University of Technology Sydney

Faculty of Engineering and Information Technology

A Study on the Behaviour of Guided Wave Propagation in Utility Timber Poles

A DISSERTATION

SUBMITTED IN PARTIAL FULFILMENT OF THE REQUIREMENTS

for the degree of

DOCTOR OF PHILOSOPHY

in the field of

Civil and Structural Engineering

by

Mahbube Subhani

March 2014

Abstract

Timber is a widely used engineering material because of its availability and good engineering properties. The round timber is suitable for electricity poles, wharfs, piles, bridge piers, etc. There are nearly 7 million utility poles in the current network in Australia, in which around 5 million timber poles are used for distribution of power and communications. The utility pole industry in Australia spends about $40~$50 million annually on maintenance and asset management to avoid failure of the utility lines. Each year about 30,000 electricity poles are replaced in the eastern states of Australia, despite the fact that up to 80% of these poles are still in a very good serviceable condition. In addition, with discovery of scour problems in bridge foundations in the past 30 years, a study on the USA's national bridge stock showed that out of approximately 580,000 highway timber bridges in the National bridge inventory, about 104,000 of these bridges had unknown foundations depth. Therefore, a reliable non-destructive evaluation technique is essential for the condition assessment of timber poles/piles to ensure public safety, operational efficiency and to reduce the maintenance cost.

Different types of non-destructive tests (NDT) were developed during the last decades to evaluate the embedment depth and the quality of materials of embedded structures. Some of these methods have also been utilised for timber piles or poles. However, the extent of knowledge developed on non-destructive tests for timber piles is far from adequate and the effectiveness and reliability of current NDTs are questionable due to uncertainty on materials, structures and environment. In addition, one dimensional assumption is usually considered while dealing with timber poles/piles which is insufficient to reflect the actual behaviour of stress wave propagation in the columnar structures. Also, the anisotropic behaviour of timber and the effects of environment are not taken into account in numerous conventional non-destructive evaluations (NDE) that leads to errors regarding the condition assessment of timber poles.

Waves propagating along a pile/pole include different clusters of waves, called guided waves (GWs). In GW, the velocities of a wave (such as phase velocity, group velocity, energy velocity) become a function of frequencies (i.e. wave dispersion behaviour) and displacement magnitude varies when waves propagate along the pole. Besides, GWs

that have the same frequencies possess shorter wavelengths than their counterpart of conventional surface wave. Hence, it is possible to detect smaller sized defects with a guided wave technique than a surface wave technique. Hence, it is essential to model the actual three dimensional behaviour of wave propagation inside the timber pole instead of one dimensional assumption, and the environmental factors in conjunction with the actual timber pole situation is necessary to be addressed before suggesting an experimental set up and verification.

This thesis investigates the GW propagation inside the timber pole using an analytical, one semi analytical and one numerical method. The actual GW equations are solved analytically considering the timber as both isotropic and transversely isotropic material to emphasize the importance of modelling timber as an anisotropic material. Some parametric studies are also carried out to show the effect of the diversity in material properties of timber on the stress wave propagation. Also, the dispersion curves, mode shapes, contribution of different branches of longitudinal and flexural waves in a signal are presented in order to propose a suitable input frequency and number of cycles, the distances among the sensors, the location and orientation of sensors, etc. Although the analytical GW solution can offer a number of suggestions for the experimental set up, the time domain results cannot represent the actual boundary conditions due to the complexity involved in solving the partial embedment of soil that reflects the actual field behaviour. Besides, the impact location and orientation cannot be implemented in the analytical GW solution. Accordingly, a semi analytical method, namely, Spectral finite element method (SFEM) is employed to model the timber pole with the actual boundary conditions together with the impact location and orientation to illustrate the propagation of different kind of waves and branches. Even though SFEM can explain both the dispersion curves and time domain reconstruction, the dispersion curves are only accurate up to a certain frequency. Further, the three dimensional behaviour is unavailable in SFEM as this method cannot present the wave propagation in the circumferential direction. To overcome this issue, a numerical technique is implemented using the Finite Element method, and based on the signal obtained from this method, the three dimensional behaviour is explained which is then utilized to separate different kind of waves. Beyond that, two popular advanced signal processing techniques are applied to the numerical signals to compare the efficiency of these two approaches leading to determining the wave velocity and the embedment length of the timber pole.

Certificate of authorship/originality

I certify that the work in this thesis has not previously been submitted for a degree nor has it been submitted as part of requirements for a degree except as fully acknowledged within the text.

I also certify that the thesis has been written by me. Any help that I have received in my research work and the preparation of the thesis itself has been acknowledged. In addition, I certify that all information sources and literature used are indicated in the thesis.

Mahbube Subhani

Date:

To my loving younger sister Ummul Afia Shammi

Acknowledgements

I would like to express my deepest appreciation to my supervisors Prof. Bijan Samali and A/Prof Jianchun Li over the last four years as the completion of my research and the dissertation would have never been possible without their guidance. From the very beginning of the postgraduate study till now, I have been receiving advice from them not only on the planning for the research study and analysing the test results but also on my future career. As an international student, it was not so easy for me to adapt to a totally new environment initially, but Prof. Samali always helped me to make a right decision and to cope with challenge. I still recall most of the meetings I had with Prof. Bijan, where I always felt very comfortable to express my opinion regarding the research and discuss my personal issues. The kindness and co-operation of him would always be memorable throughout my life. I was very lucky that A/Prof Jianchun Li's office was on the same floor as mine, which allowed me to meet him any time I required to. Specially, in the case of any new observations related to my research, I could freely discuss them with him which certainly helped me in explaining the findings. Prof Li's door was always open for discussion about technical and even for any personal issues. His constant inspiration and critical reasoning about my work gave me the enthusiasm to pursue for the better.

I would also like to give special thanks to Dr Hamid Reza Valipour who was the panel member for my Master's assessment, for his inspirations which made it possible to upgrade my course of study from Masters by research to PhD. I am also very thankful to Dr. Ali Saleh, Dr. Emre Erkmen and Prof. Keith Crews because of the time they spent with me for strengthening some of my fundamental concepts on Structural Analysis, Numerical Modelling and properties of timber materials.

I am also grateful to all the members of the timber pole project. Mr. Amir Zad always helped me to learn about all the experimental work in the laboratory and in the field. And the other members, Mr. Roman Elsener, Mr. Bahram Jozi, Ms. Ning Yan, Dr. Ulrike Dackermann, and the capstone student Mr. Andrew Tang, who always helped me to develop a holistic view of the project, and I was always comfortable to work as a

team with them. I cannot thank enough the laboratory staff, especially Mr. Peter Brown for his patient and cordial support and teaching me about the instrumentation and different equipment. Also, Mr. Rami Haddad and Mr. David Dicker always came forward to help me for conducting any kind of test under the best possible circumstances.

My parents and siblings certainly have made an invaluable contribution to the completion of my research as I would have never been able to come overseas for post-graduate studies without their support and encouragement. Many times during my PhD, I felt it was impossible to take it to the next stage; however, I was always motivated by my family to complete my research study.

I cannot but mention about some of my colleagues and friends who have contributions to the successful completion of my dissertation. Firstly, I would like to thank Mr. Aslan Hokmabadi and Mr. Mohsen Askari with whom I discussed about many technical details of my work and they helped me with their best as a friend to overcome my difficulties. Secondly, I am very thankful to Mr Chij Shrestha, Mr. Ikramul Kabir, Dr. Yancheng Li and Ms. Yukari Aoki who were not only my fellow researchers but also very good friends.

Finally, I would like to acknowledge the financial supports provided by the ARC linkage project in conjunction with Ausgrid for conducting my research. Also, the IRS scholarship offered by UTS provided me extensive support to accomplish my PhD goal.

Mahbube Subhani

March 2014

List of Publications based on this research

Journal Publications

1. **Subhani, M.**, Li, J., Gravenkamp H. & Samali, B. (2013), 'Effect of Elastic Modulus and Poisson's Ratio on Guided Wave Dispersion Using Transversely Isotropic Material Modelling', *Advanced Material Research*, vol. 778, pp. 303-311.*

2. **Subhani, M.,** Li, J., Samali, B. & Yan N. (2013), 'Determination of the embedded lengths of electricity timber poles utilising flexural wave generated from impacts', *Australian Journal of Structural Engineering, vol. 14, no. 1, pp. 85.**

3. **Subhani, M.**, Li, J. & Samali, B. (2013), 'A comparative study of guided wave propagation in timber poles with isotropic and transversely isotropic material models', *Journal of Civil Structural Health Monitoring, vol. 3, no. 2, pp. 65-79.**

4. Li, J., **Subhani, M.** & Samali, B. (2012), 'Determination of Embedment Depth of Timber Poles and Piles Using Wavelet Transform', *Advances in Structural Engineering*, vol. 15, no. 5, pp. 759-770.*

Conference Publications

1. **Subhani, M.**, Li, J., Gravenkamp H. & Samali, B. (2013), 'Effect of Elastic Modulus and Poisson's Ratio on Guided Wave Dispersion Using Transversely Isotropic Material Modelling', *Proceedings of the International Conference on Structural Health Assessment of Timber Structures (SHATIS 13)*, 4-6 September 2013, Trento, Italy.

2. **Subhani, M.**, Samali, B. & Li, J. (2012), 'Behaviour of stress wave propagation in utility timber pole', *Proceedings of the 22nd Australasian Conference on the Mechanics of Structures and Materials (ACMSM 22)*, 11-14 December 2012, University of Technology, Sydney, Australia.*

3. Li, J., Dackermann, U. & **Subhani, M.** (2012), 'R&D of NDTs for Timber Utility Poles in Service - Challenges and Applications (Extension for Bridge Sub-Structures and Wharf Structures)', *Proceedings of the Workshop on Civil Structural Health*

Monitoring (CSHM-4), 6-8 November 2012, Bundesanstaltfür Materialforschung und -prüfung (BAM), Berlin, Germany, Lecture 13, (published on CD).*

4. **Subhani, M.,** Li, J. & Samali, B. (2012), 'A comparative study of guided wave propagation in timber poles with isotropic and orthotropic material models', *Proceedings of the First International Conference on Performance-based and Life-cycle Structural Engineering (PLSE)*, 5-7 December 2012, The Hong Kong Polytechnic University, Hong Kong, (published on CD).*

5. **Subhani, M.**, Li, J., Samali, B. & Dackermann, U. (2011), 'Determinations of stress wave velocity in a timber pole using wavelet transform', Dynamics for Sustainable Engineering, *Proceeding of the 14th Asia Pacific Vibration Conference*, 5-8 December 2011, The Hong Kong Polytechnic University, Hong Kong, pp. 222-231.*

6. Li, J., Crews, K., Samali, B., **Subhani, M.** & Zad A. (2011), 'Determination of Embedment Depth of Timber Poles and Piles using wavelet transform', *Proceedings of the International Conference on Structural Health Assessment of Timber Structures (SHATIS 11)*, 16-17 June 2011, Lisbon, Portugal, (published on CD).*

(* indicated peer-reviewed publications)

Table of contents

List of Tables

List of Figures

List of Abbreviations and Notations

1D	One dimensional
3D	Three dimensional
BEM	Boundary element method
CRF	Converted flexural mode reflection
CRS	Converted shear mode reflection
CWT	Continuous wavelet transform
DFT	Discrete Fourier transforms
EBT	Euler-Bernoulli beam theory
FDM	Finite difference method
FE	Finite element
FEM	Finite element method
FFT	Fast Fourier transforms
FRF	Frequency response function
FSDT	First order shear deformation theory
FT	Fourier transforms
GW	Guided wave
HSDT	Higher order shear deformation theory
IF	Incoming flexural mode
IFFT	Inverse fast Fourier transforms
IR	Impulse response
IS	Incoming shear mode
KED	Kinetic energy density
LISA	Local interaction simulation approach
MC	Moisture content
MRA	Multi resolution analysis
MSLM	Mass spring lattice model
NA	Neutral axis
NDE	Non-destructive evaluation
NDT	Non-destructive testing
ODE	Ordinary differential equation

PDE	Partial differential equation
PEP	Polynomial eigenvalue problem
PWR	Power flow density
PWVD	Pseudo Wigner – Ville Distribution
RF	Reflected flexural mode
RS	Reflected shear mode
SAFE	Semi analytical finite element method
SBFEM	Scaled boundary finite element method
SE	Sonic echo
SED	Strain energy density
SFEM	Spectral finite element method
SHPB	Split Hopkinson pressure bar
SKM	Short kernel method
STFT	Short time Fourier transforms
SVD	Singular value decomposition
WT	Wavelet transforms
WVD	Wigner – Ville Distribution

E_r	Modulus of elasticity in the radial direction
E_z	Modulus of elasticity in the longitudinal direction
E_θ	Modulus of elasticity in the tangential direction
G_{rz}	Shear modulus on the radial – longitudinal plane
$G_{r\theta}$	Shear modulus on the radial – tangential plane
$G_{\theta z}$	Shear modulus on the tangential – longitudinal plane
L_{emb}	Embedment length of the timber pole
$\widehat{M}$	Moment in the frequency domain
$\widehat{N}$	Axial force in the frequency domain
$\widehat{V}$	Shear force in the frequency domain
$f_{Nyquist}$	Nyquist frequency
$\hat{u}(x,t)$	Axial displacement in the frequency domain
$\hat{v}(x,t)$	Transverse displacement in the frequency domain
ν_{rz}	Poisson's ratio corresponding to a contraction in longitudinal direction when an extension is applied in radial direction

$\nu_{r\theta}$	Poisson's ratio corresponding to a contraction in tangential direction when an extension is applied in radial direction
ν_{zr}	Poisson's ratio corresponding to a contraction in radial direction when an extension is applied in longitudinal direction
$\nu_{z\theta}$	Poisson's ratio corresponding to a contraction in tangential direction when an extension is applied in longitudinal direction
$\nu_{\theta r}$	Poisson's ratio corresponding to a contraction in radial direction when an extension is applied in tangential direction
$\nu_{\theta z}$	Poisson's ratio corresponding to a contraction in longitudinal direction when an extension is applied in tangential direction
$\hat{\varphi}(x,t)$	Shear contraction
$\hat{\psi}(x,t)$	Lateral contraction in the frequency domain
$\check{\psi}(\omega)$	Mother wavelet in the frequency domain
$[C]$	Stiffness matrix
$[S]$	Compliance matrix
∇	Divergence operator
A	Cross sectional area
a	Radius of cylinder
$A, B....F$	Unknown coefficients
C	Wave velocity
$C_1, C_2 \ldots C_4$	Unknown coefficients
C_f	Flexural wave velocity
C_l	Bulk longitudinal wave velocity
Cs	Bulk shear wave velocity
D	Diameter
D_{SFEM}	Dynamic stiffness matrix
E	Modulus of elasticity or Young's modulus
E_0	Longitudinal modulus of elasticity (E_L) at zero MC
E_g	E_L at temperature T
E_L	Longitudinal modulus of elasticity
f	Frequency
G	Shear modulus
$h(t)$	Translation of a window of a given length
I	Moment of inertia
J	Bessel's function of first kind
H	Hankel function

j	Imaginary number
K	Spring constant
$K_1, K_2 \ldots K_4$	Adjustable parameters
L	Length/reflection depth
l_1	Distance between the sensor and ground level
L_s	The distance between sensors
L_T	The distance between sensor and the bottom of the pole
N	Number of sampling points
NRG	Total energy
p	circumferential order of cylinder
P_m	Power flow of a mode
PWR_z	Component of poynting vector in the direction of propagation
$q(x,t)$	Externally applied load
r	Any distance from the centre of the circular cross section along the radius
R_i	Amplitude ratio
S	Cross section of the cylinder
s	Scaling parameter
T	Temperature
t	Time
u	Displacement
u_r	Displacement component along radial direction
u_z	Displacement component axial/longitudinal direction
u_θ	Displacement component along tangential/angular direction
V_{gr}	Group velocity
V_{ph}	Phase velocity
V_{soil}	Bulk wave velocity of soil
V_z	Energy velocity
w	Rotation vector
$x(t)$	Any arbitrary signal
Z	Ordinary and modified Bessel function of first kind
α_{leak}	Leakage angle
Δf	Distance between the two peaks in velocity versus frequency function
Δt	Time difference between the arrival and reflected peaks
I	Rotation vector

$u(x,t)$	Axial displacement in the time domain
$v(x,t)$	Transverse displacement in the time domain
α	Wavenumber for longitudinal waves
β	Wavenumber for shear waves
γ	Shearing strain
ε	Normal strain
η	Viscous damping
λ	Lamĕ constant
μ	Lamĕ constant or shear modulus
ν	Poisson's ratio
ξ	Wavenumber
ρ	Mass density
σ	Normal stress
τ	Shearing stress
$\varphi(x,t)$	Shear contraction in the time domain
$\psi(t)$	Mother wavelet in the time domain
$\psi(x,t)$	Lateral contraction in the time domain
ω	Angular frequency
ϕ	Slope

Chapter 1

1. Introduction

1.1 Background

Timber is a widely used structural material. As it is a natural product, controlling different properties to a desired state is difficult to achieve. Therefore, a great number of uncertainties exist in a timber structure. Moreover, these properties are very susceptible to environmental influence such as temperature, moisture content etc. Natural timbers not only contain some natural discontinuity or defect but also may be subjected to deterioration due to the direct exposure to weather. As a result, it may lose its desired strength and fail to maintain its load carrying capacity.

Utility poles represent a significant part of Australia's infrastructure as well as globally. According to Nguyen et al. [1], there are nearly 7 million utility poles in the current Australian network, around 5 million of which are timber poles and used for distribution of power and communication. The utility pole industry in Australia spends about $40~50 million annually on the maintenance and asset management to avoid the failure of the utility lines. Each year, about 30,000 electricity poles are replaced in the eastern states of Australia, despite the fact that up to 80% of these poles are still in a very good serviceable condition.

On the other hand, with discovery of scour problems in bridge foundations in the past 30 years, a study on the USA's national bridges showed that out of approximately 580,000 highway bridges in the National bridge inventory, about 104,000 had unknown foundation depth. Also, for a large number of older non-federal-aided bridges and to a

lesser extent of federal-aided bridges, there are no designs or as-built bridge plans available to document the type, depth, geometry or materials incorporated in the foundations, especially, for timber piles which are more common for bridges and railway foundations than other kinds of piles, particularly in country roads. Hence, there is a need for development of a low cost, non-destructive testing method to provide information on the depth and types of unknown bridge foundations and their likely level of damage to aid in their safety evaluations. This consideration should include all information about the timber poles/piles such as their length, defects and foundation type etc.

There are similar situations in Australia regarding timber bridges. Current estimation reveals that around 27,000 of the total 40,000 bridges are made of timber, 85% of which are in local government areas, with the other 15% owned by State Road and Rail authorities [2]. Most of them are in excess of 50 years old and are in a degraded or structurally weakened condition. Nonetheless, these bridges are highly valued for the purpose of transportation and also for their social and historical significance.

It is, therefore, of great importance to carry out research on timber columnar structures such as poles and pile for evaluation of their in-service conditions including their embedment lengths. To serve this purpose, different types of non-destructive tests (NDT) have been developed during the last decades to evaluate the embedment depth and the quality of materials of embedded structures. Some of these methods have also been utilised for timber piles or poles. However, the extent of knowledge developed on non-destructive tests for timber piles is far from adequate and the effectiveness and reliability of current NDTs are questionable due to uncertainty on materials, structures and the environment. In relation to this, advanced signal processing plays a critical role in the research and holds a key to the solution of these problems. Moreover, as determination of the length of a pole depends on the characteristics of stress wave including wave modes, wave frequencies and velocities, so analysing the wave properties and the analytical solution of this problem become equally important. And finally, presence of soil due to the partial embedment of pole reflects the need for soil structure interaction to be considered to identify its effect on stress wave propagation.

1.2 Statement of the problem and aim of the research

Most of the currently available NDT methods are mostly derived for the isotropic materials such as concrete, steel, etc. These NDT techniques are either based on one dimensional wave propagation or on the grounds of guided wave (GW) propagation. One dimensional assumption considers constant stress wave velocity, whereas the GW theory studies the frequency dependent wave velocity. Even though the one dimensional theory is easier to implement, it has some drawbacks. For instance, high accuracy on determining the embedment length or location of damage can only be achieved if the input frequency is in the low range. This is due to the fact that the stress wave shows a dispersive behaviour in the high frequency range, i.e. the wave velocity becomes a function of frequency. It is well known that high frequency input is essential to detect the smaller size damage due to its shorter wavelength and need to be employed in numerous practical situations. Additionally, the one dimensional theory cannot evaluate the effect of surrounding medium. The GW theory can incorporate the dispersion characteristics and also the embedded condition. However, the usage of the GW theory for the evaluation of structural components is mainly limited to the isotropic materials.

Timber is well known for its anisotropic behaviour. Even though the guided wave theory is derived for the anisotropic material, most of the non-destruction evaluation (NDE) techniques for timber materials are based on one dimensional theory owing to the complexities involved while searching for an analytical solution. Therefore, it is worthwhile to apply the GW theory to the anisotropic material in order to obtain sufficient accuracy to assess the current conditions of timber poles. In this research, the GW theory is investigated for two types of anisotropic behaviour, i.e. transversely isotropic and orthotropic, to associate the theory with practical implementations.

A good number of numerical and semi analytical methods are also available for the GW propagation in different media. All these methods have their own advantages and disadvantages. Similarly, the analytical solutions also have some benefits and limitations. Therefore, in conjunction with the analytical solutions, two numerical methods, namely the Spectral finite element method (SFEM) and the Finite element method (FEM), are also used to study the behaviour of the GW propagation in different media.

The acquired signal from the NDT of timber poles/piles are distorted due to the presence of dispersion which is obvious in any finite media. Even though the GW theory can suggest solutions for dispersion, it is difficult to interpret the results to serve the purpose. This research work aims at studying the GW propagation in the timber pole and minimisation techniques on the effect of dispersion are proposed by using the expositions. Consequently, some experimental considerations are provided based on the analytical and numerical solutions such as the choice of input frequencies, the shape of the input signals, sensors locations and orientations, distances among the sensors, etc. Also, two commonly used signal processing techniques are compared to examine their applicability for the evaluation of timber poles.

1.3 Objectives of the thesis

In GW propagation, the main obstacle is the distortion of the signal due to the dispersion which makes it very difficult to extract the necessary information to assess the condition of the timber pole. In general, the following phenomena lead to the distortion of the signal:

1. In a GW, different type of waves can be generated such as longitudinal wave, flexural wave, etc. These two waves have very different behaviours at various frequency ranges. However, the superposition of these waves is responsible for the dispersion.

2. In addition to the different types of wave, the same wave has a number of branches/modes. The number of branches increases at high frequencies and all these branches may have different wave velocities. Accordingly, different branches may reach the sensors at different times and as a result, it is difficult to identify the reflected peaks.

3. The most popular stress wave based NTDs are based on the reflection of the wave. In particular, mode conversions occur on reflection and may distort the signal.

4. The properties of timber are affected by the environmental factors such as temperature, moisture content, etc. which influence the stress wave propagation in timber poles. Also, timber poles are partially embedded in soil and the signal is also affected by the surrounding medium.

The primary goal of this study is to overcome or minimise all the aforementioned issues and thus, to reduce the effect of dispersion. Accordingly, the objectives of this project can be summarised as follows:

1. To solve the GW propagation in timber considering its anisotropic behaviour. The analytical equation is solved by considering timber as a transversely isotropic material.

2. To perform some parametric studies for investigating the effect of different material properties of timber since different species of timber are very diverse in terms of their material properties. The effect of temperature, moisture content and the properties of surrounding soil are also taken into account.

3. To provide suggestions to minimise the effect of dispersion in the practical field based on the analytical solution. These include choice of input frequencies, the shape of the input signals, sensors locations and orientations, distances among the sensors, etc.

4. To model the SFEM for the GW propagation in timber pole considering the anisotropic (orthotropic) behaviour with appropriate boundary conditions (partial embedment in soil). The SFEM is applied in order to model the pole as orthotropic material as the analytical equation is very complex for the same. Also, the actual boundary condition can easily be implemented using SFEM.

5. To analyse the mode conversion on the reflection based on SFEM.

6. To develop a Finite element model that is used to propose a method to separate longitudinal and flexural waves as Finite element can model actual three dimensional wave propagation in a finite media.

7. To evaluate the appropriate signal processing techniques for the condition assessment of timber poles.

1.4 Organisation of the thesis

The thesis is divided into six chapters and the outline can be described as follows:

Chapter 2 describes the background of different surface reflection techniques of non-destructive evaluation and the limitations of these methods. Also, the importance of considering GW propagation in an anisotropic material is presented. Besides, the

reviews on the current state-of-the-art about GW theory in anisotropic media are provided. Moreover, various signal processing techniques are discussed and the applicability of Continuous Wavelet Transform (CWT) and Short Kernel Method (SKM) are justified.

Chapter 3 represents the solution of GW theory considering timber as an isotropic and a transversely isotropic material. The former model is used for the parametric studies while the latter is utilised to propose the experimental set up in order to decrease the effect of dispersion. To achieve this, different dispersing curves (phase velocity, group velocity, energy velocity, attenuation, wavelength, etc.) and mode shapes (normalised displacement profile, normalised power flow etc.) are illustrated.

Chapter 4 compares different theories of SFEM and suggestions are made to solve these equations by the software MATLAB. A comparison is provided between the dispersion curves obtained from analytical solution and by SFEM. Eventually, the most appropriate theory is chosen for the analysis of timber poles. The appropriate boundary conditions for timber poles are used in this section as it is very difficult to incorporate them in the analytical study.

Chapter 5 discusses the modelling of timber poles by FEM to demonstrate the three dimensional behaviour of different types of wave. Based on the analysis, a suitable sensor network is proposed which can be used to separate longitudinal and flexural waves. In addition, CWT and SKM are compared to reflect the importance of advanced signal processing to examine the signal acquired from the testing. Also, the accuracy ranges for both of the approaches are reported.

Chapter 6 summarizes the main findings of the study and recommendations for the future works are also provided.

Chapter 2

2 Background and Literature review

2.1 Introduction

This chapter can be subdivided into four main parts. The first part will focus on different methods of non-destructive testing (NDT) which are currently available in the literature and are also used in the field of non-destructive evaluation (NDE). These methods are based on the one-dimensional (1D) wave theory. The general equations based on 1D theory are also presented in this part. The applicability and limitations of these methods are also discussed.

The second part of this chapter will describe the importance of guided wave (GW) theory in the field of NDT. The 1D theory cannot represent the actual wave propagation behaviour in the thick wave guide and is also limited to the low frequencies only. However, high frequency components are essential to detect damages in a structure due to its short wavelength. Additionally, 1D theory cannot provide any information about the attenuation of the wave energy due to the presence of a surrounding medium. Timber pole is partially embedded in soil and therefore, attenuation plays an important role for the analyses of the signal. Hence, GW theory needs to be used to interpret the signal acquired from the NDE of a timber pole.

The GW theory is used by different researchers in the NDE of isotropic plates, rods, beams, etc. However, the use of this theory related to anisotropic material is limited. Timber is an orthotropic material and to successfully interpret the wave behaviour in

timber, it is essential to focus on the theory of GW for the anisotropic material. Moreover, timber is highly affected by temperature, moisture content, growth of annual rings, etc. The second part also presents the properties of timber and discusses the relation of these parameters with the material properties of timber. The material properties are very important to solve GW propagation in an anisotropic material. Consequently, the incorporation of these properties of timber with the GW theory in an orthotropic media will be discussed in this part. Lastly, the previous works on the GW theory in an anisotropic media will be reported and the research gap between the previous works related to timber pole situation will be discussed.

The third part of this chapter will focus on the different numerical methods available for the wave propagation problems. Even though the analytical solution can give insight into the wave propagation problem, the boundary condition is simplified for the ease of calculation. For example, time domain reconstruction is difficult to obtain from the analytical solution as the mixed boundary condition for timber pole (partially embedded) is very difficult to implement in the solution. Thus, some semi analytical and numerical methods will be discussed in this part.

Finally, the last part of the chapter will deal with different advanced signal processing techniques. Signal processing is one of the most important parts of NDE as the signal usually suffers from dispersion, environmental noise, etc. Besides, it also helps to determine the embedded length of the pole and/or to determine the location of the damage when the signal is distorted by the above mentioned phenomenon.

2.2 Stress wave based Non Destructive Testing

There are a good number of non-destructive evaluation techniques available for the damage detection of structures. Among them, the NDT techniques based on stress wave propagation are very popular nowadays. Based on the geometry of the structures, different types of stress waves can be generated, such as, in a cylindrical structure, mainly three types of wave can be induced, namely, longitudinal, flexural and torsional waves. However, longitudinal and flexural waves are more popular in NDT and also easy to generate. Generation of these waves mainly depends on the impact location. If the top of the structure is easily accessible, longitudinal waves can be generated by imparting an impact in the middle of the cross section on the top of the structure. In

contrast, flexural waves are generated by striking the structure on the side of the pole. Flexural wave is typically generated if the top of the structure is obstructed by other structures (such as the piles in the jetty) or is not easily accessible (such as timber pole).

For the condition assessment of pole/pile like structures, mainly two conditions need to be determined, namely, the embedded length and location or severity of any damage. There are two ways currently available for the stress wave based assessments of these structures, i.e., surface NDT and Borehole methods. In surface NDT methods, the reflection of the stress wave is measured directly from the pile and there is no boring needed. While in borehole methods, a borehole is drilled close to the pile/pole and extends along its length. In this case, the reflection is monitored in the borehole.

The potential applications of surface NDT for pile depth determination are Sonic Echo/Impulse Response (compressional wave echo from stiffness change), Bending Wave (flexural wave echo from stiffness change) and Ultra seismic Vertical Proofing with geophysical processing of the data (compressional and flexural wave echoes). Borehole NDT includes Parallel Seismic (direct measurement of compressional and shear wave arrival to receivers in a borehole and wave travelling down the pile from an impact on the exposed substructure) and Borehole Radar (reflection of electromagnetic wave energy are measured from a nearby substructure).

Surface NDT such as Sonic Echo (SE), Impulse Response (IR), and Ultra Seismic methods, are usually more economical and easier to conduct as the dynamic exciter and the receiver are placed at accessible locations. Borehole methods, such as Parallel Seismic and Ground Penetration Radar may determine the underground length of a pile through its lengths in a more direct manner but are more expensive. In particular, for utility pole investigation in this project, it is not practical to borehole during a routine testing. Among these methods, SE, IR and bending wave methods have been used for many years and a brief description of these methods are described below:

2.2.1 The Sonic Echo and Impulse Response method

Sonic Echo/Impulse Response (SE/IR) tests are performed to evaluate the integrity of the pole / pile material and determine the length of deep foundations. These methods can be used to detect defects, soil inclusions, pile necking and diameter increases (bulbing) as well as approximate pile lengths.

The Sonic Echo methods require measurement of the travel time of stress waves (in time donmain) and Impulse Response methods use spectral analysis (in frequency domain) for interpretation. These two methodes are sometimes called Pile Integrity Testing method (PIT). The Sonic Echo method is also known as Echo, Seismic, Sonic, Impulse Echo and Pulse Echo method. Other names for the Impulse Response methods include Sonic Transient Response, Transient Dynamic Response and Sonic.

In both (SE/IR) tests, the reflection of longitudinal waves (also called compressional wave) from the bottom of the tested structural element or from a discontinuity such as a crack or a soil intrusion is measured. The generated wave from an impulse hammer travels down a shaft or a pile until a change in acoustic impedance (a function of velocity, density, and changes in diameter) is encountered, at which point the wave reflects back and is recorded by a receiver placed next to the impact point.

Sonic Echo data are used to determine the depth of the foundation based on the time separation between the first arrival and the first reflection events or between any two consecutive reflection events (Δt) according to the following equation:

$$L = C_l \frac{\Delta t}{2}, \tag{2.1}$$

where L is the reflector depth and C_l is the velocity of longitudinal waves.

A reflector can be the bottom of the foundation or any discontinuity along the embedded part of the foundation. The Sonic Echo data can also be used to determine the existence of a bulb or a neck in a shaft or the end conditions of the shaft based on the polarity of the reflection events.

The Impulse Response data are also used to determine the depth of reflectors according to the following equation:

$$L = \frac{C_l}{2\Delta f}, \tag{2.2}$$

where Δf is the distance between the two peaks in velocity versus frequency function. The Frequency Response Function (FRF) of frequency-velocity plot is also called mobility and this term is widely used for the IR method by the researchers [3].

These two methods have been used successfully to determine the stress wave velocity, necking and bulbing in the structures and also the embedded length [1-10]. However, most of these works related to isotropic materials and it has been found that the time or frequency domain results of an anisotropic medium are not as clear as the isotropic media. Hence, for the timber pole situation, these methods cannot be directly used. In timber materials, the moisture contents, annual rings, fibre direction, etc. play an important role and SE/IR methods are used with some modifications [11-17]. These include, using some factors for velocity changes related to annual rings, moisture content, etc. These modifications work quite well in the low frequency band or to determine the embedded length of the pole and the large damages. In particular, high frequency components should be taken into account to detect small sized damages and the modified SE/IR method for timber materials cannot be extended directly due to the dispersion of longitudinal wave in high frequency.

The wave velocity (in both methods) is considered to be known and usually taken as constant to calculate the length of the pile. Whereas, provided the length is known, the velocity can be determined. Since the stress wave velocity within a structure is dependent on the material properties, therefore, the wave velocity is also considered as a parameter for the evaluation of the structure. The stress wave velocity for good quality concretes are reported in countless number of literatures [4, 5].

2.2.2 The bending wave method

The bending wave method uses flexural (bending) waves, rather than longitudinal waves used in the Sonic Echo/Impulse Response method, to determine condition and unknown depth of deep foundations. The application of this method has so far been used mainly on deep foundations such as timber piles, concrete piles and drilled shafts that extend above the ground or water surface. Some experimental research work has been conducted on using the bending wave method for timber piles. In general, this method can be applied to slender members.

The bending wave method uses the propagation of flexural or bending waves in piles that are highly dispersive in nature. The bending wave velocity decreases with increasing wavelength, with most of the velocity decrease occurring at wavelengths that

are longer than the pile diameter. These longer waves propagate as flexural or bending wave energy.

In dispersive signal analysis, selected group of frequencies are extracted. These frequencies are analysed for the individual time required to travel to the tip of the pile and back or from their tops to the location of an area of damage such as a void, break, soil intrusion or material deterioration. Since the method involves striking the pile on the side and placing the receivers on the side of the pile, the method is potentially useful in cases where the top of the pile is obscured by a structure.

Due to the highly dispersive nature, advanced signal processing is vital for the bending wave method in order to determine the frequency dependent velocity. The Continuous Wavelet Transform (CWT) and the Short Kernel Method (SKM) are the most popular signal processing techniques for the dispersive waves. The SKM was developed by Douglas [6] and used successfully by Holt [7]. Wang and Chang [8] used the bending wave method for the concrete structures. The applications of bending wave method for timber materials are demonstrated in [23-25] which are in good agreement with the expected results. Nevertheless, only low frequency band is taken into account.

2.2.3 Limitations of surface NDT methods

The above mentioned surface reflection techniques use one dimensional wave or one dimensional bulk wave propagation approximation for their wave propagation analysis. Bulk waves assume that waves propagate in infinite media; hence, no boundary conditions need to be satisfied. Nevertheless, the one dimensional wave theory has been successful due to the fact that longitudinal wave velocity is almost constant at low frequency for large diameter piles and the same is true for attenuation [9]. Hence, dispersion is not a problem for longitudinal wave at low strain integrity testing or surface NDT and the one dimensional wave assumption is valid. In contrast, bending wave propagation by one-dimensional theory considers dispersive behaviour (Bernoulli-Euler beam theory). This, however, is only limited to the bending of a beam. Accordingly, the velocity of the wave increases with the increase of frequency. In general, the bending wave velocity converges at high frequency due to shear and rotary inertia which are not taken into account in the bending wave method. As a result, the one dimensional theory is only applicable for bending wave in the low frequency range.

Therefore, the velocity of the wave in SE, IR and bending wave methods are needed to be calculated before solving for the length of the pile/pole. Subsequently, if both the velocity and the length are unknown, it become very difficult to use these surface reflection techniques.

Attenuation is one of the important parameters which need to be considered while dealing with any embedded structure. Attenuation occurs due to the leakage of energy in the surrounding soil in the stress wave method which, however, is not taken into account in the case of surface reflection techniques. This issue becomes more prominent when the length to diameter (L/D) ratios of the pile/pole/shaft is high or the surrounding soil is very stiff [10]. The imparted energy will be dissipated more due to the attenuation for the case of a long shaft and thus the amplitude of the toe reflection or the reflection from any defects will be reduced significantly. Accordingly, it is possible that this weak reflected signal will be inseparable from the background noise. Therefore, it is important to plot the attenuation curves to know the amount of dissipation in a given condition which can only be derived from a guided wave (GW) theory.

Waves propagating along a pile/pole include different clusters of waves, called guided waves (GWs). These three dimensional wave clusters arise from incidence and reflections of a variety of longitudinal, shear and surface waves along the boundary and depend on the shape of the structures. In GW, the velocities of a wave (such as phase velocity, group velocity, energy velocity) become a function of frequencies (i.e. wave dispersion behaviour) and displacement magnitude varies when waves propagate along the pole. Popovics [11] showed that the predominant waves in concrete slabs excited by impact echo method are related to low frequencies of the lowest branch of guided waves. Chao [12] and Finno et al. [13] also reached the same conclusion for concrete piles and drilled shafts. Finno et al. [13] showed that the upper limit of the frequency band varies from 250 Hz to 1000 Hz for 4 m to 1 m diameter concrete piles, respectively. GWs that have the same frequencies possess shorter wavelengths than their counterpart of conventional surface waves. Hence, it is possible to detect smaller sized defects with a guided wave technique than a surface wave technique. Chao [12] identified a 7% cross section notch in a prototype concrete pile using longitudinal guided waves whereas a defect size of more than 30% of the cross sectional area of a

pile can only be detected by conventional surface wave methods [14]. Consequently, GW theory is the most appropriate theory for the analysis of wave propagation in poles.

2.3 Importance of guided wave and consideration of guided wave theory for anisotropic materials

The GW theory has successfully been used for concrete, steel and other isotropic structures with cylindrical geometry [22, 30, 32-38]. However, timber is an orthotropic material and the GW theory derived for isotropic materials cannot be directly used for an anisotropic material. This is due to the fact that the dispersion curves for isotropic and anisotropic materials are different. Accordingly, at any particular frequency, the dispersion behaviour, phase velocity, energy velocity etc. are different in an isotropic and in an anisotropic material. Nevertheless, GW theory for isotropic materials can be used for some parametric studies on timber, such as, the effect of moisture content, temperature, annual rings, etc. can be studied using the GW theory for isotropic cylinder. The properties of timber will be explained in Section 2.4 and the review of GW theory for anisotropic cylinder will be presented in Chapter 3.

There are different types of anisotropy in a material. This includes, orthotropic, transversely isotropic, transversely anisotropic, etc. Timber is an orthotropic material which has three distinct properties in three orthogonal directions. Additionally, the moduli of elasticity of timber are affected by moisture content, fibre direction and also sometimes by annual ring formation. Therefore, it is important to know the effect of these parameters on the engineering properties of timber materials.

2.4 Properties of timber

In the GW equation, material properties, such as the modulus of elasticity, the density and the Poisson's ratio play an important role in the determination of wave propagation behaviour. For timber, these material properties are greatly dependent on the species, biological diversity, temperature, number of growth rings, fibre directions, moisture content, etc. Gerhards [15], Hanhijiirvi [16] and Lenth and Sargent [17] concluded that an increase in temperature (T) results in decrease in modulus of elasticity. These variations occur until the moisture content reaches the fibre saturation point which is around 27 – 30% for most species of wood. Dinwoodie [18] reported that when the moisture content (MC) is 0% and the temperature varies between -20°C and +60°C, the

reduction of stiffness is 6%. However, when the *MC* reaches 20%, the reduction of stiffness is approximately 40%. Since temperature affects the *MC*, they are often considered at the same time during testing or analysis to evaluate their effects on modulus of elasticity (*E*). Tallavo et al. [19] adopted a statistical analysis to obtain the relationship among *E*, *T* and *MC*. The number of annual growth rings per cm is approximately 1 to 10 and is another important parameter. Modulus of elasticity increases with the increase of the number of the annual rings [44-46]. The velocities of stress waves in timber are greatly affected by variation of the material properties. Another important factor influencing the wave propagation in timber is the fibre direction of the grain. For most structural members, fibres of the wood are aligned more or less with the longitudinal axis of the member [20]. Some wood species have very strong fibre orientation in the radial direction of the cross section and sometimes it grows spirally. In this case, the behaviour of wave propagation will be completely different since the wave is travelling across the fibre when it is propagating in the longitudinal direction. In this project, although the effects of temperature, moisture content and annual ring are not directly considered in the solution, GW equation is solved for a range of *'E'* values to relate wave velocity to these effects indirectly through relation to *'E'* values. In this particular case, an isotropic material model for timber is used in the GW equation to study the relationship between modulus of elasticity and the velocity of the wave.

The relation between temperature and the longitudinal modulus of elasticity is described by Ellwood [21] and is also consistent with the results obtained by Palka [22] and Wu and Milota [23]. The equation is expressed as

$$E_g = E_0(0.475 - 0.0038T), \tag{2.3}$$

where E_0 = longitudinal modulus of elasticity (E_L) at zero *MC*; $E_g = E_L$ at temperature T.

The effect of both temperature and *MC* is given by Oliver et al.

$$(E - E_g)[E - E_0 + 5(E_0 - E_g)MC] = \frac{E_g^2}{1000}, \tag{2.4}$$

where *MC* = moisture content in kg kg^{-1} and $E = E_L$ at given *T* and *MC* [24]. The value of *E* in radial and tangential directions can be found by the ratios given by Green et al. (1999).

In NDT of timber poles, *MC* can be measured by a moisture meter. By knowing the *MC* and T, the corresponding value of the modulus of elasticity can be determined from Equations (2.3) and (2.4). The present study on the GW propagation due to changes in modulus of elasticity can, therefore, be helpful to understand the reduction/increase in velocity of the wave in timber poles.

At the time of growth of a tree, earlywood and latewood are formed. Earlywood is the part of the wood in a growth ring of a tree that is produced in its growing season (usually in spring). Similarly, latewood is the part of the wood in a growth ring that is produced later in the growing season (usually in summer). The cells of earlywood are larger and have thinner walls whereas for latewood, the opposite is true. Within a growth ring, the change of earlywood and latewood is gradual; however, each layer of earlywood from the next growing season makes an abrupt contrast with the latewood before it, thus leading to the perception of rings which is also called annual rings. The strength of a timber depends on the amount of latewood and the greater the proportion of latewood, the greater the density and strength [25].

Sometimes, it is necessary to model timber poles as a layered material for which moduli of elasticity and densities of the layers can be modelled differently. Even though the bulk wave velocity in earlywood and latewood are different, it is not very easy to model a timber considering earlywood and latewood (Figure 2.1). This is due to the fact that the thickness of latewood is much less and there are numerous layers of latewood present in a cross section of a timber.

In general, timber can be considered as a two layered material known as heartwood and sapwood (Figure 2.2). The presence of heartwood/sapwood varies among different biological species. The area of heartwood closer to the base of a tree is more than towards the top of a tree. On average, at the base and at 5% height level, the amount of heartwood is 69%. And, at the 15, 35 and 50% of tree height level, heartwood amount is 67, 62 and 58 %, respectively, of the total cross section [26]. The modulus of elasticity in sapwood is usually 10 to 20 % less than the same for heartwood [27]. The density of sapwood is also lower than the same for heartwood and some experimental results on density can be found in [28].

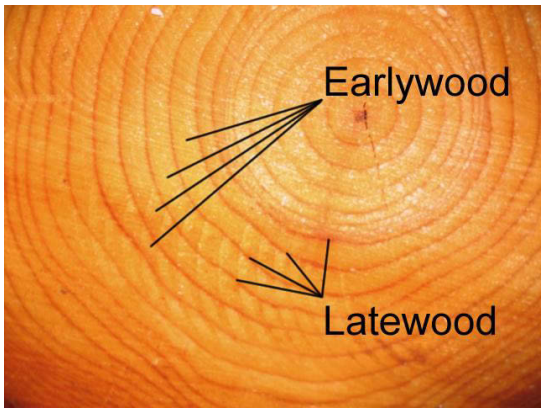

Figure 2.1 Photographs of earlywood and latewood [29]

Figure 2.2 Photographs of heartwood and sapwood [29]

2.5 Literature review of GW theory for anisotropic media

The GW theory for anisotropic media was developed for plate like structures [30]. Using theory of elasticity to solve dynamic problems for thick walled members and thick cylindrical isotropic wave guide presents severe difficulties associated with complexities of the basic system of partial differential equations and the necessity of satisfying the boundary conditions [31]. These difficulties are even more complex when the structural members are made of an anisotropic material. Nevertheless, some research work has been undertaken on orthotropic cylinder. The theory of orthotropic cylinder can be found in [32, 33]. Their work mainly focuses on hollow cylindrical cross sections with orthotropic and transversely isotropic material model. Markus and Mead [32] used the Frobenius method for solving the wave motion in anisotropic media and presented the results for hollow cylinder. Martin and Berger [34] used Neumann series for wave propagation in solid timber. However, only the free vibrations of a wooden pole are examined. Elmaimouni [35] employed a polynomial approach to elucidate the dispersion relation of a hollow cylinder. Grigorenko [31] proposed an efficient numerical-analytical approach for analysing stationary dynamic processes to study the propagation of elastic waves in anisotropic inhomogeneous cylinder and demonstrated mode shapes and dispersion relation of a hollow transversely isotropic cylinder with circular and non-circular cross section. In addition, natural vibrations of a finite length anisotropic cylinder with different conditions were also reported. Nonetheless, to the author's best knowledge, results for a thick cylindrical waveguide have not yet been reported in the literature.

In comparison to the orthotropic cylinder, several papers can be found on transversely isotropic cylinders. The theory of GW for a transversely isotropic cylinder is provided in [36, 37]. In general, timber is an orthotropic material. Nevertheless, in order to derive a GW solution for timber pole structures, some simplifications on orthotropic material characteristics can be imposed and as such timber can be considered as a transversely isotropic material. It is well-known that for timber, the ratio of modulus of elasticity in longitudinal direction to tangential direction is approximately 20 but such ratio is only around 2 for radial direction to tangential direction [38]. In other words, the modulus of elasticity in transversal direction, i.e. the radial and tangential directions can be considered the same in the analysis without causing much error.

Research on wave propagation in transversely isotropic cylinder can be divided into two categories, i.e. solid and hollow cylinder. Hollow cylinders, shafts or cylindrical shells are of prime interest for wave propagation in pipes. Tsai et al. [39] and Tsai [40] investigated the cylindrically guided waves in transversely isotropic shafts and thick hollow cylinders. Nagy [41] illustrated the wave propagation problems for longitudinal waves in fluid loaded homogeneous transversely isotropic cylinder. Ahmed [42] extended Nagy's (1995) results to include flexural modes of free and immersed transversely isotropic cylinders. Honarvar et al. [43] solved a mathematical model for longitudinal and flexural wave propagation in a solid transversely isotropic cylinder. However, Honarvar et al. [43] studied the wave propagation for a thin cylindrical composite material with traction free condition.

When the radius of the cylinder increases, it is considered as thick waveguides and the propagation can be different due to the fact that some wavelengths can be compared to the lateral dimension of the cylinder. Nonetheless, guided wave propagation in a transversely isotropic material has not yet been reported for a thick cylindrical structure considering both solid and layered material.

When it comes to the solution of GW wave theory, it is never an easy task. A great number of methods have been developed over the years to obtain the dispersion curves from the guided wave equations. Some of the widely used analytical methods are stiffness methods [44, 45], global matrix methods [46], etc. Both these methods are accurate for plate like structures, layered material and thin cylindrical waveguides. In contrast to these analytical approaches, some purely numerical methods have been

developed to obtain the dispersion curves. Among them, the semi analytical finite element method (SAFE) [47] and the scaled boundary finite element (SBFEM) [48] are very universal to use and also accurate. SAFE has so far been applied to composite plates [49], damped wave guides of arbitrary cross section [50, 51], rods and rails [52], etc. The solution for anisotropic cylindrical waveguide by SAFE can be found in [79-81] where hollow cylinder or laminated composites of very thin cross section are considered.

To solve the dispersion curves, there are three software that can be found at this stage, namely, PCDisp [53], Disperse [54] and GUIGUW [55]. Only the demo version of GUIGUW is available now which uses SAFE method whereas Disperse uses global matrix method. PCDisp is a MATLAB written code developed for an isotropic material.

2.6 The Spectral Finite Element Method (SFEM) and Conventional Finite Element Method (FEM)

Different numerical methods

Pure analytical results of guided wave propagation are derived for the simplest cases, especially when the boundary conditions are simplified. For example, only fully embedded or traction free boundary conditions can be solved for the GW propagation. In GW theory, only the side boundary conditions are satisfied and the length of the member is considered as infinity. Additionally, the GW equations are derived in such a way that the solutions are obtained in the frequency domain. Constructing the signal in the time domain is very difficult from the frequency domain solution due to the complexity involve with the boundary conditions. The solutions become very complicated when the end conditions need to be satisfied in conjunction with the side boundary conditions. Besides, analytical results do not consider any impact location or orientation. Therefore, the dispersion curves represent the output for both longitudinal and flexural wave without knowing the impact conditions. For instance, it is expected that a bar with a longitudinal impact will propagate the longitudinal wave whereas if it is struck transversely, then flexural motion will be generated. However, experimental results revealed that this assumption is not always true. In general, when a bar is impacted transversely, the wave starts propagating as a wave in a semi-infinite medium until it reaches the lateral boundary and reflects back inside. It is seen that a particle at

some location further down the guide experiences a complex superposition of the initial wave plus all the newly generated reflected waves [56]. Nevertheless, this is not a flexural motion. The factors related to this issue are the duration of the pulse, the distance between bonding surfaces and the transit time. In particular, the longer the pulse and the smaller the depth, the sooner (both in time and space) the response resembles to a flexural motion. As a result, to answer all the questions or to find out the real effects due to impact some numerical methods can be adopted.

There are a number of numerical algorithms and techniques that have been developed for wave propagation analysis, which include both time domain and frequency domain approaches. Such as, the transfer function matrix method [57], the dynamic stiffness matrix method [58], the finite difference method (FDM) [59], the finite element method (FEM) [60, 61], the mass spring lattice model (MSLM) [62], the local interaction simulation approach (LISA), the boundary element method (BEM) [63], the strip element method [64], the spectral finite element method (SFEM) [56, 65], etc.

The strip element method was applied by Oshima et al. [66] for the stress wave propagation in a beam composite fibre sensor, while Xi et al. [67] adopted the same technique for investigation of coupled fluid-structure interaction. Ultrasonic wave simulation in isotropic and transversely isotropic media by MSLM was demonstrated by Yim and Choi [68] while Chen et al. [69] described the propagation of surface acoustic wave in aluminium and copper plates. Delsanto et al. presented both the one [70] and two [71] dimensional uniform waveform propagation through a plate by LISA. Sundaraman and Adams [72] applied the same method to orthotropic plates. Related to BEM, Zhu et al. [73] analysed the elastic wave propagation and scattering by cracks in laminated composite plates. Also Cho [74] elucidated scattering of Lamb waves due to different defects by hybrid BEM approach, whereas Hayashi and Endoh [75] provided the simulation of Lamb wave propagation in plates by the same approach.

Different order finite difference schemes for solving partial differential equations were explored by Strikwerda [76]. Also various higher order finite difference schemes were proposed for the better accuracy [77, 78]. FEM was used by Verdict et al. [79] for the Lamb wave propagation in thin plate and shell like structures while Yokoyama [80] discussed about the torsional wave propagation in thin walled tube. Conry et al. [81] investigated the reflection and transmission of Lamb waves by embedded and surface

breaking defects in thin isotropic plates. Jeong and Ruzzene [82] observed the vibration and wave propagation of cylindrical periodic grid structures by FEM. Gosselin et al. [83] compared FDM and FEM and reported that FEM is more accurate than FDM. Pucket [84] also reported the effectiveness of FEM in cylindrical structures while Moser et al. [85] studied the effectiveness of this method in relation to modelling of wave propagation in annular structure.

Conventional FEM vs. SFEM

The effectiveness of FEM is justified by a number of researchers and has been used for wave propagation problems. However, there are some limitations of FEM. Even though both SFEM and FEM yield almost similar results, FEM solves the wave propagation phenomenon in the time domain and SFEM determines the same in the frequency domain first. Additionally, SFEM mainly considers the structure one dimensionally while by FEM the structure can be solved in 1D, 2D or 3D. Nevertheless, the accuracy may reduce while considering it 1D or 2D in case of FEM. The main reason behind this is the fact that FEM is based on some assumed solutions to the field variables. This assumption for wave propagation gives large system sizes due to its inability to approximate the mass distribution accurately. Moreover, at the high frequency signal, the wavelengths are very small and to capture the higher order modes by FEM, the meshes need to be very fine. This is because of the requirement that element size should be smaller than the wavelength; otherwise, the element edges will act as a free boundary and will reflect the initial response from the element edges. Accordingly, the computational cost increases significantly due to ensuring the accuracy of mass distribution/inertia by fine mesh. In contrast, SFEM is based on domain transfer method where the governing equation is transformed into the frequency domain first by Discrete Fourier Transform (DFT). Consequently, the governing partial differential equation (PDE) is reduced to a set of ordinary differential equations (ODE) with constant coefficients, where the time coordinate gives way to the frequency, which is introduced as a parameter [86]. The resultant ODEs can be solved directly. The elements are formulated using the exact solution of the governing ODEs as interpolation function. Subsequently, an exact mass distribution can be achieved which leads to the formation of exact dynamic stiffness matrix. Therefore, only one element is sufficient to handle a beam of any length if there is no discontinuity or irregularity. As a result, the size of the

global stiffness matrix reduces to a great extent. Furthermore, another advantage of SFEM is that the wave characteristics can be extracted directly from the formulation. Hence, the inside of wave propagation can be seen by SFEM. Eventually, both the dispersion curves and time domain results are possible to obtain by SFEM.

Different theories of SFEM

The most important aspect to be considered for using SFEM is the selection of the correct theory according to the practical situation. There are different theories available for both isotropic and anisotropic media. Spectral elements for elementary rod [87], elementary beam [88, 89], elementary composite beam [90], composite tube [91] and two dimensional membrane element [92] can be found in literature. The elementary rod has a non-dispersive behaviour and the velocity is constant throughout the range of all frequencies. On the other hand, elementary beam theory is based on Euler-Bernoulli beam theory (EBT) which does not consider lateral effect or shear deformation or rotary inertia. As a result, even though the theory represents the dispersive flexural wave behaviour, the velocity increases with the increase of frequency which is not true. This is due to ignoring the shear deformation and rotary inertia. Because, shear deformation and rotary inertia influence the velocity of flexural wave by converging it at a certain frequency and also the velocity becomes constant beyond that limit. Accordingly, elementary models cannot represent the dynamics of a deep structural member.

Single mode Love theory was developed [93] for isotropic rod which introduces the effect of dispersion for longitudinal wave. However, only the first mode can be captured and is accurate up to a certain frequency level. There are several higher order spectral elements proposed for both isotropic and anisotropic one dimensional wave guide. The first higher order rod theory for circular cross section was investigated by Mindlin-Hermann [94]. These higher order rod theories consider the Poisson's effect and subsequently, an additional propagating mode can be observed at high frequency. Additionally, this also gives rise to the dispersion of the first longitudinal mode. Other higher order rod theories include, higher order two mode theory [95], three mode theory [56], higher order three mode theory [95], four mode theory [96], higher order four mode theory [95], etc. For thick isotropic beam, the first order shear deformation theory (FSDT) was introduced by Timoshenko [97] where the rotary inertia and shear deformation are taken into account. Consequently, an additional propagating mode at

high frequency is observed in a deep isotropic beam which is related to the shear deformation and rotary inertia.

Spectral element for anisotropic material is mainly developed for laminated composite beams [98] and functionally graded materials [86, 99]. It is reported that in unsymmetrical laminated deep composite beams, both axial and flexural motion are coupled [100]. This axial-flexural coupled wave propagation in multi-ply connected slender composite beams was carried out by Mahapatra et al. [90] based on EBT. Even though FSDT for anisotropic beam is more accurate, it has its own limitations, for instance, the shear locking. Therefore, it becomes essential to adopt FSDT for thick beams with proper locking alleviation schemes [101]. To overcome this problem, higher order shear deformation theory (HSDT) was developed [131-133]. Due to the differences among the elastic modulus in three orthogonal directions, prediction of error while applying different beam theories is not straight forward. The studies showed that for thick composite beams with strong asymmetry ply-stacking sequence, errors due to EBT become significant [102, 103]. The modified FSDT theory for thick composite beams was explained in [98] and the solution due to the Poisson's contraction effect was also suggested. The use of FSDT for thick composite beams revealed that the coupling of axial-flexural-shear and contraction mode does exist [98, 104].

All the theories mentioned above are mainly used for rectangular cross-sections whereas in timber poles the cross section is circular. Additionally, mainly one nodded element is taken into account unless there is a structural discontinuity. However, in the case of timber pole, it is essential to analyse it as a multi node element which can easily be introduced by SFEM, although it has never been used for the timber pole condition. Moreover, only simple boundary conditions are employed in the literature such as a cantilever beam or beam with pinned end or a simple spring [105]. In contrast, timber pole's boundary conditions are a mixed situation, such as; there should a dashpot at the soil level and a spring plus dashpot at the bottom of the pole. Spring at the soil level can be ignored as the displacement is very low and there is no slip or gap due to the impact load. Furthermore, it is very practical to impact the timber pole somewhere close to the ground rather than at the top of the pole. As a result, one down going and one up going wave will be generated. It is also important to point out the effect of soil in the time domain which can be reconstructed in SFEM by inverse Fourier or Laplace or Wavelet

transform. Beyond that, and as most of the theory for anisotropic media is derived for asymmetric play stacking of composite beams, timber itself is an orthotropic material and possesses the symmetrical anisotropic behaviour. Therefore, it becomes essential to investigate the applicability of the current theories for timber. Based on the orientation and location of the impact, coupling of flexural-shear modes or axial-contraction modes or axial-flexural-shear-contraction modes can be observed and needs to be verified.

Time domain reconstruction

The first step related to the SFEM formulation is the transformation of the governing equation from time domain to frequency domain. This can be achieved by the different forward transformation techniques. Accordingly, as mentioned earlier, the PDEs are uncoupled to ODEs. The spatial variation is semi-explicitly obtained by solving the characteristic equation in wavenumber-frequency domain. As a result, a complex shape function matrix of all the wave modes is formed as linear superposition. By solving this characteristic equation, dispersion curves, such as, frequency vs. phase velocity, frequency vs. group velocity, frequency vs. wavenumber, etc. can be estimated. Then, the complex dynamic stiffness matrix can be formed by the same way as the conventional FE method; however, this matrix is exact. The basic difference between FEM and SFEM is that all the spectral amplitudes which correspond to element nodal variables are evaluated at each frequency step instead of pseudo-static variables evaluated at each time step or at each Eigen frequency. After that the global system is solved for unit spectral amplitude of the applied load history at each frequency which is very much similar to FEM (unless it is a repeated system). Next, post processing is carried out by convolving with the applied load. Consequently, frequency-displacement or frequency-velocity data can be obtained. Lastly, the time domain results can be found by inverse transform.

There are different transformation techniques available in the literature, such as, the Laplace transform, Fourier transform and the Wavelet transform. And, to get the time domain result it is important to choose an efficient technique depending on the practical condition. Obtaining an inverse Laplace transformation is not straight forward and has limited scope for the wave propagation problems. On the other hand, numerical versions of forward and inverse transforms are available for both Fourier and Wavelet transforms. The Fourier transform uses the Fast Fourier Transform (FFT) numerical

algorithm whereas the Daubechies wavelet is commonly used for time domain reconstruction by Wavelet transform.

Both these transformation techniques have their advantages and disadvantages. The main drawback of FFT based SFEM is that it cannot handle the waveguides of short lengths or un-damped waveguides [56, 98]. This is due to the fact that short length, forces multiple reflections at smaller time scales. As FFT is associated with a finite time window, shorter length of waveguides or un-damped waveguides do not allow the response to die down within the chosen time window. This is called wrap around problem where the remaining part of the response, beyond the chosen time window, will appear first which causes the distortion of the signal. In contrast, wavelet analysis can be adapted to a finite domain and initial values can be imposed using the wavelet extrapolation technique [106]. This removes the wrap around problem.

FFT based SFEM was used for elementary rod [87], elementary beam [88, 89], multiply connected one dimensional higher order isotropic guides [107, 108]. Besides, Baz [109], Palacz and Krawczulk [110], Krawczulk et al. [111], Anderson [96] also used FFT based SFEM. While, wavelet based SFEM was used for isotropic rod [112, 113], isotropic Timoshenko beam [113], higher order composite beams [106], delamination in composite beam [114] with rectangular cross section. Also, Hong and Kennet [115], Gopalakrisnan and Jha [116], Yuan et al. [117], Li et al. [118], Sohn et al. [119] used Wavelet based SFEM for damage detection of plate or beam like structures.

Even though FFT encounters this wrap around problem in time domain analysis of wave propagation, it is the best method used to study the spectrum and dispersion relation. Additionally, it is easier to implement because of the numerical superiority of the FFT algorithm. Moreover, timber poles are not a short waveguide and hence FFT based SFEM can be used for this purpose. Furthermore, different techniques are mentioned in the literature to overcome this wrap around problem for a long waveguide. Such as, adding a throw-off element [56, 98] or adding some damping [56, 98], etc. Since, damping is present in the timber pole situation due to the presence of soil, thus with the appropriate time window, wrap around problem can be minimised.

2.7 Advanced signal processing

Signal processing is an important part of NDT. The signal obtained from a NDT is not always clear enough to extract the current features of the structure. Thus, the signal needs to be processed or analysed to examine the condition of the structure. Moreover, signal processing is also essential in case of a broadband frequency input signal, dispersive wave propagation and also to filter out the noise from the environment.

Signal processing is an area of applied mathematics that deals with the operations and/or analysis of signals, in either discrete or continuous time. Signals are analogue or digital electrical representations of time-varying or spatial-varying physical quantities. Based on the understanding of wave propagation in a timber pole, advanced signal processing can be utilized for the data processing to reveal hidden information that is critical for condition and length determination of poles. Three main groups of signal processing tools are often associated with wave based analysis: time domain analysis, frequency domain analysis (i.e. Fourier transform) and time-frequency analysis.

The conventional Fourier Transform (FT) is of great importance for wave based signal analysis. Based on the FT, the mobility curve in the IR method was established. In addition, it also gives great insight into the frequency components present in the signal. Some semi analytical analysis, such as, the Spectral Finite Element methods (SFEM) is also based on Fast Fourier Transform (FFT). Accordingly, FFT is used in numerous NDT techniques. The Fourier phase method is used by researchers for analysing the dispersive signal in the frequency domain, but the accuracy is not satisfactory due to the error of computing true phase angle [7]. Moreover, the Fourier phase method can only be used to determine the embedded length of a pole rather than to determine the damage location, due to the loss of time information that is essential to find the damage location. This is due to the fact that high frequency components are susceptible to damage due to their short wavelength and it is important to determine at which time a particular frequency component is present. To overcome this deficiency, time-frequency analysis is a useful tool and the details of different time-frequency analyses are described below.

2.7.1 Time frequency analysis

Due to the dispersive nature of the signal, a good number of frequency components exist in the timber pole. Every frequency component has different velocities; therefore, every frequency component reaches the bottom of the pole at different times. Moreover, if there is interference then they will move with a group velocity rather than a phase velocity. The presence of different modes may also occur at different times; hence time frequency analysis becomes very important due to the dispersive nature of a wave. Furthermore, to analyse a non-stationary signal, (whose frequency responses vary with time) the Fourier Transform (FT) does not have any value, this is because if two signals have four spectral components and one is stationary and another one is non-stationary, the FT of both signals will be the same. This is why the time frequency analysis becomes necessary for a non-stationary signal.

Despite the fact that damage detection is often an inverse problem, and no universally applicable solution exists for all damage problems, the acquisition of knowledge with respect to diagnosis is enormous. Various damage detection techniques, approaches and methodologies have been developed over the past 30 years. A good deal of recent studies in this area are related to new developments in advanced signal processing, as reported in [120]. To date, most damage detection methods use Fourier analysis as the primary signal-processing tool. From the resulting spectra, modal properties or damage-sensitive features are extracted to detect changes in the signal properties. However, often the most important aspect is in how these characteristics change with time. Therefore, time domain analysis is not always able to reflect all the necessary features of the signal. Examination of the time-invariant modal properties of a structure neither can typically provide information about whether a system is nonlinear, nor can it identify a sudden change in the system properties. The non-stationary nature of measured signals produced by mechanical faults or structural damage suggests that time-variant procedures can be used to detect such faults as an alternative approach to the classical Fourier-based methods. Recent years have shown a tremendous progress in this area. All time-variant methods can be classified into three major groups: time-dependent models, time–frequency and time–scale analyses.

There are a great number of time frequency analysis methods such as:

Short Time Fourier Transform (STFT)

Wigner – Ville Distribution (WVD)

Pseudo Wigner – Ville Distribution (PWVD)

Choi – Williams Distribution

Staszewski et. al. [120] discussed briefly the features of above methods and compared their limitations and advantages in various situations.

Short Time Fourier Transform (STFT)

When FT is applied on a signal, all the time domain data (temporal data) are lost and only frequency components are obtained. To overcome the shortcoming of the loss of temporal data, Gabor [121] introduced short time Fourier transform (STFT) by introducing the windowing techniques, that is, by considering a section of the signal at a specific a time range. The original approach for performing time–frequency analysis relies on the well-known FT. By applying the FT to sections of a signal, an assessment of the time-varying nature of the frequency spectrum can be found. It is performed by translating a window of a given length, $h(t)$, along the signal of interest, $x(t)$

$$x(\tau) = x(\tau)h(t-\tau). \tag{2.5}$$

FT is then applied within the window, allowing for a measurement of the frequency content for that segment of the signal.

$$STFT_X^{(\omega)}(t,f) = \int_t [x(t).\omega^*(t-t')]e^{-2j\pi ft}dt. \tag{2.6}$$

In STFT, the width of the window is fixed. Thus, the resolution for the high and low frequency component is fixed.

The function extracted, using the STFT, can be displayed in a two dimensional time–frequency map, where at each time point a frequency spectrum is provided that is based on the averaged characteristics of the signal for the period of time within the window. This map is called a spectrogram and is computed by taking the square of the modulus of $F_t(\omega)$ for each window.

STFT has been used for a long time as a time frequency analysis tool. Jin-Chul Hong [122] used dispersion based STFT applied to dispersive wave analysis.

Wigner – Ville Distribution (WVD)

For STFT, high resolution cannot be obtained simultaneously for both time and frequency domains since once the time window size is chosen, it remains fixed for all frequencies [123]. The time–frequency resolution of the STFT is limited by the size of window that is used in the analysis. The WVD seeks to increase the limits of resolution by weighting the signal $f(t)$ with time and frequency translations of itself, rather than a window function. The distribution is defined by taking the FT of the instantaneous auto-correlation function, $x^*(1-1/2\tau).\ x(1+1/2\tau)$, where x^* indicates the complex conjugate of x.

The WVD is a measure of the overlap of the signal at a past time with the signal at a future time point. The drawback is that this creates interferences (cross terms) which show up as highly oscillating terms resulting from the superposition of separate spectral components of the signal, and can cause misinterpretation of the signal phenomena. These interferences can be removed by averaging, but this will reduce the resolution.

Another drawback to the WVD is the decrease in the frequency range over the STFT. When taking a FT, the resulting spectra have a periodicity equal to the rate at which the signal was sampled. The WVD distribution, however, has a periodicity equal to only half the sampling rate. To increase the frequency range of the representation, the corresponding analytical signal is first extracted using the Hilbert transform. By finding the WVD of the analytical signal, aliasing can be mitigated.

Pseudo Wigner – Ville Distribution (PWVD)

One of the ways to help alleviate the problems of cross terms in the WVD is to apply a window to the equation [120]. The window function helps to smooth the distribution while emphasizing the signal around time t, provided that the window peaks at $\tau = 0$.

Choi – Williams Distribution

The window function used in the PWVD is just one choice for a kernel function in Cohen's general class of distributions [120]. There are different other functions that can

be used to try and smooth out the cross terms resulting from the WVD. The attenuation of cross terms is better than PWVD, but there is a decrease in frequency resolution as compared with the WVD [120]. The highest mode is also difficult to identify.

To sum up, the summary on shortcoming on time frequency analysis can be listed below:

1. The most common approach, the STFT, provides a decent approximation to the frequencies present in the signal, and their changes.

2. The WVD greatly improves the resolution to which the frequency values are known, but at the cost of the introduction of artefacts in the distribution.

3. The Pseudo Wigner–Ville and Choi–Williams distributions provided results somewhere in between. Both have less artefacts present than the Wigner–Ville transform, but with a worse resolution. However, the resolution is not as poor as for the STFT.

To sum up, all these four time-frequency analyses described above have a fixed window size and so the resolution for high and low frequency components is the same.

2.7.2 Time scale or multi resolution analysis

Although the time and frequency resolution problems are results of a physical phenomenon (the Heisenberg uncertainty principle) and exist regardless of the transform used, it is possible to analyze any signal by using an alternative approach called the multi resolution analysis (MRA). MRA, as implied by its name, analyzes the signal at different frequencies with different resolutions. Every spectral component is not resolved equally as it is the case for the STFT.

MRA is designed to give a good time resolution and a poor frequency resolution at high frequencies and a good frequency resolution and a poor time resolution at low frequencies. This approach is especially useful when the signal at hand has high frequency components for short durations and low frequency components for long durations. Fortunately, the signals that are encountered in practical applications are often of this type.

There are mainly two types of wavelet transform, one is Continuous Wavelet Transform (CWT) and another one is Discrete Wavelet Transform (DWT). Most commonly, CWT is used to analyse a signal. As it has a high time resolution for high frequency component and high frequency resolution for low frequency component, it is easier to choose the desired frequency band and to determine the velocity of the wave from that frequency only. On the other hand, DWT is also useful to decompose and recompose measured signals and it is often used for de-noising the data. This is especially attractive for processing experimental data or field testing data where noise often causes a great degree of problems. Ni [124] used CWT for pile integrity testing. Ovanesova [123] and Kim [125] used both CWT and DWT for damage detection in frame structures, and the applicability of wavelet transform (WT) is justified. J.P. Seidal [126] presented a low strain integrity testing in time frequency domain and represent different aspects of response in time and frequency domain. Addison [127] used wavelet analysis for low strain integrity testing of foundation piles and introduced a method where the signal is conditioned by a wavelet filter allowing selective frequency bands. Peterson [128] used CWT to increase the accuracy of the measurement of the relative phase velocity. Due to the advantages of CWT in NDT because of its very accurate resolution in every frequency, CWT is chosen as one of the signal processing techniques in this research.

Another popular signal processing technique for analysis of dispersive wave is SKM. Douglas et al. [6] developed Short Kernel Method (SKM) which is also popular to analyse dispersive wave generated by bending wave testing. It generates the SKM plot in time domain for a selected frequency and SKM plot allows determination of the velocity of the frequency as well as echo time from which embedment length and possible damage location can be determined. Holt [7] compared the Fourier phase method and SKM to analyse a dispersive flexural wave signal and concluded that the SKM is more accurate and easier to implement.

2.8 Conclusions

To determine the embedded length and/or damage location, the velocity or the length has to be known a priori in the conventional surface reflection techniques. However, in reality, the velocity is unknown and also dispersive, i.e., the velocity changes with frequency. This dispersive behaviour is very common for the thick cylindrical waveguide, such as, timber pole. Accordingly, the velocity needs to be determined for

the condition assessment of the timber pole. Thereby, GW theory has to be used to verify the experimentally calculated stress wave velocity.

It is also discussed that the dispersive behaviour is different for isotropic and anisotropic material. As timber is an orthotropic material, hence the GW theory for the anisotropic media is essential to be considered for the actual representation of the timber behaviour. Timber is affected by temperature, *MC*, annual rings etc. and are better to consider while solving for the GW equation.

Even though the analytical solution of GW theory can give insight into the wave propagation behaviour, it is always simplified due to the complexity associated with the solution of the GW equations. For instance, timber can be considered either fully embedded or traction free in the GW theory although timber poles are partially embedded in the soil. Therefore, some numerical and semi analytical approaches can be used to solved this issue. SFEM and FEM are chosen for his purpose. Both of these methods also have their own limitations. Therefore, in conjunction with the pure analytical results both the numerical and semi analytical methods are chosen for the analysis of GW propagation in timber poles.

Lastly, advanced signal processing is needed to be used to interpret the signal in order to determine the embedded length and damage location in the timber pole. The use of appropriate signal processing techniques becomes crucial when the signal suffers from dispersion. It is presented that time-frequency analyses are better to use for this purpose. There are different time-frequency analyses that can be found in the literature; nevertheless, the CWT and SKM are the most suitable for the signal analysis. Thus, these two techniques are chosen in this project.

Chapter 3

3 A Study of behaviour of guided wave propagation in a cylindrical structure

3.1 Introduction

This chapter describes the guided wave propagation in a cylindrical structure. The results are shown in terms of mainly phase velocity and group/energy velocity curves. In addition, wavelengths of the guided wave in a cylindrical structure are also presented to illustrate the maximum size of the damage that can be detected at different frequencies. For embedded condition, attenuation curves are seen to reflect the energy loss in a cylindrical structure. Furthermore, mode shapes (displacement profile, power flow, etc.) are reported to reveal the direction of wave propagation along the radius of the structure.

Both longitudinal and flexural waves are taken into consideration in this study. Depending on the suitability of the impact location, decision has to be made on choosing the appropriate wave behaviour (longitudinal or flexural). Additionally, timber is also modelled as layered material as described in Section 2.4 to show the effect of the heartwood and sapwood. Moreover, both isotropic and transversely isotropic material models are discussed to indicate the difference of these two systems and to emphasize the importance of considering timber as an anisotropic material. The effect of temperature and moisture content (in terms of modulus of elasticity) is also investigated in the isotropic material model.

The results of comparison between GW in isotropic and transversely isotropic cylindrical structures in this thesis will highlight the importance of considering timber as an anisotropic medium for propagation of GW. Dispersion curves of a transversely isotropic material are compared for different combination of elastic constants (from orthotropic model) to investigate the effect of these parameters on transversely isotropic material model. A suggestion is carried out to consider the appropriate 5 elastic constants of transversely isotropic model from orthotropic modelling which has 9 elastic constants. This is achieved by comparing the phase velocity of curves of transversely isotropic model with orthotropic material modelling which is studied in [129].

In the current study, the software 'Disperse' is used to plot the dispersion curves for both isotropic and transversely isotropic material model. Transversely isotropic material model is compared with orthotropic model which is solved by SBFEM [129]. The reason behind choosing two different methods is that 'Disperse' cannot plot dispersion curves for an orthotropic cylinder as it is mentioned in its manual [130].

3.2 Wave theories for isotropic material

It is already discussed that, timber is an anisotropic material and needed to be considered as either transversely isotropic or orthotropic material. However, the isotropic wave behaviour is discussed in the beginning due to the fact that some parametric studies can be examined from the isotropic modelling. For example, the effect of temperature, moisture content, layered material, etc. can be investigated easily in the isotropic material modelling. Additionally, it is also important to know the differences between these two material modellings. Therefore, the wave theories for both isotropic and transversely isotropic materials will be presented here.

3.2.1 Theory of one dimensional wave

A good number of wave based NDT methods are established using 1D wave theory which is based on kinematics of deformation. This theory describes waves in a string or plane waves in an infinite space. Hence, the derivation does not consider the effect of lateral deformation (Poisson's effect). As a result, the initial condition dominates the wave behaviour. Even though it is considered an infinite media, reflection and transmission can occur if a material interface exists. Such boundary conditions, which can only be present in the direction of propagation, can only change the wave amplitude

but not its velocity. In other words, wave velocity is assumed to be constant throughout the media. The displacement equation for a wave, which propagates along the x-direction, is expressed as,

$$\frac{\partial^2 u}{\partial t^2} = C^2 \frac{\partial^2 u}{\partial x^2} \tag{3.1}$$

where u = displacement and C = wave velocity [131].

The wave velocity described by this equation can be either bulk longitudinal (C_l) or bulk shear (Cs) wave velocity which are expressed as,

$$C_l = \sqrt{\frac{E}{\rho}} \tag{3.2}$$

$$C_s = \sqrt{\frac{G}{\rho}} \tag{3.3}$$

where E = Young's modulus, G = Shear modulus and ρ = mass density.

The assumption of the bending wave propagation based on the 1D wave theory is also popular because of its good accuracy in low frequency. The governing equation for flexural wave propagation is derived for one dimensional wave equation in an infinite media. The Bernoulli-Euler beam theory of a beam is considered, i.e. only pure bending is taken into account. Therefore, if the material of the beam is considered as homogeneous, then the motion in the vertical direction (y direction) can be given by,

$$\frac{\partial^4 y}{\partial x^4} + \frac{1}{a^2}\frac{\partial^2 y}{\partial t^2} = 0, \tag{3.4}$$

$$a^2 = \frac{EI}{\rho A} \tag{3.5}$$

where I = moment of inertia of the section and A = cross sectional area [132].

If a harmonic wave is propagating, then the flexural wave velocity, C_f can be found by,

$$C_f = \sqrt{a\omega} \tag{3.6}$$

where ω = angular frequency.

From the equation, it can be seen that the wave velocity will increase with the increase of wave frequency without converging to a certain value due to neglecting the rotary inertia and shear effect. While the Rayleigh theory considers only the rotary inertia effect and the Timoshenko beam theory considers both rotary inertia and shear effect in addition to bending. Details can be found in [132].

3.2.2 Theory of elasticity

In theory of elasticity, boundary effects are considered for a three dimensional wave. Hence, this theory provides a solution for elastic waves in finite structures with surface and boundary conditions. It is usually derived for isotropic media; nevertheless, it can also be extended to orthotropic and layered media. The boundary conditions which are essential to derive the equation depend on stress and displacement constrains, Poisson's effect and the surrounding media. These factors affect wave amplitude, energy dissipation and also wave velocity. The displacement equation of motion in an isotropic elastic medium in the absence of body force can be expressed by the dynamic equation of motion,

$$(\lambda + 2\mu)\nabla \mathrm{I} - 2\mu\nabla \times w = \rho \frac{\partial^2 u}{\partial t^2} \tag{3.7}$$

where μ and λ = Lamĕ constants, $\mathrm{I} = u_{x,x} + u_{y,y} + u_{z,z}$, w = rotation vector and ∇ = divergence operator [131].

From the above equation, it can be observed that it contains dilation and rotation parts. Therefore, there are two kinds of waves travelling with different speeds in a three dimensional space, namely, longitudinal wave with dilatation and shear wave with rotation. The velocities of these two waves in a bounded medium can be derived by further analysis of Equation (3.7) and are expressed as,

$$C_l = \sqrt{\frac{(\lambda + 2\mu)}{\rho}} = \sqrt{\frac{(1-\nu)E}{(1+\nu)(1-2\nu)\rho}} \tag{3.8}$$

$$C_s = \sqrt{\frac{\mu}{\rho}} = \sqrt{\frac{G}{\rho}} = \sqrt{\frac{E}{2(1+\nu)\rho}} \tag{3.9}$$

where ν = Poisson's ratio.

More details on the derivation of these equations can be found in [9], [132] and [131].

3.2.3 Theory of guided wave

In a finite media, the boundary imposes stress and/or strain constraints, causing waves to reflect at the boundary and often yielding a change of wave type and their directions [133]. Accordingly, GW exists in any finite medium including elastic or inelastic materials [9]. The difference of the GWs in elastic or inelastic materials is that the waves in an elastic medium follow the theory of elasticity [132] and those in an inelastic medium follow the elastic-viscous constitutive law. Thus, all guided waves are dispersive in a finite medium except light in vacuum [134]. In other words, the wave velocity of a GW is a function of frequency, geometric conditions and boundary conditions. Due to the aforementioned reasons, for stress wave propagation along a timber pole, it is more appropriate to consider it as GW compared to bulk wave propagation.

The governing equation for a GW can be expressed by the Navier-Stokes equation. The details of this equation for isotropic materials are presented in [9, 135]. In addition, in GW theory the stress boundary condition must be satisfied. The stress-strain equation is given by Hooke's law as,

$$[\sigma] = [C][\varepsilon] \tag{3.10}$$

where σ = stress matrix, C = stiffness matrix and ε = strain matrix.

For an isotropic material, the elastic components depend on only two independent constants and the elastic constants/stiffness matrix of isotropic material is shown in Equation (3.11).

$$\begin{bmatrix} C_{11} & C_{12} & C_{12} & 0 & 0 & 0 \\ C_{12} & C_{11} & C_{12} & 0 & 0 & 0 \\ C_{12} & C_{12} & C_{11} & 0 & 0 & 0 \\ 0 & 0 & 0 & \frac{C_{11}-C_{12}}{2} & 0 & 0 \\ 0 & 0 & 0 & 0 & \frac{C_{11}-C_{12}}{2} & 0 \\ 0 & 0 & 0 & 0 & 0 & \frac{C_{11}-C_{12}}{2} \end{bmatrix} \quad (3.11)$$

where $C_{11} = \frac{E(1-\upsilon)}{(1+\upsilon)(1-2\upsilon)}$ and $C_{12} = \frac{E\upsilon}{(1+\upsilon)(1-2\upsilon)}$ [25].

The theoretical solution of a GW in an isotropic cylinder with different boundary conditions (traction free or embedded) can be found in [136], [132], [11], [10] and [9]. The solutions are based on displacement potential theory or superposition of partial wave techniques. The equation is solved for an angular frequency (ω) and the root of the equation is the wavenumber (ξ), which can be a complex number. The relation between the real part of a wavenumber (Re ξ) and the frequency is called dispersion relation. The imaginary part of a wavenumber (Imag ξ) may be present if the cylinder is surrounded by another medium and/or when material damping is considered. The plot of the imaginary part of the wavenumber (Imag ξ) versus the wave frequencies can illustrate the attenuation of wave branches/modes at a given frequency. The relation between the frequency and the velocity of a wave is called spectrum relation and is usually derived from the real part of the wavenumber. It is also possible to obtain one to infinite number of wavenumbers at a particular frequency, which simply means that for the given frequency a number of branches are present.

In this research, both traction free and embedded geotechnical conditions are considered. Embedded condition mainly affects the energy leakage which is related to attenuation. To author's best knowledge to date, no research work has been published on the solution of guided wave propagation in a solid or layered cylindrical structure with transversely isotropic materials under embedded condition.

In the following section, an overview is given for the determination of the parameters used to calculate GW solutions for an isotropic cylinder. The section is subdivided into dispersion relation, spectrum relation, displacement fields and mode shapes (power flow, energy velocity, etc.).

3.2.3.1 Dispersion relation

The dispersion relation for a longitudinal wave was derived by Pochhammer [137] and Chree [138]. Later, Zemanek [136] solved this dispersion relation for longitudinal and flexural waves. The dispersion relations for both longitudinal and flexural waves in a traction free isotropic cylinder are given below in Equation (3.12) and (3.13), respectively.

$$\frac{2\alpha}{a}(\beta^2+\xi^2)J_1(\alpha a)J_1(\beta a)-(\beta^2-\xi^2)^2J_0(\alpha a)J_1(\beta a)-4\xi^2\alpha\beta J_1(\alpha a)J_0(\beta a)=0, \tag{3.12}$$

$$\begin{vmatrix} \left[\frac{\lambda}{2\mu}(\alpha^2+\xi^2)a^2+(\alpha^2a^2-p^2)\right]J_p(\alpha a)+\alpha aJ_p'(\alpha a) & (\beta^2a^2-p^2)J_p(\beta a)+\beta aJ_p'(\beta a) & 2p[\beta aJ_p'(\beta a)-J_p(\beta a)] \\ p[\alpha aJ_p'(\alpha a)-J_p(\alpha a)] & p[\beta aJ_p'(\beta a)-J_p(\beta a)] & -(2p^2-\beta^2\alpha^2)J_p(\alpha a)+2\beta aJ_p'(\alpha a) \\ -\alpha aJ_p'(\alpha a) & -\left(\frac{\xi^2-\beta^2}{2\xi^2}\right)\beta aJ_p'(\beta a) & pJ_p(\beta a) \end{vmatrix}=0, \tag{3.13}$$

$$\alpha^2+\xi^2=\frac{\omega^2}{C_l^2}, \tag{3.14}$$

$$\beta^2+\xi^2=\frac{\omega^2}{C_s^2} \tag{3.15}$$

where α = wavenumber for longitudinal waves; β = wavenumber for shear waves; ξ = wavenumber in the direction of propagation; a = radius of the cylinder; J = Bessel's function of first kind; p = circumferential order of cylinder.

The circumferential order p is zero for a longitudinal wave. For a flexural wave, the condition is $p > 0$. Even though theoretically, infinite circumferential orders are expected for a flexural wave, it is believed that flexural modes induced and measured in experiments will likely to be of first circumferential order ($p = 1$). The dispersion relation for longitudinal branches in an embedded isotropic cylinder can be found in [10] and the dispersion relation for a flexural wave in an embedded cylinder is presented in [9] and are presented in Appendix A.

This dispersion relation is also called frequency equation or characteristic equation. It can be seen that at any frequency there are infinite numbers of roots that satisfy the frequency equation. These roots can be imaginary, complex or real. The imaginary roots correspond to the non-propagating wave branches whereas the real roots represent the propagating branches. These propagating longitudinal branches are denoted by L(p,q) or L(0,q) and flexural branches are represented by F(p,q) or F(1,q), where q is the branch number. The complex roots related to the branches are called evanescent modes and will be discussed later.

At the lowest frequency, only one real root can be found while other roots are imaginary or complex. This one real root corresponds to the first propagating branch. As the frequency increases, some of the complex roots of the frequency equation become real which represents the presence of more than one propagating mode. The branches which have real valued roots from the beginning are called fundamental branches (mainly L(0,1) and F(1,1)). The frequency where a root first becomes real is called the cut-off frequency of that branch. At cut-off frequency, the wavenumber is zero and it can be determined by putting $\xi = 0$ in the frequency equation. Below the cut-off frequency, wavenumbers are either imaginary or complex. The branches with a cut-off frequency are called higher order branches.

3.2.3.2 Spectrum relation

At each frequency, all the propagating branches have a phase velocity and group velocity. Phase velocity represents the propagation of a constant phase and group velocity indicates the propagation of energy of the wave. As wavenumbers are corresponding to frequencies, the relation between wavenumber and frequency is established from the dispersion relation. From a known wavenumber and frequency, the phase velocity (V_{ph}) and the group velocity (V_{gr}) at a particular frequency can be obtained by the following equations

$$V_{ph} = \frac{\omega}{Re\,(\xi)} \tag{3.16}$$

$$V_{gr} = \frac{d\omega}{Re\,(d\xi)} \tag{3.17}$$

Each of the frequency components in the wave packet will travel at different group velocities. If the difference in velocities over the range of the frequency is large, there will be a great degree of dispersion since the different frequency components arrive at different times. This spread will cause the propagating wave to change shape as it propagates. However, if the group velocities are very similar over the generated frequency range, the packet will maintain the same shape during its entire propagation length.

The phase velocity of a branch approaches infinity at the cut-off frequency (as $\xi = 0$ in Equation (3.16)). In contrast, group velocity does not have any infinite value. Group

velocity expresses how quickly the energy of the wave will progress along the structure. Equation (3.17) is only valid, if the system has less attenuation (embedded in soft soil) or no attenuation (traction free pole). Therefore, if the attenuation is large, then the solution for the group velocity may not be physically possible, such as an infinite value at cut-off frequency of a particular branch [130]. Furthermore, the group velocity is also unrepresentative of wave packet velocity if the material is anisotropic. This is because the energy of a wave does not necessarily follow the phase direction [130]. Hence, for these two circumstances, the energy velocity may need to be determined in order to obtain the propagation velocity of energy or wave packet. The results of the spectrum relations (phase, group and energy velocities) will be illustrated in the latter section of this chapter.

Group/energy velocity has great importance on NDT. All the higher order branches have a maximum peak value of group velocity at certain frequency. Zemanek [136] extensively analysed the higher order branches numerically and mentioned that axial displacement of the higher order branches is in phase near the maximum group velocity. At frequencies not associated with maximum group velocity, the axial displacement along the radius is out of phase and average displacement approaches zero. Therefore, it is better to choose the input frequency at the maximum energy velocity. The details on choosing the input frequency based on the group/energy velocity curves will be presented in the latter part of this chapter.

3.2.3.3 Displacement field

In GW propagation, the displacement distributions across a structure are a combination of different types of wave shapes due to the reflection of the longitudinal and shear waves at boundaries [132]. The displacement components for a GW in a cylindrical coordinate system (r, θ, z) is provided by Hanifah [10] as follows

$$u_r = \left[A_1 \alpha Z_p'(\alpha r) - A_4 \xi Z_p'(\beta r) + A_6 \left(\frac{p}{r}\right) Z_p(\beta r)\right] \cos p\theta \, e^{i(\xi z - \omega t)}, \tag{3.18}$$

$$u_\theta = \left[-A_1 \left(\frac{p}{r}\right) Z_p(\alpha r) + A_4 \left(\frac{p\xi}{\beta r}\right) Z_p(\beta r) - A_6 \beta Z_p'(\beta r)\right] \sin p\theta \, e^{i(\xi z - \omega t)}, \tag{3.19}$$

$$u_z = i\left[-A_1 \xi Z_p(\alpha r) - A_4 \beta Z_p(\beta r)\right] \cos p\theta \, e^{i(\xi z - \omega t)} \tag{3.20}$$

where u_r, u_θ and u_z are the displacement components along radial, tangential/angular and axial/longitudinal direction; Z is the ordinary and modified Bessel function of first

kind and A_1, A_4 and A_6 are undetermined coefficients. A_1 represents stretch (longitudinal) effects and A_4 and A_6 represent shear effects. It can also be seen from above three equations that if $p = 0$, u_θ components become zero, i.e. in a longitudinal wave, only radial and longitudinal components of displacement are present. Whereas in the case of bending wave ($p = 1$), all three displacement components are present. While, the displacement distribution is symmetric along the longitudinal axis for a longitudinal wave, it is anti-symmetric for a bending/flexural wave.

3.2.3.4 Mode shapes

Guided wave changes its shape with different wave branches and at different propagation frequency, that is, for the same branch; the shape of the wave is different at different frequency. In dispersion curve, a point on a wave branch that corresponds to a frequency is called mode. The mode shape displays how the displacements, stresses, energy, power flow etc. vary through the thickness/radius of the plate/cylinder.

The strain energy density (SED) is given by the summations of stress-strain products. These expressions assume complex values of the quantities [139]. If real values are used then these expressions should be multiplied by two [130]. For a cylindrical system, *SED* and kinetic energy density (*KED*) can be obtained by the following formulas

$$SED = \frac{1}{4}\left[\sigma_{rr}\frac{\frac{\partial}{\partial u_r}}{\frac{\partial}{\partial r}} + \sigma_{\theta\theta}\left(\frac{1}{r}\frac{\partial u_\theta}{\partial \theta} + \frac{u_r}{r}\right) + \sigma_{zz}\left(\frac{\partial u_z}{\partial z}\right)\right]$$

$$+\frac{1}{8}\left[\sigma_{rz}\left(\frac{\partial u_r}{\partial z} + \frac{\partial u_z}{\partial r}\right) + \sigma_{r\theta}\left(r\frac{\partial}{\partial r}\left(\frac{u_\theta}{r}\right) + \frac{1}{r}\frac{\partial u_r}{\partial \theta}\right) + \sigma_{\theta z}\left(\frac{\frac{\partial}{\partial u_\theta}}{\frac{\partial}{\partial z}} + \frac{1}{r}\frac{\frac{\partial}{\partial u_z}}{\frac{\partial}{\partial \theta}}\right)\right], \quad (3.21)$$

$$KED = \frac{\rho}{4}\left[\left(\frac{\partial u_r}{\partial t}\right)^2 + \left(\frac{\partial u_\theta}{\partial t}\right)^2 + \left(\frac{\partial u_z}{\partial t}\right)^2\right]. \quad (3.22)$$

The power flow density (*PWR*) is obtained from the product of the velocity vector and the stress tensor and called poynting vector, is expressed as

$$PWR = -\frac{1}{2}\begin{bmatrix} \sigma_{rr}\left(\frac{\partial u_r}{\partial t}\right)^* + \sigma_{r\theta}\left(\frac{\partial u_\theta}{\partial t}\right)^* + \sigma_{rz}\left(\frac{\partial u_z}{\partial t}\right)^* \\ \sigma_{r\theta}\left(\frac{\partial u_\theta}{\partial t}\right)^* + \sigma_{\theta\theta}\left(\frac{\partial u_\theta}{\partial t}\right)^* + \sigma_{\theta z}\left(\frac{\partial u_z}{\partial t}\right)^* \\ \sigma_{rz}\left(\frac{\partial u_z}{\partial t}\right)^* + \sigma_{\theta z}\left(\frac{\partial u_\theta}{\partial t}\right)^* + \sigma_{zz}\left(\frac{\partial u_z}{\partial t}\right)^* \end{bmatrix} \tag{3.23}$$

where * denotes complex conjugate. *PWR* reveals how the energy is flowing through the structure, i.e., the depth at which the greatest transmission of energy takes place or the manner in which energy leaves the structures by leakage.

The energy velocity (V_z) can be calculated using Equation (3.21 – 3.23)

$$V_z = \frac{\int_S \int_T (PWR_z) dT dS}{\int_S \int_T (NRG) dT dS} \tag{3.24}$$

where S = cross section of the cylinder, T = time period of the wave, PWR_z = component of poynting vector in the direction of propagation (in this case along the cylinder) and NRG = total energy = SED + KED.

The power flow of a mode (P_m) can be elucidated by the integration of PWR in the direction of the propagation of the wave. It is a quantity of the whole structure rather than a particular location and indicates the rate at which energy is transmitted along the structure. The equation for P_m is described by

$$P_m = -\frac{1}{2}\int_S \left[\sigma_{rz}\left(\frac{\partial u_r}{\partial t}\right)^* + \sigma_{\theta z}\left(\frac{\partial u_\theta}{\partial t}\right)^* + \sigma_{zz}\left(\frac{\partial u_z}{\partial t}\right)^*\right] dS. \tag{3.25}$$

It is noteworthy to state that all the mode shape results shown in this study are normalised values. Details of the normalisation can be found in [130] and the derivation of this quantities is explained in [139].

3.3 Wave theories for anisotropic material

The spectrum and dispersion relations are different for anisotropic material. However, the relations are derived from the theory of elasticity or the Hooke's law (also called constitutive equation). Therefore, the general constitutive equation is discussed first.

3.3.1 The compliance matrix

In anisotropic media, the compliance matrix [S] is used more often to define the stress strain relationship compared to the stiffness matrix [C]. The compliance matrix is defined as:

$$[\varepsilon] = [S][\sigma]. \tag{3.26}$$

The stiffness and compliance matrices of an orthotropic or transversely isotropic material are defined by Equations (3.27) and (3.28)

$$[C] = \begin{bmatrix} C_{11} & C_{12} & C_{13} & 0 & 0 & 0 \\ C_{21} & C_{22} & C_{23} & 0 & 0 & 0 \\ C_{31} & C_{32} & C_{33} & 0 & 0 & 0 \\ 0 & 0 & 0 & C_{44} & 0 & 0 \\ 0 & 0 & 0 & 0 & C_{55} & 0 \\ 0 & 0 & 0 & 0 & 0 & C_{66} \end{bmatrix} \tag{3.27}$$

$$[S] = \begin{bmatrix} \frac{1}{E_r} & \frac{\nu_{\theta r}}{E_\theta} & \frac{\nu_{zr}}{E_z} & 0 & 0 & 0 \\ \frac{\nu_{r\theta}}{E_r} & \frac{1}{E_\theta} & \frac{\nu_{z\theta}}{E_z} & 0 & 0 & 0 \\ \frac{\nu_{rz}}{E_r} & \frac{\nu_{\theta z}}{E_\theta} & \frac{1}{E_z} & 0 & 0 & 0 \\ 0 & 0 & 0 & \frac{1}{G_{\theta z}} & 0 & 0 \\ 0 & 0 & 0 & 0 & \frac{1}{G_{rz}} & 0 \\ 0 & 0 & 0 & 0 & 0 & \frac{1}{G_{r\theta}} \end{bmatrix} \tag{3.28}$$

The compliance matrix is always symmetrical and for orthotropic material, $\nu_{\theta r}/E_\theta = \nu_{r\theta}/E_r$, $\nu_{zr}/E_z = \nu_{rz}/E_r$ and $\nu_{z\theta}/E_z = \nu_{\theta z}/E_\theta$. However, for a transversely isotropic material, if the plane of isotropy is the r-θ plane then, $\nu_{\theta r} = \nu_{r\theta} = \nu_1$, $\nu_{rz} = \nu_{\theta z} = \nu_2$, $\nu_{zr} = \nu_{z\theta} = \nu_3$, $G_{\theta z} = G_{zr} = G$, $E_r = E_\theta = E$ *and* $G_{r\theta} = E/2(1 + \nu_1)$. From these equations, it is clear that, 12 elastic constants (9 independent) for an orthotropic material and 6 constants (5 independent) for a transversely isotropic material are needed to complete the compliance matrix. Since timber is an orthotropic material, most of material testing results of timber given in the literature includes 12 elastic constants. Therefore, it is essential to choose 5 appropriate elastic constants (for transversely isotropic material consideration) from available literature on timber. In the current study, dispersion

curves of a transversely isotropic material are also compared for different combination of elastic constants (from orthotropic model) to investigate the effect of these parameters on transversely isotropic material model. Furthermore, a suggestion is carried out to consider the 5 appropriate elastic constants by comparing with orthotropic material modelling. Accordingly, for a parametric study of transversely isotropic material, it is clear that if E is considered as E_θ, then v_2 and v_3 have to be chosen as $v_{\theta z}$ and $v_{z\theta}$, respectively, to keep the compliance matrix symmetric. Consequently, if $E = E_r$, then v_2 and v_3 have to be chosen as v_{rz} and v_{zr}, respectively. Based on these relations, 4 sets can be chosen from orthotropic elastic constants and results will be presented later in this chapter.

3.3.2 Dispersion relation of a transversely isotropic material

The characteristic equation of a transversely isotropic cylinder considering the wave is propagating in the z direction can be given as follows [43]

$$s^4(s^2+\xi^2)(C_{44}C_{11}s^4-\varsigma s^2+\zeta)\left(\left(\frac{C_{11}-C_{12}}{2}\right)s^2-\rho\omega^2+\xi^2\right)=0 \tag{3.29}$$

where

$$\varsigma=(C_{13}+C_{44})^2\xi^2+C_{11}(\rho\omega^2-C_{33}\xi^2)+C_{44}(\rho\omega^2-C_{44}\xi^2), \tag{3.30}$$

$$\zeta=(\rho\omega^2-C_{44}\xi^2)(\rho\omega^2-C_{33}\xi^2). \tag{3.31}$$

In Equation (3.29), s = 0 is the trivial solution and the solution corresponding to $s^2=-\xi^2$ corresponds to an imaginary wave vector in the direction of propagation (in the z direction in this case), i.e., a disturbance that will die out exponentially without propagating. Three meaningful solutions exist for Equation (3.29) [43]

$$s_1^2=\frac{\varsigma-\sqrt{\varsigma^2-4C_{11}C_{44}\zeta}}{2C_{11}C_{44}}, \tag{3.32}$$

$$s_2^2=\frac{\varsigma+\sqrt{\varsigma^2-4C_{11}C_{44}\zeta}}{2C_{11}C_{44}}, \tag{3.33}$$

$$s_3^2=\frac{2(\rho\omega^2-C_{44}\xi^2)}{2C_{11}C_{44}}. \tag{3.34}$$

From the above equations, the wavenumber can be calculated and the spectrum relation can be formed similarly as mentioned in the Section 3.2.3.2. The frequency equations for longitudinal and flexural waves for a transversely isotropic material can be

determined by satisfying the boundary conditions. For the traction free situation, the frequency equations of longitudinal and flexural waves are expressed in [140] and also presented in Appendix A.

3.3.3 Displacement field

The displacement distributions across a cylinder with transversely isotropic behaviour are expressed as follows:

$$u_r = \left\{ \begin{array}{c} A_p\left[\left(s_1\frac{p}{r} + i\xi a s_1 \frac{p}{r} q_1\right) J_p(s_1 r) + (-s_1 - i\xi a q_1 s_1) J_{p+1}(s_1 r)\right] \\ +B_p\left[\left(s_2\frac{p}{r} q_2 + i\xi a s_2 \frac{p}{r}\right) J_p(s_2 r) + (-s_2 q_2 - i\xi a s_2) J_{p+1}(s_2 r)\right] \\ +C_p\left[\left(\frac{p}{r}\right) J_p(s_3 r)\right] \end{array} \right\} \cos(p\theta) e^{i(\xi z - \omega t)}, \tag{3.35}$$

$$\begin{aligned} u_z = \{ & A_p\left[(i\xi + a q_1 s_1^2) J_p(s_1 r)\right] \\ & + B_p\left[(i\xi q_2 + a s_2^2) J_p(s_2 r)\right] \} \cos(p\theta) e^{i(\xi z - \omega t)}, \end{aligned} \tag{3.36}$$

$$\begin{aligned} u_\theta = \{ & A_p\left[\left(-\frac{p}{r} - i\xi a \frac{p}{r} q_1\right) J_p(s_1 r)\right] + B_p\left[\left(-\frac{p}{r} q_2 - i\xi a \frac{p}{r}\right) J_p(s_2 r)\right] \\ & + C_p\left[\left(-\frac{p}{r}\right) J_p(s_3 r) + s_3 J_{p+1}(s_3 r)\right] \} \sin(p\theta)\, e^{i(\xi z - \omega t)} \end{aligned} \tag{3.37}$$

where q_1 and q_2 are constants that depend on the elastic constants of the material, the frequency and the wavenumber [140] are presented in Appendix A. From the above equations, it can be seen that even though the equations are more complicated than the isotropic case, the same features are present. As such, only radial and axial components are present in the longitudinal wave (when p = 0). Moreover, like Section 3.2.3.3, the flexural wave (p = 1) has all three displacement components. Nevertheless, if θ = 0°, then Equation (3.37) becomes zero, i.e. at the impact location (θ = 0°), there will be no angular component of displacement. Again, if θ = 90°, then Equations (3.35) and (3.36) are zero, i.e. in bending/flexural wave, axial and radial displacement components are zero at a position 90° around the circumference from the impact location. The details of this feature will be presented in Chapter 5.

3.4 Dispersion curves for isotropic material

3.4.1 Traction free condition

At first, some parametric studies are carried out to investigate the effect of material properties on dispersion curves. The results are shown in terms of phase velocity at this

stage. Also, timber is considered as layered material to represent whether it is essential to assume it as a layered material or not. Accordingly, the modulus of elasticity, density, thickness of the sapwood and the differences of material properties between heartwood and sapwood are emphasized on this part of the study.

3.4.1.1 Effect of modulus and density

Table 3.1 and Table 3.2 provide the material properties used to indicate the effect of modulus and density, respectively.

Table 3.1 Different sets of material properties to show the effect of modulus on phase velocity

	Set 1	Set 2	Set 3	Set 4
E (GPa)	14	17	20	23
ρ (kg/m^3)	750	750	750	750
v	0.4	0.4	0.4	0.4

Table 3.2 Different sets of material properties to show the effect of density on phase velocity

	Set 5	Set 6	Set 7	Set 8	Set 9
E (GPa)	23	23	23	23	23
ρ (kg/m^3)	550	650	750	850	950
v	0.4	0.4	0.4	0.4	0.4

Figure 3.1 and Figure 3.2 illustrate the effect of modulus and density, respectively. The consequences of changing the dispersion curves due to the change in modulus and density are obvious and expected. The first longitudinal branch always starts from the velocity equal to the bulk longitudinal wave velocity (Equation 3.2). As a result, if the modulus of elasticity increases or density decreases, this bulk wave velocity will increase.

Accordingly, the initial phase velocity of L(0,1) branch of set 1 is lower than the same of set 4. Similarly, the initial phase velocity of L(0,1) branch of set 5 is higher than the same of set 9. In addition, for both situations, the shifting of the cut-off frequencies of different branches is observed among the sets. Consequently, fewer numbers of branches will be demonstrated within the same frequency range if modulus of elasticity increases and density decreases. However, a similar trend can be identified.

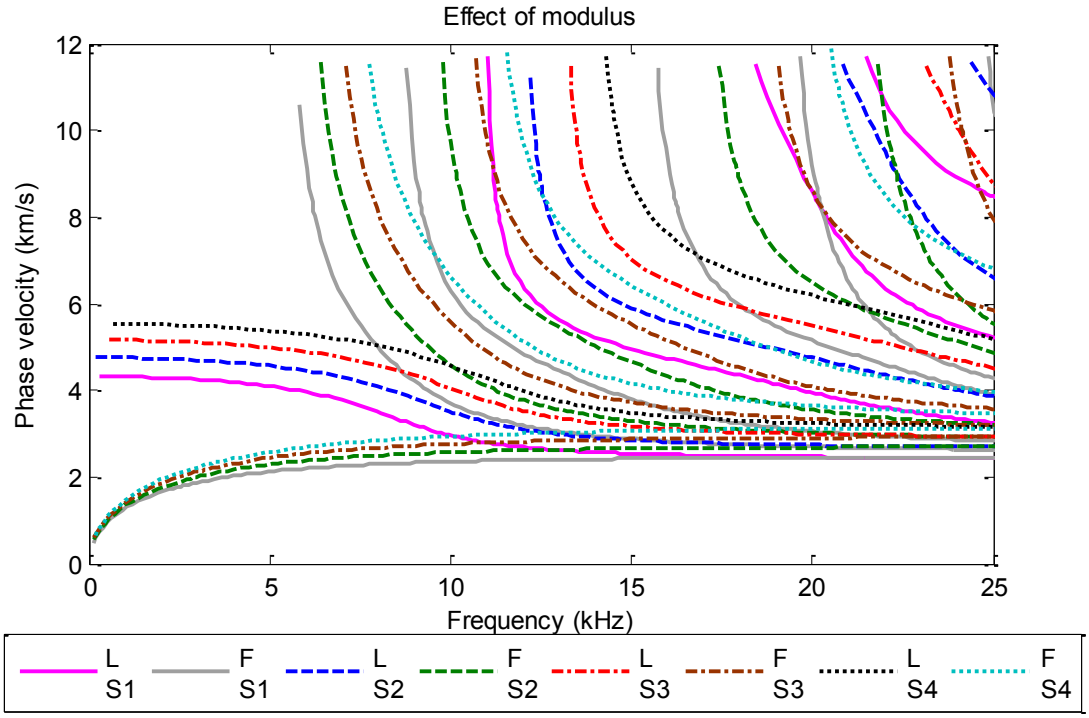

Figure 3.1 Comparison of phase velocities among sets 1 to 4 to show the effect of modulus (L= longitudinal, F=Flexural, S=Set)

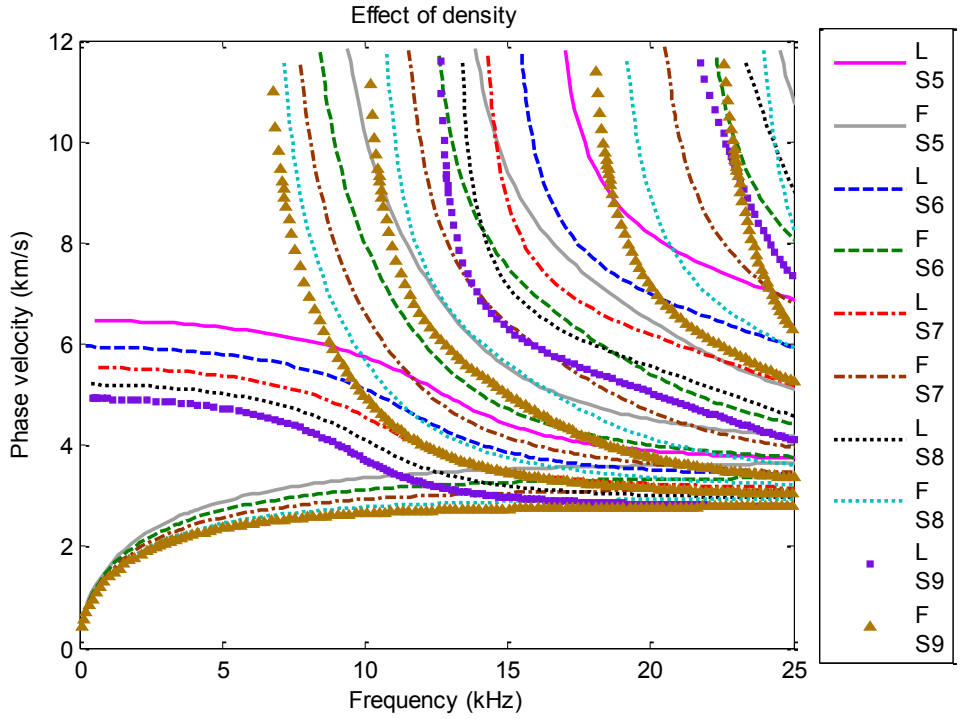

Figure 3.2 Comparison of phase velocities among sets 5 to 9 to show the effect of density (L= longitudinal, F=Flexural, S=Set)

Timber is a natural material and its Moduli of elasticity and densities vary widely among species. Usually, hardwoods are used as a timber pole and the Moduli of elasticity and density for hardwoods are commonly varied within the range mentioned in Table 3.1 and Table 3.2. Additionally, modulus of elasticity can be affected by the change of temperature, moisture content and number of annual rings per cm. Furthermore, the moisture content of the timber may vary between the layers close to surface and the layers in the middle of the pole. Subsequently, shifting of cut-off frequency or the change of initial phase velocity of L(0,1) branch may occur. Therefore, it is not very easy to find out the exact modulus of elasticity and sometimes the density as well, while the large scale NDT on timber poles are being conducted. As a result, if the exact material properties of the timber poles are unknown, it is better to allow a range for variation in terms of wave velocity while comparing the experimental velocity with the analytical phase velocity.

3.4.1.2 Effect of Poisson's ratio

In comparison with anisotropic material, isotropic material has only one Poisson's ratio whereas transversely isotropic and orthotropic materials have 3 and 6 values of Poisson's ratios, respectively. In this section, the effect of Poisson's ratio is presented within the values from 0.3 to 0.45 (Table 3.3).

Table 3.3 Different sets of material properties to show the effect of Poisson's ratio on phase velocity

	Set 10	Set 11	Set 12	Set 13
E (GPa)	23	23	23	23
ρ (kg/m^3)	950	950	950	950
v	0.3	0.35	0.4	0.45

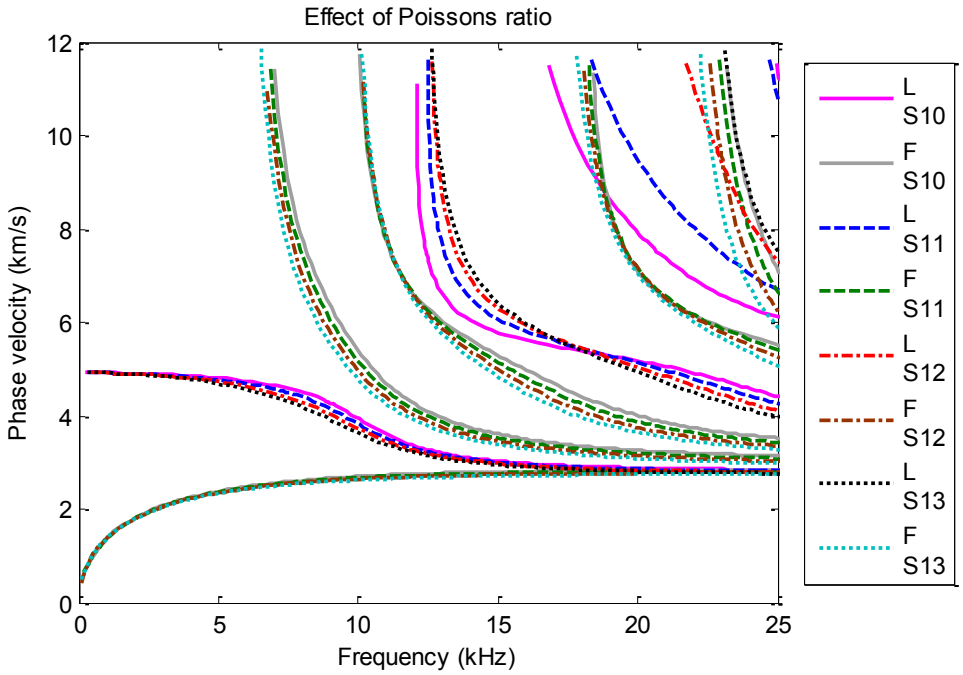

Figure 3.3 Comparison of phase velocities among sets 10 to 13 to show the effect of Poisson's ratio

Figure 3.3 depicts the phase velocity curves of sets 10 to 13 up to 25 kHz. As indicated in the figure, the effect of Poisson's ratio is less significant on the velocity curves. Longitudinal wave velocity is affected more by the Poisson's ratio compared to the same of flexural wave. However, the variation increases at higher frequencies. For example, L(0,1) branch is less affected than L(0,3) branch. Accordingly, if the impact force induces higher frequencies, Poisson's ratio has notable effect on longitudinal wave velocity and accurate value of Poisson's ratio should be taken into account. From this plot, it can be noted that little variation in Poisson's ratio for transversely isotropic material will not influence the dispersion curves greatly.

3.4.1.3 Comparison between solid and layered timber modelling

In this section, the comparison between layered and solid timber is performed. The layered timber is divided into heartwood and sapwood. According to Section 2.4, the thickness of the sapwood may vary due to biological diversity and it also depends on which part of the tree is used. Thereby, at first, the effect of thickness of sapwood is analysed (Table 3.4). Secondly, the effect of the difference of the material properties between heartwood and sapwood is conducted (Table 3.5). For both cases, comparison is made with solid wood. The properties of solid wood are considered to be the same as

set 11. And the properties of layered material are chosen based on the guidelines provided in [52-54].

Table 3.4 Different radius and thickness of heartwood and sapwood

	Heartwood E = 23 GPa, ρ = 950 kg/m^3, v = 0.35	Sapwood E = 20 GPa, ρ = 800 kg/m^3, v = 0.35
	Radius (mm)	Thickness (mm)
Set 14	103	40
Set 15	83	60
Set 16	63	80

Table 3.5 Different material properties of heartwood and sapwood

	Heartwood Radius = 103 mm, v = 0.35		Sapwood Thickness = 40 mm, v = 0.35	
	E (GPa)	ρ (kg/m^3)	E (GPa)	ρ (kg/m^3)
Set 17	23	950	20	850
Set 18	23	950	18	750
Set 19	23	950	20	750

Figure 3.4 compares the phase velocity curves of layered and solid timber. As illustrated in this figure, the variation in the thickness of the sapwood is insignificant on dispersion curves. Timber poles usually have a tapered shape and the thickness of the sapwood varies along the length of the pole. Therefore, it can be noted that this variation of the thickness does not influence the phase velocity curves.

The differences of material properties between sapwood and heartwood are depend on the species of the tree. Some species have substantially different material properties and some have similar values. Figure 3.5 displays the phase velocity curves for different values of sapwood. The material properties of heartwood are kept constant to show the variation of velocities between these two layers. The most difference which can be predicted between these two layers is represented by Set 19. Even for this situation, the variation is nominal. Thereby, it can be concluded that timber can be considered as solid material for NDT testing and to plot the dispersion curves accordingly. Thus, in the next sections of the chapter, the timber will be considered as a solid material.

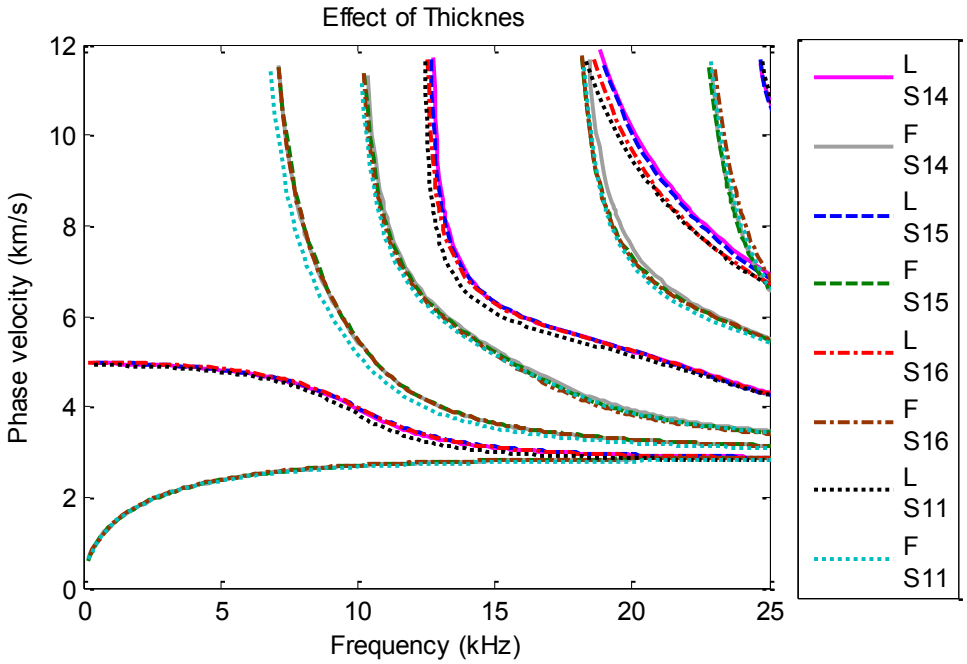

Figure 3.4 Comparison of phase velocities among sets 14 to 16 and 11 to show the effect of thickness of sapwood

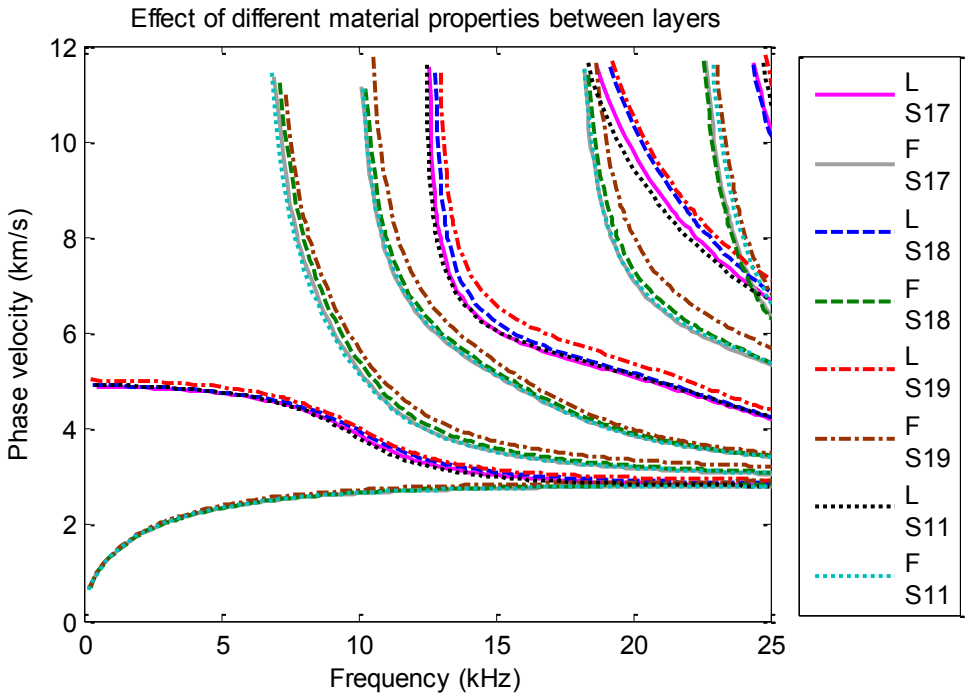

Figure 3.5 Comparison of phase velocities among sets 17 to 19 and 11 to show the effect of difference of material properties between heartwood and sapwood

3.4.1.4 Effect of temperature and moisture content

Figure 3.6 depicts the effect on phase velocity of a solid isotropic timber pole due to various values of moduli of elasticity. Modulus of elasticity of a timber pole may

decrease due to increase in temperature and *MC*. In the figure, variation of phase velocity due to '*E*' is demonstrated at frequency of 1 kHz and 4 kHz. For example, if the modulus of elasticity in a dry timber pole is 19 GPa, then such modulus at 5°C with a *MC* of 10% will drop to 14 GPa (calculated by Equations (2.3) and (2.4)). As a result the phase velocity of *F (1,1)* mode reduces by 8.7% and 11.16% at 1 kHz and 4 kHz, respectively. The reduction in phase velocity for *L (0,1)* mode at 1 kHz and 4 kHz is 14.3% and 15.16%, respectively. It can, therefore, be concluded that longitudinal wave velocity is affected more by temperature and *MC* compared to bending wave velocity. Moreover, reduction in phase velocity also increases at higher frequency for the same temperature and moisture content.

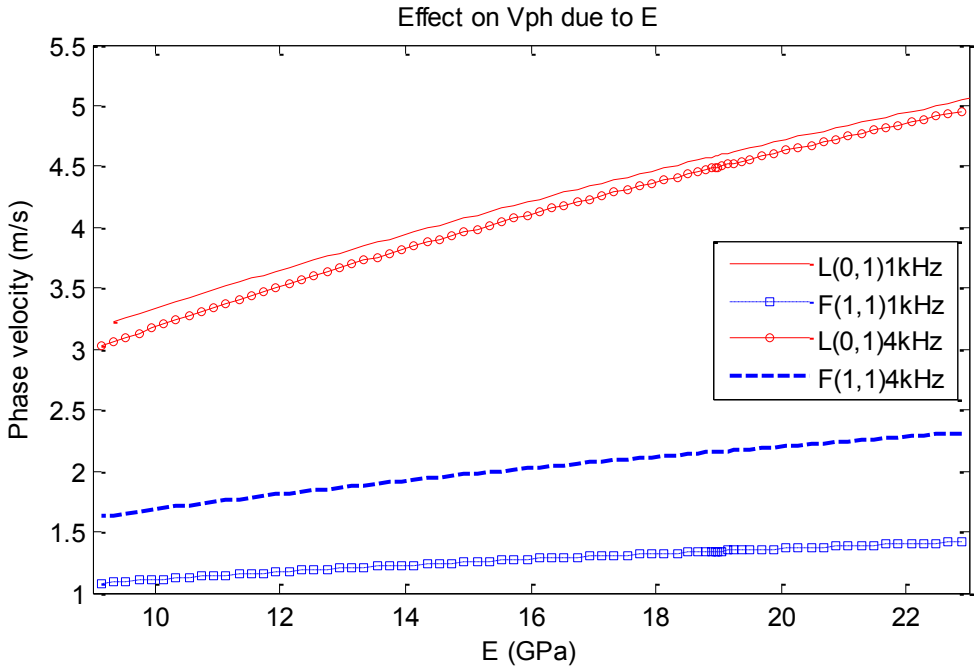

Figure 3.6 Effect of temperature and moisture content on phase velocity

3.4.1.5 Effect of radius

As timber is a natural material, the diameter of it can be varied. Usually the common diameter of timber poles is in between 250 to 350 mm. To analyse the effect of diameter, the material properties used are the same as set 11 with diameters of 250, 300 and 350 mm. Figure 3.7 shows the effect of diameter on phase velocity curves. According to the figure, the frequency range which is corresponding to the constant phase velocity of L(0,1) branch reduced with the increase in diameter. The F(1,1)

branch is affected very little within the range of 250 to 350 mm diameter. However, the shift of cut-off frequency is observed for the higher order branches in both longitudinal and flexural waves. Therefore, fewer numbers of branches can be seen with the reduction of diameter. In the field tests, the diameter can be determined easily from the circumference of the pole and thus the appropriate dispersion curve can be selected.

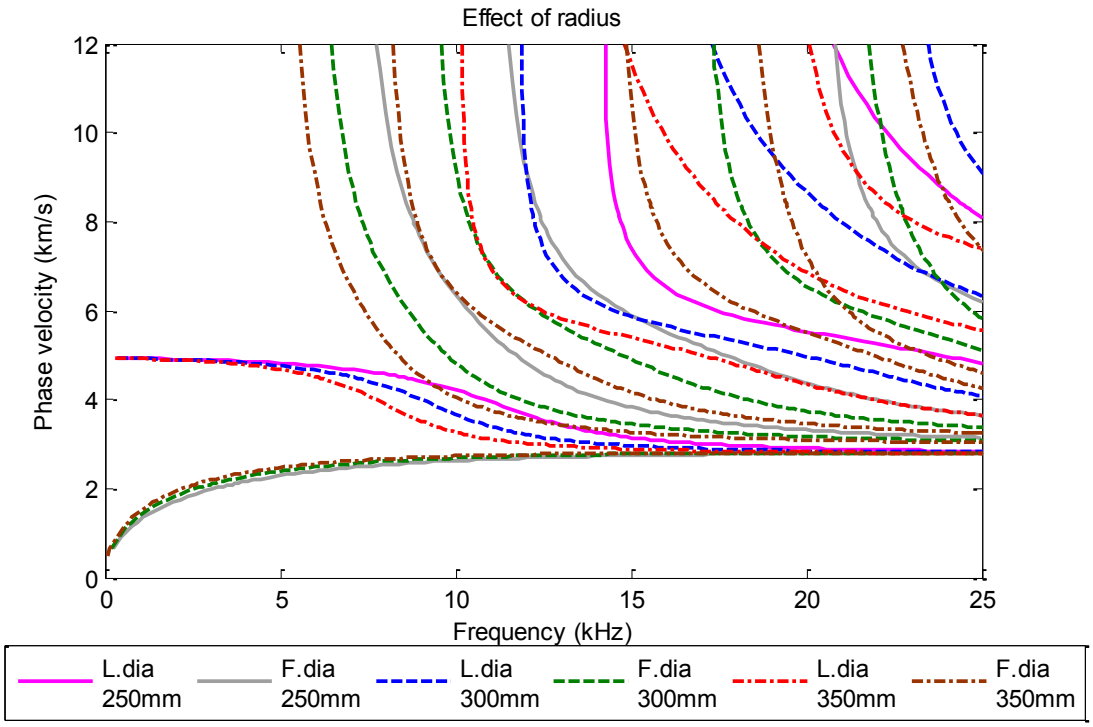

Figure 3.7 Effect of diameter of the timber pole on phase velocity

3.4.1.6 Group velocity and wavelength

In numerous NDTs, impact is induced by manual impact. Manual impact contains broadband frequency and it is usually in the low frequency range (usually up to 1-5 kHz). From the dispersive curves, it is clear that in this range, only the fundamental branches are present and the longitudinal wave velocity can be considered as constant, whereas bending wave is highly dispersive in low frequency. Usually, some signal processing techniques (such as, Short kernel method, Continuous wavelet transform, etc.) are used to determine the bending wave velocity. By using these signal processing techniques, frequency dependent velocities are usually determined for broadband

frequency band and hence, the measured velocities have to be compared with phase velocity curves.

Narrow band frequency input is also used in numerous cases, especially to generate consistent impact. Also, narrow band frequency can be generated in high frequency and is able to determine smaller damages due to its short wavelength. As input frequency is known in this case, therefore, the measured velocity from the experiment/field has to be compared with group velocity curve.

Figure 3.8 denotes the group velocity curve of set 11. The group velocity curve has great importance for choosing the input frequency. As illustrated in Figure 3.8, every branch has a maximum peak group velocity except the fundamental branches (L(0,1) and F(1,1)). While dealing with narrow band frequency, it is better to choose the input frequency which contains the maximum peak group velocity. For example, the F(0,3) branch has a maximum group velocity within the frequency range of 12.7 to 13.5 kHz. If the input frequency is chosen to be in this range, then less dispersion will be observed in the signal. The maximum dispersion will occur at the point of intersection between two branches [141]. Such as, at approximately 10 kHz, where F(0,2) and F(0,3) branch intersects, will have the most amount of dispersion. Therefore, it is better to analyse the group velocity curve to deal with the least possible amount of dispersion.

Figure 3.9 displays the wavelength curve of set 11 versus to frequency. Wavelength reflects the size of damage which can be determined from a chosen input frequency. That is, if the impact is made manually, the usual frequency range is within 1 to 7 kHz. In this range, it is clear from the figure that the damage size of 35 to 80 cm can only be determined if flexural wave is generated. It can also be noted that the fundamental longitudinal branch (L(0,1)) has longer wavelength compared to the F(1,1) branch. As a result, if longitudinal waves are generated in low frequency, damage size of only 60 cm to 1.7 m can be detected. Therefore, input frequency should be chosen based on the size of damage which is needed to be detected.

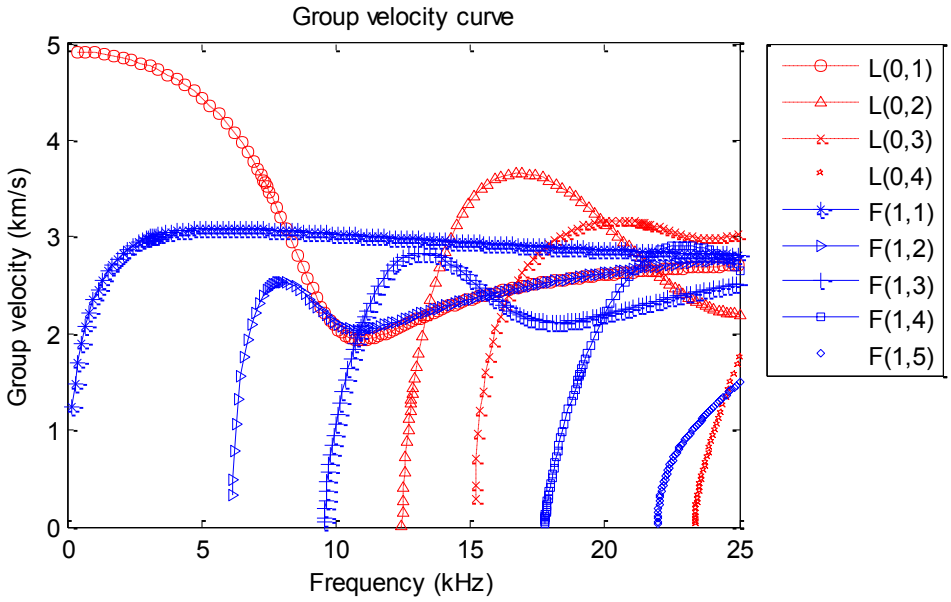

Figure 3.8 Group velocity curve of set 11

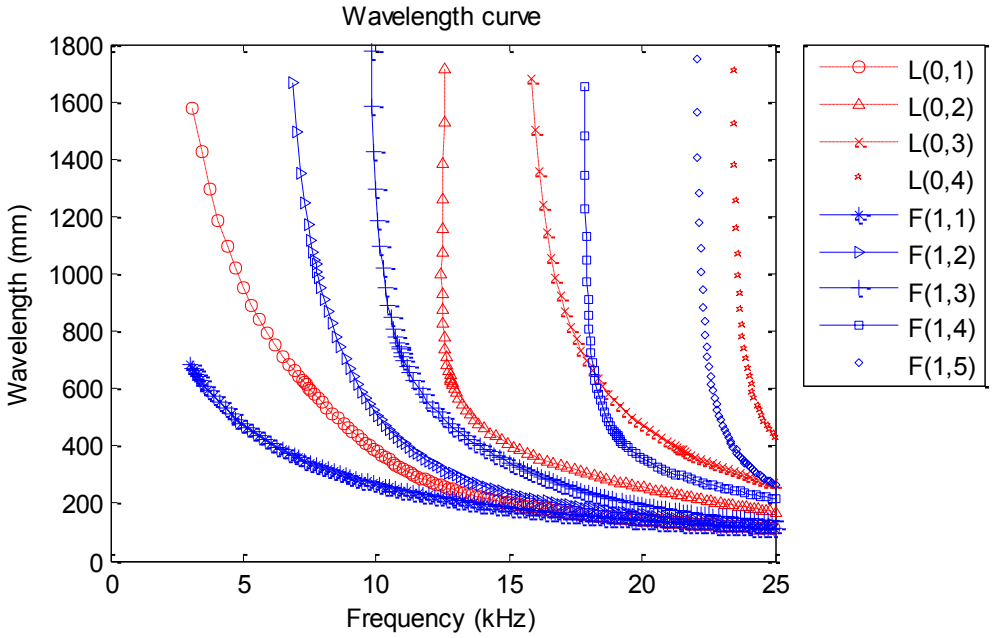

Figure 3.9 Wavelength of set 11 versus frequency

3.4.2 Embedded condition

In this section, timber is considered as embedded in soil. As timber pole is partially embedded in soil, it is important to study the effect of soil on wave propagation. However, it is not possible to model the timber partially embedded in soil while trying to solve the analytical equation. Therefore, it is considered that the timber is surrounded by soil. The effect of soil can be summarised in mainly two categories, i.e. the effect of soil on velocity and on attenuation. In this study, the dispersion curves for embedded situation are compared with traction free condition. The diameter of the timber pole is considered as 286 mm and soil is presented as half space or infinite media.

The connection between soil and timber material plays an important role to generate the dispersion curves. The connection can be rigid or can be illustrated by a spring-dashpot system. In this project, a rigid connection is employed due to the fact that the slip or gap between soil and the timber is negligible because of the low strain produced by the impact hammer. Therefore, the displacement or strain on the timber-soil interface can be considered to be the same. As a result, rigid connection can be justified.

Table 3.6 represents the material properties of soil and timber pole. The effect of different stiffness of soil is also illustrated in the study to indicate its influence on velocity and attenuation. In addition, the displacement profile along the radius of the pole is also reported. The material properties of different kinds of soil are selected based on the guidelines provided in [9, 142, 143].

Table 3.6 Properties of timber and soil used in the analysis of dispersion curves for embedded condition

Properties	Timber	Soil 1	Soft soil	Dense soil
E (GPa)	23	0.25	0.1	0.26
ρ (kg/m^3)	950	1700	1400	1800
v	0.3	0.3	0.3	0.3

3.4.2.1 Comparison of velocity curves between traction free and embedded condition

Figure 3.10 and Figure 3.11 compare the phase and group velocity plots, respectively, of isotropic solid timber poles considering traction free and embedded conditions. The material properties of timber and soil 1 are considered in this study (Table 3.6). As

indicated in the figures, phase velocity remains unaffected by the surrounding soil (except at very low frequency of the first two fundamental branches, L(0,1) and F(1,1)). The reason is that the real part of wavenumber for both traction free and embedded cases is not affected significantly by the density or shear modulus of the surrounding medium [9, 10, 12]. However, in the embedded situation, imaginary part of the wavenumber has a large value and causes attenuation (Section 3.2.3). As group velocity represents the propagation of energy and attenuation presents in the embedded structure, hence, infinite value of group velocity is observed at cut-off frequency where infinite value of attenuation is noted (Section 3.2.3.2). Thus, Equation (3.17) is no longer valid to calculate the group velocity for high attenuation cases. For GW propagation in embedded timber pole, attenuation is high due to the fact that timber soil interaction is considered to be rigid in the analysis; hence leakage of the energy in the surrounding medium is high. Accordingly, Equation (3.24) can be used to determine the energy velocity and Figure 3.12 displays the energy velocity of a timber pole in the embedded situation which is also compared with traction free condition (where group and energy velocity is the same). From both figures (Figure 3.10 and Figure 3.12), it can be concluded that wave velocity is not affected by the surrounding medium except in very low frequencies. For example, phase velocity is affected by soil below 2 kHz and energy velocity is reduced below 4 kHz due to embedment.

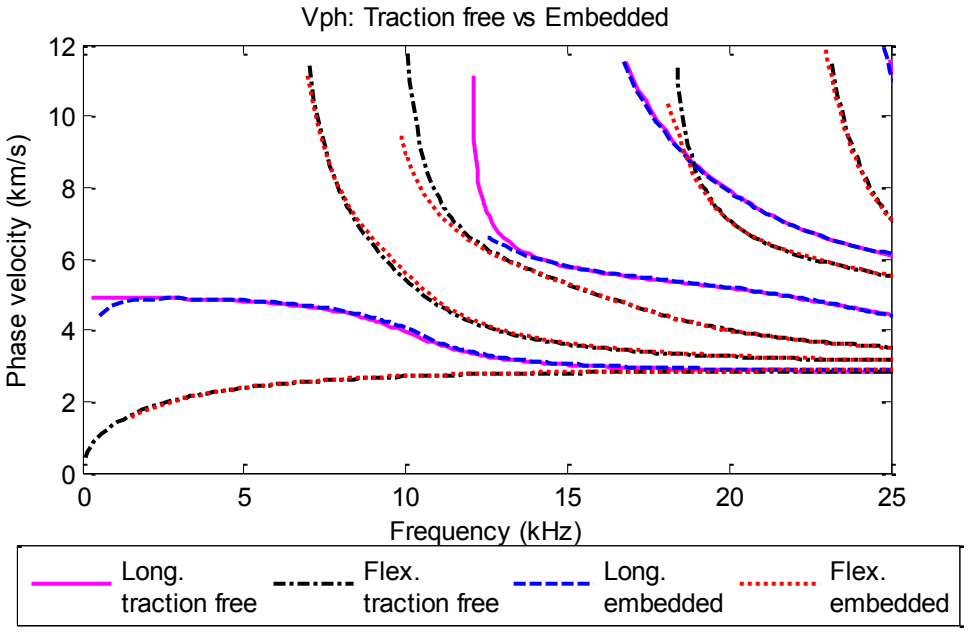

Figure 3.10 Comparison of phase velocity curves between traction free and embedded condition

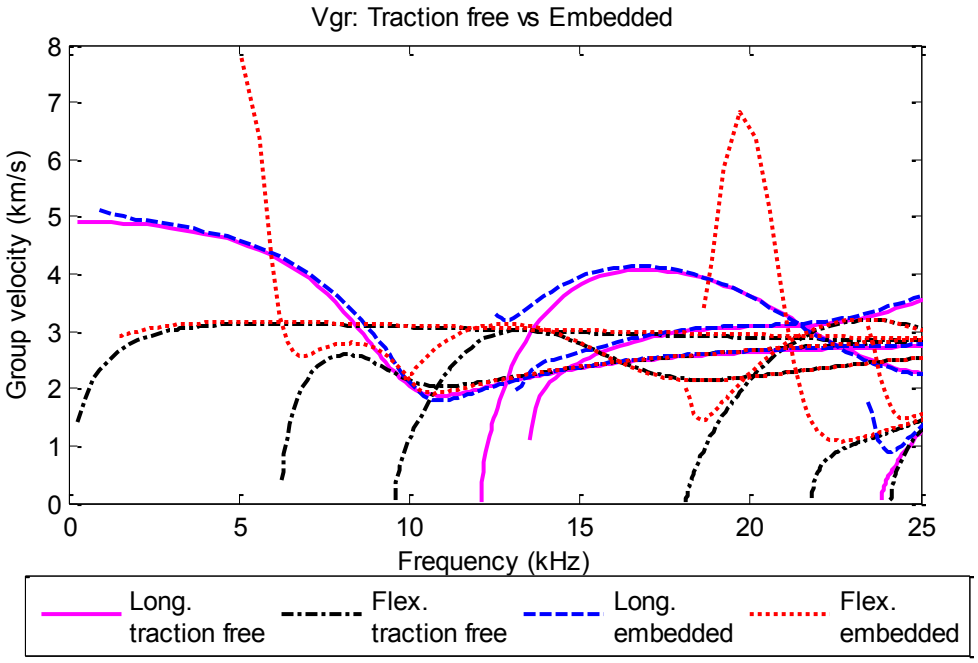

Figure 3.11 Comparison of group velocity curves between traction free and embedded condition

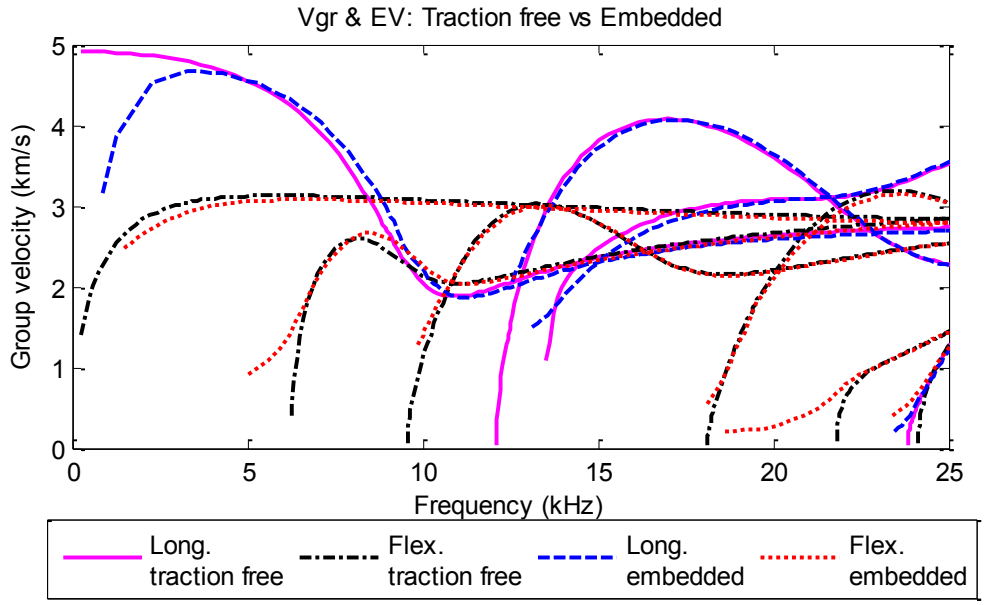

Figure 3.12 Comparison of energy velocity curves between traction free and embedded condition

3.4.2.2 Attenuation curves

Figure 3.13 depicts the attenuation curves of soil 1 (Table 3.6). It is clear from the figure that attenuation is high at cut-off frequency as mentioned in the earlier section. For higher order branches, attenuation decreases from the cut-off frequencies and reaches a local minimum around the frequency corresponding to energy velocity (Figure 3.12). It can also be seen that in the low frequency range (related to the frequency band induced by hammer impact), flexural wave has more attenuation compared to longitudinal wave velocity. Nevertheless, at high frequency no particular trends are observed.

Not all modes present in the dispersive curves are necessarily showing attenuation. The projection of the wave along the interface must match with the guided wave and the bulk wave of the surrounding media. The leakage angle (α_{leak}) of the wave in the surrounding media can be expressed by

$$\alpha_{leak} = \sin^{-1}\left(\frac{V_{soil}}{V_{ph}}\right) \tag{3.38}$$

where V_{soil} is the bulk wave velocity of soil (bulk longitudinal or bulk shear wave) which can be calculated from Equation (3.2) and (3.3) and V_{ph} is the phase velocity of guided wave in timber [130].

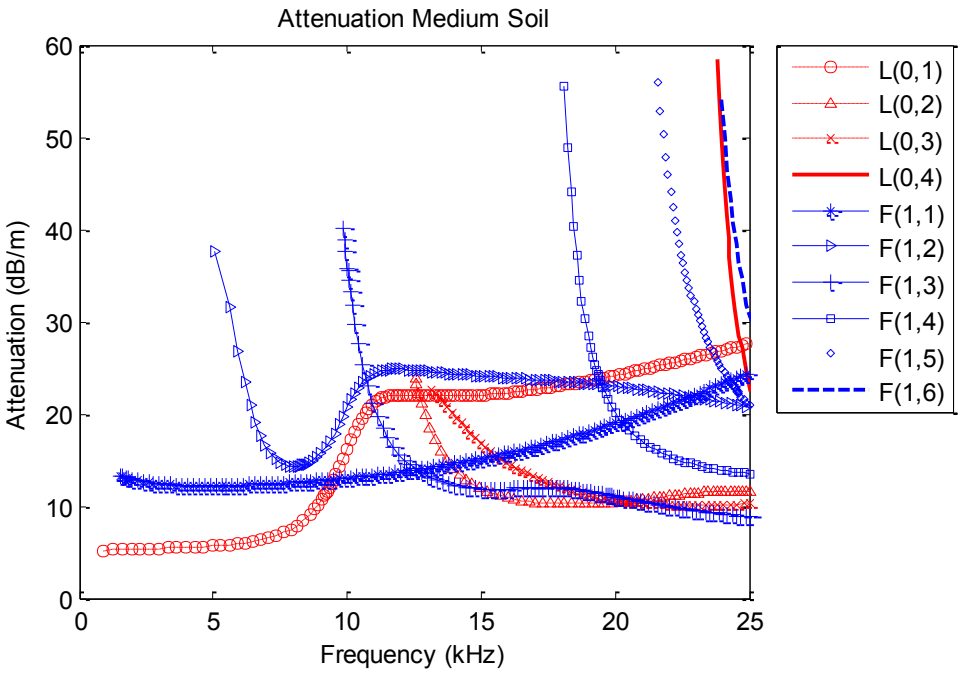

Figure 3.13 Attenuation curve of soil 1

Thus, if the phase velocity of the guided wave is less than the bulk wave velocity in the surrounding medium, then the leakage angle will be imaginary (Equation 3.38), i.e. instead of generating a wave propagating away from the pole, the displacements are damped down exponentially and the energy is trapped in the region of the pole adjacent to the soil. Therefore, the pole will leak only shear wave if the phase velocity is above the bulk shear wave velocity of the surrounding medium. On the other hand, if the phase velocity is greater than the bulk longitudinal wave velocity of the surrounding medium, the pole will leak both shear and longitudinal waves.

3.4.2.3 Effect of soil properties

Figure 3.14 compares the phase velocity curves among the traction free timber pole, pole embedded in soft soil and dense soil. Similar to the previous section, it can be noted that the phase velocity does not change due to the surrounding soil properties except in very low frequency band. In the very low frequency band, the reduction of phase velocity is more for dense soil compared to the soft one (Figure 3.15, zoomed portion of Figure 3.14). Additionally, the phase velocities of timber pole embedded in soft and dense soil converge to the phase velocity of traction free condition at the frequency of 1.8 kHz and 2.6 kHz respectively. For dense soil, it can be seen that the reduction of phase velocity is almost 11 and 5% at the frequency of 500 and 1000 Hz, respectively. Subsequently, in the hammer impact test (inducing low frequency components), the reduction of phase velocity may be observed. The flexural fundamental branch is not affected significantly by the surrounding soil parameter.

Figure 3.16 shows the energy velocity curve up to 5 kHz. Similar to the phase velocity curve, no effect of soil can be identified on energy velocity at high frequencies. Compared to phase velocity curves, energy velocities are affected more at low frequencies. In a dense soil, the reduction of energy velocity is approximately 50, 30 and 12% at the frequency of 500, 1000 and 2000 Hz, respectively. Slight reduction of energy velocity corresponding to fundamental flexural branch can be seen with a value of 7% at the frequency of 1.5 kHz.

Figure 3.17 and Figure 3.18 illustrate the attenuation curve of soft and dense soil, respectively. Clearly, attenuation curves are affected by the soil parameter to a great extent. Attenuation increases with the increase of the stiffness of soil. Consequently, in

case of high attenuation, the reflection from the bottom of the pole, to calculate the embedded length, may not be captured by the accelerometers. Furthermore, if high frequency band is induced, it will excite multi modes and the sensors or accelerometers will most probably capture the mode with lowest attenuation and highest value of displacement on the surface of the pole at particular frequency [144]. The displacement profile will be discussed in Section 3.4.2.5.

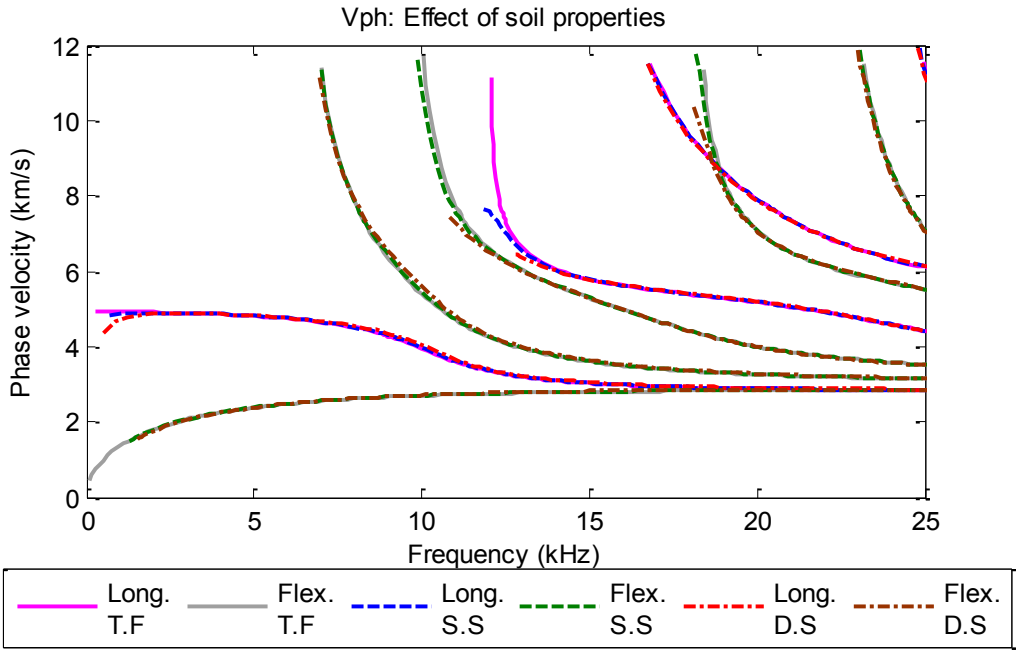

Figure 3.14 Effect of soil parameter on phase velocity (T.F = Traction Free, S.S = Soft Soil, D.S = Dense Soil)

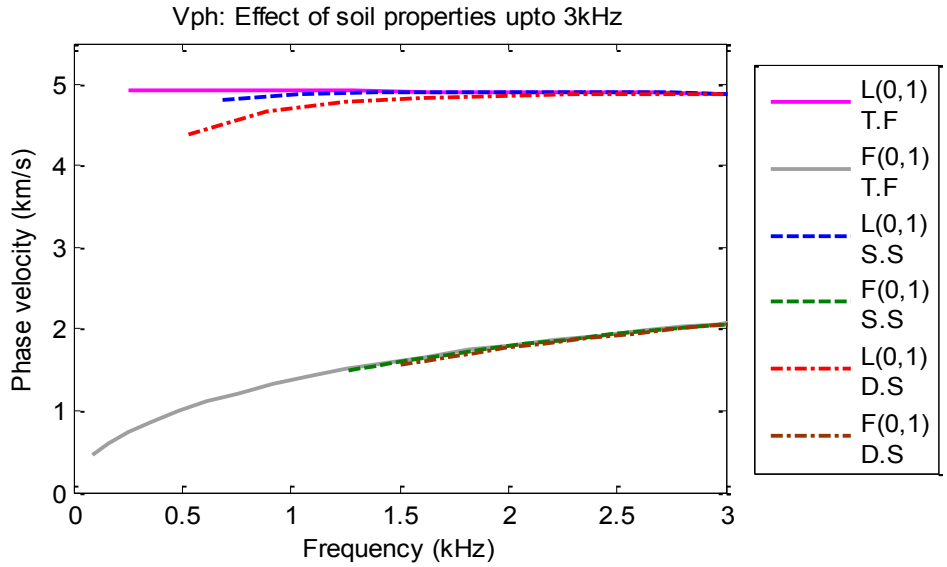

Figure 3.15 Up to 3 kHz of Figure 3.14

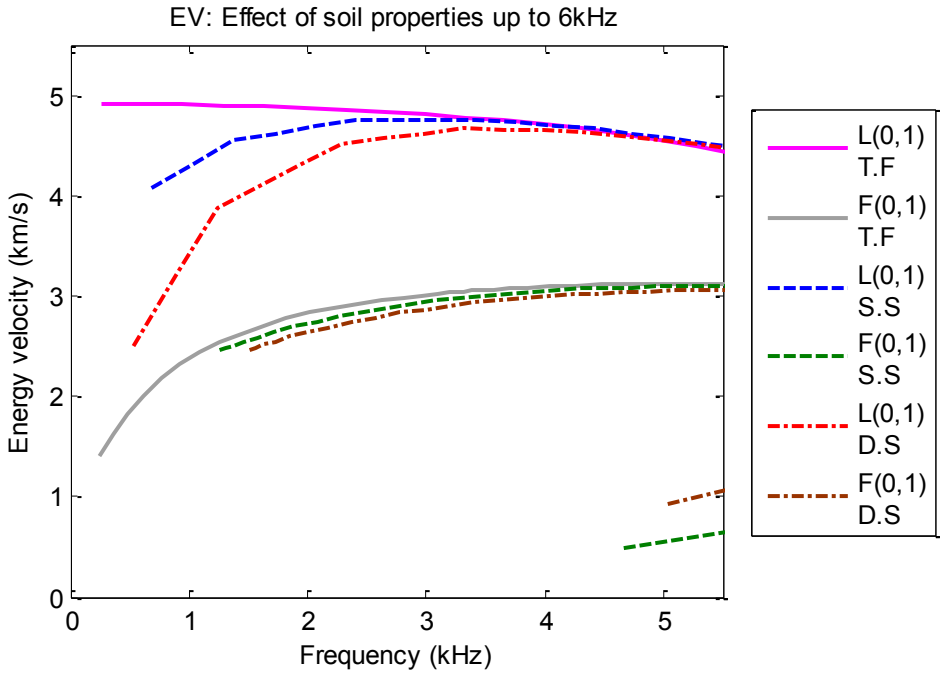

Figure 3.16 Effect of soil parameter on energy velocity (T.F = Traction Free, S.S = Soft Soil, D.S = Dense Soil)

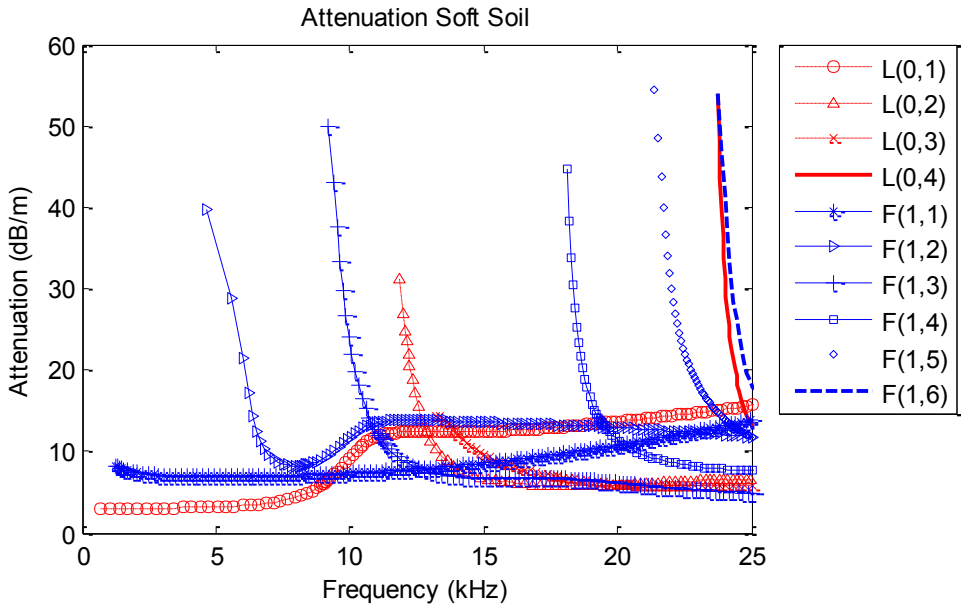

Figure 3.17 Attenuation curves of soft soil

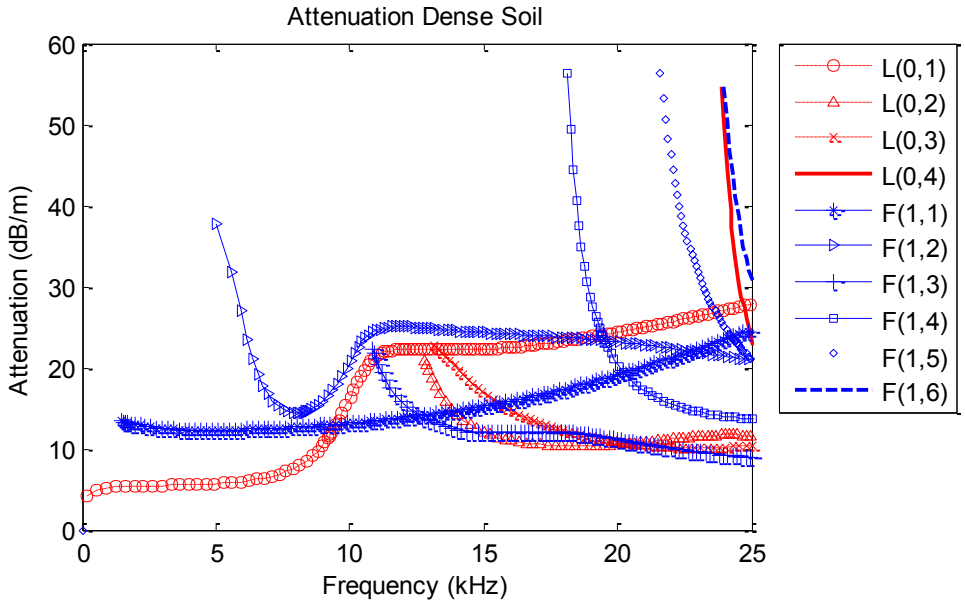

Figure 3.18 Attenuation curves of dense soil

3.4.2.4 Normalised power flow

Power flow expresses the travelling of energy, in other words, it represents the energy velocity peaks throughout the radius of the pole. Figure 3.19 to Figure 3.31 display the normalised power flow for traction free condition and Figure 3.32 to Figure 3.40 represent the same for embedded situation. Power flow is shown from the neutral axis to the surface of the pole along the radius. For embedded condition, the power flow in the half space is also illustrated up to the adjacent 150 mm of timber pole. A solid line indicates the interface of timber and soil for the embedded situation. The power flow of the longitudinal wave is symmetrical and for flexural wave it is anti-symmetrical.

In low frequency, the energy is almost evenly distributed along the radius of the pole or maximum energy is flowing along the surface (Figure 3.19 and Figure 3.24). The power flow is elucidated at the frequency of 3 kHz and only fundamental branches can be seen within this range. From Figure 3.19 to Figure 3.23, it is also clear that only axial power flow exists in longitudinal branches, i.e. in the case of the generation of longitudinal wave, the energy will flow only in the axial direction. In contrast, angular power flow also exists in flexural wave in addition to the axial power flow (Figure 3.24 to Figure 3.31). Hence, at the impact location or at r-z plane (where $\theta = 0°$), pure vertical shear movement can be seen (no angular component of displacement). In contrast, due to the energy flow in the circumferential direction, angular component of displacement can be

observed where $0° < \theta < 180°$ and $180° < \theta < 360°$. In traction free condition, no power flow is identified along the radial direction of the pole.

In particular, local maxima and minima occur along the radius of the pole in higher branches. For example, local maxima or minima can be observed at 120 mm from neutral axis (N.A) in L(0,2) mode at 20 kHz (Figure 3.22), at 100 mm from N.A in L(0,1) mode at 20 kHz (Figure 3.21), at 50 mm from N.A in F(1,4) mode at 20 kHz (Figure 3.31) etc. It is also important to note that some modes may have zero or much less power flow on the surface of the pole. Such as, axial power flow (P_r) of L(0,1) mode at 10 kHz (Figure 3.20), P_r of L(0,3) mode at 20 kHz (Figure 3.23), both axial and circumferential power flow of F(1,3) mode at 20 kHz (Figure 3.30), etc. The modes with zero or less amount of power flow on the surface of the pole may not be captured by the accelerometers, as sensors are mounted on the surface of the pole. Furthermore, displacement at some particular direction may not be prominent enough to be captured by the accelerometer. For example, the sensors oriented in the tangential direction may not be able to show the presence of F(1,4) mode at 20 kHz (Figure 3.31) as the power flow in the tangential direction is lower than the axial power flow. Therefore, in this situation, it is better to attach the sensor in the axial direction if F(1,4) mode is essential to capture at 20 kHz. In contrast, accelerometers in the tangential direction can successfully capture the presence of F(1,3) mode at 10 kHz (Figure 3.29) due to its high energy on the surface.

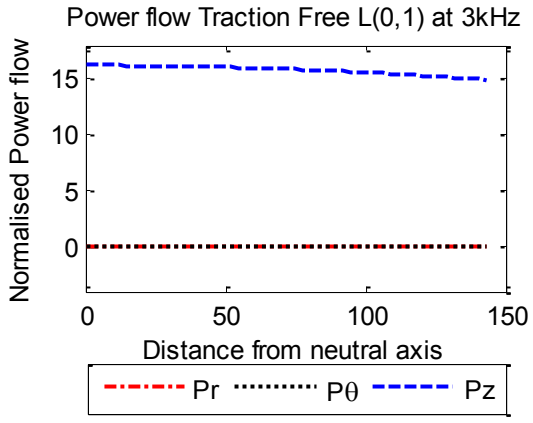

Figure 3.19 Power flow of L(0,1) at 3 kHz (traction free)

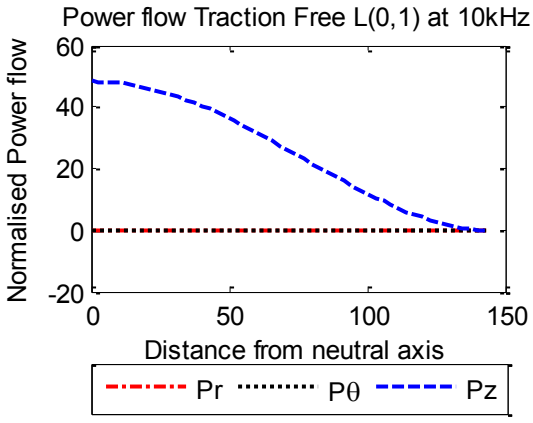

Figure 3.20 Power flow of L(0,1) at 10 kHz (traction free)

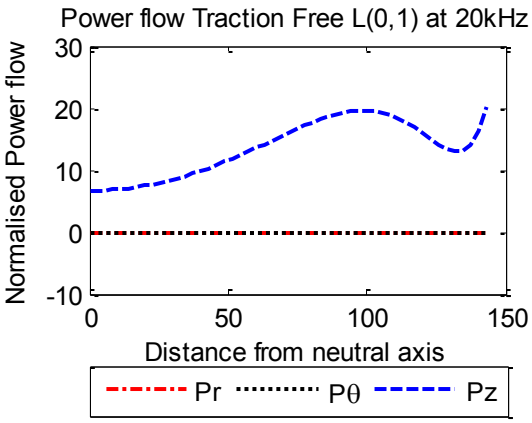

Figure 3.21 Power flow of L(0,1) at 20 kHz (traction free)

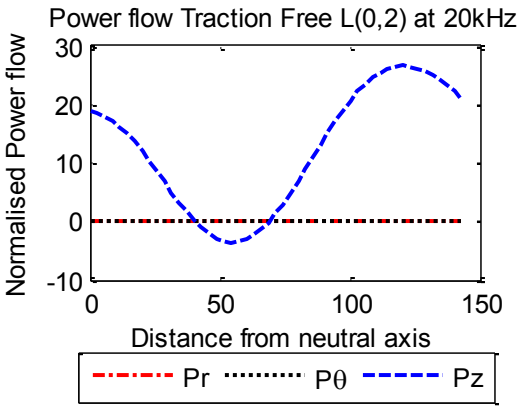

Figure 3.22 Power flow of L(0,2) at 20 kHz (traction free)

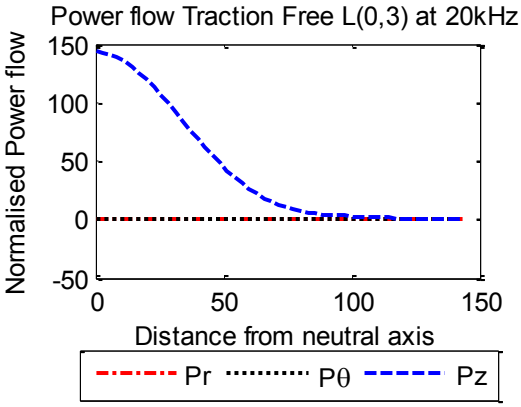

Figure 3.23 Power flow of L(0,3) at 20 kHz (traction free)

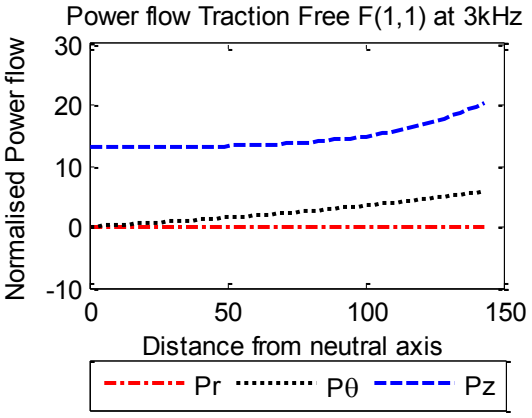

Figure 3.24 Power flow of F(1,1) at 3 kHz (traction free)

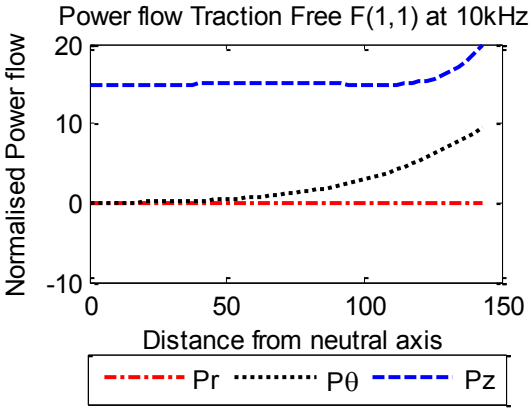

Figure 3.25 Power flow of F(1,1) at 10 kHz (traction free)

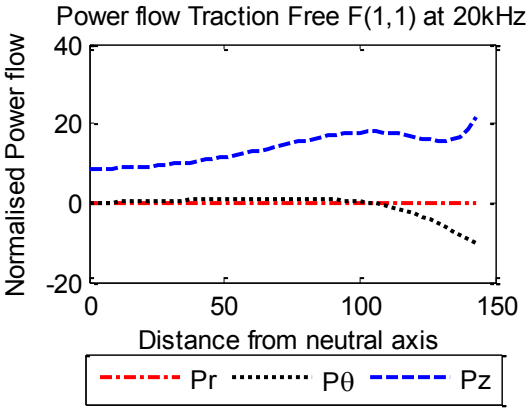

Figure 3.26 Power flow of F(1,1) at 20 kHz (traction free)

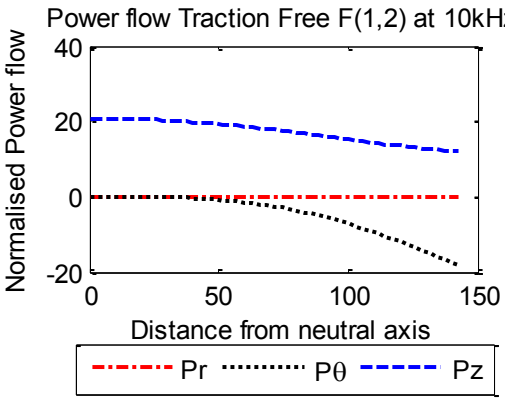

Figure 3.27 Power flow of F(1,2) at 10 kHz (traction free)

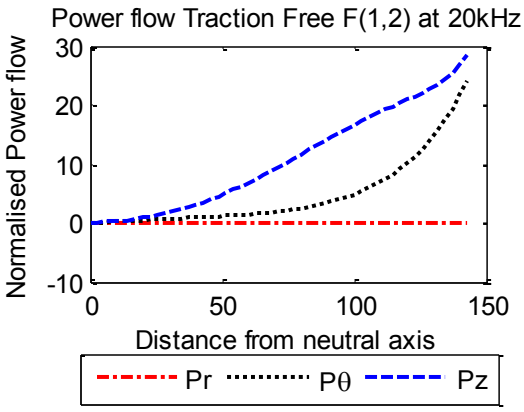

Figure 3.28 Power flow of F(1,2) at 20 kHz (traction free)

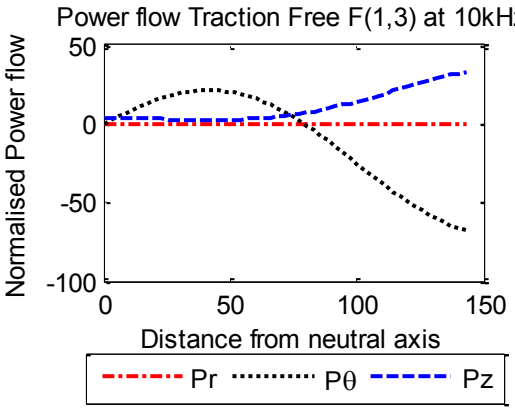

Figure 3.29 Power flow of F(1,3) at 10 kHz (traction free)

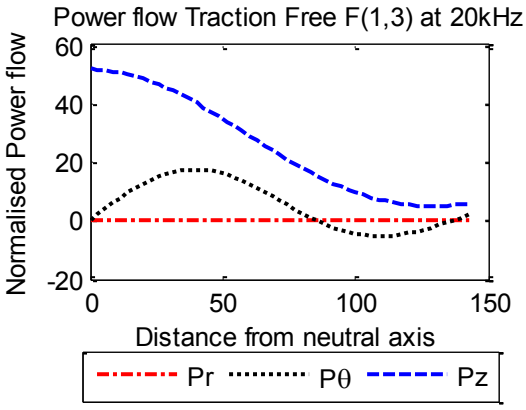

Figure 3.30 Power flow of F(1,3) at 20 kHz (traction free)

It is well established that radial power flow exists for the embedded condition which is an indication of attenuation or damping [51, 130] and can be seen in Figure 3.32 to Figure 3.40 where the timber pole is surrounded by soil. From these figures, it can be observed that radial power flow in the half space (in this case, it is soil) is more comparable to the axial or tangential power flow in the soil. Therefore, if the radial power flow increases then the attenuation will increase. As expected, the power flow inside the pole is the same as traction free pole except for the presence of the radial flow. Since, flexural wave propagation in an embedded medium has axial, radial and tangential power flows, therefore, bending wave usually loses more energy than longitudinal wave. The power flow of L(0,2) mode at 20 kHz, F(1,2) and F(1,3) mode at 10 kHz and F(1,4) mode at 20 kHz are presented in Appendix B.

Power flow expresses the concentration of energy along the radius of the pole. Hence, the mode with high attenuation and those with local maxima inside the pole cannot

possibly be detected by the sensors on the surface of the structure. Therefore, in wave based NDTs, power flow can help to understand the possible wave modes present in the signals captured by the sensors. Velocity curves can also help to determine the wave mode. However, if the velocity of some wave modes at certain frequencies is almost the same, power flow can be utilised to recognise the presence of the possible wave mode.

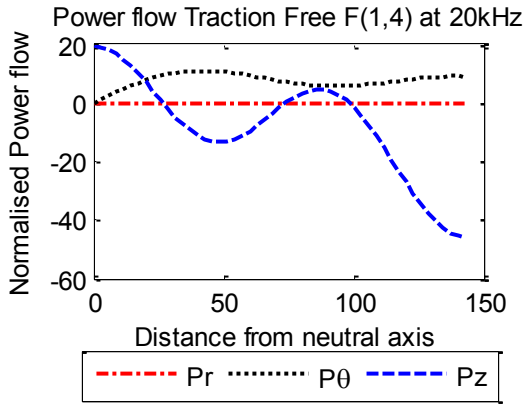

Figure 3.31 Power flow of F(1,4) at 20 kHz (traction free)

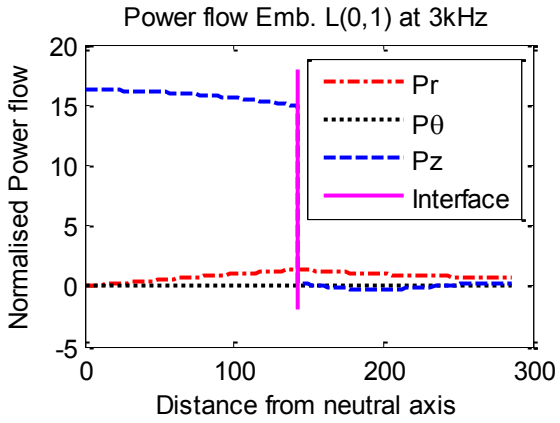

Figure 3.32 Power flow of L(0,1) at 3 kHz (embedded)

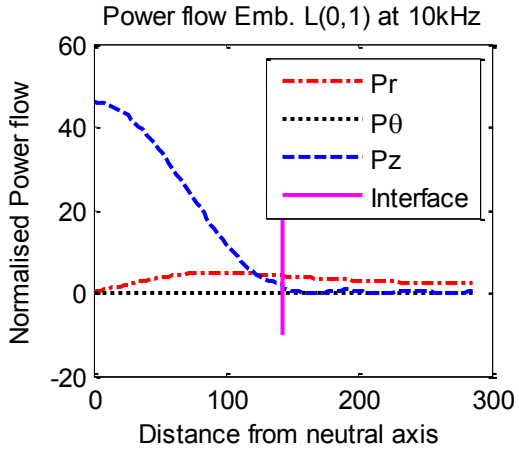

Figure 3.33 Power flow of L(0,1) at 10 kHz (embedded)

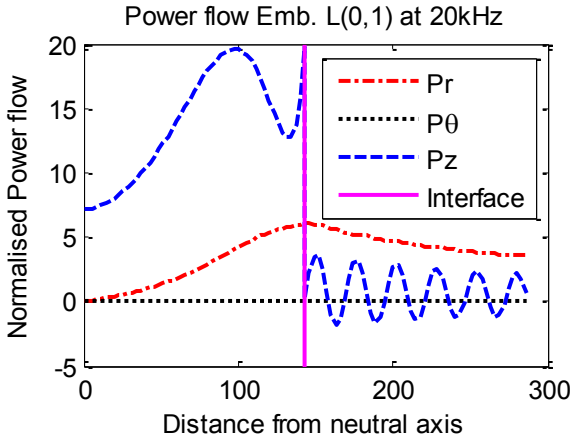

Figure 3.34 Power flow of L(0,1) at 20 kHz (embedded)

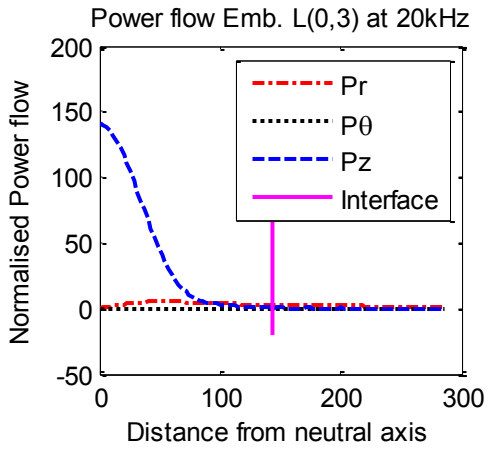

Figure 3.35 Power flow of L(0,3) at 20 kHz (embedded)

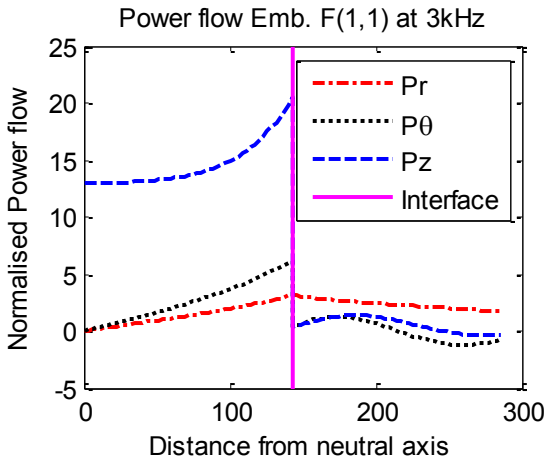

Figure 3.36 Power flow of F(1,1) at 3 kHz (embedded)

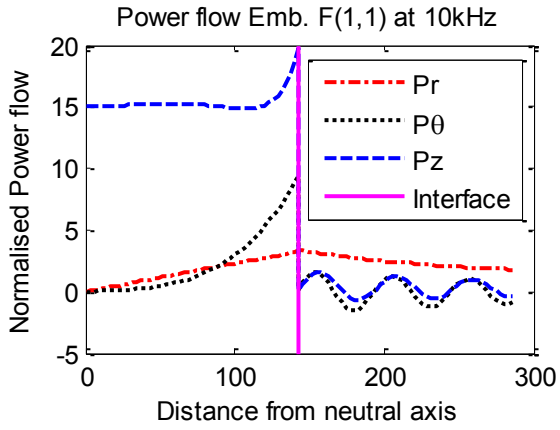

Figure 3.37 Power flow of F(1,1) at 10 kHz (embedded)

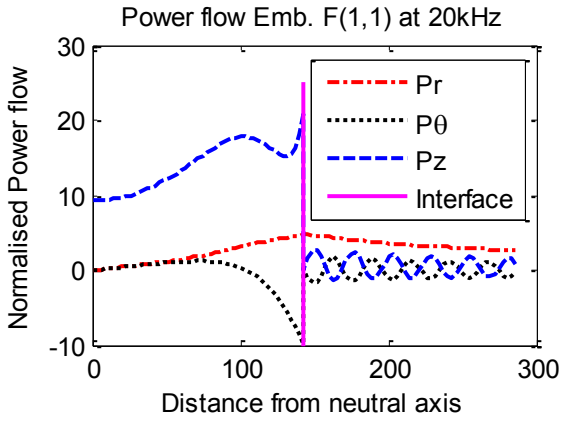

Figure 3.38 Power flow of F(1,1) at 20 kHz (embedded)

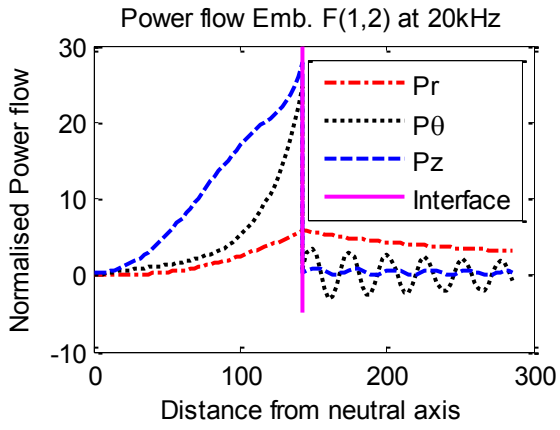

Figure 3.39 Power flow of F(1,2) at 20 kHz (embedded)

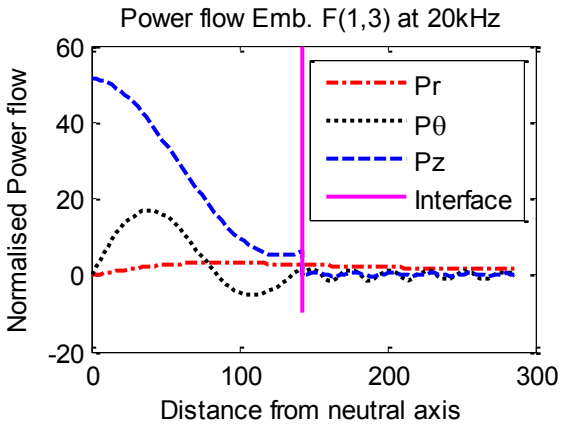

Figure 3.40 Power flow of F(1,3) at 20 kHz (embedded)

3.4.2.5 Normalised displacement

Figure 3.41 to Figure 3.50 depict the normalised displacement profile of different modes for an isotropic traction embedded cylinder while the wave is propagating along the z direction. The displacement profiles for the traction free condition are not presented due to the fact that they are the same as the embedded condition except the displacements on the surrounding soil part. The figures start from the origin or neutral axis (denoted by zero) to the surface/interface (where radius, r = 143 mm). Again, the displacement profile of the first 150 mm of adjacent soil is shown in the figure. A solid line is drawn at the interface between timber and soil.

Even though power flows in the axial direction in longitudinal wave, axial and radial (vertical shear) displacement can be observed in this wave as predicted by Equations 3.18 and 3.20. Similarly, all three components of displacement are observed in the flexural wave where power flows in the axial and tangential direction (Equations 3.18 – 3.20). This is due to the polarization of the wave. It is noteworthy to state that displacement components of flexural wave vary along the circumference of the cylinder. From Equations (3.18 – 3.20) it can be seen that in the r-z plane, where $\theta = 0°$ (can be defined as the impact plane), there is no angular component. In contrast, only angular component is present at $\theta = 90°$. Therefore, it is possible to obtain pure bending wave or longitudinal wave at selected sensor locations and directions along the cylinder and this will be discussed in Chapter 5. Finally, as this is an embedded condition, hence radial power flow also exists and will also contribute to the radial displacement.

From Figure 3.41 to Figure 3.45, it is noticed that angular/tangential component in longitudinal wave is zero as expected whereas flexural wave has all components (Figure 3.46 to Figure 3.50). Axial/longitudinal component of displacement in flexural wave and radial component in longitudinal waves always reach zero at the origin. It is of interest to note that axial components are symmetrical in longitudinal wave and anti-symmetrical in flexural wave. However, the radial components are anti-symmetrical in longitudinal wave and symmetrical in flexural wave. As a result, practically, vertically oriented two sensors (capturing axial displacement) placed 180° apart on a cross section will show the opposite phase for flexural wave but the same phase for longitudinal wave. The opposite is true if the sensors are placed to capture the radial displacement of the wave. The details will be presented in Chapter 5.

Similar to the power flow, displacement profiles are evenly distributed or linearly increasing towards the surface of the pole in low frequency. However, local maxima and minima will occur in the higher order modes (or in high frequency) and also the distributions are no longer linear. Also, for the multi modes propagation, small displacements corresponding to a particular mode on the surface of the pole may not be detected by the sensors. For example, by generating 20 kHz of input frequency, F(1,2) mode (Figure 3.48) may not be detected irrespective of the orientation of the sensors due to the almost zero displacement value of radial, axial and tangential components on the surface of the pole. Additionally, sensors oriented in the longitudinal direction, sensors oriented in the radial direction, sensors mounted in the axial direction, sensors placed in the radial/tangential direction at 20 kHz and sensors attached in the axial direction are better in clearly capturing the modes L(0,1) at 3kHz (Figure 3.41), L(0,1) at 10 kHz (Figure 3.42), L(0,2) at 20 kHz (Figure 3.44), F(1,3) at 20 kHz (Figure 3.49) and F(1,4) at 20 kHz (Figure 3.50), respectively.

From these figures, it can be seen that most of the attenuation is attributed to the amount of radial displacement on the outer surface of the pole. The reason is that radial displacement permits the energy to be coupled from the guided wave into the surrounding medium. The radial displacement in the half space usually increases as the frequency increases and hence the attenuation increases at high frequency. The displacement profile of F(1,1) mode, F(1,2) mode and F(1,3) mode at 10 kHz is presented in Appendix B.

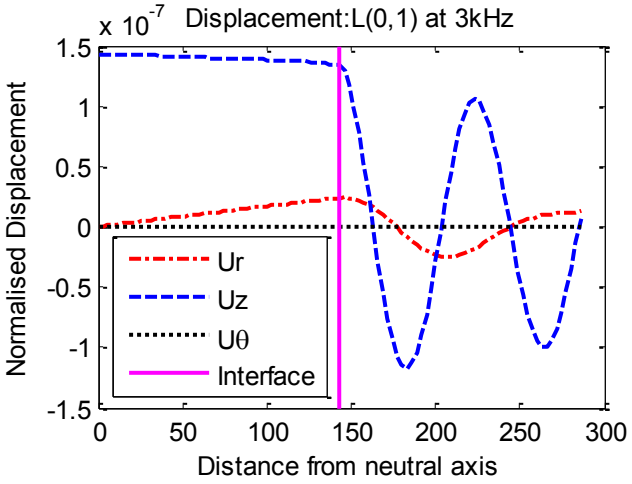

Figure 3.41 Normalised displacement of L(0,1) at 3 kHz (embedded)

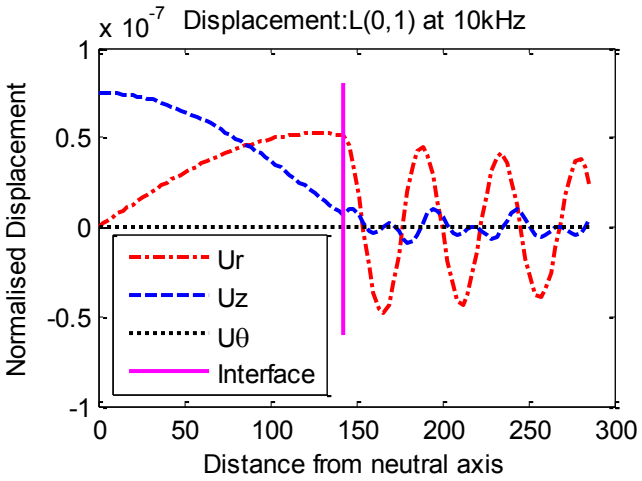

Figure 3.42 Normalised displacement of L(0,1) at 10 kHz (embedded)

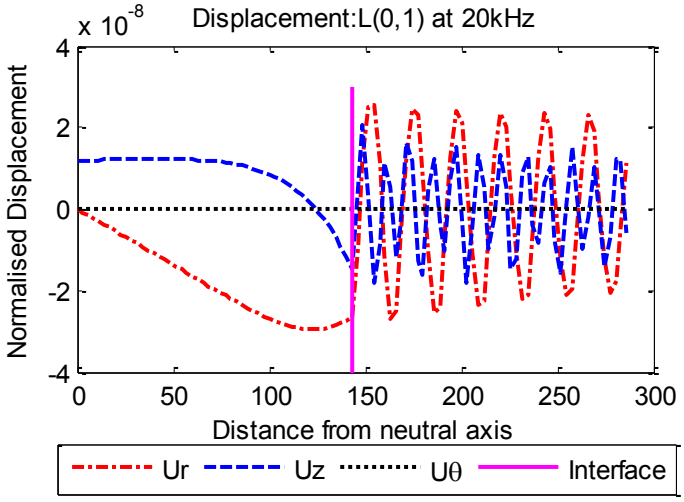

Figure 3.43 Normalised displacement of L(0,1) at 20 kHz (embedded)

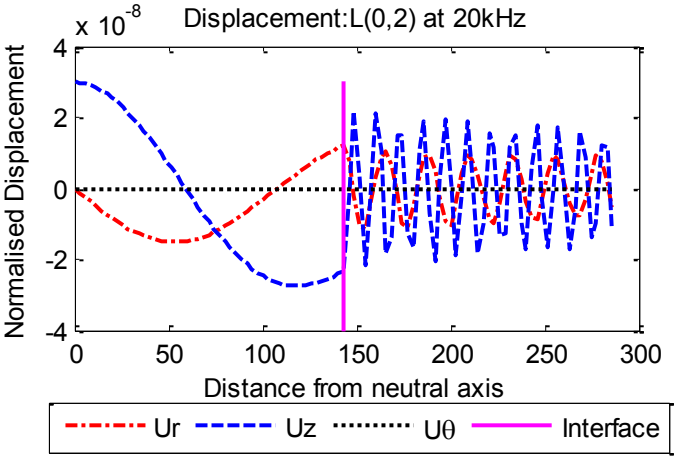

Figure 3.44 Normalised displacement of L(0,2) at 20 kHz (embedded)

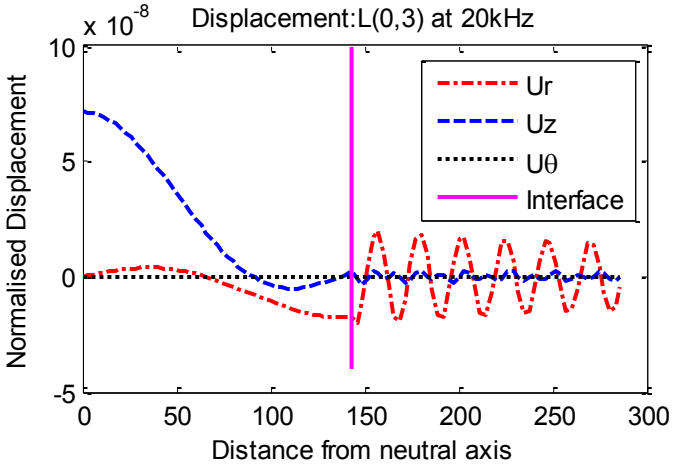

Figure 3.45 Normalised displacement of L(0,3) at 20 kHz (embedded)

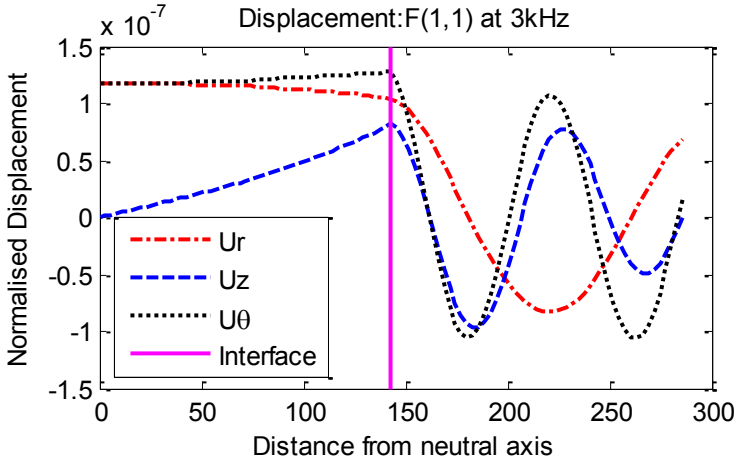

Figure 3.46 Normalised displacement of F(1,1) at 3 kHz (embedded)

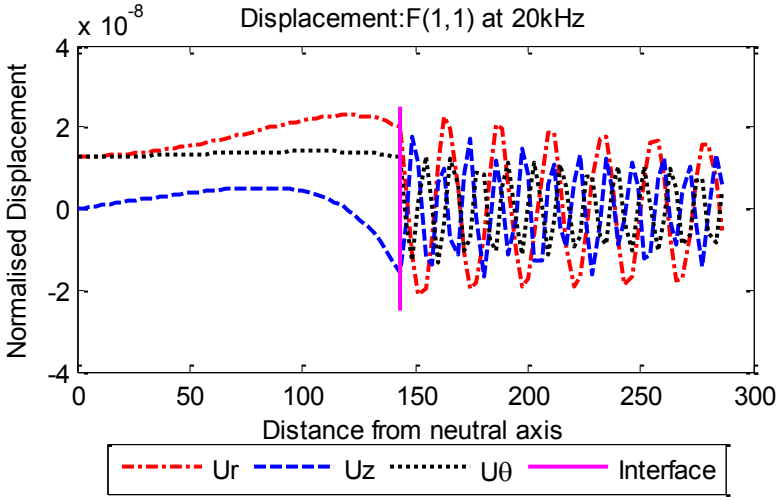

Figure 3.47 Normalised displacement of F(1,1) at 20 kHz (embedded)

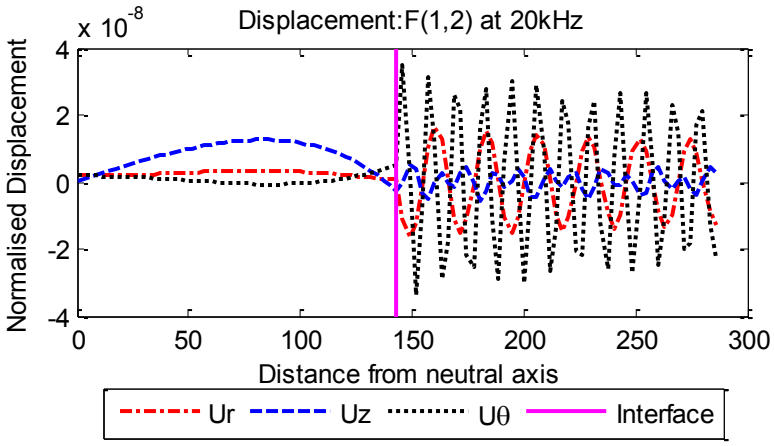

Figure 3.48 Normalised displacement of F(1,2) at 20 kHz (embedded)

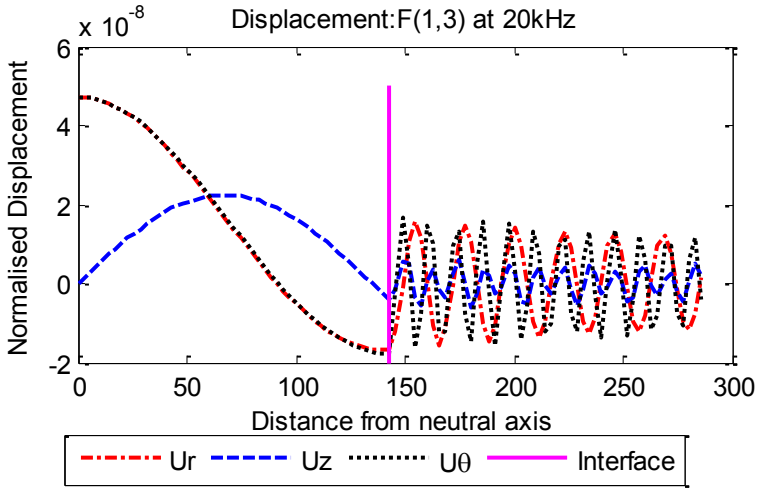

Figure 3.49 Normalised displacement of F(1,3) at 20 kHz (embedded)

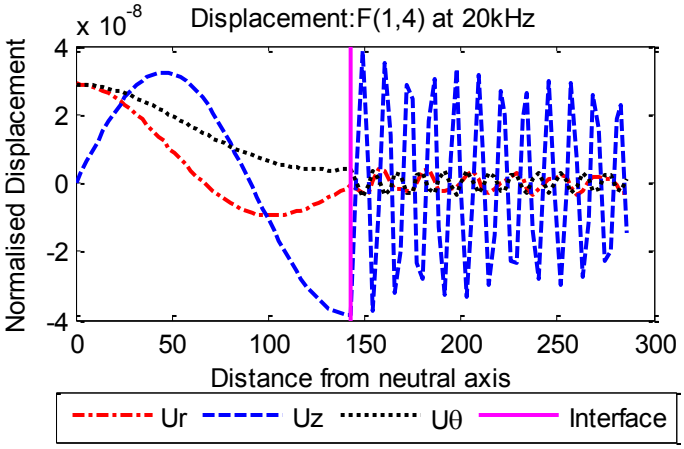

Figure 3.50 Normalised displacement of F(1,4) at 20 kHz (embedded)

For applications of wave based NDTs, the location of sensors should be selected where there is less attenuation and maximum displacement can be seen [144]. Consequently, a

sensor arrangement or sensor network is established from these analyses and will be presented in Chapter 5.

An example can be given here to detect the possible modes from displacement profile, attenuation curve and energy velocity based on excited input frequency and sensor's orientation. Provided that the input frequency is 20 kHz, there are 7 modes observable from the group velocity/attenuation curve in that range, namely L(0,1), L(0,2), L(0,3), F(1,1), F(1,2), F(1,3) and F(1,4). In case of the sensors orientation in the longitudinal direction, it can be predicted from the displacement profile (comparing Figure 3.43 to Figure 3.45) that mainly L(0,1) and L(0,2) will be present if longitudinal wave is generated. Despite this fact, normalised displacement of L(0,1) mode at 20 kHz is much less comparable to the L(0,2) mode at 20 kHz and also the attenuation of L(0,1) at 20 kHz is higher than L(0,2) at that frequency (Figure 3.13). Eventually, depending on the depth of the embedded length, only L(0,2) mode may only be detected by the sensors. For flexural wave propagation at 20 kHz, longitudinally oriented sensors possibly detect the F(1,1) and F(1,4) mode at 20 kHz as displayed in the displacement profile (comparing Figure 3.47 to Figure 3.50). The attenuations of these two modes are almost the same at 20 kHz as illustrated in Figure 3.13. Subsequently, two modes with two different velocities will propagate within the pole and can be seen in the captured sensor data. These velocities can be identified from the energy velocity curve (Figure 3.12) with the values of 2.9 km/s and 2.2 km/s for F(1,1) and F(1,4) modes, respectively.

3.5 Effect of elastic modulus and Poisson's ratio on guided wave dispersion using transversely isotropic material modelling

In this section of the chapter, a comparison will be made between orthotropic and transversely isotropic material to suggest the accuracy of considering timber as transversely isotropic material. As mentioned in Section 3.3.1, an orthotropic material has 9 independent constants, whereas a transversely isotropic material has only 5. Based on the symmetry of the compliance (Equation 3.27) or stiffness matrix (Equation 3.28) and the relations explained in Section 3.3.1, four sets can be formed for transversely isotropic modelling from the elastic constants of orthotropic situation.

Only traction free condition is considered for transversely isotropic case as the effect of soil on velocity can be ignored. First, the comparison is made between isotropic and

orthotropic material to reflect the importance of considering timber as an anisotropic material. The material properties of timber, considering it as an orthotropic material, are given in Table 3.7. The data is selected based on the available literature [38]. The dispersion curves of an isotropic material are obtained with modulus of elasticity = 23 GPa and Poisson's ratio = 0.40. The aforementioned 4 sets of transversely isotropic material properties are presented in Table 3.8. For all cases, the density is 900 kg/m^3 and the radius is considered as 150 mm. It is noted that the dispersion curves for isotropic and transversely isotropic material model is solved by Disperse and compared with the work of Subhani et. al. [129] where SBFEM is employed.

Table 3.7 Material properties used in the analyses of orthotropic material

Properties	E_z [GPa]	E_θ [GPa]	E_r [GPa]	G_{zr} [GPa]	$G_{z\theta}$ [GPa]	$G_{r\theta}$ [GPa]
Values	23	1.177	2.665	2.047	1.403	0.483
Properties	v_{zr}	$v_{z\theta}$	$v_{r\theta}$	$v_{\theta r}$	v_{rz}	$v_{\theta z}$
Values	0.35	0.43	0.7	0.309	0.041	0.022

Table 3.8 Different sets of material properties used in the analyses of transversely isotropic material

Properties	E [GPa]	E_z [GPa]	G [GPa]	v_1	v_2
Set 1	1.177	23	1.403	0.7	0.022
Set 2	1.177	23	1.403	0.309	0.022
Set 3	2.665	23	2.047	0.309	0.041
Set 4	2.665	23	2.047	0.7	0.041

Effect of material modelling

Figure 3.51 and Figure 3.52 display the phase velocity (V_{ph}) curve of an isotropic and orthotropic cylinder, respectively. The difference between these two material modelling is clearly notable from the figures. In isotropic material, 2 longitudinal branches (solid lines) and 3 flexural branches (dashed lines) are present within 15 kHz whereas 3 longitudinal branches (solid lines) and mainly 6 branches of flexural waves (dashed lines) are observed in orthotropic model within 10 kHz. Therefore, it is obvious that timber needs to be considered as an anisotropic material.

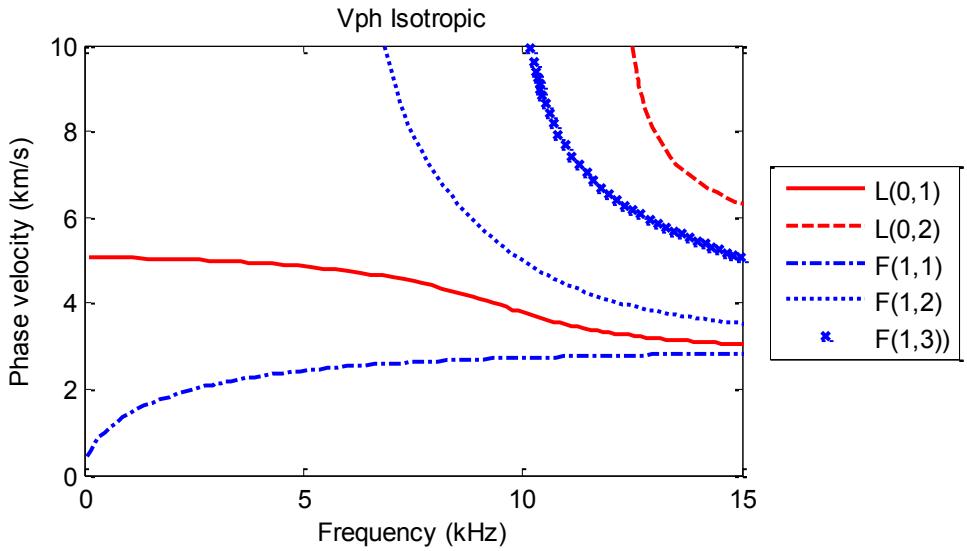

Figure 3.51 Phase velocity curve for isotropic traction free cylinder

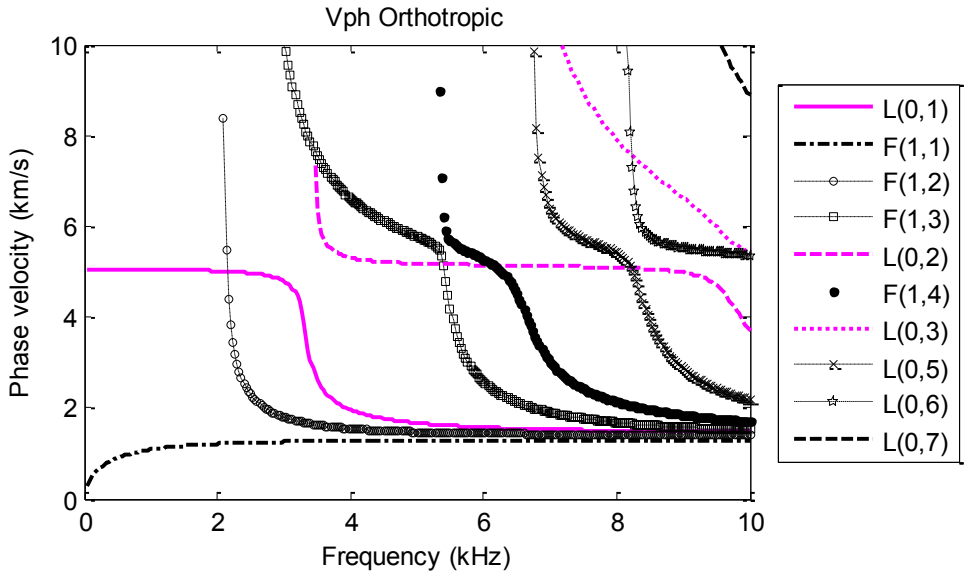

Figure 3.52 Phase velocity curve for orthotropic cylinder [129]

Effect of modulus and Poisson's ratio

Figure 3.53 compares the dispersion curves between sets 1 and 4, while Figure 3.54 shows the same between sets 2 and 3 to show the effect of modulus. Similar trends can be depicted between the two sets in both figures. The constant velocity of L(0,1) is identical up to 2.5 kHz and 2 kHz in Figure 3.53 and Figure 3.54, respectively. In addition, significant similarities can be observed in F(1,1) branches for both sets. For the higher order branches, shifting of the cut-off frequency can be seen from these two figures. Due to shifting of the cut-off frequency, fewer branches can be seen within the

same frequency range. For example, 4 longitudinal branches in sets 2 and 3 branches of longitudinal wave can be displayed from Figure 3.54 within the range of 10 kHz. Similarly, the number of flexural branches for sets 2 and 3 are 7 and 5, respectively.

Figure 3.55 and Figure 3.56 represent the effect of Poisson's ratio on dispersion curves. Unlike Figure 3.53 and Figure 3.54, no particular trend can be seen from Figure 3.55 and Figure 3.56. Poisson's ratio does not affect the F(1,1) branch over the whole frequency range. Considerable similarities is observed in F(1,2) branch and L(0,1) branch with constant velocity up to a certain frequency range. Consequently, it can be summarised that any of the aforementioned sets can be considered for low frequency NDT which is based on flexural wave propagation. However, for longitudinal wave propagation and flexural wave in high frequency, it becomes essential to choose the correct set while timber is considered as a transversely isotropic material. Accordingly, the phase velocity curves of these 4 sets are compared with the orthotropic material to reveal the appropriate set which needs to be considered for transversely isotropic simplification and the results are presented in the next section.

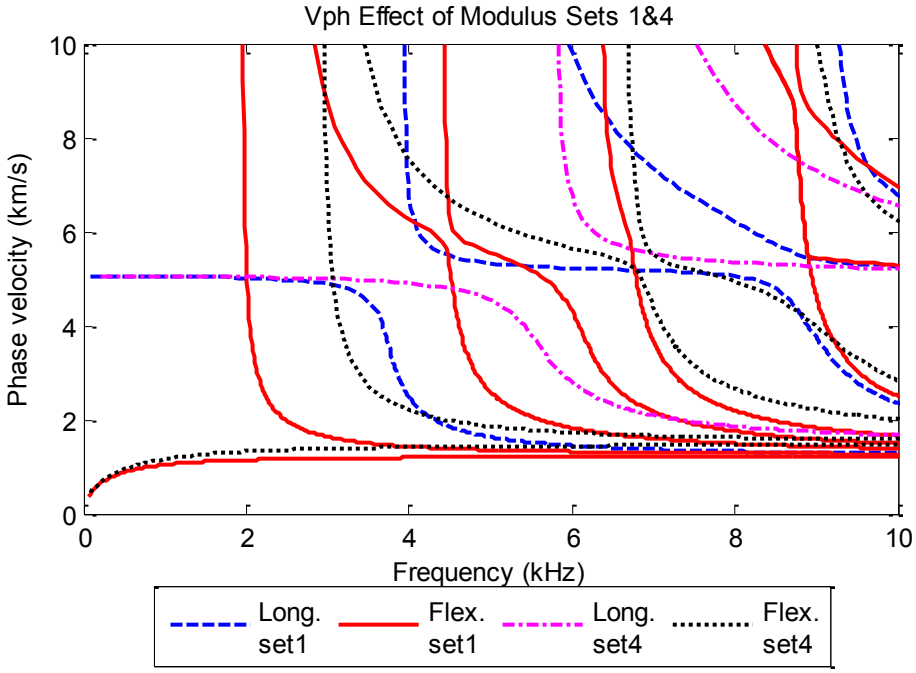

Figure 3.53 Comparison between sets 1 and 4 for transversely isotropic cylinder

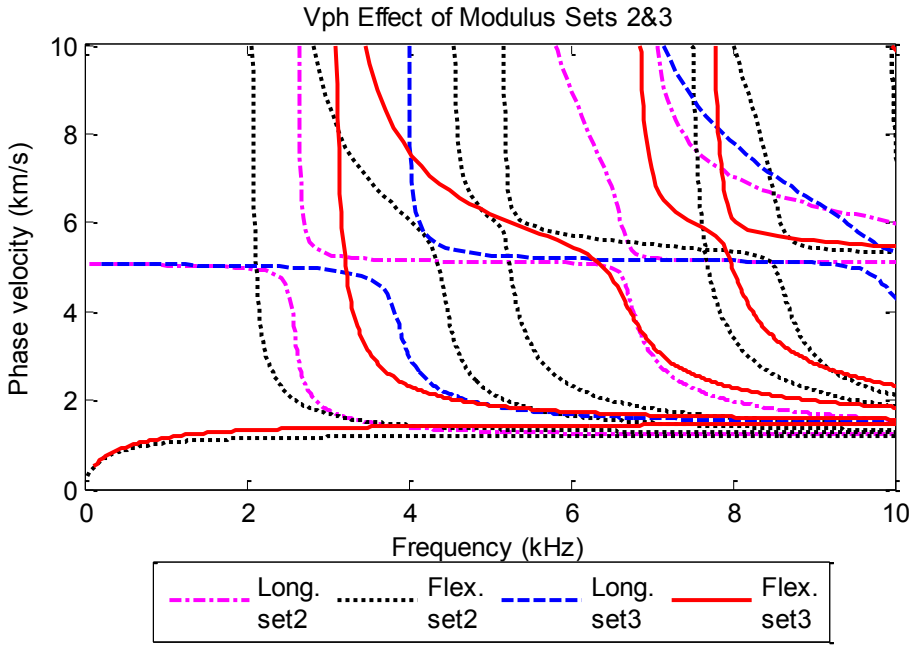

Figure 3.54 Comparison between sets 2 and 3 for transversely isotropic cylinder

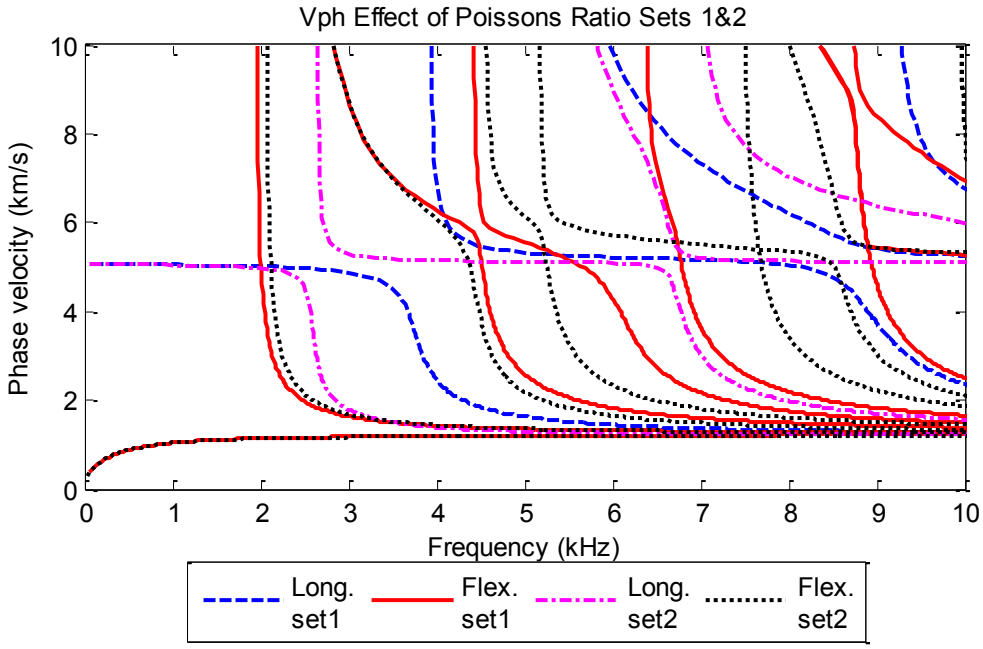

Figure 3.55 Comparison between sets 1 and 2 for transversely isotropic cylinder

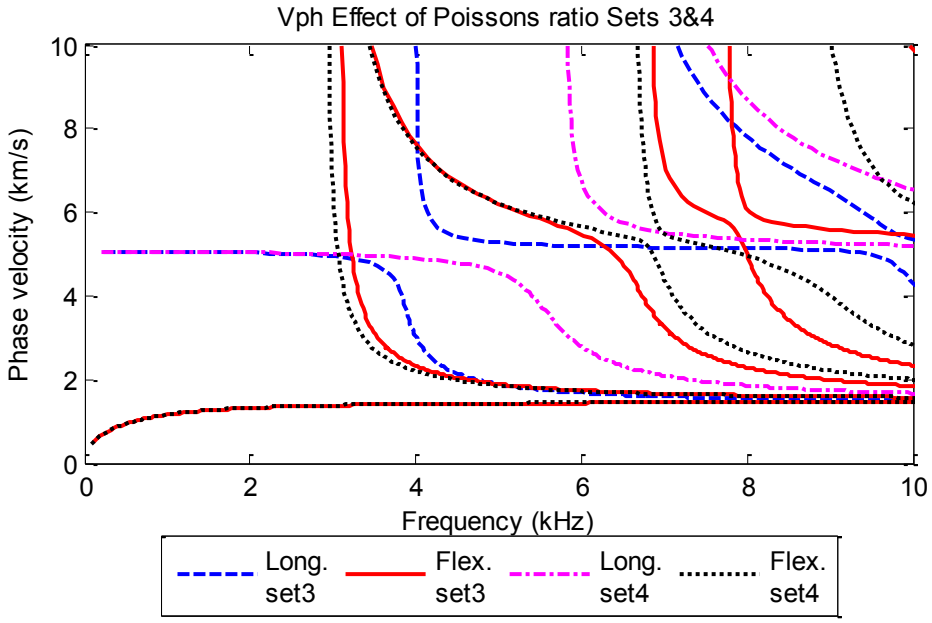

Figure 3.56 Comparison between sets 3 and 4 for transversely isotropic cylinder

Comparison between orthotropic and transversely isotropic (TI) material

To choose the correct set(s), a comparison is made with orthotropic dispersion curves. Figure 3.57 and Figure 3.58 show the comparison of sets 1 and 2, respectively, with orthotropic model. From both figures, it is clear that transversely isotropic material consideration gives better results than isotropic model, however, the similarities between orthotropic and transversely isotropic is unsatisfactory. Nevertheless, set 2 gives better results compared to set 1 as the F(1,1) and F(1,2) branches of set 2 are in good agreement with the same branches of orthotropic model. In Figure 3.58, the numbers of longitudinal branches for transversely isotropic and orthotropic models are 4 and 3, respectively, whereas the same for flexural wave are found to be 7 and 6, respectively. The most unsatisfactory part of set 1 is related to the cut-off frequency of longitudinal branches and shift of cut-off frequency of F(1,3) and F(1,4).

Figure 3.59 and Figure 3.60 depict the comparison of sets 3 and 4, respectively, with orthotropic model. Set 4 shows inadequate similarities with orthotropic model. In contrast, set 3 (Figure 3.59) shows significant matches of the longitudinal branches with the same for orthotropic material. Additionally, some flexural branches of set 3 agree considerably well even though the number of flexural branches is less than the same for orthotropic model.

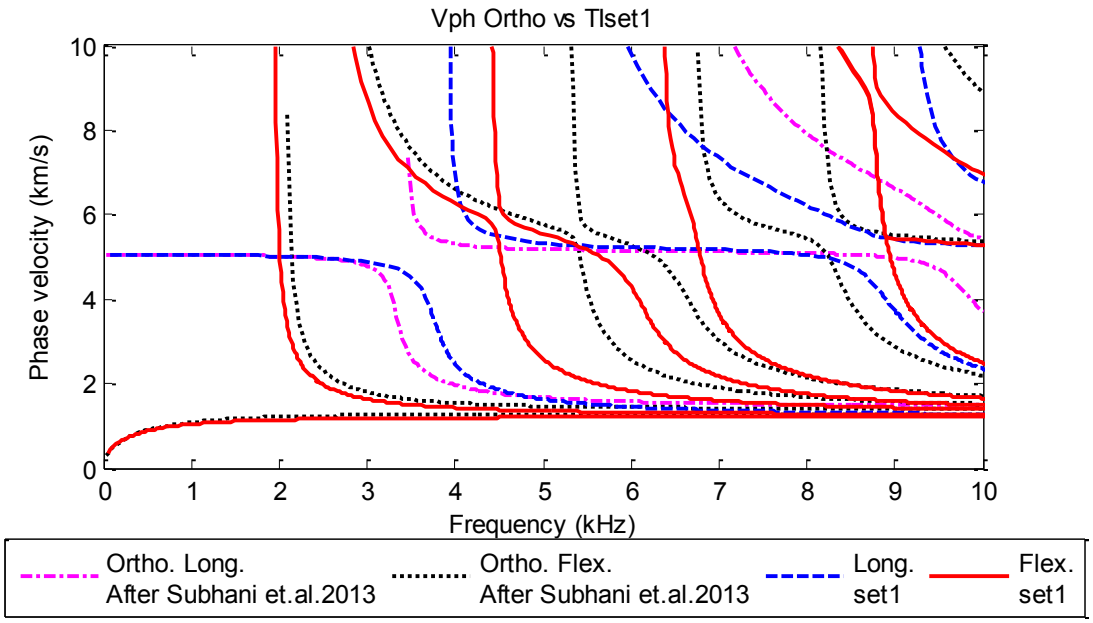

Figure 3.57 Comparison of Vph between orthotropic and transversely isotropic (Set 1) material

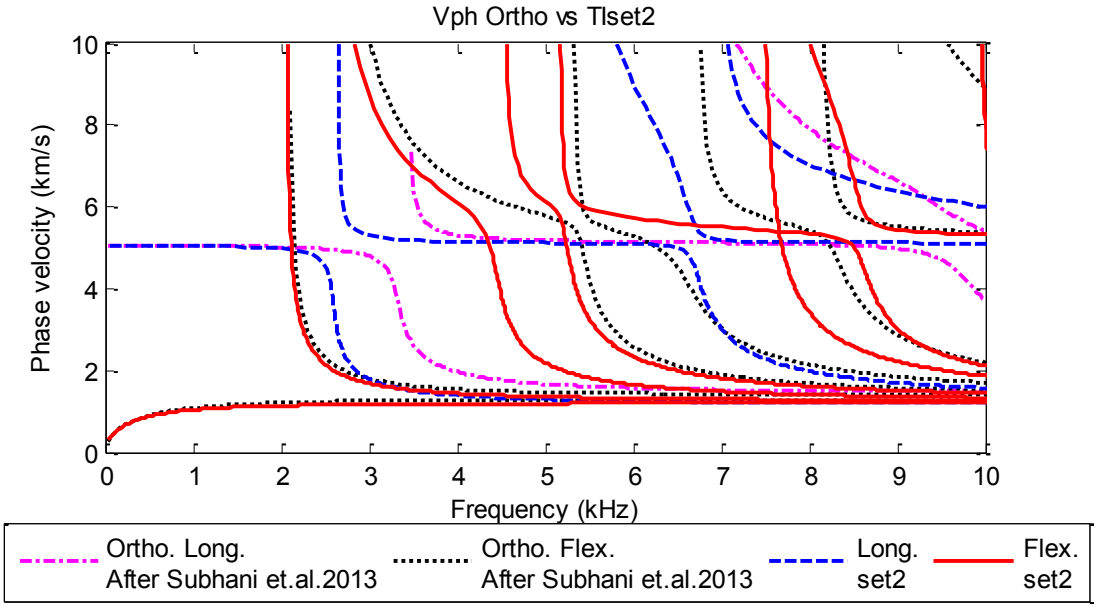

Figure 3.58 Comparison of Vph between orthotropic and transversely isotropic (Set 2) material

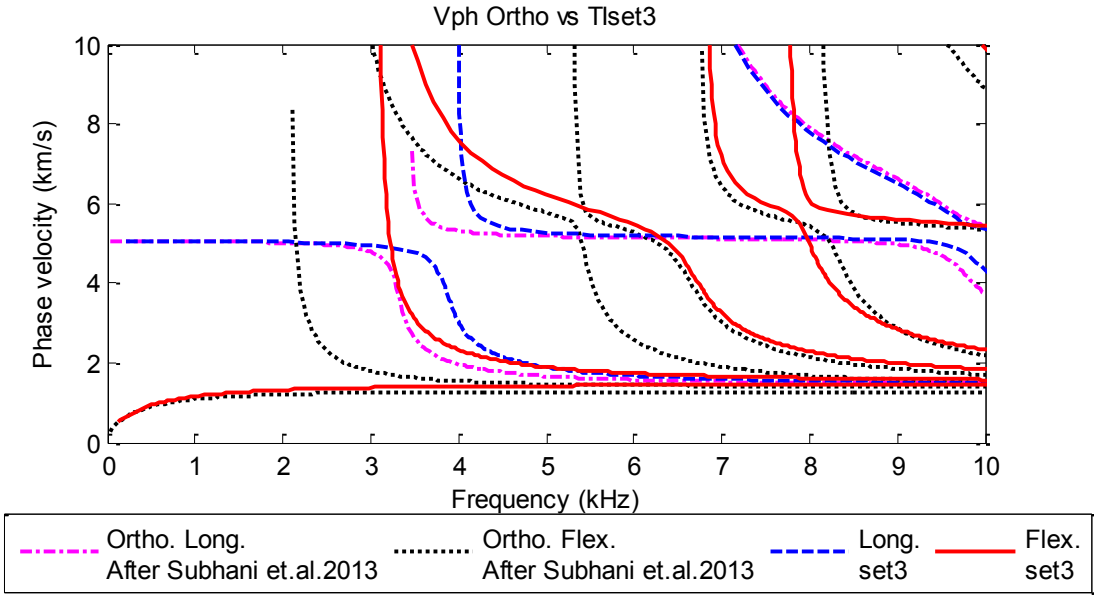

Figure 3.59 Comparison of Vph between orthotropic and transversely isotropic (Set 3) material

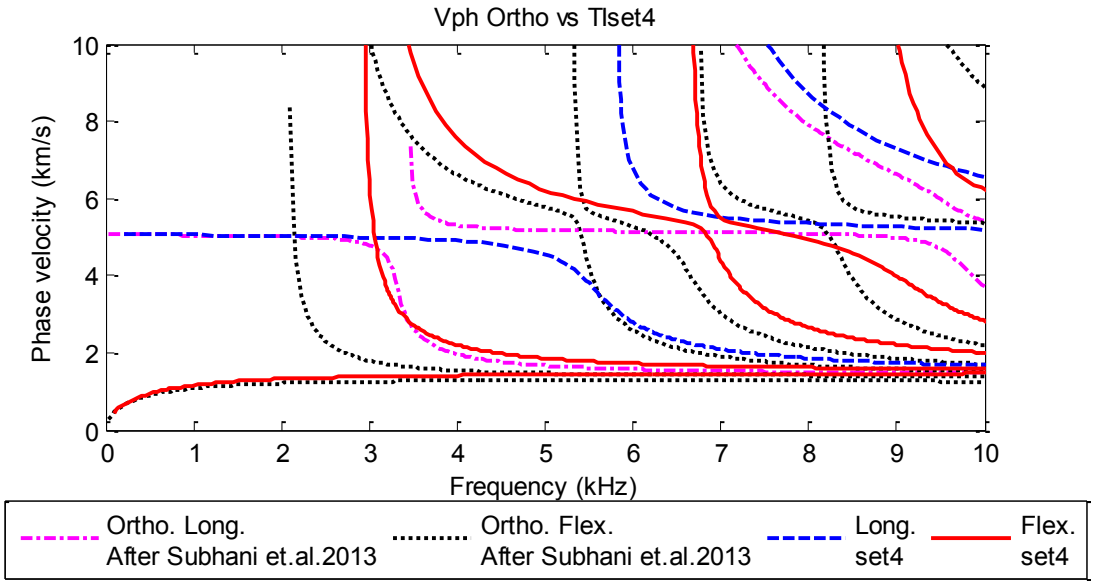

Figure 3.60 Comparison of Vph between orthotropic and transversely isotropic (Set 4) material

From the above discussion, it can be summarised that transversely isotropic model for timber can be considered as it gives better results compared to the isotropic model. However, appropriate material properties have to be chosen from the orthotropic model to get the correct dispersion curves. For the case of low frequency NDT, set 2 ($E = E_\theta$, $v_1 = v_{\theta r}$, $v_2 = v_{\theta z}$ and $G = G_{z\theta}$) is better to consider. On the other hand, for high frequency NDT, set 3 ($E = E_r$, $v_1 = v_{\theta r}$, $v_2 = v_{rz}$ and $G = G_{zr}$) can be selected if the longitudinal wave is generated. For flexural wave propagation in high frequency, it becomes crucial

to predict the appropriate set of transversely isotropic model. Therefore, it is suggested to use the orthotropic material model for this condition. Nevertheless, depending on the desired accuracy of the wave velocity, the combination of set 2 and 3 can be used if dispersion curve for orthotropic material model is unavailable. Set 2 can give a better idea about the possible number of branches that may be present in that frequency range whereas set 3 can be used to predict the velocity.

3.6 Dispersion curves for transversely isotropic material

In this section, the wavelength, energy velocity curve, displacement profile and propagation shape of transversely isotropic material are presented. Again, only traction free condition is considered for transversely isotropic material model as from the previous study, and it is concluded that the velocity of the wave is affected negligibly by the surrounding soil. However, attenuation can affect the signal in terms of the presence of different modes in the signal when it reflects back from the bottom. In Disperse, embedded transversely isotropic material can be modelled. Nonetheless, numerical instability is observed if thick cylindrical waveguide is the point of interest in this regard. Timber has large diameter and to model it as an embedded structure causes this instability. Due to the presence of large magnitude imaginary part (which is attenuation) there are three unknowns in the characteristic equation (i.e. frequency and real and imaginary parts of the wavenumber) compared to two unknowns in traction free condition. Accordingly, finding out the roots in the embedded condition is always more difficult than traction free condition. That is why manual tracing is used in conjunction with automatic tracing for embedded isotropic waveguide while modelling with Disperse. In the case of embedded transversely isotropic material with large diameter, automatic tracing cannot find any root and manual tracing can only be done. The results of the embedded transversely isotropic material with thick waveguide can be found in [145]. In this project, only traction free condition is considered for the transversely isotropic material modelling.

3.6.1 Wavelength

Figure 3.61 and Figure 3.62 show the wavelength curve of set 2 and set 3, respectively. By comparing the wavelengths of transversely isotropic material (set 2 and set 3) with isotropic material (Figure 3.9), shorter wavelengths can be seen in low frequency for

transversely isotropic material. For instance, the wavelengths at 5kHz for L(0,1) mode for isotropic material, set 2 of transversely isotropic material and set 3 of transversely isotropic material are 0.95 , 0.28 and 0.37 m, respectively. Similar behaviour can be observed in F(0,1) mode at 5 kHz. The wavelengths for all these 3 cases are almost similar below 3 kHz for L(0,1) modes whereas shorter wavelength can again be seen in F(0,1) modes. As a result, it can be concluded that smaller damage can be detected in low frequency NDT (such as, manual impact loading) while transversely isotropic material is used for the analysis.

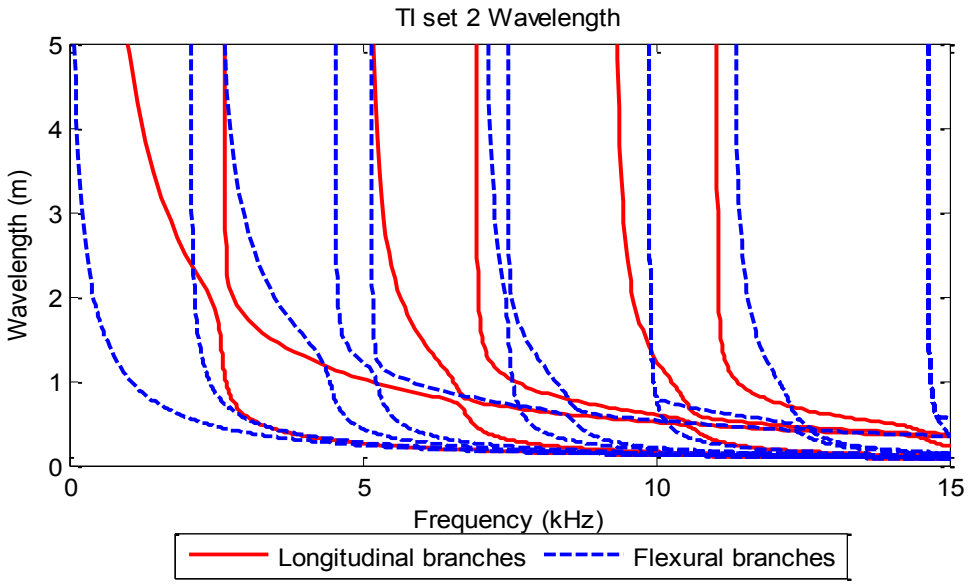

Figure 3.61 Wavelength curve of transversely isotropic material (set 2)

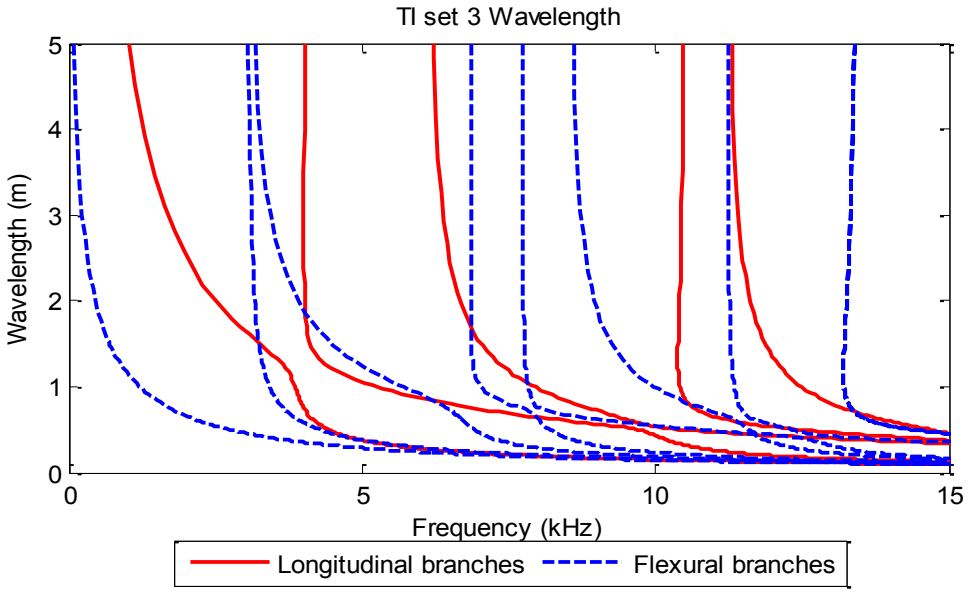

Figure 3.62 Wavelength curve of transversely isotropic material (set 3)

3.6.2 Energy velocity

As mentioned earlier, energy velocity can be used to choose the input frequency. Figure 3.63 and Figure 3.64 represent the energy velocity curves of sets 2 and 3, respectively, of transversely isotropic material. Even though the trend of energy velocity of a transversely isotropic material looks similar to the same of isotropic material, there is an important difference between the energy velocity of isotropic and transversely isotropic material. According to the discussion in Section 3.4.1.6, all the branches have a high peak in their energy velocity. In a transversely isotropic material, the highest peak is constant for a wide frequency band and also reaches the velocity of bulk longitudinal wave at this highest peak. This phenomenon reflects that the particular branch with the maximum constant energy velocity equal to the bulk longitudinal wave velocity dominates over a specific frequency range. This is also consistent with work done by Zemanek [136]. Zemanek pointed out that the axial displacement is in phase over a range of frequencies where the branch's energy velocity (or group velocity in traction free isotropic cylinder) is near the bulk longitudinal wave speed.

From Figure 3.63, it can be noted that L(0,3) branch has a constant velocity up to a frequency range from 7.8 kHz to 9.68 kHz. Consequently, an input frequency with a central value of 8.5 kHz, for example, will dominate the L(0,3) branch and this branch will contain most of the energy. Moreover, less dispersion will be observed because of the constant velocity of this dominating mode. The highest amount of dispersion will occur at the point of intersection among the branches, for example, at the frequency of 6.6 kHz, the first 3 longitudinal wave modes intersect and hence, an input frequency of 6.6 kHz will cause the maximum dispersion and thus, maximum distortion of signal can be seen.

In an anisotropic material, sometimes it is hard to induce purely longitudinal or flexural waves. For anisotropic materials, an axially symmetric excitation of a cylindrical bar may excite flexural modes in addition to the axially symmetric mode [141]. From Figure 3.63 and Figure 3.64, an alteration of maximum energy velocity can be pointed out between flexural and longitudinal branches. It is clear from the figures that, at the frequency of less dispersive flexural mode (constant energy velocity of a mode) are actually related to the maximum dispersive longitudinal mode (energy velocity at the intersection of different modes). For example, according to the aforementioned

frequency at 6.6 kHz, maximum dispersion will occur for the longitudinal branches; in contrast, at that frequency one flexural branch has the constant peak energy velocity equal to the bulk longitudinal wave velocity which is the representative of minimum dispersion. As a result, the signal in a transversely isotropic material usually suffers more dispersion than an isotropic material if both the longitudinal and flexural waves are generated. The time domain explanation of this discussion will be presented in Section 3.7.

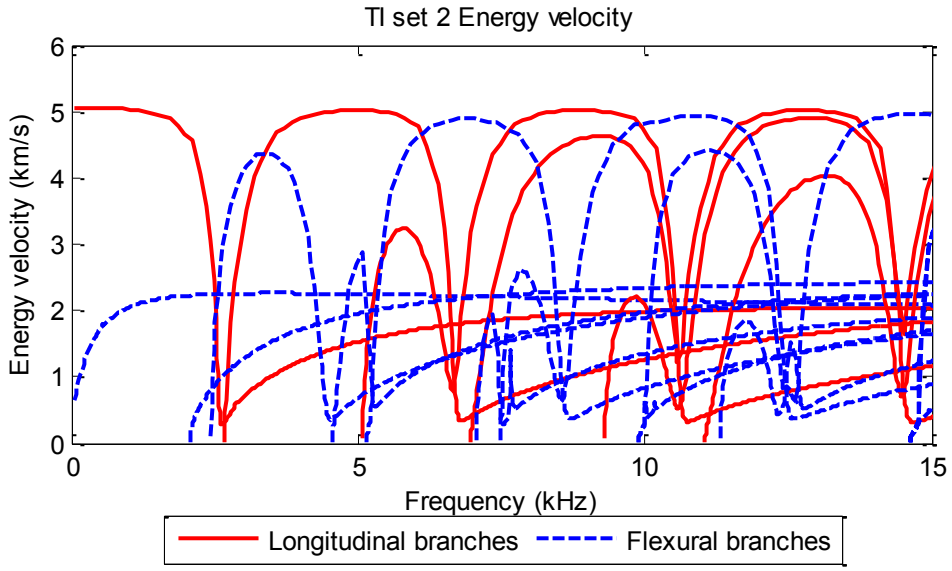

Figure 3.63 Energy velocity curve of transversely isotropic material (set 2)

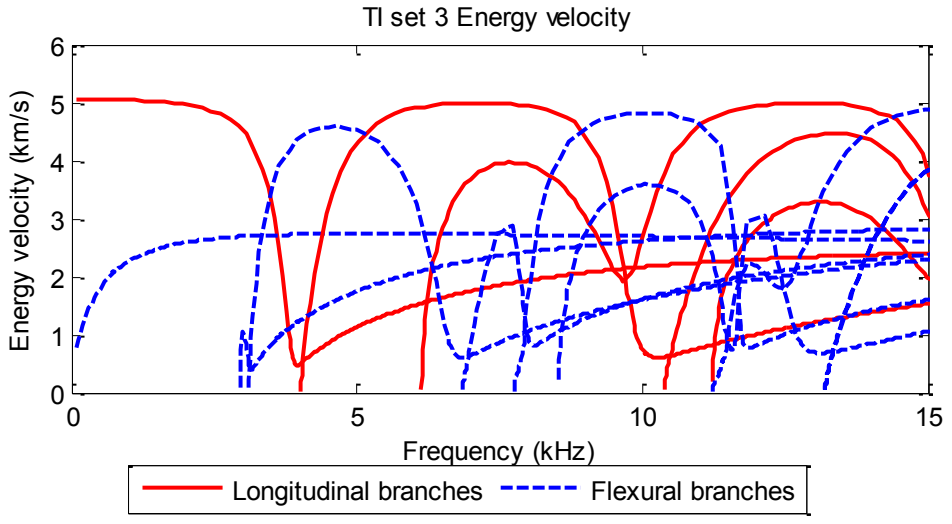

Figure 3.64 Energy velocity curve of transversely isotropic material (set 3)

3.6.3 Normalised displacement and propagation shape

The power flow in a transversely isotropic material is the same as isotropic material, i.e. only axial power flow exists in longitudinal wave and axial and tangential power flow can be observed in flexural wave for traction free condition. In addition, axial components are symmetrical in longitudinal wave and anti-symmetrical in flexural wave. Also, the radial components are anti-symmetrical in longitudinal wave and symmetrical in flexural wave. As a result, practically, two vertically oriented sensors (capturing axial displacement) placed 180° apart on a cross section will show the opposite phase for flexural wave but the same phase for longitudinal wave. The opposite is true if the sensors are placed to capture the radial displacement of the wave.

Again, in longitudinal wave, radial (vertical shear) and axial displacement can be observed in this wave as shown by Equations 3.35 and 3.36. Similarly, all three components of displacement are observed in the flexural wave where power flows in the axial and tangential direction (Equations 3.35 – 3.37). Nevertheless, it is noteworthy to state that flexural wave displacement components vary along the circumference of the cylinder. From Equations (3.35 – 3.37) it can be observed that in the r-z plane, where θ = 0° (can be defined as the impact plane), there is no angular component. In contrast, only angular component is present at θ = 90°. Therefore, it is possible to obtain pure bending wave or longitudinal wave at selected sensor locations and directions along the cylinder.

Even though, the propagation properties and components are the same, the displacement profiles are different in a transversely isotropic material. Figure 3.65 shows the radial, axial and tangential displacements of L(0,1) and F(1,1) mode at 2 kHz. Unlike isotropic material, the displacement profile is not very linear in low frequency. However, maximum displacement occurs at the surface of the pole at low frequency and no local maxima and minima can be observed along the radius. In this figure, also the propagation shapes in r-z plane are presented at the corner of the figure. The top propagation shape represents the L(0,1) mode at 2 kHz and the bottom propagation shape plots the F(1,1) mode at 2 kHz. From the propagation shape it is also clear that longitudinal wave is symmetrical and flexural wave is anti-symmetrical and additionally, maximum displacement occurs on the surface.

Figure 3.66 to Figure 3.70 show the displacement profile of different modes at the frequency of 8 kHz. At this frequency, 4 longitudinal branches and 6 flexural branches are present. From Figure 3.66, it is clear that L(0,2) mode has a local minima at a distance of 50 mm from the neutral axis. Accordingly, local maxima and minima can be observed along the radius from the propagation shape. Similarly, local maxima and minima behaviour can be seen from Figure 3.67 and Figure 3.68. Both the displacement profile and propagation shape show this characteristic. From the displacement profiles, it can be seen that axial components of L(0,1) and L(0,2) mode (at 8 kHz) have almost zero displacement on the surface of the pole, whereas, the radial components of L(0,3) and L(0,4) mode (at 8 kHz) have almost zero magnitude on the surface. Thus, the propagation shape of L(0,1) and L(0,2) (at 8 kHz) modes depict the maximum displacement on the surface which is in the radial direction. In contrast, the propagation shape of L(0,3) and L(0,4) modes show very little displacement on the surface. Therefore, an input signal with a central frequency of 8 kHz with the accelerometers orientated in the longitudinal direction, most probably capture the L(0,3) and L(0,4) modes and sensors oriented in the radial direction possibly record the L(0,1) and L(0,2) modes.

Similar conclusions can be drawn from the flexural modes at 8 kHz (Figure 3.68 - Figure 3.70). F(1,1) and F(1,2) (at 8 kHz) do not have any local maxima and minima along the radius which can also be observed from the propagation shape. Additionally, a small radial displacement at the surface of the pole can be seen from F(1,2) mode and consequently the propagation shape shows less magnitude on the surface. Again, F(1,3) to F(1,6) modes (at 8 kHz) display local maxima and minima which can be seen from both displacement profiles and propagation shapes. F(1,4) and F(1,5) have much less energy propagating on the surface of the pole and hence, almost zero displacement can be noted from the propagation shape on the surface. From the magnitude of the different displacement components of flexural wave on the surface of the pole at 8 kHz, it can be observed that an input signal with a central frequency of 8 kHz with the accelerometers orientated in the longitudinal direction most probably capture the F(1,6) mode and the sensors oriented in the radial direction possibly record the F(1,1), F(1,2) and F(1,4) modes. The displacement profiles of different modes at 15 kHz is shown in Appendix B. Also, the displacement profiles of set 3 at 2 kHz, 8 kHz and 15 kHz are presented in Appendix B.

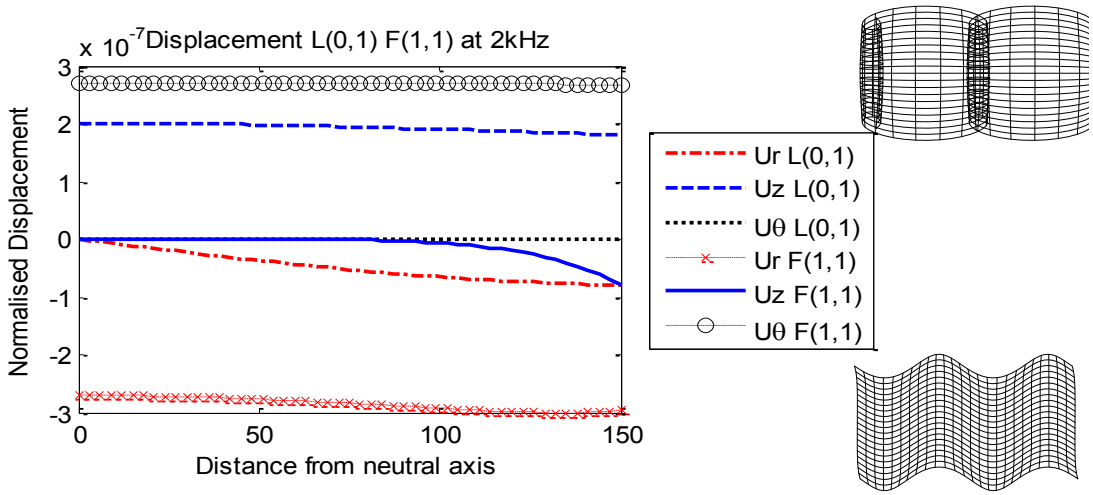

Figure 3.65 Normalised displacement and propagation shape of L(0,1) and F(1,1) mode at 2 kHz

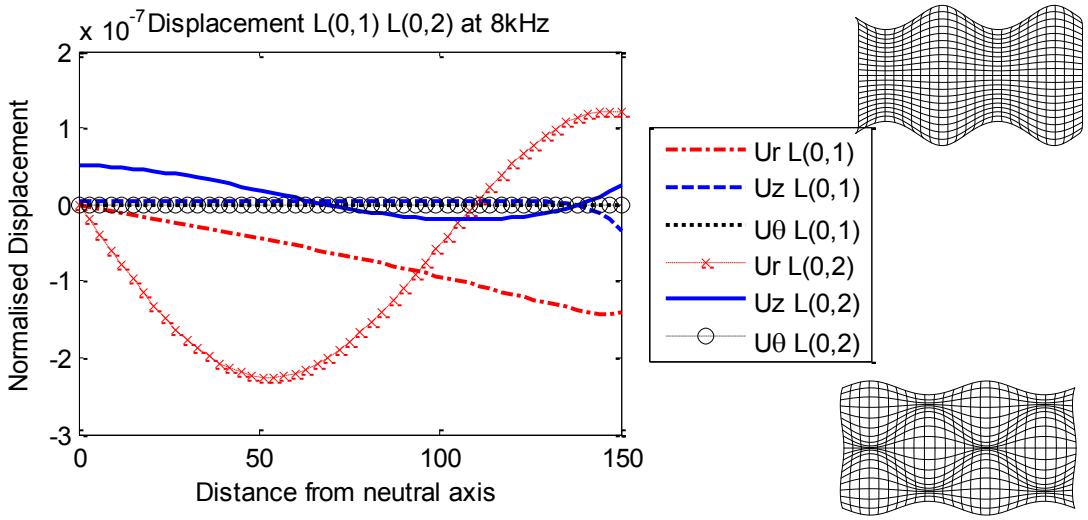

Figure 3.66 Normalised displacement and propagation shape of L(0,1) and L(0,2) mode at 8 kHz

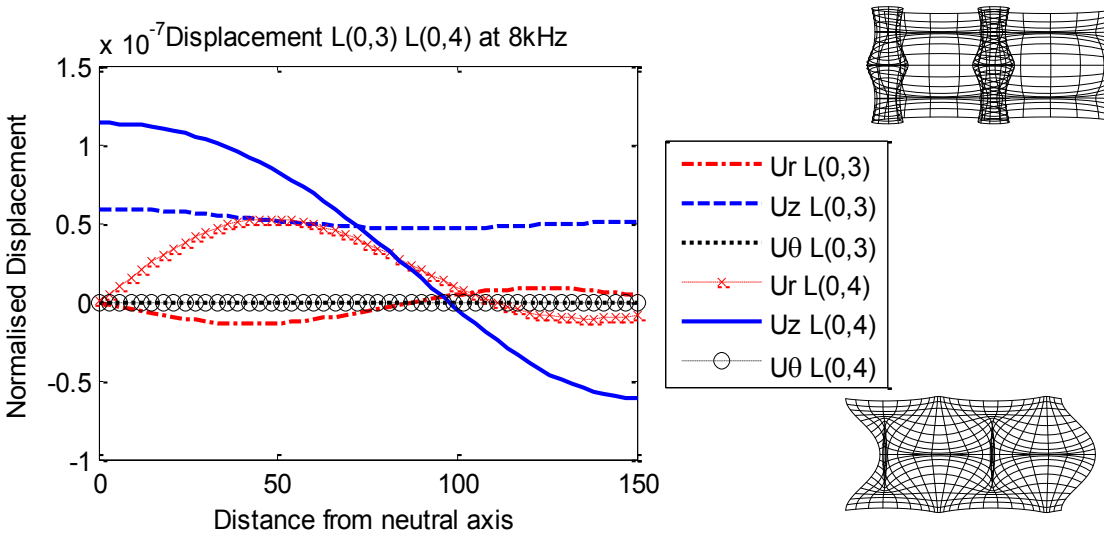

Figure 3.67 Normalised displacement and propagation shape of L(0,3) and L(0,4) mode at 8 kHz

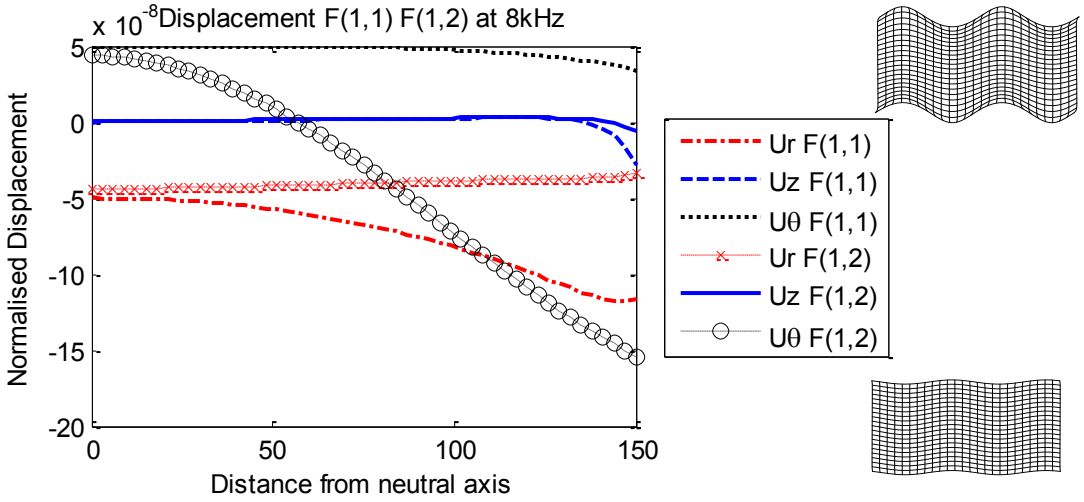

Figure 3.68 Normalised displacement and propagation shape of F(1,1) and F(1,2) mode at 8 kHz

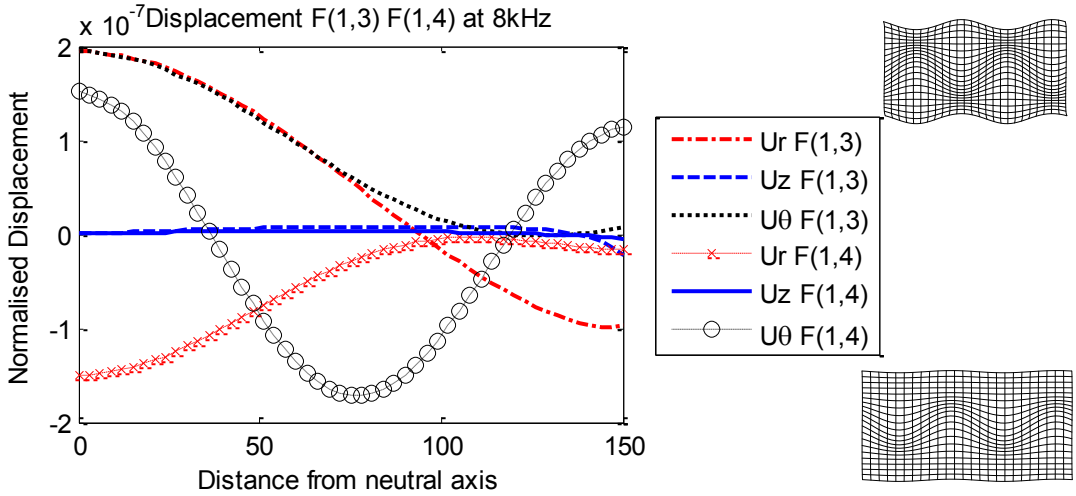

Figure 3.69 Normalised displacement and propagation shape of F(1,3) and F(1,4) mode at 8 kHz

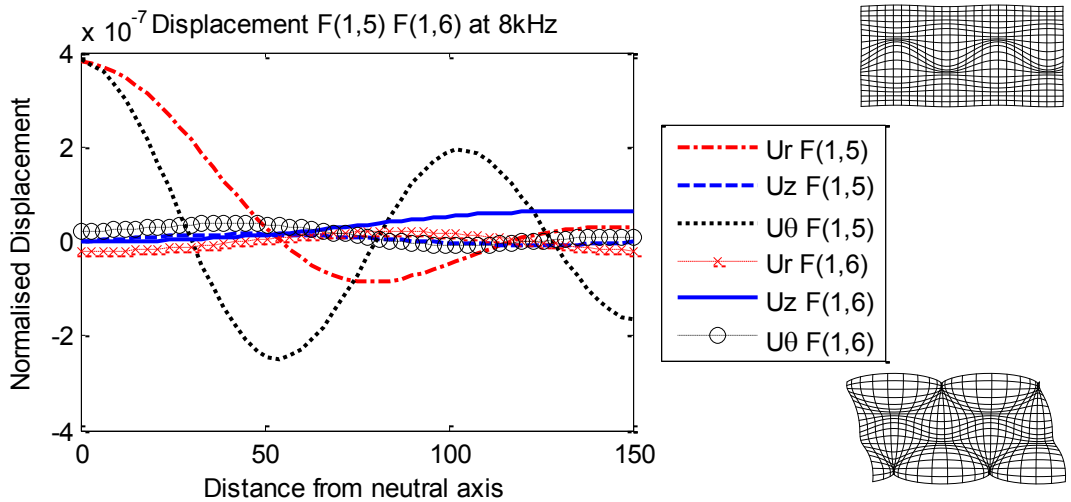

Figure 3.70 Normalised displacement and propagation shape of F(1,5) and F(1,6) mode at 8 kHz

3.7 Simulated signal

In this project, a signal is simulated based on the dispersion curves. Both longitudinal and flexural waves are considered for this purpose. In NDT, sometimes a wave packet is used to excite a signal in the structure. The shape of this input signal changes while it propagates through the structure because of the dispersion. This is very common in the multi-mode analysis of the signal due to the spreading out of the faster branch which separates from the slower branch. Accordingly, the appearance of several secondary pulses of similar shape trailing the main pulse is illustrated in the propagating signal. This is known as trailing pulse and were investigated first by Mason and McSkimin [146]. Each of these trailing pulses contains energy from each propagating mode which is induced by the selected input excitation.

The input frequency for a particular structure is usually chosen from the energy velocity curve. It is usually chosen in such a way that least amount of dispersion occurs in the signal. Simulated signal can help to investigate the possible amount of distortion occurring in a signal under a selected input frequency. Additionally, it can also give an indication of the amount of attenuation present in that frequency band due to the presence of surrounding media.

Puckett [141] developed an analytical model and investigated the effect of trailing pulse on a traction free isotropic cylinder. He focused on longitudinal wave only. In this study, both longitudinal and flexural waves are considered for two different geometrical conditions, i.e. traction free and embedded. Moreover, traction free transversely isotropic material is also taken into account to plot the simulated signal for longitudinal and flexural wave propagation. The software “Disperse” is used to plot this simulated signal.

In this section, the time signal at different frequencies will be presented. Depending on the input frequency, various numbers of branches may be present in the signal. The contribution of different branches is influenced by the amount of energy contained in that particular mode. As mentioned in the earlier sections input frequency can be chosen from the energy velocity curve and the effect of the chosen input frequency on signal is also investigated in this section. Besides, the effect of narrow band and broad band frequency is demonstrated. The central frequency is selected from the energy velocity

curve and the number of cycles determines the narrowness of the signal. For example, a 15 kHz frequency signal with 10 cycle sine burst has broader frequency range than a 15 kHz signal with 30 cycle sine burst. The narrower the signal, the less dispersion will occur.

The multi-mode simulation in this section is shown as both pitch catch and pulse echo method. Pitch catch is used when there is one transducer to induce the signal and one receiver to receive the signal. In this timber pole project, multiple sensors are used to capture the data and wave velocity is determined from the time taken by the wave to reach one sensor from another. Accordingly, pitch catch can give ideas about the most probable distorted shape of the signal from one sensor to another. Embedded length of the timber is determined from the reflection of the signal and therefore, pulse echo can be useful for this condition. Pulse echo method considers a single transducer which is used to act as a generator and also a receiver. As embedded length or damage location is usually determined from one sensor; hence, pulse echo gives a better estimation of the shape of the dispersive signal on reflection.

In the pitch catch method, the contribution of different modes can be shown. In contrary, it is important to note that mode conversion occurs on reflection and thus, pulse echo method cannot capture the contribution of individual modes. Nevertheless, it shows the summation of different modes. For example, provided that the first 4 flexural branches are present in an excited signal, then pulse echo will show the contribution of F(1,1) mode, F(1,1) – F(1,2) mode, F(1,1) – F(1,3) mode, F(1,1) – F(1,4) mode, etc.

Traction free condition is selected only for transversely isotropic material and both embedded and traction free situations are considered for the isotropic material.

3.7.1 Transversely isotropic material

For transversely isotropic material, set 2 (Table 3.8) is considered for the analysis of this simulated signal.

3.7.1.1 Effect of bandwidth

From the energy velocity curve (Figure 3.63), it can be seen that one longitudinal mode at 8.5 kHz and one flexural mode at 10.7 kHz have constant peak velocity. According to the aforementioned discussion, less amount of dispersion should occur at the constant

peak velocity of any particular mode and also, the mode corresponding to the constant peak velocity is supposed to dominate the signal in terms of energy. To demonstrate the effect of bandwidth, these two frequencies are considered separately for longitudinal and flexural wave propagation. In addition, the time signal for pitch catch and pulse echo methods are reported. The propagation distance for pitch catch method is considered as 0.6 m. The timber pole usually has an embedded length of 1 to 2.5 m; hence, propagation distance is employed as 5 m for pulse echo method. Finally, both 10 cycle and 30 cycle sine burst are taken into account to investigate the effect of bandwidth.

From the energy velocity curve, it is clear that there are mainly 4 longitudinal branches present at the frequency of 8.5 kHz. Figure 3.71 displays the excitation signal at the input frequency of 8.5 kHz with 10 cycles. The propagation of this excited signal is depicted in Figure 3.72 where the propagation distance is 0.6 m. The dispersion of the signal is very clear from this figure as the main signal is distorted due to the presence of 4 longitudinal modes at that frequency. Figure 3.73 illustrates the propagation of the same signal with a distance of 5m due to reflection. As the propagation distance increases, possible mode conversion may occur on the reflection; hence, more distortion of the signal (because of higher dispersion) is clearly visible in the pulse echo method. In this reflected signal, two major groups of packet can be observed at approximately 6 and 9.5 ms. These two groups most possibly belong to the L(0,3) and L(0,4) mode, since the highest energy velocity (Figure 3.63) at 8.5 kHz belongs to L(0,3) mode and second highest velocity corresponds to L(0,4) mode. The contribution of individual modes will be presented in the latter section of the chapter.

Figure 3.74 indicates the excitation signal at the frequency of 8.5 kHz with 30 cycle sine burst. Due to the higher number of cycles, the frequency band is narrower compared to the 10 cycle signal. As a result, the 30 cycle signal will stay within the frequency range of constant peak energy velocity around 8.5 kHz. In other words, since the constant peak energy velocity of L(0,3) mode is within the range of 8 to 10 kHz; thereby, a narrower frequency band has the possibility to stay within this range whereas the 10 cycle sine burst may fall outside this range. By performing the FFT, this phenomenon can be ensured and will be presented later in this section.

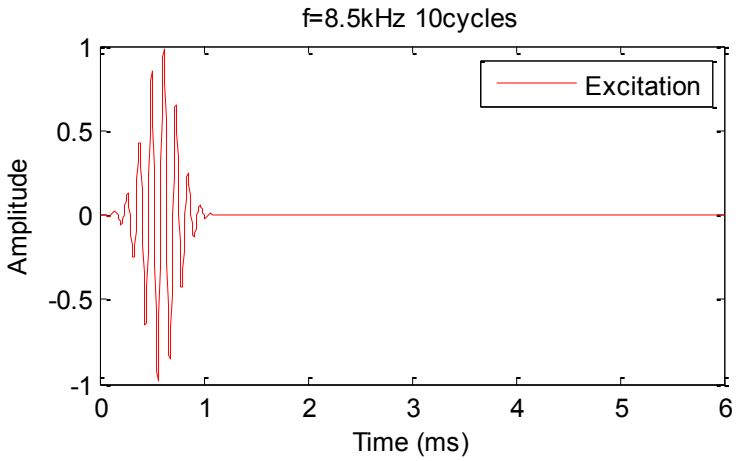

Figure 3.71 Excitation at 8.5 kHz with 10 cycle sine burst

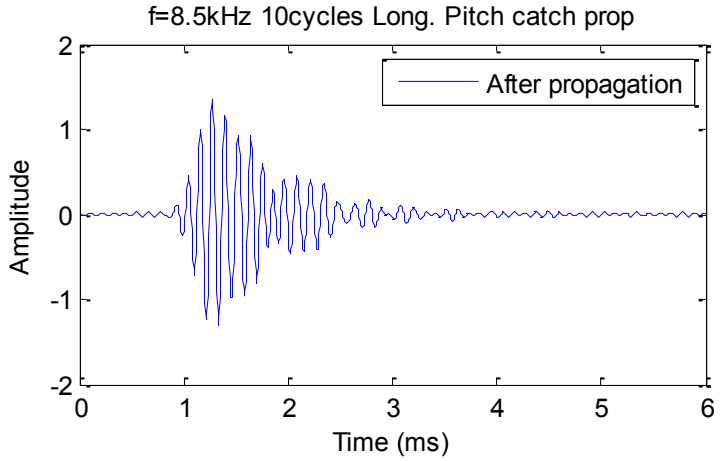

Figure 3.72 Propagation of longitudinal waves at 8.5 kHz signal with 10 cycle sine burst (pitch catch)

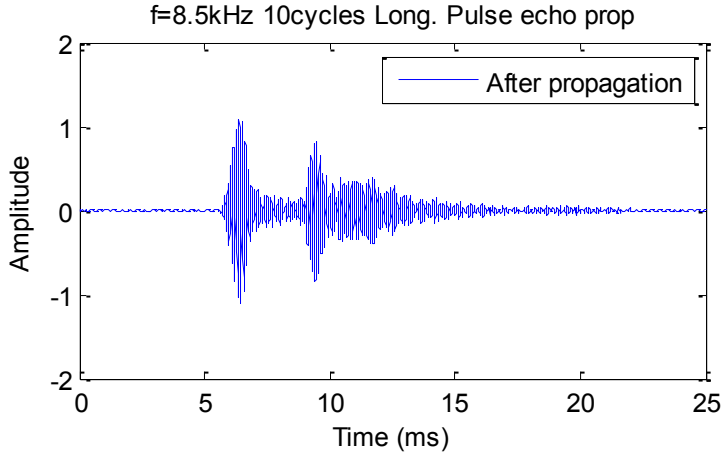

Figure 3.73 Propagation of longitudinal waves at 8.5 kHz signal with 10 cycle sine burst (pulse echo)

The advantage of the narrower frequency band can be clearly seen from Figure 3.75. As the frequency band gets narrower in the 30 cycle input signal and stays on the constant part of the energy velocity curve; hence, very little amount of dispersion can be observed by the pitch catch method. The result of pulse echo method (Figure 3.76) is also satisfactory. Three groups of pack can be seen in Figure 3.76 which belongs to three different longitudinal branches. Due to different velocities of these three longitudinal branches, they reach the receiver at different times. Also, they keep almost the same shape of the excitation signal and as a result, very little dispersion occurs in this signal. Consequently, it can be concluded that narrow band frequency can reduce the dispersion to a great extent. It is also noteworthy to state that the distance between the transducer and receiver should be reduced to decrease the effect of dispersion for the case of 10 cycle sine burst. Otherwise, this distortion of the signal creates the trailing pulse and makes it difficult to determine the stress wave velocity from the sensors. The effect of this propagation distance will be reported later in this section.

For the flexural wave propagation, the situation is more complicated. For example, the central frequency of the excitation is chosen at 10.7 kHz because of the constant peak energy velocity at that range in case of flexural wave. Mainly 9 flexural branches can be seen at this frequency. Figure 3.77 and Figure 3.80 show the excitation frequency of 10.7 kHz with 10 and 30 cycles, respectively. Clearly, significant amount of dispersion is observed in flexural wave even with the same propagation distance of 0.6 m (Figure 3.78). The same is true for the pulse echo method (Figure 3.79). An improvement can be seen for the 30 cycle signal both in the pitch catch (Figure 3.81) and pulse echo (Figure 3.82) method. However, the modification is not as good as the longitudinal wave due to the presence of more flexural branches in the frequency range. Mainly two dominating groups can be observed in the 30 cycle signal (Figure 3.81) which are possibly corresponding to the highest two energy velocities (Figure 3.63). In contrast, four main groups of packet are seen in the pulse echo method with 30 cycle sine burst. Finally, it can be concluded that the distance of 0.6 m between the transducer and receiver in flexural wave propagation should be reduced, even though 30 cycle sine burst is used, to decrease the amount of dispersion.

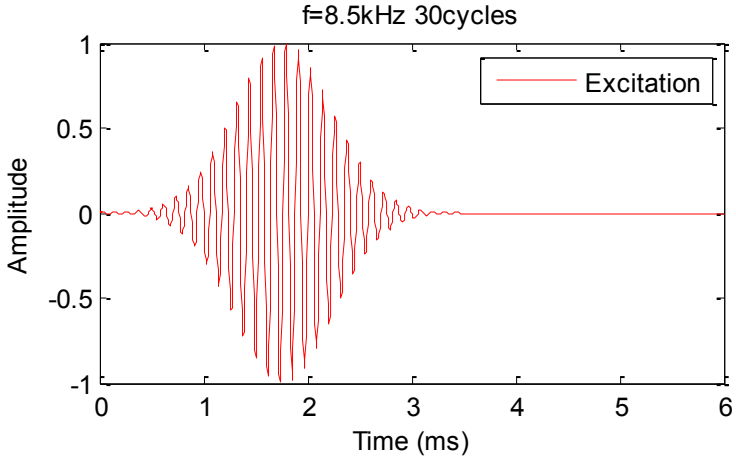

Figure 3.74 Excitation at 8.5 kHz with 30 cycle sine burst

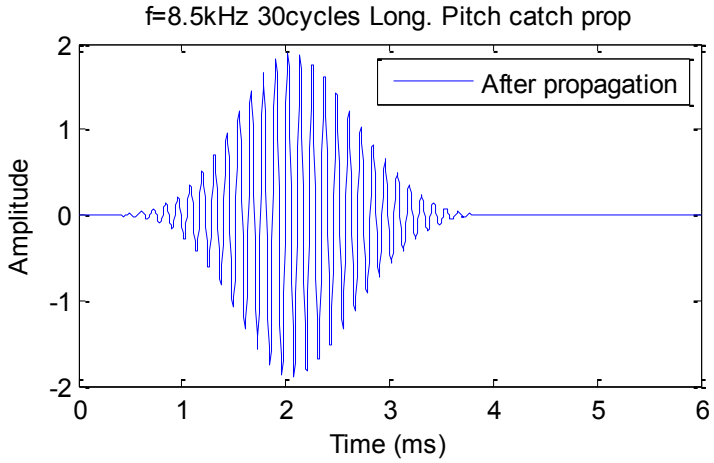

Figure 3.75 Propagation of longitudinal waves at 8.5 kHz signal with 30 cycle sine burst (pitch catch)

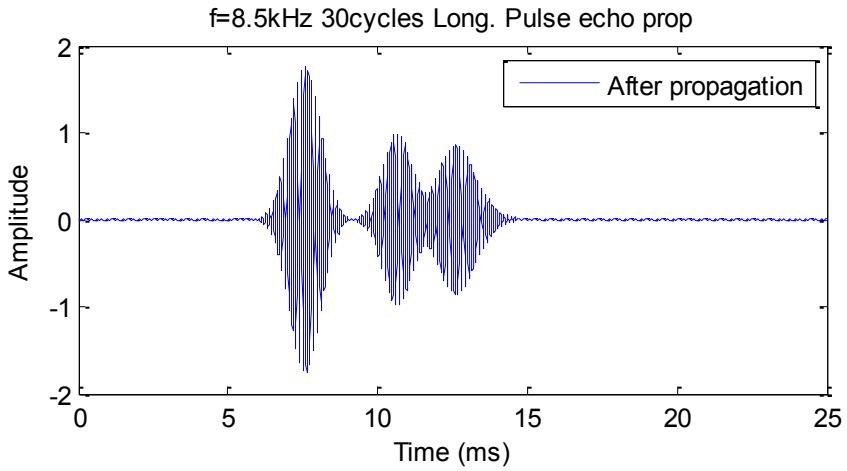

Figure 3.76 Propagation of longitudinal waves at 8.5 kHz signal with 30 cycle sine burst (pulse echo)

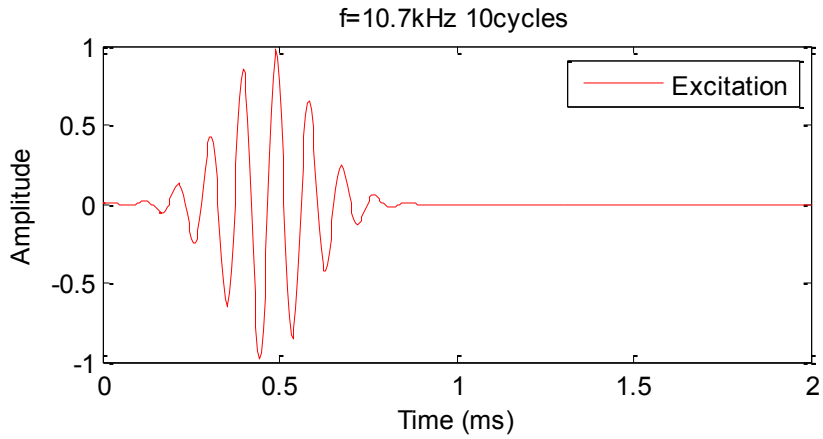

Figure 3.77 Excitation at 10.7 kHz with 10 cycle sine burst

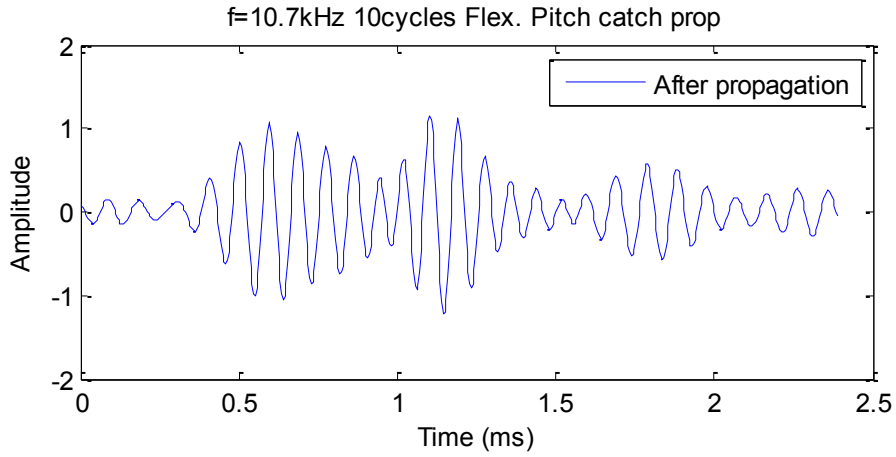

Figure 3.78 Propagation of flexural waves at 10.7 kHz signal with 10 cycle sine burst (pitch catch)

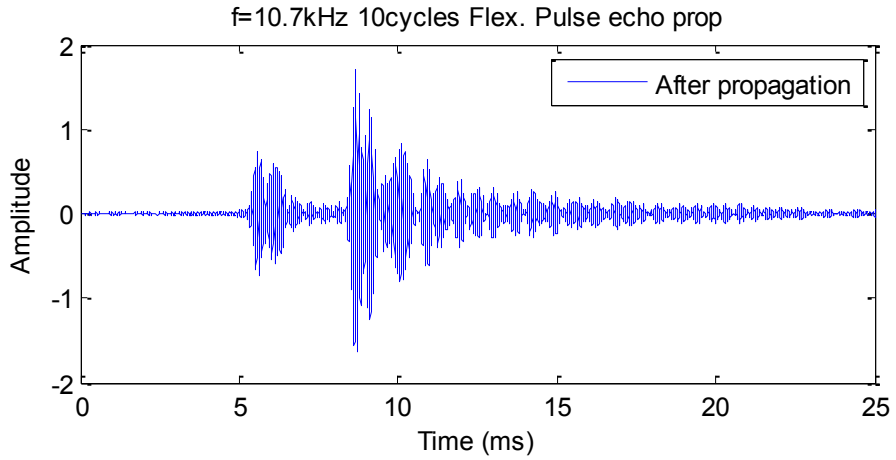

Figure 3.79 Propagation of flexural waves at 10.7 kHz signal with 10 cycle sine burst (pulse echo)

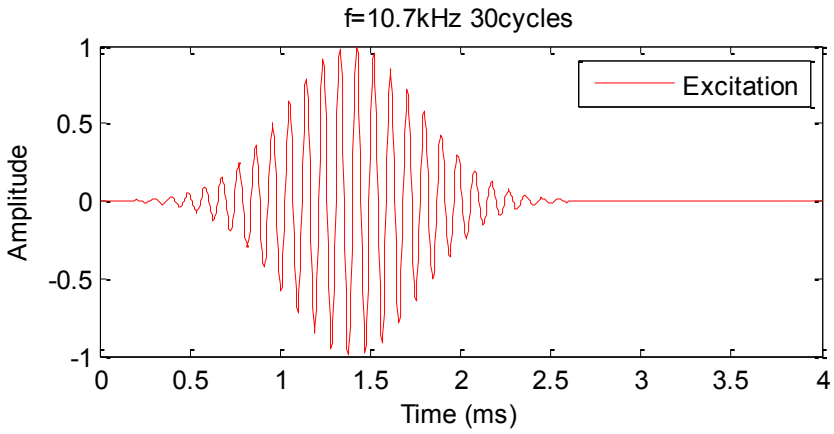

Figure 3.80 Excitation at 10.7 kHz with 30 cycle sine burst

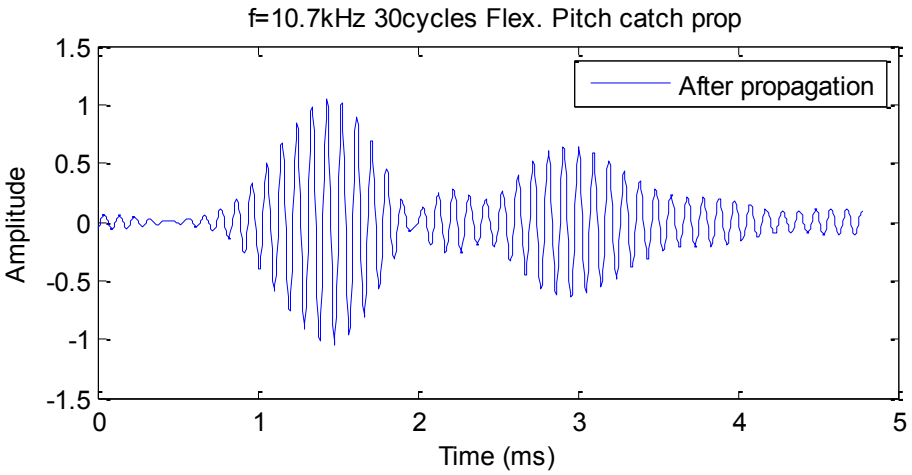

Figure 3.81 Propagation of flexural waves at 10.7 kHz signal with 30 cycle sine burst (pitch catch)

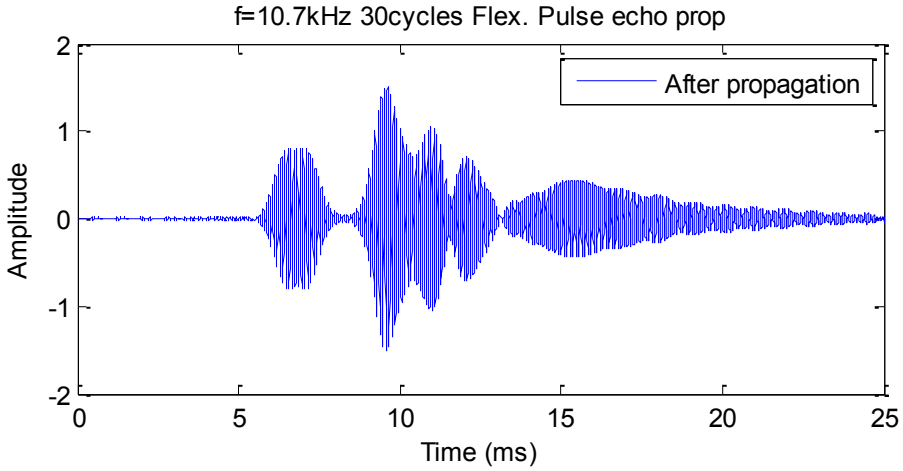

Figure 3.82 Propagation of flexural waves at 10.7 kHz signal with 30 cycle sine burst (pulse echo)

3.7.1.2 Effect of input frequency

In the previous section, the input frequency was chosen where the constant peak energy velocity was shown. As mentioned earlier, the highest dispersion will occur at the point of intersection among the branches. From the energy velocity curve, it can be seen that one of the frequencies with maximum dispersion, where longitudinal branches intersect each other, is 11 kHz. Similarly, one of the intersection points of flexural branches can be observed at 12.6 kHz. In this section, these two frequencies will be investigated separately for longitudinal and flexural branches. For this study, only 30 cycle sine burst is considered as 10 cycle sine burst should show more dispersion.

Figure 3.83 shows the excitation frequency at 11 kHz with 30 cycle sine burst. Five branches of longitudinal modes can be seen at this frequency. The dispersion is notable even by the pitch catch method (Figure 3.84). Despite this, dispersion does not cause substantial dispersion and may be reduced by decreasing the distance between the generator and receiver. In contrast, the pulse echo method extensively distorts the signal (Figure 3.85). Therefore, if this frequency is chosen, it may be possible to calculate the stress wave velocity from two consecutive sensors; however, the embedded length calculation will not be very easy.

For flexural wave propagation, the previous input frequency (10.7 kHz) was not satisfactory. The same feature can be seen at 12.6 kHz. The excitation frequency of 12.6 kHz with 30 cycle sine burst (Figure 3.87) excites almost 11 flexural branches. Similar to the longitudinal case, at 11 kHz, the pitch catch method (Figure 3.87) shows considerably good results and again can be reduced by decreasing the distance between generator and receiver. Nonetheless, the pulse echo method (Figure 3.88) significantly distorts the excitation signal as expected compared to the 10.7 kHz excitation frequency with 30 cycle sine burst.

Therefore, it can be concluded that while choosing the input frequency, it is better to select the frequency where any particular mode has the constant peak energy velocity. Additionally, number of cycles should be increased to make the frequency band narrower. These two conditions are important to determine if the embedded length of the pole or damage location has to be determined. To calculate the stress wave velocity, the generator and transducer can be placed closer to reduce the effect of dispersion.

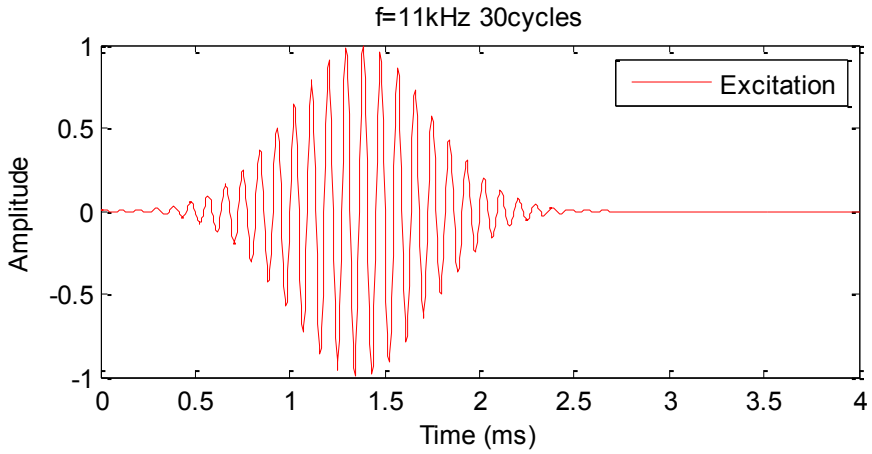

Figure 3.83 Excitation at 11 kHz with 30 cycle sine burst

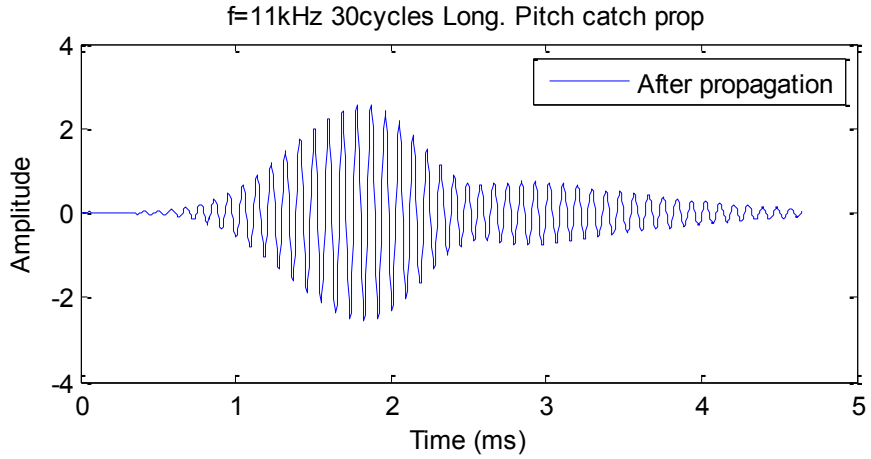

Figure 3.84 Propagation of longitudinal waves at 11 kHz signal with 30 cycle sine burst (pitch catch)

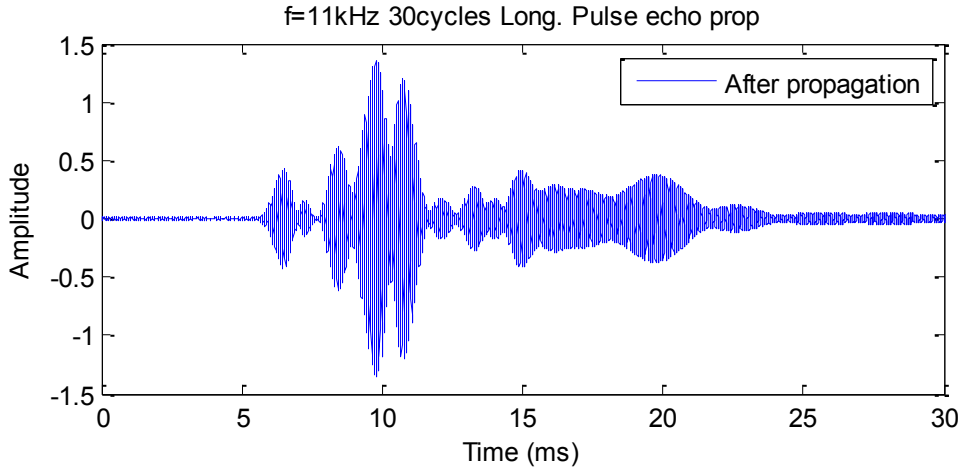

Figure 3.85 Propagation of longitudinal waves at 11 kHz signal with 30 cycle sine burst (pulse echo)

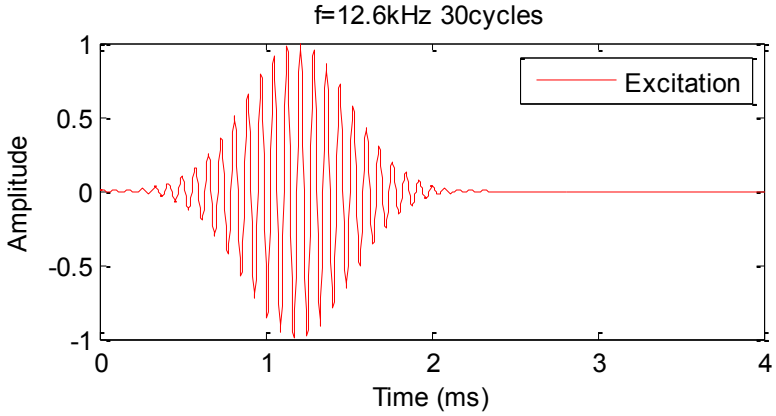

Figure 3.86 Excitation at 12.6 kHz with 30 cycle sine burst

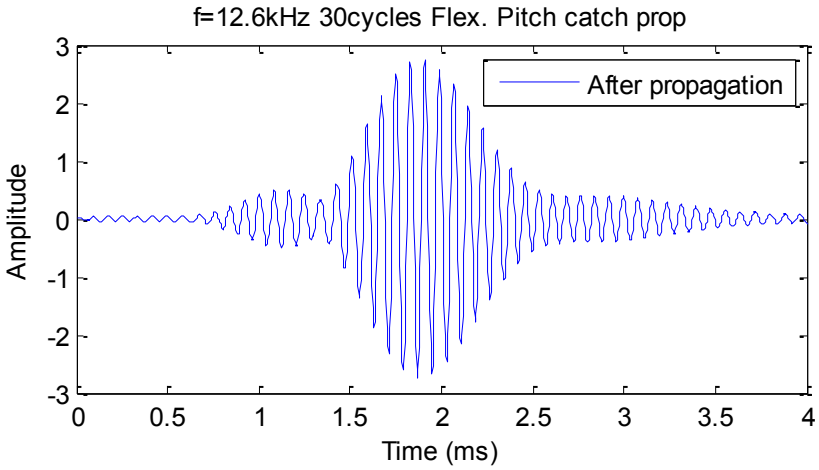

Figure 3.87 Propagation of flexural waves at 12.6 kHz signal with 30 cycle sine burst (pitch catch)

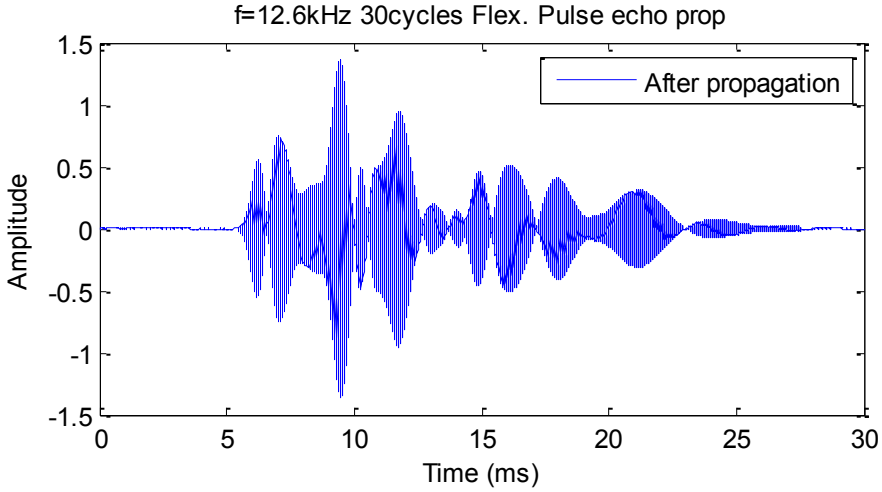

Figure 3.88 Propagation of flexural waves at 12.6 kHz signal with 30 cycle sine burst (pulse echo)

3.7.1.3 Combination of longitudinal and flexural wave and contribution of individual modes

In the previous section, flexural and longitudinal waves were discussed separately. However, in reality, both waves may be generated when anisotropic media is considered. As timber is an anisotropic material, hence, while considering it as a transversely isotropic material, it is of interest to consider both waves at the same time. In this section, both waves are chosen to show the distorted shape of the signal due to dispersion. Again, pitch catch and pulse echo methods are used. The propagation distance corresponding to pitch catch and pulse echo methods are kept the same as the previous section.

While considering the longitudinal and flexural waves at the same time, it is not very straight forward to choose the input frequency. It can be seen from the energy velocity curve (Figure 3.63) that the constant peak energy velocities of longitudinal and flexural waves come alternatively. Additionally, the frequencies, where the constant peak energy velocities of longitudinal waves are observed, actually relate to the intersection of the flexural branches. As a result, the frequencies of minimum dispersion of a longitudinal wave are corresponding to the maximum dispersion of a flexural wave. Also the opposite is true, i.e. the maximum dispersion in a longitudinal wave and minimum dispersion of a flexural wave can be observed at the same frequency. Consequently, sometimes it is very hard to get a less dispersive signal in case of transversely isotropic material.

Both 10 cycle and 30 cycle sine burst are considered in this section and the temporal (time domain) and spectral (frequency domain) data of the excitation are demonstrated in Figure 3.89 to Figure 3.92. As noted earlier, the 30 cycle burst sine signal has a narrower frequency band compared to the 10 cycle one. The central frequency is chosen at 12.5 kHz, where the constant peak energy velocity is related to longitudinal wave and intersection among the flexural branches are seen. In Figure 3.87 (input frequency of 12.6 kHz), only the flexural waves were considered. And in Figure 3.94 (12.5 kHz with 30 cycles), both the longitudinal and flexural waves are taken into account. However, the shape of the signal is considerably similar to Figure 3.87 (12.6 kHz with 30 cycles). This is obvious due to the fact that longitudinal waves are less dispersive in this input

frequency and thereby, the contributions from longitudinal modes are less on dispersion.

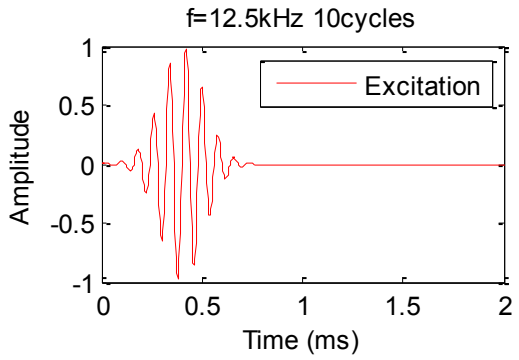

Figure 3.89 Excitation at 12.5 kHz with 10 cycle sine burst (time domain)

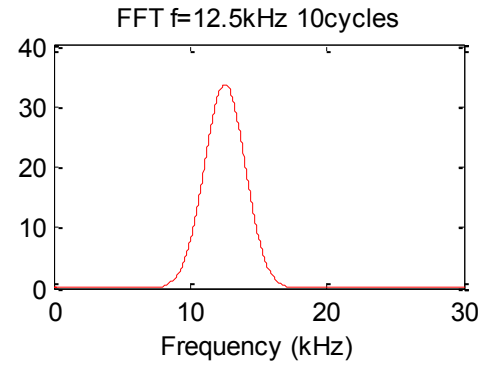

Figure 3.90 Excitation at 12.5 kHz with 10 cycle sine burst (frequency domain)

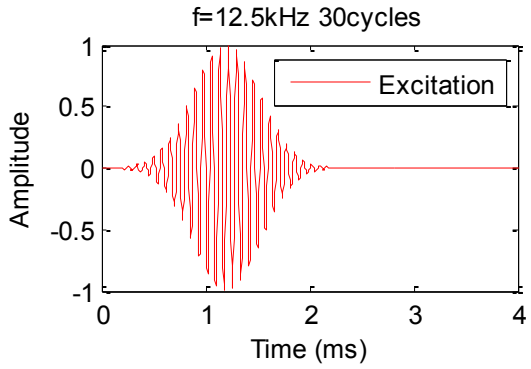

Figure 3.91 Excitation at 12.5 kHz with 30 cycle sine burst (time domain)

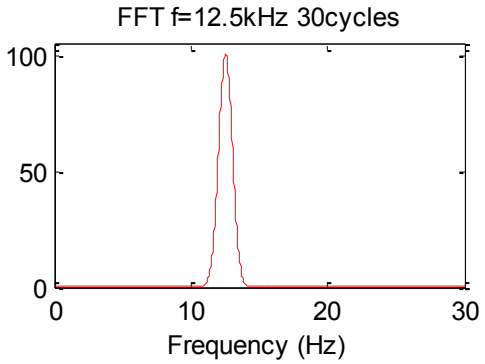

Figure 3.92 Excitation at 12.5 kHz with 30 cycle sine burst (frequency domain)

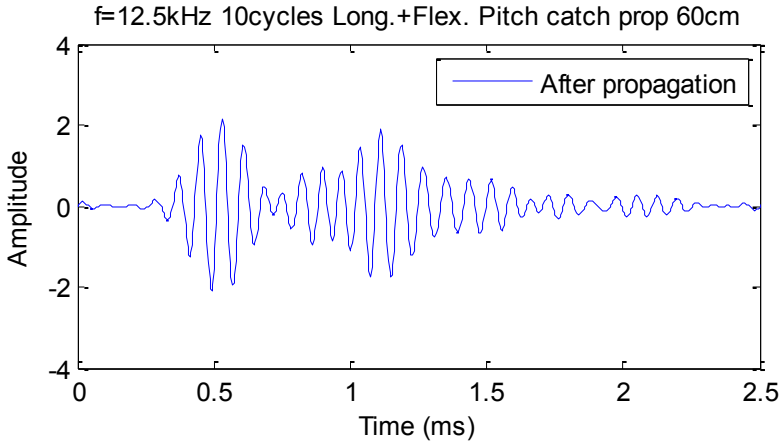

Figure 3.93 Propagation of longitudinal and flexural waves at 12.5 kHz signal with 10 cycle sine burst (pitch catch)

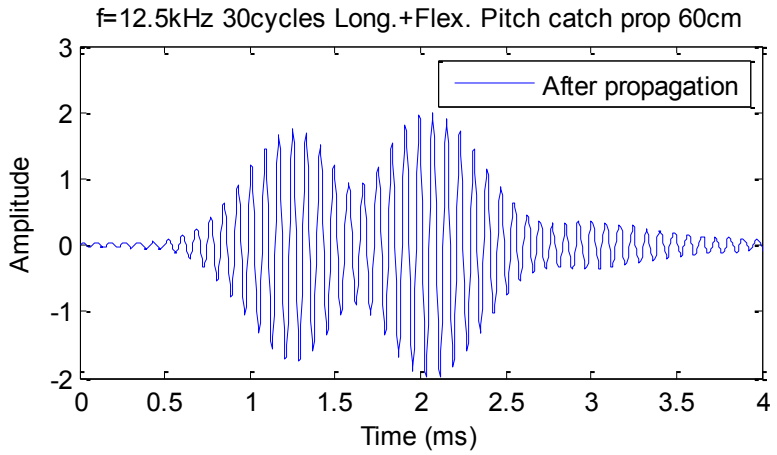

Figure 3.94 Propagation of longitudinal and flexural waves at 12.5 kHz signal with 30 cycle sine burst (pitch catch)

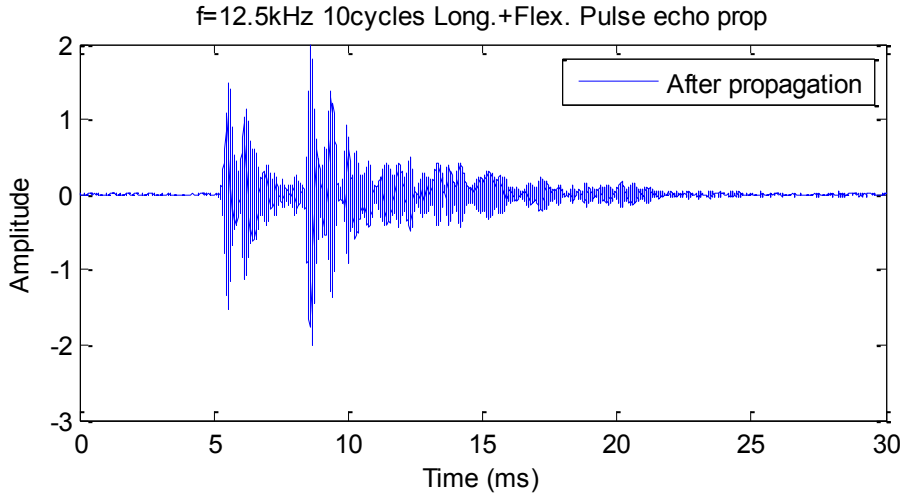

Figure 3.95 Propagation of longitudinal and flexural waves at 12.5 kHz signal with 10 cycle sine burst (pulse echo)

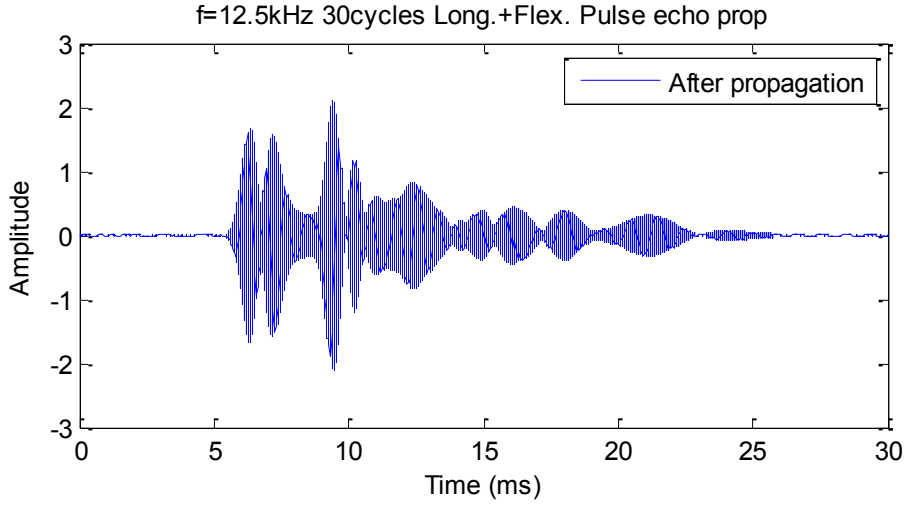

Figure 3.96 Propagation of longitudinal and flexural waves at 12.5 kHz signal with 30 cycle sine burst (pulse echo)

Same observations can be made on pulse echo method where notable similarities are seen between Figure 3.88 and Figure 3.96. Both these two figures have almost the same excitation. The excitations with 10 cycle sine burst is more dispersive as investigated in the previous sections and the propagation signals of 10 cycle sine burst with 12.5 kHz central frequency are presented in Figure 3.93 and Figure 3.95 which are corresponding to pitch catch and pulse echo, respectively.

Figure 3.97 to Figure 3.100 represent the contribution of individual modes. In the pitch catch method, the contribution of different modes is shown. In contrast, pulse echo method cannot present the contribution of individual modes as noted previously. It shows the summation of different modes, such as, provided that the first 4 flexural branches are present in an excitation signal, then pulse echo will show the contribution of F(1,1) mode, F(1,1) – F(1,2) mode, F(1,1) – F(1,3) mode, F(1,1) – F(1,4) mode, etc.

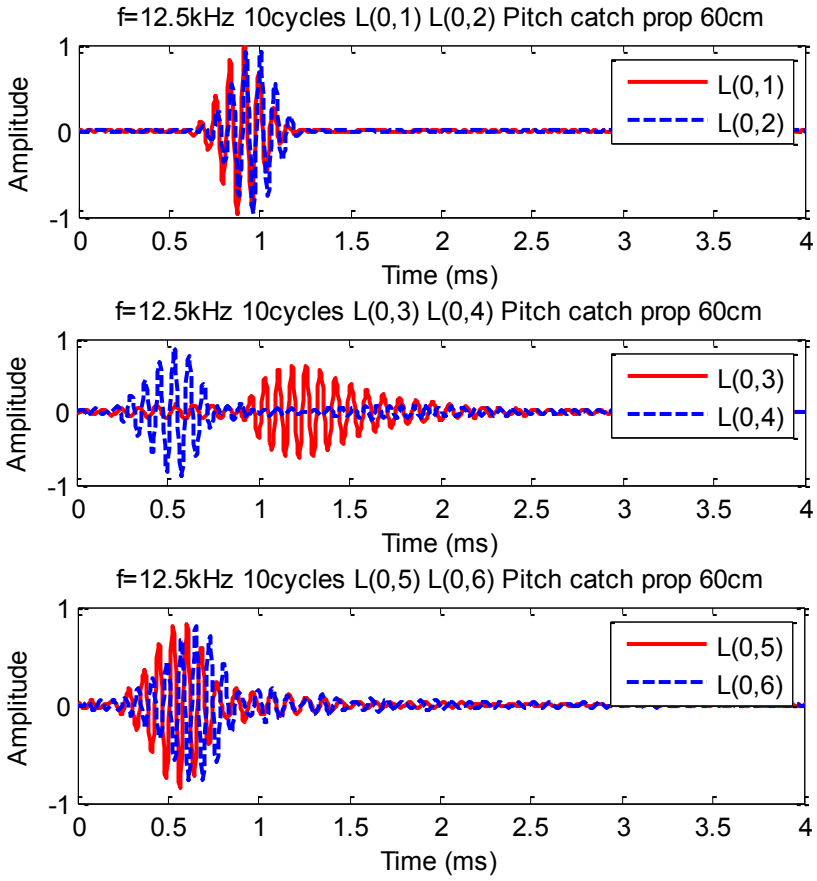

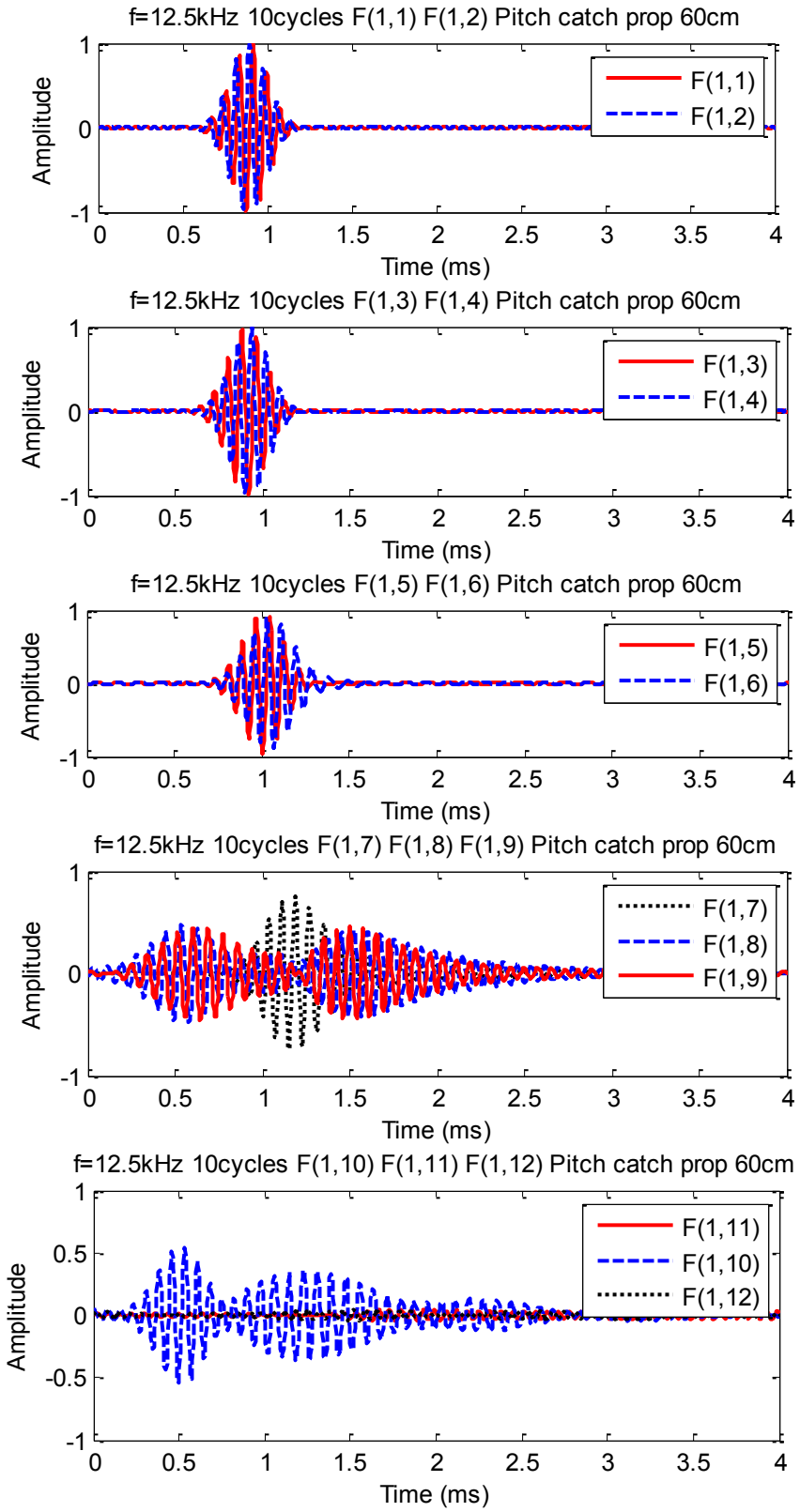

Figure 3.97 Contribution of individual modes on the propagation of a 12.5 kHz input signal with 10 cycle sine burst (pitch catch)

In Figure 3.97, contribution of 6 longitudinal modes and 12 flexural modes are depicted. Even though from the energy velocity curve, only 11 flexural modes can be observed exactly at 12.5 kHz, however, the 12^{th} mode is included because the 10 cycle sine burst has a wide band of frequencies. From this figure, it can be seen that most of the modes contain almost the same shape of excitation signal except F(1,8), F(1,9) and F(1,10). The latter 3 modes distorted the most and are responsible for the dispersion. Although the other modes are not very dispersive, nonetheless, the arriving times are different due to different velocity at 12.5 kHz which is also contributing to the dispersion of the signal. The contribution of F(1,11) and F(1,12) is very little because F(1,11) branch starts propagating just after 12.5 kHz and F(1,12) may fall outside the input frequency range. The summation of the modes or the final signal can be seen from Figure 3.93.

In the 30 cycle sine burst signal, the individual modes show less dispersion as expected (Figure 3.98). Again the F(1,8) to F(1,10) modes are mainly responsible for distorting the shape as indicated by Figure 3.94. The shapes of the other modes are similar to the excitation signal. The F(1,11) and F(1,12) modes are zero valued for 30 cycle signal due to the narrow frequency band.

The dispersion on the reflection or by pulse echo method is inevitable and can be seen clearly from Figure 3.99. Almost all modes are distorted except L(0,1) and from F(1,1) to F(1,4). L(0,3), F(1,8) to F(1,10) modes are again mainly responsible for the dispersion. The distortions of most modes are reduced in the 30 cycle sine burst (Figure 3.100). Nevertheless, L(0,3) modes reach at different times because it has the lowest velocity at 12.5 kHz. Also, F(1,8) to F(1,10) modes are again very dispersive.

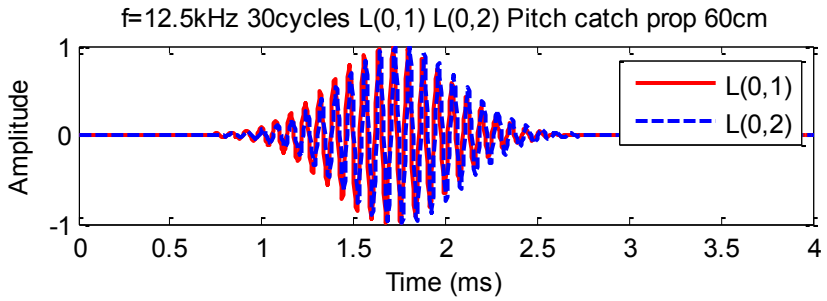
f=12.5kHz 30cycles L(0,1) L(0,2) Pitch catch prop 60cm
Amplitude
Time (ms)
L(0,1)
L(0,2)

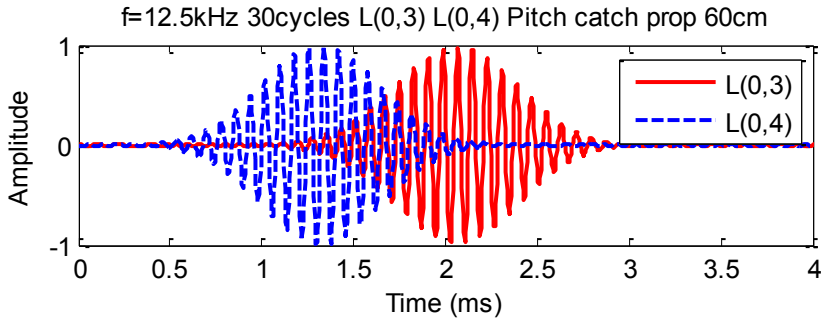
f=12.5kHz 30cycles L(0,3) L(0,4) Pitch catch prop 60cm
Amplitude
Time (ms)
L(0,3)
L(0,4)

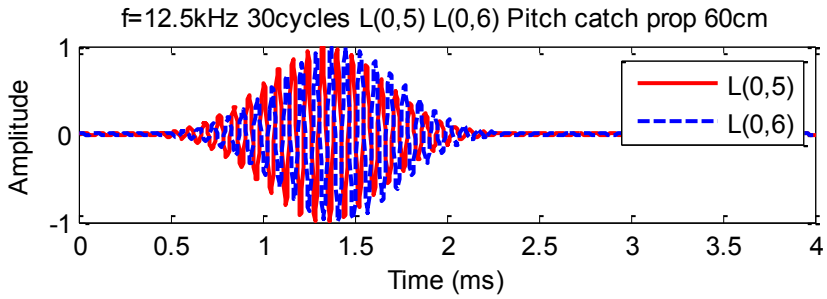
f=12.5kHz 30cycles L(0,5) L(0,6) Pitch catch prop 60cm
Amplitude
Time (ms)
L(0,5)
L(0,6)

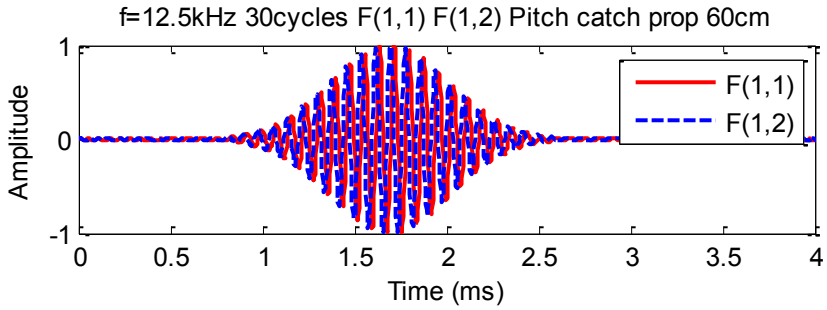
f=12.5kHz 30cycles F(1,1) F(1,2) Pitch catch prop 60cm
Amplitude
Time (ms)
F(1,1)
F(1,2)

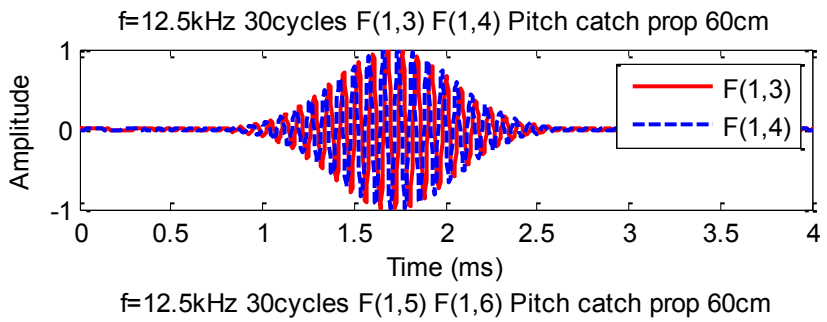
f=12.5kHz 30cycles F(1,3) F(1,4) Pitch catch prop 60cm
Amplitude
Time (ms)
F(1,3)
F(1,4)

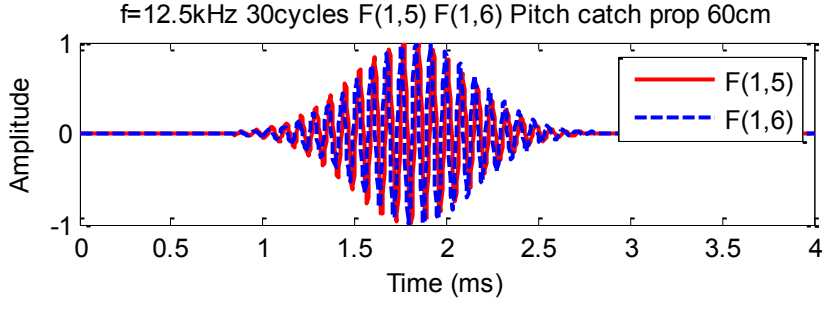
f=12.5kHz 30cycles F(1,5) F(1,6) Pitch catch prop 60cm
Amplitude
Time (ms)
F(1,5)
F(1,6)

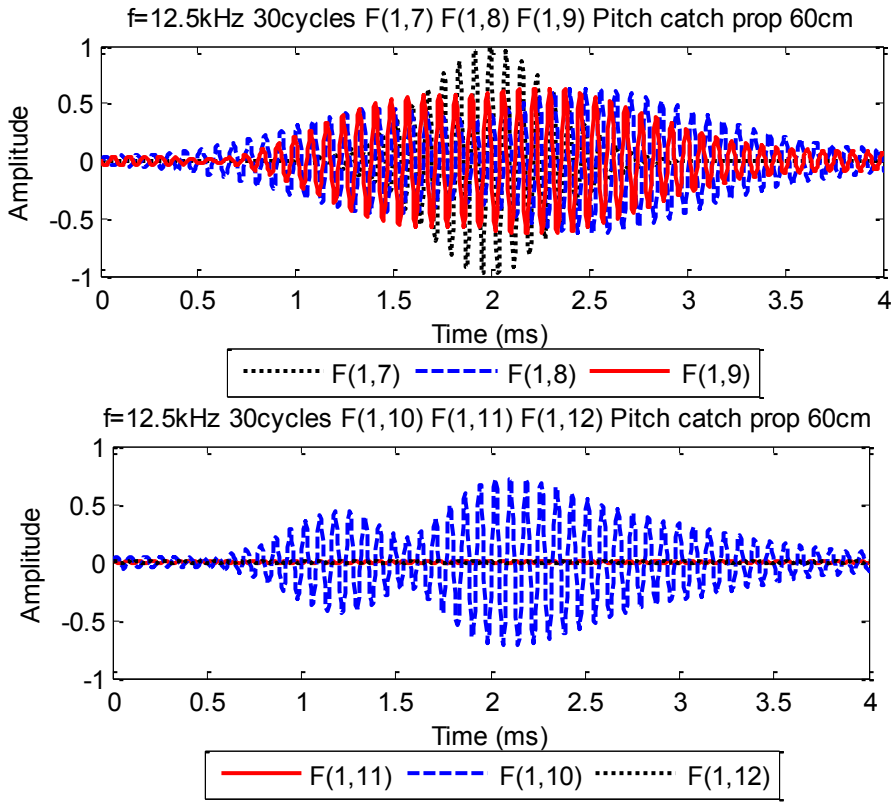

Figure 3.98 Contribution of individual modes on the propagation of a 12.5 kHz input signal with 30 cycle sine burst (pitch catch)

It is noteworthy to state that in this study all the modes are considered to simulate the signal. However, practically, it may not be possible to detect all the modes by the sensors as discussed in the displacement profile section. From the above discussion it is clear that by choosing the correct input frequency and making the frequency band narrower, dispersion of some modes can be reduced. From the energy velocity curve and also from the simulated signal, it is also clear that number of modes arrive almost at the same time because they have similar energy velocity at a particular frequency. To eliminate the most dispersive modes, displacement profiles can be used. From the discussion on displacement profile, it was proposed that not all the modes have highest displacement on the surface of the pole. Moreover, some modes may have almost zero radial and tangential displacements on the surface or some modes also have almost zero axial displacement on the surface of the pole. Consequently, it can be concluded that by placing the sensors in any particular direction (radial/longitudinal/tangential) it is possible to eliminate some modes to be captured by the sensors. Furthermore, attenuation (which is not considered in the simulated signal) may occur because of the

embedded part of the timber pole and some modes may not reflect back from the bottom of the pole due to the high amount of attenuation. In the next section, a comparison will be made between traction free and embedded timber pole based on isotropic material model to analyse the effect of attenuation.

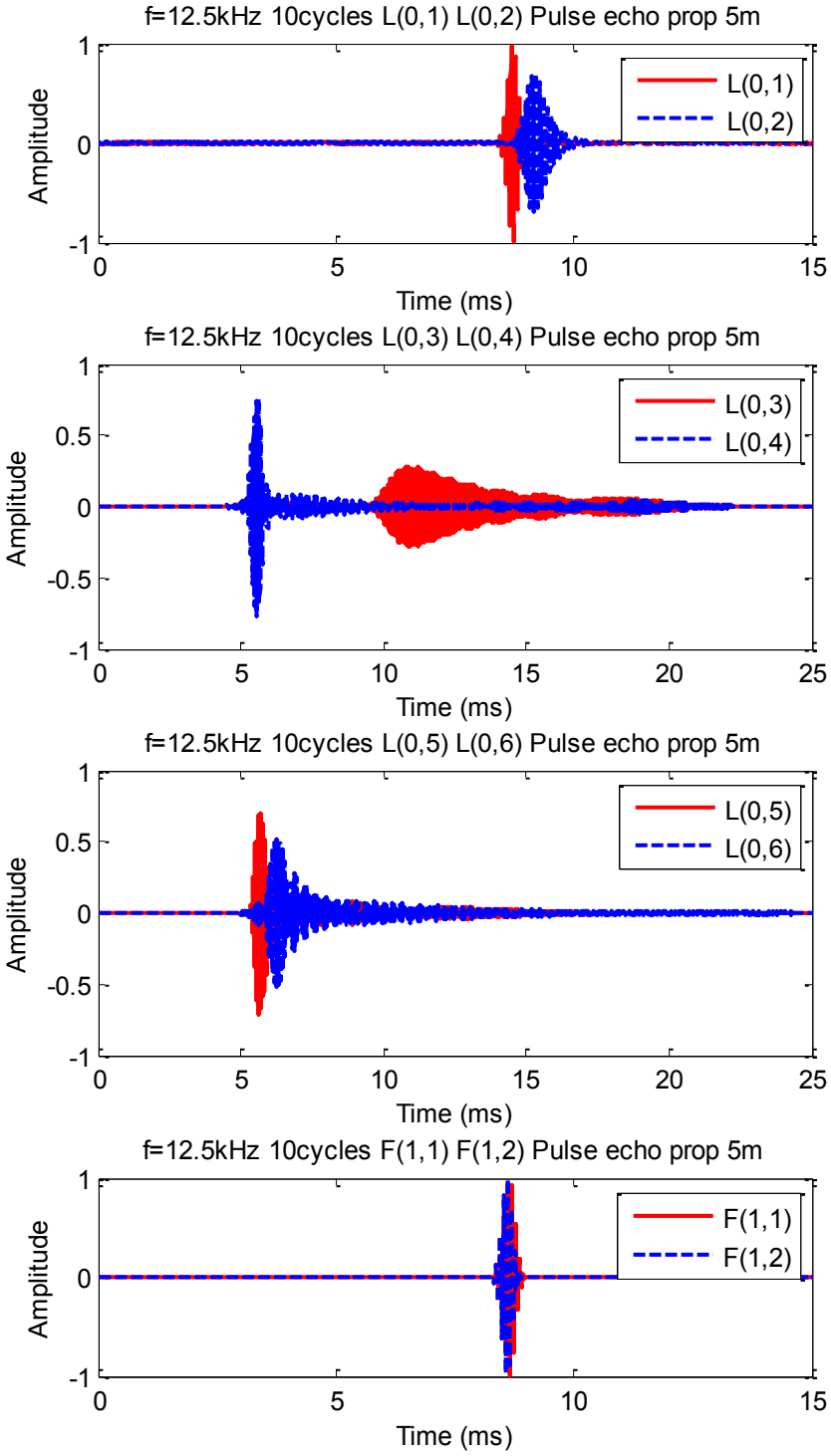

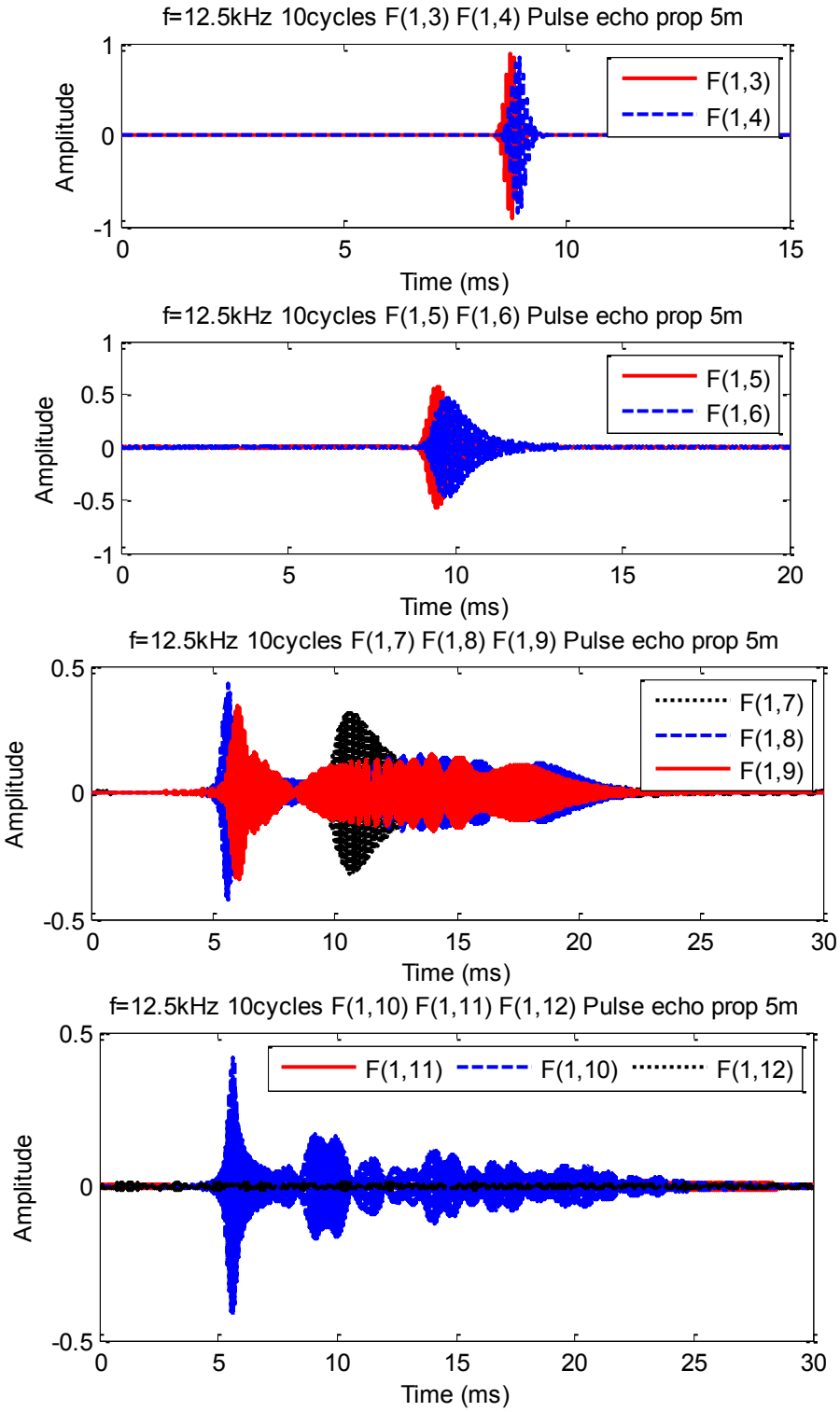

Figure 3.99 Contribution of individual modes for the propagation of a 12.5 kHz input signal with 10 cycle sine burst (pulse echo)

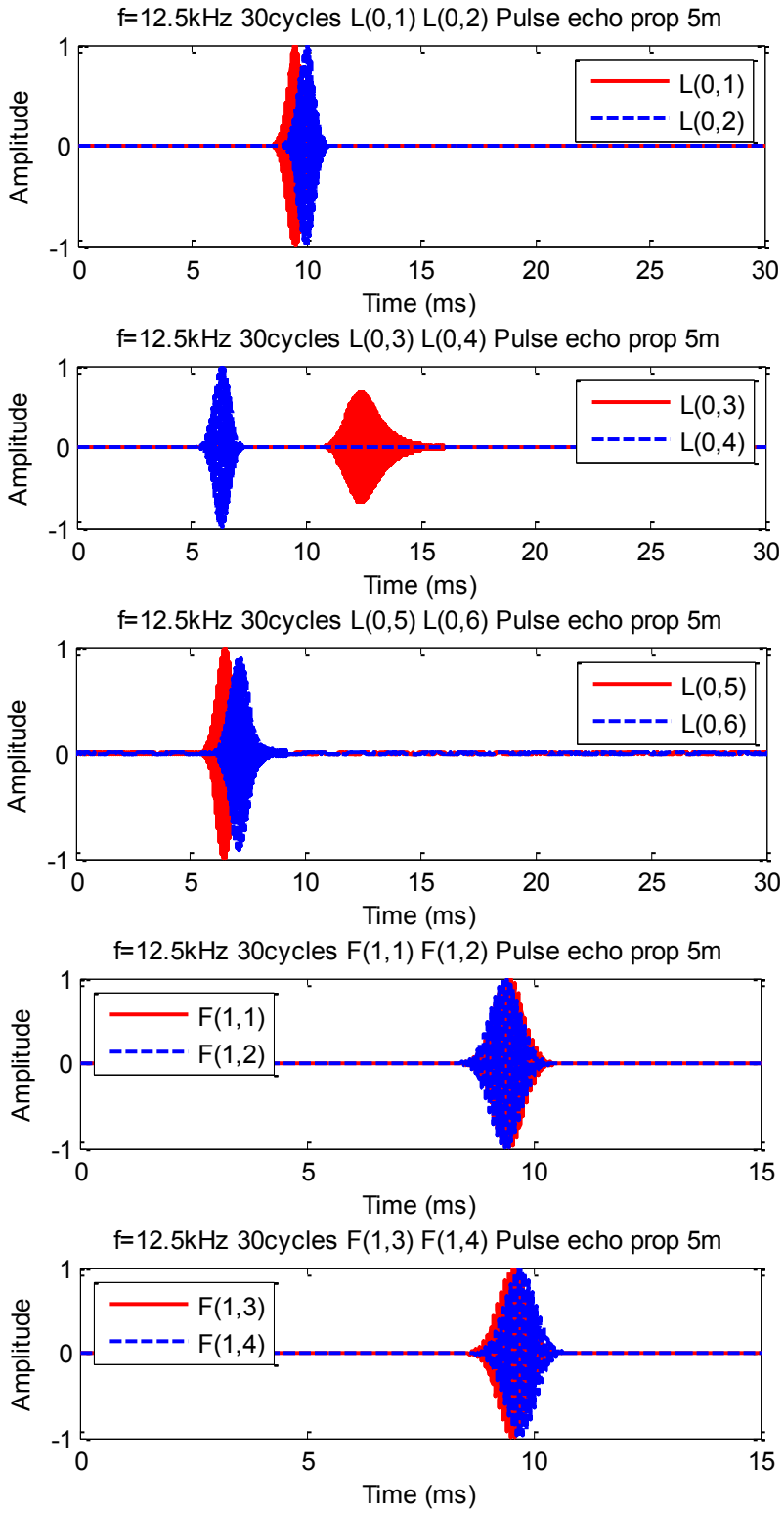
f=12.5kHz 30cycles L(0,1) L(0,2) Pulse echo prop 5m
Amplitude
Time (ms)
L(0,1)
L(0,2)
f=12.5kHz 30cycles L(0,3) L(0,4) Pulse echo prop 5m
Amplitude
Time (ms)
L(0,3)
L(0,4)
f=12.5kHz 30cycles L(0,5) L(0,6) Pulse echo prop 5m
Amplitude
Time (ms)
L(0,5)
L(0,6)
f=12.5kHz 30cycles F(1,1) F(1,2) Pulse echo prop 5m
Amplitude
Time (ms)
F(1,1)
F(1,2)
f=12.5kHz 30cycles F(1,3) F(1,4) Pulse echo prop 5m
Amplitude
Time (ms)
F(1,3)
F(1,4)

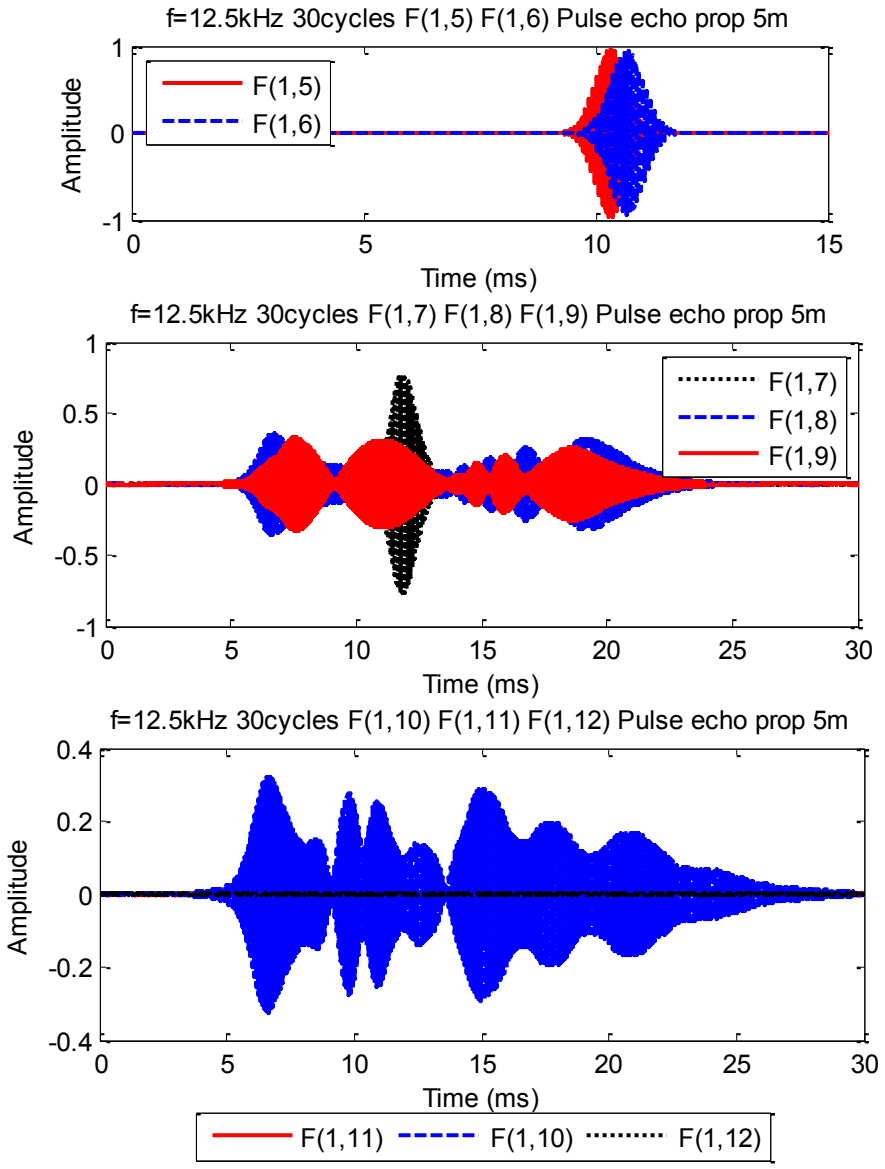

Figure 3.100 Contribution of individual modes for the propagation of a 12.5 kHz input signal with 30 cycle sine burst (pulse echo)

By analysing the energy velocity curves, displacement profiles and simulated signals, it can be concluded that dispersion can be reduced as follows:

1. The input frequency can be chosen in a manner that corresponds to the constant peak energy velocity related to any longitudinal or flexural mode.

2. The appropriate numbers of cycle or sine burst can be selected in order to obtain a narrow band frequency.

3. From the simulated signals, the most dispersive modes can be determined.

4. Possible embedment length can be assumed to check the probability of the reflection of a particular mode since the attenuation can be very high for some modes. If the undesired modes (dispersive) are not reflected back, then reduction in dispersion will be acquired.

5. To eliminate the most dispersive modes (selected from the simulated signals), displacement profiles on the induced frequency can be plotted. From the displacement profiles, the most dispersive modes with the zero displacement components (axial/radial/tangential) can be determined.

6. Depending on the zero displacement components of the dispersive modes on the surface of the pole, the orientation of the sensors can be finalised.

3.7.1.4 Effect of propagation distance

In the pulse echo method, the embedded length is unknown; hence, it is not possible to change the propagation distance. Additionally, dispersion is inevitable in the pulse echo method due to the mode conversion on reflection and also the propagation distance is usually more compared to the pitch catch method. When the propagation distance is higher, even the smallest change in energy velocity among the branches makes a significant difference on reaching the sensor because of the different arrival time of the modes. Thereby, distortion is observed. However, in the pitch catch method, it is possible to change the distance between the generator and receiver or between the sensors in multi sensors arrangement. In this section, the effect of this propagation distance in the pitch catch method will be demonstrated.

As an example regarding propagation distance, the input frequency is chosen at 7 kHz with 10 and 30 cycles (Figure 3.101). Both longitudinal and flexural waves are considered at the same time. The reduction in propagation distance clearly decreases the dispersion as indicated by Figure 3.102. From this figure, it is clear that even with 10 cycle sine burst, distortion of the signal is decreased immensely when the propagation distance is changed from 60 cm to 20 cm. For 30 cycle sine burst, the dispersion is already less because of the narrow frequency band as discussed in previous sections and is shown in Figure 3.103. Therefore, for 30 cycle sine burst, 60 cm distance between the generator and receiver is acceptable. Although an improvement can be made by reducing the propagation distance to 20 cm as depicted in Figure 3.103 (bottom figure).

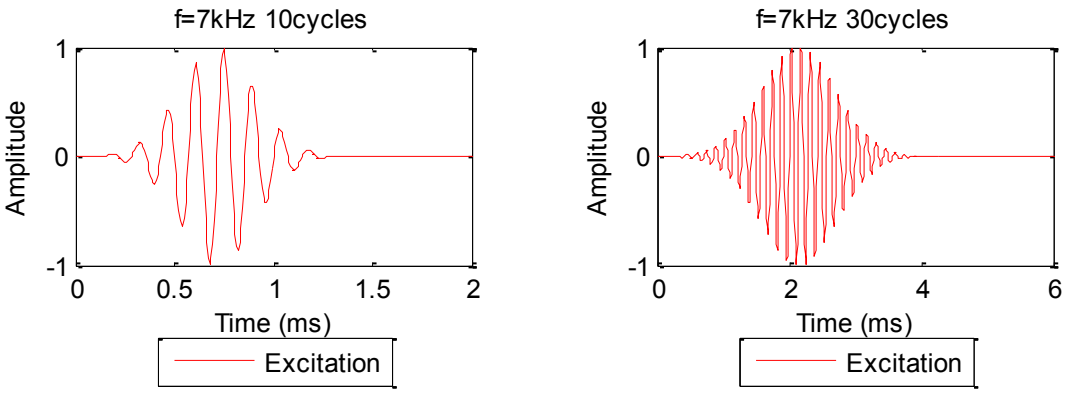

Figure 3.101 Excitation at 7 kHz frequency with 10 (left) and 30 cycles (right)

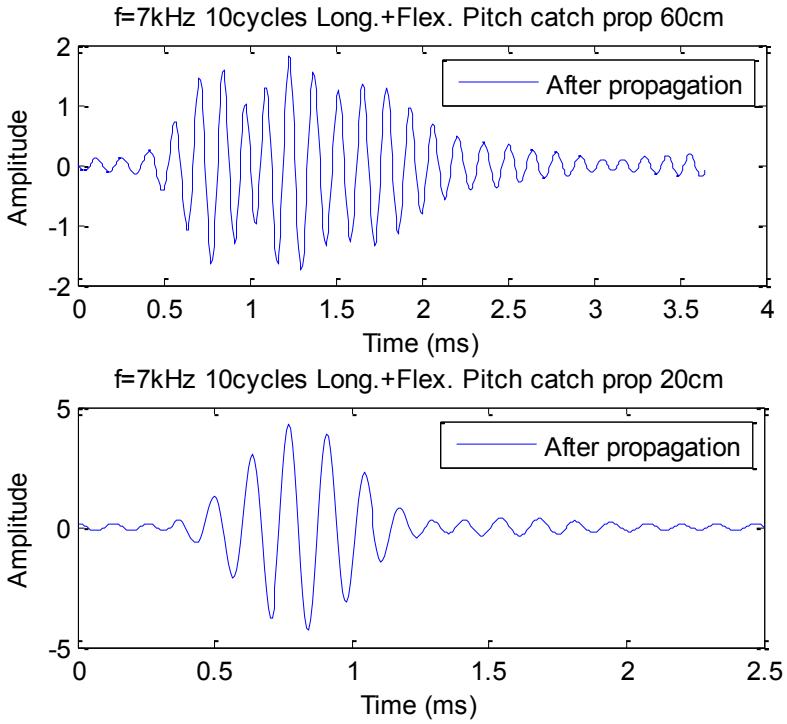

Figure 3.102 Propagation of longitudinal and flexural modes at 7 kHz with 10 cycle sine burst with a propagation distance of 60 cm (top) and 20 cm (bottom)

In Section 3.7.1.3, the input frequency was used as 12.5 kHz where high amount of dispersion was observed as a great number of longitudinal modes intersect at this frequency. The results for pitch method with a 60 cm propagation distance were displayed in that section which suffers from dispersion. Figure 3.104 plots the propagation of 12.5 kHz wave with 10 and 30 cycle sine burst where the propagation

distance is 20 cm. It is clear from the figure that the modification of 10 cycle sine burst on dispersion is not satisfactory when the propagation distance is reduced. This is due to the high amount of dispersion at 12.5 kHz. In contrast, 30 cycle sine burst gives better results compared to 10 cycle one. However, some distortion can be observed. Therefore, it can be concluded that 30 cycle sine burst is better to use for 12.5 kHz and 20 cm distance between the generator and receiver is the marginal range. To get a less distorted signal at 12.5 kHz, the number of cycles can be increased or the propagation distance reduced.

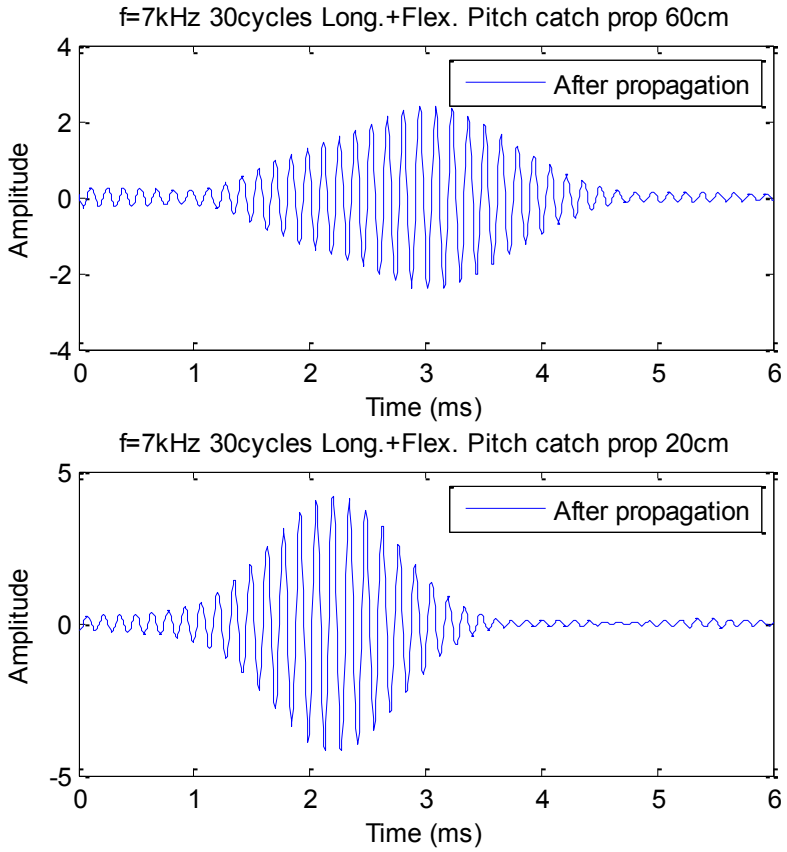

Figure 3.103 Propagation of longitudinal and flexural modes at 7 kHz with 30 cycle sine burst with a propagation distance of 60 cm (top) and 20 cm (bottom)

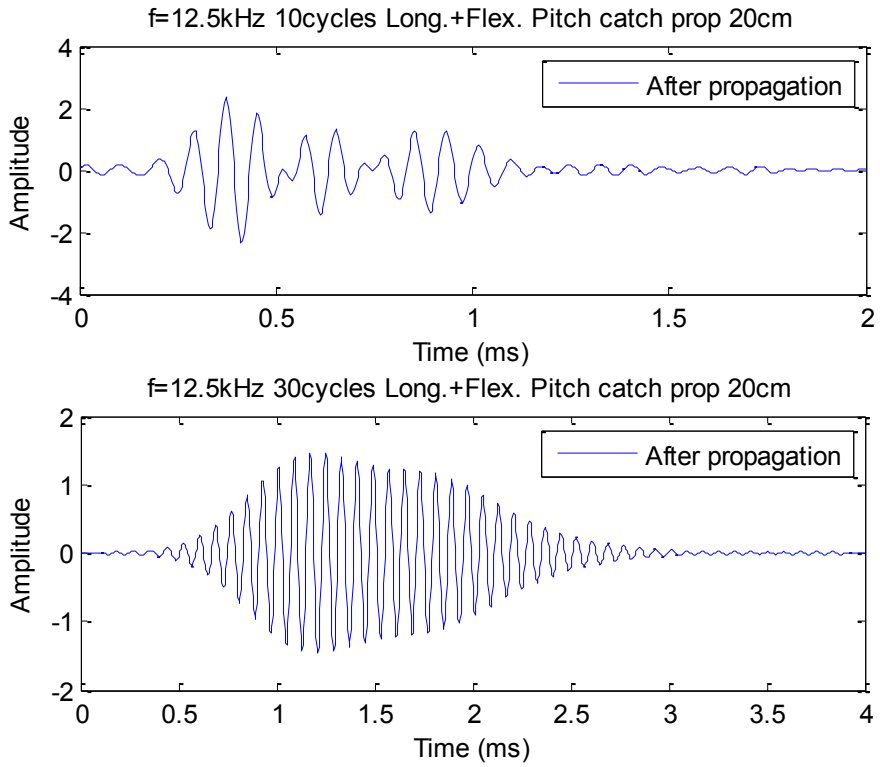

Figure 3.104 Propagation of longitudinal and flexural modes at 12.5 kHz with 10 cycle (top) and 30 cycle (bottom) sine burst with a propagation distance of 20 cm

3.7.2 Isotropic material

For the isotropic material, both traction free and embedded conditions are taken into account. For both conditions, set 10 (Table 3.3) is used as the properties of timber and for embedded situation, the properties of soil 1 are chosen for soil (Table 3.6). The energy velocity curve (Figure 3.105) and attenuation curve (Figure 3.106) up to 65 kHz is presented here. From the energy velocity, it is clear that the energy velocity curve of an isotropic material is very much different from transversely isotropic material. The peak energy velocities of each branch in an isotropic cylinder do not reach the bulk longitudinal wave velocity which is a common phenomenon in a transversely isotropic material. Additionally, the peak energy velocity of each branch remains constant for a very small frequency range. Hence the input frequency range has to be very narrow to avoid dispersion. However, very narrow band frequency is practically hard to induce. Therefore, dispersion is also inevitable in an isotropic material.

In a transversely isotropic material, longitudinal and flexural waves are often induced simultaneously and they have peak maximum energy velocity in an alternate fashion.

Thereby, even though the input frequency is chosen at the peak constant energy velocity of a longitudinal wave, distortion is observed due to the maximum dispersion point at that frequency which is corresponding to the flexural wave. In contrast, in an isotropic material it is possible to create longitudinal and flexural wave solely. However, no input frequency can reduce the dispersion because of the absence of peak constant energy velocity over a broad range of frequency.

In this section, isotropic material is taken into account mainly to show the effect of attenuation in the signal. Two input frequency is chosen for isotropic material, i.e. 16.5 kHz and 50 kHz and also both 10 cycles and 30 cycles are selected. The results of 16.5 kHz and the plot of 50 kHz input frequency with 10 cycles are presented in Appendix C. In this section, the results of 50 kHz with 30 cycle sine burst are demonstrated. Propagation distances in pitch catch method are considered as 60 cm and in pulse echo method, 5 m propagation distance is employed. For the pitch catch method, only traction free condition is taken into account which is the practical situation. However, in the pulse echo method, both traction free and embedded situation are investigated to point out the effect of soil or attenuation. Longitudinal and flexural waves are displayed separately for the isotropic condition.

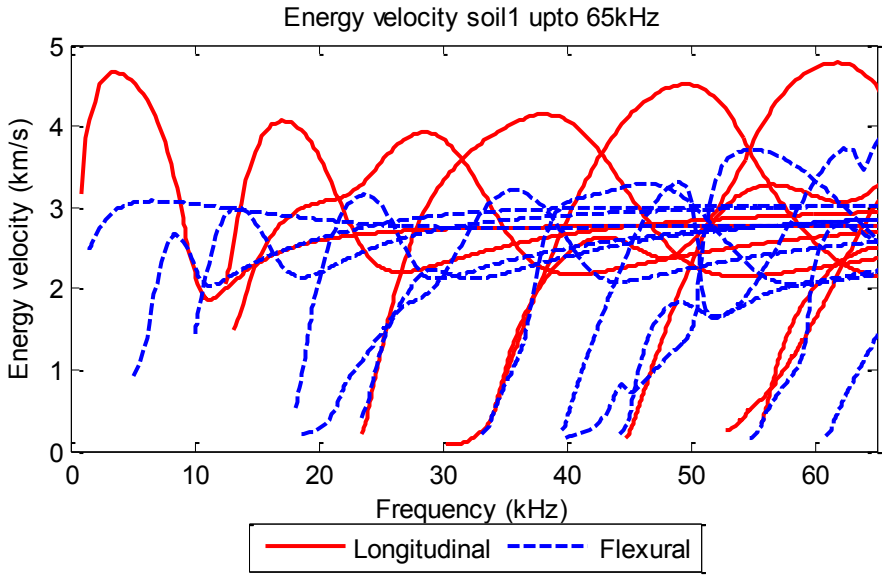

Figure 3.105 Energy velocity curve of an isotropic cylinder embedded in soil up to 65 kHz

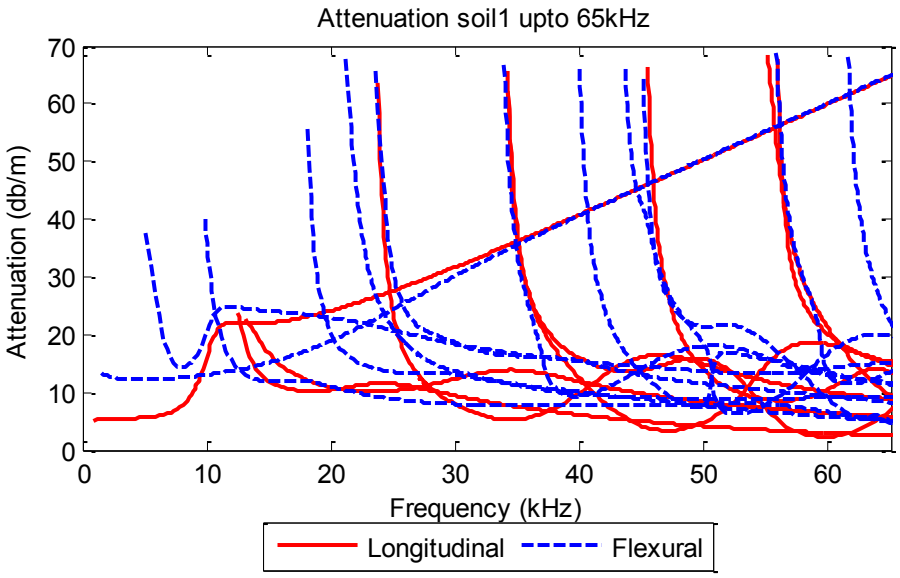

Figure 3.106 Attenuation curve of an isotropic cylinder in soil up to 62 kHz

3.7.2.1 Final signal or summation of all modes

Figure 3.107 plots the excitation signal with 30 cycle sine burst at the central frequency of 50 kHz. Figure 3.108 and Figure 3.109 represent the propagation of longitudinal and flexural modes, respectively, with a distance of 60 cm. It can be seen that the longitudinal modes are less dispersive compared to the flexural waves. This is because of the chosen input frequency which is corresponding to the peak energy velocity of a longitudinal mode (Figure 3.105). In addition, the 30 cycle sine burst produces a narrow band signal. Hence, it can be justified that this distance between the generator and receiver for longitudinal wave propagation at this frequency is sufficient to reduce the amount of dispersion. For the flexural wave propagation, the signal is distorted, however, not to a great extent. Thus, reducing the propagation distance may solve this problem.

The plots of pulse echo method of a traction free cylinder are illustrated in Figure 3.110 and Figure 3.111 where the former one is corresponding to the longitudinal modes and the latter is related to the flexural modes. Again more dispersion can be observed out in the flexural wave. To reduce the effect of dispersion, the contribution of individual mode and normalised displacement should be analysed as discussed in the previous sections.

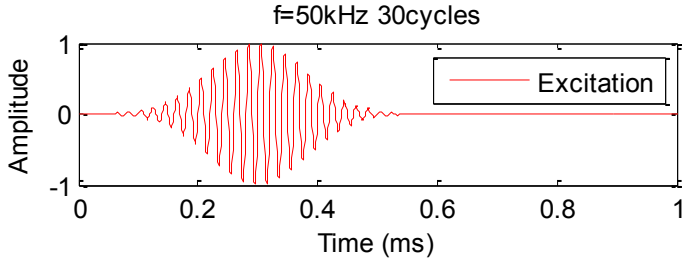

Figure 3.107 Excitation at 50 kHz frequency with 30 cycles

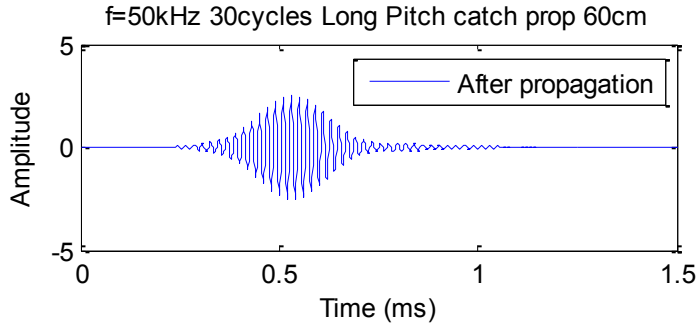

Figure 3.108 Propagation of longitudinal modes with a distance of 60 cm (pitch catch)

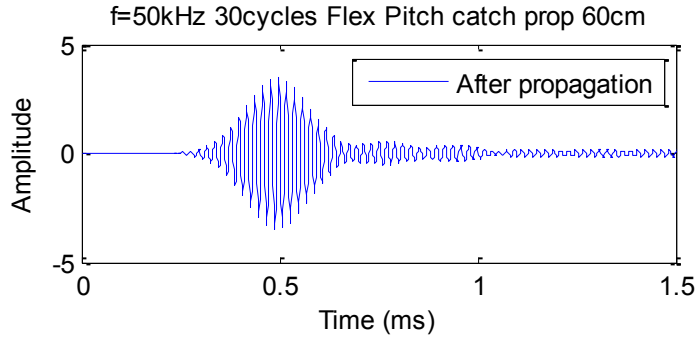

Figure 3.109 Propagation of flexural modes with a distance of 60 cm (pitch catch)

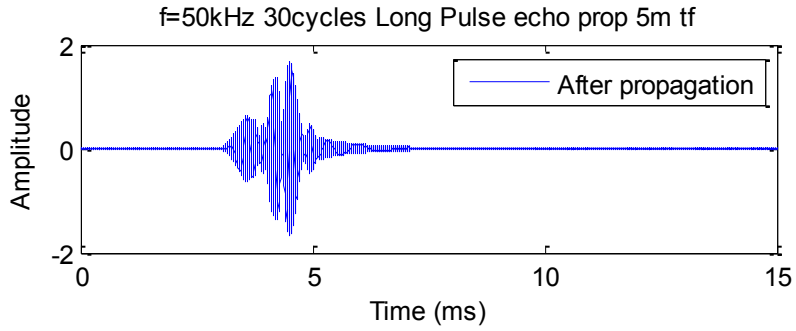

Figure 3.110 Propagation of longitudinal modes with a distance of 5 m (pulse echo) in traction free isotropic cylinder

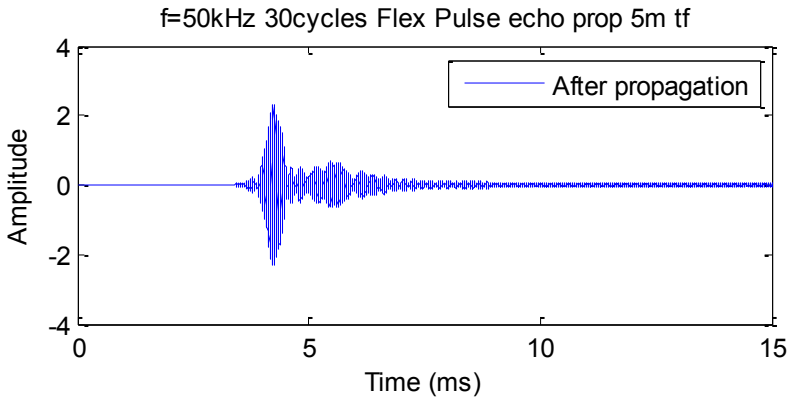

Figure 3.111 Propagation of flexural modes with a distance of 5 m (pulse echo) in traction free isotropic cylinder

Figure 3.112 and Figure 3.113 represent the propagation of longitudinal and flexural modes, respectively, with a distance of 5 m by pulse echo method. In particular, the modes with very high attenuation may not come back on reflection or will have very small amplitude. As a result, a great number of modes will have less contribution in the final signal as illustrated in Figure 3.112 and Figure 3.113. By comparing these two figures with traction free condition, it is clear that the shape of the reflected signal in the pulse echo method is totally different when attenuation is present. Moreover, the group behaviour is almost absent in the reflected signal when the timber or the cylinder is surrounded by soil. Furthermore, a distinct peak is observed in the signal. Therefore, it is not easy to select the reflected peak while the embedded length is needed to be determined or if damage is present below the soil. Furthermore, the substantial amount of amplitude reduction is also elucidated due to the loss of energy in the soil. In the stiff soil, the attenuation is more and some amplifier may need to be used.

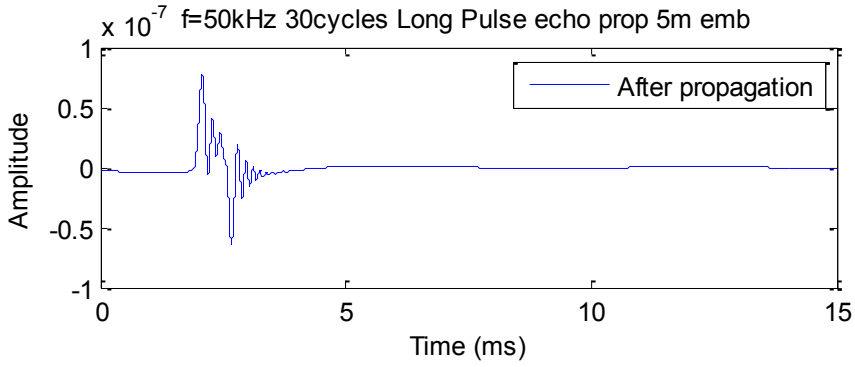

Figure 3.112 Propagation of longitudinal modes with a distance of 5 m (pulse echo) in embedded isotropic cylinder

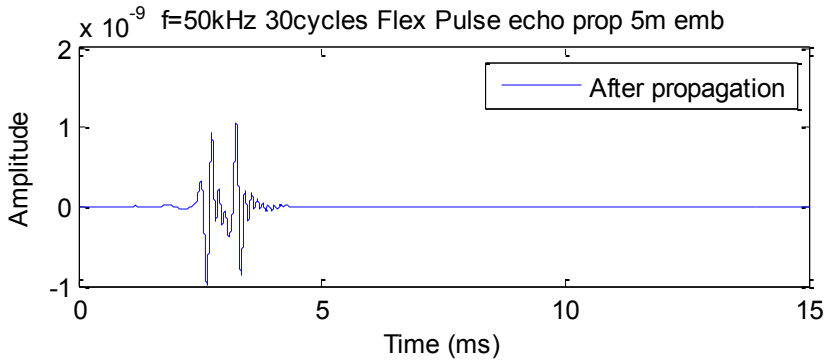

Figure 3.113 Propagation of flexural modes with a distance of 5 m (pulse echo) in embedded isotropic cylinder

From the discussion and investigation, it can be predicted that least dispersion will be observed at 16.5 kHz input signal with 30 cycle sine burst. Additionally, longitudinal waves should have less dispersion as mentioned in the previous paragraph. It can also be predicted that 60 cm propagation distance in the pitch catch method is sufficient for this condition. Moreover, for the 16.5 kHz signal with 10 cycles burst, it may be essential to reduce this propagation distance. As mentioned earlier, the results of 16.5 kHz signal with different propagation distance, with 10 and 30 cycle sine burst, for traction free and embedded condition is presented in Appendix C. The longitudinal and flexural waves are plotted separately. The results of 50 kHz with 10 cycle sine burst can be also seen in Appendix C.

3.7.2.2 Contribution of individual modes

The contributions of individual modes with the propagation distance of 60 cm (pitch catch method) for the 50 kHz input signal with 30 cycles are not essential to analyse due to the fact that the minimisation of dispersion is satisfactory. However, the pulse echo method suffers extensively from dispersion and the contribution of individual modes may help to reduce this effect. Figure 3.114 displays the contribution of the longitudinal modes in a traction free isotropic cylinder for the 50 kHz input signal with 30 cycles where the most distorted mode is L(0,7). Also, L(0,8) and L(0,9) modes have very little amplitude because at this frequency range, these two modes just start propagating with very little energy. The final signal is depicted in Figure 3.110 where different packets are formed due to the arrival of different modes at different times (different energy velocity) and distortion is observed due to the L(0,7) modes.

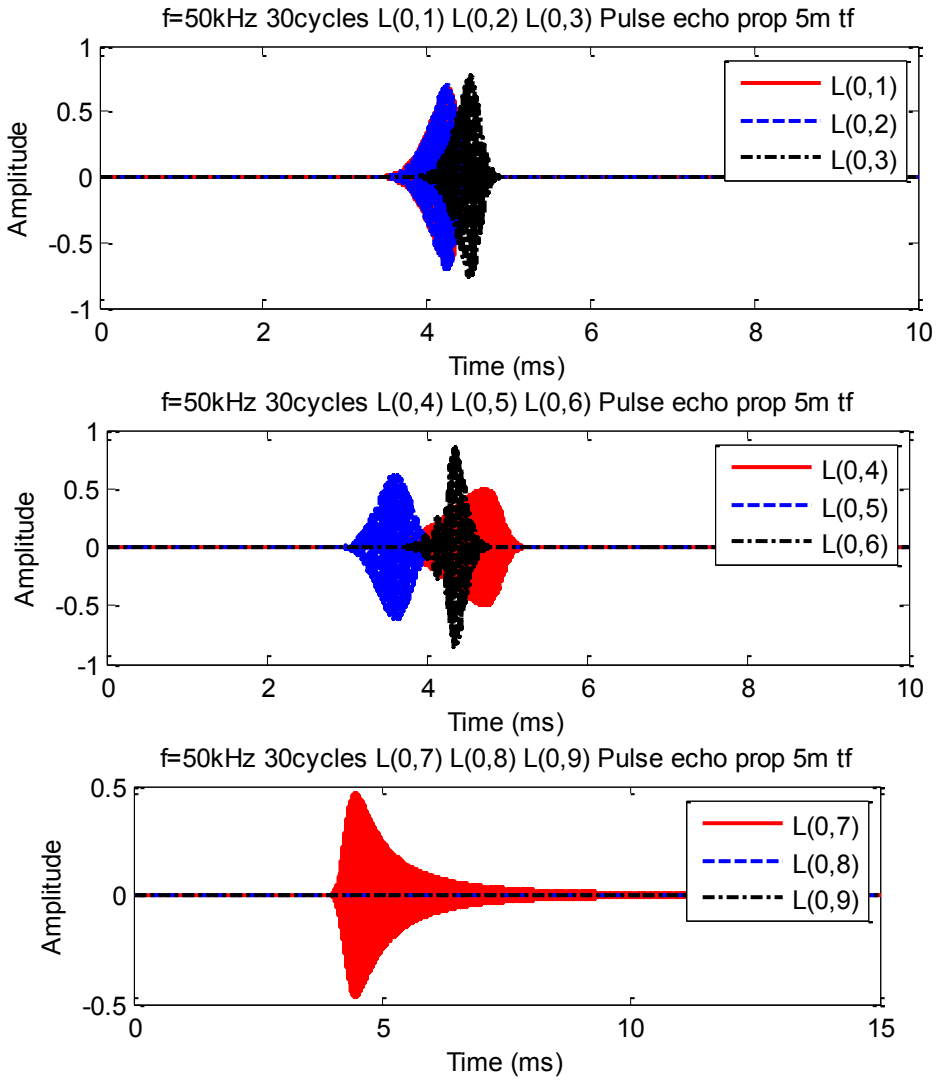

Figure 3.114 Contribution of individual longitudinal modes in traction free isotropic material (tf= traction free)

In comparison with the traction free condition, significant amount of distortion can be illustrated in the embedded condition (Figure 3.115). The L(0,1) mode is distorted in a totally different shape and has the highest amount of amplitude. The amplitude of the L(0,2) and L(0,3) modes are so less compared to L(0,1) mode that in the same scale these cannot be seen. The contribution of other modes are also substantially low compared to L(0,1) mode. The reductions in amplitudes are clearly due to the attenuation or losing of energy in the soil. Although the shape matched notably well with the same mode in the traction free condition (except L(0,1) mode) because of the vast attenuation of these modes, the final signal (Figure 3.112) is dominated by the L(0,1) mode.

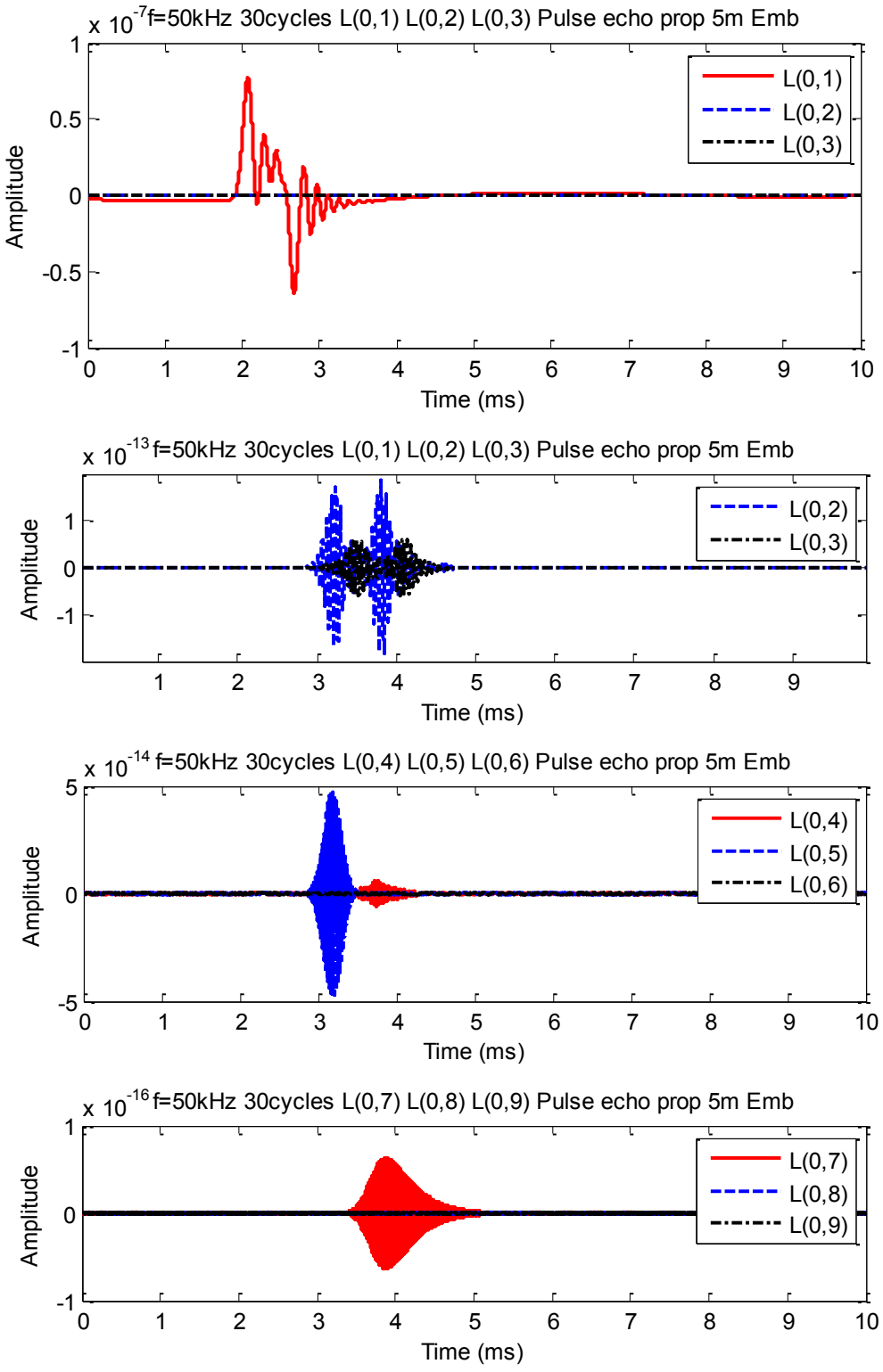

Figure 3.115 Contribution of individual longitudinal modes in embedded isotropic material (Emb = Embedded)

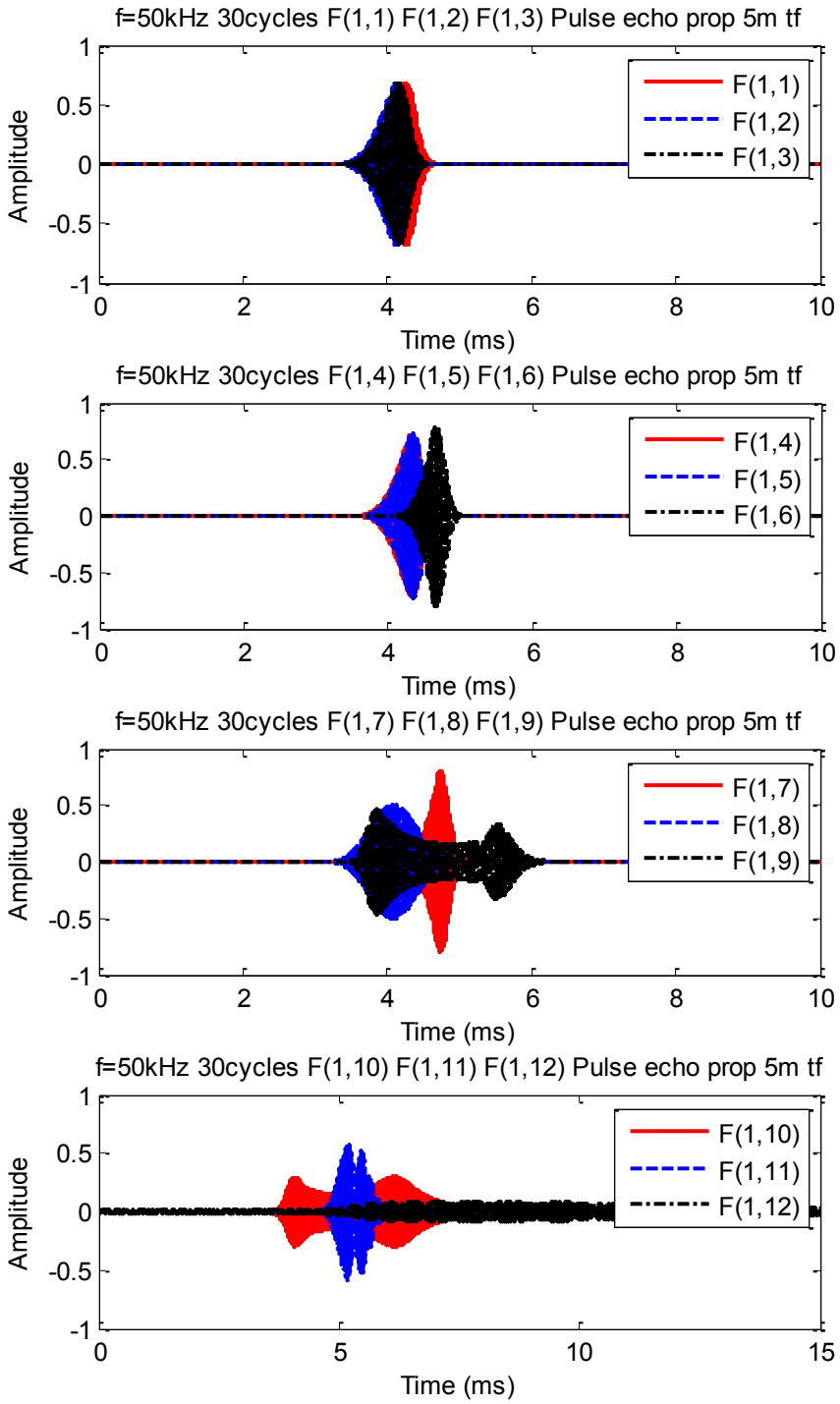

Figure 3.116 Contribution of individual flexural modes in traction free isotropic material

For the flexural wave propagation, more dispersion is expected as depicted in Figure 3.116. In this figure, the F(1,8) to F(1,12) modes show extensive amount of dispersion to the signal while the cylinder is isotropic. For the embedded condition, the reduction in amplitude can again be seen from Figure 3.117. The F(1,1) mode distorted the most

and has the highest amplitude in comparison with the other modes. F(1,4) mode is also distorted, however the loss of energy is more in this mode. The F(1,6), F(1,11) and F(1,12) modes have very high attenuation and their contribution to the reflected signal is very low at the input frequency of 50 kHz and with a propagation distance of 5m. Therefore, the final signal (Figure 3.113) is dominated by the F(1,1) mode.

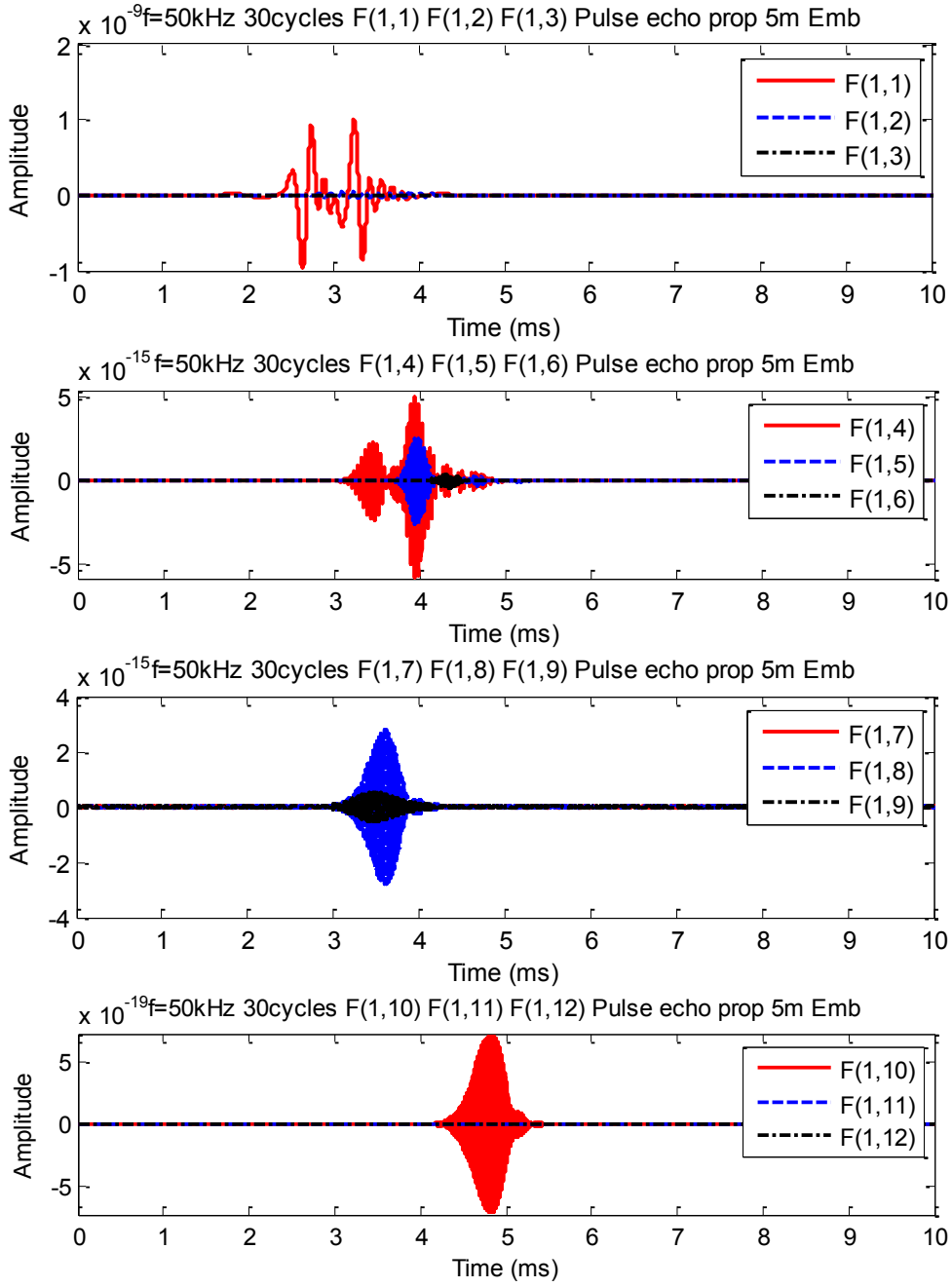

Figure 3.117 Contribution of individual flexural modes in embedded isotropic material

3.8 Limitations of guided wave theory

The GW theory can suggest a great number of solutions while solving for a plate or cylinder. The great advantage is that it allows for the lateral confinement of the cylinder or plate and thus, the guided wave is formed. It also reflects the three dimensional behaviour and also gives ideas about the velocities of different modes, normalised displacements, normalised power flow etc. However, it has some limitations. The main limitations are, it considers infinite length of the plate or cylinder, it cannot model partial embedment of the structure and hence, the time domain reconstruction cannot reflect the actual field behaviour.

The reasons behind the difficulties of solving the wave propagation in finite or semi-infinite media can be explained from the dispersion relation. As discussed in Section 3.2.3, the characteristic or frequency equations can have three kinds of roots. These are real (related to propagating modes), imaginary (related to non-propagating modes) and complex (also called evanescent modes). All the roots are essential to solve the frequency equation. The evanescent roots with complex numbers have both imaginary and real parts. The real part indicates the propagation of the branch and the imaginary component indicates that the branch attenuates spatially. Pilant [147] pointed out that a pair of complex modes, one traveling in the +z direction and one travelling in the –z direction, are always generated simultaneously. Therefore, a standing wave is formed which loses energy very fast spatially and does not transport any energy. These evanescent branches are important for problems involving semi-infinite and finite waveguides which are required to satisfy the boundary conditions at the end of the bar. For low frequencies with only a single propagating mode, the mode shape of the first mode is not sufficient to satisfy an arbitrary stress function at the end of the bar. The shapes of the infinite number of evanescent modes allow an arbitrary stress function to be represented by an expansion over the modes [141].

The frequency equations based on Pochhammer - Chree theory describes the solution for the wave propagation in an infinite cylindrical waveguide. The dispersion relation developed from these equations can be used to check the velocities from the experimental results. However, experimental results are collected in the time domain and thereby, conversion of the Pochammer – Chree equation in the time domain is required for finite or semi-infinite media which is difficult due to the additional face at

the bottom of the cylinder and the complications associated with the boundary conditions.

In NDE of timber pole, the most important aspect of a signal is to detect the reflection from the end of the pole or from a damage to determine the embedded length and location of damage, respectively. Subsequently, the reflection behaviour of a signal is very important. Kolsky [131] showed the reflection characteristics for a plane wave between two media based on Snell's law and concluded that the phase change on reflection at the boundary depends on the characteristic impedance (product of density and wave velocity). When the characteristic impedance of the second medium (in timber pole situation, it is soil) is higher than that of the first (timber), then there will be a 180° phase change in the vibration, but the phase will remain the same if the soil impedance is less than timber. This is also true for the longitudinal wave propagation in a wave guide.

For guided wave propagation, few analytical solutions can be found for different end conditions and few literatures are also reported on considering the impact load on the structures. Two approaches have been developed for the solution of end condition, namely integral transform method and solving the boundary value problem for a semi-infinite cylindrical rod subjected to an initial condition. Skalak [148] considered an infinite cylinder, solving the differential equations for a set of boundary conditions that modelled the collision of two semi-infinite cylinders. Folk et. al. [149] introduced a solution for a semi-infinite bar loaded with a step pressure function at the end of the bar. Jones and Norwood [150] used the method of Folk et al. to investigate the axially symmetric longitudinal response of a semi-infinite elastic bar to a pressure step end loading and to a velocity impact end loading. Kennedy and Jones [151] further explored the effects of different radial distributions on the response of a waveguide to a pressure step end loading. Goldberg and Folk [152] extended the method of Folk et al. to solve the pure-end-condition problem. They obtained the solution to two mixed-end-condition problems, and used these solutions to solve the pure-end-condition problem. Their results agree well with the experimental work of Curtis and Fox [153].

Davies [154] used the phase velocities from the frequency equation and a Fourier decomposition to predict the change in shape of a trapezoidal (first mode only) excitation in a finite cylindrical bar. In a similar method Follansbee and Frantz (1983)

calculated a dispersion correction for signals measured in the split Hopkinson pressure bar (SHPB). Zemanek [136] considered the stresses of the modes to determine the reflection of the first branch incident at the free end of a cylindrical bar. In addition to the fundamental branch, modes with complex wave numbers were considered in an expansion to satisfy the stress free boundary conditions. Reflection coefficients were calculated from a system of equations equal to the number of modes considered, and an end resonance was observed. Gregory and Gladwell [155] also considered the reflection of the first mode but calculated the coefficients in the expansion using an integral formulation of least squares. The resonant frequency observed by both Zemanek and Gregory and Gladwell was very close to the experimental frequency measured by Oliver [156].

Peterson [157] combined the techniques of Davies and Zemanek. A system of equations was used to determine the coefficients of the propagating modes in a finite cylindrical waveguide with a broadband excitation, and Fourier decomposition was used to determine the phase shift of each mode. Puckett [158] also developed an excellent analytical model to determine the reflection and also verified this experimentally.

Graff [132] considered a steady train of harmonic incident waves in a semi-infinite beam and determined the frequency dependent amplitude ratio of the reflected flexural waves. The reflective characteristics for different boundaries of a semi-infinite thin beam were also investigated. It was reported that the phase shift of a flexural wave depends on the end condition of the beam and also on frequency component. However, most of these analytical works are complicated and can only be used for simple boundary conditions (such as pinned, hinged, fixed end etc.), simple geometry (constant diameter) and mainly for isotropic materials.

From the above discussions, it can be concluded that most of the analytical works are performed on semi-infinite cylinder or on limited numbers of modes for finite cylinder while dealing with the end conditions of the structures. Also, the load is applied in the longitudinal direction and mainly symmetrical loading is considered. Therefore, some simplifications are always made in the analytical solutions. Consequently, some numerical methods are reported to incorporate the location and orientation of the load, different types of loads, finite length of the structures etc.

There are a good number of numerical methods available to draw the dispersion curves and also for the reversal of the signal in the time domain. Alterman and Karal [159] used finite difference method for the elastic wave propagation in a semi-infinite cylindrical rod. Puckett [84] developed an finite element model (FEM) to plot the dispersion relation and also the time domain plots for a finite rod were presented. Another widely used numerical or semi-analytical tool is the Spectral finite element method (SFEM). Both of these methods have their own advantages and disadvantages. Such as, in the FEM, the approximation of the mass matrix, the appropriate stiffness matrix etc. cannot be determined accurately and also time consuming for the necessity of fine mesh. Whereas, SFEM is very accurate in these regards and is very good for the wave propagation problems. By SFEM, different boundary conditions (such as timber pole situation), different shapes (tapered etc.) can be modelled easily. Additionally, both the dispersion curves and time domain data can be investigated. On the other hand, SFEM can only predict the signal on the surface of the pole since SFEM is mainly based on 1D or 2D simplification whereas, 3D model can be generated easily using the FEM. 3D model or the wave propagation in a three dimensional space is sometimes helpful as the displacement of the particles have different properties (polarization of the stress wave) along the circumference of the cylinder as discussed in this chapter (Section 3.2.3.3, 3.3.3, 3.4.2.5, 3.6.3) and it is useful to develop a 3D sensor network system to reduce the effect of dispersion.

At the end, both methods can easily deal with the locations and orientation of load of any desired shape/properties. The GW propagation by SFEM is explained in Chapter 4 while FEM modelling of timber pole is described in Chapter 5.

3.9 Conclusions

In this chapter, different wave theories were described and it was justified that, GW theory is the most relevant theory while dealing with the timber pole situation. GW theory can be derived for isotropic and anisotropic materials. For the isotropic model, some parametric studies were undertaken on the effect of different material properties on the GW propagation. It is found that, even though modulus of elasticity and density change the velocity, the trend remain similar. Poisson's ratio has very little effect on the dispersion curves. It is also shown that, moisture content and temperature affect the stiffness or modulus of elasticity of the material and thus, the GW propagation is

affected. Hence, it is better to measure the amount of moisture content in a timber pole and also the temperature on a given day to accurately calculate the modulus of elasticity of timber pole. When the pole is considered as embedded in soil, the properties of the surrounding material also influence the dispersion curves. Leakage of the energy or attenuation occurs due to the presence of soil and it increases with the increase of soil stiffness. The surrounding medium does not affect the wave velocity except in the very low frequency range.

Even though the timber can be modelled as an isotropic material to perform some parametric studies, it cannot give the correct dispersion curves for timber. Timber is an orthotropic material and any anisotropic material has more wave branches within the same frequency range compared to the isotropic dispersion curves. For simplification, timber can be considered as a transversely isotropic material, provided that correct parameters are chosen from the orthotropic properties of timber. By choosing the correct parameters, transversely isotropic material modelling can be used successfully for the longitudinal wave propagation and low frequency flexural wave propagation. However, for the high frequency flexural wave propagation, an orthotropic model is suggested, if high accuracy is required.

This chapter also discussed reducing the effect of dispersion. This can be achieved by analysing the energy velocity curve, normalised displacement and simulated signal. It is shown that, the input frequency corresponding to any constant peak energy velocity of any particular mode can reduce the dispersion. The narrower the input frequency band, the less will be the dispersion. Therefore, 30 cycle sine burst (or more) can be used to reduce this effect. If distortion of the signal still exists, the sensors distance can be decreased to obtain the signal in the expected form which is essential to determine the stress wave velocity accurately. It is also presented that, not all the modes are responsible for dispersion. Therefore, the modes which are causing the most dispersion can be determined from the contribution of individual modes in a simulated signal. Based on the displacement profile of those modes, further reduction of dispersion can be achieved. This is due to the fact that the particles on the surface have different polarisation of displacement and some of them are zero on the surface. By placing the sensors in the orientation of zero amplitude displacement components related to the most dispersive modes, the undesired mode/s can be eliminated.

To wrap up, it can be mentioned that, GW theory can be used successfully to choose the correct input frequency, number of cycles and also to arrange a 3D sensor network system to reduce the effect of dispersion. However, the time domain reconstruction for a finite length structure is difficult to achieve due to the simplifications in the boundary conditions. Besides, GW theory does not consider the load in the characteristic equation. As a result, some numerical methods can be used to serve this purpose.

Chapter 4

4 Study of guided wave propagation using the Spectral Finite Element Method

4.1 Introduction

This chapter discusses the guided wave propagation in a cylindrical structure using the Spectral Finite Element Method (SFEM). The first part of the chapter describes different available theories for both rod and beam like structures. It is noteworthy to state that SFEM considers the one dimensional simplification of a real structure with the highest accuracy. The theories for both isotropic and anisotropic cylindrical waveguides are presented. Some issues related to solving the equation associated with different theories of SFEM are also discussed in this part. The theories which are considered for isotropic rod like structures are the elementary theory [87], the single mode Love theory [56], the two modes Mindlin-Hermann theory [56] and the three mode theory [56]. The theories are related to an isotropic beam using the Bernoulli-Euler theory (EBT) [88] and the Timoshenko beam theory [98]. It must be noted that the rotary inertia and the shear deformation is taken into account in the Timoshenko beam theory. Accordingly, an additional mode (shear mode) can be observed in addition to the flexural mode. For the anisotropic beam, the Timoshenko beam theory for anisotropic materials [86, 98-100] is considered. The theory for anisotropic materials is derived for unsymmetrical laminated composite beams and functionally graded materials. As a result, the equation related to this expresses the coupling of longitudinal, flexural, shear and contraction

modes. The contraction mode which has the same behaviour as the longitudinal mode, comes into the equation because of the Poisson's effect in a deep beam.

In the second part of the chapter, comparisons are made between the different theories in the frequency domain to demonstrate the differences and limitations of various theories. The results are shown in terms of the phase velocity curves. Also, the dispersion curves of different theories are compared to the actual analytical curves presented in Chapter 3. From these studies, the correct theories, which can resemble the closest practical solution for the timber pole situation, are chosen for an isotropic rod, an isotropic beam and an anisotropic cylinder. Then, the appropriate theories are used to reconstruct the signal in the time domain.

Part three of the chapter describes the time domain solutions under different boundary conditions. Mainly two boundary conditions are investigated. The first one considers the timber pole standing on the soil and the second one considers the timber pole as partially embedded in soil which is the practical situation. These two boundary conditions are adopted to illustrate the effect of soil on wave propagation when the structure is partially embedded. The soil is represented by a spring and dashpot system. Again, isotropic and anisotropic material modelling is discussed. Different impact locations and orientations are explained to show the effect of various impact situations. Also, the coupling of different modes due the impact orientation is pointed out in this part. The input frequency is chosen from group velocity curves as described in Chapter 3. A narrowband input frequency is considered to reduce the effect of dispersion.

4.2 Theories of SFEM

SFEM is based on domain transfer method where the governing equation is transformed into the frequency domain by Discrete Fourier Transform (DFT). As a result, the governing partial differential equation (PDE) is reduced to a set of ordinary differential equations (ODE) with constant coefficients, where the time coordinate gives way to the frequency, which is introduced as a parameter [86]. The resultant ODEs can be solved directly. The elements are formulated using the exact solution of the governing ODEs as interpolation function. Therefore, an exact mass distribution can be achieved which leads to the establishment of exact dynamic stiffness matrix. Therefore, only one element is sufficient to handle a beam of any length if there is no discontinuity or

irregularity. Accordingly, the size of the global stiffness matrix reduces to a great extent. In short, SFEM generates the dynamic stiffness matrix very accurately and it takes only 15-30 minutes to run a code. Furthermore, another advantage of SFEM is that the wave characteristics can be extracted directly from the formulation. Hence, the inside of wave propagation can be seen by SFEM. Eventually, both the dispersion curves and time domain results are possible to obtain by SFEM.

SFEM requires solving some equations in order to obtain the final results. However, there are a good number of theories available to serve the purpose. In the next section, some theories will be explained which are used to explain these methods and to also compare on the grounds of choosing the appropriate theory.

4.2.1 Theories related to isotropic rod like structures

The theory for SFEM can be divided into two parts. The first part is related to the spectrum and dispersion relation (spectral analysis) and the second part deals with the determination of the displacement or velocity at any particular point (solution for displacement).

4.2.1.1 Spectral analysis

Elementary theory

The elementary theory is derived for a long and slender rod subjected to one dimensional axial stress. The equation is similar to Equation (3.1), however, in this equation the damping is not considered. Therefore, the equation of motion can be represented as [56]

$$\frac{\partial}{\partial x}\left[EA\frac{\partial u}{\partial x}\right] = \rho A\frac{\partial^2 u}{\partial t^2} + \eta A\frac{\partial u}{\partial t} - q \tag{4.1}$$

where E = Young's modulus; A = cross sectional area; ρ = mass density; η = viscous damping; $q = q(x,t)$ = externally applied load, $u = u(x,t)$ = axial displacement.

A solution of the form

$$u(x,t) = \sum_{n=1}^{N} \hat{u}(x,\omega_n)e^{-j\omega_n t} \tag{4.2}$$

is assumed, where the time dependency is replaced by the angular frequency (ω_n) and the summation needs to be determined up to the Nyquist frequency ω_n and j is the imaginary number. Now substituting Equation (4.2) into Equation (4.1), the partial differential equation (PDE) is reduced to the governing ordinary differential equation (ODE) as

$$\frac{d}{dx}\left[EA\frac{d\hat{u}}{dx}\right] + \omega_n^2 \rho A\hat{u} - j\omega_n \eta A\hat{u} = -q. \tag{4.3}$$

Now, if both the Young's modulus and cross sectional area do not vary with position, then the following homogeneous differential equation can be obtained,

$$EA\frac{d^2\hat{u}}{dx^2} + (\omega_n^2 \rho A - j\omega_n \eta A)\hat{u} = 0. \tag{4.4}$$

This equation is an ordinary differential equation with constant coefficients where the frequency is considered as a parameter and the solution is of the form $u_0 e^{-j\xi x}$. By substituting the solution into Equation (4.4), the discretised form of the governing equation becomes,

$$(EA\xi^2 + \omega_n^2 \rho A - j\omega_n \eta A)u_0 = 0 \tag{4.5}$$

where ξ is the wavenumber and can be computed trivially in this case as,

$$\xi = \pm\sqrt{\frac{\omega_n^2 \rho A - j\omega_n \eta A}{EA}}. \tag{4.6}$$

For the undamped case,

$$\xi = \pm\omega_n\sqrt{\frac{\rho A}{EA}}. \tag{4.7}$$

After getting the wavenumber, the spectrum relation can be obtained.

Love theory

The wavenumber for the single mode Love theory is indicated as [56]

$$\xi = \pm\omega\sqrt{\frac{\rho A}{EA - \upsilon^2 \rho J\omega^2}} \tag{4.8}$$

where $J = \int_A r^2 dA$ = polar moment of inertia.

Mindlin-Hermann theory

Similarly, the wavenumber can be determined using the Mindlin-Hermann theory. As this theory considers two modes, two pairs of roots relating to two wavenumbers, can be determined. In this theory, the lateral contraction (ψ) is taken into account because of the two considered modes. One of these modes is related to the longitudinal and the other one to the contraction mode. Therefore, the governing equation related to this theory is proposed as

$$\begin{bmatrix} -(\lambda+2\mu)A\xi^2+\rho A\omega^2 & -j\xi\lambda A \\ j\xi\lambda A & -\mu IK_1\xi^2-(2\mu+\lambda)A+\rho IK_2\omega^2 \end{bmatrix}\begin{Bmatrix} u_0 \\ \psi_0 \end{Bmatrix}=0 \tag{4.9}$$

where λ and μ are Lame's constants, I is the moment of inertia, and K_1 and K_2 are adjustable parameters. The adjustable parameters are determined in numerous ways [56] and the values related to these two parameters are K_1 = 1.68 and K_2 = 1.80. Equation (4.9) can be solved by considering the polynomial eigenvalue problem (PEP) or by using the companion matrix method [160] or even by forming the polynomial equation. The characteristic equation can be obtained by setting the determinant equal to zero. Since the characteristic equation is quadratic in ξ^2, the polynomial equation can be easily solved. The equation is expressed as

$$a_2\xi^4+a_1\xi^2+a_0=0 \tag{4.10}$$

where

$$\begin{aligned} a_2 &= A\mu IK_1(2\mu+\lambda), \\ a_1 &= [4\mu(\mu+\lambda)A^2-\rho IK_2\omega^2A(2\mu+\lambda)-\rho A\omega^2\mu IK_1], \\ a_0 &= -\rho A\omega^2[A(2\mu+\lambda)-\rho IK_2\omega^2]. \end{aligned} \tag{4.11}$$

As mentioned earlier, Equation (4.10) can be solved for ξ^2 and two pairs of roots can be determined.

Three mode theory

From the Mindlin-Herman theory it is clear that there are two degrees of freedom at each node. Likewise, in the three mode theory [56], three degrees of freedom are considered. These three degrees of freedom are related to the longitudinal displacement and two rotations (lateral contraction ψ and shear contraction φ). The governing equation related to this theory is presented as [161]

$$\begin{bmatrix} -(\lambda+2\mu)A\xi^2+\rho A\omega^2 & -j\xi\lambda A & 0 \\ j\xi\lambda A & -\mu IK_1\xi^2-(2\mu+\lambda)A+\rho I\omega^2 & 2j\xi\mu Ah \\ 0 & -\frac{10}{48}j\mu Ah & -(2\mu+\lambda)I\xi^2-5\mu A+\rho I\omega^2 \end{bmatrix} \begin{Bmatrix} u_0 \\ \psi_0 \\ \varphi_0 \end{Bmatrix} = 0. \tag{4.12}$$

where h is the diameter of the cylinder or thickness of the plate. The characteristic equation can be obtained by setting the determinant equal to zero. Since the characteristic equation is cubic in ξ^2, the polynomial equation can be solved for ξ^2. Again, to solve the equation for wavenumbers, the PEP or the companion matrix or the polynomial equation can be used. The problem related to solving the equation for wavenumbers is the magnitude of the coefficients. When the polynomial equation is formed, the coefficients related to the wavenumber become very large which causes forward and backward errors [162]. Therefore, it is better to use the PEP or to form the companion matrix [160] from the characteristic equation to reduce the magnitude of the coefficient. In this present study, Cardano's method [163, 164] for solving the cubic is used. It is well known that Cardano's method can only be used for cubic equations. It gives very accurate results even with high coefficient values. The polynomial characteristic equation can thereby be formed as

$$a_3(\xi^2)^3+a_2(\xi^2)^2+a_1\xi^2+a_0=0 \tag{4.13}$$

where

$$\begin{aligned} a_3 &= -A\mu I^2(2\mu+\lambda)^2, \\ a_2 &= -AI(2\mu+\lambda)[4A\mu(\mu+\lambda)-I(4\mu+\lambda)\rho\omega^2], \\ a_1 &= A[-20A^2\mu^2(\mu+\lambda)+AI(\lambda^2+13\lambda\mu+18\mu^2)\rho\omega^2-I^2(5\mu+2\lambda)\rho^2\omega^4], \\ a_0 &= \rho A\omega^2(5A\mu-\rho I\omega^2)[A(2\mu+\lambda)-\rho I\omega^2]. \end{aligned} \tag{4.14}$$

The spectrum relation can be obtained from the wavenumber as described in Equation (3.16) and Equation (3.17).

4.2.1.2 Solution for displacement

After the wavenumber(s) is/are determined, the displacement can be calculated. At first, the displacements of nodes are determined and then the displacements at any arbitrary location can be obtained. The results related to phase velocities of the different theories are presented later in the chapter. Since these results illustrate that the three mode theory is the closest to the practical situation, only the solution for displacement related to the

three mode theory is presented here. Details on displacement calculations using other theories can be found in [161].

Six roots or wavenumbers can be determined by solving Equation (4.13) and are denoted as $\pm\xi_1, \pm\xi_2, \pm\xi_3$. The general longitudinal displacement and rotations of a rod at any arbitrary location, having a length of L, can be written as

$$\begin{aligned}
\hat{u}_0(x,\omega_n) &= A_0R_4e^{-j\xi_1x} + B_0R_5e^{-j\xi_2x} + C_0R_6e^{-j\xi_3x} + D_0R_4e^{-j\xi_1(L-x)} \\
&\quad + E_0R_5e^{-j\xi_2(L-x)} + F_0R_6e^{-j\xi_3(L-x)}, \\
\hat{\psi}_0(x,\omega_n) &= A_0R_1e^{-j\xi_1x} + B_0R_2e^{-j\xi_2x} + C_0R_3e^{-j\xi_3x} - D_0R_1e^{-j\xi_1(L-x)} \\
&\quad - E_0R_2e^{-j\xi_2(L-x)} - F_0R_3e^{-j\xi_3(L-x)}, \\
\hat{\varphi}_0(x,\omega_n) &= A_0e^{-j\xi_1x} + B_0e^{-j\xi_2x} + C_0e^{-j\xi_3x} + D_0e^{-j\xi_1(L-x)} + E_0e^{-j\xi_2(L-x)} \\
&\quad + F_0e^{-j\xi_3(L-x)},
\end{aligned} \tag{4.15}$$

where,

$$\begin{aligned}
R_i &= \frac{(2\mu+\lambda)I\xi_i^2 + 5\mu A - \rho I\omega^2}{-\frac{10}{48}\mu Ah}, i = 1,2,3, \\
R_i &= \frac{j\xi_j\lambda A}{-(2\mu+\lambda)A\xi_i^2 + \rho A\omega^2}R_j, \qquad i = 4,5,6, \qquad j = 1,2,3.
\end{aligned} \tag{4.16}$$

The unknown constants A_0, B_0, C_0, D_0, E_0 and F_0 can be found from the nodal conditions.

If the rod is considered as two nodded element, where $x = x_1$ and $x = x_2$ ($|(x_2 - x_1)| = L$), the nodal displacements can be represented as $\hat{u}_1 = \hat{u}_0(x_1,\omega_n)$, $\hat{\psi}_1 = \hat{\psi}_0(x_1,\omega_n)$, $\hat{\varphi}_1 = \hat{\varphi}_0(x_1,\omega_n)$ and $\hat{u}_2 = \hat{u}_0(x_2,\omega_n)$, $\hat{\psi}_2 = \hat{\psi}_0(x_2,\omega_n)$, $\hat{\varphi}_2 = \hat{\varphi}_0(x_2,\omega_n)$. Consequently, the relation between nodal displacements and the unknown constants (or amplitudes) can be expressed as

$$\begin{Bmatrix} \hat{u}_1 \\ \hat{\psi}_1 \\ \hat{\varphi}_1 \\ \hat{u}_2 \\ \hat{\psi}_2 \\ \hat{\varphi}_2 \end{Bmatrix} = \begin{bmatrix} R_4 & R_5 & R_6 & R_4e^{-j\xi_1L} & R_5e^{-j\xi_2L} & R_6e^{-j\xi_3L} \\ R_1 & R_2 & R_3 & -R_1e^{-j\xi_1L} & -R_2e^{-j\xi_2L} & -R_3e^{-j\xi_3L} \\ 1 & 1 & 1 & e^{-j\xi_1L} & e^{-j\xi_2L} & e^{-j\xi_3L} \\ R_4e^{-j\xi_1L} & R_5e^{-j\xi_2L} & R_6e^{-j\xi_3L} & R_4 & R_5 & R_6 \\ R_1e^{-j\xi_1L} & R_2e^{-j\xi_2L} & R_3e^{-j\xi_3L} & -R_1 & -R_2 & -R_3 \\ e^{-j\xi_1L} & e^{-j\xi_2L} & e^{-j\xi_3L} & 1 & 1 & 1 \end{bmatrix} \begin{Bmatrix} A_0 \\ B_0 \\ C_0 \\ D_0 \\ E_0 \\ F_0 \end{Bmatrix}. \tag{4.17}$$

The matrix in Equation (4.17) can be denoted as [$\mathbf{T_1}$].

Similarly, the force in the frequency domain, $\hat{F}(x,\omega_n) = \{\hat{N}(x,\omega_n) \quad \hat{Q}(x,\omega_n) \quad \hat{M}(x,\omega_n)\}^T$ can be calculated for x_1 and x_2 where the nodal forces are represented as [161]

$$\begin{aligned}
\hat{N}(x_1,\omega_n) &= (2\mu+\lambda)A\frac{\partial \hat{u}_0}{\partial x} + \lambda A\hat{\psi}_0,\\
\hat{Q}(x_1,\omega_n) &= \mu I\left(\frac{\partial \hat{\psi}_0}{\partial x} - 24\frac{\hat{\varphi}_0}{h}\right),\\
\hat{M}(x_1,\omega_n) &= \frac{48}{5}(2\mu+\lambda)I\frac{\partial \hat{\varphi}_0}{\partial x},\\
\hat{N}(x_2,\omega_n) &= -\hat{N}(x_1,\omega_n),\\
\hat{Q}(x_2,\omega_n) &= -\hat{Q}(x_1,\omega_n),\\
\hat{M}(x_2,\omega_n) &= -\hat{M}(x_1,\omega_n).
\end{aligned} \tag{4.18}$$

Now, by substituting the values of $\hat{u}_0$, $\hat{\psi}_0$ and $\hat{\varphi}_0$ in Equation (4.18), the relation between nodal forces and the unknown constants (or amplitudes) can be determined and is represented in the following equation

$$\begin{Bmatrix} \hat{N}_1 \\ \hat{Q}_1 \\ \hat{M}_1 \\ \hat{N}_2 \\ \hat{Q}_2 \\ \hat{M}_2 \end{Bmatrix} = \begin{bmatrix} m_{11} & m_{12} & m_{13} & m_{14} & m_{15} & m_{16} \\ m_{21} & m_{22} & m_{23} & m_{24} & m_{25} & m_{26} \\ m_{31} & m_{32} & m_{33} & m_{34} & m_{35} & m_{36} \\ m_{41} & m_{42} & m_{43} & m_{44} & m_{45} & m_{46} \\ m_{51} & m_{52} & m_{53} & m_{54} & m_{55} & m_{56} \\ m_{61} & m_{62} & m_{63} & m_{64} & m_{65} & m_{66} \end{bmatrix} \begin{Bmatrix} A_0 \\ B_0 \\ C_0 \\ D_0 \\ E_0 \\ F_0 \end{Bmatrix} \tag{4.19}$$

where

$$\begin{aligned}
m_{11} &= -j\xi_1(2\mu+\lambda)AR_4 + \lambda AR_1, & m_{12} &= -j\xi_2(2\mu+\lambda)AR_5 + \lambda AR_2,\\
m_{13} &= -j\xi_3(2\mu+\lambda)AR_6 + \lambda AR_3, & m_{14} &= (j\xi_1(2\mu+\lambda)AR_4 - \lambda AR_1)e^{-j\xi_1 L},\\
m_{15} &= (j\xi_2(2\mu+\lambda)AR_5 - \lambda AR_2)e^{-j\xi_2 L}, & m_{16} &= (j\xi_3(2\mu+\lambda)AR_6 - \lambda AR_3)e^{-j\xi_3 L},\\
m_{21} &= -j\xi_1\mu AR_1 - (24/h)\mu I, & m_{22} &= -j\xi_2\mu AR_2 - (24/h)\mu I,\\
m_{23} &= -j\xi_3\mu AR_3 - (24/h)\mu I, & m_{24} &= (-j\xi_1\mu AR_1 - (24/h)\mu I)e^{-j\xi_1 L},\\
m_{25} &= (-j\xi_2\mu AR_2 - (24/h)\mu I)e^{-j\xi_2 L}, & m_{26} &= (-j\xi_3\mu AR_3 - (24/h)\mu I)e^{-j\xi_3 L},\\
m_{31} &= -j\xi_1(48/5)(2\mu+\lambda)I, & m_{32} &= -j\xi_2(48/5)(2\mu+\lambda)I,\\
m_{33} &= -j\xi_3(48/5)(2\mu+\lambda)I, & m_{34} &= j\xi_1(48/5)(2\mu+\lambda)Ie^{-j\xi_1 L},
\end{aligned}$$

$$m_{35} = j\xi_2(48/5)(2\mu+\lambda)Ie^{-j\xi_2 L}, \quad m_{36} = j\xi_3(48/5)(2\mu+\lambda)Ie^{-j\xi_3 L},$$
$$m_{41} = m_{14}, \quad m_{42} = m_{15}, \quad m_{43} = m_{16}, \quad m_{44} = -m_{11},$$
$$m_{45} = -m_{12}, \quad m_{46} = -m_{13}, \quad m_{51} = -m_{24}, \quad m_{52} = -m_{25},$$
$$m_{53} = -m_{26}, \quad m_{54} = -m_{21}, \quad m_{55} = -m_{22}, \quad m_{56} = -m_{23},$$
$$m_{61} = m_{34}, \quad m_{62} = m_{35}, \quad m_{63} = m_{36}, \quad m_{64} = m_{31}.$$
$$m_{65} = m_{32}, \quad m_{66} = m_{33}, \tag{4.20}$$

The matrix in Equation (4.19) can be denoted as $[\mathbf{T_2}]$.

Thereby, the nodal forces are related to nodal displacements by

$$\begin{Bmatrix} \widehat{N}_1 \\ \widehat{Q}_1 \\ \widehat{M}_1 \\ \widehat{N}_2 \\ \widehat{Q}_2 \\ \widehat{M}_2 \end{Bmatrix} = [\boldsymbol{T_2}][\boldsymbol{T_1}]^{-1} \begin{Bmatrix} \hat{u}_1 \\ \hat{\psi}_1 \\ \hat{\varphi}_1 \\ \hat{u}_2 \\ \hat{\psi}_2 \\ \hat{\varphi}_2 \end{Bmatrix}. \tag{4.21}$$

The dynamic stiffness matrix for the rod at frequency ω_n is therefore $D_{SFEM} = [\boldsymbol{T_2}][\boldsymbol{T_1}]^{-1}$. Accordingly, the displacement can be obtained at the N^{th} sampling point. In this equation, the force is known. For instance, if the load is applied longitudinally at node 2 (x_2), then all the forces will be zero except $\widehat{N}_2$. The value of $\widehat{N}_2$ is the forward FFT of the impact load in the time domain. Subsequently, the nodal displacements can be acquired. After calculating the nodal displacements, the unknown coefficients can be determined from Equation (4.17). Now the deformations at any arbitrary location can be obtained using Equation (4.15). It is noteworthy to mention that the final displacement or total solution is the summation of $\hat{u}_0(x,\omega_n)$, $\hat{\psi}_0(x,\omega_n)$ and $\hat{\varphi}_0(x,\omega_n)$.

Finally, the time domain results can be achieved by inverse fast Fourier transform (IFFT) and will be discussed in details in a latter part of this chapter.

4.2.2 Theories related to isotropic beam like structures

4.2.2.1 Spectral analysis

Elementary beam theory (EBT)

Similar to the elementary rod theory, the governing equation in the time domain is represented as

$$\frac{\partial^2}{\partial x^2}\left[EI\frac{\partial^2 v}{\partial x^2}\right] + \rho A\frac{\partial^2 v}{\partial t^2} + \eta A\frac{\partial v}{\partial t} = q(x,t). \tag{4.22}$$

In the frequency domain, this equation will again be

$$EI\frac{d^4\hat{v}}{dx^4} + (\omega_n^2\rho A - j\omega_n\eta A)\hat{v} = 0. \tag{4.23}$$

This equation can also be represented as

$$\frac{d^4\hat{v}}{dx^4} + \beta^4\hat{v} = 0, \qquad \beta^2 = \sqrt{\frac{\omega^2\rho A - j\omega\eta A}{EI}}. \tag{4.24}$$

A solution can be obtained from the particular solution of the following two equations

$$\frac{d^2\hat{v}}{dx^2} + \beta^2\hat{v} = 0, \qquad \frac{d^2\hat{v}}{dx^2} - \beta^2\hat{v} = 0. \tag{4.25}$$

Hence, the wavenumber can be calculated as

$$\xi_1 = \pm\beta, \qquad \xi_2 = \pm j\beta. \tag{4.26}$$

Likewise, for the undamped case,

$$\beta^2 = \omega\sqrt{\frac{\rho A}{EI}}. \tag{4.27}$$

Timoshenko beam theory

The Timoshenko beam theory considers rotary inertia and shear deformation which is essential for the deep beam. Additionally, at high frequencies the Euler-Bernoulli beam theory can be used. In the Timoshenko theory, shear is taken into account and thus the governing equation can be shown as [165]

$$\begin{bmatrix} GAK_1\xi^2 - \rho A{\omega_n}^2 & -j\xi GAK_1 \\ j\xi GAK_1 & EI\xi^2 + GAK_1 - \rho I{\omega_n}^2 \end{bmatrix}\begin{Bmatrix} v_0 \\ \varphi_0 \end{Bmatrix} = 0 \tag{4.28}$$

where G is the shear modulus and the adjustable parameter $K_1 = 0.86$.

Again, to solve this equation for wavenumbers, the determinant of the matrix is set to zero. Instead of forming the polynomial equation from the determinant, the polynomial eigenvalue problem is formed (PEP) to solve for wavenumbers. The method is universal and easy to solve with very high accuracy. As Equation (4.25) is a polynomial of ξ, the

problem of finding wavenumber ξ and v_0 or φ_0 is a standard PEP of determining non-zero **v** and ξ such that

$$\boldsymbol{W}(\xi)\mathbf{v} = \left(\sum_{i=0}^{p} \xi^i \boldsymbol{A}_i\right)\mathbf{v} = 0, \boldsymbol{A}_i \in \mathbb{C}^{N_v \times N_v}, \mathbf{v} \in \mathbb{C}^{N_v \times 1} \tag{4.29}$$

where p is the polynomial order (or power of ξ) and N_v is the size of $\boldsymbol{W}$ [165]. Each $\boldsymbol{A}_i$ depends on the material properties, frequency and wavenumber.

The PEP for the Timoshenko theory can thus be formed as follows:

$$\left\{\xi^2\begin{bmatrix} GAK_1 & 0 \\ 0 & EI \end{bmatrix} + \xi\begin{bmatrix} 0 & -jGAK_1 \\ jGAK_1 & 0 \end{bmatrix} + \begin{bmatrix} -\rho A\omega^2 & 0 \\ 0 & GAK_1 - \rho I\omega^2 \end{bmatrix}\right\} \tag{4.30}$$

Or it can be written as

$$\xi^2\boldsymbol{A}_2 + \xi\boldsymbol{A}_1 + \boldsymbol{A}_0 \tag{4.31}$$

where p = 2 and N_v = 2. Now the roots at each frequency (N sampling points of FFT) can easily be found using MATLAB after defining A_2, A_1 and A_0 and then by using the command "polyeig(A_2, A_1,A_0)".

4.2.2.2 Solution for displacement

The results related to phase velocities regarding an elementary beam (or EBT) and Timoshenko beam theories are explained later in the chapter. Since the results illustrate that the Timoshenko theory is the closest to the practical situation, only the solution for displacement related to this theory is presented here.

Four roots or wavenumbers can be obtained by solving Equation (4.31) and are denoted as $\xi_1, \xi_2, -\xi_1$ and $-\xi_2$. The complete solutions for the deformations are

$$\begin{aligned} \hat{v}(x,\omega_n) &= C_1 e^{-j\xi_1 x} + C_2 e^{-j\xi_2 x} + C_3 e^{j\xi_1 x} + C_4 e^{j\xi_2 x}, \\ \hat{\varphi}(x,\omega_n) &= C_5 e^{-j\xi_1 x} + C_6 e^{-j\xi_2 x} + C_7 e^{j\xi_1 x} + C_8 e^{j\xi_2 x}. \end{aligned} \tag{4.32}$$

The unknown constants C_1, C_2, C_3 … C_8 can be calculated from the nodal conditions. It can be noted that unlike the three mode theory, the amplitudes or unknown coefficients related to transverse deformation are not represented by the amplitude ratio $\boldsymbol{R}$ (Equation (4.16) between transverse deformation and rotation. The reason for this is that another elegant method can be used to determine these coefficients. This way the ratio can be

obtained directly from Singular Value Decomposition (SVD). This method is proposed in [86] and can be explained as follows.

After obtaining the eigenvalues (or wavenumbers), the eigenvectors can be arranged in a matrix $\boldsymbol{R}$ so that

$$\left\{\xi_p^2\boldsymbol{A}_2 + \xi_p\boldsymbol{A}_1 + \boldsymbol{A}_0\right\}\begin{Bmatrix}R_{1p}\\R_{2p}\end{Bmatrix} = 0. \tag{4.33}$$

The complete solution at each frequency ω_n can be denoted as

$$\begin{Bmatrix}\hat{v}(x,\omega_n)\\\hat{\varphi}(x,\omega_n)\end{Bmatrix} = \sum_{m=1}^{4} C_m \begin{Bmatrix}R_{1m}\\R_{2m}\end{Bmatrix} e^{-j\xi_m x}. \tag{4.34}$$

The amplitude ratios $\boldsymbol{R}$ are determined from the concept given in Equation (4.29) and SVD is applied for this purpose. It is beneficial not to use the direct command "[X,V]=eig(R)" (in MATLAB) for calculating the eigenvectors. This is due to the fact that using the direct command, it is not possible to determine which vectors are related to which particular wavenumber. From Equation (4.34), it can be seen that the elements of R_{1m} or R_{2m} are the coefficients of the solution corresponding to the wavenumber ξ_m by the relation $R_{1m}e^{-j\xi_m x}$. The details of the SVD technique are presented in the next section of this chapter.

If a beam is considered as two nodded elements where $x = x_1 = 0$ and $x = x_2 = L$, the nodal displacements can be represented as $\hat{v}_1 = \hat{v}(x_1,\omega_n)$, $\hat{\varphi}_1 = \hat{\varphi}(x_1,\omega_n)$ and $\hat{v}_2 = \hat{v}(x_2,\omega_n)$, $\hat{\varphi}_2 = \hat{\varphi}(x_2,\omega_n)$. Consequently, the relation between nodal displacements and the unknown constants (or amplitudes) can be expressed as

$$\begin{Bmatrix}\hat{v}_1\\\hat{\varphi}_1\\\hat{v}_2\\\hat{\varphi}_2\end{Bmatrix} = \begin{bmatrix} R_{11} & R_{12} & R_{13} & R_{14} \\ R_{21} & R_{22} & R_{23} & R_{24} \\ R_{11}e^{-j\xi_1 L} & R_{12}e^{-j\xi_2 L} & R_{13}e^{j\xi_1 L} & R_{14}e^{j\xi_2 L} \\ R_{21}e^{-j\xi_1 L} & R_{22}e^{-j\xi_2 L} & R_{23}e^{j\xi_1 L} & R_{24}e^{j\xi_2 L} \end{bmatrix}\begin{Bmatrix}C_1\\C_2\\C_3\\C_4\end{Bmatrix}. \tag{4.35}$$

The matrix in Equation (4.35) can be denoted as $[\mathbf{T_1}]$.

Similarly, the forces at the nodes can be expressed as

$$\begin{Bmatrix} \hat{V}_1 \\ \hat{M}_1 \\ \hat{V}_2 \\ \hat{M}_2 \end{Bmatrix} = [\boldsymbol{T_2}] \begin{Bmatrix} C_1 \\ C_2 \\ C_3 \\ C_4 \end{Bmatrix} \tag{4.36}$$

where $\hat{V}_1 = -V(x_1)$, $\hat{V}_2 = V(x_2)$, $\hat{M}_1 = -M(x_1)$, $\hat{M}_2 = M(x_2)$ and the explicit form of matrix $[\mathbf{T_2}]$ can be represented as [98]

$$\begin{gathered} T_2(1,m) = -GA\big(-j\xi_m R(1,m) - R(2,m)\big), \\ T_2(2,m) = -EI(-j\xi_m)R(2,m), \\ T_2(3,m) = -T_2(1,m), \qquad T_2(4,m) = -T_2(2,m). \end{gathered} \tag{4.37}$$

Thereby, the nodal forces are related to nodal displacement by

$$\begin{Bmatrix} \hat{V}_1 \\ \hat{M}_1 \\ \hat{V}_2 \\ \hat{M}_2 \end{Bmatrix} = [\boldsymbol{T_2}][\boldsymbol{T_1}]^{-1} \begin{Bmatrix} \hat{v}_1 \\ \hat{\varphi}_1 \\ \hat{v}_2 \\ \hat{\varphi}_2 \end{Bmatrix}. \tag{4.38}$$

Therefore, the dynamic stiffness matrix for the beam at frequency ω_n is $D_{SFEM} = [\boldsymbol{T_2}][\boldsymbol{T_1}]^{-1}$. Accordingly, the displacement can be obtained at the N^{th} sampling point. In this case, the load is applied transversely at node 2 (x_2); hence, all the forces will be zero except $\hat{V}_2$. Again, the final displacement or total solution is the summation of $\hat{v}(x,\omega_n)$ and $\hat{\varphi}(x,\omega_n)$. Lastly, the time domain results can be determined by using the inverse fast Fourier transform (IFFT).

4.2.3 Theories for anisotropic material

The constitutive model for an orthotropic laminated composite beam is proposed in [166] and states that the plane stress condition can be derived from the stress strain relationship. For the timber pole situation, the plane stress is considered in the *L*-*R* plane. Therefore, the stress strain relationship for an orthotropic beam can be represented as

$$\begin{Bmatrix} \sigma_{11} \\ \sigma_{33} \\ \tau_{13} \end{Bmatrix} = \begin{bmatrix} C_{11} & C_{13} & 0 \\ C_{13} & C_{33} & 0 \\ 0 & 0 & C_{55} \end{bmatrix} \begin{Bmatrix} \varepsilon_{11} \\ \varepsilon_{33} \\ \gamma_{13} \end{Bmatrix} \tag{4.39}$$

where 1 is related to the *L*-axis and 3 is corresponding to *R*-axis. In addition, the Poisson's effect is considered when determining the stiffness from the compliance matrix. By considering the Poisson's effect, the stiffness can be named as reduced

stiffness matrix. The arbitrary orientation of timber fibres is not taken into account for the timber pole situation, as in almost all timber poles the fibres are orientated longitudinally. Hence, the reduced stiffness can be expressed as

$$C_{11} = \frac{E_L}{1 - \nu_{LR}\nu_{RL}}, \qquad C_{33} = \frac{E_R}{1 - \nu_{LR}\nu_{RL}},$$
$$C_{13} = \nu_{RL}C_{11}, \qquad C_{55} = G_{LR}. \tag{4.40}$$

For a composite beam, the stiffness coefficients can be determined from the individual ply properties, ply orientation, etc. and can be obtained by integration over the beam cross section which can be expressed as [100],

$$[A_{ij} \quad B_{ij} \quad D_{ij}] = \int_A C_{ij}[1 \quad r \quad r^2]dA. \tag{4.41}$$

Similarly, the coefficients associated with the inertial terms can be represented as

$$[I_0 \quad I_1 \quad I_2] = \int_A \rho[1 \quad r \quad r^2]dA. \tag{4.42}$$

However, Equations (4.41) and (4.42) are derived for a composite beam and it must be noted that for the timber pole situation, there is no such thing as individual ply stacking. Hence, the material of a timber pole cannot be considered as a layered material with different properties as showed in Chapter 3. Therefore, $\int_A C_{ij}\, r\, dA = 0$ and $\int_A \rho\, r\, dA = 0$. Accordingly, $B_{ij} = I_1 = 0$. Hence, the coefficients related to A_{ij} and D_{ij} can be calculated as

$$A_{11} = C_{11}A, \qquad A_{13} = C_{13}A, \qquad A_{33} = C_{33}A, \qquad A_{55} = C_{55}A$$
$$D_{11} = C_{11}\frac{\pi r^4}{4} = C_{11}I, \qquad D_{55} = C_{55}\frac{\pi r^4}{4} = C_{55}I. \tag{4.43}$$

4.2.3.1 Spectral analysis

As mentioned above, for a composite beam or bar with asymmetric ply stacking, the coupling of longitudinal and flexural waves occurs. The theory based on EBT considers only axial and transverse displacements. Similar to isotropic materials, the longitudinal wave has a constant velocity and the flexural wave's velocity increases with the increase in frequency due to neglecting shear deformation and rotary inertia. In contrast, the fast order shear deformation theory (FSDT) considers additional two modes

(contraction mode and shear mode) and illustrates very accurate dispersion relations. Therefore, longitudinal-flexural-shear-contraction coupling is considered in the FSDT. A corresponding comparison will be presented later in the chapter.

Elementary theory/based on EBT

The PEP of the EBT can be expressed as follows

$$\left\{\xi^4\begin{bmatrix}0 & 0\\ 0 & D_{11}\end{bmatrix}+\xi^2\begin{bmatrix}A_{11} & 0\\ 0 & 0\end{bmatrix}+\begin{bmatrix}-\rho A\omega_n^2 & 0\\ 0 & -\rho A\omega_n^2\end{bmatrix}\right\}\begin{Bmatrix}u_0\\ v_0\end{Bmatrix}=0. \tag{4.44}$$

After solving this equation for each frequency (N sampling points of FFT), the dispersion relation can be obtained.

First order shear deformation theory (FSDT)

The displacement field $\{\boldsymbol{u}\}=\{u,\psi,v,\varphi\}(x,t)$ based on a plane wave element is

$$\{\boldsymbol{u}\}=\sum_{n=1}^{N}\{\tilde{u},\tilde{\psi},\tilde{v},\tilde{\varphi}\}(x)e^{-j\omega_n t}=\sum_{n=1}^{N}\{\tilde{\boldsymbol{u}}\}(x)e^{-j\omega_n t}. \tag{4.45}$$

Again, ω_n is the circular frequency at the n^{th} sampling point and N is the frequency index corresponding to the Nyquist frequency in the FFT.

After obtaining the ODEs in the frequency domain [98], $\tilde{\boldsymbol{u}}(x)$ can be determined. Since ODEs have constant coefficients, the solution is of the form $\{\tilde{\boldsymbol{u}}_0\}e^{-j\xi x}$, where $\{\tilde{\boldsymbol{u}}_0\}$ is the vector of unknown constants. This can also be written as $\{\tilde{\boldsymbol{u}}_0\}=\{u_0,\psi_0,v_0,\varphi_0\}$. Hence, the characteristic equation can be expressed as

$$[\boldsymbol{W}]\begin{Bmatrix}u_0\\ \psi_0\\ v_0\\ \varphi_0\end{Bmatrix}=0. \tag{4.46}$$

By setting the determinant of $[\boldsymbol{W}]$ equal to zero, the wavenumbers can be determined. After forming the PEP for $[\boldsymbol{W}]$, it can be represented as

$$\left\{ \xi^2 \begin{bmatrix} A_{11} & 0 & 0 & -B_{11} \\ 0 & D_{55} & B_{55} & 0 \\ 0 & B_{55} & A_{55} & 0 \\ -B_{11} & 0 & 0 & D_{11} \end{bmatrix} + \xi \begin{bmatrix} 0 & jA_{13} & 0 & 0 \\ -jA_{13} & 0 & 0 & j(B_{13}-B_{55}) \\ 0 & 0 & 0 & -jA_{55} \\ 0 & -j(B_{13}-B_{55}) & jA_{55} & 0 \end{bmatrix} \right.$$
$$\left. + \begin{bmatrix} -I_0\omega_n^2 & 0 & 0 & I_1\omega_n^2 \\ 0 & -I_2\omega_n^2 + A_{33} & -I_1\omega_n^2 & 0 \\ 0 & -I_1\omega_n^2 & -I_0\omega_n^2 & 0 \\ I_1\omega_n^2 & 0 & 0 & -I_2\omega_n^2 + A_{55} \end{bmatrix} \right\}$$
$$or \ \xi^2 \boldsymbol{A}_2 + \xi \boldsymbol{A}_1 + \boldsymbol{A}_0 \tag{4.47}$$

where $p = 2$ and $N_v = 4$. Now the roots at each frequency (N sampling points of FFT) can be easily found.

4.2.3.2 Solution for displacement

By solving Equation (4.47), eight roots are found where four are forward moving and four backward moving waves. In other words, eight wavenumbers can be obtained, namely, $\xi_1, \xi_2, \xi_3, \xi_4, \xi_5(=-\xi_1), \xi_6(=-\xi_2), \xi_7(=-\xi_3)$ and $\xi_8(=-\xi_4)$. These wave-numbers are related to longitudinal (ξ_1), flexural (ξ_2), shear (ξ_3) and contraction (ξ_4) modes. Similar to Equation (4.34), the displacement at any point can be denoted as

$$\{\tilde{\boldsymbol{u}}\}_n = \begin{Bmatrix} \hat{u}(x,\omega_n) \\ \hat{\psi}(x,\omega_n) \\ \hat{v}(x,\omega_n) \\ \hat{\varphi}(x,\omega_n) \end{Bmatrix} = \begin{bmatrix} R_{11} & \dots & R_{18} \\ R_{21} & \dots & R_{28} \\ R_{31} & \dots & R_{38} \\ R_{41} & \dots & R_{48} \end{bmatrix} \begin{bmatrix} e^{-j\xi_1 x} & 0 & \cdots & 0 \\ 0 & e^{-j\xi_2 x} & \cdots & 0 \\ \vdots & \ddots & \ddots & \vdots \\ 0 & \cdots & \cdots & e^{-j\xi_8 x} \end{bmatrix} \{\boldsymbol{a}\}_n \tag{4.48}$$

where $[\boldsymbol{R}]_n$ are the amplitude ratios and $\{\mathbf{a}\}_n$ is the unknown constant vector. Before going to the next step, the amplitude ratios matrix needs to be determined. Again, it is important to determine the amplitude ratios corresponding to a particular wavenumber. As mentioned earlier, amplitude ratios are the eigenvectors and according to Equation (4.29), they can be written as

$$[\boldsymbol{W}(\xi_m)]_n[\boldsymbol{R}]_n = 0. \tag{4.49}$$

From the spectral analysis, the roots or wavenumbers can be determined; hence $[\boldsymbol{W}]$ at any frequency for any particular wavenumber (ξ_m) can be obtained. It is obvious that for particular wavenumbers (which are roots of $[\boldsymbol{W}]$), $[\boldsymbol{W}]$ is singular, and therefore, nontrivial $[\boldsymbol{R}]_n$ can be calculated. This $[\boldsymbol{R}]_n$ matrix is nothing but the null space of $[\boldsymbol{W}(\xi_m)]$. As the wavenumber ξ_m renders the $[\boldsymbol{W}(\xi_m)]$ singular, hence $[\boldsymbol{W}(\xi_m)]$ has a

nontrivial null space. In other words, by calculating the null space of $[\boldsymbol{W}(\xi_m)]$, the amplitude ratios can be determined, and SVD is very efficient for this purpose.

The $[\boldsymbol{R}]_n$ matrix is solved in the present study by the method proposed in [86, 98] where SVD is used. According to SVD, any rectangular matrix F can be written as $F = USV^H$, where U and V are unitary matrices and S is a diagonal matrix containing the singular values [167] and the superscript H represents the Hermitian conjugate. In this decomposition, the diagonal or the S matrix will have at least one zero singular value and the column of V that corresponds to a zero singular value of F forms the null space of F. It is worthwhile to mention that it is almost practically impossible to obtain an exactly zero singular value. In this situation, the column of V vector corresponding to the lowest singular value can be considered as the null space of F.

For example, if $\xi_m = \xi_1$, then by substituting the value of ξ_1 in Equation (4.47), the matrix $[\boldsymbol{W}(\xi_1)]$ (=$\boldsymbol{W}_1$ (say)) at any frequency ω_n can be obtained. Then, by using the flowing MATLAB command, the amplitude ratios related to ξ_1 at ω_n can be calculated as

```
[U1,S1,V1] = svd(W1,0);
R1 = V1(:,end);
```

By entering zero in the command "svd(W1,0)", the S matrix is sorted in ascending order and hence the zero or smallest singular value is related to the last diagonal value. Thus, the last column of the V1 matrix will give the amplitude ratios R_{11}, R_{21}, R_{31} and R_{41}. Similarly, for $\xi_m = \xi_2$, R_{12}, R_{22}, R_{32} and R_{42} can be determined.

The next step is similar to the previous section, i.e. to form the relation between nodal displacements and the unknown constants as

$$\begin{Bmatrix} \tilde{\boldsymbol{u}}_1 \\ \tilde{\boldsymbol{u}}_2 \end{Bmatrix}_n = [\boldsymbol{T_1}]_n \{\boldsymbol{a}\}_n. \tag{4.50}$$

The explicit form of the $[\boldsymbol{T_1}]$ matrix can be expressed as [98]

$$T_1(1:4,1:8) = R(1:4,1:8),$$
$$\mathrm{T_1(l,m) = R(l-4,m)e^{-j\xi_m L}}, \qquad \mathrm{l = 5,\dots\dots 8}, \qquad \mathrm{m = 1,\dots\dots 8}. \tag{4.51}$$

The nodal forces can also be represented in terms of unknown constants as follows

$$\{\hat{f}\}_n = \begin{Bmatrix} \tilde{f}_1 \\ \tilde{f}_2 \end{Bmatrix}_n = [\boldsymbol{T_2}]_n \{\boldsymbol{a}\}_n \tag{4.52}$$

where $\tilde{f}_1 = \{N_{x1}, Q_{x1}, V_{x1,} M_{x1}\}^T$ and $\tilde{f}_2 = \{N_{x2}, Q_{x2}, V_{x2,} M_{x2}\}^T$. The $[\boldsymbol{T_2}]$ matrix can be expressed as

$$\begin{aligned}
T_2(1,i) &= j(A_{11}R(1,i) - B_{11}R(4,i))\xi_i - A_{13}R(2,i) \\
T_2(2,i) &= -B_{55}\left(-jR(3,i)\xi_i - R(4,i)\right) + jD_{55}R(2,i)\xi_i \\
T_2(3,i) &= -A_{55}\left(-jR(3,i)\xi_i - R(4,i)\right) + jB_{55}R(2,i)\xi_i \\
T_2(4,i) &= j(B_{11}R(1,i) - D_{11}R(4,i))\xi_i + B_{13}R(2,i) \\
T_2(5{:}8,i) &= -T_2(1{:}4,i)e^{-j\xi_i L}, \qquad i = 1, \dots \dots 8
\end{aligned} \tag{4.53}$$

Thereby, the nodal forces are related to nodal displacements by

$$\begin{Bmatrix} \tilde{f}_1 \\ \tilde{f}_2 \end{Bmatrix}_n = [\boldsymbol{T_2}][\boldsymbol{T_1}]^{-1} \begin{Bmatrix} \tilde{\boldsymbol{u}}_1 \\ \tilde{\boldsymbol{u}}_2 \end{Bmatrix}_n \tag{4.54}$$

Thus, the dynamic stiffness matrix at frequency ω_n is $D_{SFEM} = [\boldsymbol{T_2}][\boldsymbol{T_1}]^{-1}$. Accordingly, the displacements can be obtained at the N^{th} sampling point. If the load is applied longitudinally at node 2 (x_2), then all the forces will be zero except $\hat{N}_2$. If the impact is imparted transversely, then all forces, except $\hat{V}_2$, will be zero. Subsequently, the nodal displacements can be acquired. After obtaining the nodal displacements, the unknown coefficients can be determined from Equation (4.50). Next, the deformations at any arbitrary location can be calculated using Equation (4.48). Lastly, the final displacement or total solution is the summation of $\hat{u}(x, \omega_n)$, $\hat{\psi}(x, \omega_n)$, $\hat{v}(x, \omega_n)$ and $\hat{\varphi}(x, \omega_n)$. The time domain results can be determined by using the inverse fast Fourier transform (IFFT).

4.2.4 Boundary conditions for timber pole situation

In a finite length rod or beam (contrary to an infinite structure), the reflection of waves is very important to be considered. The wave reflection mainly depends on the boundary conditions of the structure. From the above discussion, it is clear that an equal number of forward and backward propagating waves are taken into account in the infinite length element (or spectral relation as the spectral relation is solved for infinite length element) solution. However, for a finite length element, the energy is trapped in the element, and as a result a wraparound problem is present in the FFT based SFEM.

Hence, it is important to damp the energy or leakage of energy. There are different ways to damp the signal, such as to increase the number of FFT points and/or to increase the time sampling rate, which, however, causes aliasing problems. Alternatively, a small amount of damping can be added to the wavenumber as $\xi = \xi(1 - j\eta)$, where η is a small damping constant [165]. Nevertheless, all the methods mentioned above cannot be applied if the boundary is fixed or rigid (such as a cantilever beam). Therefore, another very effective method is used to add damping in the waveguide which is called throw off element [56, 98]. A throw off element is a one-noded infinite length element. In the throw off element method, only forward propagating waves (or forward propagating wavenumbers) are used to form the D_{SFEM} matrix for the throw off element and then the D_{SFEM} matrix for the finite length element is added to form the global stiffness matrix by the similar method used for the conventional FEM [168]. Details of using the throw off element method can be found in [56, 98, 161].

However, the throw off element cannot be used in the timber pole situation. The reason is that an embedded timber pole does not have any rigid boundaries. The timber pole is partially embedded in soil and energy leaks due to damping in the soil. Hence, in the current study, mainly two types of boundary conditions are investigated. The first one is standing on soil and second one is partially embedded in soil. This comparison is made to see the effect of soil when the pole is surrounded by it. The soil is replaced by spring and dashpot elements. When the pole is standing on soil, it is modelled as standing on a spring and dashpot element. In contrast, for the partial embedment condition, in addition to the spring and dashpot at the bottom, one dashpot is added at the soil level. It is not important to consider the spring at the soil level since the displacement is very small and no slipping or gaping occurs due to impact. As a result, by adding a dashpot at the top of the soil level, only energy leakage at the soil level is taken into account.

Details on applying boundary conditions as spring and dashpot elements in a rod and beam element are described in [56]. For a rod element, the boundary condition is related to axial forces, whereas for a beam element, two boundary conditions related to shear forces and moments are considered. Corresponding equations for the boundary conditions of a rod and beam element are presented in Table 4.1 and Table 4.2.

Table 4.1 Equations of typical boundary conditions for rods [56]

Boundary condition	Time domain	Frequency domain
Spring	$EA\frac{\partial u(0,t)}{\partial x} = -Ku(0,t)$	$EA\frac{d\hat{u}(0,t)}{dx} = -K\hat{u}(0)$
Dashpot	$EA\frac{\partial u(0,t)}{\partial x} = -\eta\frac{\partial u(0,t)}{\partial t}$	$EA\frac{d\hat{u}(0,t)}{dx} = -\eta j\omega\hat{u}(0)$

where the boundary is considered to be applied at node 1 (where x=0) and the force is $EA\frac{\partial u(0,t)}{\partial x}$ and the displacement is u.

Table 4.2 Equations of typical boundary conditions for beams [56]

Boundary condition (BC)	Imposed BC1	Imposed BC2
Linear spring	$EI\frac{\partial^2 v(0,t)}{\partial x^2} = 0$	$EI\frac{\partial^3 v(0,t)}{\partial x^3} = +Kv(0,t)$
Dashpot	$EI\frac{\partial^2 v(0,t)}{\partial x^2} = 0$	$EI\frac{\partial^3 v(0,t)}{\partial x^3} = +\eta\frac{\partial v(0,t)}{\partial t}$

In Table 4.2, two boundary conditions are given in the time domain, which become conditions on the various space derivatives in the frequency domain similar to Table 4.1.

The displacement, slope, moment and shear forces are different order derivatives of $\hat{v}(x,\omega)$ and can be expressed as

$$\text{Displacement}, \hat{v} = \hat{v}(x,\omega),$$
$$\text{Slope}, \hat{\phi} = \frac{d\hat{v}}{dx},$$
$$\text{Moment}, \hat{M} = EI\frac{d^2\hat{v}}{\partial x^2},$$
$$\text{Shear force}, \hat{V} = -EI\frac{d^3\hat{v}}{\partial x^3}.$$

According to the boundary conditions of a particular node, the forces related to spring and dashpot can be inserted in Equation (4.21), (4.38) and (4.53) to solve the displacement equation.

Different methods have been proposed to replace the soil by spring and dashpot [169-172]. The spring which represents the stiffness of soil can be horizontal and/or vertical. Similarly, both horizontal and vertical dashpot elements have different values. According to the charts and tables shown in [169], it is found that both the horizontal

damping and stiffness at the bottom of the soil is 1.5 times larger than the values in the vertical direction (for timber pole material properties). In the corresponding study, it is considered that the timber has a diameter of 300 mm and an embedded length of 2 m. To determine the stiffness and damping values, the density of soil is considered as 1,700 kg/m^3 and the elastic modulus of soil as 0.25 GPa. In the study, it is further found that the vertical damping coefficient on the bottom of the pile is almost 20 times larger than the value on the surface. However, the aforementioned literatures consider the low frequency dynamic stiffness. Ding et al. also used the spring and dashpot system for soil [173], so for the current investigation, the value for the vertical spring (or stiffness) is taken from this article with a value of 10^7 N/m^3. The horizontal stiffness is considered to be 1.5 times of the vertical stiffness and taken as 1.5×10^7 N/m^3. Similarly, the damping coefficient at the bottom of the pole is considered as 10^5 Ns/m^3 and 1.5×10^5 N/m^3 for the vertical and horizontal directions, respectively. The damping coefficient of the surrounding soil or on the surface are taken as 5×10^3 Ns/m^3 and 7.5×10^3 N/m^3 for the vertical and horizontal directions, respectively.

In SFEM, any structural member can be considered as a two-noded element (due to the dynamic stiffness matrix) if there is no irregularity or discontinuity in the structure. Despite from the above discussions, it is clear that the actual timber pole situation cannot be considered as a two-noded element. If the impact is imparted at the top of the pole, three nodes need to be taken into account. The extra node is the soil level where the vertical and/or horizontal dashpot is set up. Similarly, provided that the impact is imparted at the middle section of the pole, then four nodes need to be considered. Due to practical reasons, the impact strike is typically imparted at 1.5 m above the soil. In this case, the global stiffness matrix needs to be formed before solving the nodal displacement. Forming the global dynamic stiffness matrix follows the same procedure as for forming the global stiffness matrix in the conventional FEM. Details of forming the global stiffness matrix can be found in [56, 60, 107, 168]. For instance, the global dynamic stiffness matrix for a three-noded anisotropic cylinder is a 12 by 12 matrix. Again, the impact force can be determined from the FFT of the input signal and the forces related to spring and dashpot can be obtained from Table 4.1 and Table 4.2 while all the forces will be zero.

In the presented analysis, time-velocity data is sometimes required. Such velocity data can easily be found from the displacement values. After determining the final displacement or total solution at any point, the velocity can simply be calculated by multiplying the displacement values with $j\omega$ [56].

4.2.5 The forward and inverse FFT

Since in the present study the SFEM is performed based on FFT, it is important to present some basic requirements of the FFT. From the above discussion it is found that the first step related to the SFEM is to convert the time domain impact data to the frequency domain. In this study, the Gaussian signal is used as time domain signal. The Gaussian signal *P(t)* can be expressed as

$$P(t) = \frac{A}{\sigma\sqrt{2\pi}} e^{-\frac{1}{2}\left(\frac{t-\mu}{\sigma}\right)^2} \sin(2\pi t f) \tag{4.55}$$

where σ = standard deviation; $1/\sigma$ gives the frequency range of the spectrum; f = central frequency of the input signal; A = constant amplitude; μ = mean or the point in the time domain where the Gaussian distribution has a maximum value [84]. In this study, the input frequency f is taken as 12 kHz and 20 kHz and the frequency range as 8 kHz, i.e. σ = 1/8000. Also, μ = 4e-3 s and A = 0.004 are considered as values to determine *P(t)*.

The most important part of choosing the input signal is to choose the total time T and the time increment. A large time increment ΔT can cause aliasing problems while leakage can be avoided by choosing a large T. Besides, total time affects the frequency steps in the frequency domain. For a signal of time duration T sampled as N points, the discretisation rates in the two domains can be represented as

$$\Delta T = \frac{T}{N} \qquad \Delta f = \frac{1}{T} \tag{4.56}$$

In this study, T is chosen as 1 sec and ΔT as 1 μs to avoid leakage and aliasing problems. This gives a frequency step Δf of 1 Hz and hence the final frequency will be 1,000,000 Hz. It is important to mention that the analysis for solving the displacement is only required up to the Nyquist frequency. This is because in the FFT algorithm, N real points are transformed into $N/2$ complex points. The Nyquist frequency is thus defined as

$$f_{Nyquist} = \frac{N}{2T} = \frac{1}{2\Delta T} = \frac{N\Delta f}{2}. \tag{4.57}$$

Therefore, in the present study, the displacement at each point needs to be solved for each N^{th} sampling point (in this case at each frequency, as the frequency step is 1 Hz) up to the Nyquist frequency of 500,000 Hz. After obtaining the FFT of the input Gaussian signal, the impact force at each N^{th} frequency can also be determined and inserted in the nodal force-displacement relationship.

After calculating the displacement for each frequency, the inverse FFT is required to obtain the time domain signal. Since displacements can only be determined up to the Nyquist frequency, before the IFFT algorithm is implied, the displacement values related to the frequencies beyond the Nyquist frequency must be organized in such a way that they are the complex conjugates of the displacements related to the frequencies up to the Nyquist frequency. This ensures real valued time domain signals.

Another important aspect when applying the IFFT algorithm is that the zero frequency component is undetermined since it does not propagate. It is advantageous to remove its arbitrariness by imposing that the first value of the reconstruction is zero, i.e. [56]

$$\hat{u}_0 = -\sum_{1}^{N-1} \hat{u}_n. \tag{4.58}$$

For the same reason, all the actual signals are formed with a zero header to emphasize this point.

4.3 Frequency domain comparison

In this section, the dispersion curves determined using different theories are compared. Dispersion curves for both rod and beam like structures are presented. In addition, the results are also compared to the analytical results presented in Chapter 3. Furthermore, the dispersion curves of anisotropic material are also compared to the curves of orthotropic and transversely isotropic materials.

Before presenting the spectrum relation, it is essential to also present the dispersion relation which is especially important for a multi-mode analysis. This is due to differentiating the wavenumbers that correspond to the specific mode. Hence, the

dispersion relations for the anisotropic cylinder and isotropic Timoshenko beam are presented first.

4.3.1 Input signal and dispersion relation

The first step of SFEM is to define the load history. A Gaussian signal with an input frequency of 12 kHz and 20 kHz is used for the analysis (see Figure 4.1 and Figure 4.2). The number of sampling points is the same as mentioned above. The amplitude in the frequency domain is reduced to decrease the amount of energy.

The material properties used for the anisotropic material modelling are calculated from Equations (4.40) to (4.43) and are presented in Table 4.3.

Table 4.3 Material properties used for the anisotropic material modelling

Radius (m)	0.15	C_{11} (N/m^2)	2.3335 x 10^{10}
Density (kg/m^3)	900	C_{33} (N/m^2)	2.7038 x 10^{9}
Area (m^2)	0.0707	C_{13} (N/m^2)	9.5673 x 10^{8}
I (m^4)	3.9766 x 10^{-4}	G_{LR} (N/m^2)	2.047 x 10^{9}
I_0 (kg/m)	63.6255	D_{11} (N.m^2)	9.2793 x 10^{6}
I_2 (kg.m)	0.3579	D_{55} (N.m^2)	8.1401 x 10^{5}
ν_{LR}	0.35	A_{13} (N)	6.7636 x 10^{7}
ν_{RL}	0.041	A_{55} (N)	1.447 x 10^{8}
A_{11} (N)	1.6497 x 10^{9}	A_{33} (N)	1.9115 x 10^{8}

Sometimes, it is important to use some factors related to A_{55}, A_{33}, D_{55} and I_2 if the range of excitation frequency ω_{max} is such that

$$\omega_{max} > min\left(\sqrt{\frac{A_{55}}{I_2\left(1-(I_1^2/I_0I_2)\right)}}, \sqrt{\frac{A_{33}}{I_2\left(1-(I_1^2/I_0I_2)\right)}}\right). \quad (4.59)$$

Therefore, a sufficient accuracy can be obtained using the following factors $A_{55} = K_1A_{55}$, $D_{55} = K_2D_{55}$, $I_2 = K_3\, I_2$ and $A_{33} = K_4A_{33}$. Factors are determined as $K_1 = 0.86$, $K_2 = 0.89$, $K_3 = 1.216$ and $K_4 = 0.98$ [104].

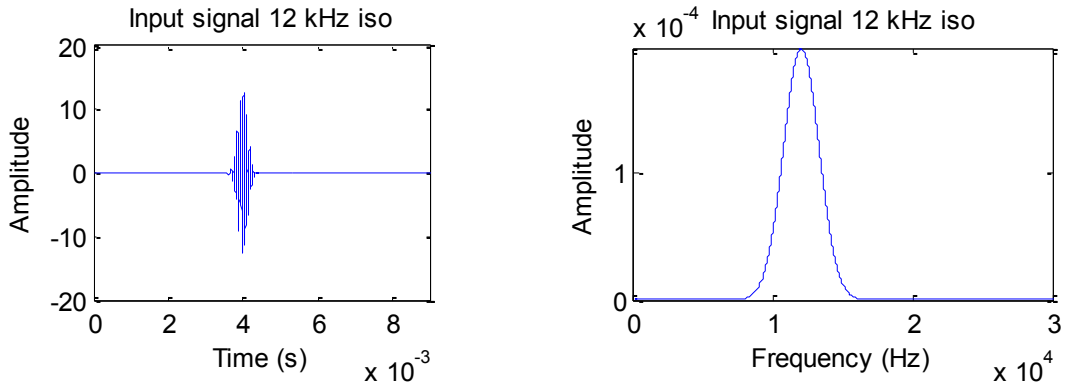

Figure 4.1 Excitation at 12 kHz signal

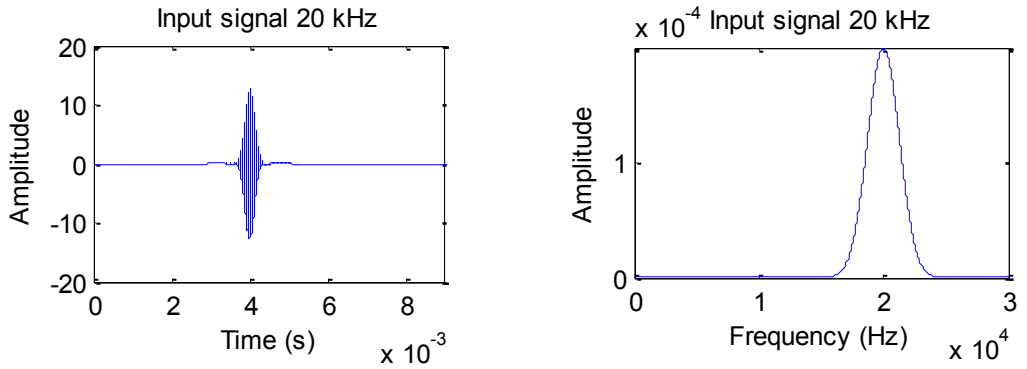

Figure 4.2 Excitation at 20 kHz signal

For the case of an anisotropic cylinder, there are four modes which are related to the longitudinal, flexural, shear and contraction modes. The longitudinal and the flexural modes start from zero frequency while the shear and contraction modes have their own cut-off frequencies. These cut-off frequencies can be obtained by implying $\omega_n = 0$; hence the Equation (4.47) shows that

$$\xi(0)_{1.....,6} = 0, \;\; \xi(0)_{7,8} = \pm\sqrt{\frac{A_{13}^2 - A_{11}A_{33}}{A_{55}D_{55}}}. \tag{4.60}$$

From the equation it can be seen that six roots start from zero frequency which are related to the longitudinal, flexural and shear modes and the non-zero one is related to the contraction mode. For the timber pole situation, the stiffness coefficients $C_{11} > C_{13}$ and $C_{33} > C_{13}$, and consequently, the non-zero roots must be imaginary at and near $\omega_n = 0$.

Next, the cut-off frequency can be obtained by setting $\xi = 0$ in Equation (4.47) giving

$$\omega_{cut-off} = 0,0,0,0, \sqrt{\frac{A_{55}}{I_2\left(1-(I_1^2/I_0I_2)\right)}}, \sqrt{\frac{A_{33}}{I_2\left(1-(I_1^2/I_0I_2)\right)}}. \quad (4.61)$$

From the equation it can be noted that initially there are two forward propagating waves (one flexural and one longitudinal), and two backward propagating waves (one flexural and one longitudinal). Also, below the cut-off frequency, two evanescent or non-propagating shear modes (one forward and one backward) and two evanescent or non-propagating contraction modes (one forward and one backward) are present. Since $A_{33} > A_{55}$, the contraction mode will propagate later than the shear mode. For the same reason, the wavenumber associated with the evanescent components in the contraction mode before the cut-of frequency is much higher than the wavenumber due to shear. Further, the flexural mode has a higher magnitude of wavenumber compared to the magnitude of the longitudinal mode. By knowing these criteria, it is possible to determine which roots are related to which wavenumbers, and hence, the dispersion relation can be obtained. As an example, Figure 4.3 illustrates the dispersion relation of an anisotropic cylinder. The flexural mode has the largest wavenumber as expected and the shear mode starts to propagate before the contraction mode.

For the isotropic Timoshenko beam, two modes are present, namely, the flexural and shear modes. Similar to the previous condition, the flexural mode starts from the zero frequency and the shear mode has a cut-off frequency. The cut-off frequency of the shear mode can be obtained from Equation (4.30) by implying $\xi = 0$. The material properties used for the isotropic Timoshenko beam are presented in Table 4.4.

Table 4.4 Material properties used for isotropic material model

Radius (m)	0.15	E (N/m^2)	23 x 10^9
Density (kg/m^3)	900	G (N/m^2)	8.8462 x 10^9
Area (m^2)	0.0707	ν	0.3
I (m^4)	3.9766 x 10^{-4}		

Figure 4.4 displays the dispersion relation for the isotropic Timoshenko beam. From the figure, it can be seen that for the isotropic beam, the cut-off frequency of the shear mode is higher than the cut-off frequency for anisotropic material.

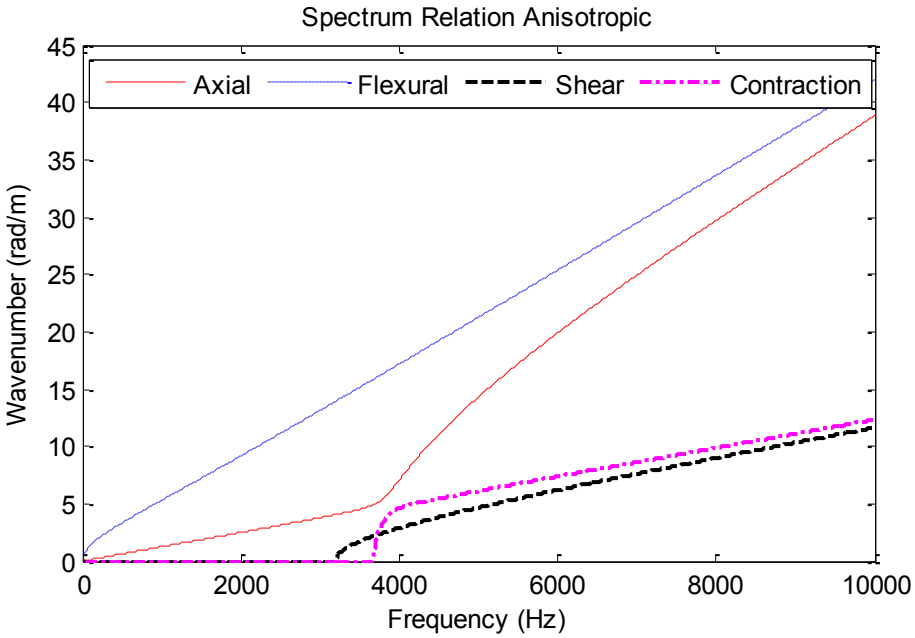

Figure 4.3 Dispersion relation of an anisotropic cylinder considering the properties of timber pole

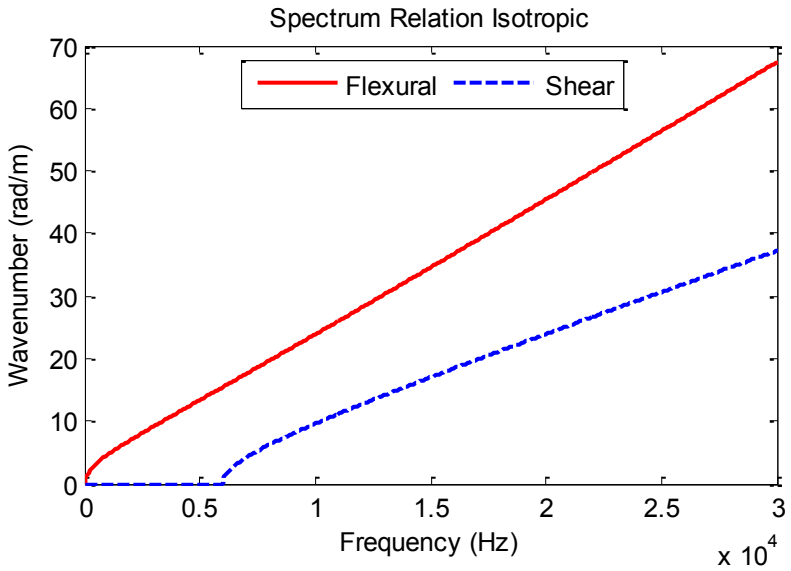

Figure 4.4 Dispersion relation of an isotropic Timoshenko beam considering the properties of timber pole

4.3.2 Spectrum relation

First, the phase velocity curves related to different theories are compared to determine the most appropriate theory which can best represent the timber pole situation. Second, the obtained dispersion curves are compared to the analytical curves presented in

Chapter 3. For this comparison, this section can be divided into isotropic rod theories, isotropic beam theories and anisotropic cylinders.

4.3.2.1 Isotropic rod and beam

Figure 4.5 and Figure 4.6 show the phase and group velocity curves of different rod theories. The elementary theory, the single mode Love theory, the two modes Mindlin-Hermann theory and the three mode theory are considered. From the figure, it can be seen that the elementary theory has constant phase velocity and hence is non-dispersive. The Love theory captures only the first longitudinal mode although only in the low frequency range. In addition, the velocity does not converge with an increase in frequency. The Mindlin-Hermann theory and the three mode theory have both very good agreement of the L(0,1) mode. Similarly, the three mode theory captures the L(0,2) mode better than the Mindlin-Hermann theory. Hence, it can be concluded that to obtain accurate lower order modes, it is essential to consider a higher order mode theory. For instance, provided that the input frequency falls above the cut-off frequency of the third mode, the four mode theory can interpret the third mode more accurately than the three mode theory. However, as the input frequencies in this research are considered as 12 kHz and 20 kHz, the three mode theory is sufficient to represent the actual timber pole situation.

A comparison between the three mode theory and the analytical results (or the Pochhammer-Chree equation) is presented in Figure 4.7. As mentioned earlier, notable similarities can be seen for the L(0,1) mode whereas the L(0,3) mode agrees the least. Even though, the cut-off frequency of the L(0,2) mode is almost the same for both theories, the difference increases with an increase in frequency. Especially the L(0,2) mode of the three mode theory cannot capture the change in slope at the frequency around 20 kHz which can clearly be seen in the analytical result. This is due to the same reason mentioned earlier that a higher order theory needs to be considered if it is essential to interpret higher frequencies. Zak and Krawczuk pointed out that even the normal four mode theory cannot represent the exact L(0,2) mode and thus the higher order four mode theory is proposed [95]. Nonetheless, the three mode theory is chosen for the analysis of the timber pole owing to the comparatively low frequency content.

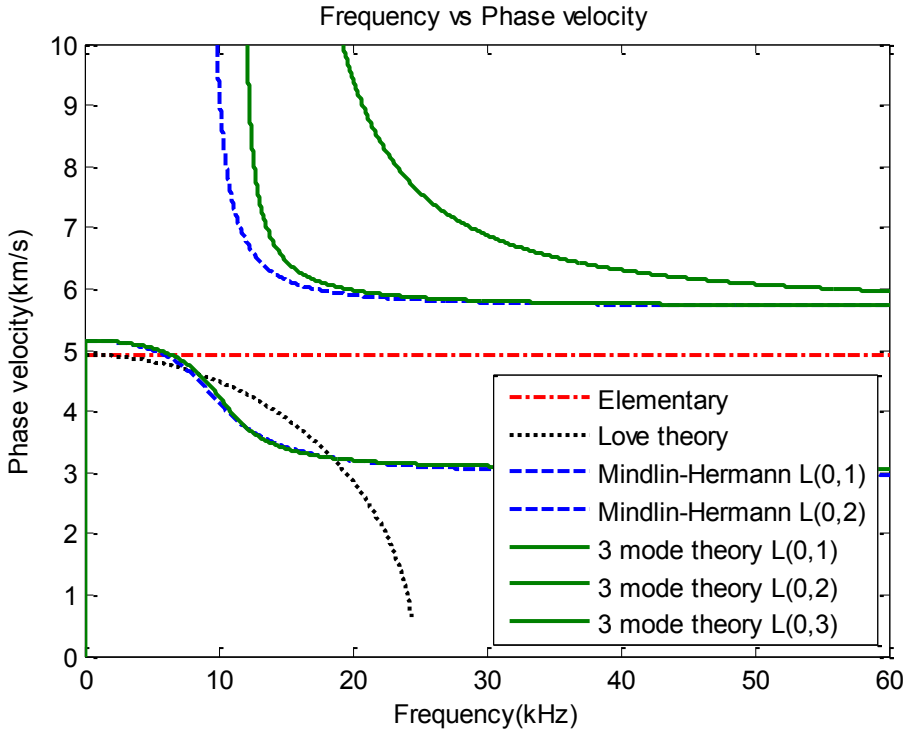

Figure 4.5 Comparison of phase velocity among different isotropic rod theories

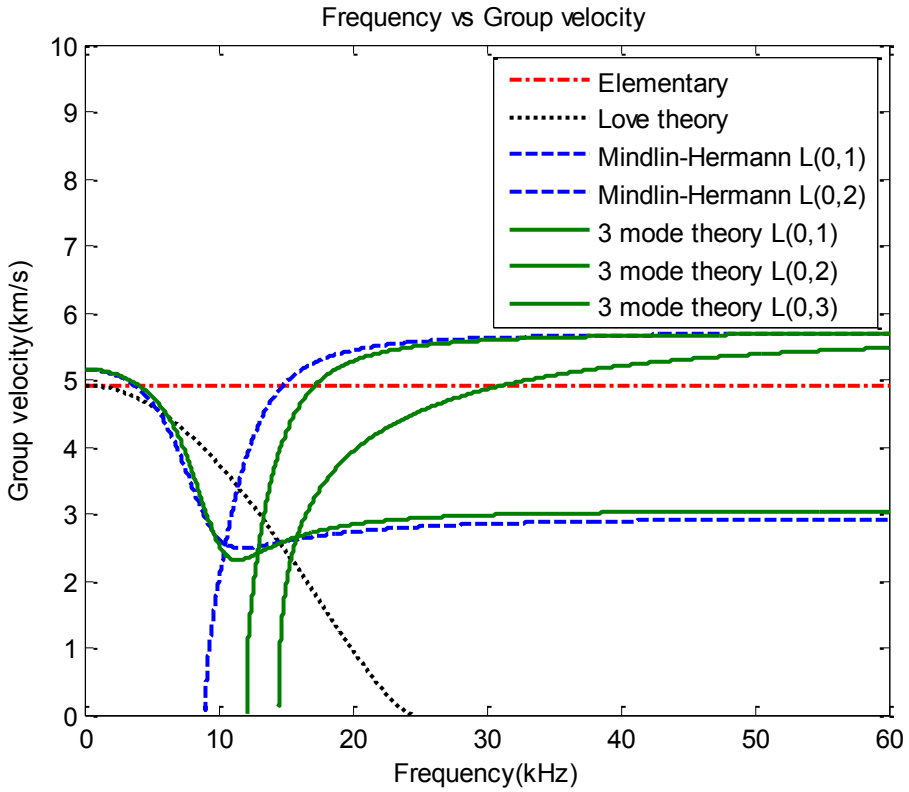

Figure 4.6 Comparison of group velocity among different isotropic rod theories

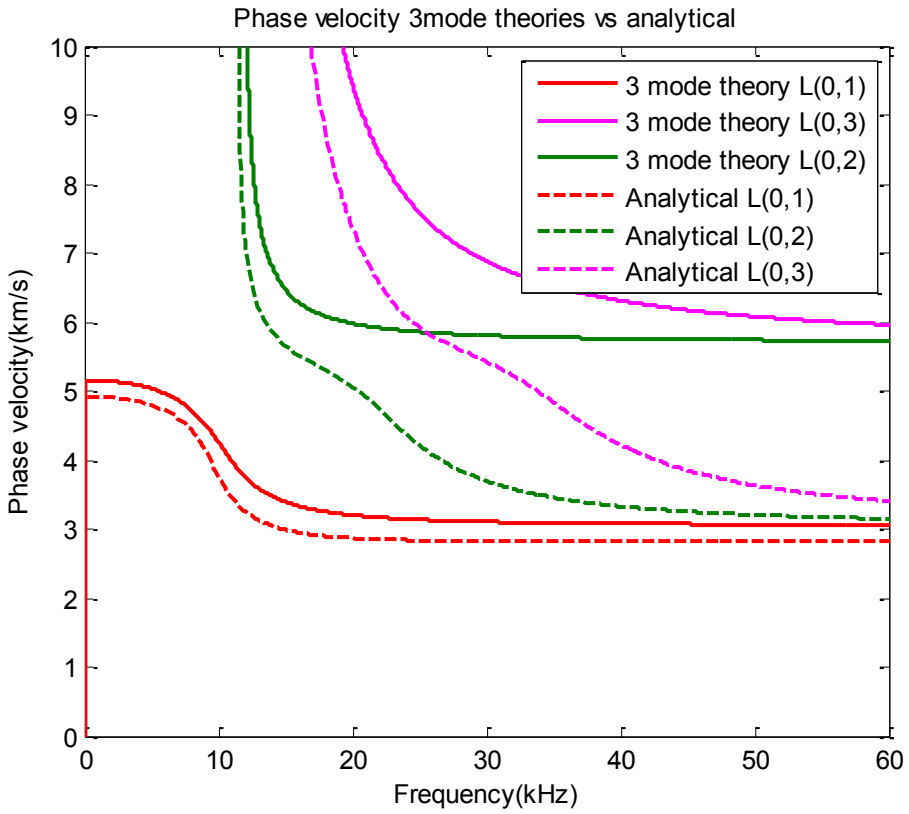

Figure 4.7 Comparison of phase velocity between 3 mode theory and analytical results

Figure 4.8 compares the phase velocity curves of the EBT to the Timoshenko beam theory. From Equation (4.25) and (4.27) it can be concluded that the phase velocity increases with an increase in frequency for EBT as can be seen from the figure. However, the EBT captures the first mode (or flexural mode) very well in very low frequencies (below 1.15 kHz). In contrast, the Timoshenko beam theory takes account of both the flexural and shear modes, with the flexural mode converging due to considering the shear deformation and rotary inertia. The shear mode has a cut-off frequency and starts to propagate from around 7 kHz. As a result, only the Timoshenko beam theory can represent the closest practical situation.

Figure 4.9 depicts the comparison between the analytical result and the Timoshenko beam theory. According to this figure, significant similarities can be observed for the flexural mode. In addition, the shear mode is related to the F(1,2) mode of the analytical result and both of the modes have the same cut-off frequency. Again, the difference increases with an increase in frequency and both converge in higher frequencies. The

dissimilarities of the shear mode can be observed more prominently in the group velocity curves. Figure 4.10 illustrates that the group velocity of the shear mode is higher than the same of the flexural mode (above 7.3 kHz), while analytically, it is actually lower than the flexural mode (Figure 3.12). Nevertheless, no better theory was found to represent the flexural wave propagation and hence the Timoshenko beam theory is considered for the time domain reconstruction.

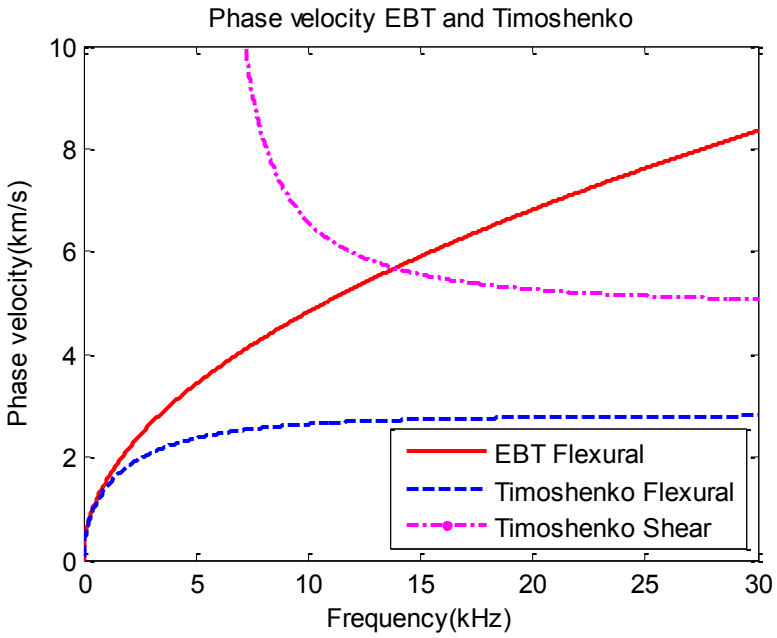

Figure 4.8 Comparison of phase velocity between different isotropic beam theories

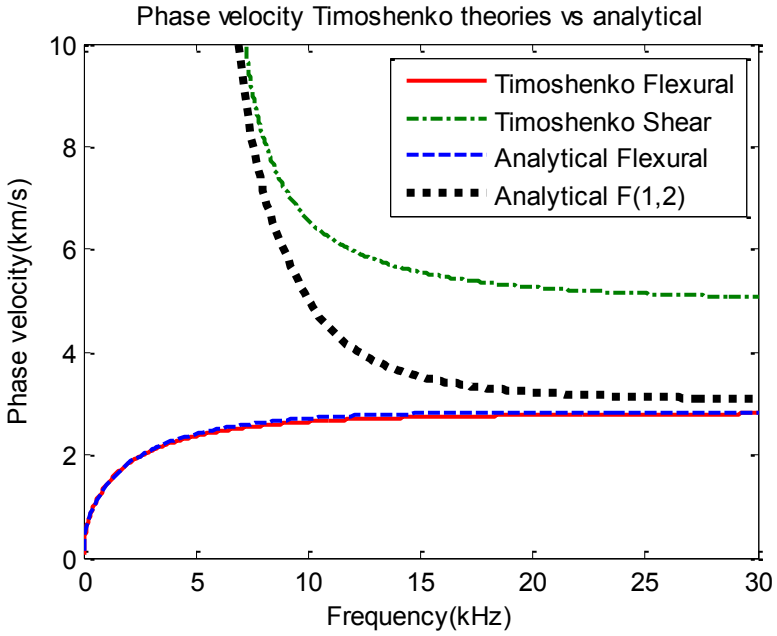

Figure 4.9 Comparison of phase velocity between Timoshenko beam theory and analytical result

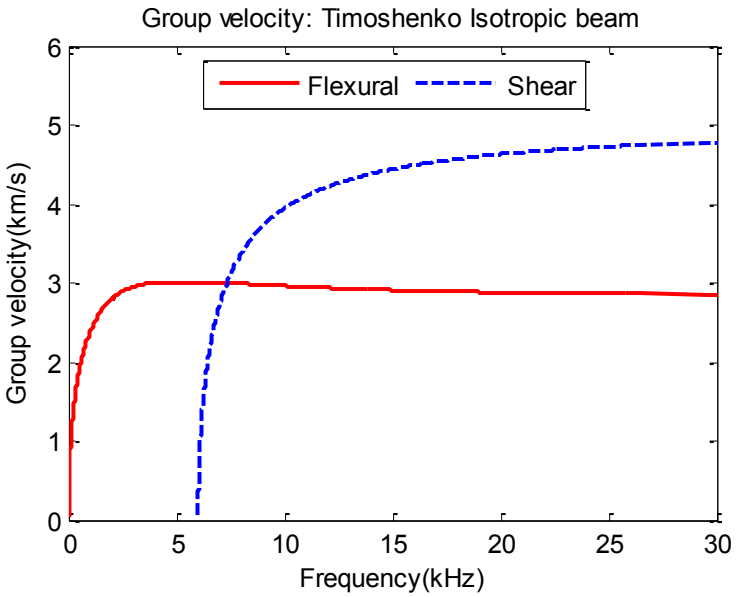

Figure 4.10 Group velocity curves of Timoshenko isotropic beam

4.3.2.2 Anisotropic cylinder

Figure 4.11 presents a comparison between the EBT and Timoshenko theory for a cylinder of anisotropic material considering plane stresses. Similar to the isotropic case, the longitudinal wave is non-dispersive. For the flexural wave of the EBT, the phase velocity increases with an increase in frequency. However, the longitudinal wave of the EBT captures the phase velocity correctly up to 2.8 kHz, whereas in the isotropic case, the non-dispersive part of the longitudinal wave, plotted for the elementary theory, is correct until 8 kHz. The same observation is made for the flexural mode, where, for instance, the flexural mode obtained from the EBT matches with the Timoshenko beam theory up to 1.15 kHz for the isotropic condition, while it matches only up to 300 Hz for the anisotropic material condition. Accordingly, the Timoshenko theory is again chosen for the comparison with the analytical results.

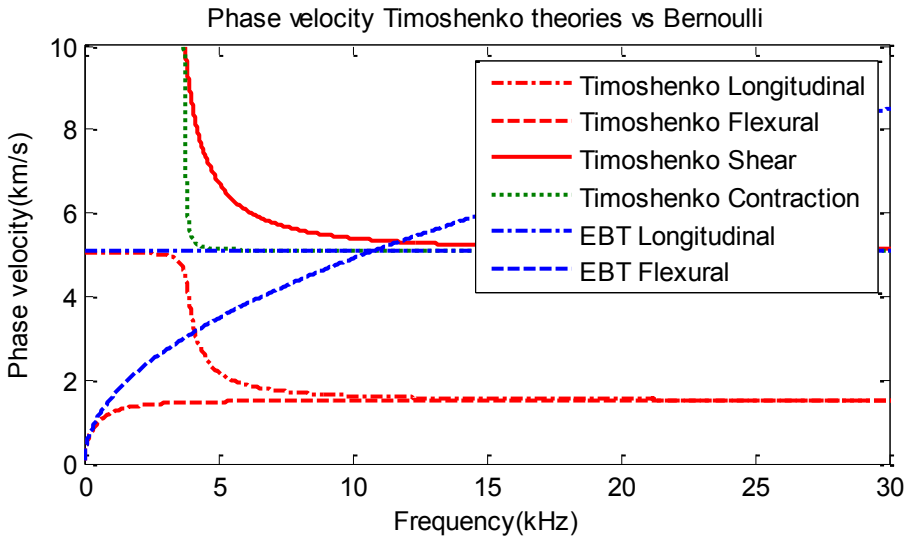

Figure 4.11 Comparison of phase velocity between different anisotropic wave theories

Figure 4.12 presents the comparison between the anisotropic cylinder of the Timoshenko theory and the material properties mentioned in set 2 of the transversely isotropic material presented in Chapter 3. From the figure, a clear difference can be seen between the two theories, and hence, it can be concluded that the set 2 of the transversely isotropic material cannot represent the orthotropic behaviour correctly. In comparison, the set 3 of the transversely isotropic material matches very well with the Timoshenko theory, which is shown in Figure 4.13. The figure indicates that the longitudinal and the flexural modes of the Timoshenko theory and the set 3 of the transversely isotropic material are in good agreement. The cut-off frequency of the contraction mode of the Timoshenko theory has the same value as its counterpart of the transversely isotropic material which is the L(0,2) mode. Again, the similarities between the L(0,2) mode and the contraction mode can be observed up to 9 kHz beyond which the contraction mode becomes constant while the L(0,2) mode converges from 15 kHz. Therefore, these two frequencies are chosen for time domain reconstruction due to the explanation given in Chapter 3 which is related to the peak constant group velocity. It can also be seen that the Timoshenko theory cannot interpret the F(1,2) mode of the transversely isotropic material. Further, the shear mode matches well with the F(1,3) mode although the similarity is not very satisfactory. The cut-off frequency of the F(1,3) and the shear mode is almost the same; however, the shear mode cannot represent the actual behaviour after 6 kHz.

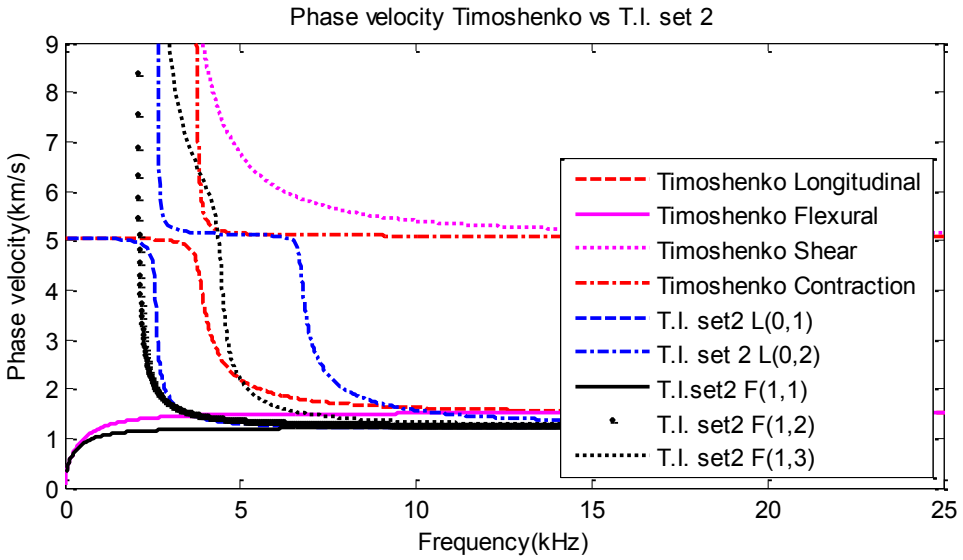

Figure 4.12 Comparison of phase velocity between Timoshenko theory and transversely isotropic material modelling (set 2)

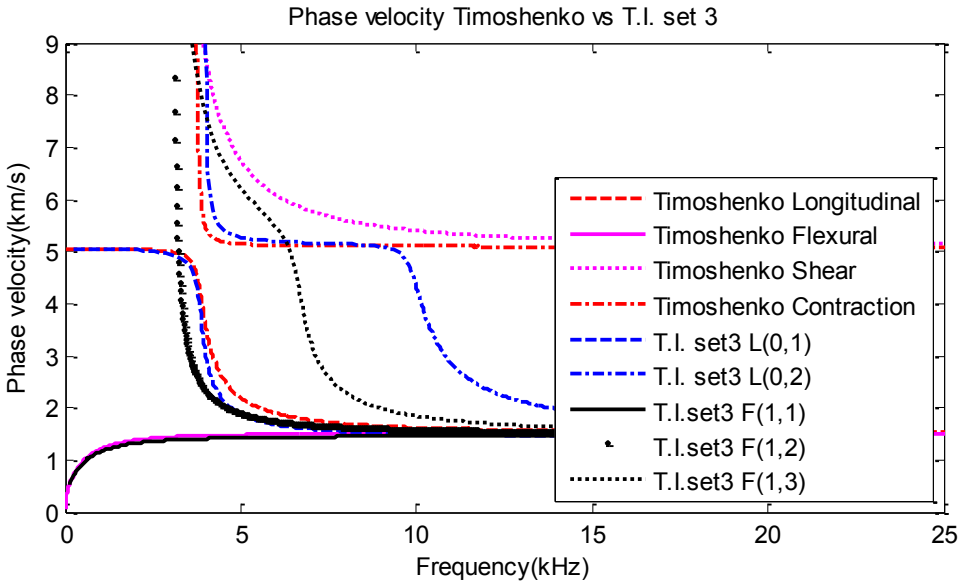

Figure 4.13 Comparison of phase velocity between Timoshenko theory and transversely isotropic material modelling (set 3)

Figure 4.14 displays the phase velocity curves of the anisotropic cylinder using the Timoshenko theory and the phase velocity curves of the actual orthotropic cylinder. For this case, the same observations can be made as with the comparison between set 3 of the transversely isotropic cylinder and the Timoshenko theory. While the longitudinal mode of the Timoshenko theory is non-dispersive up to 3.4 kHz, this range drops to 2.5 kHz for the orthotropic material modelling. Small changes can be seen between the flexural mode and the F(1,1) mode. Also, the cut-off frequency of the contraction mode is the almost same as the L(0,2) mode; and it has the same velocity for both cases until

9 kHz. The shear mode and the F(1,3) mode depict the same behaviour as mentioned earlier for the set 3 of the transversely isotropic model.

Even though there are some dissimilarities, the Timoshenko theory is chosen for the anisotropic behaviour since no theory was found that can simulate the anisotropic case closer than the Timoshenko theory. It is also noted that the Timoshenko theory reflects the transversely isotropic behaviour better than the orthotropic counterpart.

For further information, the group velocity curves for the Timoshenko anisotropic cylinder is presented in Figure 4.15. Since the group velocity is critical for the wave input, the group velocity curve is of special importance.

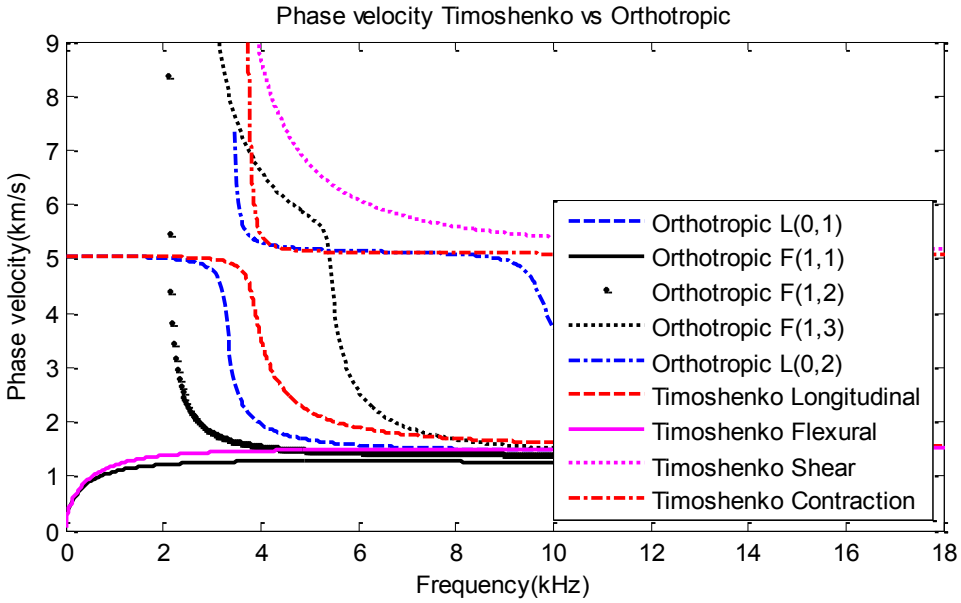

Figure 4.14 Comparison of phase velocity between Timoshenko theory and orthotropic material modelling

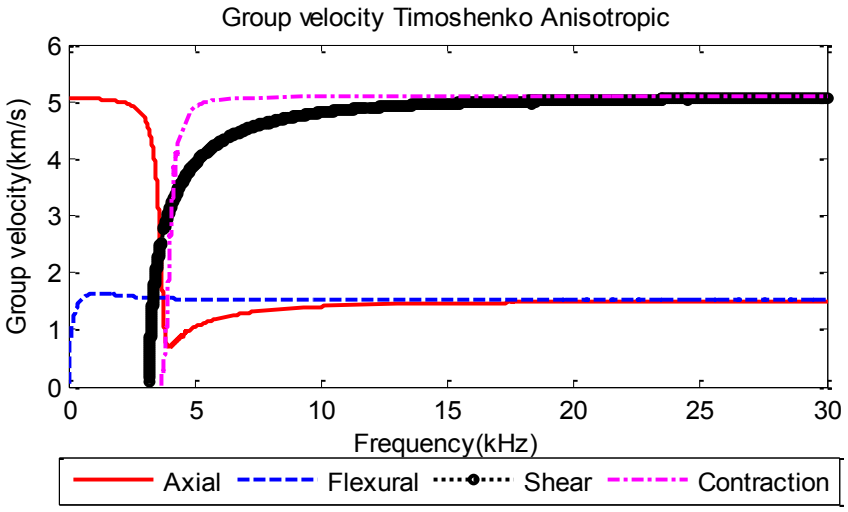

Figure 4.15 Group velocity curve of anisotropic cylinder

4.4 Time domain reconstruction

For the time domain reconstruction, two different boundary conditions are considered, namely, directly standing on soil and partial soil embedment (real timber pole situation). Also, different impact locations and directions are investigated. For example, for the isotropic rod behaviour, the impact is imparted vertically at the top of the timber pole, whereas for the isotropic Timoshenko beam, the impact direction is chosen to be horizontal at the top of the beam. Regarding the anisotropic cylinder, two different locations are taken into account, i.e. impact on top of the cylinder and impact from 1.5 m from the ground. At these two locations, the impact directions are considered as vertical and horizontal (both separately and combined). The combination of vertical and horizontal directions is investigated due to the fact that sometimes the impact is imparted through a 45 degree inclined waveguide. Figure 4.16 shows different impact locations, directions and boundary conditions (for longitudinal impact).

Two impact locations (at top and middle of the pole) are chosen due to analyse the wave behaviour. Impact top at creates only one directional wave whereas impact at the middle produces two wave, one upward going wave and the other one is downward going wave. Therefore, impact at top is chosen to investigate the longitudinal (vertical impact) and flexural wave (horizontal impact) behaviour without any interference of bi-directional wave. However, in reality, the impact is imparted at the middle of the pole as the top of the pole is not easily accessible. Horizontal, vertical and inclined impact is considered at the latter location to produce longitudinal and flexural wave separately and combined.

For the longitudinal wave propagation, the spring and dashpot are placed in the longitudinal direction, while for the transverse loading (or bending wave), they are placed in the transverse direction. For the anisotropic condition, the springs and dashpots are placed in both the longitudinal and transverse directions.

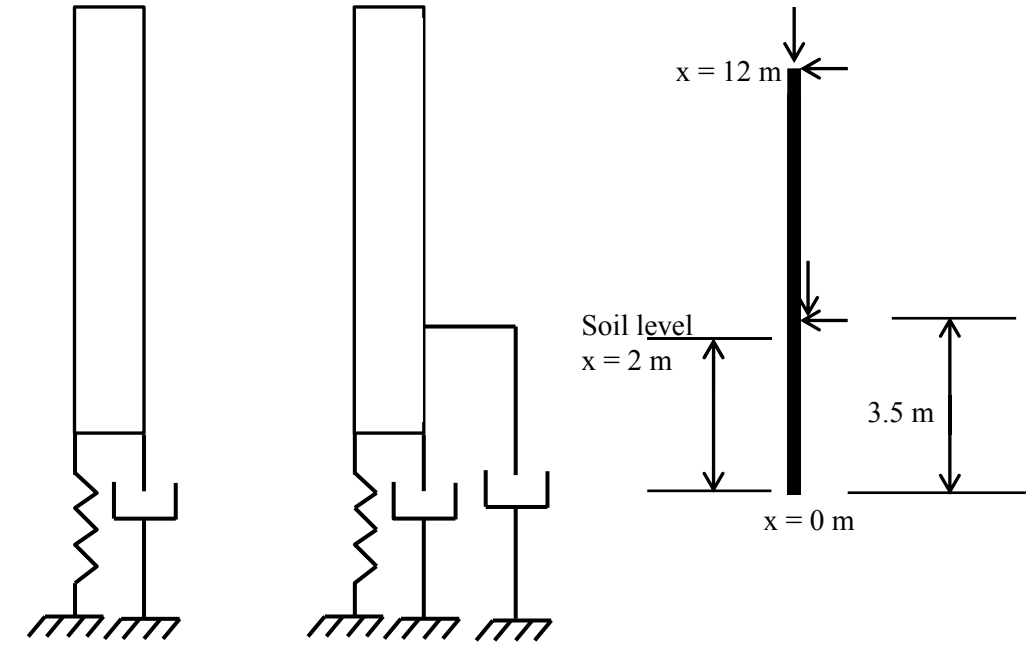

Figure 4.16 Boundary conditions and different impact locations and orientations

4.4.1 Isotropic rod element

For the isotropic rod investigation, the input frequency is chosen to be 20 kHz and the impact is imparted longitudinally at x = 12 m (on top of the pole). From Figure 4.6 it can be seen that all three modes are present at this input frequency and the velocities relating to mode 1, 2 and 3 are approximately 2,860 m/s, 3,860 m/s and 5,320 m/s, respectively. Therefore, all three modes can be seen in the time domain results.

In the first investigation, the pole is considered to be standing on the soil. For this case, the pole is simplified to a two-nodded element only. Figure 4.17 illustrates the time domain signals at x = 12 m, 8 m, 4 m and 0 m (bottom of the pole) for the standing on soil situation. It can be seen that in the beginning at x = 12 m (when the impact is imparted), all the modes are generated together. However, they start separating while traveling down the pole. At x = 8 m, the 2nd mode has already separated from mode 1 whereas the 3rd mode is clearly visible at x = 4 m. At the bottom of the pole (x = 0m), all three modes can clearly be observed. In the figure, the dashed line connects the 1st arrival (and also reflection) of mode 1 at different locations (or sensors), while the solid and dashed dot line connects the arrival (and also reflection) of mode 2 and 3,

respectively. The slopes of these lines represent the group velocities corresponding to these three modes. From the slopes, three group velocities can be calculated which match accurately with the group velocity curves (Figure 4.6). Since mode 3 has the highest velocity, it reaches all the sensors first, this is followed by mode 2 and lastly mode 1 due to its lowest velocity. It can also be observed that the reflected waves reach the lower sensors first and then the sensors with longer distances. Or in other words, the reflected wave reaches the location x = 4 m before it reaches x = 8 m. This trend is also very clear from the figure.

Figure 4.18 displays the time domain results for the real timber pole situation (partially embedded) based on the three modes theory with the same input frequency as mentioned above. For this situation, the timber pole is modelled as a three-nodded element. The signal capturing (sensor) locations are chosen at x = 12 m, 8 m, 4 m, 2 m (soil level) and 0 m (the bottom of the pole). In comparison with Figure 4.17, it can be observed that there is not much difference in the longitudinal wave propagation due to the presence of the soil. However, as the time increases, the amplitude reduces owing to the loss of energy due to the soil embedment.

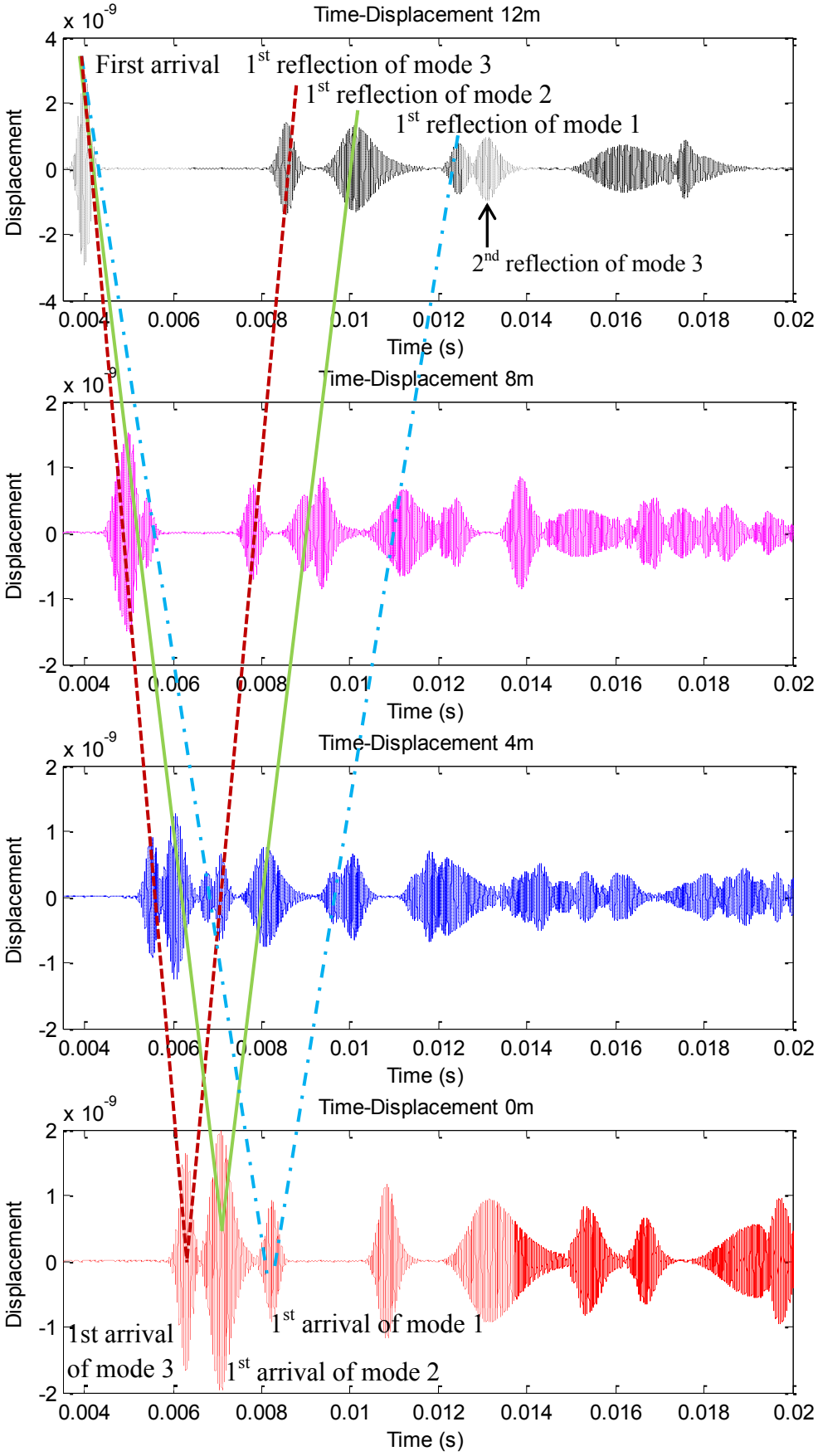

Figure 4.17 Time domain results of isotropic rod element based on 3 mode theory

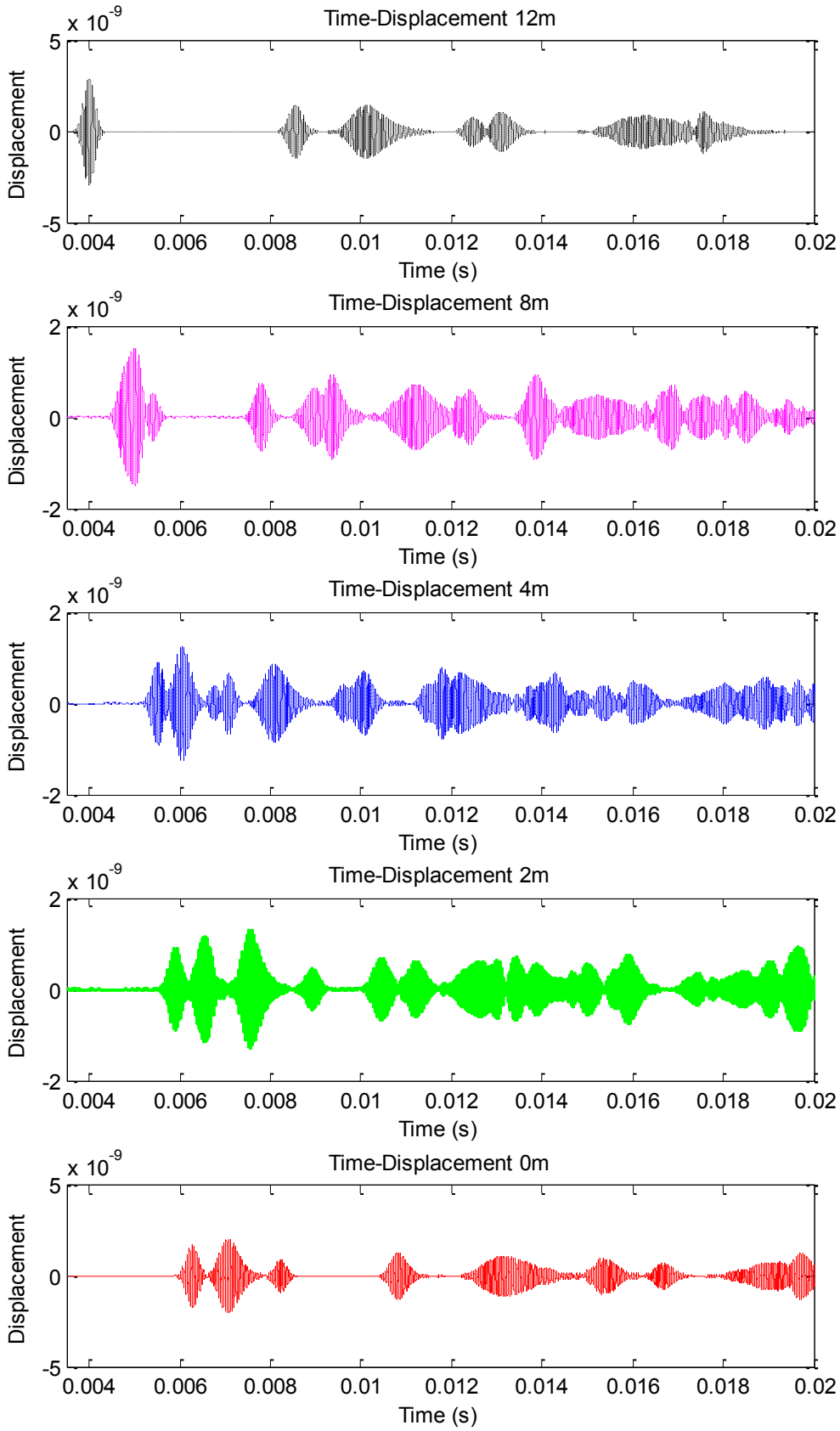

Figure 4.18 Time domain results of isotropic rod element (partially embedded) based on 3 mode theory

For the real timber pole situation, the sensor at the soil level (x = 2 m) is affected by the superposition of the different modes. For instance, the reflection of mode 1 is interfering with the first arrival of mode 2 and similarly the first arrival of mode 3 is superimposed with the reflection of mode 2. From this investigation, it can be concluded that the presence of soil does not affect the longitudinal wave propagation.

4.4.2 Isotropic beam element

The input frequency is chosen to be 20 kHz for this situation and the impact is imparted transversely at x = 12 m or at the top the pole. It is clear from Figure 4.10 that both the flexural and shear modes are present at this input frequency and the velocities related to flexural and shear modes are approximately 2,900 m/s and 4,600 m/s, respectively. Therefore, both these modes can be seen in the time domain results.

Figure 4.19 illustrates the time domain signal at x = 12m, 9m, 6m, 3m and 0m (bottom of the pole) for the standing on soil situation. It can be seen that at the beginning (x =12m) where the impact is imparted, both modes are generated together. However, they start separating while traveling down the pole. At x = 9m, the flexural mode has already separated from the shear mode due to its slower velocity. At the bottom of the pole (x = 0m), both modes can clearly be observed. The dashed line connects the 1st arrival (and also reflection) of the shear mode at different locations (or sensors) while the dashed dot line connects the arrival (and also reflection) of the flexural mode. The slopes of these lines should represent the group velocities corresponding to these three modes. From the slopes, these two group velocities can be calculated which matched accurately with the group velocity curves (Figure 4.10). Since the shear wave has the higher velocity, it reaches all the sensors first before the flexural wave. It is also obvious that the reflected waves will reach the lower sensors first and then the sensors on longer distance. This trend is also very clear from the figure. Also, the reflection of shear mode and the arrival of the flexural mode are superimposed at x = 3m. The only discrepancy is observed at x = 9m where a spurious wave packet can be seen at 0.0059 sec.

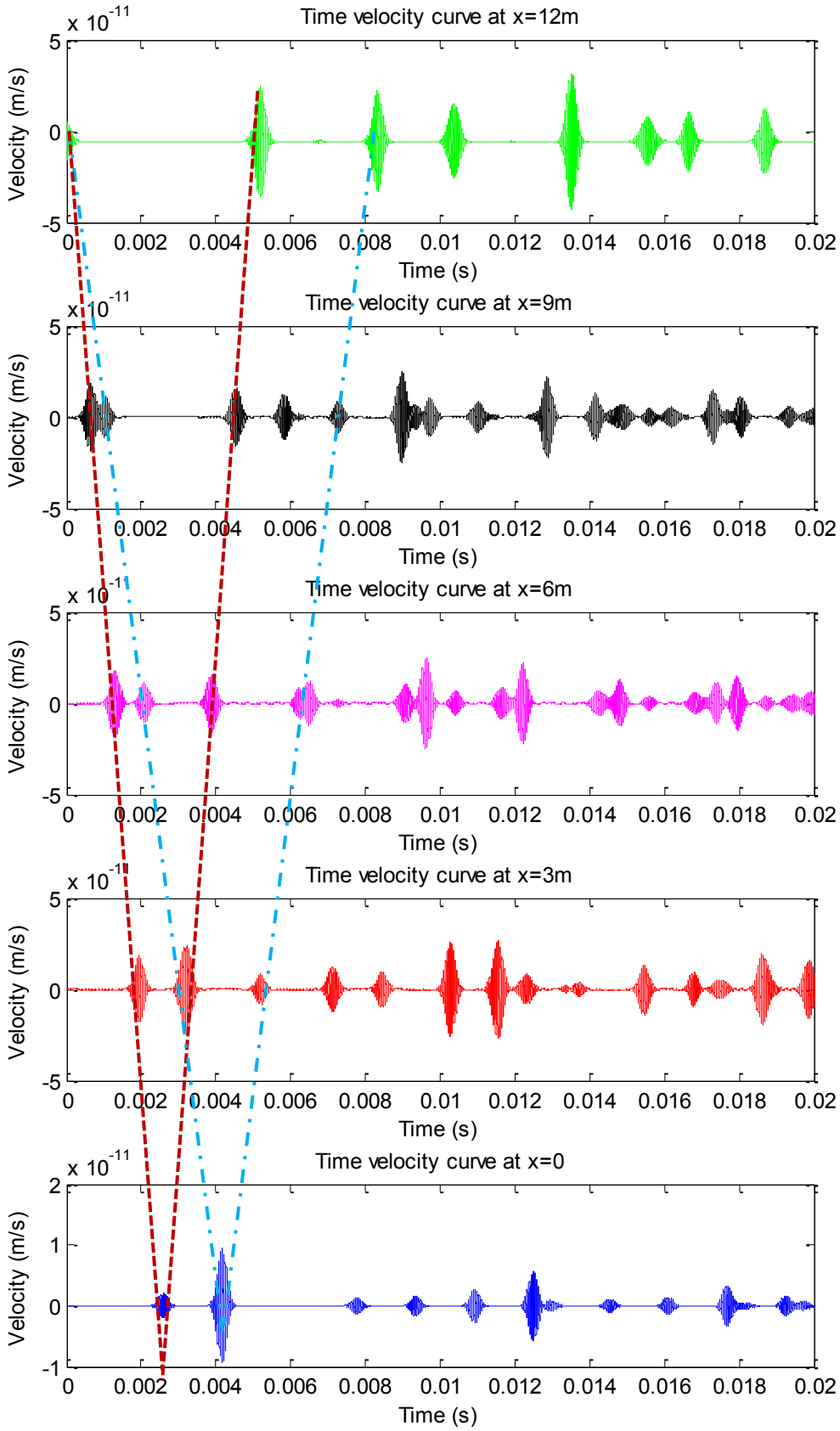

Figure 4.19 Time domain results of isotropic beam element based on Timoshenko beam theory

In Figure 4.20, the time domain results are plotted for the timber pole situation based on the Timoshenko beam theory with the same input frequency used for the previous situation. The locations are chosen at x = 12 m, 10 m, 6 m, 2 m (soil level) and 0 m (the bottom of the pole). By comparing Figure 4.20 to Figure 4.19, the effect of soil can clearly be observed for the flexural wave propagation. For the real timber pole condition, there are more peaks compared to the standing on soil situation. A possible reason for this phenomenon is the mode conversion. As the flexural wave reaches the bottom of the pole it is converted to one flexural wave and a shear wave and the same behaviour can be noted for the shear wave. Due to the mode conversion, more peaks are present with increase in time, and hence, the signal becomes more cluttered.

At x = 12 m, one more peak can be seen at 0.00674 sec which is, however, absent from the previous case. In Figure 4.20, two arrows are depicted for the reflection of the shear wave and also two arrows are plotted for the reflection of the flexural wave. As mentioned before, it is assumed that the first shear waves are converted to one shear wave and one flexural wave. Hence, the peak at 0.00519 sec (at x = 12 m) is related to the reflected shear wave (same as for the standing on soil situation). Similar to the shear wave, the flexural wave is also converted to one shear mode and one flexural mode. Accordingly, the peak at 0.00674 sec (x = 12 m) is actually the superposition of two modes and one of the modes is the converted flexural mode from the reflected shear mode and the other one is the converted shear mode from the reflected flexural mode. Lastly, the peak at 0.00832 sec (x = 12 m) is related to the reflected flexural wave (same as for the standing on soil situation). These can also be verified by determining the velocity from the slope of the arrowed lines (dashed and dashed dot arrowed lines). These arrowed lines are termed IS (incoming shear mode), IF (incoming flexural mode), RS (reflected shear mode), CRF (converted reflected flexural mode), RF (reflected flexural mode) and CRS (converted reflected shear mode). After calculating the slopes of these lines, it is found that the velocity of the incoming shear mode (IS) and flexural mode (IF) are approximately 4,600 m/s and 2,900 m/s, respectively. Similarly, the velocities calculated from the slopes of the RS and CRS are also found to be 4,600 m/s which is the same as for the shear mode velocity. Further, the velocities calculated from the slopes of the RF and CRF are also found to be 2900 m/s which is the same as for the flexural mode velocity.

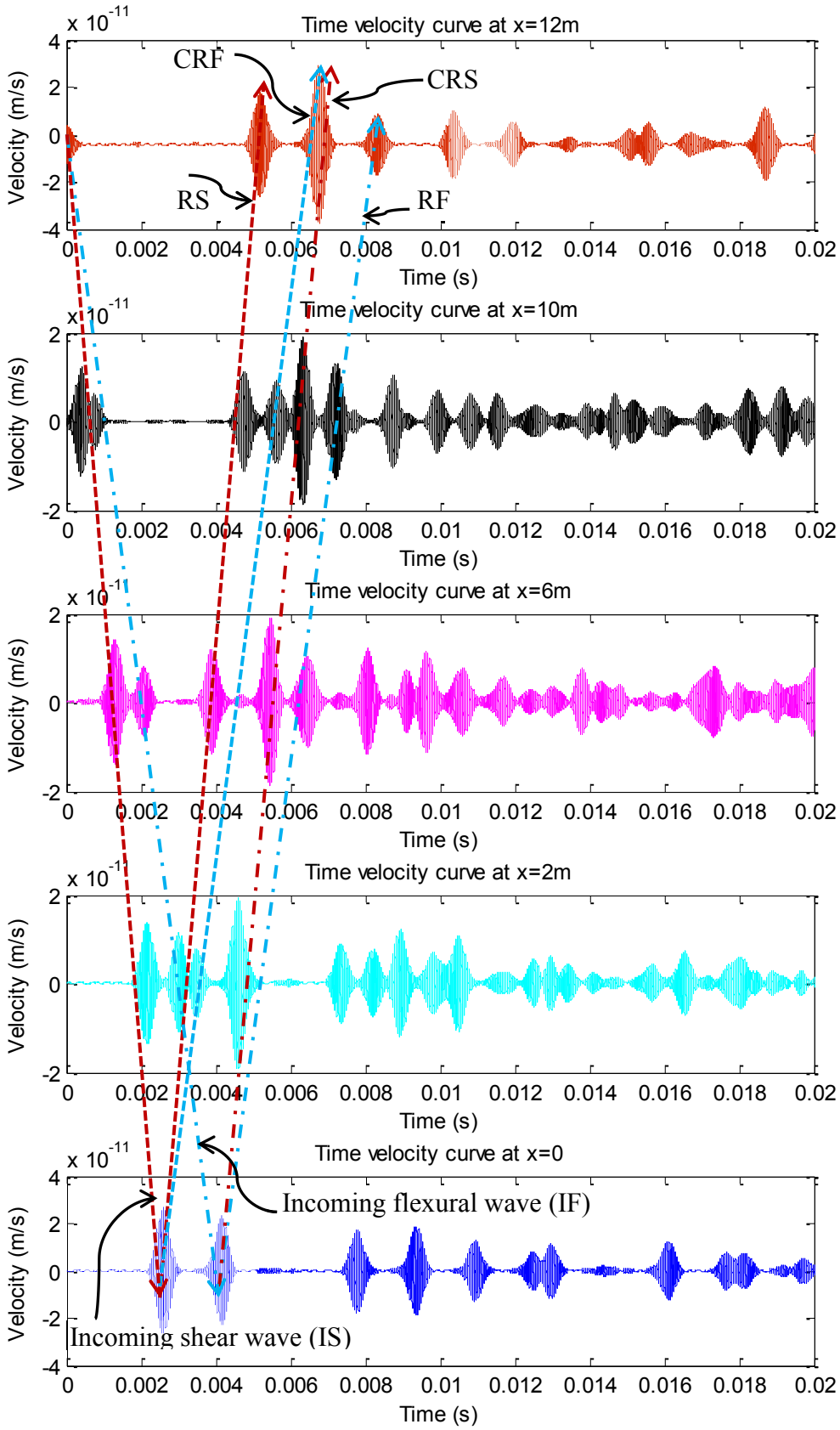

Figure 4.20 Time domain results of isotropic beam element (partially embedded) based on Timoshenko beam theory

Therefore, it can be concluded that the flexural wave propagation is affected by the presence of soil and mode conversion happens at the bottom of the pole.

4.4.3 Anisotropic cylinder

In the following sections, SFEM is performed for an anisotropic cylinder with different impact scenarios including: impact on top (vertical, horizontal and inclined direction) and impact from the middle section of the cylinder/pole.

4.4.3.1 Impact at top (vertically)

In the first study, the impact is imparted vertically from the top of the cylinder/pole. As mentioned earlier, for the anisotropic case, flexural and longitudinal waves are coupled. This, however, may not be true for the real timber pole situation since the equations are derived for laminated composite materials. Nevertheless, for the current investigation, the impact frequency is chosen as 12 kHz (central frequency). At this frequency, the group velocities of flexural and longitudinal waves are approximately 1,600 m/s for both types of wave, while the shear and the contraction modes have a velocity of 5,000 m/s (Figure 4.15). From the figure, the differences in velocities among these modes are clearly visible. Again, five locations are chosen for the time domain results; these are x = 12 m, 9 m, 6 m, 3 m and 0 m (bottom of the pole). Figure 4.21 demonstrates the time domain results at different locations.

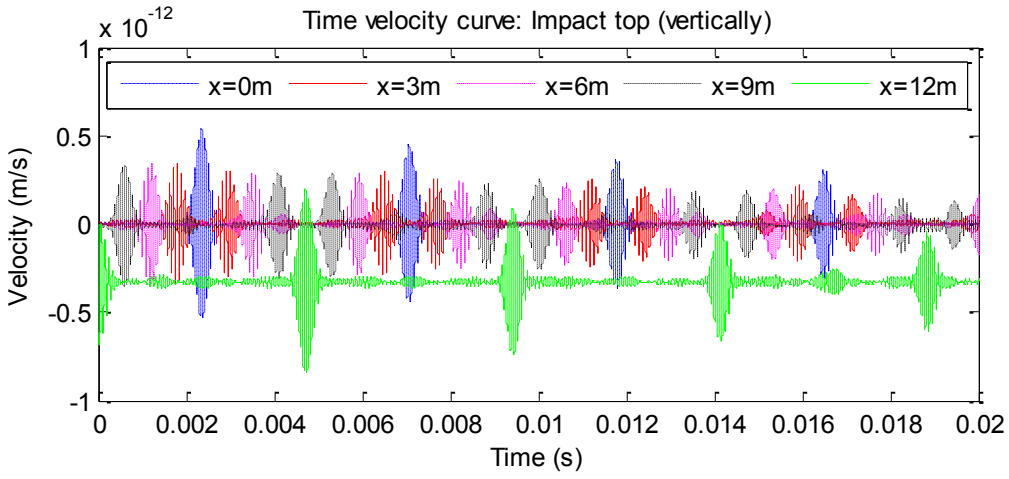

Figure 4.21 Time domain results of anisotropic cylinder with impact at top (vertically) considering the pole standing on soil

From the figure, clearly separated waves are visible and it is hard to imagine the superposition of different modes. From the time differences, the wave velocity is calculated to be 5,000 m/s. Therefore, it can either be the shear or contraction mode. From the figure and the calculated wave velocity, one can conclude that the flexural and shear waves are absent in the results. Hence, in Figure 4.22 the wave velocities are plotted separately for the longitudinal, flexural, shear and contraction parts of the final signal.

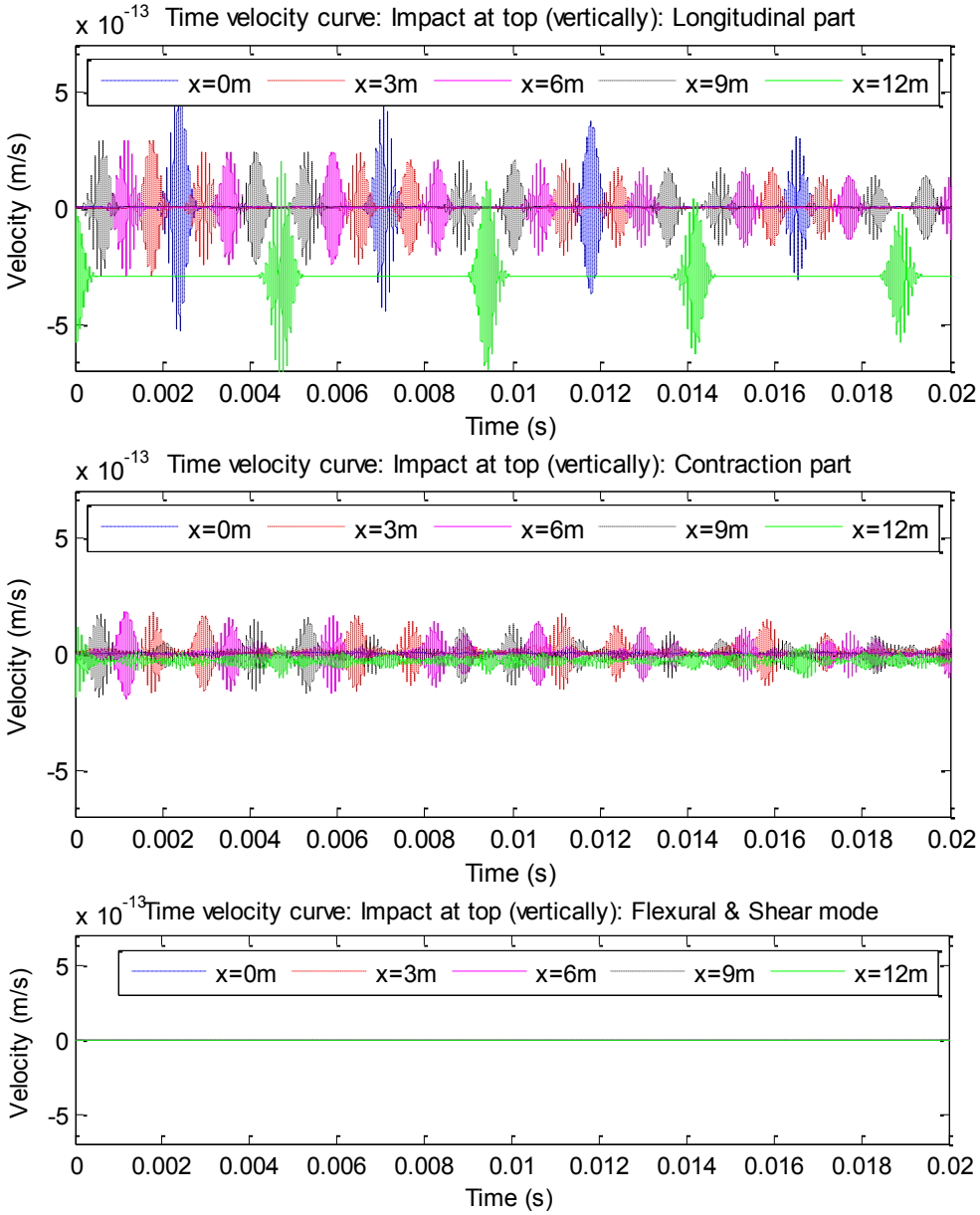

Figure 4.22 Contribution of different modes in an anisotropic cylinder with impact at top (vertically) considering the pole standing on soil

From the figure it can be seen that the flexural and shear modes are not present since the impact is imparted vertically at the top of the pole. Further, the contraction mode has lower amplitude when compared to the longitudinal mode, and thus, the final wave plot (Figure 4.21) is dominated by the longitudinal mode and behaves as non-dispersive. It is also observed that the longitudinal mode contains the same features as the contraction mode and shows the same velocity as the contraction mode, even though the contraction mode contains some intermediate small peaks. A possible reason for this phenomenon is that the longitudinal wave usually propagates with a constant velocity since the constant velocity part is always dominating.

Using the same impact frequency as in the 'standing on the soil' situation, the time domain results for the timber pole situation (partially embedded) is presented in Figure 4.23. The locations of the sensors are also shown in the figure. Unlike the isotropic case, for the anisotropic modelling of the timber pole here, the presence of soil does affect the longitudinal wave propagation. From the figure, it can also be observed that there are a number of peaks in the final time-velocity curve, and hence, the longitudinal and contraction modes are drawn again separately in Figure 4.24 and Figure 4.25, respectively.

In the figures, it can be seen that the longitudinal mode of the signal is very clear and almost follows the same trend as the standing on soil situation. The contraction part displays more dispersion effects as can be seen from Figure 4.25, and, thereby, it affects the final time-velocity curve. The possible reason for this can be the input frequency. Consequently, the input frequency is changed to 20 kHz.

The time domain results related to an input frequency of 20 kHz are presented in Figure 4.26. From the figure, it can be seen that the signal gets clearer by changing the frequency. This can also be explained from the group velocity curves. As such, the group velocity becomes constant at 20 kHz whereas at 12 kHz it has some slope which causes more dispersion. Again, the velocity of the contraction mode is dominant and equals to 5,000 m/s. Therefore, similar to the timber pole situation of the isotropic case, for the anisotropic modelling of the timber pole, soil also does not affect the wave propagation if an appropriate input frequency is chosen. The individual contributions of the longitudinal and contraction modes are presented in Appendix D.

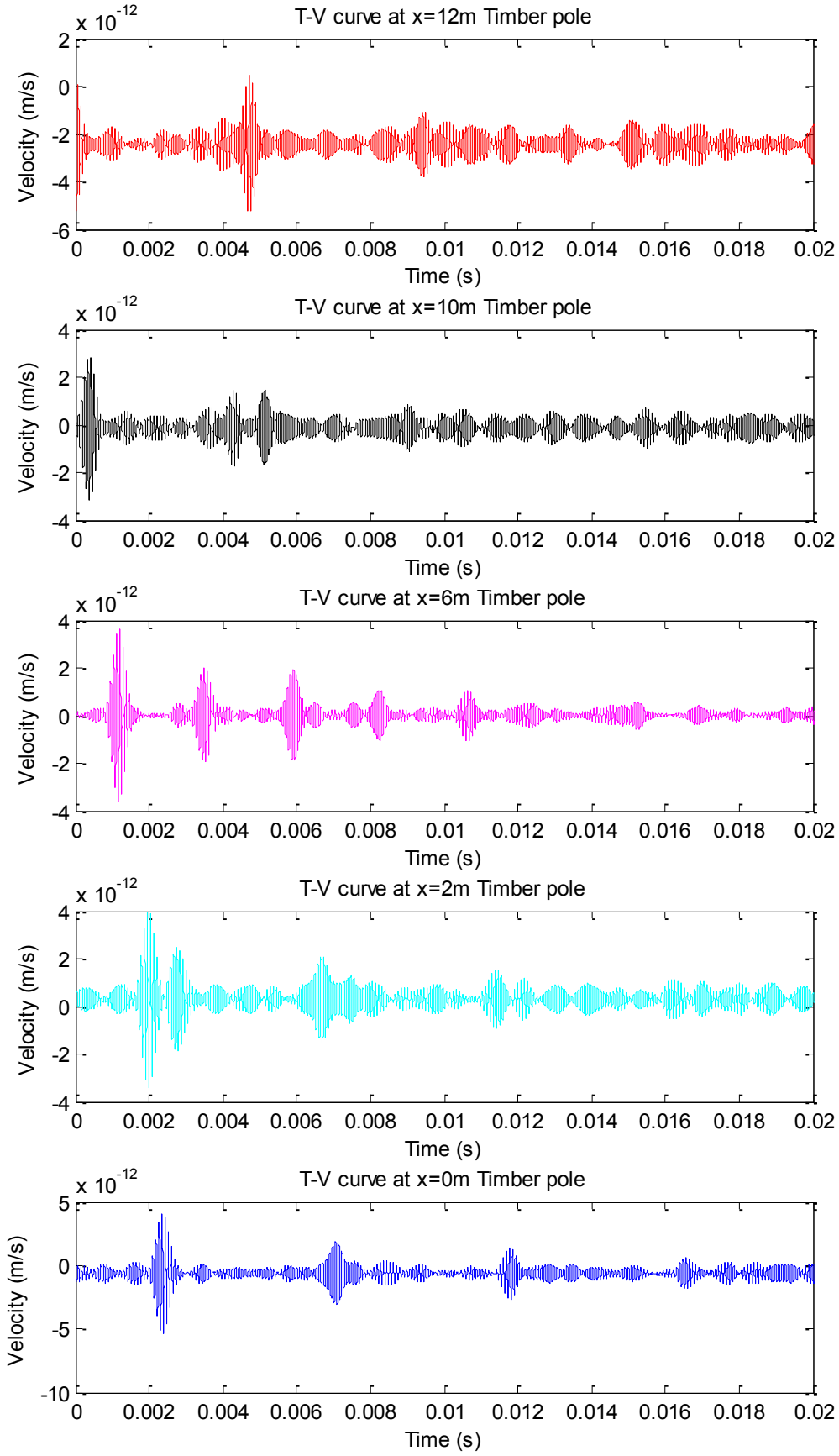

Figure 4.23 Time domain results of anisotropic cylinder with impact at top (vertically) considering the timber pole situation

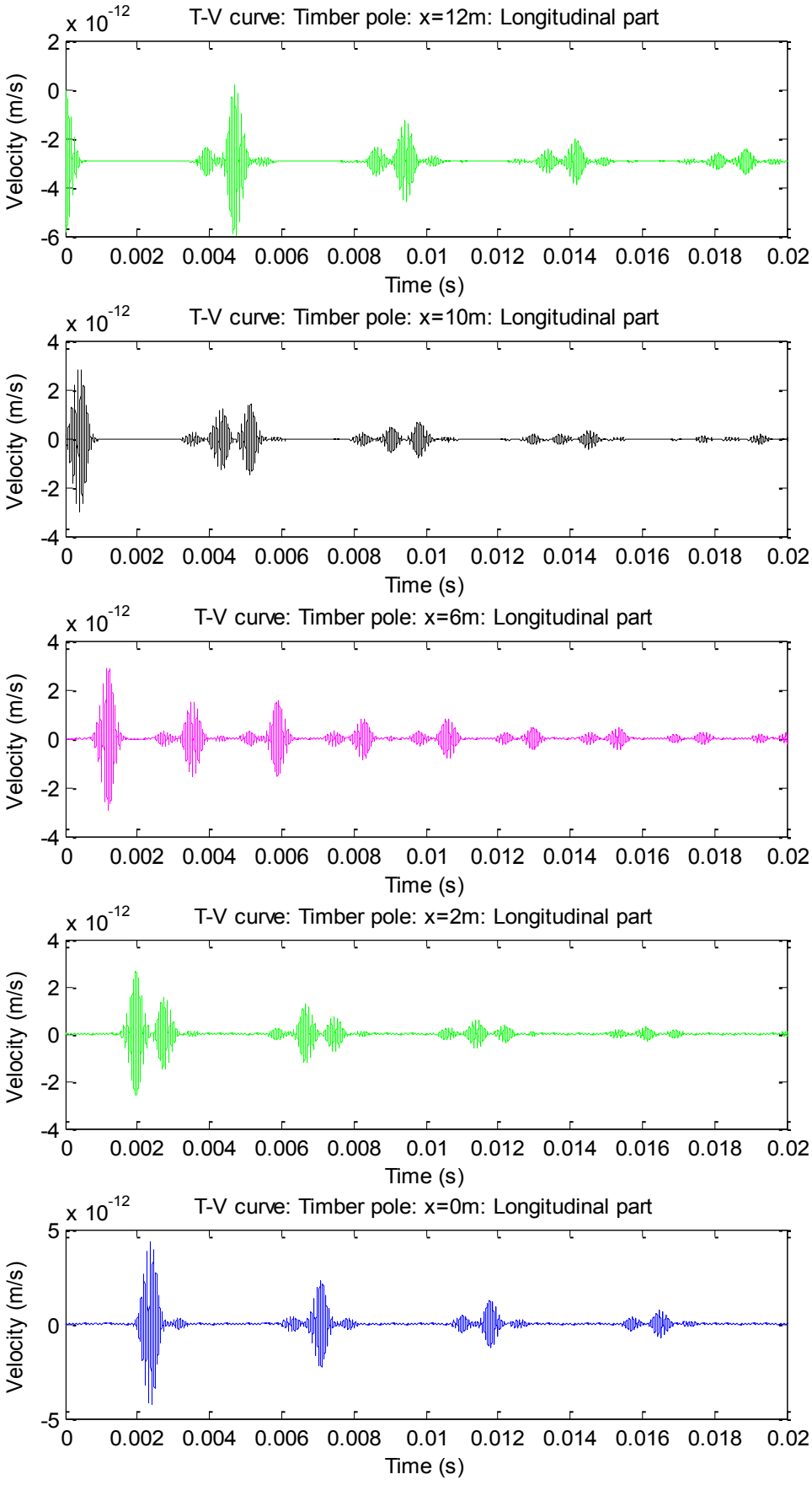

Figure 4.24 Contribution of longitudinal modes in an anisotropic cylinder with impact at top (vertically) considering timber pole situation

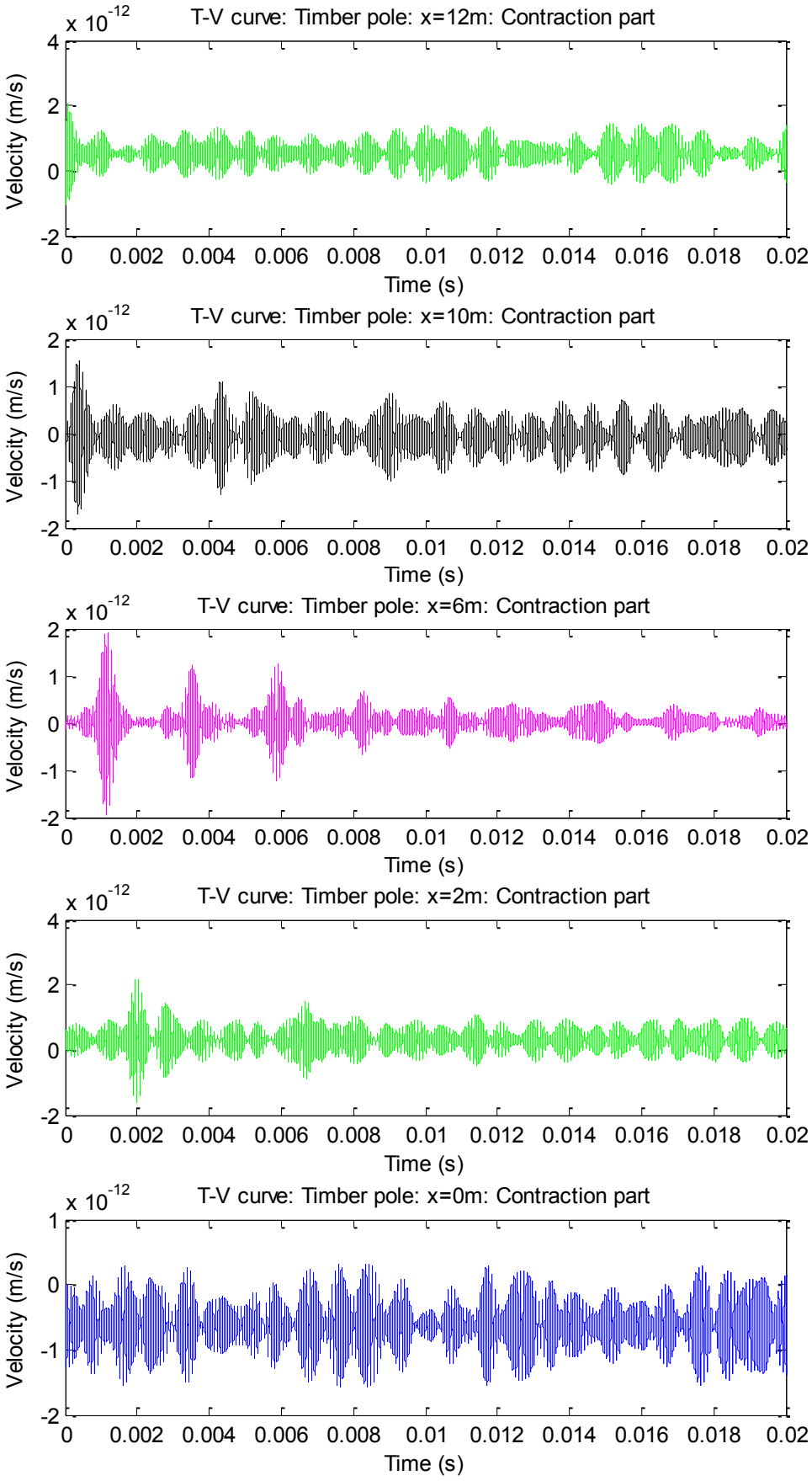

Figure 4.25 Contribution of contraction modes in an anisotropic cylinder with impact at top (vertically) considering timber pole situation

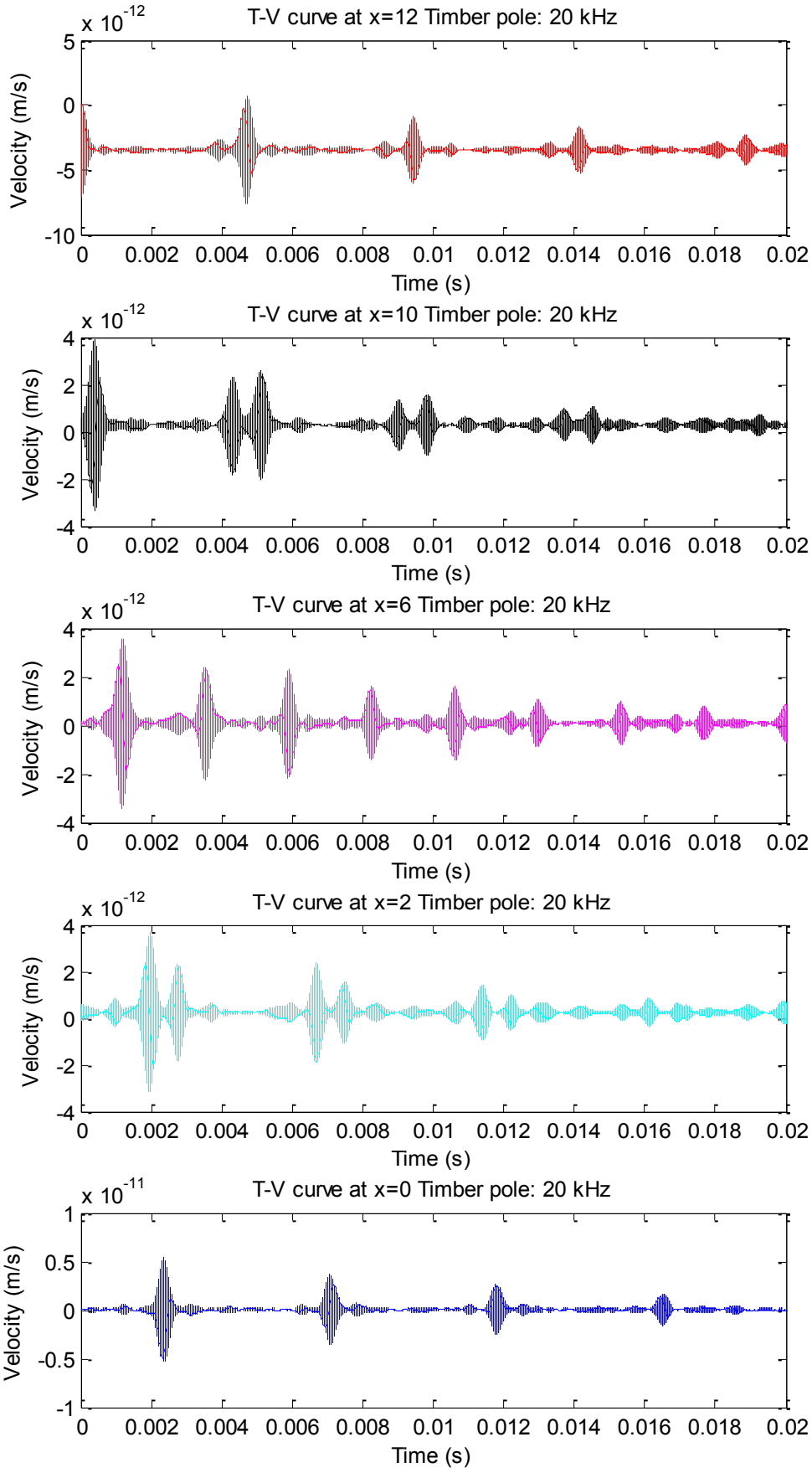

Figure 4.26 Time domain results of anisotropic cylinder with impact at top (vertically) considering the timber pole situation (input frequency 20 kHz)

4.4.3.2 Impact at top (horizontally)

In the next investigation, the impact is imparted horizontally on top of the cylinder/pole with an input frequency of 12 kHz as the cental frequency. First, the timber is considered to stand on the soil. Figure 4.27 (a) presents the time domain results at different locations. The contributions of the flexural and shear modes are displayed separately in Figure 4.27 (b) and (c). Since the impact is imparted horizontally, the longitudinal and contraction modes are absent. This is the reason why the individual contributions of these modes are not presented in the figure.

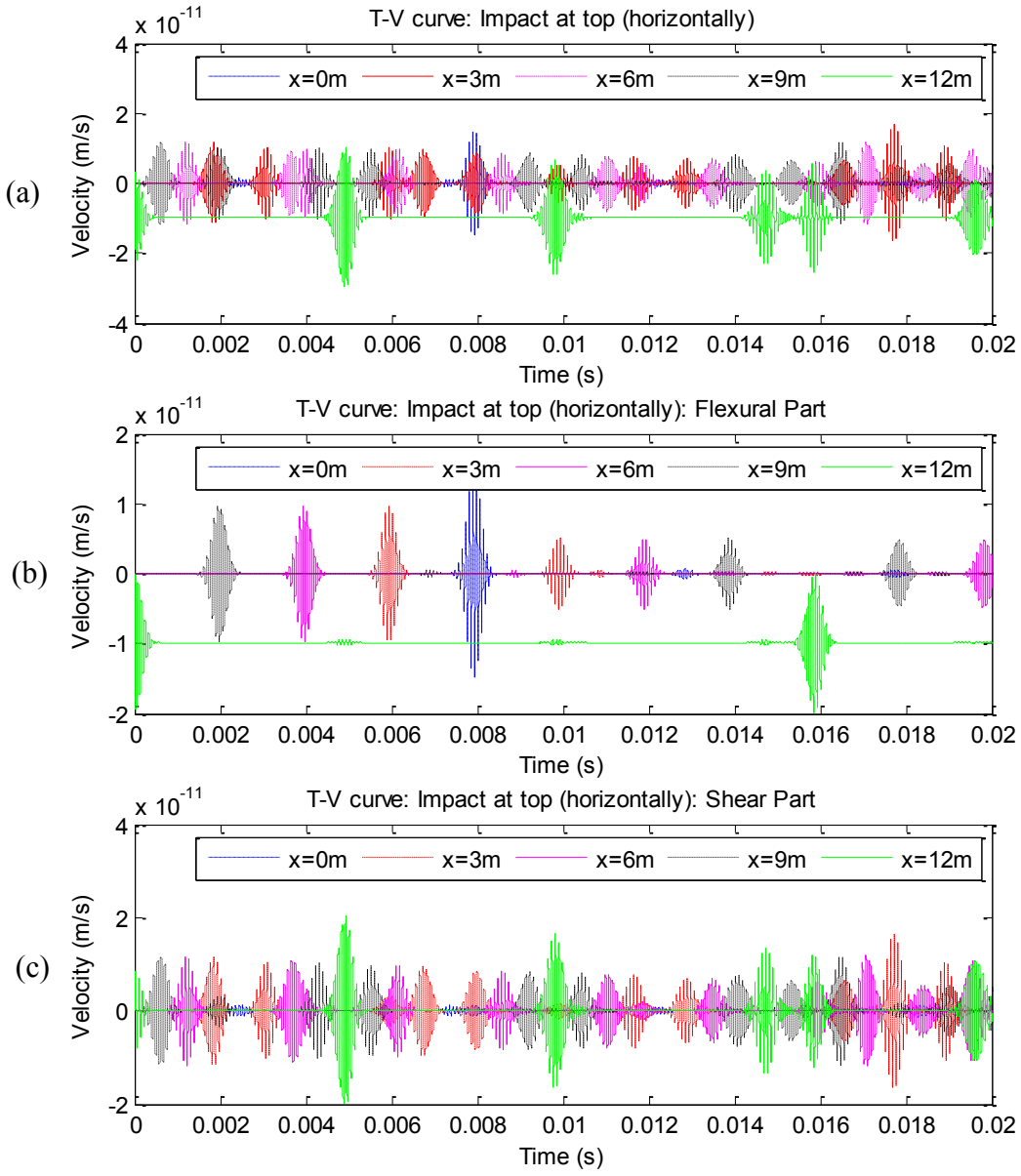

Figure 4.27 Time domain results and contribution of different modes of anisotropic cylinder with horizontal impact at top considering the pole on the soil

As the difference between the shear and flexural wave velocities is significantly large (5,000 m/s and 1,600 m/s, respectively), the reflection time related to these modes has a very large time lag. By analysing the individual contributions of the flexural and shear modes, it can be seen that the reflected flexural mode reaches the sensors very late. For instance, by comparing plots (a) and (c) of Figure 4.27, the peaks at 0.005 sec, 0.01 sec and 0.015 sec (x =12 m) are actually related to the shear mode. Similarly, the reflected flexural mode can be observed at 0.016 sec by comparing plots (a) and (b) of Figure 4.27. Since the shear mode velocity is almost three times higher than the flexural mode velocity, the three reflections of the shear mode are received before the first reflection of the flexural mode.

With the same impact frequency as with the 'standing on the soil' situation, the time domain results for the timber pole situation (partially embedded) are presented in Figure 4.28. The locations of the sensors are also shown in the figure. Similar to the isotropic case, the presence of soil greatly affects the flexural wave propagation. It can also be observed from the figure that there are a number of peaks in the final time-velocity curve and also more dispersion. From the group velocity curves, it can be seen that the shear wave velocity has a slope for an input frequency of 12 kHz which possibly causes the dispersion effect. The individual contributions of the shear and flexural modes are presented in Appendix D. Again, to minimize the dispersion effect, a different input frequency (20 kHz) is chosen as input.

As such, Figure 4.29 illustrates the time domain results for an input frequency of 20 kHz. From the figure, it can be seen that not much improvement is achieved by changing the frequency. This highlights the complex wave behaviour related to the flexural wave propagation in the anisotropic media. To determine which peaks are related to the flexural and shear waves, the individual contributions of the two modes are depicted in Figure 4.30 and Figure 4.31, respectively. From Figure 4.30, it is observed that the flexural mode suffers greatly from attenuation. The first arrival peaks at different locations have a large amplitude; however, after the wave reflection, the amplitudes decrease by a great extent. In addition, similar to the isotropic case, mode conversion occurs during the flexural wave propagation. For example, the flexural mode converts on reflection to one flexural and one shear mode. The converted shear mode reaches the

x = 12 m location at 0.013 sec while the flexural mode reaches the same point at 0.016 sec.

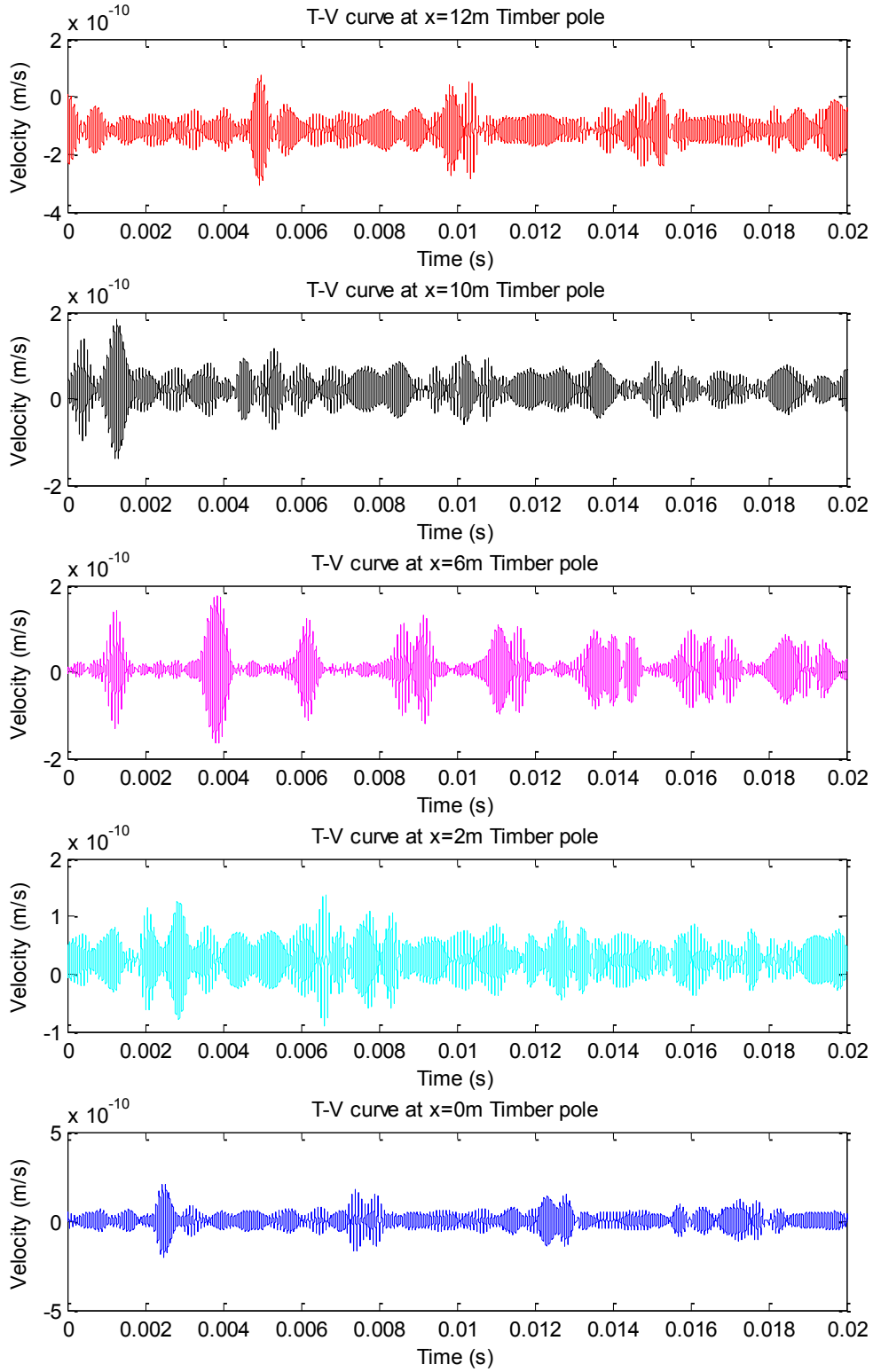

Figure 4.28 Time domain results of anisotropic cylinder with horizontal impact at top considering timber pole situation (Input frequency 12 kHz)

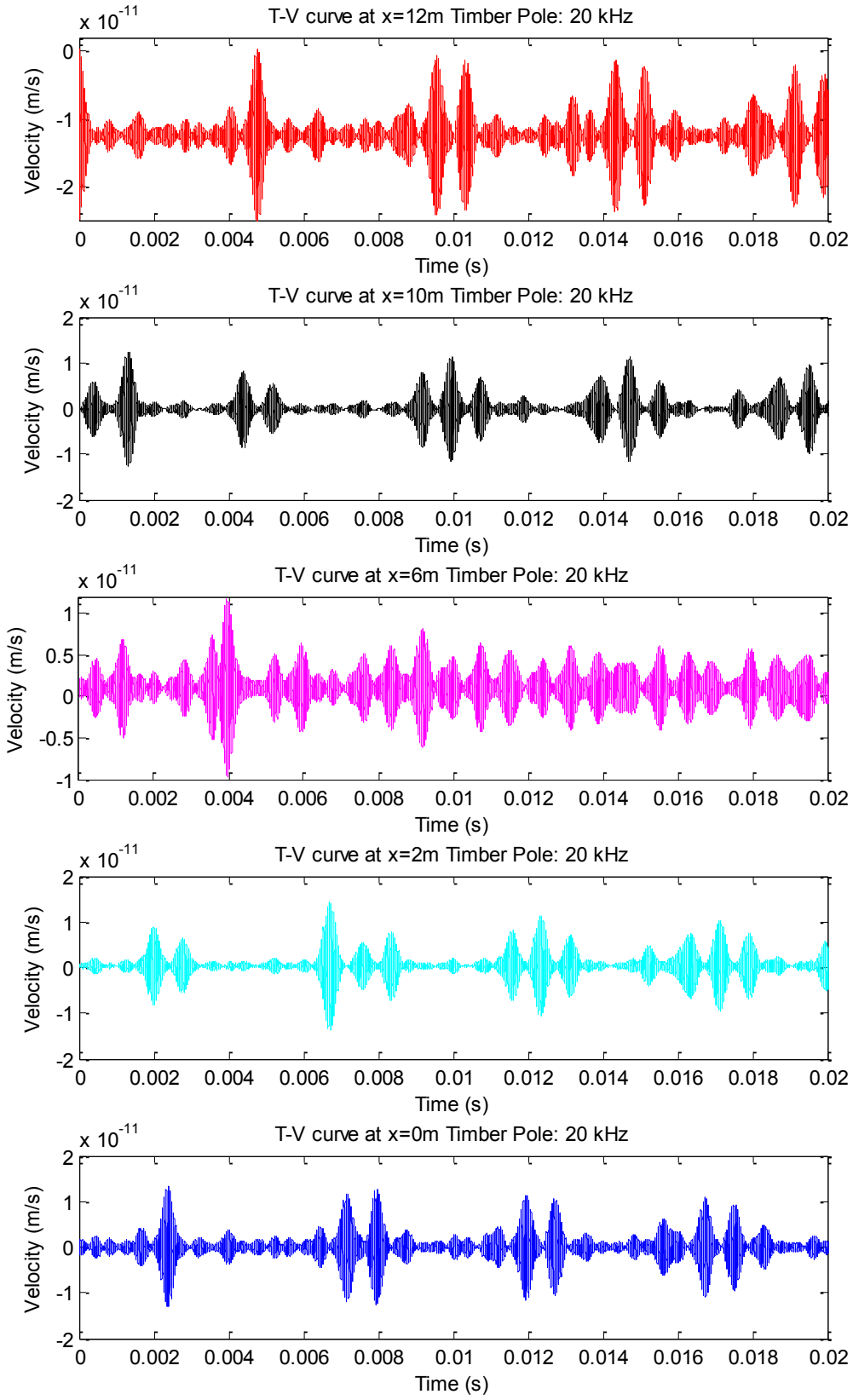

Figure 4.29 Time domain results of anisotropic cylinder with horizontal impact at top considering timber pole situation (Input frequency 20 kHz)

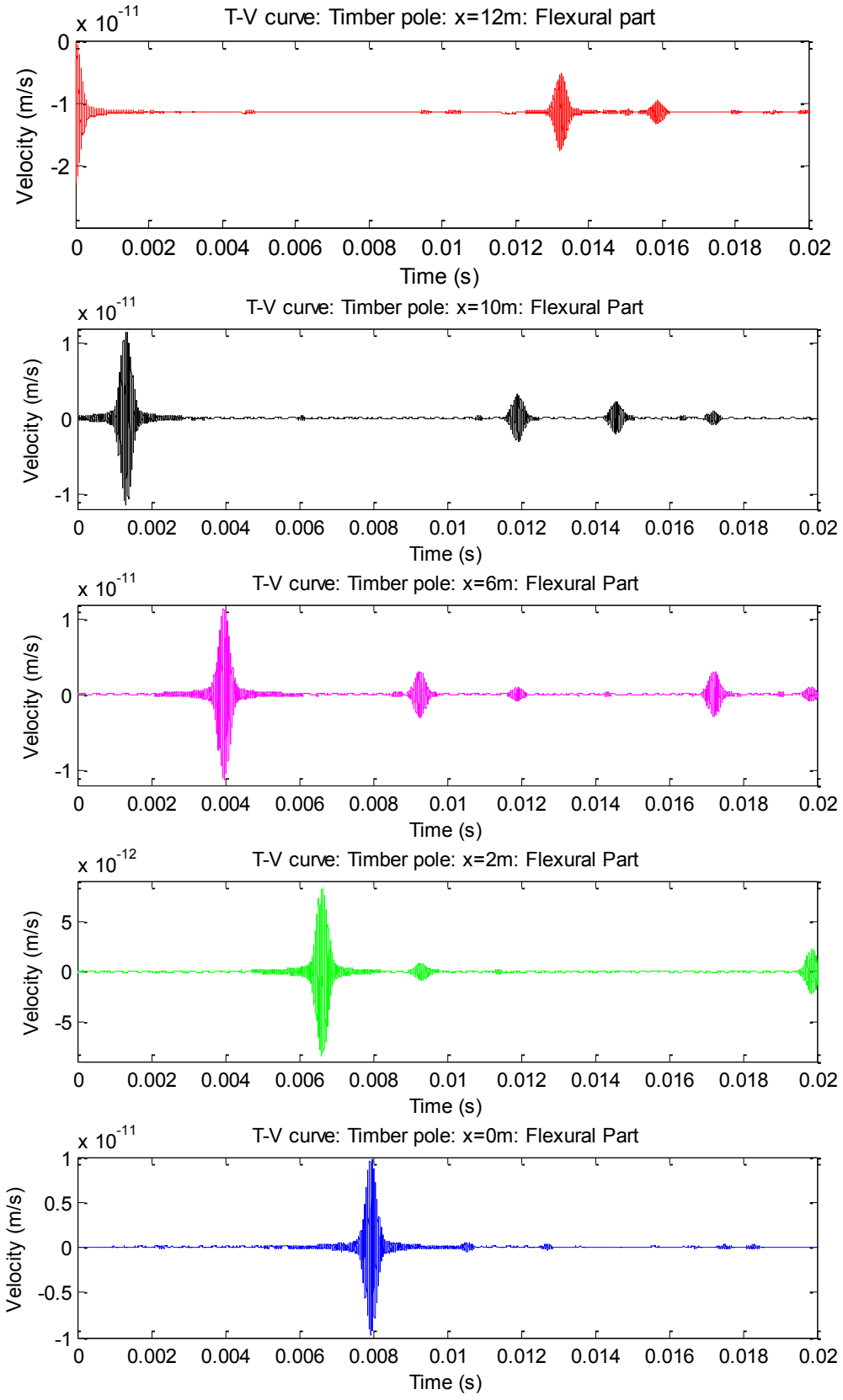

Figure 4.30 Contribution of flexural mode in an anisotropic cylinder with impact at top (horizontally) considering timber pole situation

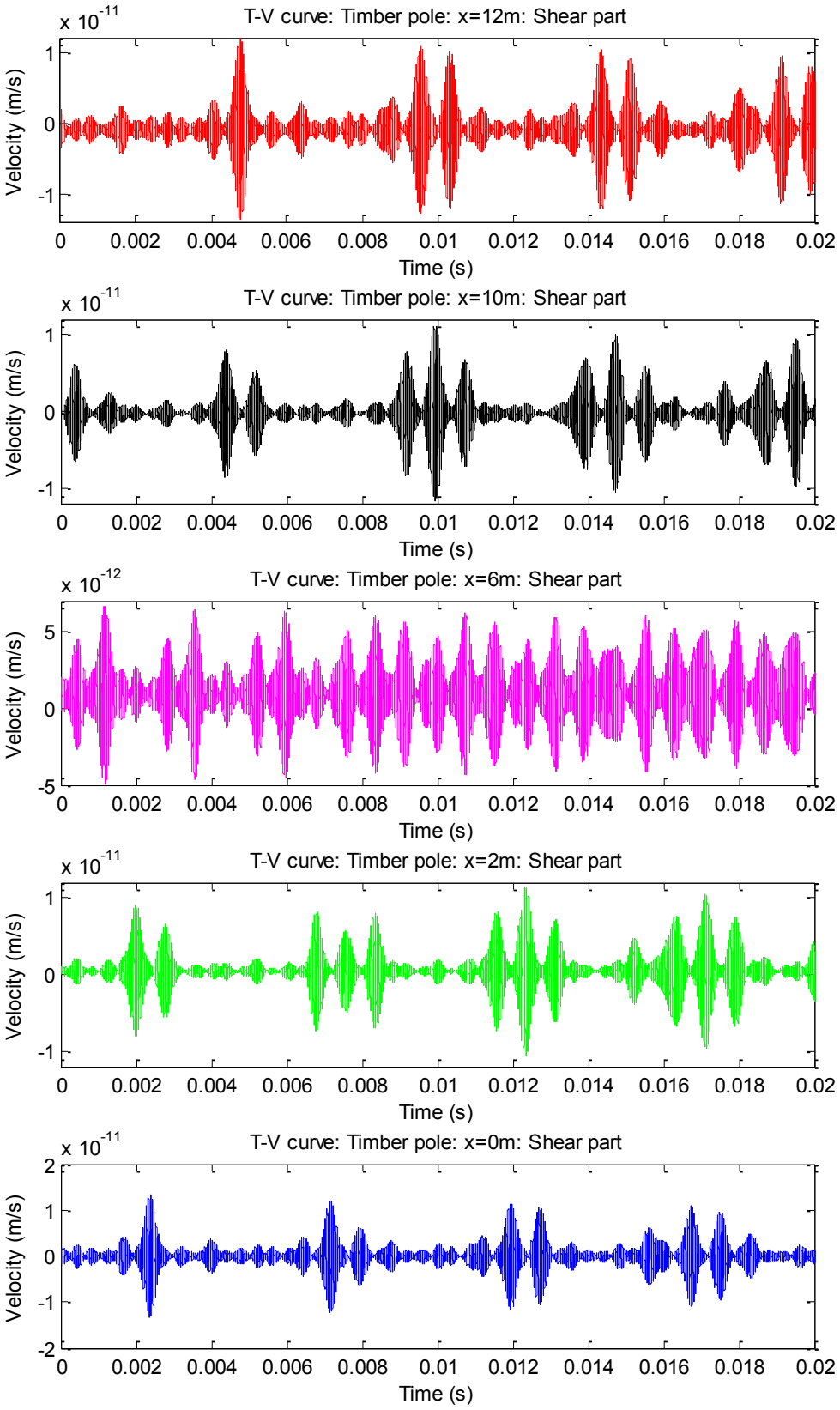

Figure 4.31 Contribution of shear mode in an anisotropic cylinder with impact at top (horizontally) considering timber pole situation

Again, the shear mode is mainly responsible for the dispersion as it can be seen from Figure 4.31. Here, the shear mode is also affected by the wrap around problem as the wave related to this mode does not die down within the chosen window, and hence, starts to appear in the beginning of the window. The peaks in between the large peaks are possibly the peaks related to this problem. This shows that the shear wave has very small attenuation and hence contaminated the final signal results.

4.4.3.3 Impact at top (inclined load)

In this investigation, the load is imparted on top of the pole with an inclined direction. In real testing situations, this is typically performed using a waveguide which is attached to the pole. The impact is then imparted directly on the waveguide. Using this method, the Rayleigh wave can be avoided and hence clearer signals can be obtained close to the impact location. In the SFEM, the loading of the inclined force is divided into horizontal and vertical components and applied simultaneously on the structure. Thereby, all four modes are being generated.

For the timber pole situation, the obtained results are presented in Figure 4.32. Here, the two components of the impact force are applied on the top with an input frequency of 20 kHz. Due to the presence of the four modes, more peaks are observed in the signal. The contributions of the longitudinal, flexural, contraction and shear modes are presented in Figure 4.33, Figure 4.34, Figure 4.35 and Figure 4.36, respectively. In Figure 4.33, it can be seen that the longitudinal mode is propagating with a group velocity of 5,000 m/s which does not match with the group velocity curve. As mentioned earlier, this phenomenon is also observed in the previous investigations. The arrivals and the reflections of the waves are very clear in the longitudinal modes. The propagation of the flexural mode shows the same behaviour as for the horizontal impact situation (Figure 4.34). That is, it has the slowest velocity among these four modes and mode conversion can be observed on wave reflection. Further, the flexural mode is converted to both shear and flexural waves.

Both the shear and contraction modes are suffering from the wrap around problem. That is why the signals towards the end of the plot start to appear and distort the signal. However, owing to the presence of damping, the amplitudes decrease.

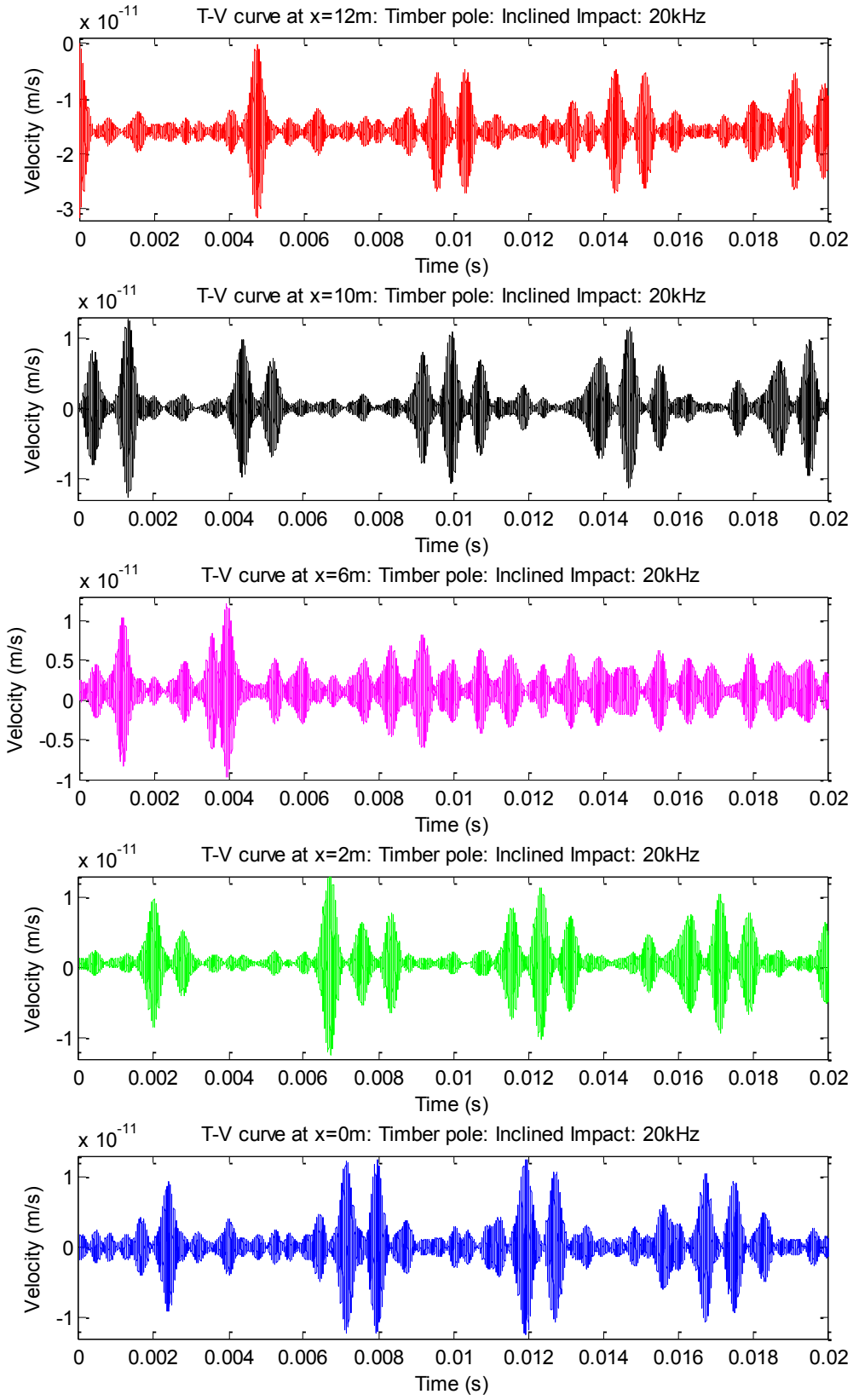

Figure 4.32 Time domain results of anisotropic cylinder with inclined impact at top considering timber pole situation (Input frequency 20 kHz)

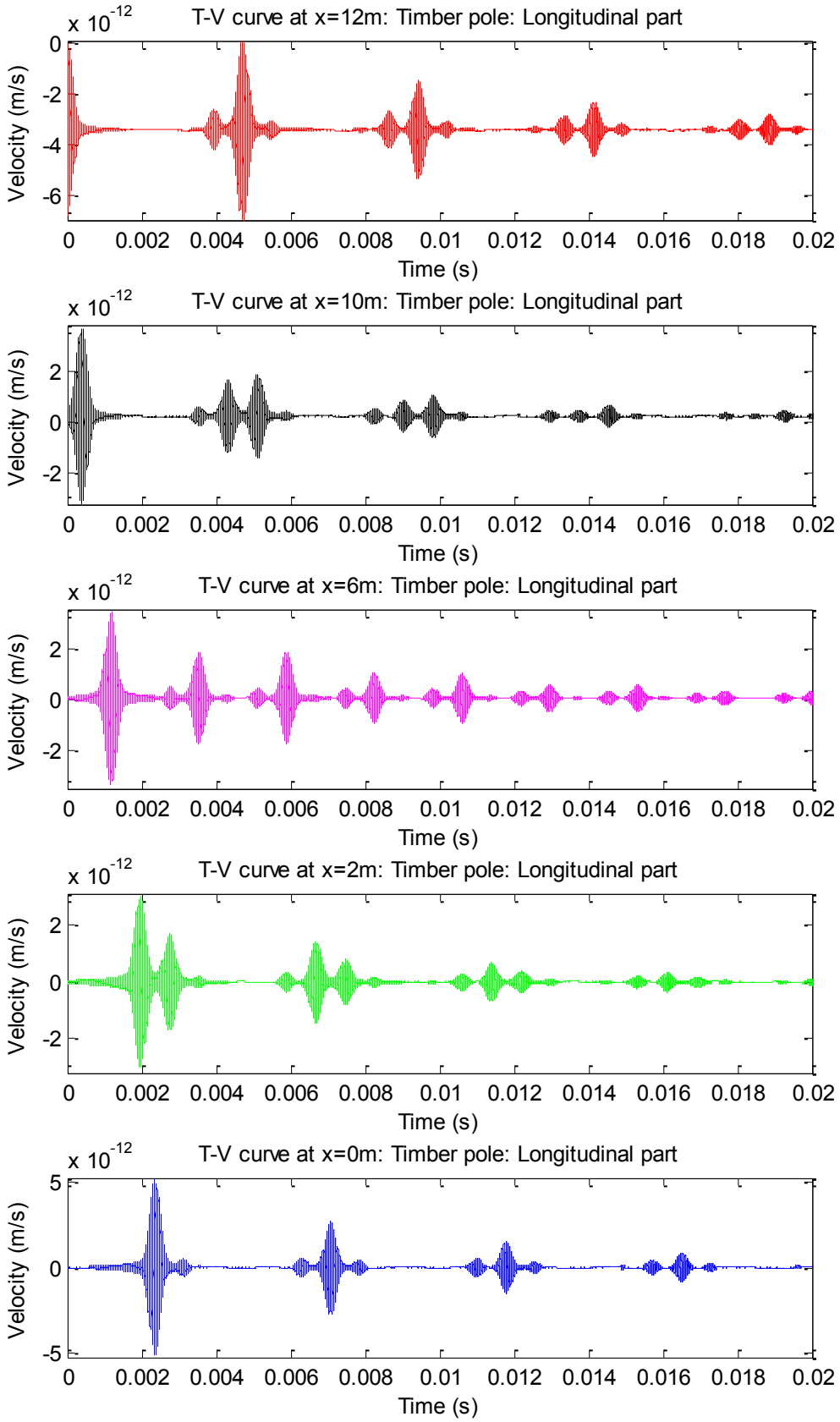

Figure 4.33 Contribution of longitudinal mode in an anisotropic cylinder with inclined impact at top considering timber pole situation (input frequency 20 kHz)

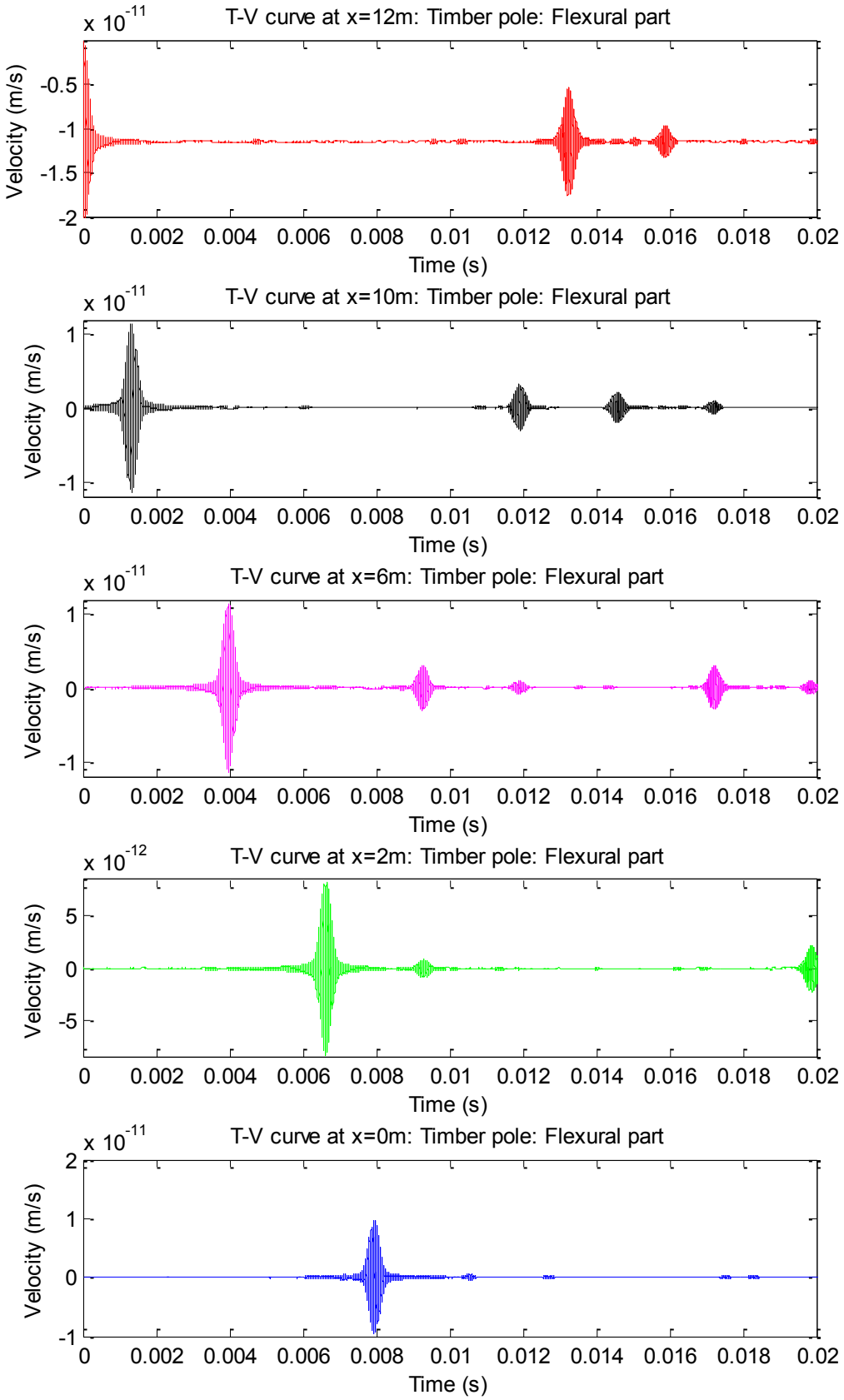

Figure 4.34 Contribution of flexural mode in an anisotropic cylinder with inclined impact at top considering timber pole situation (input frequency 20 kHz)

Consequently, only the peaks with the higher amplitude need to be considered. Nonetheless, as the time increases, it becomes harder to differentiate between the real peaks and the peaks due to the wrap around problem. From the time difference between the arrival peaks at different locations, the velocity of the contraction mode is determined to be 5,000 m/s. This matches precisely with the group velocity curve, although it is hard to say whether any mode conversion occurs or not due to the same signal processing problem. For the contraction mode propagation, the signal at x = 0 m is the most complex among all the signals from different locations.

The shear mode velocity is also calculated from the arrival peaks at different locations and the velocity is in good agreement with the group velocity curve. Further, mode conversion occurs for the shear wave, with the shear mode being converted to the flexural and the shear mode. For the shear mode, the middle location of the pole (x = 6 m) gives the most complex results when compared to other locations.

4.4.3.4 Impact at the middle of the pole

Under field conditions, the most practical application is to impart the load in the middle section of the pole since the timber poles are usually 10 to 13 m long. Accordingly, the impact is usually imparted at 1.5 m from the ground level. If the impact is applied in the middle section of the pole, then two propagating waves will be generated; one will propagate in the upward direction and the other one in the downward direction. For the upward-going wave, the investigated locations are at x = 4 m, 6 m, 10 m and 12 m while the impact is applied at x = 3.5 m. In addition, for the downward travelling wave, the signals are captured at x = 3 m, 2 m, 1 m and at the bottom of the pole. Similar to the previous conditions, the soil level modelled at x = 2 m. The input frequency is 20 kHz.

For the mid-section impact condition, only the timber pole situation is investigated. The impact orientation is considered as vertical, horizontal and inclined. While the results related to the vertical and horizontal cases are presented in Appendix D, the inclined impact results are presented and discussed in this chapter. In the SFEM, the modelled timber pole is divided into three elements (four nodes), for the impact in the middle section situation. The four nodes are situated at the top and bottom of the pole, at the soil level and at the impact location.

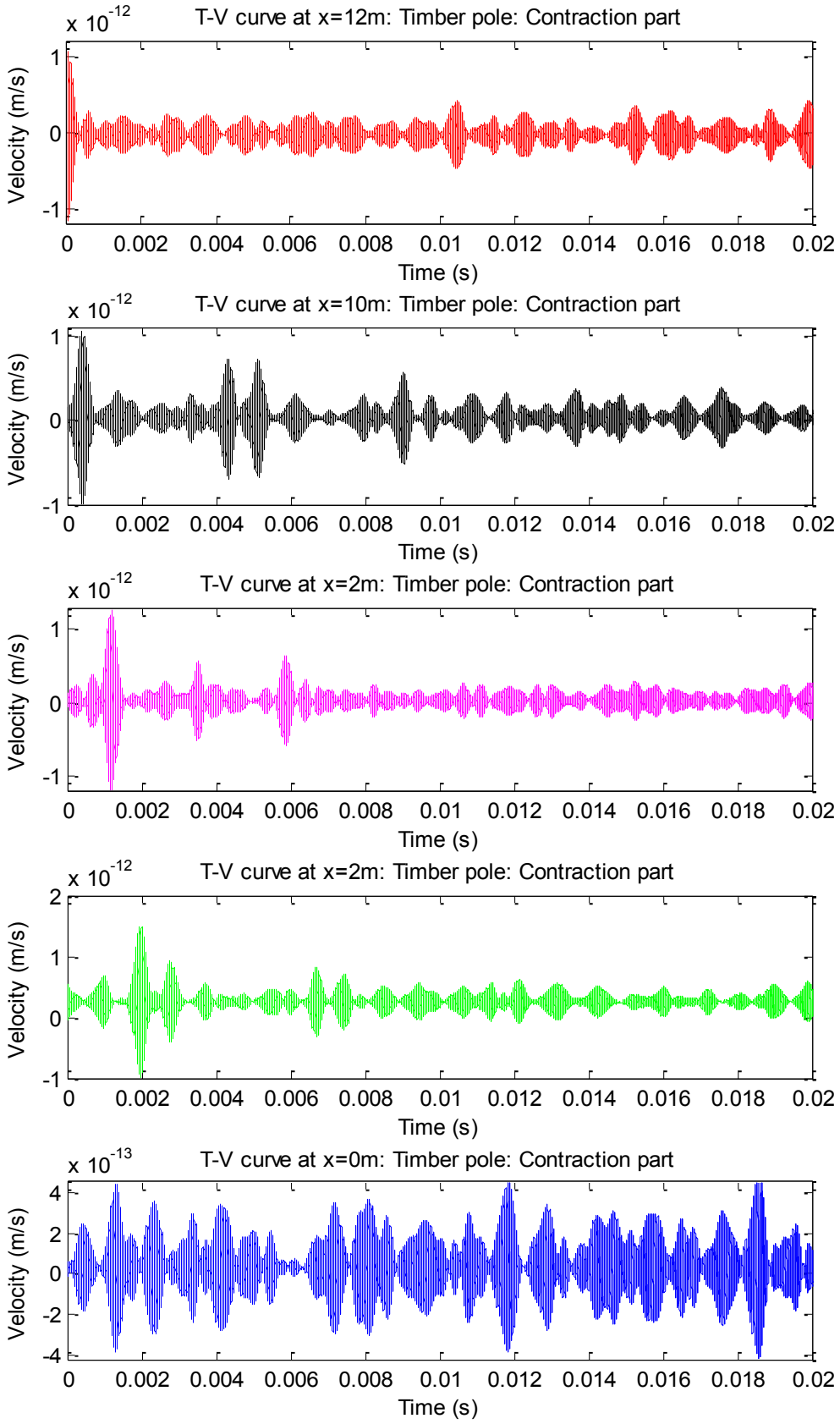

Figure 4.35 Contribution of contraction mode in an anisotropic cylinder with inclined impact at top considering timber pole situation (input frequency 20 kHz)

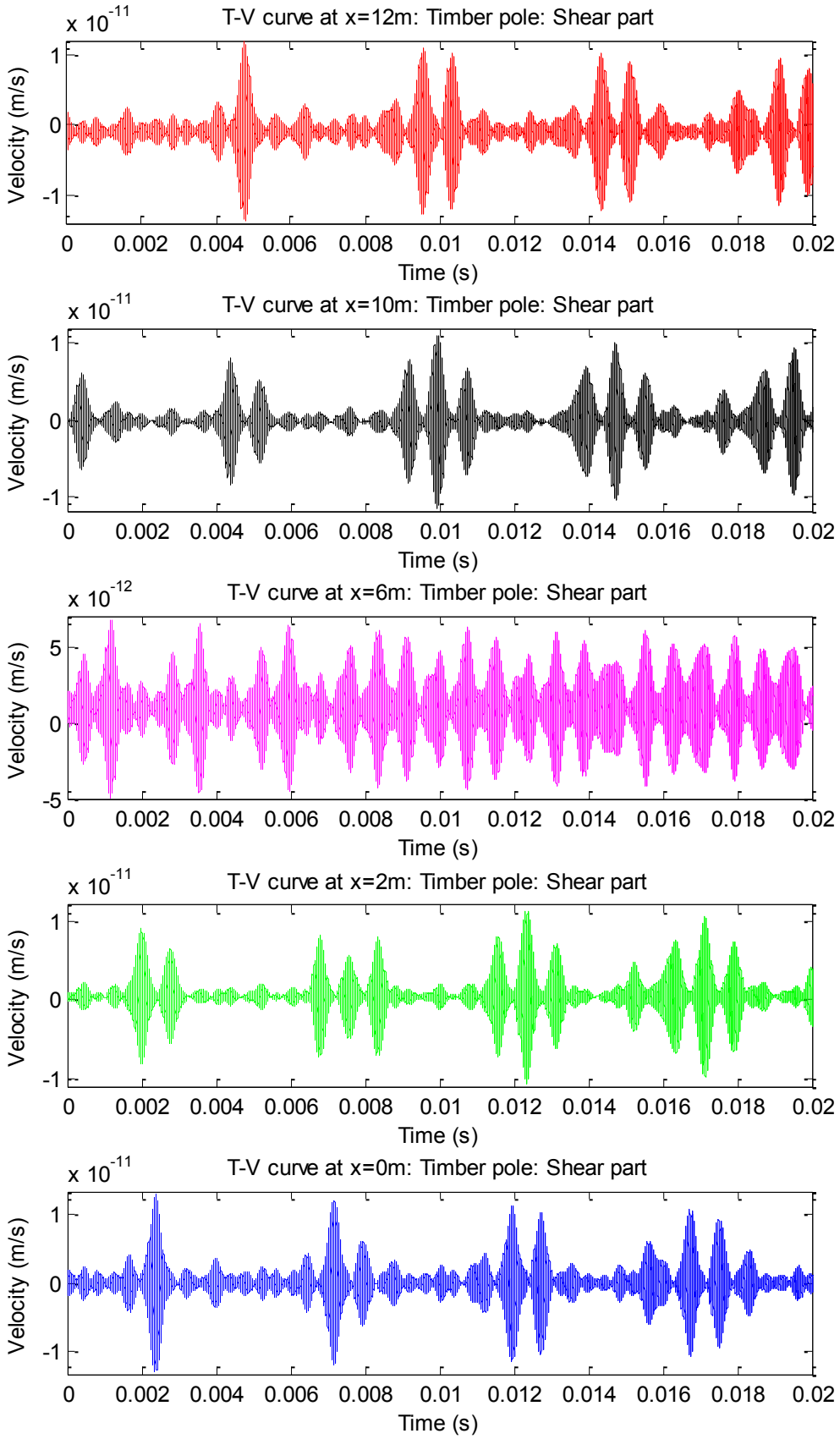

Figure 4.36 Contribution of shear mode in an anisotropic cylinder with inclined impact at top considering timber pole situation (input frequency 20 kHz)

Figure 4.37 displays the time domain results for the downward-going wave, whereas Figure 4.38 presents the results for the upward travelling wave. As previously mentioned, all four modes are generated in the situation where the impact is imparted in the inclined direction. Here, both the vertical and horizontal components are present and act as longitudinal and transverse impact. Due to the multi-mode propagation, more peaks are present. The larger number of peaks is, however, due to the multiple reflections of the upward and downward travelling waves. It can further be seen that the peaks have different amplitudes which illustrates that different modes contain different amounts of energy. Consequently, the individual contributions of the longitudinal, flexural, contraction and shear modes are studied. For this study, only five locations are chosen for comparison with two locations being above the impact location (x = 10 m and 12 m), two locations being below the impact location (x = 2 m and 0 m) and one location being at the impact location itself (x = 3.5 m).

Figure 4.39 depicts the propagation of the longitudinal mode and Figure 4.40 shows the flexural mode propagation. The impact location is situated in the middle section. The propagation of these two modes is very clear and the signal is clean as can be seen in the figures. For both cases, one wave starts propagating upwards and one wave propagates downwards. The downward wave reflects from the bottom of the pole and reaches the top just after the first arrival of the up-going wave at the same location. Both waves then reflect from the top. Again, the velocity of the longitudinal mode is calculated to be 5,000 m/s and the flexural mode has a group velocity of 1,600 m/s.

Figure 4.41 and Figure 4.42 show the individual contributions of the contraction and shear modes, respectively. Unlike the longitudinal and flexural cases, the time domain results are not very clear for the contraction and shear modes. Nevertheless, the wrap around problem of the shear and contraction modes is reduced by adding dashpots in these two directions. The boundary conditions for the dashpot can be found in Table 4.1 and by substituting the boundary conditions in Equation (4.54). From Figure 4.41, it can be noted that the contraction mode is the most dispersive mode as no clear trend can be observed. Nonetheless, the final signal is not affected even though the attenuation is also high in the contraction mode. It is further observed that the amplitude reduces in the down-going contraction mode, especially when the wave reaches the soil level.

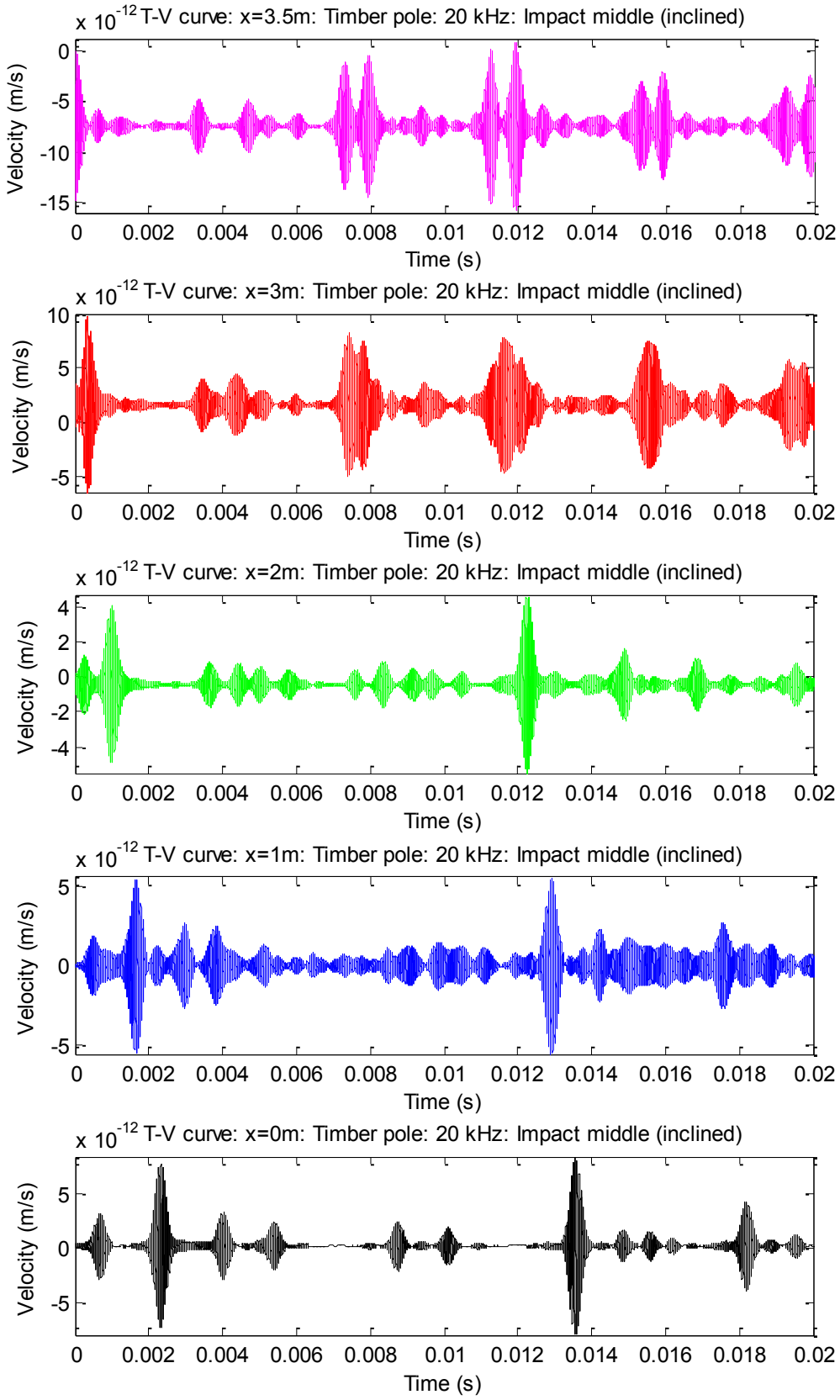

Figure 4.37 Time domain results of anisotropic cylinder with inclined impact at the middle considering timber pole situation (down going wave)

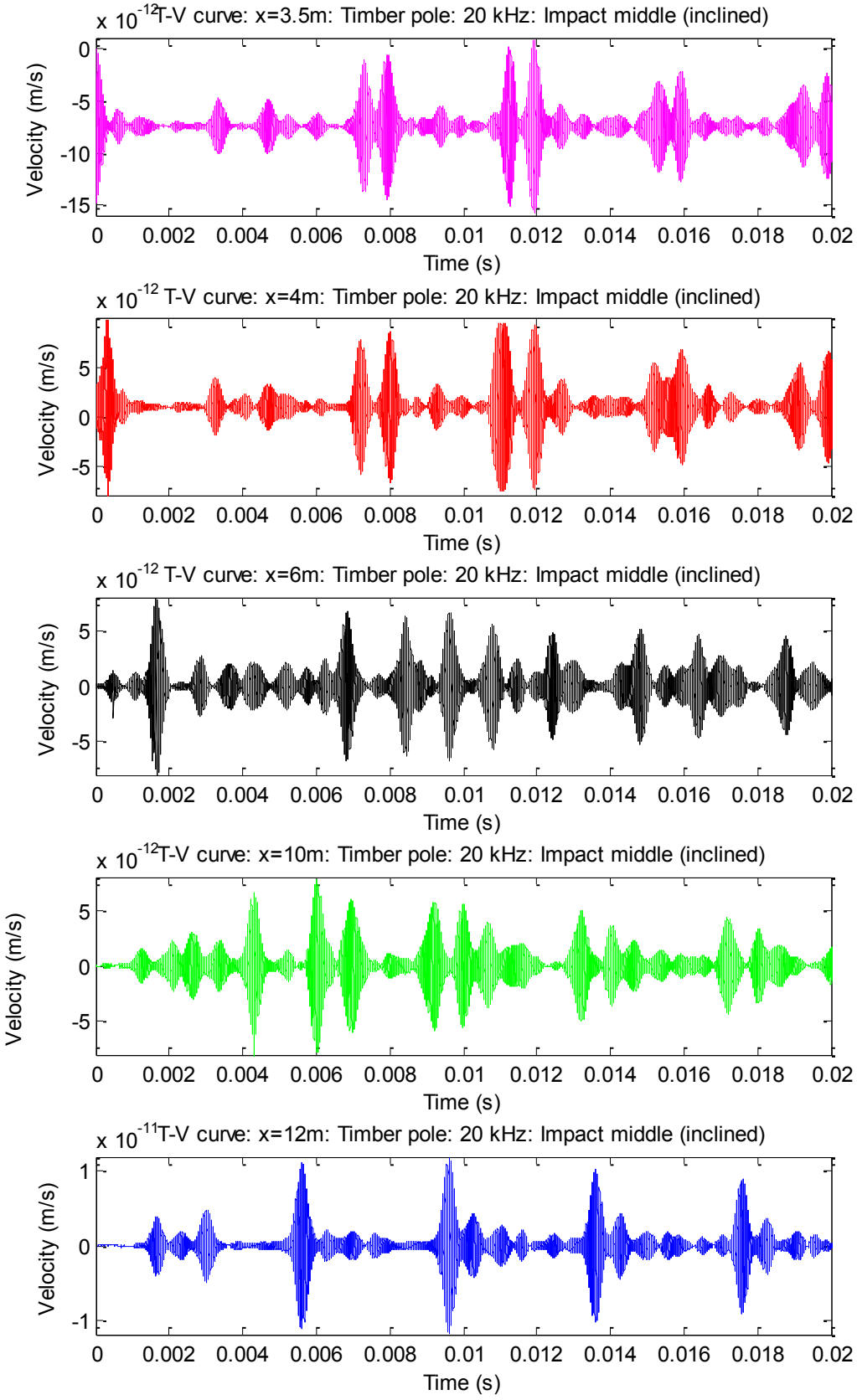

Figure 4.38 Time domain results of anisotropic cylinder with inclined impact at the middle considering timber pole situation (up going wave)

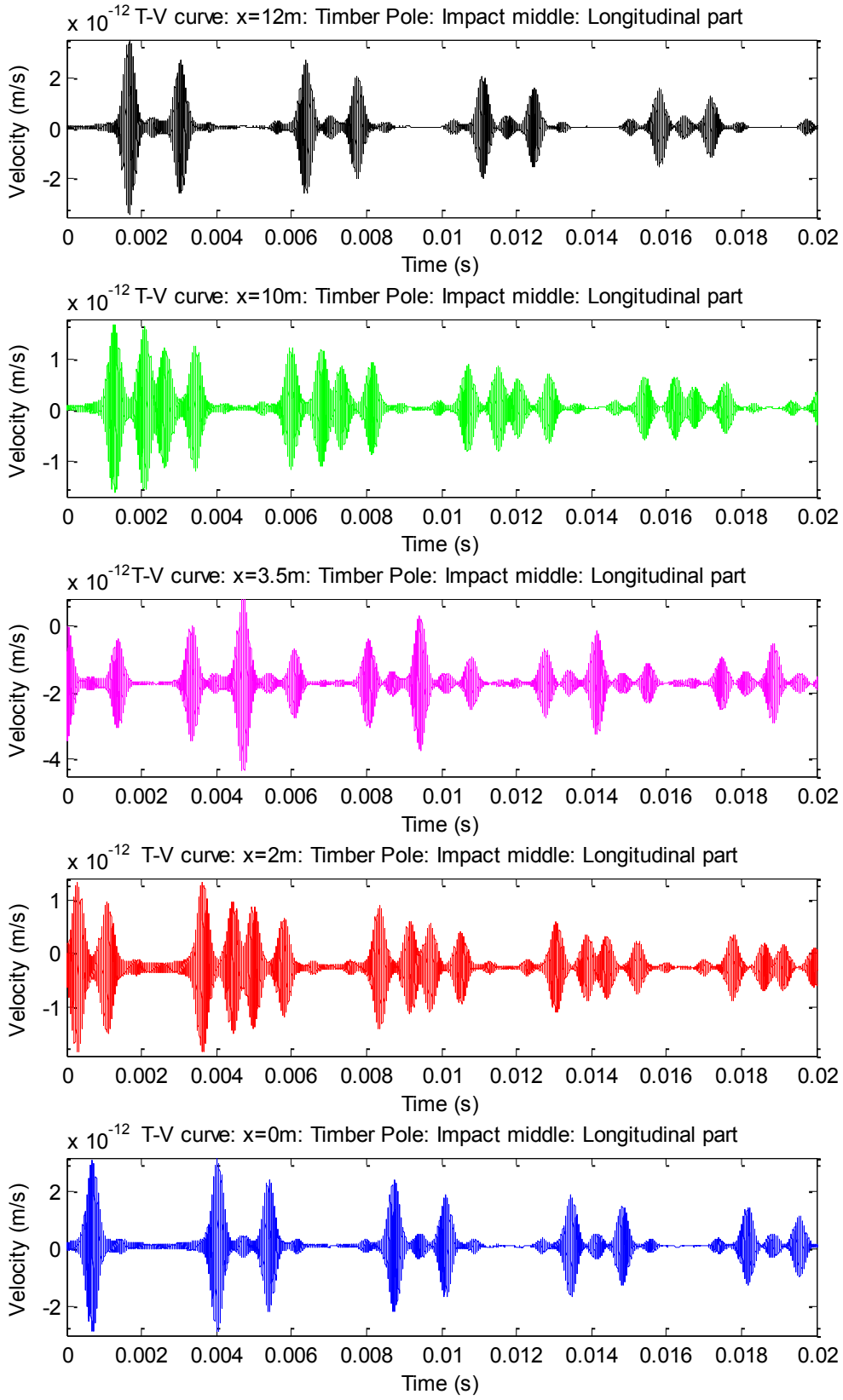

Figure 4.39 Contribution of longitudinal mode in an anisotropic cylinder with inclined impact at the middle considering timber pole situation

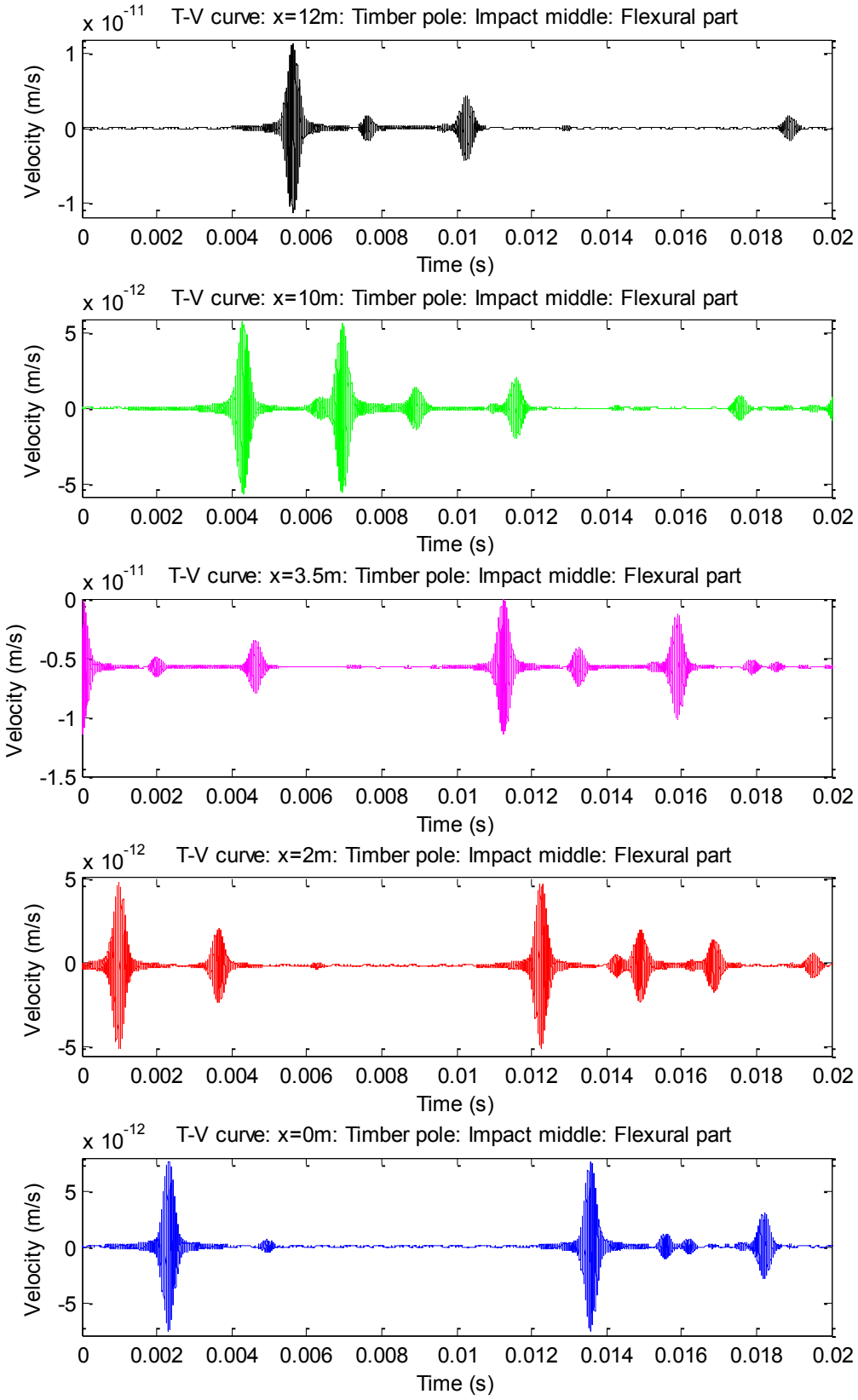

Figure 4.40 Contribution of flexural mode in an anisotropic cylinder with inclined impact at the middle considering timber pole situation

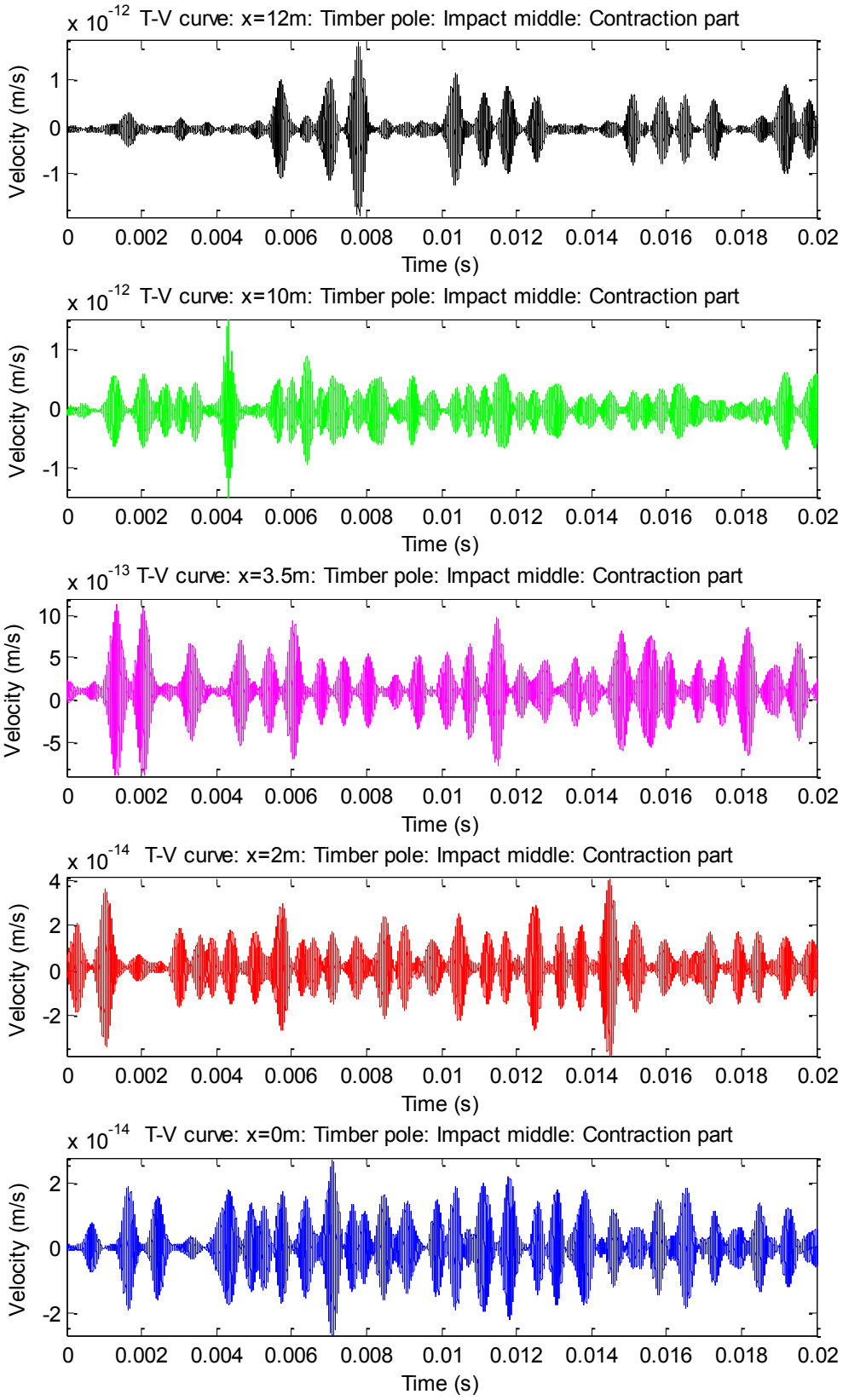

Figure 4.41 Contribution of contraction mode in an anisotropic cylinder with inclined impact at the middle considering timber pole situation

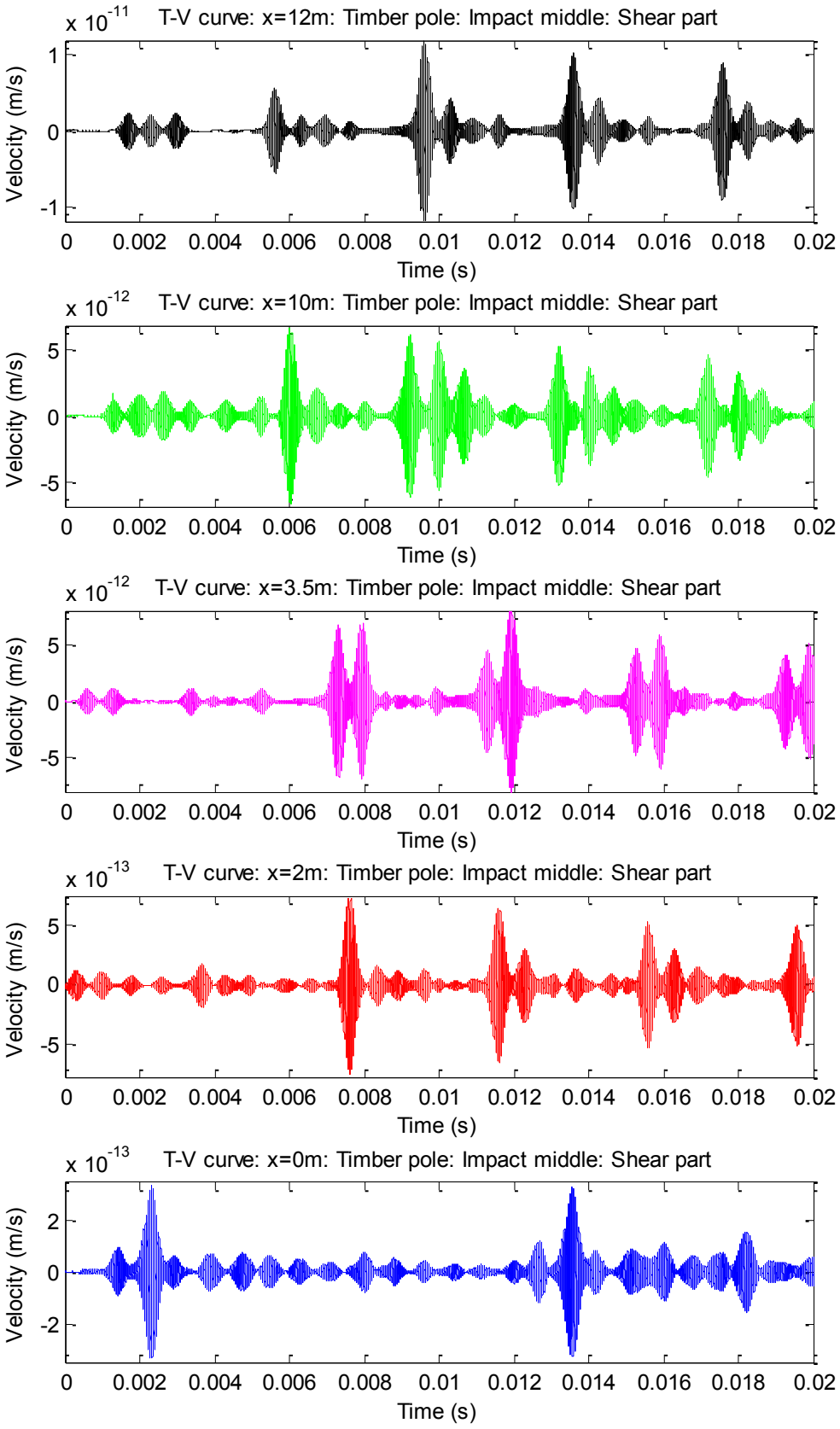

Figure 4.42 Contribution of shear mode in an anisotropic cylinder with inclined impact at the middle considering timber pole situation

It is further observed that the shear mode propagation is not as clear as the longitudinal or flexural wave propagation; nonetheless it is better than the contraction mode. In the beginning, the shear mode starts to propagate with very small amplitude which means that the shear wave contains very low energy. However, it can be observed from the figure that higher amplitude peaks occur at a later time. This is possibly due to the mode conversion since it was previously observed that the shear mode converted to one shear and one flexural mode upon reflection.

From the investigation above, it can be seen that due to the presence of soil and when the impact is imparted in the middle section of the pole, the signal becomes much more complicated and it is not possible to analyse the signal by simple observation. Thus, advanced signal processing techniques are essential to solve these issues, which are presented in the next chapter.

4.5 Conclusions

This chapter presented different analytical theories of the Spectral Finite Element method. Both isotropic and anisotropic material modellings were discussed. Based on the spectrum relation of different theories, it was found that the closest theories for the timber pole situation were the three mode theory (for isotropic rod modelling) and the Timoshenko beam theory (for the isotropic beam modelling) and the Timoshenko theory (for the anisotropic medium modelling). Based on this finding, these theories were chosen for the corresponding investigations and were used for the time domain reconstruction.

Even though the SFEM is very accurate for one-dimensional structures, the modelling of the spectrum relation has some limitations. For example, higher number of modes cannot be solved. As such, the three mode theory can only determine the first three longitudinal modes, whereas the Timoshenko beam theory can only calculate two modes for the isotropic case and four modes for anisotropic materials. However, the SFEM is accurate to a great extent up to a certain frequency limit. SFEM is very effective and after the spectrum relations are obtained, the time domain results can easily be determined. IFFT is usually used to reconstruct the results in the time domain.

In the investigations, numerical issues were also discussed in relation to solving for wavenumber (or dispersion relation), displacement (in the frequency domain) and time

domain reconstruction (using IFFT). Since only a few nodes were needed in the SFEM, the global stiffness matrix could easily be formed. In addition, it was also very easy to apply the necessary boundary conditions. As such, different kinds of boundary conditions could successfully be implemented in the SFEM. For the actual timber pole situation and the pole standing on soil, time domain reconstruction was investigated.

From the studies, it was found that when the pole was considered to be standing on soil, the wave propagation is not complicated. If the group velocities of the different modes are different, then they arrive at different times and the modes can easily be recognised. In contrast, for the timber pole situation, the wave propagation is somewhat more complicated. While the longitudinal wave is not influenced much by the presence of soil, mode conversion was observed in the flexural wave propagation.

For the anisotropic modelling of the timber pole, it was observed that if the impact was imparted vertically, only the longitudinal and contraction modes propagated, while if the impact was applied transversely, only the shear and flexural modes propagated. If the input frequency was above the cut-off frequencies of these modes, then the shear and contraction modes would also propagate. It was also observed that the longitudinal and contraction modes had usually the same group velocity. Further, the contraction mode was more dispersive, and hence, inconclusive in some cases. For the timber pole situation, mode conversion could again be seen for the transverse impact. For the inclined impact, all four modes were present in the signal. The flexural and longitudinal modes were usually very clear, whereas the shear and contraction modes contained a great number of peaks and suffered from wrap around problems. In some cases, the dispersion of the contraction and shear modes could be reduced by changing the input frequency.

For the anisotropic model, the timber pole was also analysed with the impact applied in the middle section of the pole, which is the most practical condition for field testing. In this case, both downward and upward travelling waves are present. Again, for the inclined impact, all the modes were present, with the contraction mode being affected most by the dispersion. The shear mode generally contained less energy, depending on the input frequency. However, when mode conversion happened, i.e. the shear mode converted to the flexural mode and then the amplitudes increased. The attenuation of the contraction mode was also noticed. Generally, for the impact at the middle section

situation, the wrap around problem did not occur. Further, it was observed that due to multi-mode propagation and multiple reflections, it was very difficult to analyse the signals. Hence, it is recommended to use advanced signal processing techniques.

SFEM has also some limitations in the time domain, even though it can easily deal with wave reflections and arbitrary boundary conditions. This limitation is mainly related to the one dimensional simplification. Nevertheless, for one-dimensional structures, the SFEM can give exactly the same results as the conventional FEM. However, the SFEM cannot represent the wave behaviour in the circumferential direction or the displacement profile along the radius of the pole. In addition, the spectrum relations have also some limitations. As discussed in Chapter 3, the longitudinal and flexural waves have different properties along the circumference of the pole; and as such, it can be beneficial to use circumferential properties for the differentiation of these modes. Hence, some analysis using the conventional FEM in conjunction with the appropriate signal processing method can be helpful in some aspects. This is irrespective of the fact that the FEM is time consuming and the spectrum relations cannot be obtained very easily. Therefore, some numerical analysis based on the conventional FEM is presented in Chapter 5.

Chapter 5

5 Study of guided wave propagation using Finite Element Method

5.1 Introduction

In Chapter 4, it was discussed that, different modes can be distinctly recognised in the time domain if dispersion is controlled. However, wave propagation in the anisotropic material with the impact in the middle shows complications. Also, sometimes in the field, impact hammer is used instead of wave packet to apply the impact on the pole. This manual impact usually produces broadband frequency which is in the low frequency range. Additionally, due to the inclined impact orientation, the superposition of the flexural and longitudinal waves also occurs. Because of the following reasons, sometimes it becomes essential to separate the longitudinal and flexural waves if possible. To do so, it is important to model the structure three dimensionally since longitudinal and flexural waves have different behaviour in three orthogonal directions. The conventional finite element is used for the following purpose. As broadband frequency range is considered; hence, continuous wavelet transform is used as a signal processing technique.

In this chapter, the wave behaviour in three dimensional systems is analysed numerically. Different impact locations are chosen for the impact to show the formulation of longitudinal and flexural waves. The displacement components in the axial, radial and tangential directions are taken into account to represent the properties

of the longitudinal and flexural wave propagation. Based on continuous wave transform, a method is proposed to separate the longitudinal and flexural waves. At the end of the chapter, a comparison is made between the short kernel method and continuous wavelet transform method to analyse the flexural wave propagation. Also the embedment length of the pole is determined by these two methods and compared.

5.2 Theories of signal processing techniques

In this study, two signal processing techniques, namely CWT and SKM are used for the analysis of broadband input signal. The reviews of these techniques are given in the following sections.

5.2.1 Continuous Wavelet Transform (CWT)

The definition of the CWT [174] is given by:

$$Wf(\tau,s) = \int_{-\infty}^{+\infty} f(t)\psi_{\tau,s}^{*}(t)dt = \int_{-\infty}^{+\infty} f(t)\frac{1}{\sqrt{s}}\psi^{*}\left(\frac{t-\tau}{s}\right)dt \tag{5.1}$$

where $*$ denotes the complex conjugate and

$$\psi_{(\tau,s)}(t) = \frac{1}{\sqrt{s}}\psi\left(\frac{t-\tau}{s}\right). \tag{5.2}$$

The function $\psi(t)$ is called mother wavelet satisfying the admissibility condition

$$\int_{-\infty}^{+\infty} \frac{\left|\breve{\psi}(\omega)\right|^2}{|\omega|}d\omega < 0 \tag{5.3}$$

where $\breve{\psi}(\omega)$ is the Fourier transform of $\psi(t)$.

To satisfy the admissibility condition, the requirement is

$$\breve{\psi}(\omega) = 0 \; and \int_{-\infty}^{+\infty} \psi(t)dt = 0\,. \tag{5.4}$$

From the equation of CWT it is found that the mother wavelet $\psi(t)$ is translated by the translation parameter τ and dilated by the scaling parameter s when a signal is analyzed. If the central frequency of $\breve{\psi}(\omega)$ is η and the time and frequency spread of $\psi(t)$ are g_t and g_w, respectively, then the time and frequency spread of $\psi_{(\tau,s)}(t)$ are sg_t and g_w/s,

respectively. Therefore, the time can be determined from translation and the frequency can be determined from scale.

The choice of the mother wavelet is very important for CWT analysis. Depending on the data characteristics and analysis purposes, the choice of the mother wavelet differs. Gabor wavelet (which is a complex valued modulated Gaussian function) can be adjusted to have a shorter time support [175]. This characteristic makes Gabor wavelet very suitable for damage detection. Although a Gabor wavelet of G_S = 5 (also called Morlet wavelet) is used by many researchers [176], lower values of G_S may sometimes give better results. Nevertheless, it should not be too low, as then it may breach the admissibility condition [175]. In this thesis, Morlet wavelet is used.

5.2.2 Short Kernel Method (SKM)

A single value SKM at a specific frequency can be stated as [7]

$$SKM_{j,k} = \sum_{i=1}^{N_2-N_1} h(\tau_i) f[(\tau_i + j.\Delta t), k]\Delta t \tag{5.5}$$

where $SKM_{j,k}$ = the j^{th} term of the cross-correlation currently being performed at the k^{th} frequency; h = time record at any sensor; f = the kernel of the k^{th} frequency used to perform the cross correlation; N_1 = number of data points in f; N_2 = number of data points in h; Δt = the time step at which the time record (h) is stored.

A user defined frequency for comparison with the sensor record is called kernel seed. The method places the kernel whose length is also determined by the user, next to the time record so its individual data points coincide with the data points in the signal. The process begins by cross multiplying the amplitude of the kernel at each time step with the corresponding signal amplitude. Products from all multiplications are then summed keeping all algebraic signs to obtain a single number. This summation is one SKM value representing how well the kernel is aligned with its frequency counterpart inside the data string. The value is graphed on an SKM plot at the point where the beginning of the kernel was placed. The kernel is then shifted along the data string by a predetermined number of points and the cross products are formed again. Another SKM value results s plotted at the point where the kernel is now placed. This procedure is continued for some specified number of kernel shifts. A positive global maximum peak

represents the location where the kernel fits best and is in phase with its frequency counterpart and a negative global maximum is a location where the kernel is also well aligned but out of phase by 180° with its frequency counterpart [7].

5.3 Numerical modelling of timber pole

The length of the timber pole in this chapter is considered as 5 m and 12 m, respectively. The diameter of the pole is considered as 30 cm and divided in 4 layers in the radial direction. The highest mesh is considered to be 5 cm. For the low frequency input (below 2-4 kHz), 5 cm is dense enough. The mesh density should be less than the wavelength of the input frequency; otherwise, the element interface will work as a boundary for the reflection. From the wavelength curve presented in Chapter 3, it is clear that for the isotropic material the wavelength is notably higher than 5 cm at the frequency of 2 kHz or less. Also, for the modelling, element SOLID45 in ANSYS is chosen to simulate the timber pole.

As the timber pole is partially embedded in soil, the interaction between the soil and the timber pole become important when a dynamic load is applied. The interface can be modelled as perfectly bonded or by frictional interface. The frictional interface, representing high nonlinear behaviour, allows modelling of slipping and gapping between the soil and the pile/pole, and thus, takes more computational time and computer resources. Hence, if the slipping and gapping is negligible or will not influence the analysis results, perfect bonding can be considered [177]. In this research, negligible slipping and gapping between soil and pole is caused by low strain testing; therefore, perfect bonding is considered to simulate the interaction behaviour.

The soil is modelled as rectangular box with the distance from the timber equal to five times the diameter of the pole, i.e. the distance from the pole to the end of the soil layer is considered as 150 cm. The reason for choosing this distance is due to the fact that the energy of the wave which is propagating through the soil will be fully attenuated before reaching the soil boundary. As a result, the soil boundary cannot reflect the wave and thus, will not affect the output signal. The modulus of elasticity, density and Poisson's ratio of the soil is considered as 155567 kPa, 1850 kg/m^3 and 0.45.

Triangular loading with duration of 550 micro second is chosen as input frequency. This is one of the common ranges in the practical situation. As a result, the broadband

frequency band usually covers up to 2,000 kHz. The low frequency range is usually considered because only the first mode of longitudinal and/or flexural waves is/are present in this range and the attenuation is usually low. The amplitude of the impact load is considered as 1,570 N.

Isotropic material properties are used for the numerical modelling. In this chapter, the main focus is not on the anisotropic behaviour but to separate the longitudinal and flexural waves from an induced input. Moreover, anisotropic modelling is time consuming and also it requires fine meshes as the wavelengths are smaller than the isotropic material. However, the method explained here can be extended for the transversely isotropic or orthotropic material modelling.

5.4 Guided wave behaviour in three dimensional analysis

To analyse the properties of the displacement component, three impact locations and orientations are considered. For the first case, the impact is imparted vertically at the centre of the cross section on the top of the pole. For the second case, the impact is applied transversely on the side of the pole while inclined impact is imparted with an angle of 45° in case 3. The sensors location, soil level, impact location and orientation are shown in Figure 5.1. For case 1, the sensors are located at 3m and 2m from the bottom of the pole whereas for cases 2 and 3, the sensor locations are chosen at 2.5 and 1.5 m from the bottom of the pole. For cases 2 and 3, the impact load is applied at 1m below the top of the pole. The loading conditions are named as top, side transverse and side 45° impact. At each sensor location, three positions along the circumference are taken into account. The sensor which is aligned with the impact line is named as 0° and the sensor opposite to 0° is called 180°. Similarly, the sensor which is located 90° around the circumference from the impact location is called as 90°. Again, at every position, the displacement is captured in three orthogonal directions of polar coordinate (r–θ–z), i.e. in the longitudinal/axial (L), radial (R) and tangential/angular (θ) directions.

The location of sensor is chosen such a way that they are very close to the ground since practically this is very convenient. Additionally, the sensors are located at the same line of the impact location, 90° along the circumference from the impact and also at 180° apart from the impact location due to the fact that the wave properties of longitudinal and flexural wave are different along the circumference as described in Section 3.3.3.

And this advantage will be taken into account in order to differentiate between longitudinal and flexural wave. All the orientations (longitudinal, radial and tangential) are also considered for the same reasons. Three different impact location and orientation are chosen in the study to induce longitudinal and flexural wave separately and also combined to investigate the effect and difference of these waves. Case 3 is the most useful impact orientation which is usually imparted through a wave guide and thus, the signal quality is better. However, this case may induces both waves simultaneously. Accordingly, comparing case 3 with case 1 and case 2 will give the inside of longitudinal and flexural wave propagation.

Hence, a notation 'S2.5R90' means that the sensor is located at 2.5m from the ground and the position is 90° along the circumference from the impact location and the displacement component is the radial one. In ANSYS, the output is the displacement while in the field usually the acceleration is captured. Therefore, the displacements are converted into acceleration by double differentiation.

5.4.1 Displacement components

Figure 5.2 illustrates the displacement/acceleration components for case 1 for the sensor at 3m from the bottom of the pole. The top plot of this figure compares the accelerations among S3L0, S3R0 and S3θ0 and the middle compares the same among S3L90, S3R90 and S3θ90 and lastly the bottom plot represents the comparison among the sensors S3L180, S3R180 and S3θ180. From these three plots, it is clear that in the case of impact at top, longitudinal wave is generated. This is owing to the fact that longitudinal wave does not have any angular/tangential component. This can be also be verified from Equations (3.18) – (3.20). Also, most of the energy is carried by the axial component of displacement.

The top plot of Figure 5.3 denotes the comparison of longitudinal component among the sensors at 3m with the orientation of 0°, 90° and 180° and the bottom plot represents the same for the radial component. Again from the figure, it can be seen that the longitudinal/axial component of displacement/acceleration has the same phase whereas the radial components at 0° and 180° are 180° out of phase from each other. Due to the contraction effect, the radial components are in out of phase situation. Thus the symmetric behaviour of the longitudinal wave is justified. As the circumferential order

is zero for the longitudinal wave (Equations (3.18) – (3.20)), hence this wave is not affected by the angle from the impact location. Or in other words, axial component of the longitudinal wave has the same phase throughout the pole.

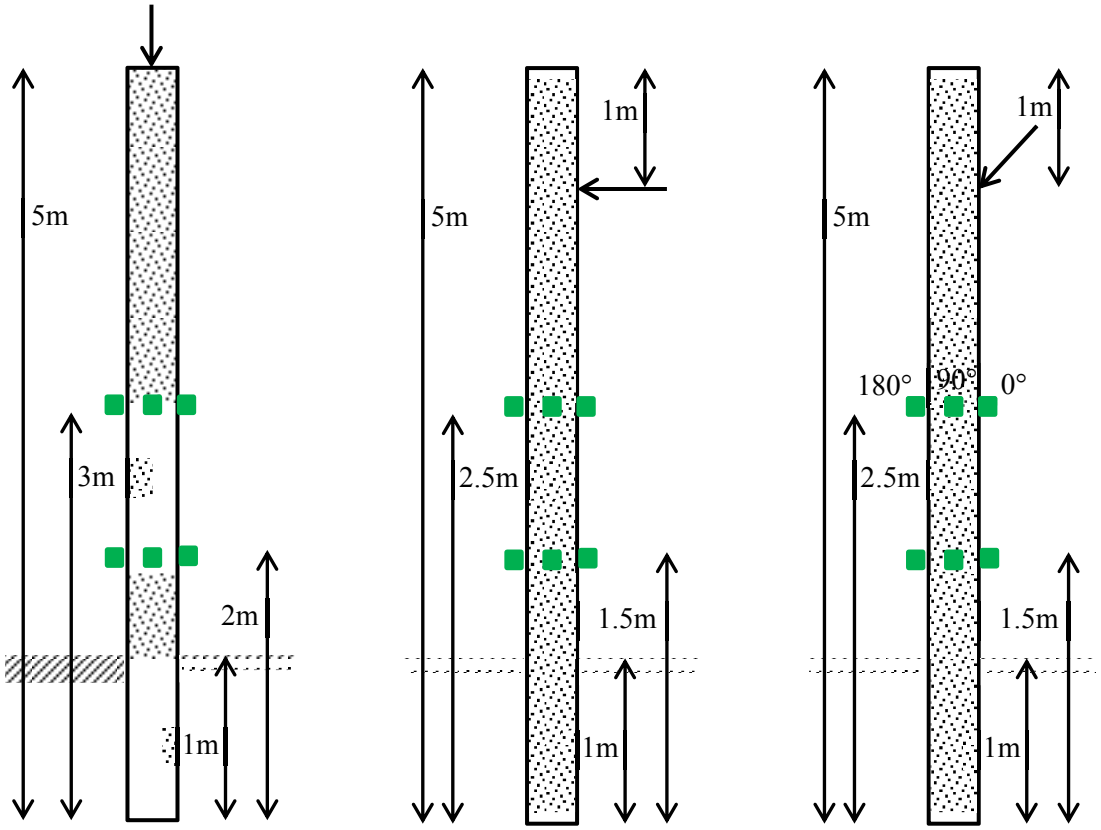

Case 1 Case 2 Case 3

Figure 5.1 Three different cases of numerical modelling of timber pole

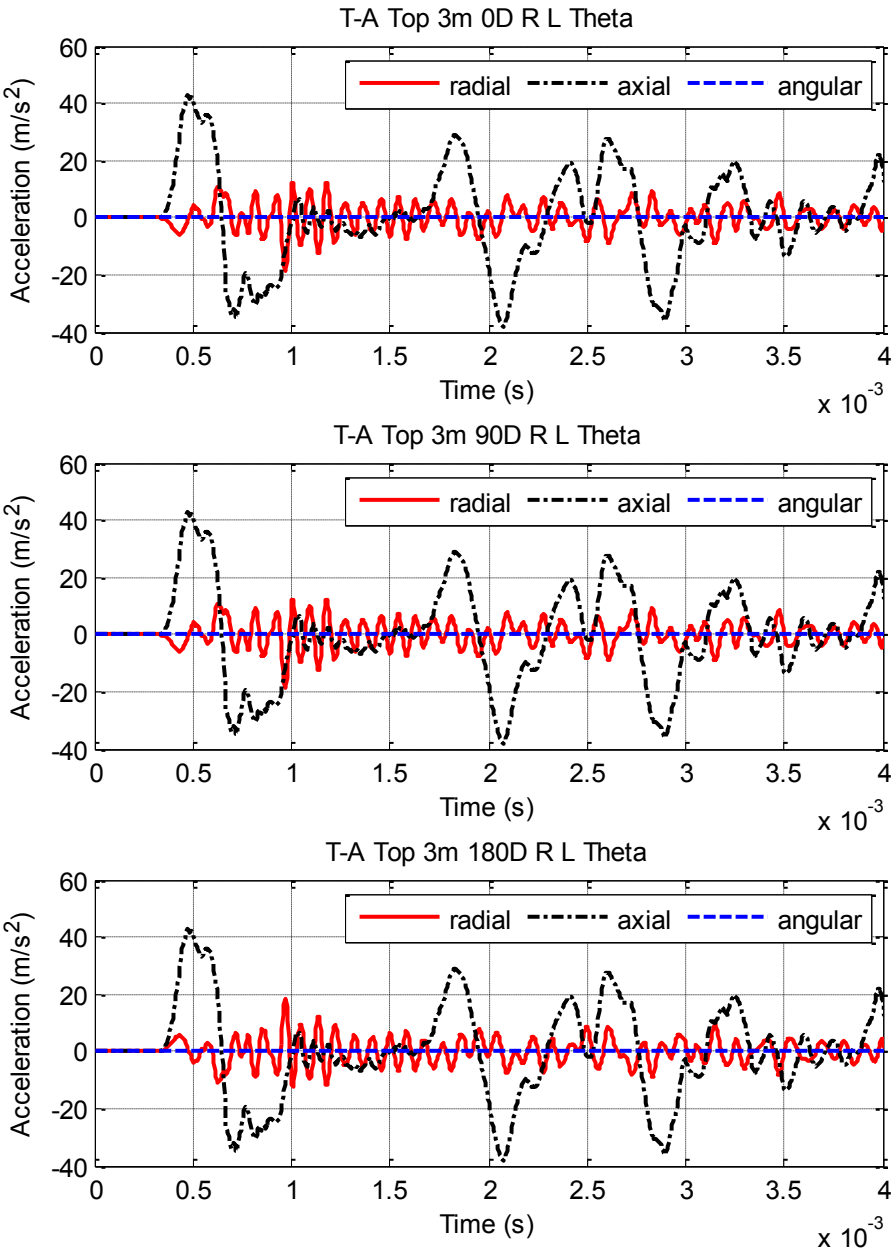

Figure 5.2 Comparison of time acceleration data in three orthogonal directions at sensor at 3m (impact at top)

Thereby, it can again be concluded that if the impact is applied at the top centre of the cross section, purely longitudinal wave can be generated. Further verification based on velocity will be provided in the latter section.

Figure 5.4 depicts the displacement/acceleration components for case 2 for the sensor at 2.5m from the bottom of the pole. The top plot of this figure compares the accelerations among S2.5L0, S2.5R0 and S2.5θ0 and the middle compares the same among S2.5L90, S2.5R90 and S2.5θ90 and lastly the bottom plot shows the comparison among the

sensors S2.5L180, S2.5R180 and S2.5θ180. From top and bottom plots, it can be seen that the angular component is zero at the sensor S3θ0 and S3θ180. This can be also verified from Equations (3.18) – (3.20). According to these equations, the axial and radial component should be zero at 90°. From the middle figure, it is obvious that the only angular component is present at 90° and contains most of the energy. The unexpected small amplitude of radial and axial components at 90° may be due to the conversion of displacement component into acceleration. Clearly, the transverse impact from the side of the pole represents the purely bending/flexural behaviour of the wave.

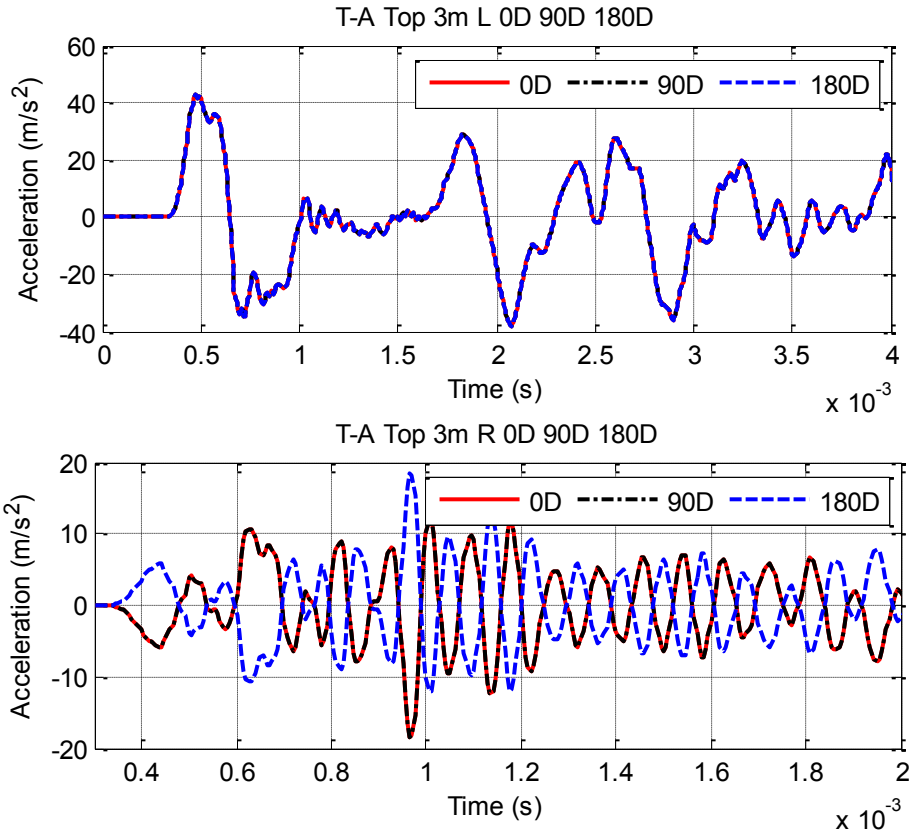

Figure 5.3 Comparison of time acceleration data in longitudinal and radial directions at sensor at 3m in different positions (impact at top)

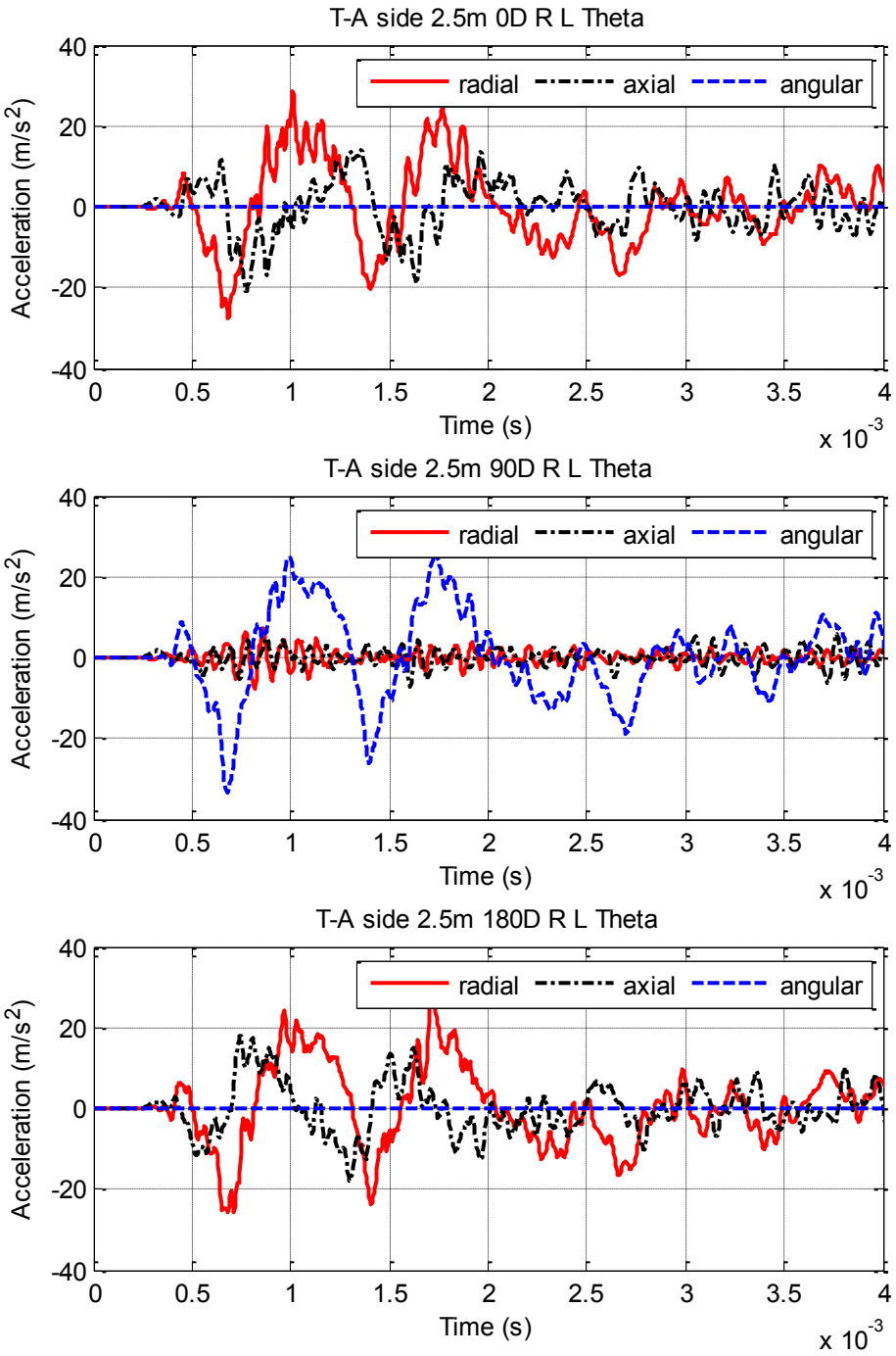

Figure 5.4 Comparison of time acceleration data in three orthogonal directions at sensor at 2.5m (impact from side transverse)

The top plot of Figure 5.5 compares the longitudinal component among the sensors at 2.5m with the orientation of 0°, 90° and 180° whereas the bottom plot demonstrates the same for the radial component. Unlike longitudinal wave, the radial components of displacement/acceleration have the same phase for the side 45° impact whereas the axial components at 0° and 180° are 180° out of phase from each other. Thus the anti-

symmetric behaviour of the flexural wave is justified. As the circumferential order is greater than one for the flexural wave (Equations (3.18) – (3.20)); hence, this wave is affected by the angle from the impact location. It can also be noted that the angular component at 90° along the circumference from the impact location represents the pure flexural wave due to the absence of tangential component in longitudinal wave.

Thereby, it can be concluded that if the impact is applied transversely from the side of the pole, purely flexural wave can be generated. Further verification based on velocity will be provided in the later section.

Figure 5.6 indicates the acceleration components for case 3 for the sensor at 2.5m from the bottom of the pole. The top plot of this figure compares the acceleration among S2.5L0, S2.5R0 and S2.5θ0 and the middle compares the same among S2.5L90, S2.5R90 and S2.5θ90 and lastly the bottom plot represents the comparison among the sensors S2.5L180, S2.5R180 and S2.5θ180. The signals are not as clear as compared to

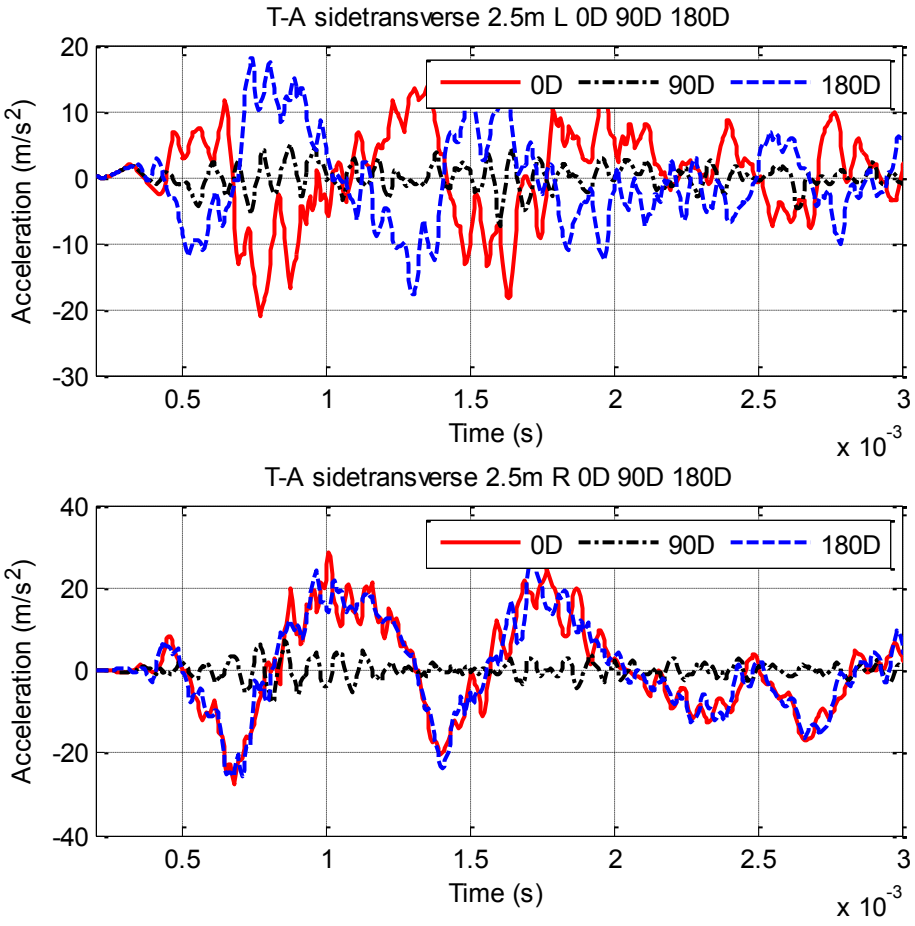

Figure 5.5 Comparison of time acceleration data in longitudinal and radial directions at sensor at 2.5m in different positions (impact from side transverse)

the two previous cases. However, some observations can be made. Such as, the angular component is zero at both sensors of 0° and 180°. This is owing to the fact that both the longitudinal or flexural waves have zero angular components at 0° and 180°. In contrast, at the 90° location, all three components of displacements can be noticed. Therefore, it can be said that inclined impact produces both the longitudinal and flexural waves at the same time. Nevertheless, it is worthwhile to mention that the angular component at 90° should be solely related to the flexural wave while the radial and axial component at 90° should represents the pure longitudinal wave since flexural wave does not have the radial and axial components at this location and orientation.

The top plot of Figure 5.7 compares the acceleration among S2.5L0, S2.5L90 and S2.5L180 and the middle compares the same among S2.5R0, S2.5R90 and S2.5R180 and lastly the bottom plot represents the comparison among the sensors S2.5θ0, S2.5θ90 and S2.5θ180. It can be seen that the symmetric or anti-symmetric behaviour of the wave is not very clear. For example, the longitudinal component at 0° and 180° do not have the same phase and at the same time they are not 180° out of phase as well. The radial component at 0° and 180° are almost at the same phase which represents the flexural behaviour. This may be in spite of the fact that the radial component has very small amplitude in the longitudinal wave propagation as previously shown and consequently, the radial component is dominated by the flexural behaviour.

The angular component solely represents the flexural wave behaviour at 90° as mentioned earlier. Subsequently, for the inclined impact, it is important to consider which waves are taken into account. An effective approach can be the separation of the longitudinal and flexural waves by their radial, axial and angular components at the 90° location or some other means to calculate the exact wave velocity as the wave velocity related to longitudinal and flexural waves is very much different. Continuous Wavelet Transform (CWT) is used as a signal processing tool to determine the velocity of the wave for Case 1, 2 and 3 and will be presented in the next section.

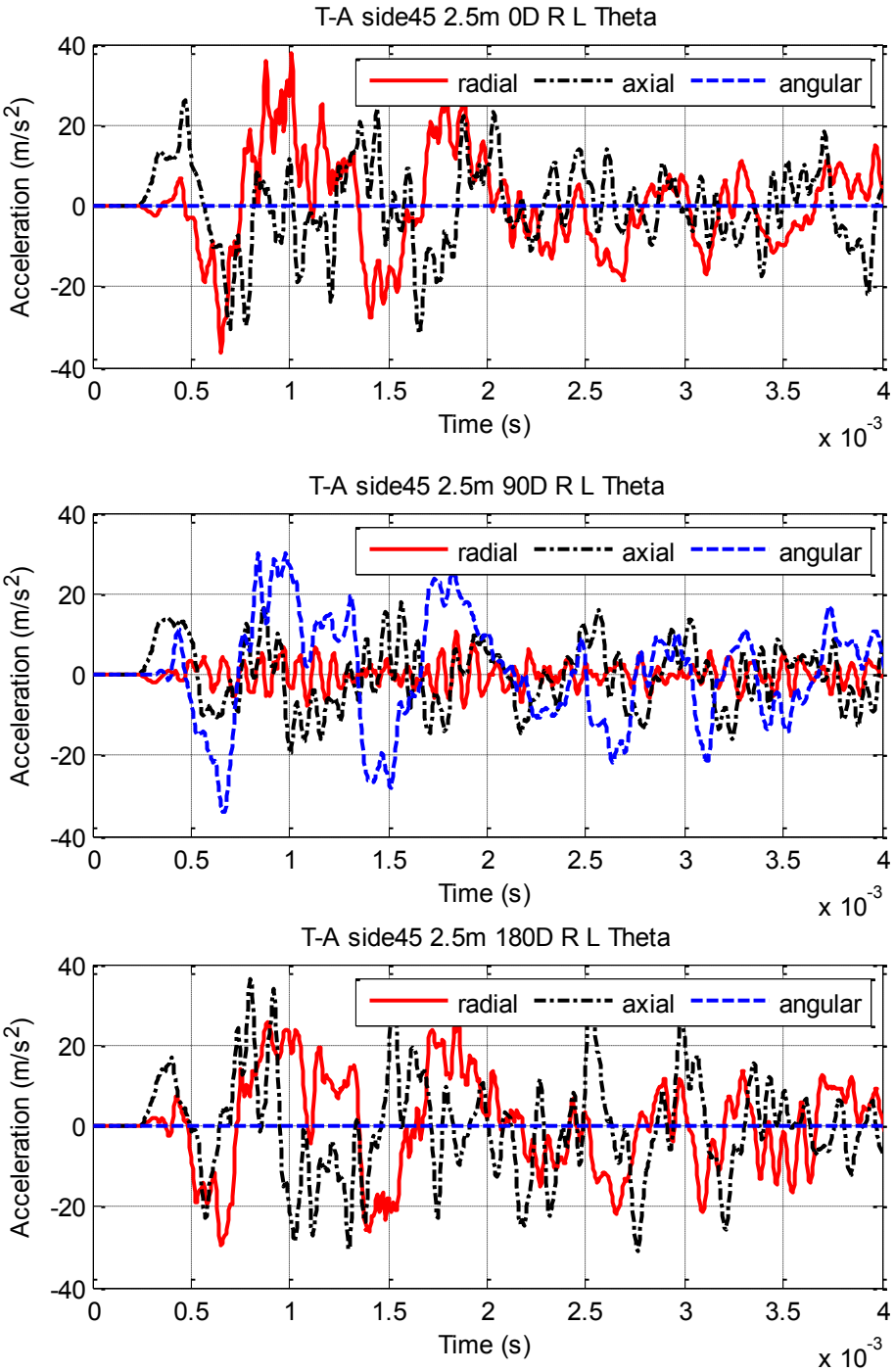

Figure 5.6 Comparison of time acceleration data in three orthogonal directions at sensor at 2.5m (impact: side 45°)

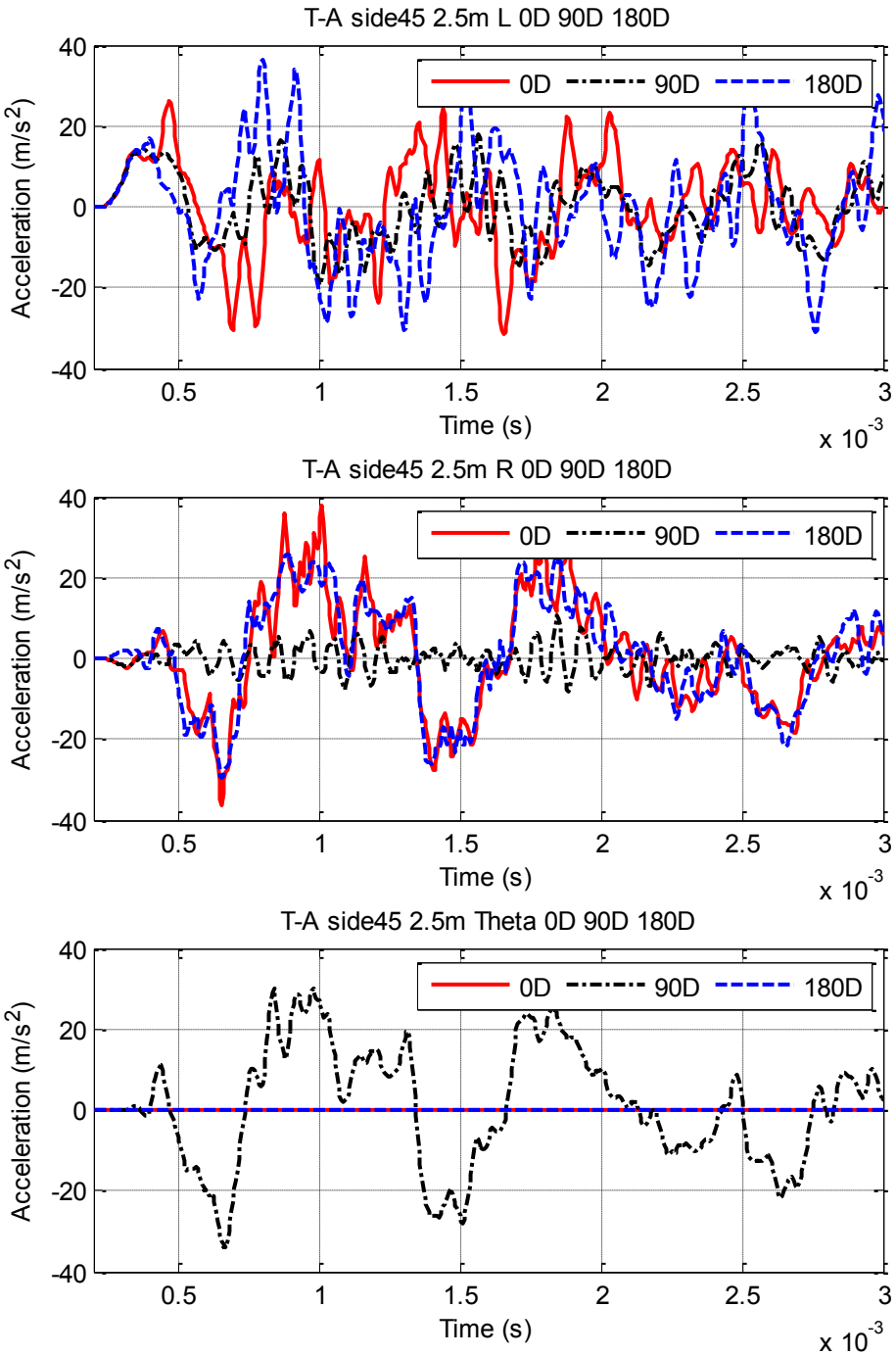

Figure 5.7 Comparison of time acceleration data in longitudinal, radial and angular directions at sensor at 2.5m in different positions (impact: Side 45°)

5.4.2 Velocity calculation

To calculate the velocity, CWT technique is used since the signals are not always very clear and CWT can separate the frequency dependent time domain data. CWT transforms the time domain data to another domain where the x-axis represents the

translation and the y-axis is related to the scale. The translation can be converted to time and the frequency is related to the scale.

Figure 5.8 shows the time-frequency contour for case 1 for the sensor S3L0 while Figure 5.9 presents the same for the sensor S2L0. From these figures, it is clear that most of the energy is below 2 kHz which is expected due to the manual impact that excites low frequency components.

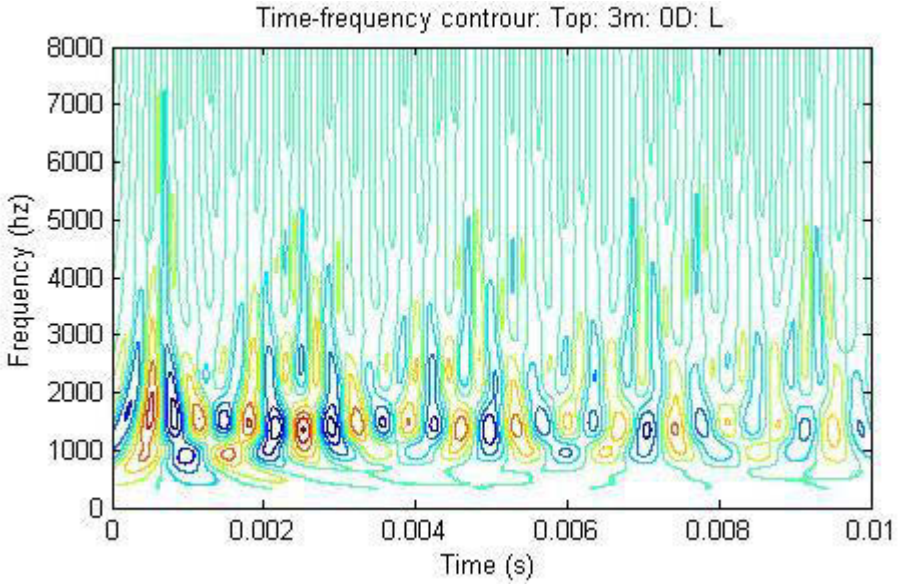

Figure 5.8 Time frequency contour of the axial displacement component for case 1 at the sensor 3m from the bottom pole with 0° orientation

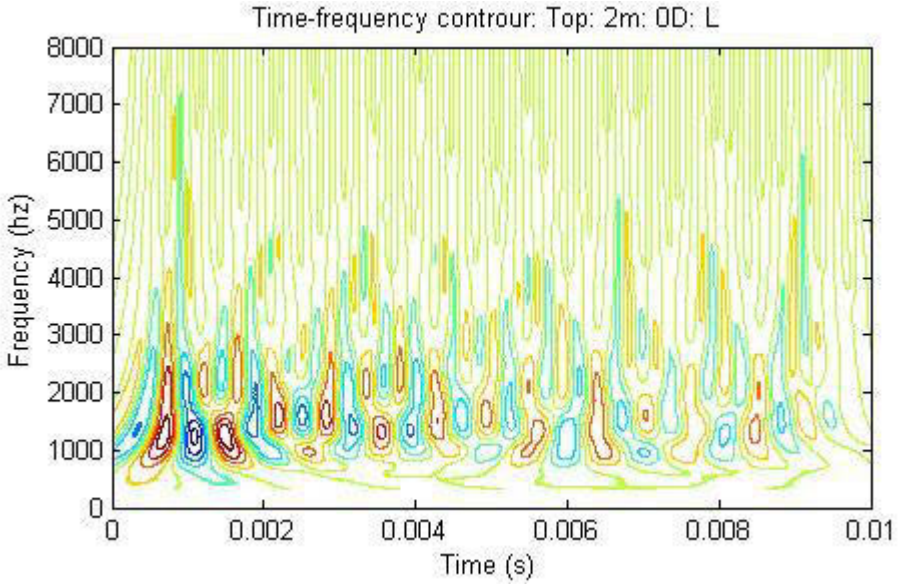

Figure 5.9 Time frequency contour of the axial displacement component for case 1 at the sensor 2m from the bottom pole with 0° orientation

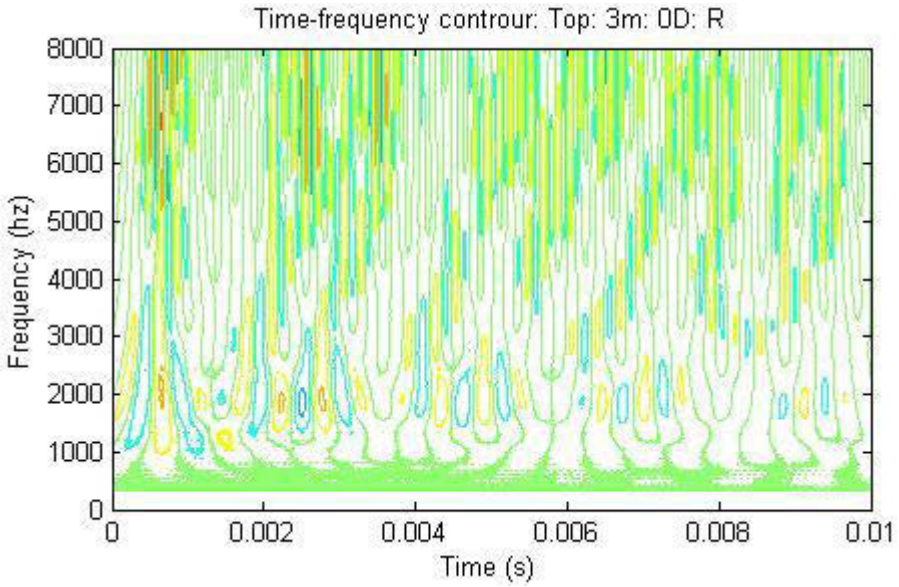

Figure 5.10 Time frequency contour of the radial displacement component for case 1 at the sensor 3m from the bottom pole with 0° orientation

The contours represent the presence of different frequencies at various times and it can be noted that the frequency component is almost constant at both of these sensors.

From the time domain plots, it was mentioned that the radial component of acceleration contains very little energy which is also depicted in Figure 5.10. From this figure, it is clear that the radial component does not have any contours with high energy level and hence, cannot be used to determine the velocity of the wave from the radial component.

The Figure 5.11 and Figure 5.12 display the time-frequency plot for the sensor S3L90 and S2L90, respectively. Similar to the time-frequency plot for the 0° orientation, the wave contains most of the energy below 2 kHz, however, for the 90° orientation; the common frequencies between two sensors are different. To determine the velocity of the wave, it is better to consider the common frequencies between two sensors. By looking at the contour plots of these two sensors, the common frequencies are chosen at 1,200, 1,500 and 1,800 Hz. Similarly, for the 0° orientation, the common frequencies between sensor S3L0 and S2L0 are taken at 1,300 and 1,700 Hz.

The top plot of the Figure 5.13 compares the coefficient plot of S3L0 and S2L0 at the frequency of 1,700 Hz whereas the bottom plot compares the same between S3L90 and S2L90 at 1,800 Hz. The coefficient plots at other common frequencies are presented in

the Appendix E. From these coefficient plots the phase velocity can easily be calculated from the time lag between two sensors by using the following formula

$$V_{ph} = \frac{L_s}{\Delta t} \tag{5.6}$$

where L_s = the distance between sensors and Δt is the time lag between two sensors.

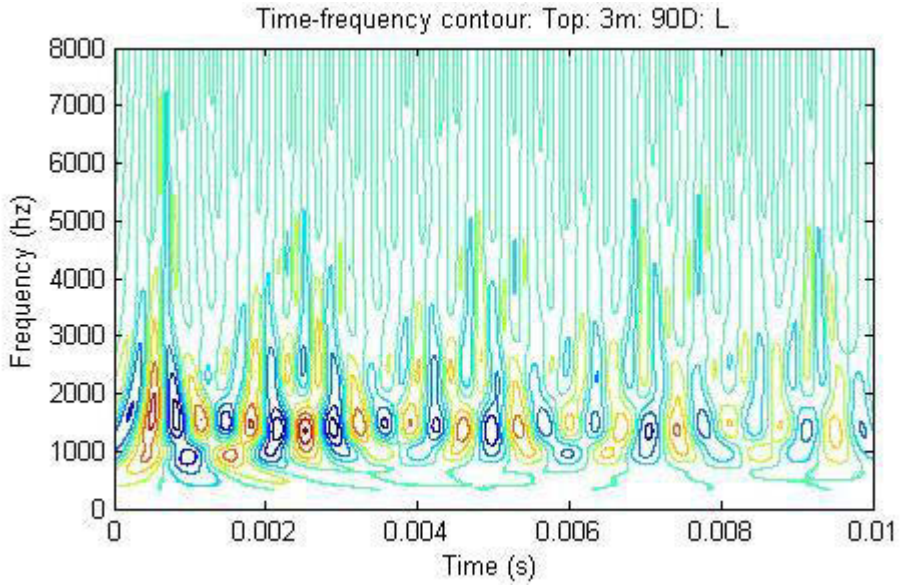

Figure 5.11 Time frequency contour of the axial displacement component for case 1 at the sensor 3m from the bottom pole with 90° orientation

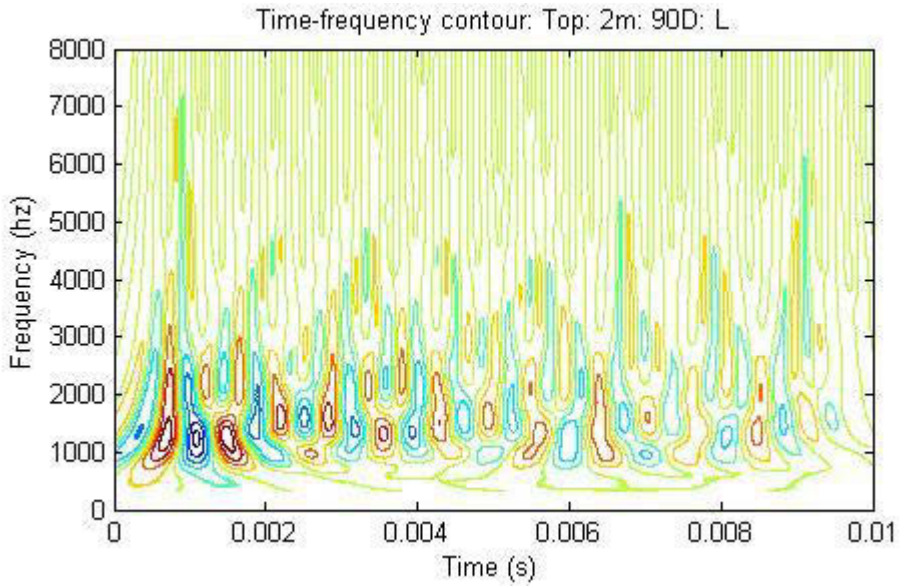

Figure 5.12 Time frequency contour of the axial displacement component for case 1 at the sensor 2m from the bottom pole with 90° orientation

The time lag can be calculated by time difference between the arrivals of the first peak at the sensors. The first peak can be easily identified from the time-CWT coefficient plot from the figures. Accordingly, the phase velocities at different common frequencies are determined and represented in Figure 5.14. It can be noticed that the velocities match considerably well with the analytical phase velocity curve of the longitudinal wave. Thereby, again it can be concluded that case 1 generates purely longitudinal wave. Among the phase velocities at the aforementioned common frequencies, two phase velocities match significantly well with the analytical value. These two frequencies are 1700 Hz for the 0° orientation and 1800 Hz for the 90° orientation. The possible reason for the better prediction may be due to the fact that these frequencies are the most common frequencies between two sensors at which most of the energy is contained.

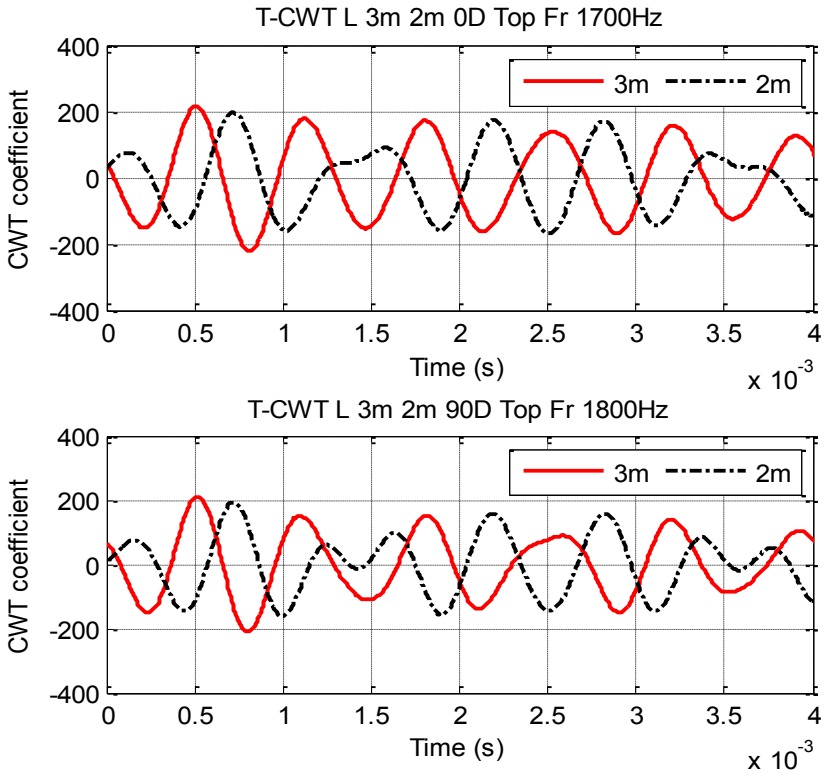

Figure 5.13 CWT coefficient plot of different components at different frequencies for case 1

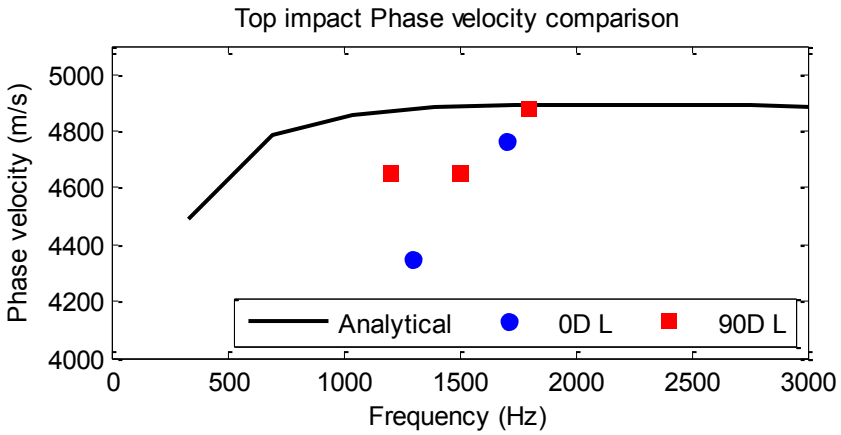

Figure 5.14 Phase velocity comparison for case 1

Figure 5.15 shows the time-frequency contour for case 2 for sensor S2.5L0 while Figure 5.16 presents the same for sensor S1.5L0. From these figures, it is clear that most of the energy is again below 2 kHz which is expected due to the manual impact. It can be seen that the frequency component is different at these sensors and the energy level is also very small in S1.5L0 compared to same in S2.5L0. There is only one common frequency found between these two sensors which is 1,500 Hz. The radial components of displacement at 0° show almost the same behaviour as the longitudinal component as can be seen from Figure 5.17 and Figure 5.18. The energy level is almost the same between these two sensors and the common frequency is also 1,500 Hz.

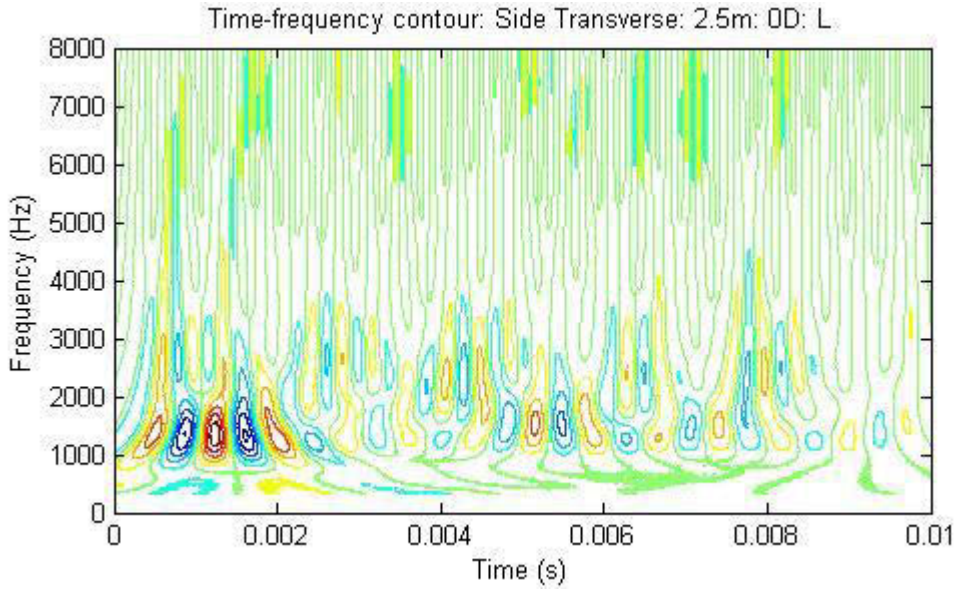

Figure 5.15 Time frequency contour of the axial displacement component for case 2 at sensor 2.5m from the bottom pole with 0° orientation

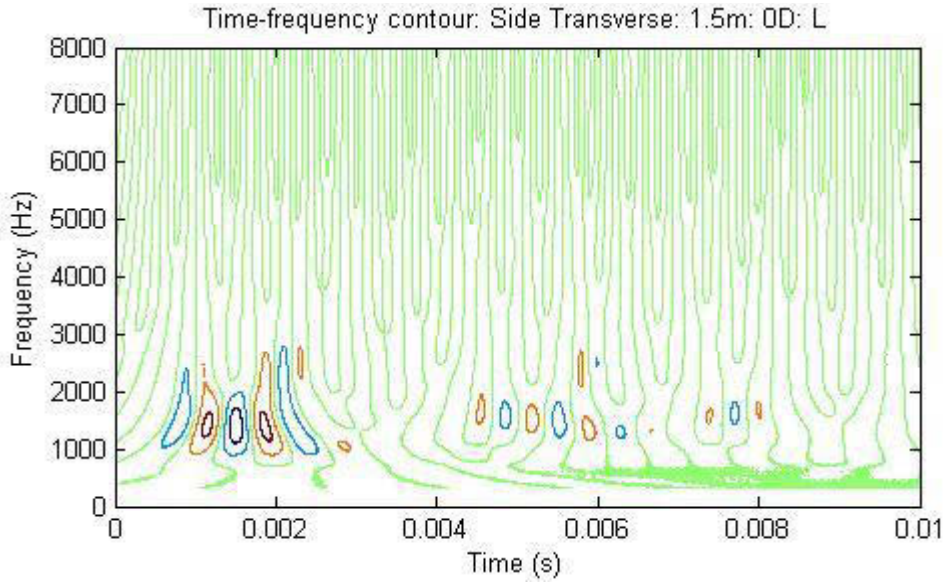

Figure 5.16 Time frequency contour of the axial displacement component for case 2 at sensor 1.5m from the bottom pole with 0° orientation

Figure 5.19 and Figure 5.20 display the time-frequency plot for the sensor S2.5L90 and S1.5L90, respectively. Similar to the time-frequency plot for the 0° orientation, the wave contains most of the energy below 2 kHz; however, some contours can be seen at 2,600 Hz especially at S2.5L90. Besides the 2,600 Hz, another common frequency between these two sensors can be chosen at 1,200 Hz. The time-coefficient plots at these chosen common frequencies are determined to calculate the phase velocities.

The top plot of the Figure 5.21 compares the coefficient plot of S2.5L0 and S1.5L0 at the frequency of 1,500 Hz whereas the bottom plot compares the same between S2.5L90 and S1.5L90 at 2,600 Hz and the middle plot shows the time coefficient plot of the sensors S2.5R0 and S1.5R0 at 1,500 Hz. The coefficient plot at 1,200 Hz is presented in Appendix E. From these coefficient plots, group behaviour at these frequencies is observed. Hence, to calculate the velocity, instead of determining the time lag between two peaks, the beginning of the wave packet (or group) is taken into account to calculate the phase velocity of the bending wave.

Due to the group behaviour it is sometimes essential to know the wavelength of the bending wave at different frequencies. For example, the wavelengths are 1.21, 1.07 and 0.75m at 1,200, 1,500 and 2,600 Hz, respectively, which is illustrated in Figure 3.9. Therefore, the wavelengths at 1,200 Hz and 1,500 Hz are longer than the distance between two sensors.

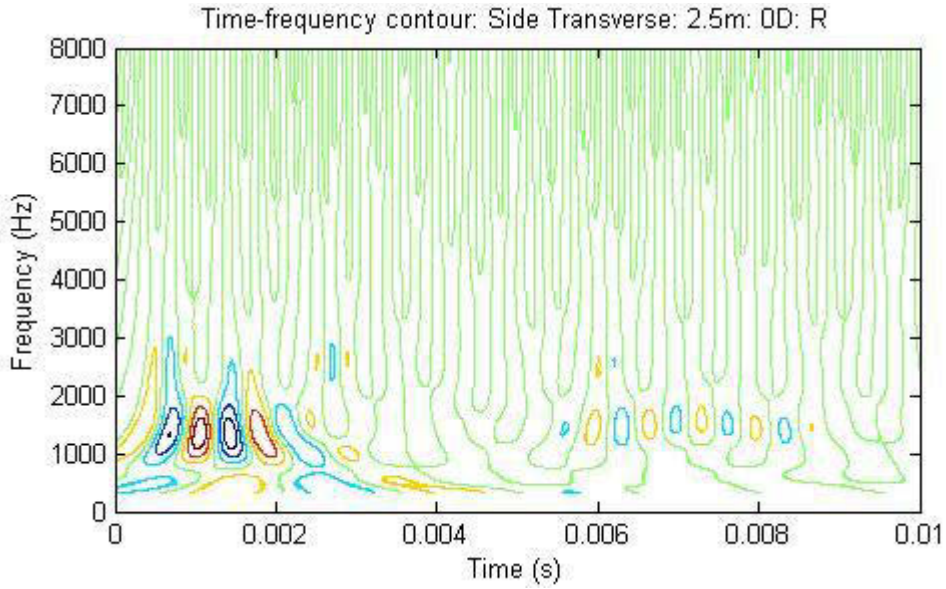

Figure 5.17 Time frequency contour of the radial displacement component for case 2 at sensor 2.5m from the bottom pole with 0° orientation

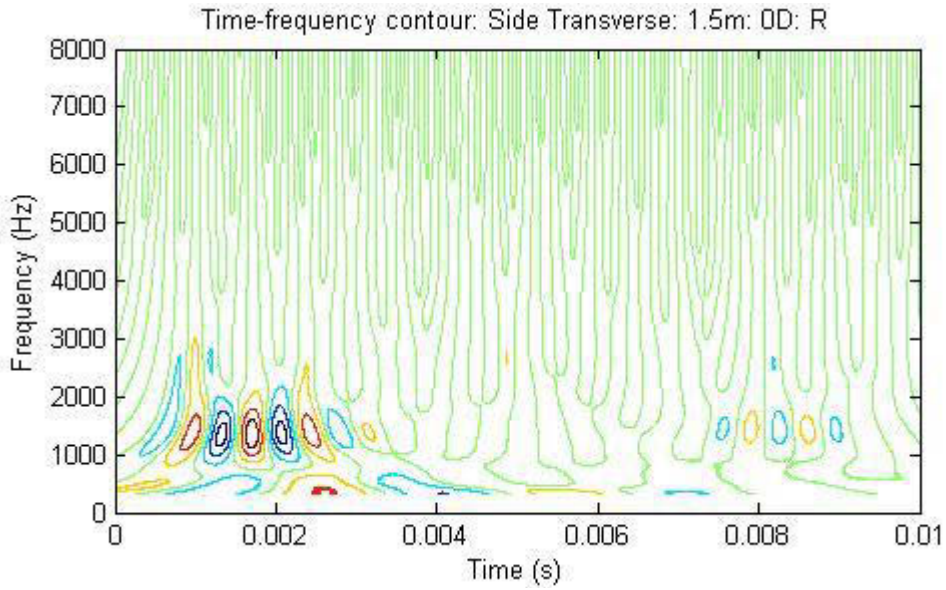

Figure 5.18 Time frequency contour of the radial displacement component for case 2 at sensor 1.5m from the bottom pole with 0° orientation

As a result, the time lag is calculated from reflection of the wave instead of the distance between two sensors. The formula for calculating phase velocity for this situation can be presented as

$$V_{ph} = \frac{L_T}{2\Delta t} \tag{5.7}$$

where L_T = the distance between sensor and the bottom of the pole and Δt is the time taken for the wave to reflect back to the sensor.

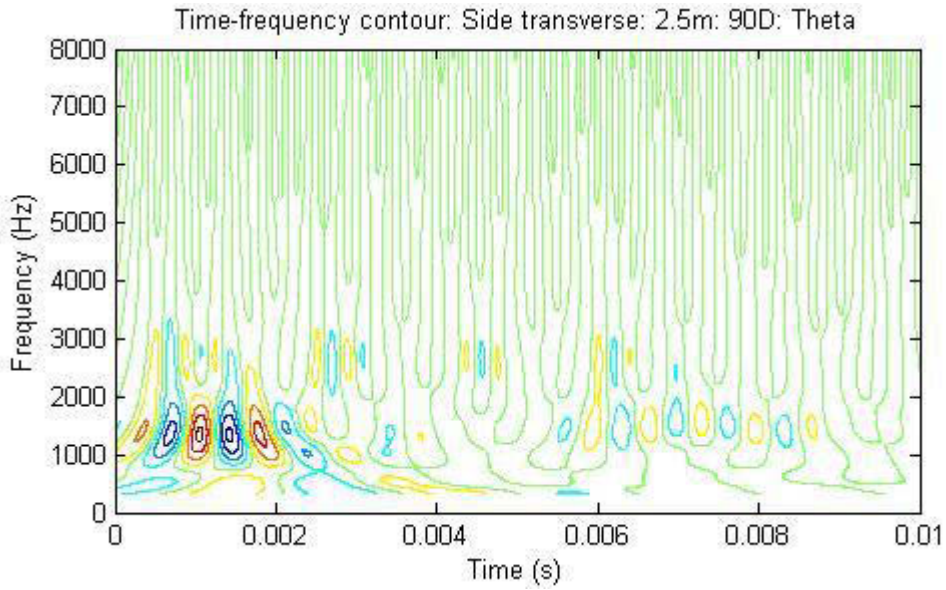

Figure 5.19 Time frequency contour of the tangential displacement component for case 2 at sensor 2.5m from the bottom pole with 90° orientation

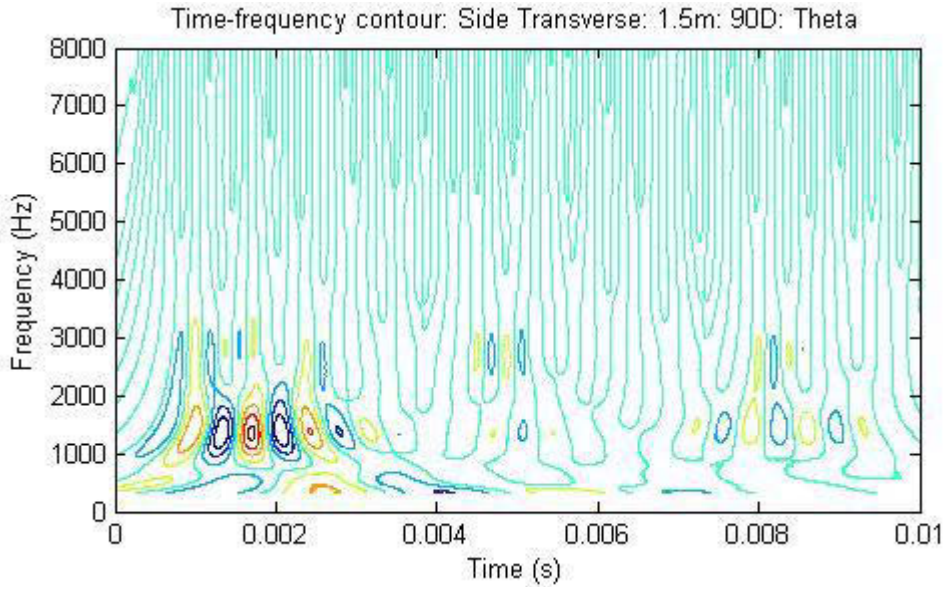

Figure 5.20 Time frequency contour of the tangential displacement component for case 2 at sensor 1.5m from the bottom pole with 90° orientation

However, the phase velocity can be determined from two sensors if the wavelength is smaller than the distance between two sensors. For instance, for the 2,600 Hz, the wavelength is 0.75m and hence, Equation (5.6) can be used to calculate the time lag. It should be mentioned here that, the distance (L_s) in this situation will be equal to the subtraction of the wavelength at that frequency from the distance between two sensors.

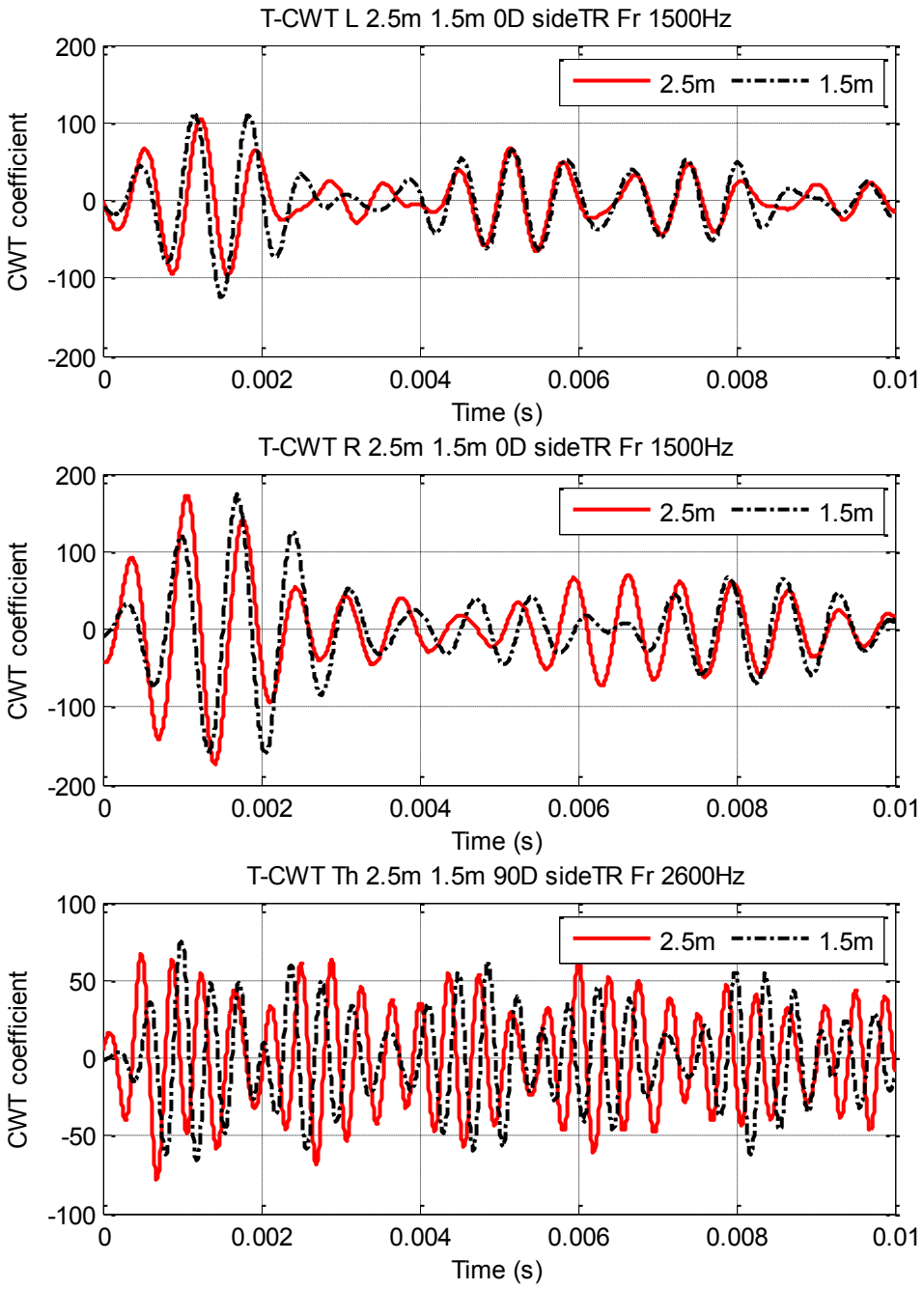

Figure 5.21 CWT coefficient plot of different components at different frequencies for case 2

For the 1,200 Hz and 1,500 Hz, the phase velocity is calculated from Equation (5.7), and Equation (5.6) is used to determine the phase velocity at 2,600 Hz. For all three situations, the time lag is calculated from the beginning of the group or wave packet. Accordingly, the phase velocities at different common frequencies are determined and illustrated in Figure 5.22. It can be noticed that the velocities match considerably well with the analytical phase velocity curves of the bending/flexural waves. Thereby, again it can be concluded that case 2 generates purely flexural waves. The phase velocities related to the sensor at 2.5m from the bottom of the pole shows better approximation compared to the sensors at 1.5m. The reasons are not very clear. However, the best approximation can be obtained from the tangential component at 90° orientation at the frequency of 2,600 Hz.

In general, the embedment length is one of the points of interest for the condition assessment of the timber pole. Hence, it is not possible to determine the phase velocity from the reflection and accordingly, it can be calculated from the wavelength. It is observed that the phase velocity approximation from the wavelength demonstrates notably good results in terms of calculating the phase velocity. Nevertheless, to use this concept of calculating velocity from wavelength, it is essential to plot the dispersion curve (frequency-wavelength) to know the exact wavelength at the chosen frequency. Additionally, the sensor distance should be set up in such a way that it is higher than the wavelength at the selected frequency.

Figure 5.23 and Figure 5.24 display the time-frequency contours for case 3 for the sensors S2.5L0 and S1.5L0, respectively, whereas Figure 5.25 and Figure 5.26 represent the same for the sensors S2.5R0 and S1.5R0, respectively. Besides, Figure 5.27 and Figure 5.28 display the time frequency contour for case 3 for the sensors at S2.5L90 and S1.5L90, respectively. Additionally, the time frequency contours for the sensors S2.5θ90 and S1.5θ90, which are related to case 3, are also indicated by Figure 5.29 and Figure 5.30, respectively. From these figures, the common frequencies between two sensors for the above conditions can be obtained. As expected from the previous discussions, the longitudinal components at 90° orientation and the tangential components at 90° should represent pure longitudinal and pure flexural waves, respectively. The common frequencies for these conditions are summarised in Table 5.1

Table 5.1 Common frequencies between sensors

Sensor 1	Sensor 2	Common frequencies (Hz)
S2.5L0	S1.5L0	1900, 2100, 2200, 2400
S2.5R0	S1.5R0	1900, 2200, 2400
S2.5L90	S1.5L90	1700, 2000, 2400
S2.5θ90	S1.5θ90	1200, 2200

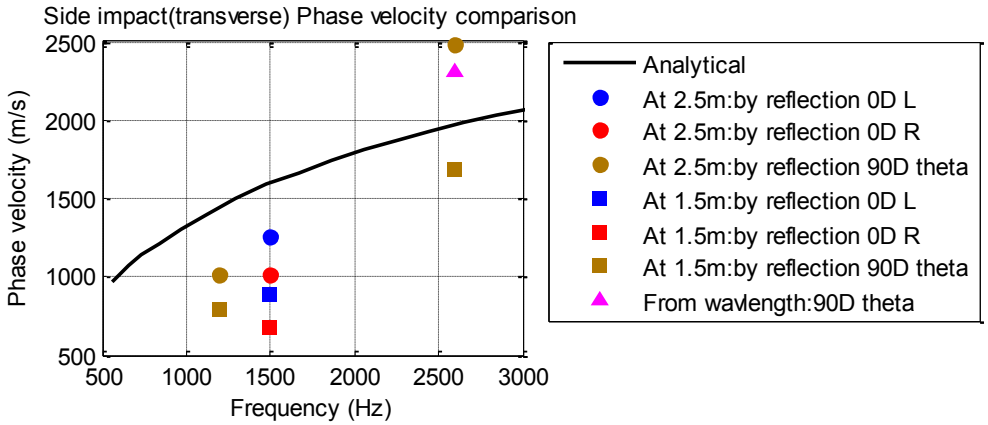

Figure 5.22 Phase velocity comparison for case 2

The time-CWT coefficient plots of two sensors at these frequencies are presented in Appendix E and used to calculate the phase velocities at these frequencies. The phase velocities related to the different orientations and various displacements for case 3 are plotted in Figure 5.31.

At first, the longitudinal components of displacements at 0° orientation are taken into account. The top plot of Figure 5.31 shows the phase velocities for the longitudinal components at 0° orientation. It is shown that if the wave is considered as longitudinal wave and Equation (5.6) is used to calculate the phase velocity, it does not agree with the analytical curve. The reason is obvious as for the inclined impact, both the flexural and longitudinal waves are generated, and considering the wave purely longitudinal leads to error in calculating the phase velocity of the generated wave. In contrast, if it is assumed that the flexural wave is generated then the calculated phase velocities from Equation (5.7) match reasonably well with the analytical phase velocity. This is possibly in spite of the fact that the longitudinal components of displacement at 0° orientation from an inclined impact contain the most energy that is related to the flexural wave. However, when the phase velocities are determined between two sensors

with the flexural wave assumptions from the wavelengths at that frequency, the discrepancies increase. The wavelengths at the above mentioned frequencies which are less than the distance between two sensors are tabulated in Table 5.2.

Table 5.2 Wavelengths of flexural wave at various frequencies

Frequency (Hz)	Wavelength (m)	Frequency (Hz)	Wavelength (m)
1,900	0.924	2,200	0.832
2,100	0.869	2,400	0.79

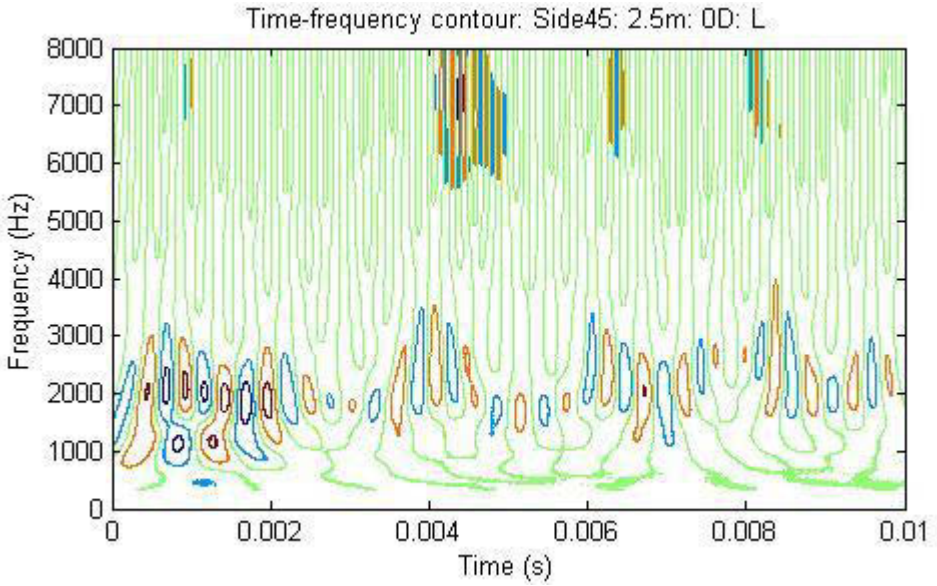

Figure 5.23 Time frequency contour of the axial displacement component for case 3 at sensor 2.5m from the bottom pole with 0° orientation

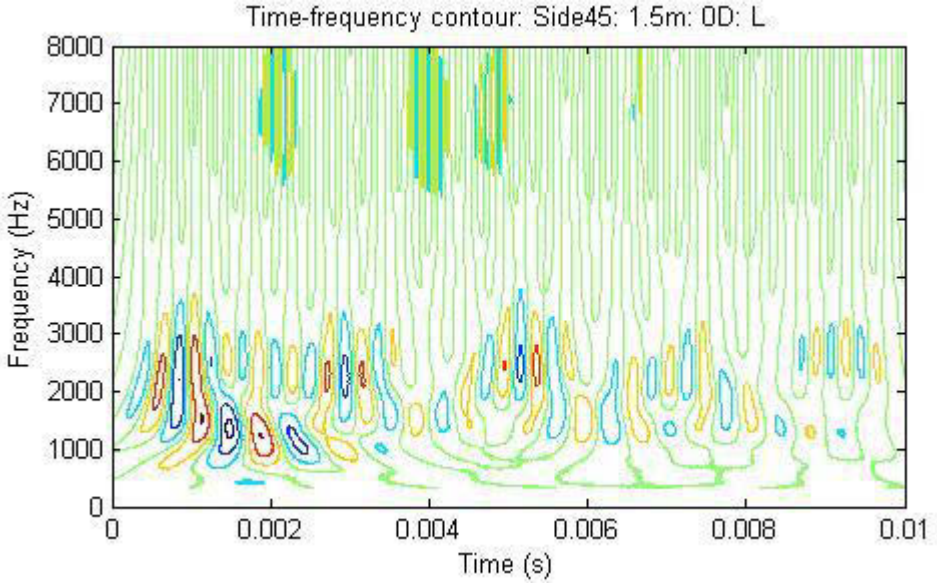

Figure 5.24 Time frequency contour of the axial displacement component for case 3 at sensor 1.5m from the bottom pole with 0° orientation

In the table, the wavelengths are taken from Figure 3.9 which is related to the first branch (F(1,1)) of flexural wave. Since, it is predicted that both longitudinal and flexural waves are generated for the inclined impact; hence, the wavelengths may be related to neither longitudinal nor flexural waves. Accordingly, the flexural wave assumption is not valid. Consequently, it can be concluded that longitudinal component of displacement at 0° orientation cannot be used to calculate the wave phase velocity, especially if the embedded length is unknown. In short, the purely longitudinal or purely flexural assumption is invalid for the inclined impact.

The middle plot of Figure 5.31 shows the phase velocities for the radial components at 0° orientation. It was shown for case 1 that the energy of the radial component, related to longitudinal wave, is less compared to the same of the flexural wave. Therefore, for the radial component, only the flexural wave assumption is used and the phase velocity is calculated from Equation (5.7) with the concept of wavelength. The phase velocities do not agree with analytical curve very well except at the frequency of 1,900 Hz. The phase velocities calculated from the concept of wavelengths present more error.

The bottom plot of Figure 5.31 shows the phase velocities for the longitudinal and tangential components at 90° orientation. It is expected that the longitudinal component at 90° should represent the pure longitudinal wave while the tangential component should reflect the pure flexural behaviour. From the figure, this behaviour is also justified. For instance, the longitudinal component agrees with the longitudinal wave's phase velocity to a great extent. Similarly, the tangential component agrees notably well with the analytical flexural phase velocity including the velocity calculated from the wavelength of the wave at 2,200 Hz.

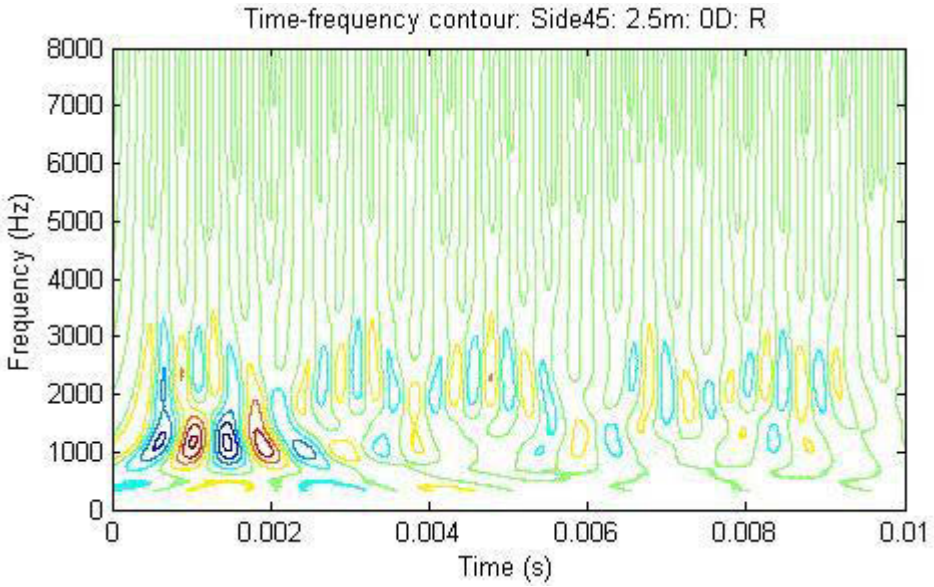

Figure 5.25 Time frequency contour of the radial displacement component for case 3 at sensor 2.5m from the bottom pole with 0° orientation

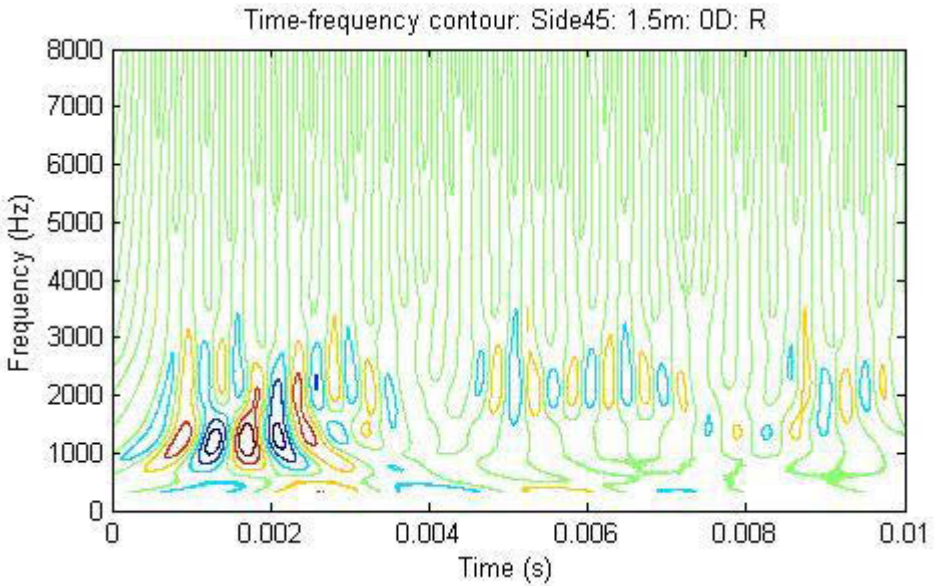

Figure 5.26 Time frequency contour of the radial displacement component for case 3 at sensor 1.5m from the bottom pole with 0° orientation

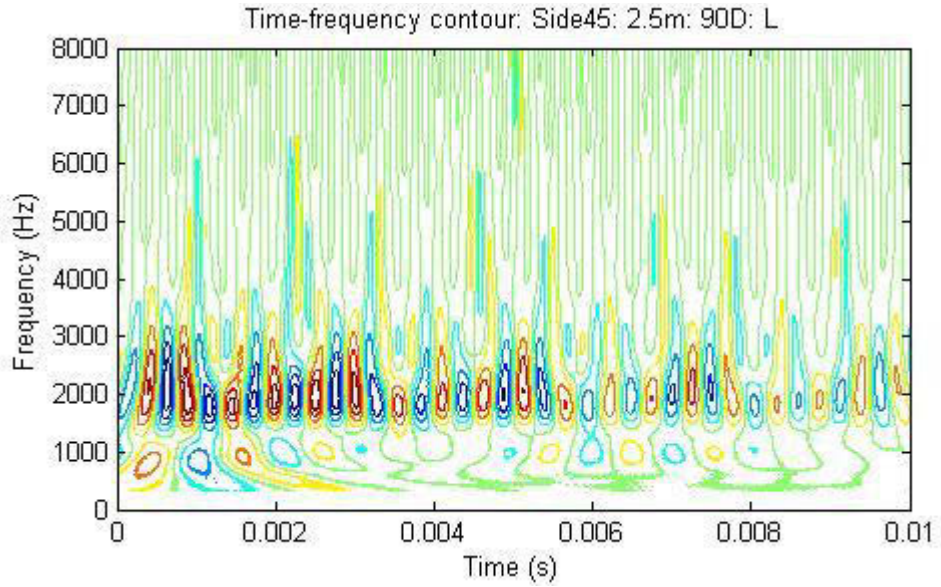

Figure 5.27 Time frequency contour of the axial displacement component for case 3 at sensor 2.5m from the bottom pole with 90° orientation

Therefore, it can be concluded that for the inclined impact or for the case of the superposition of longitudinal and flexural waves, it is important to separate these two waves. To achieve this goal, the sensors can be placed at 90° around the circumference from the impact location. And the orientation of the sensors can be chosen in the longitudinal and in the tangential directions.

Previously, for cases 1 and 2, the sensor at 180° was not taken into account due to the fact that the longitudinal components at 0° and 180° are in the same phase as in case 1 and the radial component at 0° and 180° are also in the same phase for case 2. Additionally, the radial component at 0° and 180° orientations from the impact location are 180° out of phase for case 1 and for case 2, and longitudinal components show the same behaviour. Accordingly, the sensors at 0° and 180° for case 1 and 2 represent the same time-frequency contours. However, the sensors at 180 orientations can be used for case 3 due to the summation of both waves.

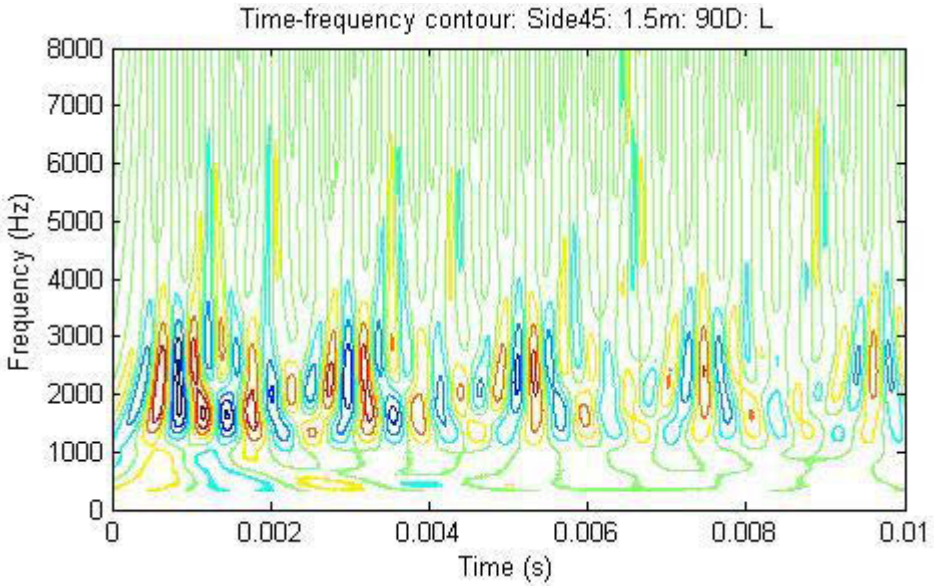

Figure 5.28 Time frequency contour of the axial displacement component for case 3 at sensor 1.5m from the bottom pole with 90° orientation

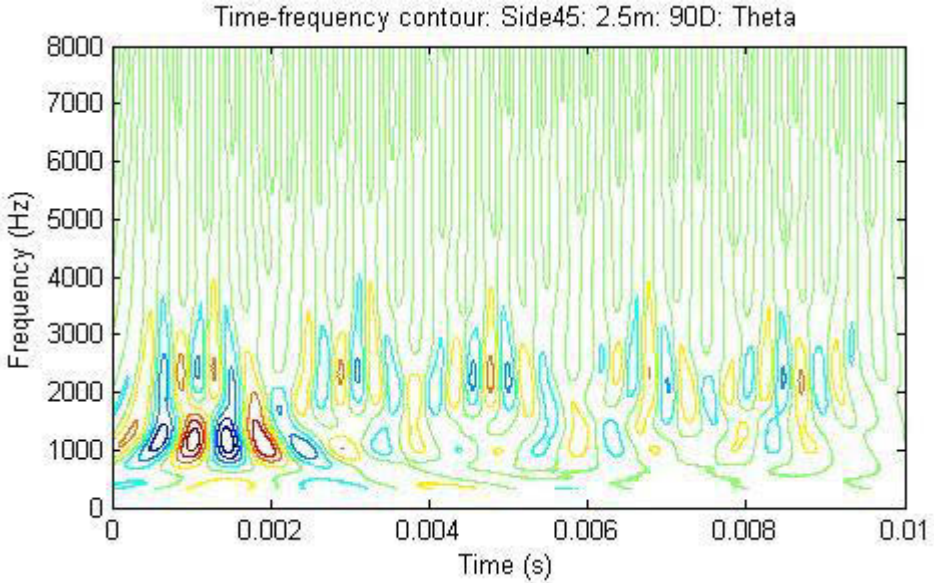

Figure 5.29 Time frequency contour of the tangential displacement component for case 3 at sensor 2.5m from the bottom pole with 90° orientation

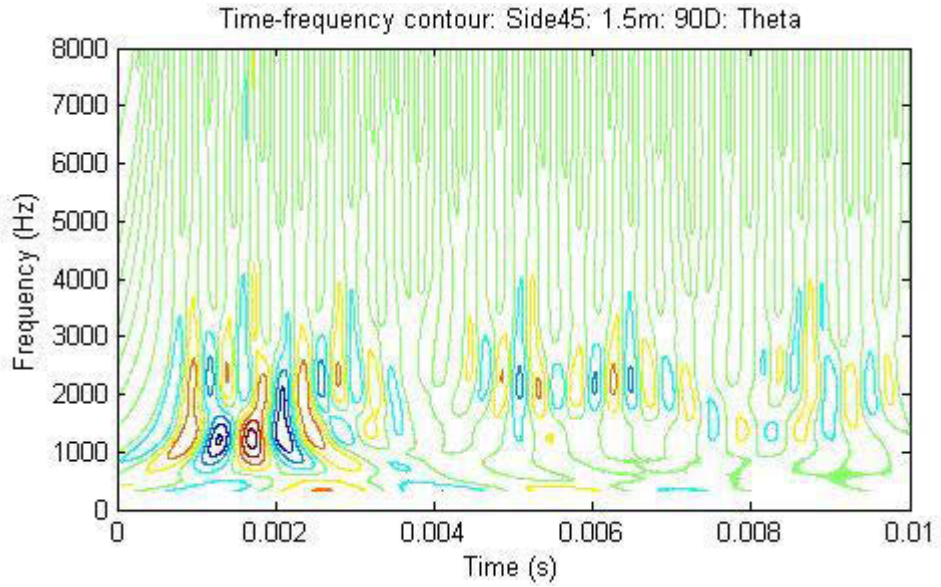

Figure 5.30 Time frequency contour of the tangential displacement component for case 3 at sensor 1.5m from the bottom pole with 90° orientation

From the aforementioned displacement behaviour of the longitudinal and flexural waves at 0° and 180°, it can be assumed that the summation of longitudinal component at 0° and 180° should represent the pure longitudinal wave owing to the fact that the longitudinal components of flexural wave at this two location should be eliminated by the summation because of the 180° out of phase situation. Also, the same is true for the radial components and thereby; summation of the radial component at 0° and 180° orientations should reflect the pure flexural behaviour.

To validate this assumption, the CWT is performed on the longitudinal and radial components at the 180° as illustrated in Figure 5.32 to Figure 5.35. By comparing the contours of the sensors at 0° and 180°, it can be seen that the time-frequency curves are not exactly the same in case 3. Nevertheless, the most common frequencies are chosen among the sensors S2.5L0, S1.5L0, S2.5L180 and S1.5L180. Likewise, the common frequencies among S2.5R0, S1.5R0, S2.5R180 and S1.5R180 are also determined and summarised in Table 5.3

Table 5.3 Common frequencies among sensors at 0° and 180° orientation

Sensors	Common frequencies (Hz)
S2.5L0, S1.5L0, S2.5L180 and S1.5L180	1900, 2100, 2200, 2400
S2.5R0, S1.5R0, S2.5R180 and S1.5R180	1200, 1500, 1900, 2200

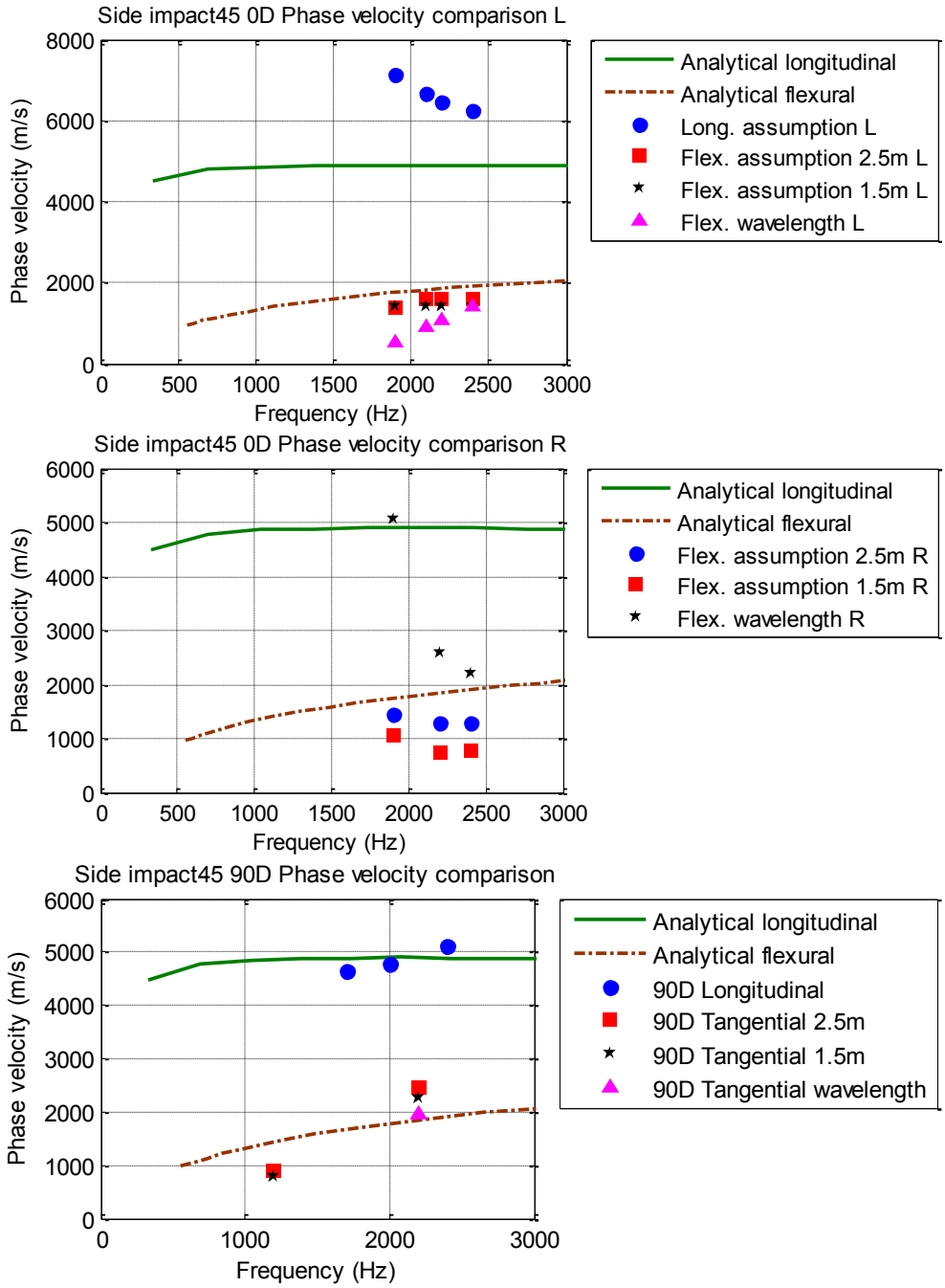

Figure 5.31 Phase velocity comparison for case 3 for the 0° and 90° orientations

The time-coefficient values at the selected frequencies are found and then summation is performed between S2.5L0 and S2.5L180 before plotting. Similarly, the summation is performed between S1.5L0 and S1.5L180, S2.5R0 and S2.5R180 and lastly, between S1.5R0 and S1.5R180. The time-CWT coefficient plots after the summations are shown in Appendix E and are used to determine the phase velocity.

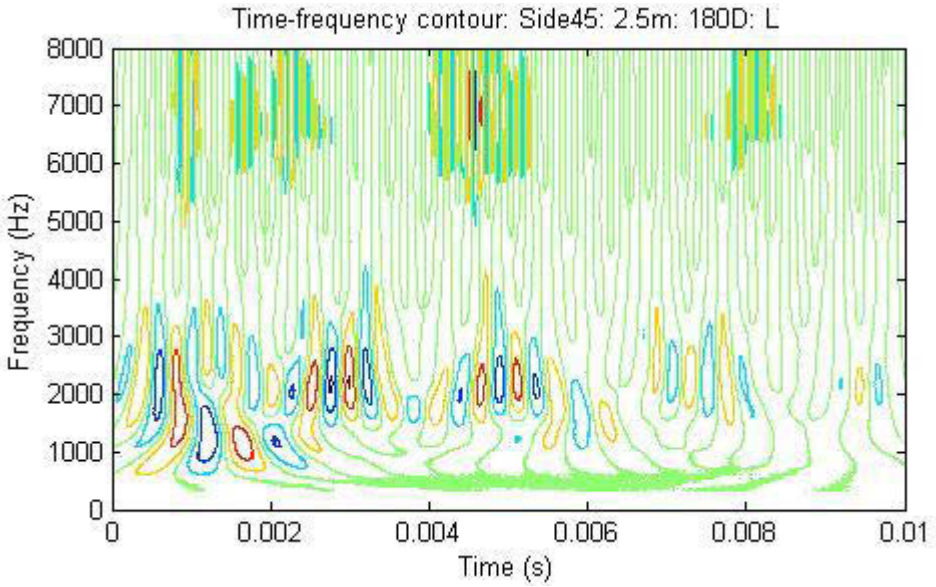

Figure 5.32 Time frequency contour of the axial displacement component for case 3 at sensor 2.5m from the bottom pole with 180° orientation

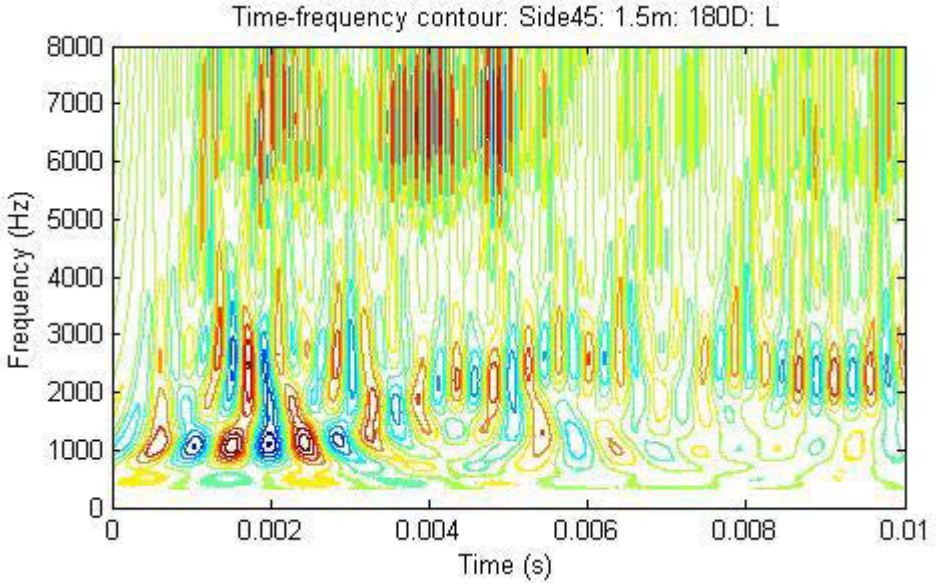

Figure 5.33 Time frequency contour of the axial displacement component for case 3 at sensor 1.5m from the bottom pole with 180° orientation

Figure 5.36 shows the phase velocity curves for this condition. From the curves, it is clear that the summation of the longitudinal components at 0° and 180° represent the pure longitudinal wave as it agrees significantly well with the analytical longitudinal wave velocity. On the other hand, the summation of the radial components at 0° and 180° represent the pure flexural wave. Nonetheless, the error for the flexural wave is more compared to the error in the longitudinal wave. The sensors at 1.5m have more

error when approximating the flexural wave velocity. In contrast, the wave velocities calculated from the wavelengths have better approximation when determining the phase velocity of the flexural wave. Hence, if the sensors are placed at 0° and 180° orientations instead of the 90°, then it is better to eliminate the flexural wave rather than the longitudinal wave. As a result, the sensors should be oriented in the longitudinal directions at these locations.

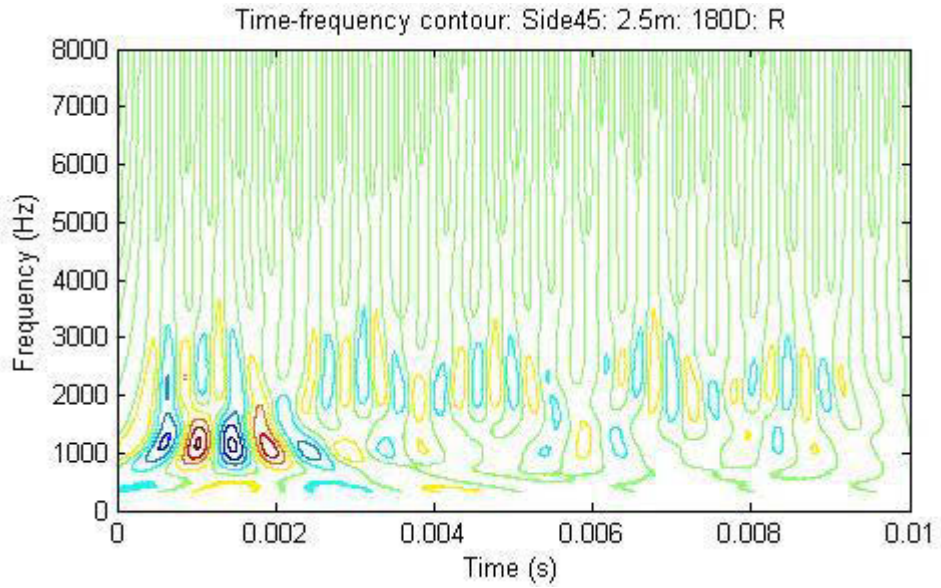

Figure 5.34 Time frequency contour of the radial displacement component for case 3 at sensor 2.5m from the bottom pole with 180° orientation

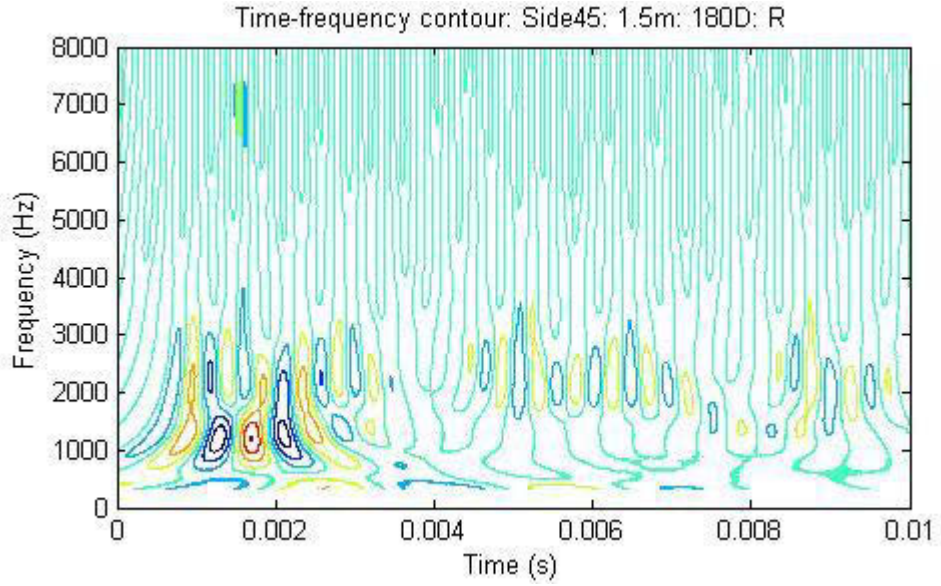

Figure 5.35 Time frequency contour of the radial displacement component for case 3 at sensor 1.5m from the bottom pole with 180° orientation

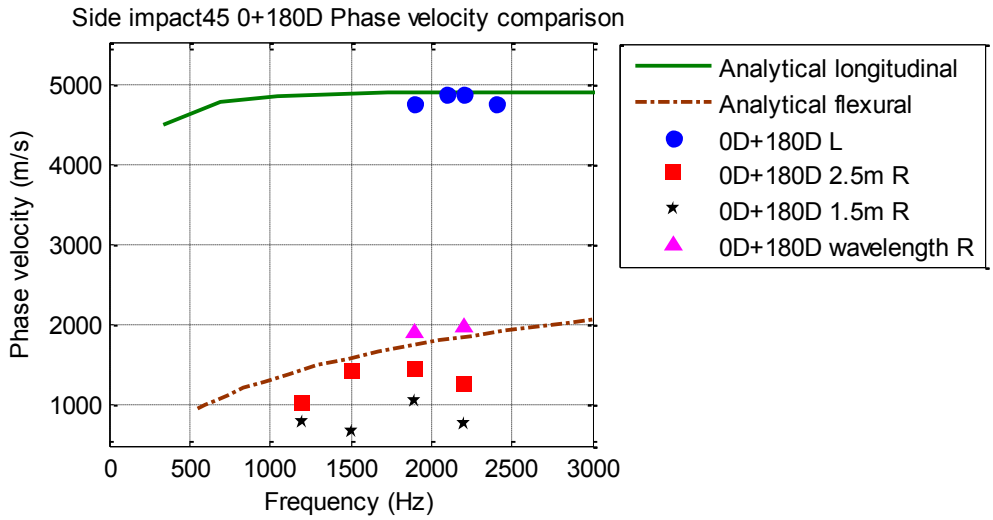

Figure 5.36 Phase velocity comparison for case 3 for the summation of 0° and 180° orientations

5.4.3 Calculation of embedment length

The embedded length can be predicted if the reflection peak can be determined. For the longitudinal wave, it is easier to find the reflection peak compared to the flexural wave. To calculate the embedded length, it is essential to find out the wave velocity between the sensors. After obtaining the velocity, the embedded length can be determined by the following formula

$$L_{emb} = \frac{V_{ph}.t}{2} - l_1 \tag{5.8}$$

where V_{ph} = velocity determined from Equation (5.6) for a particular frequency, t = time difference between first arrival and reflection peak and l_1 = distance between the sensor and ground level.

To select the reflection peak, it is important to remember that the first arrival of the wave will reach sensor 1 or S1 (the sensor at 3m from the bottom of the pole) first and then sensor 2 or S2 (the sensor at 2m from the bottom of the pole), but after reflection it will reach sensor 2 first [178]. Therefore, the embedded length for case 1 can be determined. All the phase velocities calculated for case 1 are used to find the embedded length of the pole. An example is illustrated to select the reflection peak in Figure 5.37. The time-CWT coefficient plots of sensor S3L90 at the frequency of 1,500 Hz is chosen for this purpose.

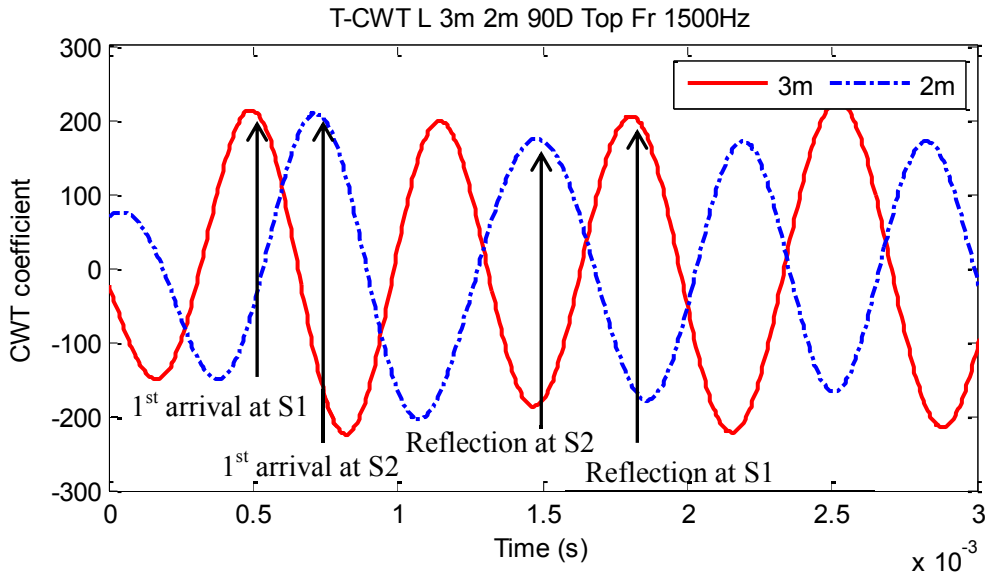

Figure 5.37 The selection of first arrival and reflection peaks from two sensors (case 1)

The first arrival of the peak between two sensors is used to calculate the phase velocity as described in Section 5.4.2. On the other hand, the embedded length is calculated from the same sensors after determining the velocity. When the reflection peak is selected, the embedment length can be obtaining from Equation (5.8). The embedment length calculated at different frequencies and at various sensors are summarised in Table 5.4. The actual embedded length is 1m as shown in Figure 5.1.

Table 5.4 Calculation of embedded length for case 1

Location & orientation	Frequency (Hz)	Velocity (m/s)	L_{emb} from S1 (m)	L_{emb} from S2 (m)	Error (S1) %	Error (S2) %
0° L	1,300	4347.83	0.88	0.72	12	28
0° L	1,700	4761.90	1.10	1.06	10	6
90° L	1,200	4651.16	1.03	0.93	3	7
90° L	1,500	4651.16	1.06	0.80	6	20
90° L	1,800	4878.05	1.17	1.23	17	23
0° R	1,300	6060.61	0.53	0.98	47	2
0° R	1,700	4878.05	0.72	0.39	28	61

As depicted in the table, the range of error is considerably broad depending on the sensors and frequencies. However, the sensors at the 90° orientation show notably best result for all the common frequencies compared to the 0° orientation.

For case 2, only one frequency (2,600 Hz) is used to calculate the embedded length as the wavelength at this frequency is lower than the distance between sensors SθL2.5 and

SθL1.5. If the wavelength is higher than the distance between two sensors, then the peak selection is different and will be presented in the next section of this chapter. For this case, the reflection peak is selected from the beginning of the group as described earlier and an example is presented in Figure 5.38. The beginning of the group can be determined from the fact that due to pulse distortion, the amplitude of the consecutive peaks will reduce until there will be an increase in amplitude of certain peak. This higher amplitude peak, corresponding to the previous peak is considered as reflection or this peak is the beginning of the reflected wave [144]. The embedment length calculated for this particular situation is presented in Table 5.5.

Table 5.5 Calculation of embedded length for case 2

Location & orientation	Frequency (Hz)	Velocity (m/s)	L_{emb} from S1 (m)	L_{emb} from S2 (m)	Error (S1) %	Error (S2) %
0° θ	2,600	2309.09	0.83	1.50	17	50

The embedded length calculation for the flexural wave shows more error and the details of determining the embedded length for the flexural wave by two different signal processing techniques will be presented later in this chapter.

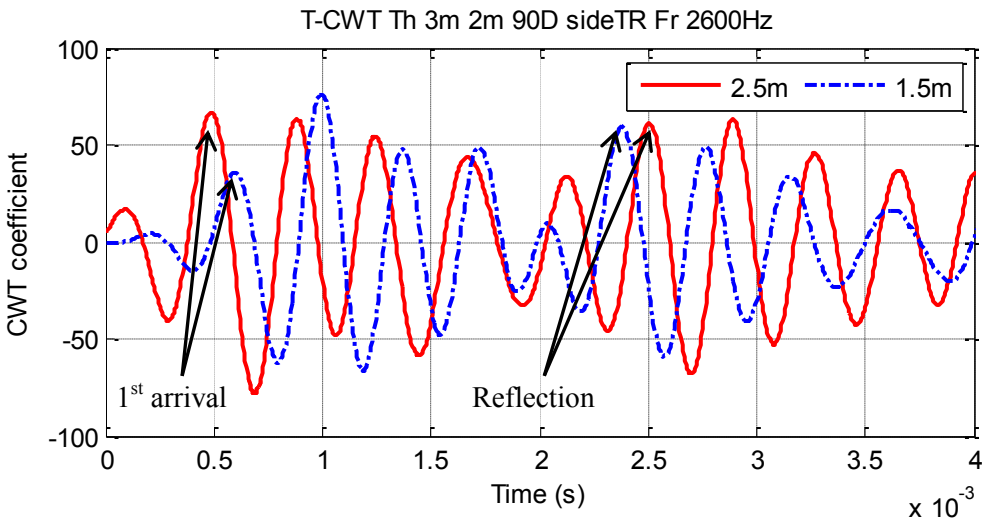

Figure 5.38 The selection of first arrival and reflection peak from two sensors (case 2)

For case 3, two conditions can be taken into account. The first one is the pure longitudinal wave and secondly, the pure flexural wave. The former situation can be found for the longitudinal displacement component at 90° orientation and also for the summation of the axial displacement component at 0° and 180° whereas the latter condition or the pure flexural behaviour can be seen at the tangential component at 90° orientation and the summation of the radial component of 0° and 180° orientation. For the pure longitudinal wave, the reflection peak can be determined in the same way mentioned for the case 1, while the method described for case 2 is used to select the reflection peak for the pure flexural behaviour. The calculated embedded length for the pure longitudinal case is tabulated in Table 5.6

Table 5.6 Calculation of embedded length for case 3 (longitudinal wave)

Location & orientation	Frequency (Hz)	Velocity (m/s)	L_{emb} from S1 (m)	L_{emb} from S2 (m)	Error (S1) %	Error (S2) %
90° L	1,700	4651.16	1.05	0.87	5	13
90° L	2,000	4761.90	1.04	0.70	4	30
90° L	2,400	5128.21	0.55	0.58	35	42
0°L+180°L	1,900	4761.90	1.05	0.78	5	22
0°L+180°L	2,100	4878.05	1.13	0.65	13	35
0°L+180°L	2,200	4878.05	1.17	0.59	17	41
0°L+180°L	2,400	4761.90	0.52	0.49	48	51

From the table, it can be noticed that the range of error is again very high. The error is more at the frequencies beyond 2,000 Hz. The main reason can be that the input frequency is supposed to excite the frequency band up to 2,000 kHz. However, the frequencies above 2,000 kHz are chosen sometimes due to selection of the common frequencies between the sensors. The error from sensor 2 is again more than the same of sensor 1. The reason is again not very clear. The best results are obtained at 1,700 and 1,900 Hz owing to the fact that both frequencies are below the excited frequency range. Therefore, it can be concluded that, in general, it is better to choose the common frequencies between two sensors which are below the excited frequency range.

The calculated embedded length for the pure flexural case is depicted in Table 5.7. The error for the flexural wave propagation is very obvious as also seen from the previous case. Lower frequencies are not used due to their long wavelength. However, when the excitation frequency is below 2,000 Hz (and wavelengths are long and below this range) and thus, large errors are observed and the results are not very satisfactory.

Table 5.7 Calculation of embedded length for case 3 (flexural wave)

Location & orientation	Frequency (Hz)	Velocity (m/s)	L_{emb} from S1 (m)	L_{emb} from S2 (m)	Error (S1) %	Error (S2) %
90° θ	2,200	1977	0.50	0.82	50.32	18.04
0°R+180°R	1,900	1900	1.77	2.70	76.80	169.80
0°R+180°R	2,200	1977	2.37	3.89	136.50	288.97

From the above discussions, it can be summarised that the velocity of the longitudinal wave can be determined very efficiently and the wavelength method can also be used to calculate the flexural wave velocity between two sensors. Even though the arrival peak can be detected correctly to calculate the phase velocity, the selection of reflection peak is not very easy for the propagation of both longitudinal and flexural waves. Nevertheless, the longitudinal wave is more accurate compared to the flexural wave. Subsequently, in the next section another technique is used for the flexural wave propagation which is a little different to the technique mentioned here. Also, in conjunction with the CWT, the SKM is also used for the flexural wave propagation and a comparison is made between these two signal processing techniques in terms of calculating the phase velocity and embedment length of the timber pole.

5.5 Calculation of embedment length for the flexural wave propagation

5.5.1 Numerical properties

For the comparison of two signal processing techniques, the CWT and the SKM, purely flexural wave propagation is considered or in other words the impact is applied in the transverse direction. Therefore, pure flexural wave will be generated. If inclined impact is used then it is better to separate the flexural wave (based on the sensor location and orientation as described in the last section) and then this procedure can be applied. For this particular situation, practical considerations are taken into account. Hence, the length of the pole is taken as 12 m with a diameter of 30 cm. The density and the Poisson's ratio are 900 kg/m^3 and 0.3, respectively. The impact is imparted at 3.5m from the bottom of the pole or 1.5 from the soil level as the embedment length is considered as 2 m. Practically, it is the most comfortable location for the manual impact. The impact direction is transverse and the sensors are orientated in the longitudinal direction. Two sensors are used, one is placed at 1m from the soil level

(Sensor 1 or S1) and the second one is placed at the soil level (Sensor 2 or S2). The impact duration is 900 µs and the amplitude is 1,576N.

5.5.2 Velocity calculation

The FFT of the sensors will represent the frequency component of the signal at the sensor as demonstrated in Figure 5.39. Since the impact duration is increased in this situation compared to the previous section, thereby the frequency band is reduced. For this condition, the frequency band is again below 2000 Hz. However, most of the energy can be seen up to 1000 Hz. This impact duration for the manual impact is mainly controlled by the materials of the hammer tip. It is found in the UTS lab that if the Teflon tips are used in the impact hammer, then the impact duration is usually approximately 900 µs while by the steel tip the frequency band can be increased and the impact duration reduced to 500 - 600 µs.

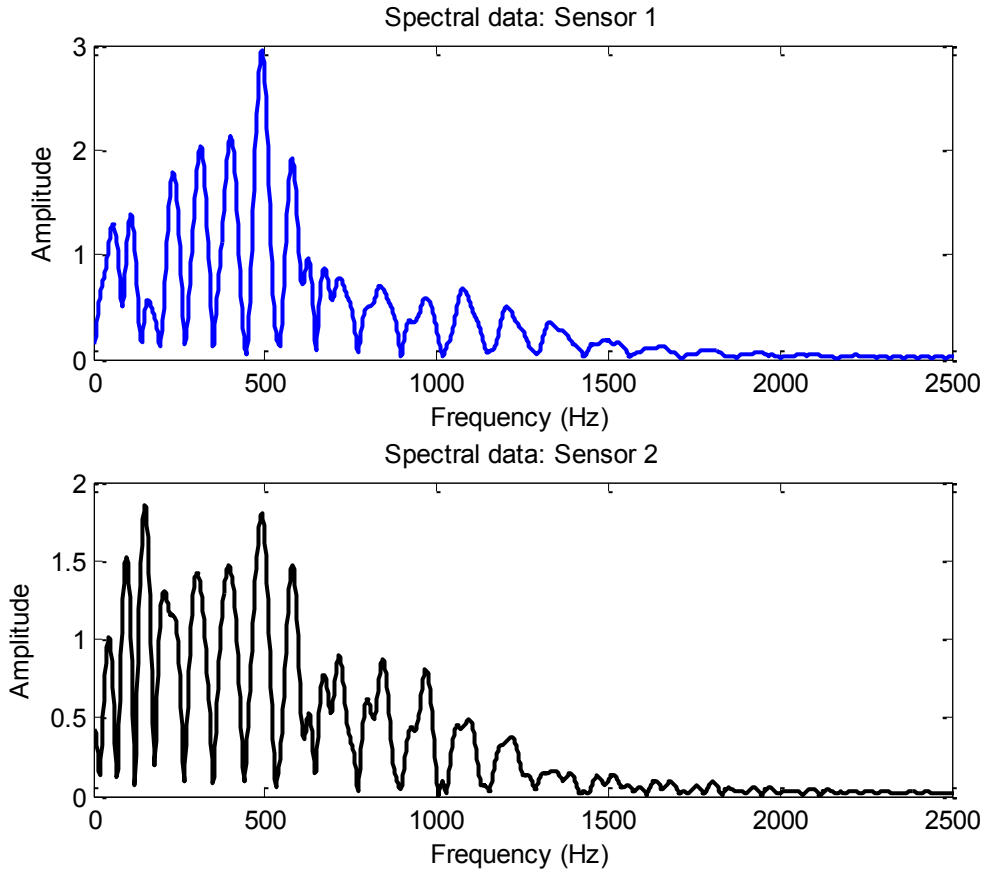

Figure 5.39 Frequency content of the applied signal at the sensors

To calculate the velocity, CWT or SKM is applied at certain frequencies (chosen from FFT) which are again chosen from the common frequencies between two sensors. For CWT, these frequencies can also be chosen from the CWT plot directly. However, for SKM, FFT is usually used to choose the frequencies. After selecting these frequencies, the time-CWT coefficient or time-SKM correlation plot is drawn and velocity is calculated between two sensors. The time difference of the first arrival or the first peak of two sensors is determined and the velocity is calculated from Equation (5.6). For this purpose, the wavelength consideration is ignored. Instead, only the first peak is taken into account. Figure 5.40 gives the time coefficient plots for both CWT and SKM and also the first arrival of these two peaks are shown by arrows. Same phase is considered from both sensors to determine the phase velocity. In the figure, only 944 Hz is shown and the other time coefficient plots at other common frequencies, such as, 586, 692, 796, 841, 1003, 1069, 1152, 1240, 1365 and 1675 Hz are presented in Appendix E.

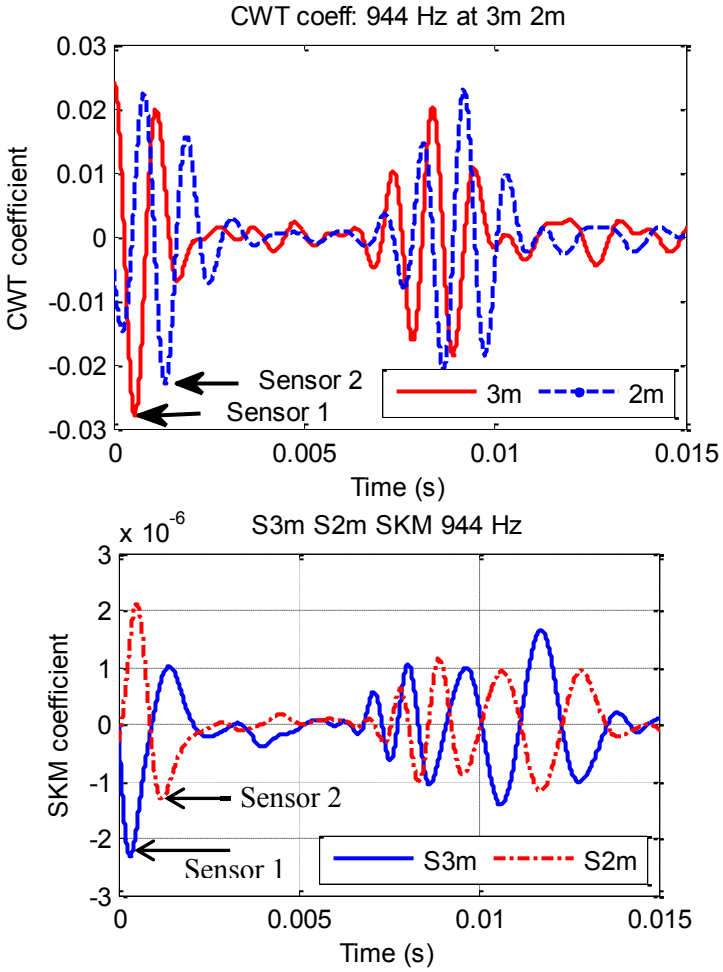

Figure 5.40 Time-coefficient plots at 944 Hz (CWT: top plot, SKM: bottom plot)

Figure 5.41 shows the calculated phase velocity by CWT and SKM and compared with the guided wave theory and also with the Bernoulli-Euler beam theory (EBT). As in the low frequency, the Bernoulli-Euler theory is also notably accurate; hence, both are shown in the figure. It is observed that the velocity is predicted better by CWT compared to the same by SKM and also the calculated velocities are closer to the guided wave curve than the Bernoulli-Euler theory. Therefore, even though the wavelength is not considered, the prediction of phase velocities is still satisfactory.

5.5.3 Calculation of embedment length

To determine the embedment length, two features are considered as mentioned earlier. Firstly, the reflected peak can be determined from the fact that due to pulse distortion the amplitude of the consecutive peaks will reduce until there will be an increase in amplitude of certain peak. This higher amplitude peak, corresponding to the previous peak is considered as reflection or this peak is the beginning of the reflected wave. Secondly, the arrival of the wave will reach sensor 1 first in the first path and then sensor 2, but after reflection it will reach sensor 2 first. Also, the same phase is considered to determine the first arrival and reflection of the same sensor. An example of choosing the first arrival and reflection is shown in Figure 5.42 and Figure 5.43. Solid arrow shows the first arrival and dashed arrow shows the reflection.

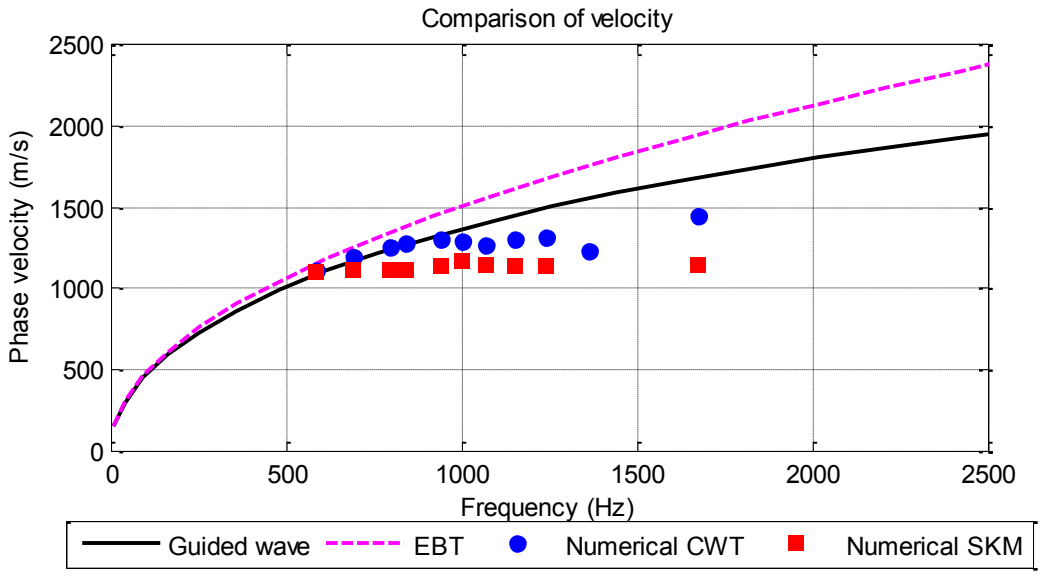

Figure 5.41 Phase velocity comparison among GW, 1D theory and numerical results

It can be seen that according to the aforementioned method, the reflection should be at approximately 0.004s for sensor 1 (bottom plot of Figure 5.43). However, it is not chosen as reflection, because this peak arrives in sensor 1 before sensor 2. Dashed arrow is showing the reflection peak which is after the reflection of sensor 2 and also satisfies the aforementioned method of choosing reflected peak.

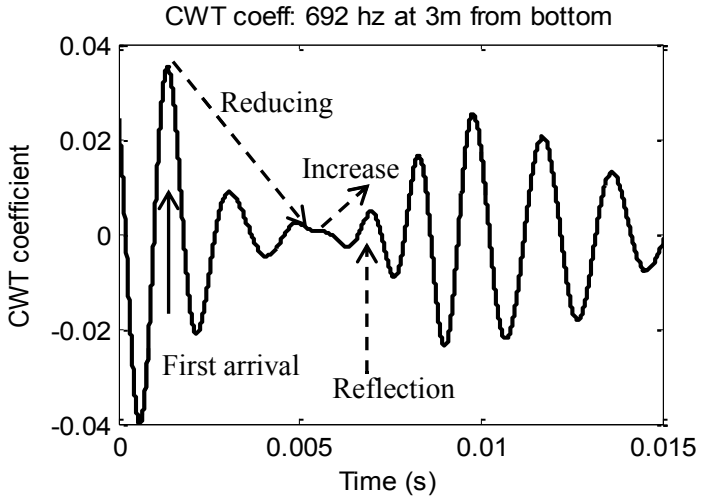

Figure 5.42 Time-coefficient plot at 692 Hz (CWT)

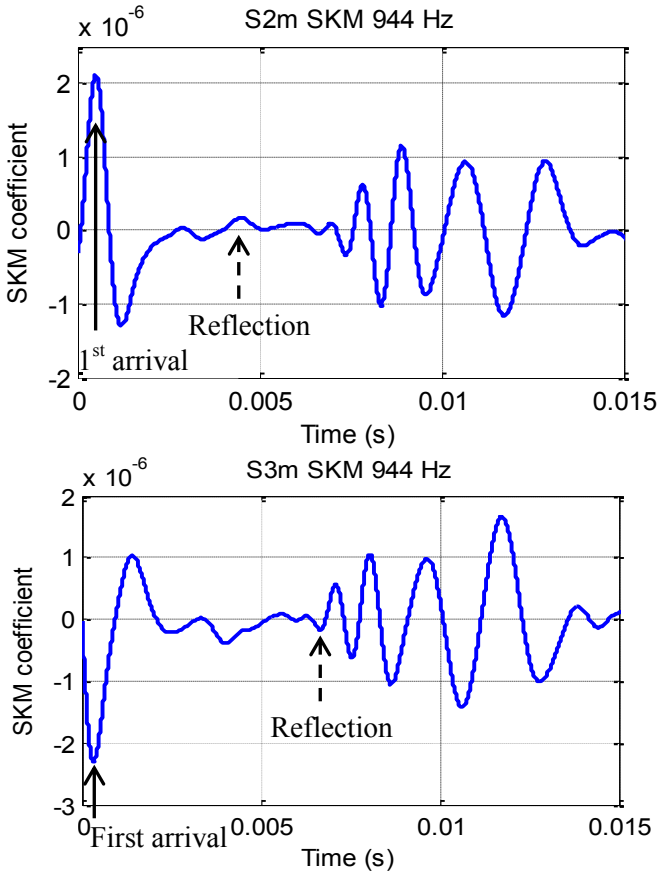

Figure 5.43 Time-coefficient plot by SKM at 944 Hz (top plot: sensor 2, bottom plot: sensor 1)

The calculated phase velocity and embedded length by CWT and SKM are presented in Table 5.8 and Table 5.9, respectively. The actual embedded length is 2m and the errors related to both sensors are indicated as well. It can be seen from Table 5.8 that, even though, the velocity approximation is in good agreement with CWT, the error related to calculating the embedded length by CWT is very high. In low frequency, the approximation is significantly high. Only two frequencies, 1,152 and 1,240 Hz show considerably better results compared to the other frequencies. Therefore, in summary, in CWT, it is hard to choose the reflection peak to calculate the embedded length. Hence, even if the wavelength is considered, as mentioned earlier, to obtain the more accurate velocity, the problem will still exist when calculating the embedment length as selecting the reflection peak is the main challenge.

Table 5.8 Calculation of embedded length by CWT

Frequency (Hz)	Velocity (m/s)	L_{emb} from S1 (m)	L_{emb} from S2 (m)	Error (S1) %	Error (S2) %
586	1117.32	3.19	3.89	59.64	94.41
692	1197.60	2.82	3.36	41.02	67.81
796	1250.00	3.11	3.81	55.47	90.31
841	1275.51	3.23	3.95	61.58	97.39
944	1298.70	1.71	3.40	14.45	69.97
1003	1290.32	1.70	2.60	14.84	30.16
1069	1273.89	1.67	2.59	16.40	29.30
1152	1298.70	1.71	2.14	14.29	6.82
1240	1315.79	1.75	2.15	12.34	7.73
1365	1233.05	1.62	2.31	18.96	15.29
1675	1449.28	1.47	2.72	26.27	36.23

Table 5.9 Calculation of embedded length by SKM

Frequency (Hz)	Velocity (m/s)	L_{emb} from S1 (m)	L_{emb} from S2 (m)	Error (S1) %	Error (S2) %
586	1098.90	2.63	2.21	31.46	10.44
692	1117.32	2.40	2.25	19.97	12.57
796	1111.11	2.46	2.24	22.78	12.08
841	1111.11	2.47	2.22	23.47	10.97
944	1129.94	2.58	2.26	28.95	13.14
1003	1169.59	2.71	2.37	35.53	18.57
1069	1142.86	2.65	2.30	32.43	14.86
1152	1136.36	2.28	2.28	13.92	13.92
1240	1129.94	2.27	2.27	13.70	13.42
1675	1142.86	2.35	2.29	17.43	14.43

In CWT, the low frequencies suffer more in terms of determining the embedment length; however, the calculated phase velocity is very accurate in low frequencies as can be seen from Figure 5.41. In CWT, the group behaviour is not very clear at every frequency and if the wavelength is very long which is normal in low frequencies, the calculation of phase velocity is not accurate enough. In contrast, even though the wavelength is long, SKM is not affected by it. The error in calculating phase velocity by SKM is substantially high in comparison with the same by CWT. Nevertheless, the embedment length calculation agrees well to a great extent. Similar to CWT, the best approximation for embedment length are found at the frequency of 1,152 and 1,240 Hz in SKM. Moreover, it can be noticed that the embedded length is overestimated at every frequency when SKM is used. In contrast, no particular trend can be found in CWT. Therefore, if the embedment length is the point of interest, then SKM is better to be used for the flexural wave propagation. On the other hand, provided that the phase velocities need to be determined, the CWT can be used with sufficient accuracy.

5.6 Conclusions

This chapter addresses, comprehensively, the three dimensional behaviour of the stress wave propagation in an isotropic cylindrical structure and focuses on the broadband low frequencies. This is due to the fact that practically low frequencies are used very frequently, and for the low frequency range the group behaviour cannot be seen clearly. The stress wave behaviour is different in three dimensions and the chapter discusses broadly the idea of taking advantage of the differences of its properties in three orthogonal directions of the cylindrical structures.

Similar to the previous chapter, this one also validates that the fully transverse impact generates purely flexural wave whereas the top impact at the middle of the cross-section produces purely longitudinal wave. Inclined load has both the vertical and horizontal components and thus, generates both waves. It is also revealed that longitudinal wave is not affected by the angle of the impact load as it is symmetrical. Additionally, longitudinal wave has radial and longitudinal components of displacement at any point on the cylinder and the longitudinal components are in the same phase between two points which are 180° apart along the circumference from the first point. Whereas, the radial components are 180° out of phase for the same two points.

However, the flexural wave is affected by the angle from the impact location. At the line of the impact location and the line 180° apart along the circumference from the impact location, have both the longitudinal and radial components of the displacement while axial and longitudinal components of displacement are zero at a position 90° around the circumference from the impact location. Also, only tangential component is present at the 90° location. In contrast with the longitudinal wave, the radial components are in the same phase at 0° and 180° from the impact location while longitudinal components are in the opposite phase due to the anti-symmetrical properties of flexural wave.

For the inclined impact or any cases, where the superposition of the longitudinal and flexural waves occurs, the separation can be done due to the fact that the longitudinal/radial and tangential components of displacement at 90° around the circumference from the impact location should represent the pure longitudinal and pure flexural wave, respectively. Another way of separating the longitudinal and flexural waves is by the summation of the longitudinal and radial components of displacement at 0° and 180° from the impact location. The former will represent purely longitudinal waves and the latter shows the purely flexural behaviour.

Different signal processing techniques can be used to calculate the phase velocity of the waves and this chapter evaluates and compares continuous wavelet transform and short kernel method. To calculate the phase velocity, time-coefficient plots are drawn and for the flexural wave, group behaviour is observed. Therefore, the determination of the reflection peak is not easy and two approaches were discussed regarding these issues. It is also shown that CWT predicts the phase velocity better than the SKM. In general, SKM is only used for the flexural wave propagation and thereby, CWT is sufficient to calculate the velocity and embedded length of the pole while longitudinal wave is propagating. In contrast, for the flexural wave propagation, the CWT predicts the phase velocity better; nevertheless, selecting the reflection peak is not easy and therefore, the approximation of embedment length by CWT is poor. On the other hand, the velocity prediction by SKM is not very precise; however, the embedded length can be determined more accurately by this method.

In this chapter, only isotropic behaviour of the wave was discussed for the cylindrical structures. However, the separation techniques of the longitudinal and flexural waves

can also be used for the transversely isotropic material, as transversely isotropic material also shows the symmetric behaviour of the wave. Besides, the displacement components have the same properties as the isotropic material. Despite this, transversely isotropic material has more branches in low frequencies and thus, suffers more from dispersion. The reduction of the dispersion behaviour was discussed in Chapter 3 and the separation of the branches can be achieved if the wave packet is used as the input frequency as reported in Chapter 4.

Chapter 6

6 Conclusions

6.1 Summary

This thesis focuses on the guided wave propagation in a cylindrical structure to emphasize the importance of analysing the analytical and numerical solutions in order to understand the inside of stress wave propagation in a timber pole/pile. To examine the guided wave behaviour, different methods are employed due to the fact that every technique has its own advantages and limitations. The first method used to study the GW behaviour involved solving the actual theory derived from the constitutive equation of material motion. Some numerical schemes were applied for solving the analytical equations. The second method can be regarded as semi-analytical procedure and known as the Spectral finite element method. There are different theories available related to this method which were compared to choose the most appropriate one that reflects the actual field condition. Lastly, the popular numerical technique, namely, the Finite element method, was implemented to simulate the actual field condition, and two signal processing techniques were performed on the signal obtained numerically.

The analytical equation is solved in the frequency domain and is very accurate to develop the dispersion curves and mode shapes of the GW. However, the time domain reconstruction is not very precise owing to the simplification of the boundary condition. Applying the mixed boundary conditions such as the partial embedment of the timber pole leads to complexity during solving the equation analytically. This limitation can easily be overcome using the SFEM since any arbitrary boundary conditions can be

implemented properly. Accordingly, the finite length element is possible to be modelled in SFEM without any complication. However, the SFEM for the cylindrical structures are usually based on the one dimensional assumption and thus, the three dimensional behaviour of the stress wave is absent in this method. In contrast, the FEM comprehensively describes the three dimensional characteristics of different types of wave and therefore, the distinct properties of various wave clusters in three orthogonal directions are beneficial on the ground of sensor arrangement that attributes to the separation of wave. Although the time domain results of FEM are very useful, it is difficult to acquire the dispersion curves using this technique. Whereas the SFEM shows sufficient accuracy for plotting the dispersion curves which, however, is only accurate up to a certain frequency range. Therefore, all the three methods are investigated and discussed in this thesis which led to the conclusions on the features of GW propagation inside the timber pole/pile that resulted in suggesting the experimental set up for non-destructive evaluation of timber pole/pile.

6.2 Main findings

Based on the results obtained from the aforementioned three methods, the following conclusions are drawn.

1. A wide variety of material properties is observed among different species of timber pole. The modulus of elasticity and density change the cut-off frequencies of different branches, however, the trend remains similar. With the increase of modulus of elasticity and the decrease in density, the phase velocity and the value of cut-off frequency of different branches increase. The Poisson's ratio has very little effect on the dispersion curves.

2. The properties of timber are affected by temperature and moisture content, and the modulus of elasticity reduces with the increase in these two parameters. Sometimes, moisture content outside the pole is different from that inside the pole. Accordingly, the stiffness varies within the pole that leads to the variation of wave velocity. However, the change in velocity is not very significant and therefore, can be ignored.

3. The partial embedment of soil around the timber pole is responsible for the leakage of energy from the system which results in the attenuation of the wave amplitude. It is found that the attenuation increases with the increase in the stiffness of soil.

Nonetheless, the phase or energy velocity is not affected by the surrounding medium except in the very low frequency range.

4. It is important to consider timber as an anisotropic material in order to obtain the correct dispersion curves as the isotropic material simplification can lead to substantial amount of error. For instance, the numbers of branches in the anisotropic material modelling are more in comparison with the same of isotropic material model while dealing with the same frequency range. As a result, more dispersion may be observed in the anisotropic modelling. Additionally, due to the complexity involved in solving the analytical equation for an orthotropic material, some simplification can be employed on the material properties of timber that makes it a transversely isotropic material. It is shown that the transversely isotropic assumption is considerably accurate for the longitudinal wave propagation and also in the case of low frequency flexural wave transmission. However, it is recommended to use the actual orthotropic material modelling provided that the flexural wave is excited in the high frequency range.

5. Based on the analytical energy velocity curve, the input frequency can be selected for the experimental/field test. In a transversely isotropic energy velocity curve, all the branches of the flexural and longitudinal wave have a constant maximum velocity under a certain frequency range. It is suggested to choose an input frequency around this range (related to any branch) in order to reduce the effect of dispersion which is accountable for the distortion of the signal. The distortion can be further reduced by increasing the number of cycles of the input frequency and also by decreasing the sensors' distances.

6. Even though the correct input frequency is chosen, some modes may show significant amount of dispersion. This can be seen from the contribution of individual modes and can be eliminated based on the normalised displacement profiles. Normalised displacement profiles illustrate the normalised amplitude of the axial, radial and tangential components of displacement. By knowing the zero amplitude of any displacement component related to the most dispersive mode(s), the sensor orientation can be selected. It is shown that the sensor can be oriented in the direction of the zero amplitude component of displacement on the surface of the pole to minimise the dispersive behaviour of the signal.

7. For the high frequency input signal, the attenuation of some modes is notably high. As a result, it is possible that the sensors may not be able to capture the reflection of some modes due to the attenuation related to the corresponding one. Therefore, it is advised to analyse the attenuation curves properly before choosing the input frequency. Specially, if the desired modes are losing all of the energy on a particular input frequency, it is better to select another input frequency based on the energy velocity curves. Similarly, some of the most dispersive modes can also be removed by choosing the input frequency associated with high attenuation of these modes.

8. The SFEM models the actual timber pole situation i.e. the length of the pole is finite unlike the analytical solution, and the partial embedment is also considered. It is depicted that the longitudinal waves or modes are less affected by the presence of soil, whereas mode conversion can be illustrated in the flexural wave propagation. Consequently, the flexural wave suffers more from dispersion compared to the longitudinal wave. In addition, unlike the analytical solution, the impact location and orientation can easily be implemented using the SFEM. It is observed that if the impact is imparted vertically, only the longitudinal and contraction modes propagate, while provided that the impact is applied transversely, only the shear and flexural modes propagate. It is also shown that the inclined impact imparted in the middle section of the pole will lead to the generation of all the modes (longitudinal, flexural, contraction and shear). Also, both the upward and downward travelling waves are present in this situation and as a result, the signal is distorted the most in this loading condition.

9. As inclined impact at the middle of the section of the pole is the most practical situation, hence, it is important to separate the longitudinal and flexural wave to clarify the signal. To achieve this, FEM is used for the low frequency input signal based on the isotropic model to suggest a three dimensional sensor array. It is proved that for the inclined impact or any cases, where the superposition of the longitudinal and flexural waves occurs, the separation can be done by placing the sensors axially and tangentially at the position which is located at 90° around the circumference from the impact location. The former should represent the pure longitudinal wave while the latter reflects the pure flexural behaviour. Another way of separating the longitudinal and flexural waves can be achieved by the summation of the longitudinal and radial

component of displacement at 0° and 180° from the impact location in order to obtain the pure longitudinal and flexural waves, respectively.

10. Two signal processing techniques, namely, CWT and SKM are compared in terms of calculating the phase velocity of the wave and the embedment length of the timber pole. CWT predicts the phase velocity better than the SKM. In general, SKM is only used for the flexural wave propagation and thereby, CWT is sufficient to calculate the velocity and embedded length of the pole when longitudinal wave is propagating. In contrast, the CWT predicts the phase velocity better in the case of the flexural wave propagation; however, the approximation of embedment length by CWT is poor. On the contrary, the velocity prediction using SKM is not very precise; nevertheless, the embedded length can be determined more accurately.

6.3 Recommendations for future work

Based on the current study, several recommendations can be made as further studies.

1. Analytical equations can be solved for the orthotropic material modelling as it is advised to use it for the flexural wave propagation in the high frequency range. Therefore, all the dispersion curves and mode shapes can be plotted for this condition and the same procedure as explained in this thesis can be employed to select the input frequency, number of cycles of the input signal, sensor locations and orientations, etc.

2. Since wrap around problem was observed in the SFEM for the real field situation, i.e. the inclined impact imparted in the middle of the section, hence, wavelet based SFEM can be applied instead of using the FFT based SFEM for this particular situation.

3. The separation of longitudinal and flexural waves is based on the numerical modelling of an isotropic pole. Even though the same strategy can be used for the transversely isotropic and orthotropic model, it is better to extend the model for the anisotropic behaviour to verify the procedure.

4. Experimental verification is needed for all the main findings discussed in this thesis.

References

1. Nguyen, M., G. Foliente, and X.M. Wang, *State-of-the-Practice & Challenges in Non-Destructive Evaluation of Utility Poles in Service.* Key Engineering Materials, 2004. **270**: p. 1521-1528.
2. Ariyaratne, W. and K. Crews, *Design and Asset Management of Bridges.* Post Graduate Lecture Notes, 2003.
3. Lo, K.F., S.H. Ni, and Y.H. Huang, *Non-destructive test for pile beneath bridge in the time, frequency, and time-frequency domains using transient loading.* Nonlinear Dynamics, 2010. **62**(1): p. 349-360.
4. Baker, C.N., *Drilled shafts for bridge foundations*. 1993: Federal Highway Administration.
5. Hearne, T.M., L.C. Reese, and K.H. Stokoe, *Drilled-shaft integrity by wave propagation method.* Journal of the Geotechnical Engineering Division, 1981. **107**(10): p. 1327-1344.
6. Douglas, R.A., J.L. Eddy, and H.E. Wahls, *On transforms and the dispersion computations used for evaluating layer properties.* ASTM special technical publication, 1989(1026): p. 612-627.
7. Holt, J.D., *Comparing the fourier phase and short kernel methods for finding overall lengths of installed timber piles*. 1994, North Carolina State University.
8. Wang, H. and T. Chang. *Non-destructive evaluations of in-service concrete piles by flexural wave approach*. 2008: Ios Pr Inc.
9. Wang, H., *Theoretical evaluation of embedded plate-like and solid cylindrical concrete structures with guided waves*. 2004, Northwestern University.
10. Hanifah, A.A., *A theoretical evaluation of guided waves in deep foundations.* Civil Engineering. Evanston, Northwestern University, 1999. **215**.
11. Popovics, J.S., *Some Theoretical and Experimental Aspects of the Use of Guided Waves for the Nondestructive Evaluation of Concrete*. 1994, Pennsylvania State University.
12. Chao, H.C., *An experimental model for non-destructive evaluation on pile foundations using guided wave approach*. 2002, Ph. D. Dissertation, Northwestern University, Evanston, IL.
13. Finno, R., et al., *Guided wave interpretation of surface reflection techniques for deep foundations.* Italian Geotechnical Journal, 2001. **35**(1): p. 76-91.
14. Committe, G.-I.D.F., *Nondestructive evaluation of drilled shafts*, in *Journal of geotechnical and geoenvironmental engineering*. 2000. p. 92-95.
15. Gerhards, C.C., *Effect of moisture content and temperature on the mechanical properties of wood: An analysis of immediate effects.* Wood and Fiber Science, 1982. **14**(1): p. 4-36.
16. Hanhijiirvi, A., *Advances in the knowledge of the influence of moisture changes on the long-term mechanical performance of timber structures.* Materials and Structures, 2000. **33**(1): p. 43-49.
17. Lenth, C. and R. Sargent. *Investigating the influence of moisture content and temperature on the tensile stiffness of radiata pine*. 2004.
18. Dinwoodie, J.M., *Timber, its nature and behaviour*. 2000: Taylor & Francis.

19. Tallavo, F., G. Cascante, and M.D. Pandey, *Estimation of the Probability Distribution of Wave Velocity in Wood Poles.* Journal of Materials in Civil Engineering, 2011. **23**: p. 1272-1280.
20. Ross, R.J., et al., *Inspection of timber bridges using stress wave timing nondestructive evaluation tools.* Madison: US Department of Agriculture, Forest Service, Forest Products Laboratory, Report FPL-GTR, 1999. **114**.
21. Ellwood, E.L., *Properties of American beech in tension and compression perpendicular to the grain and their relation to drying*. 1954: Yale University.
22. Palka, L., *Predicting the effect of specific gravity, moisture content, temperature and strain rate on the elastic properties of softwoods.* Wood Science and Technology, 1973. **7**(2): p. 127-141.
23. Wu, Q. and M.R. Milota, *Rheological behavior of Douglas-fir perpendicular to the grain at elevated temperatures.* Wood and Fiber Science, 1995. **27**(3): p. 285-295.
24. Oliver, A., U.o.T. Civil, and M.E. Dept, *A Model of the Behaviour of Wood as it Dries:(with Special Reference to Eucalypt Materials)*. 1991: Civil & Mechanical Engineering Department, Faculty of Engineering, University of Tasmania.
25. Bucur, V., *Acoustic of wood.* Spreinger series in wood sciences, Editors: TE Timell, R. Wimm, 2006.
26. Knapic, S., F.t. Tavares, and H. Pereira, *Heartwood and sapwood variation in Acacia melanoxylon R. Br. trees in Portugal.* Forestry, 2006. **79**(4): p. 371-380.
27. Metsa-Kortelainen, S. and H. Viitanen, *Effect of fungal exposure on the strength of thermally modified Norway spruce and Scots pine.* Wood Material Science and Engineering, 2010. **5**(1): p. 13-23.
28. Metsa-Kortelainen, S., T. Antikainen, and P. Viitaniemi, *The water absorption of sapwood and heartwood of Scots pine and Norway spruce heat-treated at 170 C, 190 C, 210 C and 230 C.* European Journal of Wood and Wood Products, 2006. **64**(3): p. 192-197.
29. Available from http://www.copperman.co.uk/didgeridoo/how_to_make_a_wooden_didgeridoo/what_is_wood.php.
30. Haskell, N.A., *The dispersion of surface waves on multilayered media.* Bulletin of the Seismological Society of America, 1953. **43**(1): p. 17-34.
31. Grigorenko, A.Y., *Numerical analysis of stationary dynamic processes in anisotropic inhomogeneous cylinders.* International Applied Mechanics, 2005. **41**(8): p. 831-866.
32. Markus, S. and D. Mead, *Axisymmetric and asymmetric wave motion in orthotropic cylinders.* Journal of sound and vibration, 1995. **181**(1): p. 127-147.
33. Mirsky, I., *Axisymmetric vibrations of orthotropic cylinders.* The Journal of the Acoustical Society of America, 1964. **36**(11): p. 2106-2112.
34. Martin, P. and J. Berger, *Waves in wood: free vibrations of a wooden pole.* Journal of the Mechanics and Physics of Solids, 2001. **49**(5): p. 1155-1178.
35. Elmaimouni, L., et al., *A polynomial approach to the analysis of guided waves in anisotropic cylinders of infinite length.* Wave motion, 2005. **42**(2): p. 177-189.
36. McNiven, H. and Y. Mengi, *Transient wave propagation in a semi-infinite, transversely isotropic rod.* Journal of sound and vibration, 1971. **17**(1): p. 41-49.

37. Mirsky, I., *Wave propagation in transversely isotropic circular cylinders Part I: Theory.* The Journal of the Acoustical Society of America, 1965. **37**(6): p. 1016-1021.
38. Green, D.W., J.E. Winandy, and D.E. Kretschmann, *Mechanical properties of wood.* Wood handbook: wood as an engineering material, 1999.
39. Tsai, Y., S. Liu, and G. Light, *Cylindrically guided waves in a transversely isotropic shaft.* Review of Progress in Quantitative Nondestructive Testing, 1990. **9**.
40. Tsai, Y., *Longitudinal motion of a thick transversely isotropic hollow cylinder.* Journal of pressure vessel technology, 1991. **113**: p. 585.
41. Nagy, P.B., *Longitudinal guided wave propagation in a transversely isotropic rod immersed in fluid.* The Journal of the Acoustical Society of America, 1995. **98**: p. 454.
42. Ahmad, F., *Guided waves in a transversely isotropic cylinder immersed in a fluid.* The Journal of the Acoustical Society of America, 2001. **109**: p. 886.
43. Honarvar, F., et al., *Wave propagation in transversely isotropic cylinders.* International journal of solids and structures, 2007. **44**(16): p. 5236-5246.
44. Rokhlin, S. and L. Wang, *Ultrasonic waves in layered anisotropic media: characterization of multidirectional composites.* International journal of solids and structures, 2002. **39**(16): p. 4133-4149.
45. Shah, A. and S. Datta, *Harmonic waves in a periodically laminated medium.* International journal of solids and structures, 1982. **18**(5): p. 397-410.
46. Habeger, C., R.W. Mann, and G.A. Baum, *Ultrasonic plate waves in paper.* Ultrasonics, 1979. **17**(2): p. 57-62.
47. Aalami, B., *Waves in prismatic guides of arbitrary cross section.* Journal of Applied Mechanics, 1973. **40**: p. 1067.
48. Gravenkamp, H., C. Song, and J. Prager, *A numerical approach for the computation of dispersion relations for the plate structures using scaled boundary finite element method.* Journal of sound and vibration, 2012. **331**: p. 2543-2557.
49. Datta, S.K., et al., *Wave propagation in laminated composite plates.* The Journal of the Acoustical Society of America, 1988. **83**: p. 2020.
50. Bartoli, I., et al., *Modeling wave propagation in damped waveguides of arbitrary cross-section.* Journal of sound and vibration, 2006. **295**(3): p. 685-707.
51. Marzani, A., et al., *A semi-analytical finite element formulation for modeling stress wave propagation in axisymmetric damped waveguides.* Journal of sound and vibration, 2008. **318**(3): p. 488-505.
52. Hayashi, T., W.J. Song, and J.L. Rose, *Guided wave dispersion curves for a bar with an arbitrary cross-section, a rod and rail example.* Ultrasonics, 2003. **41**(3): p. 175-183.
53. Seco, F., et al. *PCDISP: a tool for the simulation of wave propagation in cylindrical waveguides*. in *9th International Congress on Sound and Vibration*. 2002.
54. Pavlakovic, B., et al., *Disperse: a general purpose program for creating dispersion curves.* Review of progress in quantitative nondestructive evaluation, 1997. **16**: p. 185-192.
55. Bocchini, P., A. Marzani, and E. Viola, *Graphical user interface for guided acoustic waves.* Journal of Computing in Civil Engineering. **25**(3): p. 202-210.

56. Doyle, J.F., *Wave propagation in structures*. 1989: Springer.
57. Pao, Y.-H., D.-C. Keh, and S.M. Howard, *Dynamic response and wave propagation in plane trusses and frames.* AIAA journal, 1999. **37**(5): p. 594-603.
58. Langley, R., *Application of the dynamic stiffness method to the free and forced vibrations of aircraft panels.* Journal of sound and vibration, 1989. **135**(2): p. 319-331.
59. Hackbusch, W., *Multi-grid methods and applications*. Vol. 4. 1985: Springer-Verlag Berlin.
60. Reddy, J.N., *An introduction to the finite element method*. Vol. 2. 1993: McGraw-Hill New York.
61. Zienkiewicz, O.C. and R.L. Taylor, *The finite element method*. Vol. 3. 1977: McGraw-hill London.
62. Delsanto, P.P. and M. Scalerandi, *A spring model for the simulation of the propagation of ultrasonic pulses through imperfect contact interfaces.* The Journal of the Acoustical Society of America, 1998. **104**: p. 2584.
63. Brebbia, C.A., J.C.F. Telles, and L.C. Wrobel, *Boundary element techniques: theory and applications in engineering.* Berlin and New York, Springer-Verlag, 1984, 478 p, 1984.
64. Liu, G. and J. Achenbach, *Strip element method to analyze wave scattering by cracks in anisotropic laminated plates.* Journal of Applied Mechanics, 1995. **62**(3): p. 607-613.
65. Patera, A.T., *A spectral element method for fluid dynamics: laminar flow in a channel expansion.* Journal of Computational Physics, 1984. **54**(3): p. 468-488.
66. Oshima, T., R.D. Kriz, and S.G. Nomachi, *Simulation and Visualization of Stress Wave Propagation in Composite Laminate with Interphase Layer.* Nondestructive Testing And Evaluation, 1992. **8**(1-6): p. 391-403.
67. Xi, Z., et al., *A strip-element method for analyzing wave scattering by a crack in a fluid-filled composite cylindrical shell.* Composites science and technology, 2000. **60**(10): p. 1985-1996.
68. Yim, H. and Y. Choi, *Simulation of ultrasonic waves in various types of elastic media using the mass spring lattice model.* Materials evaluation, 2000. **58**(7): p. 889-896.
69. Chen, T., et al., *Numerical simulation of the surface acoustic wave propagation on the plate surface by mass spring lattice model.* Journal of Nanjing Institute of Posts and Telecommunications 2005. **25**: p. 75 - 78.
70. Delsanto, P., et al., *Connection machine simulation of ultrasonic wave propagation in materials. I: the one-dimensional case.* Wave motion, 1992. **16**(1): p. 65-80.
71. Delsanto, P., et al., *Connection machine simulation of ultrasonic wave propagation in materials. II: The two-dimensional case.* Wave motion, 1994. **20**(4): p. 295-314.
72. Sundararaman, S. and D.E. Adams, *Modeling guided waves for damage identification in isotropic and orthotropic plates using a local interaction simulation approach.* Journal of vibration and acoustics, 2008. **130**(4).
73. Zhu, J., A. Shah, and S. Datta. *BEM for Scattering of Elastic Waves by Cracks in Laminated Plates*. in *Engineering Mechanics (1995)*. 1995: ASCE.

74. Cho, Y., *Estimation of ultrasonic guided wave mode conversion in a plate with thickness variation.* Ultrasonics, Ferroelectrics and Frequency Control, IEEE Transactions on, 2000. **47**(3): p. 591-603.
75. Hayashi, T. and S. Endoh, *Calculation and visualization of Lamb wave motion.* Ultrasonics, 2000. **38**(1): p. 770-773.
76. Strikwerda, J.C., *Finite difference schemes and partial differential equations, Wadsworth & Brooks.* Cole, Pacific Grove, CA, 1989.
77. Harari, I. and E. Turkel, *Accurate finite difference methods for time-harmonic wave propagation.* Journal of Computational Physics, 1995. **119**(2): p. 252-270.
78. Zingg, D.W., *Comparison of high-accuracy finite-difference methods for linear wave propagation.* SIAM Journal on Scientific Computing, 2000. **22**(2): p. 476-502.
79. Verdict, G., P. Glen, and C. Burger, *A Finite Element Study of Lamb Waves in a Uni-Directional Graphite/Epoxy Plate.* Composite Material Technology) 1992, 1992: p. 31-38.
80. Yokoyama, T., *Finite element computation of torsional plastic waves in a thin-walled tube.* Archive of Applied Mechanics, 2001. **71**(6-7): p. 359-370.
81. Conry, M., L. Crane, and M. Gilchrist. *Ultrasonic detection of embedded and surface defects in thin plates using Lamb waves*. in *European Workshop on Smart Structures in Engineering and Technology*. 2003: International Society for Optics and Photonics.
82. Jeong, S.M. and M. Ruzzene. *Analysis of Vibration and Wave Propagation in Cylindrical Grid-Like Structures*. 2003: ASME.
83. Gosselin, O., J. Teron, and L. Nicoletis. *Modeling of elastic wave propagation by finite difference and finite element methods*. in *From Res. Towards Operational Use*. 1984.
84. Puckett, A.D., *Fidelity of a finite element model for longitudinal wave propagation in thick cylindrical wave guides*. 2000, Los Alamos National Lab., NM (US).
85. Moser, F., L.J. Jacobs, and J. Qu, *Modeling elastic wave propagation in waveguides with the finite element method.* NDT & E International, 1999. **32**(4): p. 225-234.
86. Chakraborty, A. and S. Gopalakrishnan, *A higher-order spectral element for wave propagation analysis in functionally graded materials.* Acta mechanica, 2004. **172**(1-2): p. 17-43.
87. Doyle, J., *A spectrally formulated finite element for longitudinal wave propagation.* International Journal of Analytical and Experimental Modal Analysis, 1988. **3**: p. 1-5.
88. Doyle, J. and T. Farris, *A spectrally formulated finite element for flexural wave propagation in beams.* International Journal of Analytical and Experimental Modal Analysis, 1990. **5**: p. 99-107.
89. Doyle, J. and T. Farris, *A spectrally formulated finite element for wave propagation in 3-D frame structures.* International Journal of Analytical and Experimental Modal Analysis, 1990. **5**: p. 223-237.
90. Mahapatra, R., S. Gopalakrishnan, and T. Sankar, *Spectral-element-based solutions for wave propagation analysis of multiply connected unsymmetric laminated composite beams.* Journal of sound and vibration, 2000. **237**(5): p. 819-836.

91. Mahapatra, D.R. and S. Gopalakrishnan, *A spectral finite element for analysis of wave propagation in uniform composite tubes.* Journal of sound and vibration, 2003. **268**(3): p. 429-463.
92. Rizzi, S. and J. Doyle, *Force identification for impact of a layered system.* Computational aspects of contact, impact and penetration, 1991: p. 222-241.
93. Love, A.E.H., *A treatise on the mathematical theory of elasticity*. 1927: Cambridge University Press.
94. Mindlin, R. and G. Herrmann. *A one-dimensional theory of compressional waves in an elastic rod*. in *Proceedings of the 1st US National Congress of Applied Mechanics*. 1951.
95. Zak, A. and M. Krawczuk, *Assessment of rod behaviour theories used in spectral finite element modelling.* Journal of sound and vibration, 2010. **329**(11): p. 2099-2113.
96. Anderson, S.P., *Higher-order rod approximations for the propagation of longitudinal stress waves in elastic bars.* Journal of sound and vibration, 2006. **290**(1): p. 290-308.
97. Timoshenko, S.P., *On the correction for shear of the differential equation for transverse vibrations of prismatic bars.* The London, Edinburgh, and Dublin Philosophical Magazine and Journal of Science, 1921. **41**(245): p. 744-746.
98. Gopalakrishnan, S., A. Chakraborty, and D.R. Mahapatra, *Spectral finite element method: wave propagation, diagnostics and control in anisotropic and inhomogenous structures*. 2008: Springer Verlag.
99. Chakraborty, A. and S. Gopalakrishnan, *A spectrally formulated finite element for wave propagation analysis in functionally graded beams.* International journal of solids and structures, 2003. **40**(10): p. 2421-2448.
100. Chakraborty, A. and S. Gopalakrishnan, *Poisson's contraction effects in a deep laminated composite beam.* Mechanics of Advanced Materials and Structures, 2003. **10**(3): p. 205-225.
101. Roy Mahapatra, D. and S. Gopalakrishnan, *A spectral finite element model for analysis of axial flexural shear coupled wave propagation in laminated composite beams.* Composite Structures, 2003. **59**(1): p. 67-88.
102. Bhimaraddi, A., *Computation of ply thickness of laminated beam for which Euler-Bernoulli theory is adequate.* Composite Structures, 1994. **29**(4): p. 415-420.
103. Chakraborty, A., D. Roy Mahapatra, and S. Gopalakrishnan, *Finite element analysis of free vibration and wave propagation in asymmetric composite beams with structural discontinuities.* Composite Structures, 2002. **55**(1): p. 23-36.
104. Roy Mahapatra, D. and S. Gopalakrishnan, *A spectral finite element model for analysis of axial-flexural-shear coupled wave propagation in laminated composite beams.* Composite Structures, 2003. **59**(1): p. 67-88.
105. Kudela, P., M. Krawczuk, and W. Ostachowicz, *Wave propagation modelling in 1D structures using spectral finite elements.* Journal of sound and vibration, 2007. **300**(1): p. 88-100.
106. Mitra, M. and S. Gopalakrishnan, *Wavelet based spectral finite element for analysis of coupled wave propagation in higher order composite beams.* Composite Structures, 2006. **73**(3): p. 263-277.
107. Gopalakrishnan, S., M. Martin, and J. Doyle, *A matrix methodology for spectral analysis of wave propagation in multiple connected Timoshenko beams.* Journal of sound and vibration, 1992. **158**(1): p. 11-24.

108. Martin, M., S. Gopalakrishnan, and J. Doyle, *Wave propagation in multiply connected deep waveguides.* Journal of sound and vibration, 1994. **174**(4): p. 521-538.
109. Baz, A., *Spectral finite-element modeling of the longitudinal wave propagation in rods treated with active constrained layer damping.* Smart Materials and Structures, 2000. **9**(3): p. 372.
110. Palacz, M. and M. Krawczuk, *Analysis of longitudinal wave propagation in a cracked rod by the spectral element method.* Computers & structures, 2002. **80**(24): p. 1809-1816.
111. Krawczuk, M., M. Palacz, and W. Ostachowicz, *Flexural-Shear Wave Propagation in Cracked Composite Beam.* Science and Engineering of Composite Materials, 2004. **11**(1): p. 55-68.
112. Mitra, M. and S. Gopalakrishnan, *Spectrally formulated wavelet finite element for wave propagation and impact force identification in connected 1-D waveguides.* International journal of solids and structures, 2005. **42**(16-17): p. 4695-4721.
113. Mitra, M. and S. Gopalakrishnan, *Extraction of wave characteristics from wavelet-based spectral finite element formulation.* Mechanical systems and signal processing, 2006. **20**(8): p. 2046-2079.
114. Mitra, M. and S. Gopalakrishnan, *Wavelet based spectral finite element modelling and detection of de-lamination in composite beams.* Proceedings of the Royal Society A: Mathematical, Physical and Engineering Science, 2006. **462**(2070): p. 1721.
115. Hong, T.K. and B. Kennett, *On a wavelet-based method for the numerical simulation of wave propagation.* Journal of Computational Physics, 2002. **183**(2): p. 577-622.
116. Gopalakrishnan, S. and R. Jha, *A wavelet spectral element for laminated composite plate with delamination and transverse damage.* American society of Civil Engineers, Engineering Mechanical Division Journal, 2010.
117. Yuan, S., W. Lei, and L. Shi, *Active monitoring for on-line damage detection in composite structures.* Journal of vibration and acoustics, 2003. **125**(2): p. 178-186.
118. Li, Z., et al., *Damage detection of beams based on experimental wavelet analysis of flexible waves.* Key Engineering Materials, 2004. **261**: p. 1373-1378.
119. Sohn, H., et al., *Wavelet-based active sensing for delamination detection in composite structures.* Smart Materials and Structures, 2004. **13**(1): p. 153.
120. Staszewski, W.J. and A.N. Robertson, *Time–frequency and time–scale analyses for structural health monitoring.* Philosophical Transactions of the Royal Society A: Mathematical, Physical and Engineering Sciences, 2007. **365**(1851): p. 449.
121. Gabor, D., *Theory of communication. Part 1: The analysis of information.* Electrical Engineers-Part III: Radio and Communication Engineering, Journal of the Institution of, 1946. **93**(26): p. 429-441.
122. Hong, J.C., K.H. Sun, and Y.Y. Kim, *Dispersion-based short-time Fourier transform applied to dispersive wave analysis.* The Journal of the Acoustical Society of America, 2005. **117**: p. 2949.
123. Ovanesova, A. and L. Suarez, *Applications of wavelet transforms to damage detection in frame structures.* Engineering Structures, 2004. **26**(1): p. 39-49.

124. Ni, S.H., et al., *Time-frequency analyses of pile-integrity testing using wavelet transform.* Computers and Geotechnics, 2008. **35**(4): p. 600-607.
125. Kim, H. and H. Melhem, *Damage detection of structures by wavelet analysis.* Engineering Structures, 2004. **26**(3): p. 347-362.
126. Seidel, J., *Presentation of low strain integrity testing in the time-frequency domain.* Proceeding of The 16th International Conferenee on The Application of Stress-Wavelet Theory to Piles, Sao Paulo, Brazil, 2000.
127. Addison, P. and J. Watson. *Wavelet analysis for low strain integrity testing of foundation piles, 5th Intl*. 1997.
128. Peterson, M., *A method for increased accuracy of the measurement of relative phase velocity.* Ultrasonics, 1997. **35**(1): p. 17-29.
129. Subhani, M., et al., *Effect of Elastic Modulus and Poisson's Ratio on Guided Wave Dispersion Using Transversely Isotropic Material Modelling.* Advanced Materials Research, 2013. **778**: p. 303-311.
130. Pavlakovic, B. and M. Lowe, *Disperse software manual Version 2.0.16B.* Imperial College, London, UK, 2003.
131. Kolsky, H., *Stress Waves inSolids*. 1963, Dover.
132. Graff, K.F., *Wave motion in elastic solids*. 1975: Dover Pubns.
133. Dieulesaint, E. and D.J. Royer, *Elastic waves in solids*. 1980: Springer.
134. Brillouin, L., *Wave propagation and group velocity*. Vol. 304. 1960: Academic Press New York.
135. Rose, J., *Ultrasonic waves in solid media. 1999*. 1999, Cambridge: Cambridge University Press.
136. Zemanek Jr, J., *An experimental and theoretical investigation of elastic wave propagation in a cylinder*. 1962, DTIC Document.
137. Pochhammer, L., *über die fortplanzungsgeschwindigkeiten schwingungen in einem unbegrentzten isotropen kreiscylinder.* für die reine angewandte Mathematik, 1876. **81**: p. 324 - 336.
138. C. Chree, M.A.F., *The equation of an isotropic solid in polar and cylindrical coordinates, their solution and application.* Cambridge Philosophical Society - Transactions, 1889. **14**: p. 250.
139. Auld, B.A., *Acoustic fields and waves in solids*. Vol. 2. 1990: RE Krieger.
140. Honarvar, F., E. Enjilela, and A. Sinclair, *Guided ultrasonic waves in composite cylinders.* Mechanics of Composite Materials, 2007. **43**(3): p. 277-288.
141. Puckett, A., *An experimental and theoretical investigation of axially symmetric wave propagation in thick cylindrical waveguides*. 2004, The University of Maine.
142. Board, A.B.C. and A.U.B.R. Co-ordinating, *Building code of Australia*. 2003: CCH Australia.
143. Das, B.M., *Fundamentals of geotechnical engineering*. 2008: Cengage Learning.
144. Lynch, J., *Experimental verification of concrete piles subjected to flexural guided waves*. 2007, Ph. D. Dissertation, Northwestern University, Evanston, IL.
145. Subhani, M., J. Li, and B. Samali, *A comparative study of guided wave propagation in timber poles with isotropic and transversely isotropic material models.* Journal of Civil Structural Health Monitoring, 2012: p. 1-15.
146. Mason, W. and H. McSkimin, *Attenuation and scattering of high frequency sound waves in metals and glasses.* The Journal of the Acoustical Society of America, 1947. **19**(3): p. 464-473.

147. Pilant, W.L., *The propagation of elastic waves in thin plates*. 1960, University of California: Los Angeles.
148. Skalak, R., *Longitudinal impact of a semi-infinite circular elastic bar.* J. Appl. Mech, 1957. **24**(1): p. 59-64.
149. Folk, R., et al., *Elastic strain produced by sudden application of pressure to one end of a cylindrical bar. I. Theory.* The Journal of the Acoustical Society of America, 1958. **30**: p. 552.
150. Jones, O. and F.R. Norwood, *Axially symmetric cross-sectional strain and stress distributions in suddenly loaded cylindrical elastic bars.* Journal of Applied Mechanics, 1967. **34**: p. 718.
151. Kennedy, L. and O. Jones, *Longitudinal wave propagation in a circular bar loaded suddenly by a radially distributed end stress.* Journal of Applied Mechanics, 1969. **36**: p. 470.
152. Goldberg, I.S. and R.T. Folk, *Solutions to Time-Dependent Pure-End-Condition Problems of Elasticity Pressure-Step Wave Propagation and End-Resonance Effects.* SIAM Journal on Applied Mathematics, 1993: p. 1264-1292.
153. Fox, G. and C. Curtis, *Elastic strain produced by sudden application of pressure to one end of a cylindrical bar. II. Experimental observations.* The Journal of the Acoustical Society of America, 1958. **30**: p. 559.
154. Davies, R., *A critical study of the Hopkinson pressure bar.* Philosophical Transactions of the Royal Society of London. Series A. Mathematical and Physical Sciences, 1948: p. 375-457.
155. Gregory, R. and I. Gladwell, *Axisymmetric waves in a semi-infinite elastic rod.* The Quarterly Journal of Mechanics and Applied Mathematics, 1989. **42**(2): p. 327-337.
156. Oliver, J., *Elastic Wave Dispersion in a Cylindrical Rod by a Wideâ€• Band Shortâ€• Duration Pulse Technique.* The Journal of the Acoustical Society of America, 1957. **29**(2): p. 189-194.
157. Peterson, M., *Prediction of longitudinal disturbances in a multimode cylindrical waveguide.* Experimental mechanics, 1999. **39**(1): p. 36-42.
158. Puckett, A.D. and M. Peterson, *A semi-analytical model for predicting multiple propagating axially symmetric modes in cylindrical waveguides.* Ultrasonics, 2005. **43**(3): p. 197-207.
159. Alterman, Z. and F. Karal Jr, *Propagation of elastic waves in a semi-infinite cylindrical rod using finite difference methods.* Journal of sound and vibration, 1970. **13**(2): p. 115-145, IN1.
160. Edelman, A. and H. Murakami, *Polynomial roots from companion matrix eigenvalues.* Mathematics of Computation, 1995. **64**(210): p. 763-776.
161. Krawczuk, M., J. Grabowska, and M. Palacz, *Longitudinal wave propagation. Part I Comparison of rod theories.* Journal of sound and vibration, 2006. **295**(3): p. 461-478.
162. Zeng, Z., *Algorithm 835: MultRoot---a Matlab package for computing polynomial roots and multiplicities.* ACM Transactions on Mathematical Software (TOMS), 2004. **30**(2): p. 218-236.
163. Ballou, K., *Cardano's Solution to the Cubic: A Mathematical Soap Opera.* Editorial: Social Justice, Taxicabs and Soap-Operatic Mathematics pp. 1-2, 2005. **2**(1): p. 65.
164. Kalman, D. and J. White, *A Simple Solution of the General Cubic.* 1998.

165. Gopalakrishnan, S., M. Ruzzene, and S.V. Hanagud, *Springer Series In Reliability Engineering: Computational Techniques for Structural Health Monitoring*: Springer.
166. Reddy, J.N., *Mechanics of laminated composite plates: theory and analysis*. Vol. 1. 1997: CRC press Boca Raton.
167. Golub, G.H. and C.F. Van Loan, *Matrix computations*. Vol. 3: JHU Press.
168. Cook, R.D., *Concepts and applications of finite element analysis*. 2007: Wiley. com.
169. Gazetas, G., *Formulas and charts for impedances of surface and embedded foundations.* Journal of geotechnical engineering, 1991. **117**(9): p. 1363-1381.
170. Novak, M., *Dynamic stiffness and damping of piles.* Canadian Geotechnical Journal, 1974. **11**(4): p. 574-598.
171. Pacheco, G., L.E. Suarez, and M. Pando. *Dynamic lateral response of single piles considering soil inertia contributions*. in *World Conference on Earthquake Engineering*. 2008. Beijing, China.
172. Comartin, C.D., et al., *Seismic evaluation and retrofit of concrete buildings: A practical overview of the ATC 40 document.* Earthquake Spectra, 2000. **16**(1): p. 241-261.
173. Ding, X., L. Hanlong, and Y. Chen. *Analytical Solution of Wave Propagation in Large Diameter Piles for Low Strain Integrity Testing*. 2011: ASCE.
174. Mallat, S.G., *A theory for multiresolution signal decomposition: The wavelet representation.* Pattern Analysis and Machine Intelligence, IEEE Transactions on, 1989. **11**(7): p. 674-693.
175. Kim, Y.Y. and E.H. Kim, *Effectiveness of the continuous wavelet transform in the analysis of some dispersive elastic waves.* The Journal of the Acoustical Society of America, 2001. **110**: p. 86.
176. Inoue, H., K. Kishimoto, and T. Shibuya, *Experimental wavelet analysis of flexural waves in beams.* Experimental mechanics, 1996. **36**(3): p. 212-217.
177. Balendra, S., *Numerical modeling of dynamic soil-pile-structure interaction*. 2005, Washington State University.
178. Kim, Y.R. and S.R. Ranjithan, *Nondestructive Evaluation of the Structural Condition of Timber Piles. Volumes 1 and 2*. 2000.

Appendices

A. The dispersion relation of guided wave equation for cylindrical structures

A – 1 Dispersion relation of longitudinal wave for an embedded isotropic cylinder

A – 2 Dispersion relation of flexural wave for an embedded isotropic cylinder

A – 3 Dispersion relation of longitudinal and flexural wave for a traction free transversely isotropic cylinder

B. The mode shapes of analytical guided wave equation for cylindrical structures

B – 1 Power flow of an embedded isotropic cylinder

B – 2 Normalised displacement profile of an embedded isotropic cylinder

B – 3 Normalised displacement profile of a traction free transversely isotropic cylinder

C. The time domain results of analytical guided wave equation for cylindrical structures

C – 1 Time domain signal of isotropic cylinder for the input frequency of 16.5 kHz with 10 cycle sine burst

C – 2 Time domain signal of isotropic cylinder for the input frequency of 16.5 kHz with 30 cycle sine burst

C – 3 Time domain signal of isotropic cylinder for the input frequency of 50 kHz with 10 cycle sine burst

D. The time domain reconstruction of guided wave equation for cylindrical structures using SFEM

D – 1 Individual contribution of longitudinal and contraction modes for the anisotropic cylinder with the vertical impact at the top of the pole

D – 2 Individual contribution of flexural and shear modes for the anisotropic cylinder with the horizontal impact at the top of the pole

D – 3 Time domain reconstruction of the anisotropic cylinder with the vertical impact at the middle section of the pole

E. The CWT and SKM coefficient plot of a signal from timber pole obtained using FEM

Appendix A: The dispersion relation of guided wave equation for cylindrical structures

A – 1 Dispersion relation of longitudinal wave for an embedded isotropic cylinder

The dispersion relation of a longitudinal wave for an embedded isotropic cylinder is presented in [10]

$$\begin{vmatrix} b_{11} & b_{12} & b_{13} & b_{14} \\ b_{21} & b_{22} & b_{23} & b_{24} \\ b_{31} & b_{32} & b_{33} & b_{34} \\ b_{41} & b_{42} & b_{43} & b_{44} \end{vmatrix} = 0 \tag{A1.1}$$

where

$$b_{11} = -\alpha a Z_1(\alpha a), \qquad b_{12} = \underline{\xi^*} Z_1(\beta a),$$

$$b_{13} = -\alpha' a H_1^{(2)}(\alpha' a), \qquad b_{14} = \underline{\xi^*} H_1^{(2)}(\beta' a),$$

$$b_{21} = -\alpha a Z_0(\alpha a), \qquad b_{22} = -\underline{\xi^*} Z_1(\beta a),$$

$$b_{23} = \underline{\xi^*} H_0^{(2)}(\alpha' a), \qquad b_{24} = \beta' a H_0^{(2)}(\beta' a),$$

$$b_{31} = -\left(\frac{\lambda}{\mu}\right)\left((\alpha a)^2 + \underline{\xi^{*2}}\right) Z_0(\alpha a) + 2(\alpha a)^2 Z_0(\alpha a) + 2(\alpha a)^2 Z_1(\alpha a),$$

$$b_{32} = 2\underline{\xi^*}[\beta a Z_0(\beta a) - Z_1(\beta a)],$$

$$b_{33} = -\left(\frac{\lambda'}{\mu}\right)\left((\alpha' a)^2 + \underline{\xi^{*2}}\right) H_0^{(2)}(\alpha' a) + 2\left(\frac{\mu'}{\mu}\right)(\alpha' a)^2 H_0^{(2)}(\alpha' a) + 2\left(\frac{\mu'}{\mu}\right)(\alpha' a)^2 H_1^{(2)}(\alpha' a),$$

$$b_{34} = -2\left(\frac{\mu'}{\mu}\right)\underline{\xi^*}\left[\beta' a H_0^{(2)}(\beta' a) - H_0^{(2)}(\beta' a)\right],$$

$$b_{41} = 2\underline{\xi^*}\alpha a Z_1(\alpha a), \qquad b_{42} = -\left[\underline{\xi^{*2}} - (\beta a)^2\right] Z_1(\beta a),$$

$$b_{43} = -2\left(\frac{\mu'}{\mu}\right)\underline{\xi^*}\alpha' a H_1^{(2)}(\alpha' a), \qquad b_{44} = \left(\frac{\mu'}{\mu}\right)\left[\underline{\xi^{*2}} - (\beta' a)^2\right] H_0^{(2)}(\beta' a), \tag{A1.2}$$

$\underline{\xi^*} = \xi a = dimensionless\ wavenumber$, H = Hankel function and the ‘’ denotes the corresponding material properties of surrounding medium (in pile situation, it is soil).

A – 2 Dispersion relation of flexural wave for an embedded isotropic cylinder

The dispersion relation of a flexural wave for an embedded isotropic cylinder is presented in [9]

$$\begin{vmatrix} m_{11} & m_{12} & m_{13} & m_{14} & m_{15} & m_{16} \\ m_{21} & m_{22} & m_{23} & m_{24} & m_{25} & m_{26} \\ m_{31} & m_{32} & m_{33} & m_{34} & m_{35} & m_{36} \\ m_{41} & m_{42} & m_{43} & m_{44} & m_{45} & m_{46} \\ m_{51} & m_{52} & m_{53} & m_{54} & m_{55} & m_{56} \\ m_{61} & m_{62} & m_{63} & m_{64} & m_{65} & m_{66} \end{vmatrix} = 0 \tag{A1.3}$$

where

$$m_{11} = \alpha a Z_0(\alpha a), \qquad m_{12} = -2\beta a Z_0(\beta a),$$

$$m_{13} = \beta a Z_0(\beta a), \qquad m_{14} = \alpha' a H_0^{(1)}(\alpha' a),$$

$$m_{15} = -2\beta' a H_0^{(1)}(\beta' a), \qquad m_{16} = \beta' a H_0^{(1)}(\beta' a),$$

$$m_{21} = -Z_1(\alpha a), \qquad m_{22} = \beta a Z_0(\beta a),$$

$$m_{23} = -\beta a Z_0(\beta a) + Z_1(\beta a), \qquad m_{24} = -H_1^{(1)}(\alpha' a),$$

$$m_{25} = \beta' a H_0^{(1)}(\beta' a), \qquad m_{26} = -\beta' a H_0^{(1)}(\beta' a) + H_1^{(1)}(\beta' a),$$

$$m_{31} = \xi a Z_1(\alpha a), \qquad m_{32} = \frac{\beta^2 a^2}{\xi a} \beta a Z_1(\beta a),$$

$$m_{33} = 0, \qquad m_{34} = \xi a H_1^{(1)}(\alpha' a),$$

$$m_{35} = \frac{\beta'^2 a^2}{\xi a} H_1^{(1)}(\beta' a), \qquad m_{36} = 0,$$

$$m_{41} = \left[-\frac{\lambda}{\mu}(\alpha^2 + \xi^2)a^2 - 2\alpha^2 a^2 \right] Z_1(\alpha a),$$

$$m_{42} = 3\beta^2 a^2 Z_1(\beta a), \qquad m_{43} = -\beta^2 a^2 Z_1(\beta a),$$

$$m_{44} = \left[-\frac{\lambda'}{\mu}(\alpha'^2 + \xi^2)a^2 - 2\frac{\mu'}{\mu}\alpha'^2 a^2 \right] H_1^{(1)}(\alpha' a),$$

$$m_{45} = 3\frac{\mu'}{\mu}\beta'^2 a^2 H_1^{(1)}(\beta' a), \qquad m_{46} = -\frac{\mu'}{\mu}\beta'^2 a^2 H_1^{(1)}(\beta' a),$$

$$m_{51} = 2[Z_1(\alpha a) - \alpha a Z_1'(\alpha a)], \qquad m_{52} = -\beta^2 a^2 Z_1(\beta a),$$

$$m_{53} = 2\beta\alpha Z_1'(\beta a) - (2 - \beta^2 a^2) Z_1(\beta a),$$

$$m_{54} = 2\left(\frac{\mu'}{\mu}\right)\left[H_1^{(1)}(\alpha' a) - \alpha' a H_1'^{(1)}(\alpha' a) \right],$$

$$m_{55} = \frac{\mu'}{\mu}\beta'^2 a^2 H_1^{(1)}(\beta' a),$$

$$m_{56} = \frac{\mu'}{\mu}\left[2\beta' a H_1'^{(1)}(\beta' a) - (2-\beta'^2 a^2)H_1^{(1)}(\beta' a)\right],$$

$$m_{61} = 2\alpha a Z_1'(\alpha a), \qquad m_{62} = \left(\frac{\beta^2}{\xi^2} - 1\right)\beta a Z_1'(\beta a) - Z_1(\beta a),$$

$$m_{63} = Z_1(\beta a), \qquad m_{64} = 2\frac{\mu'}{\mu}\alpha' a H_1^{(1)}(\alpha' a),$$

$$m_{65} = \frac{\mu'}{\mu}\left[\left(\frac{\beta'^2}{\xi^2} - 1\right)\beta' a H_1'^{(1)}(\beta' a) - H_1^{(1)}(\beta' a)\right],$$

$$m_{66} = \frac{\mu'}{\mu}H_1^{(1)}(\beta' a), \tag{A1.4}$$

A – 3 Dispersion relation of longitudinal and flexural wave for a traction free transversely isotropic cylinder

The dispersion relation of a longitudinal wave for an embedded isotropic cylinder is presented in [43].

Longitudinal wave

$$\begin{vmatrix} a_{11} & a_{12} \\ a_{21} & a_{22} \end{vmatrix} = 0 \tag{A1.5}$$

Flexural wave

$$\begin{vmatrix} a_{11} & a_{12} & a_{13} \\ a_{21} & a_{22} & a_{23} \\ a_{31} & a_{32} & a_{33} \end{vmatrix} = 0 \tag{A1.6}$$

where

$$\begin{aligned} a_{11} = {} & [C_{11} + j\xi a q_1(C_{11} - C_{13})]\left[(p^2 - p - s_1^2 a^2)J_p(s_1 a) + (s_1 a)J_{p+1}(s_1 a)\right] \\ & + [C_{12} + j\xi a q_1(C_{12} - C_{13})]\left[p^2 J_p(s_1 a) - (s_1 a)J_{p+1}(s_1 a)\right] \\ & + [-C_{13}\xi^2 a^2 - C_{12}p^2 + jp^2\xi a q_1(C_{13} - C_{12})]J_p(s_1 a), \end{aligned}$$

$$
\begin{aligned}
a_{12} &= [C_{11}q_2 + j\xi a(C_{11} - C_{13})]\left[(p^2 - p - s_2^2a^2)J_p(s_2a) + (s_2a)J_{p+1}(s_2a)\right] \\
&\quad + [C_{12}q_2 + j\xi a(C_{12} - C_{13})]\left[p^2J_p(s_2a) - (s_2a)J_{p+1}(s_2a)\right] \\
&\quad + [-C_{13}q_2\xi^2a^2 - C_{12}q_2p^2 + jp^2\xi a(C_{13} - C_{12})]J_p(s_2a), \\
a_{13} &= p(C_{11} - C_{12})\left[(p-1)J_p(s_3a) - (s_3a)J_{p+1}(s_3a)\right], \\
a_{21} &= C_{44}[q_1(s_1^2a^2 - \xi^2a^2) + 2j\xi a]\left[pJ_p(s_1a) - (s_1a)J_{p+1}(s_1a)\right], \\
a_{22} &= C_{44}[(s_2^2a^2 - \xi^2a^2) + 2j\xi aq_2]\left[pJ_p(s_2a) - (s_2a)J_{p+1}(s_2a)\right], \\
a_{23} &= C_{44}jp\xi aJ_p(s_3a), \\
a_{31} &= p(C_{11} - C_{12})(1 + j\xi aq_1)\left[(1-p)J_p(s_1a) + (s_1a)J_{p+1}(s_1a)\right], \\
a_{32} &= p(C_{11} - C_{12})(q_2 + j\xi a)\left[(1-p)J_p(s_2a) + (s_2a)J_{p+1}(s_2a)\right], \\
a_{32} &= \frac{(C_{11} - C_{12})}{2}\left\{[s_3^2a^2 - 2p(p-1)]J_p(s_3a) - 2(s_3a)J_{p+1}(s_3a)\right\}.
\end{aligned}
$$

(A1.7)

And, also

$$
\begin{aligned}
q_1 &= -\frac{[C_{11}s_1^2 - (\rho\omega^2 - (C_{13} + 2C_{44})\xi^2)]}{aj\xi\left[(C_{11} - C_{13} - C_{44})s_1^2 - \left(\rho\omega^2 - (C_{44}\xi^2)\right)\right]} \\
q_2 &= -\frac{aj\xi\left[(C_{11} - C_{13} - C_{44})s_2^2 - \left(\rho\omega^2 - (C_{44}\xi^2)\right)\right]}{[C_{11}s_2^2 - (\rho\omega^2 - (C_{13} + 2C_{44})\xi^2)]}
\end{aligned}
$$

(A1.8)

In the equation, if $p = 0$, then the dispersion relation for the longitudinal wave can be obtained, whereas $p = 1$ represents the same for the flexural wave.

Appendix B: The mode shapes of analytical guided wave equation for cylindrical structures

B – 1 Power flow of an embedded isotropic cylinder

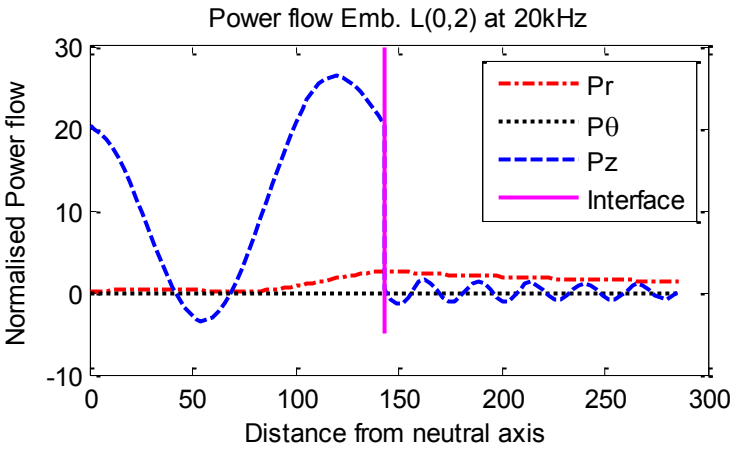

Figure B-1.1: Power flow of L(0,2) at 20 kHz (embedded)

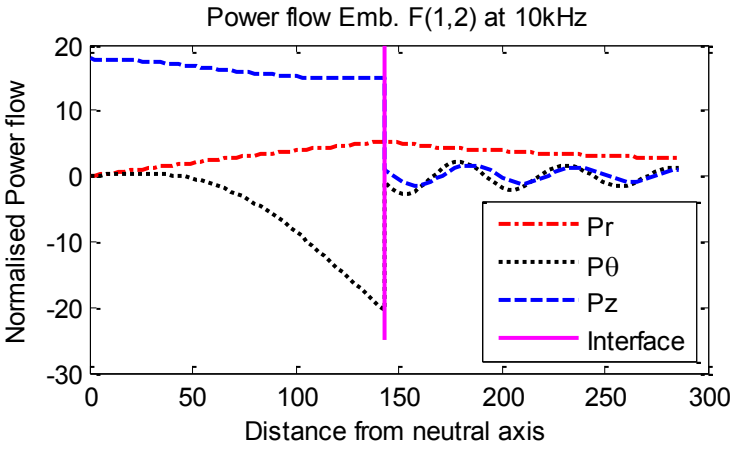

Figure B-1.2: Power flow of F(1,2) at 10 kHz (embedded)

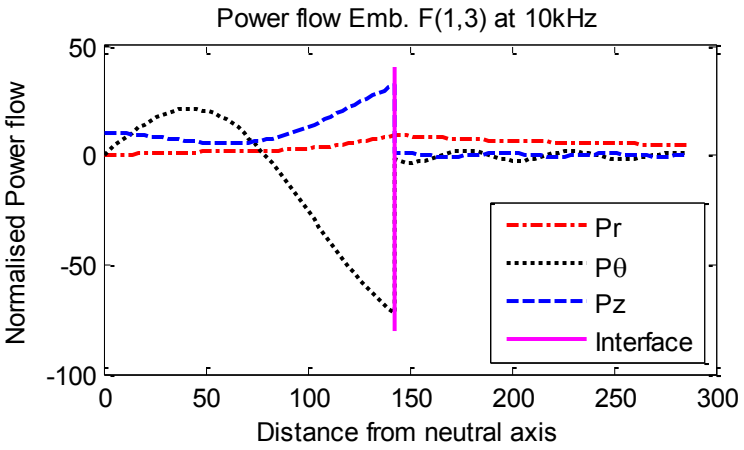

Figure B-1.3: Power flow of F(1,3) at 10 kHz (embedded)

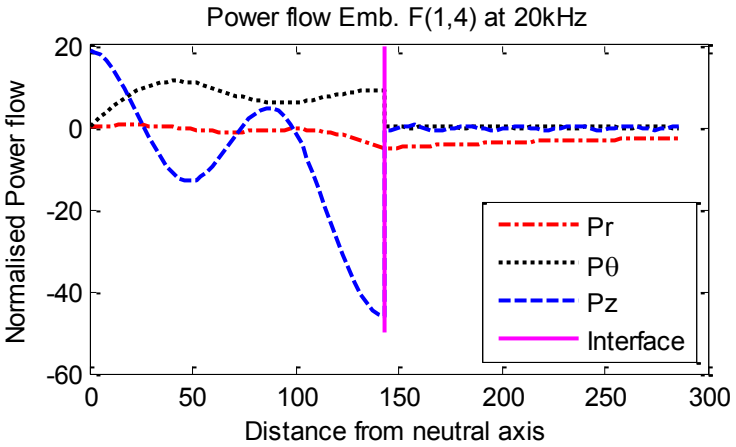

Figure B-1.4: Power flow of F(1,4) at 20 kHz (embedded)

B – 2 Normalised displacement profile of an embedded isotropic cylinder

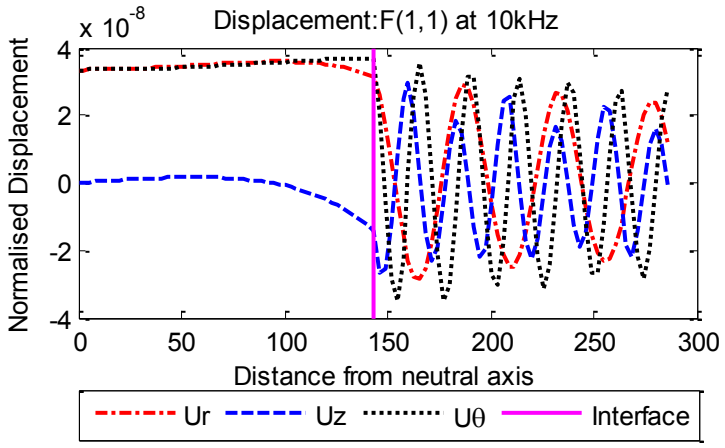

Figure B-2.1: Normalised displacement of F(1,1) at 10 kHz (embedded)

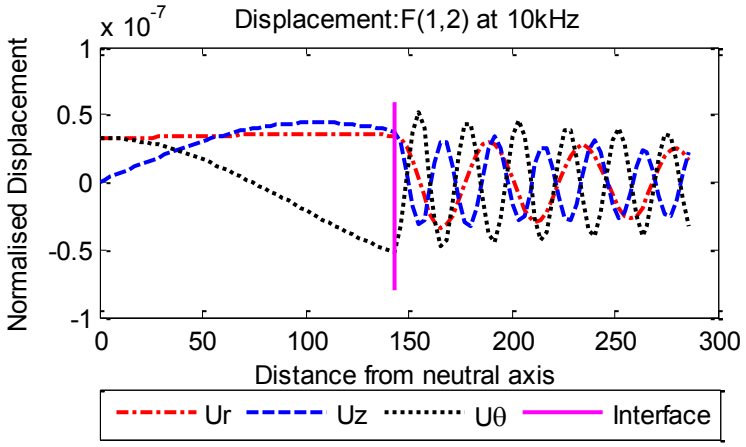

Figure B-2.2: Normalised displacement of F(1,2) at 10 kHz (embedded)

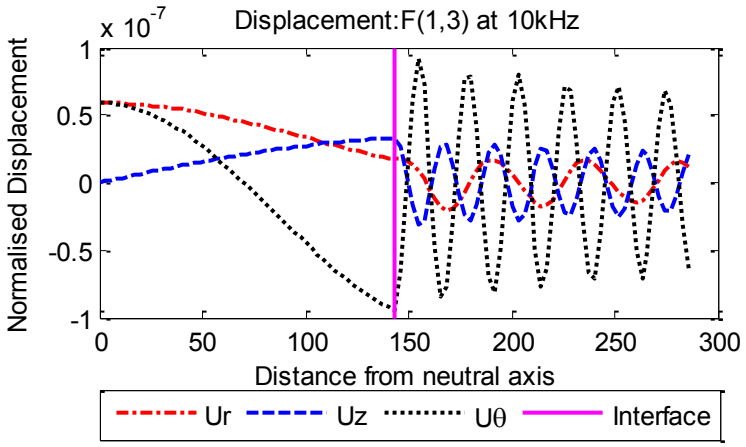

Figure B-2.3: Normalised displacement of F(1,3) at 10 kHz (embedded)

B – 3 Normalised displacement profile of a traction free transversely isotropic cylinder

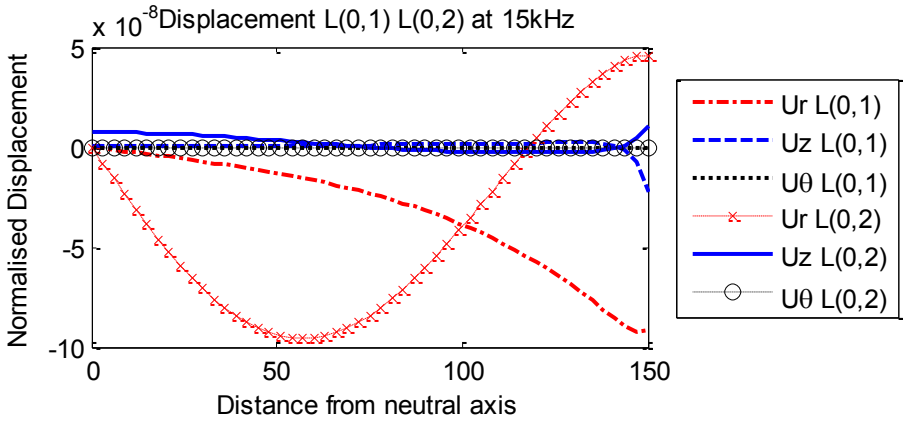

Figure B-3.1: Normalised displacement of L(0,1) and L(0,2) at 15 kHz (set 2)

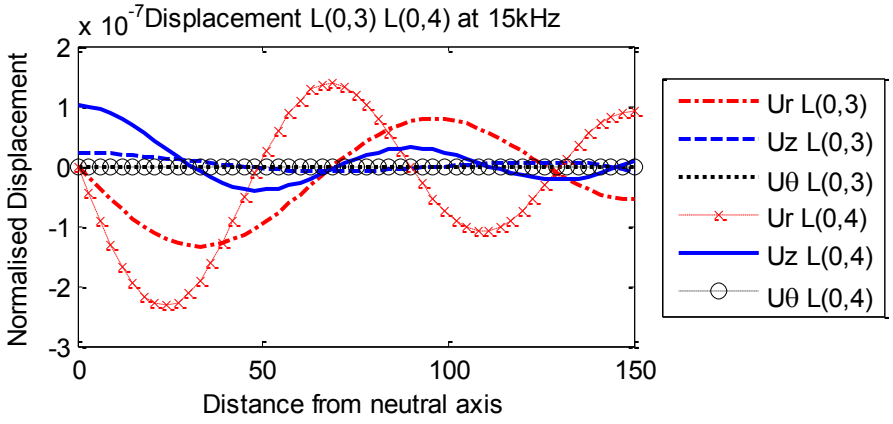

Figure B-3.2: Normalised displacement of L(0,3) and L(0,4) at 15 kHz (set 2)

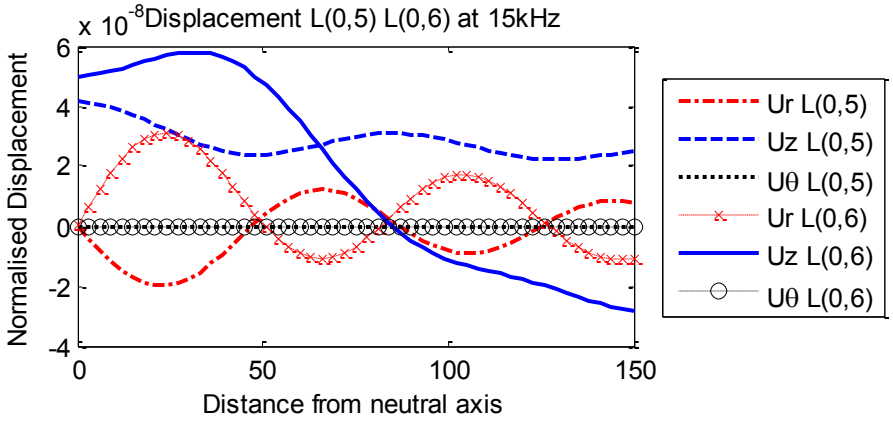

Figure B-3.3: Normalised displacement of L(0,5) and L(0,6) at 15 kHz (set 2)

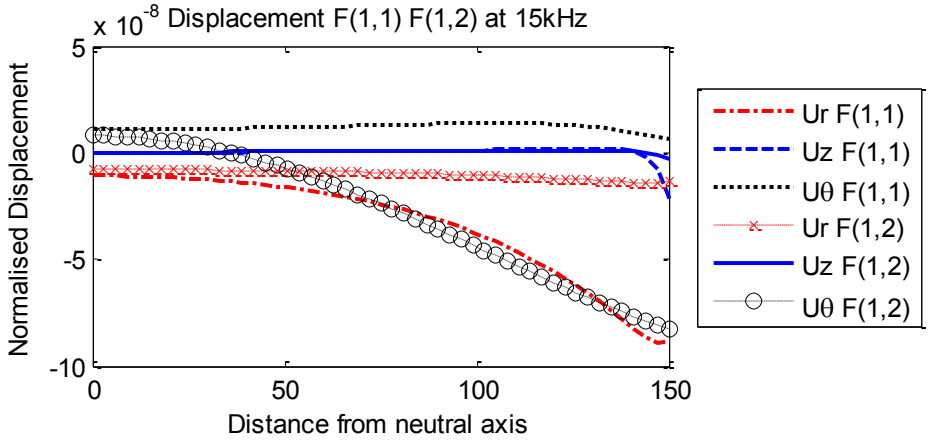

Figure B-3.4: Normalised displacement of F(1,1) and F(1,2) at 15 kHz (set 2)

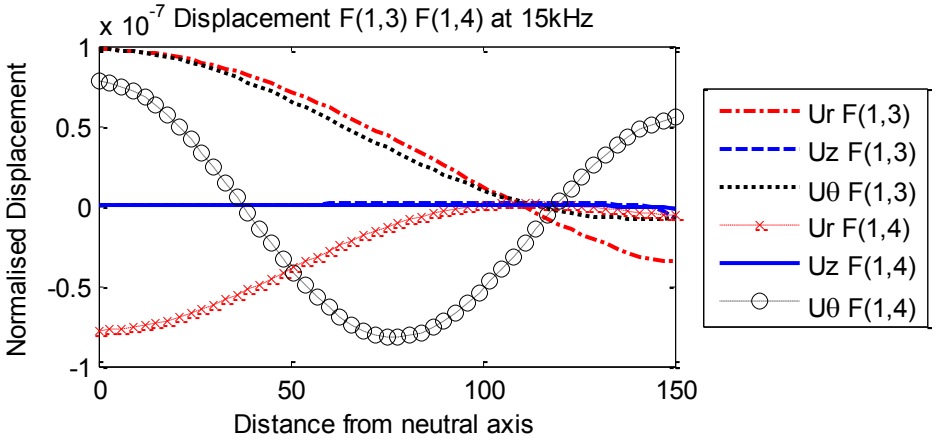

Figure B-3.5: Normalised displacement of F(1,3) and F(1,4) at 15 kHz (set 2)

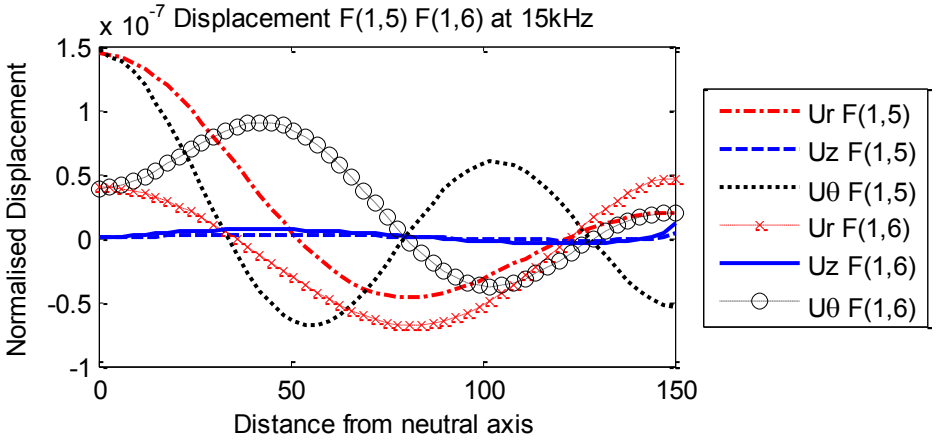

Figure B-3.6: Normalised displacement of F(1,5) and F(1,6) at 15 kHz (set 2)

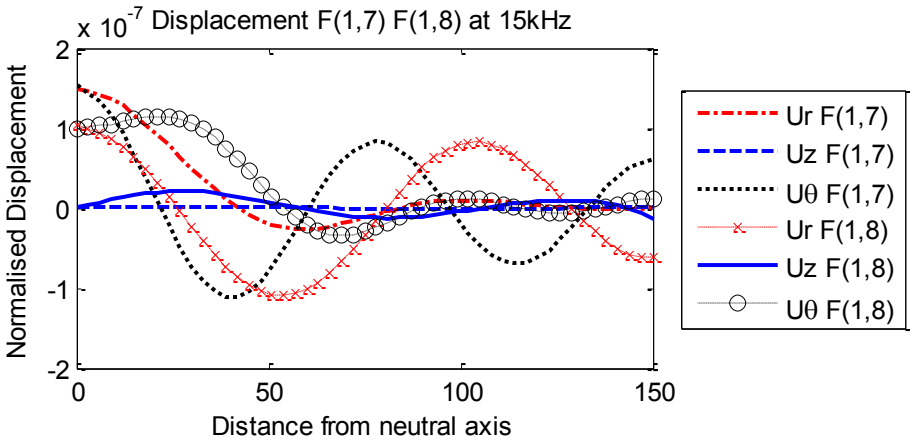

Figure B-3.7: Normalised displacement of F(1,7) and F(1,8) at 15 kHz (set 2)

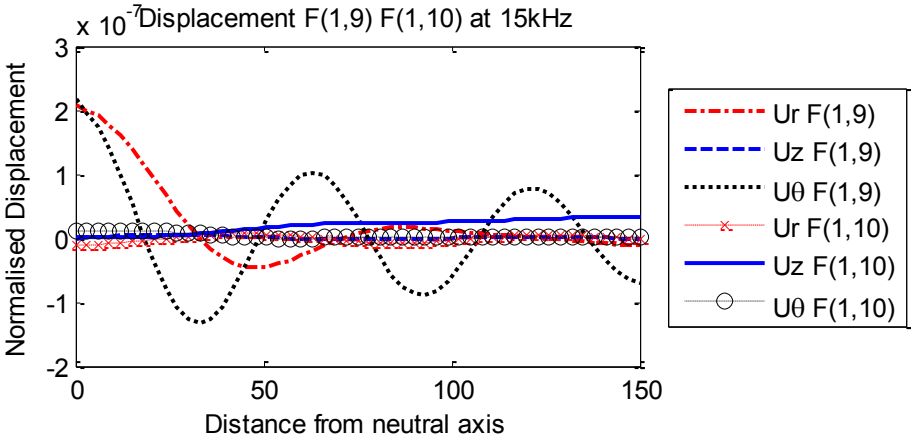

Figure B-3.8: Normalised displacement of F(1,9) and F(1,10) at 15 kHz (set 2)

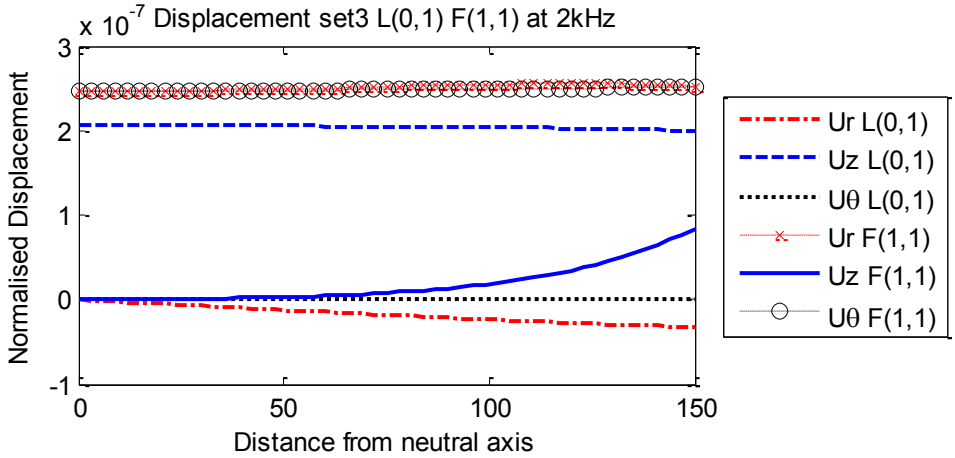

Figure B-3.9: Normalised displacement of L(0,1) and F(1,1) at 2 kHz (set 3)

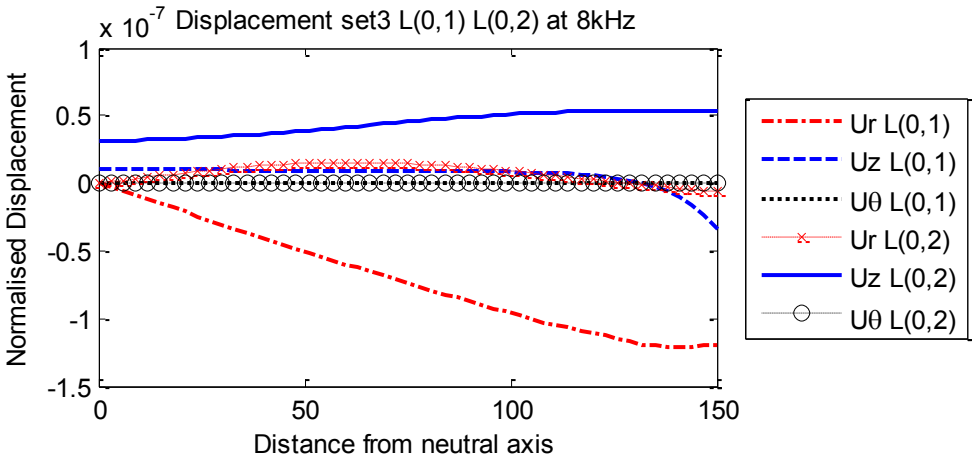

Figure B-3.10: Normalised displacement of L(0,1) and L(0,2) at 8 kHz (set 3)

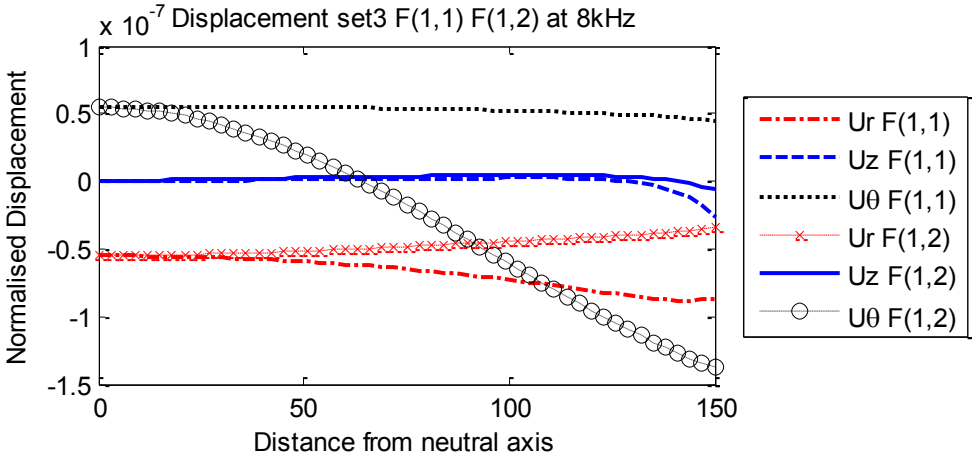

Figure B-3.11: Normalised displacement of F(1,1) and F(1,2) at 8 kHz (set 3)

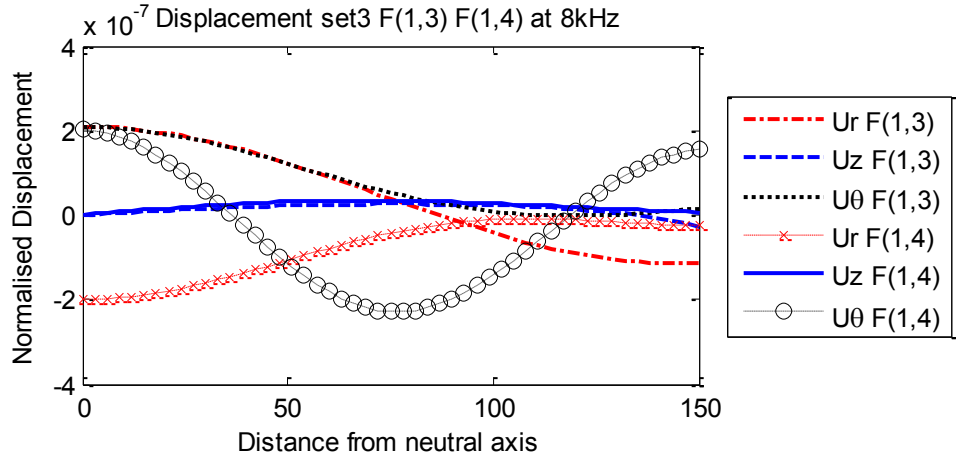

Figure B-3.12: Normalised displacement of F(1,3) and F(1,4) at 8 kHz (set 3)

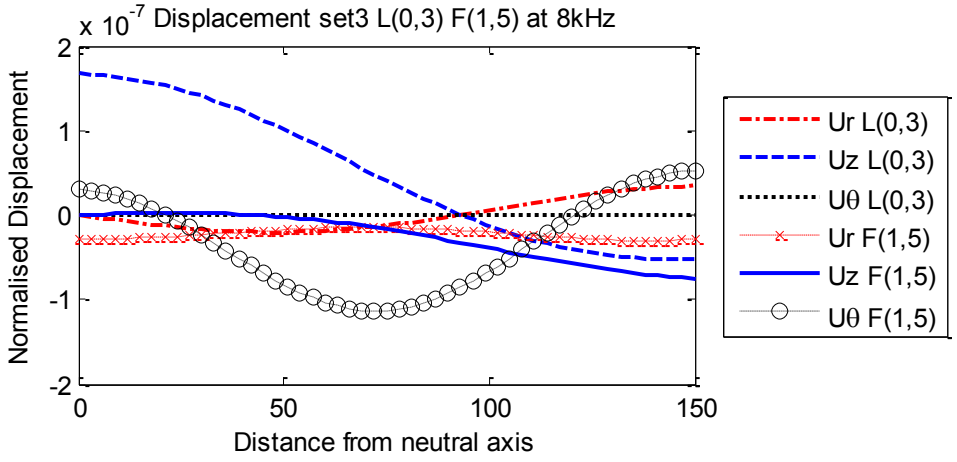

Figure B-3.13: Normalised displacement of L(0,3) and F(1,5) at 8 kHz (set 3)

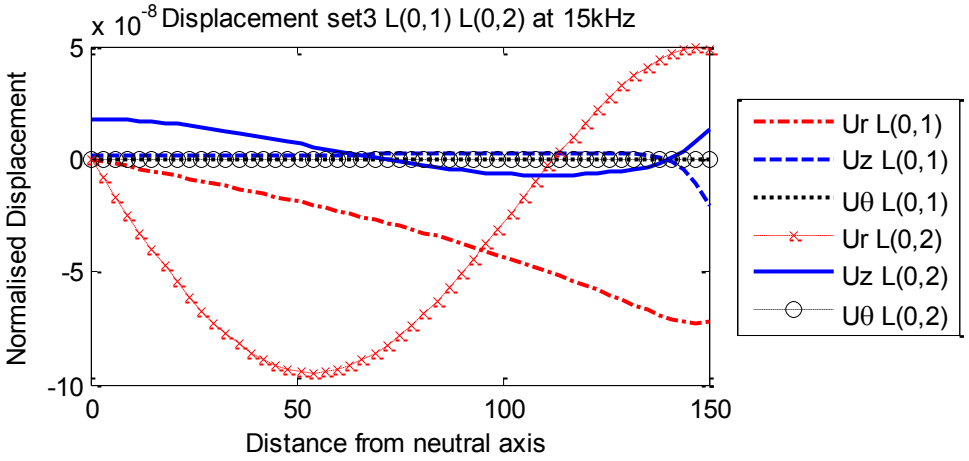

Figure B-3.14: Normalised displacement of L(0,1) and L(0,2) at 15 kHz (set 3)

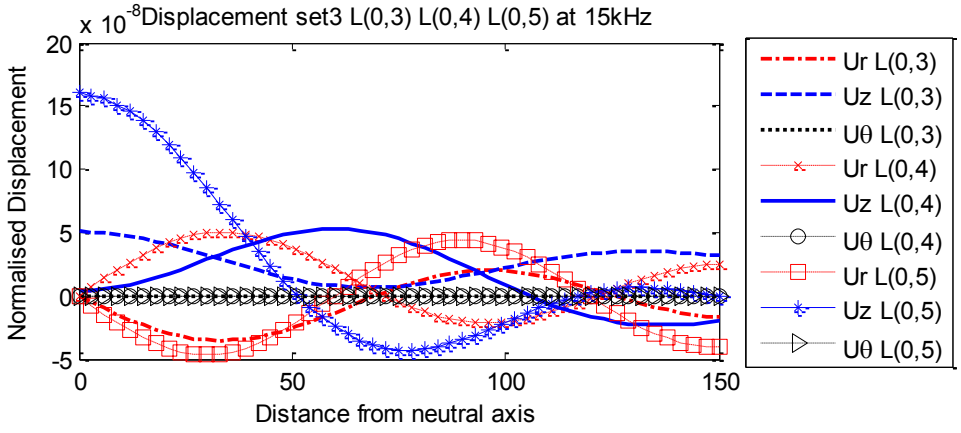

Figure B-3.15: Normalised displacement of L(0,3), L(0,4) and L(0,5) at 15 kHz (set 3)

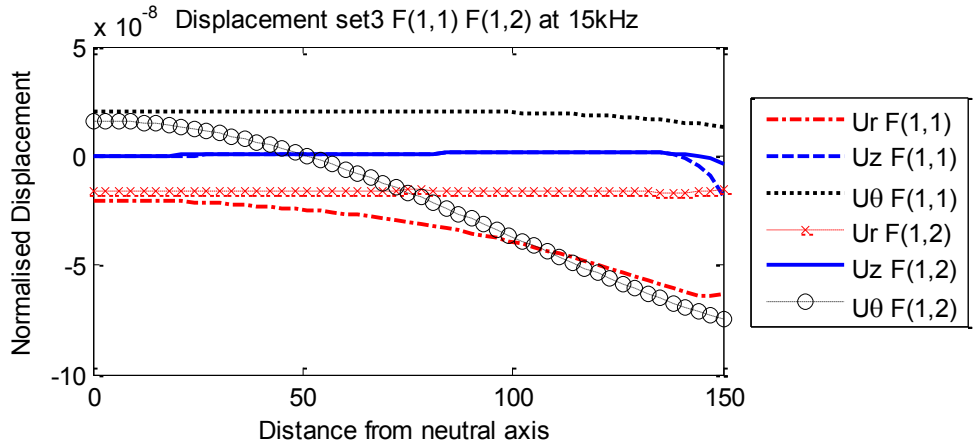

Figure B-3.16: Normalised displacement of F(1,1) and F(1,2) at 15 kHz (set 3)

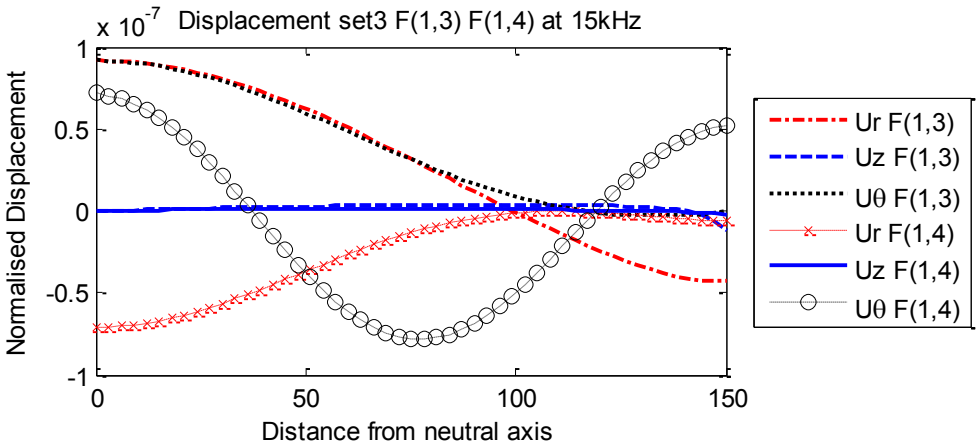

Figure B-3.17: Normalised displacement of F(1,3) and F(1,4) at 15 kHz (set 3)

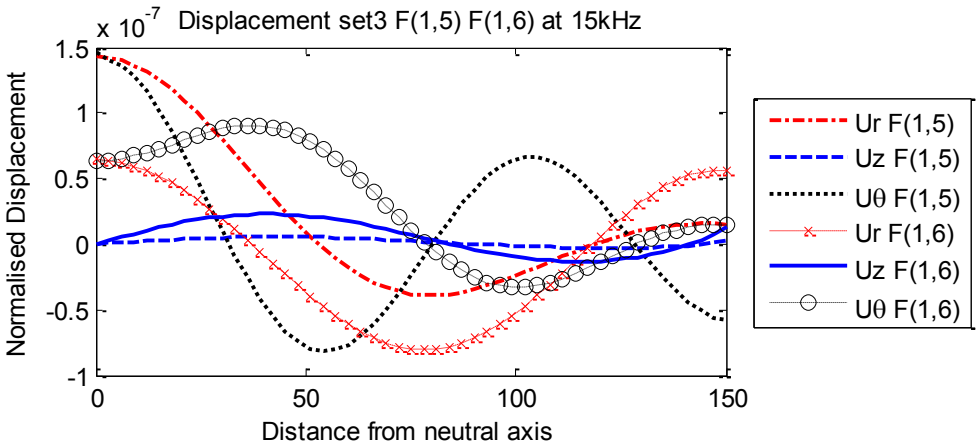

Figure B-3.18: Normalised displacement of F(1,5) and F(1,6) at 15 kHz (set 3)

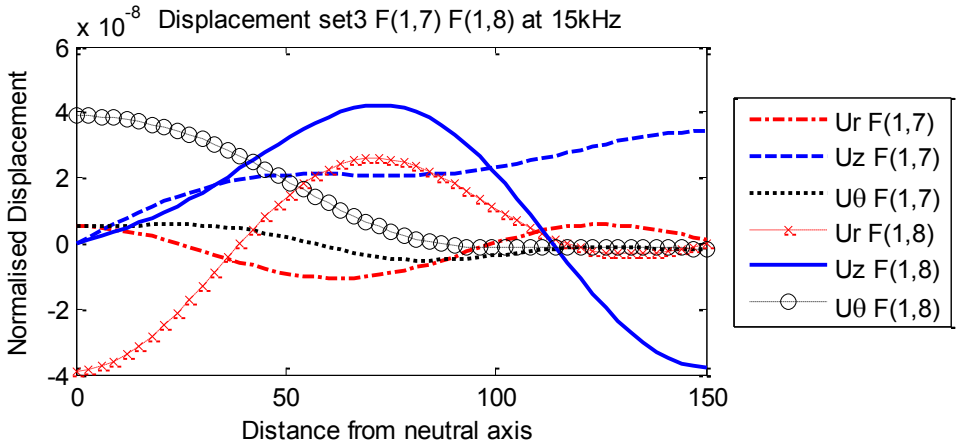

Figure B-3.19: Normalised displacement of F(1,7) and F(1,8) at 15 kHz (set 3)

Appendix C: The time domain results of analytical guided wave equation for cylindrical structures

C – 1 Time domain signal of isotropic cylinder for the input frequency of 16.5 kHz with 10 cycle sine burst

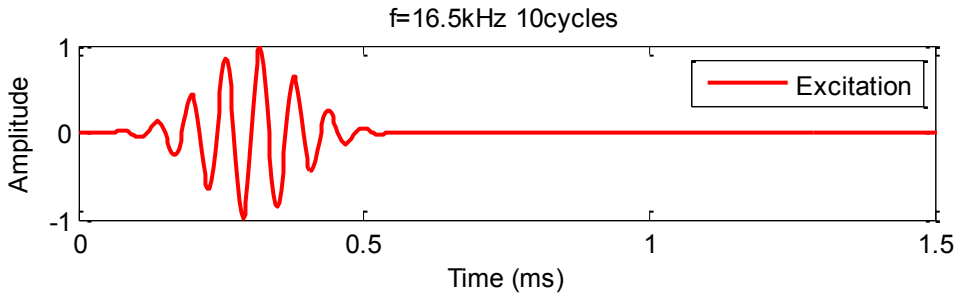

Figure C-1.1: Excitation of 16.5 kHz frequency with 10 cycles

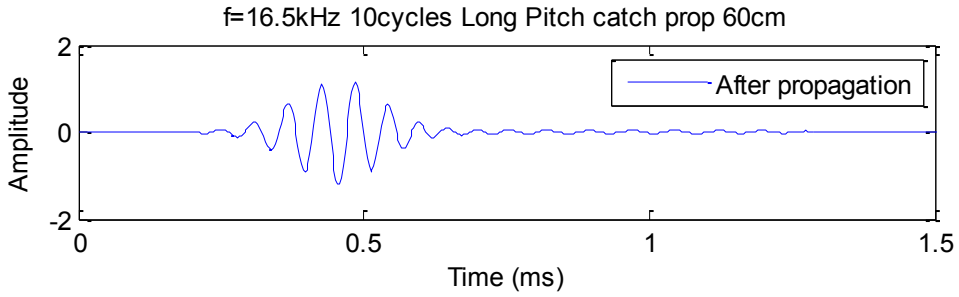

Figure C-1.2: Propagation of the longitudinal modes with a distance of 60 cm (pitch catch)

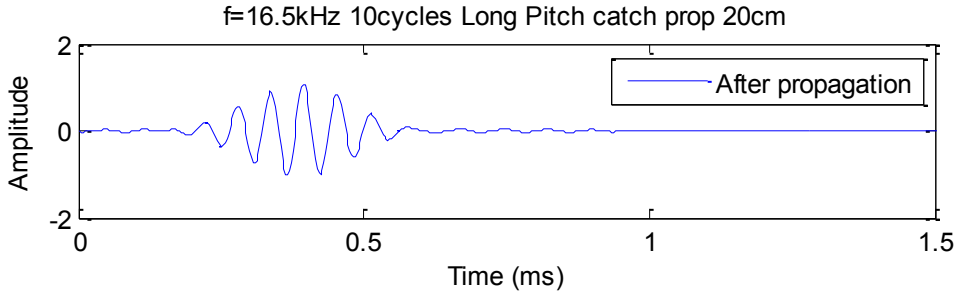

Figure C-1.3: Propagation of the longitudinal modes with a distance of 20 cm (pitch catch)

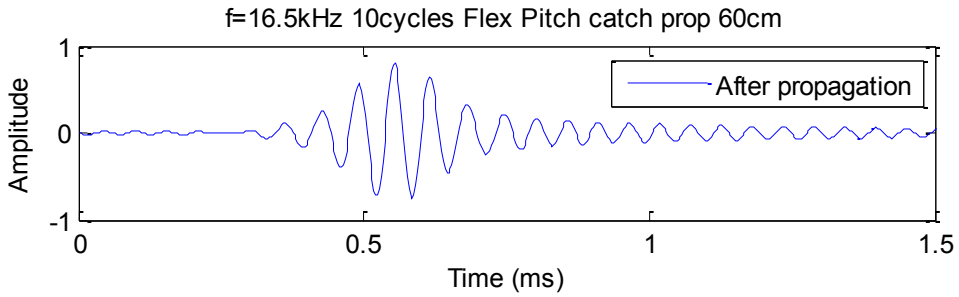

Figure C-1.4: Propagation of the flexural modes with a distance of 60 cm (pitch catch)

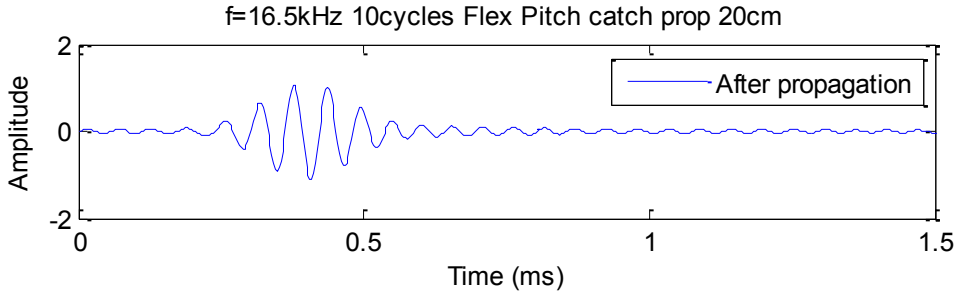

Figure C-1.5: Propagation of the flexural modes with a distance of 20 cm (pitch catch)

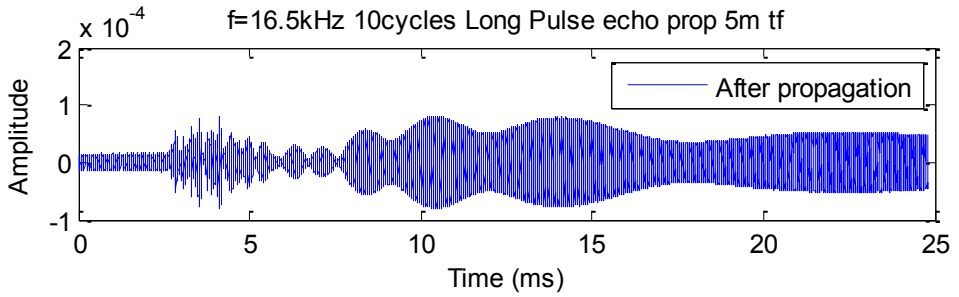

Figure C-1.6: Propagation of the longitudinal modes with a distance of 5 m (pulse echo) in traction free isotropic cylinder

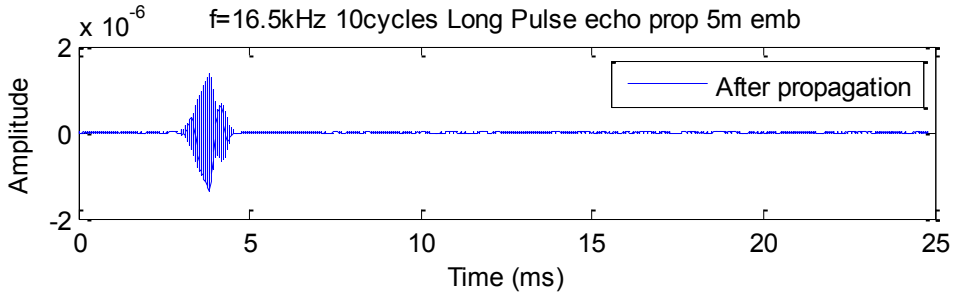

Figure C-1.7: Propagation of the longitudinal modes with a distance of 5 m (pulse echo) in embedded isotropic cylinder

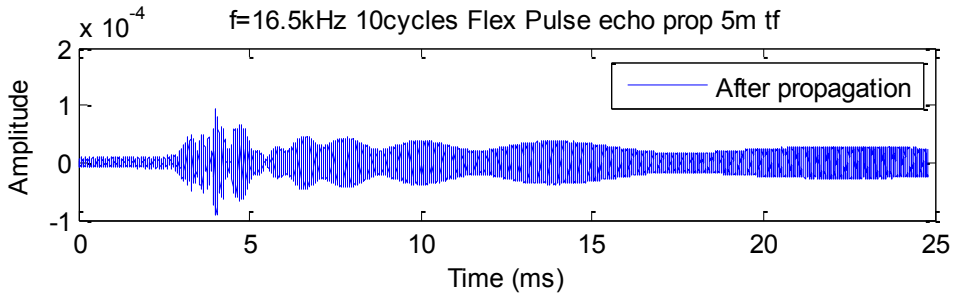

Figure C-1.8: Propagation of the flexural modes with a distance of 5 m (pulse echo) in traction free isotropic cylinder

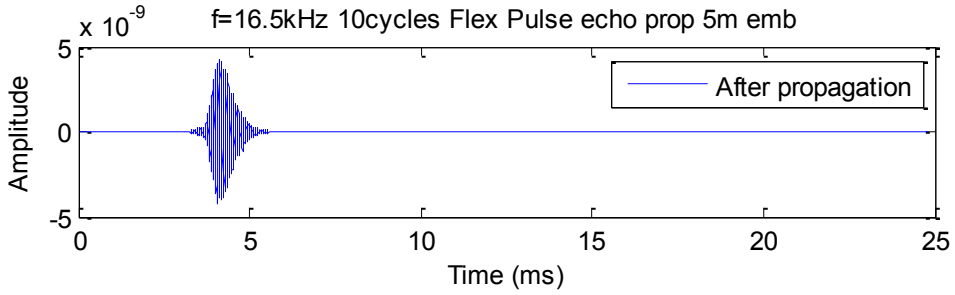

Figure C-1.9: Propagation of the flexural modes with a distance of 5 m (pulse echo) in embedded cylinder

C – 2 Time domain signal of isotropic cylinder for the input frequency of 16.5 kHz with 30 cycle sine burst

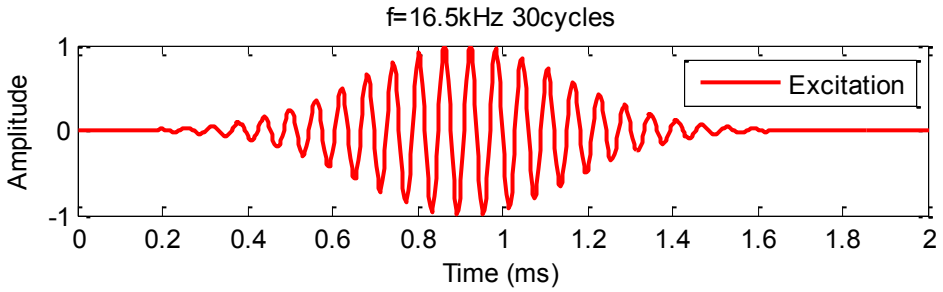

Figure C-2.1: Excitation of 16.5 kHz frequency with 30 cycles

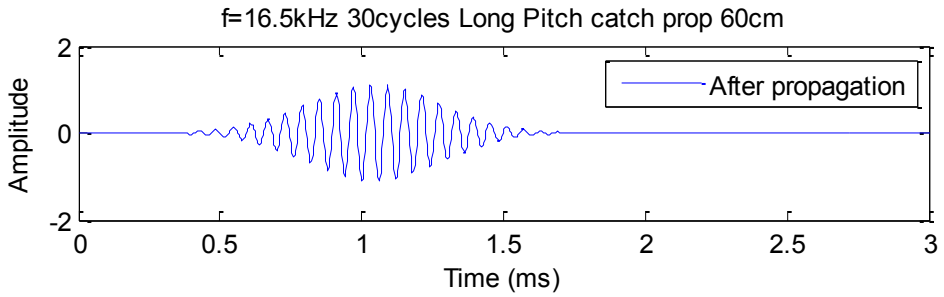

Figure C-2.2: Propagation of the longitudinal modes with a distance of 60 cm (pitch catch)

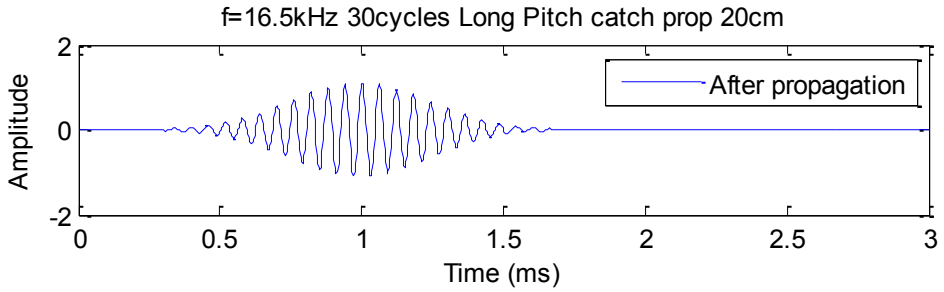

Figure C-2.3: Propagation of the longitudinal modes with a distance of 20 cm (pitch catch)

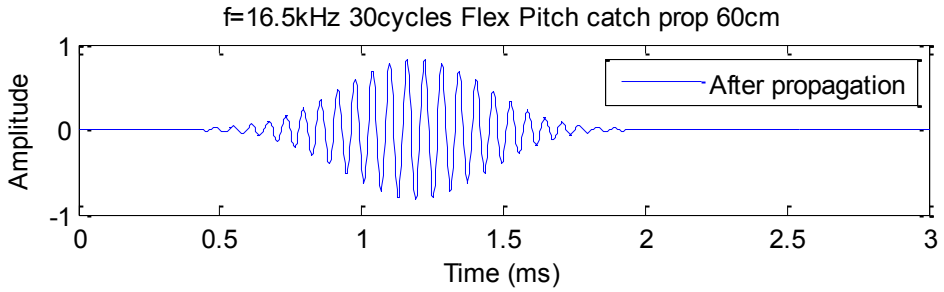

Figure C-2.4: Propagation of the flexural modes with a distance of 60 cm (pitch catch)

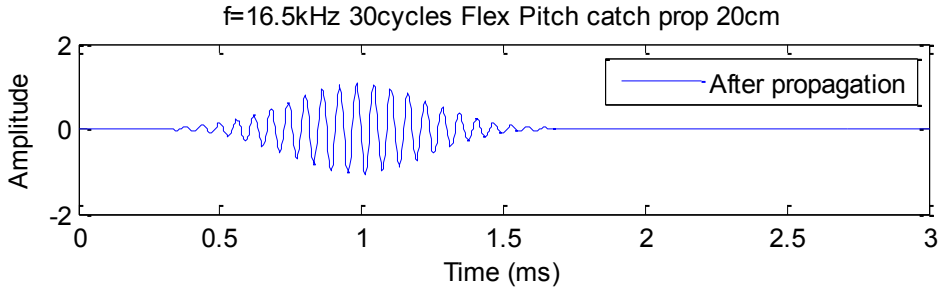

Figure C-2.5: Propagation of the flexural modes with a distance of 20 cm (pitch catch)

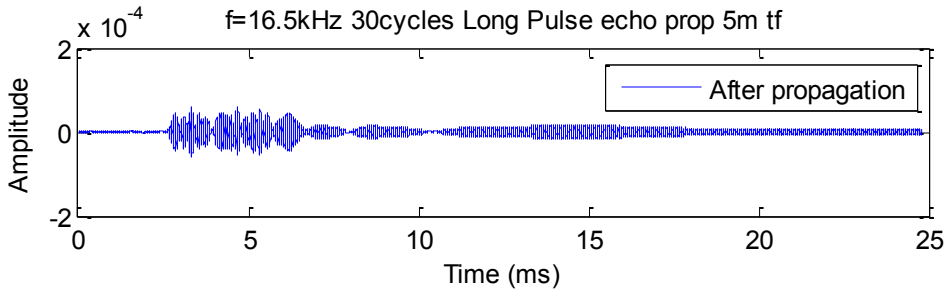

Figure C-2.6: Propagation of the longitudinal modes with a distance of 5 m (pulse echo) in traction free isotropic cylinder

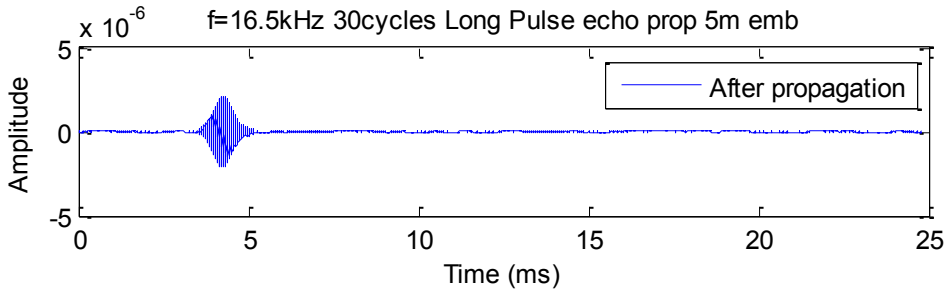

Figure C-2.7: Propagation of the longitudinal modes with a distance of 5 m (pulse echo) in embedded isotropic cylinder

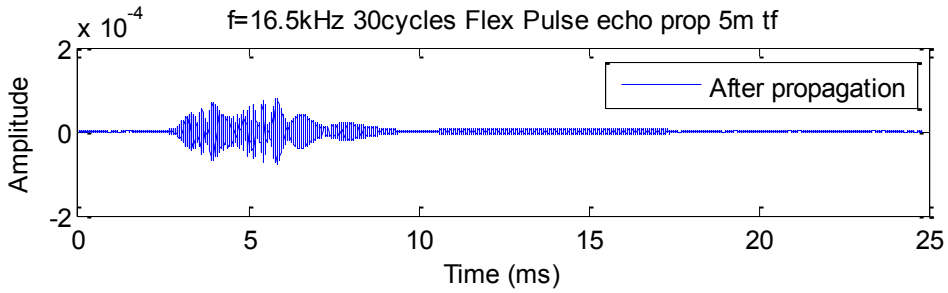

Figure C-2.8: Propagation of the flexural modes with a distance of 5 m (pulse echo) in traction free isotropic cylinder

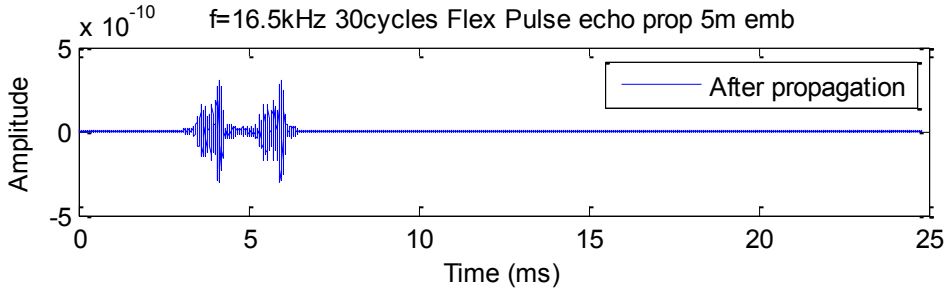

Figure C-2.9: Propagation of the flexural modes with a distance of 5 m (pulse echo) in embedded cylinder

C – 3 Time domain signal of isotropic cylinder for the input frequency of 50 kHz with 10 cycle sine burst

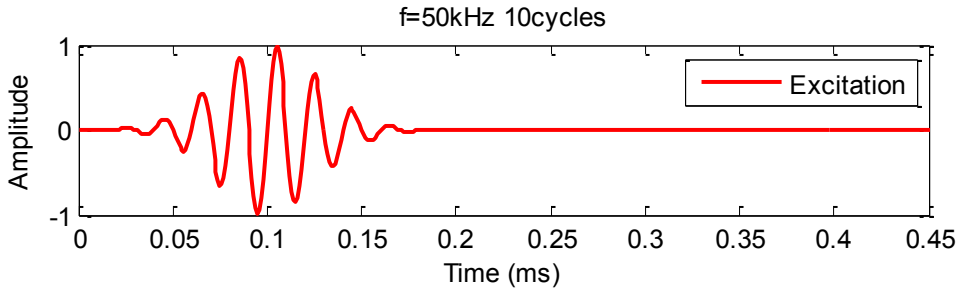

Figure C-3.1: Excitation of 50 kHz frequency with 10 cycles

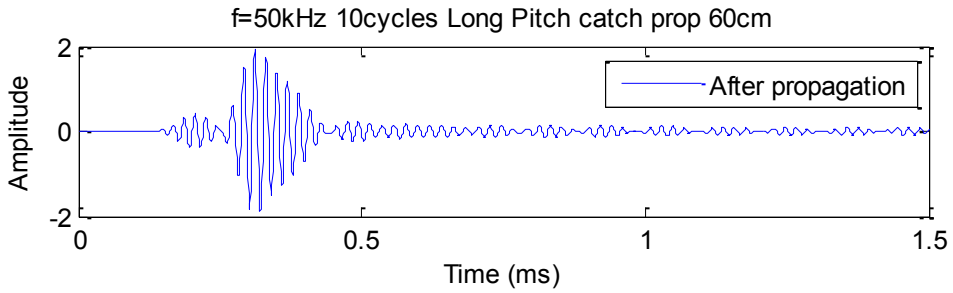

Figure C-3.2: Propagation of the longitudinal modes with a distance of 60 cm (pitch catch)

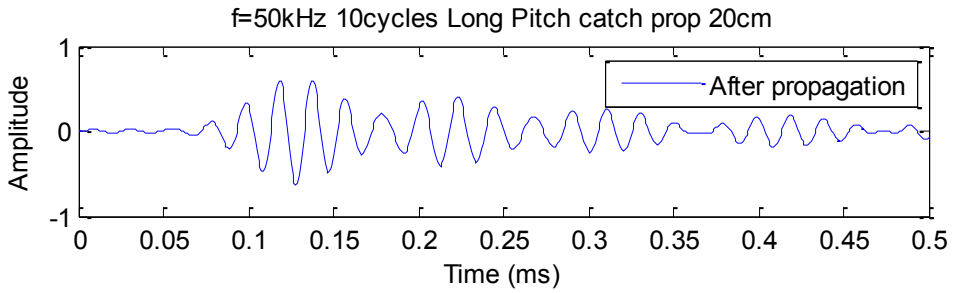

Figure C-3.3: Propagation of the longitudinal modes with a distance of 20 cm (pitch catch)

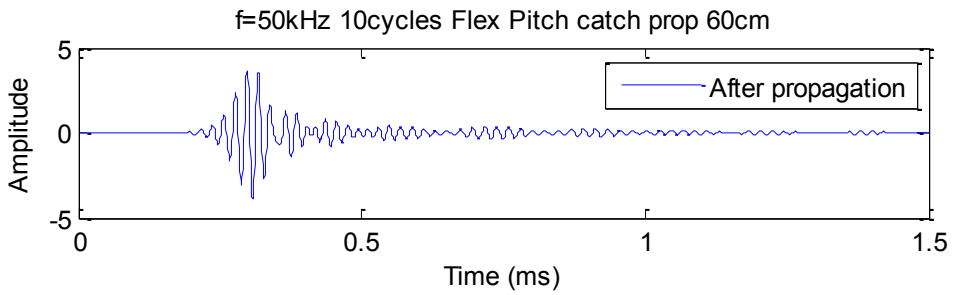

Figure C-3.4: Propagation of the flexural modes with a distance of 60 cm (pitch catch)

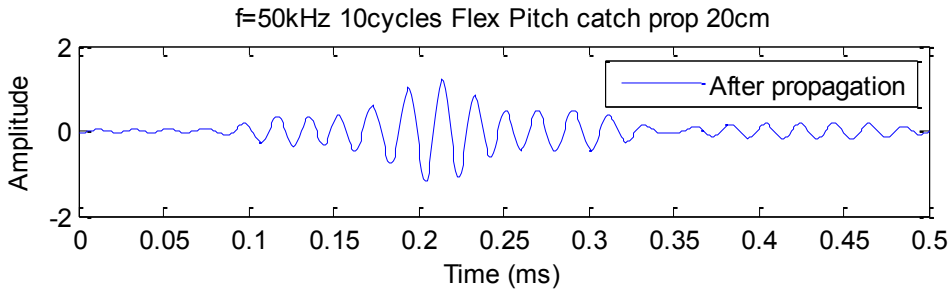

Figure C-3.5: Propagation of the flexural modes with a distance of 20 cm (pitch catch)

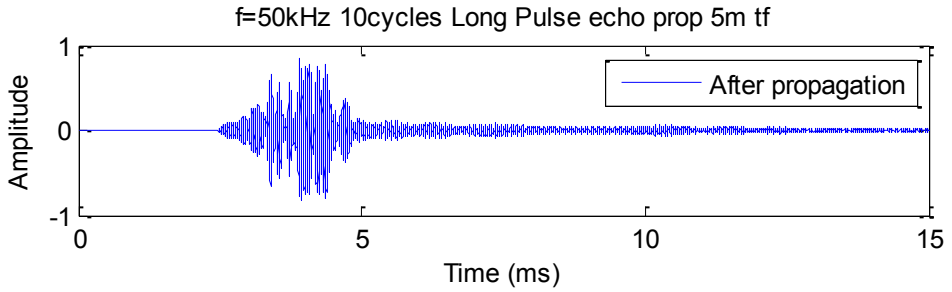

Figure C-3.6: Propagation of the longitudinal modes with a distance of 5 m (pulse echo) in traction free isotropic cylinder

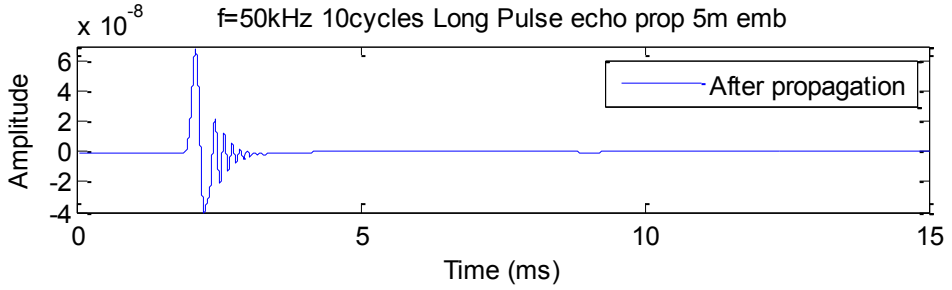

Figure C-3.7: Propagation of the longitudinal modes with a distance of 5 m (pulse echo) in embedded isotropic cylinder

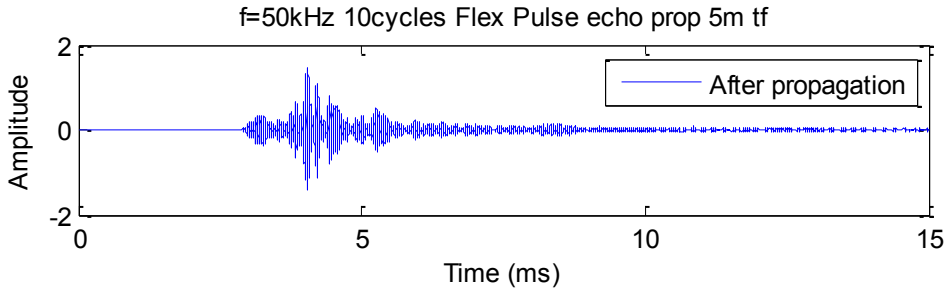

Figure C-3.8: Propagation of the flexural modes with a distance of 5 m (pulse echo) in traction free isotropic cylinder

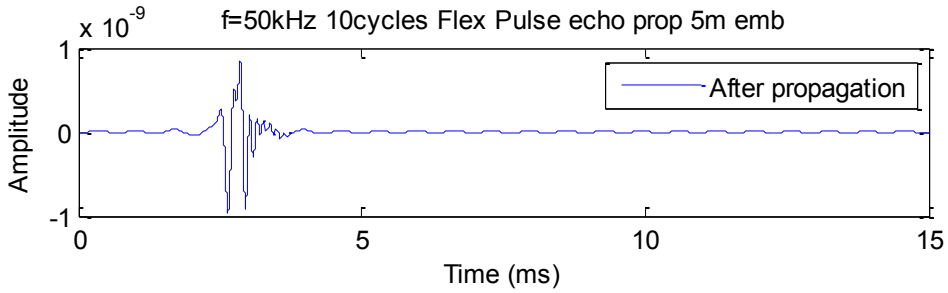

Figure C-3.9: Propagation of the flexural modes with a distance of 5 m (pulse echo) in embedded cylinder

Appendix D: The time domain reconstruction of guided wave equation for cylindrical structures using SFEM

D – 1 Individual contribution of longitudinal and contraction modes for the anisotropic cylinder with the vertical impact at the top of the pole

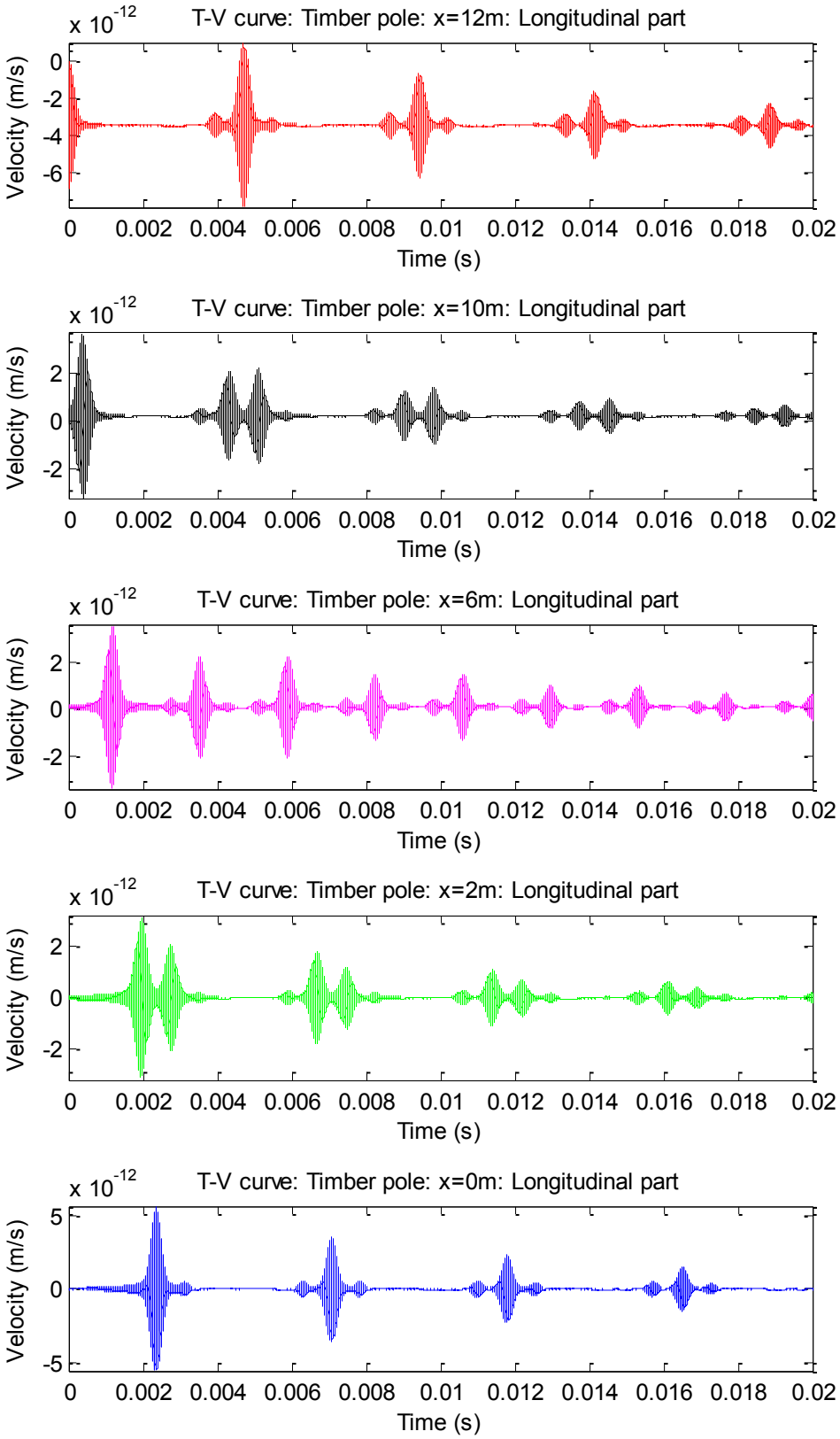

Figure D-1.1: Contribution of longitudinal modes in an anisotropic cylinder with impact at top (vertically) considering timber pole situation (input frequency 20 kHz)

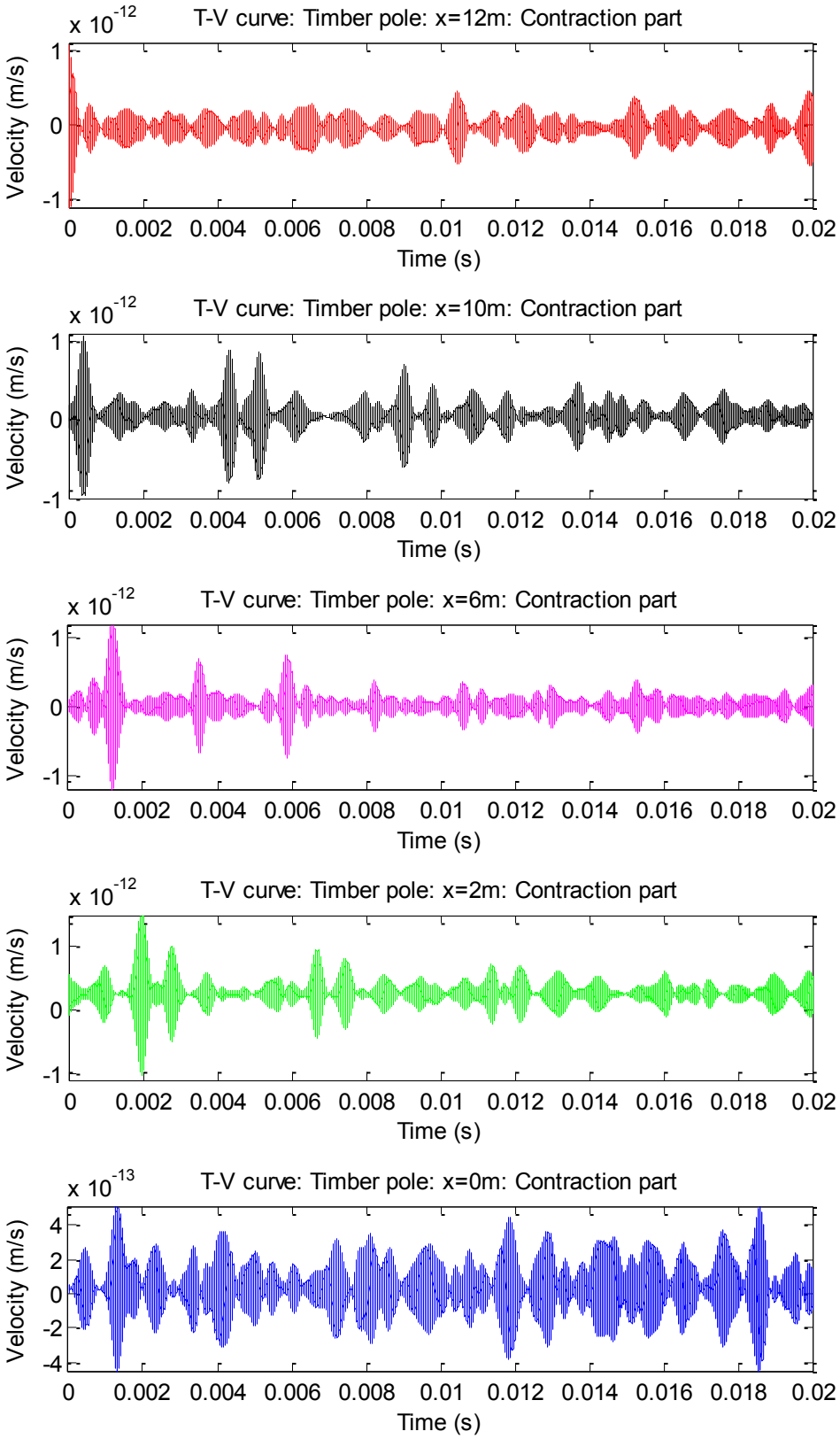

Figure D-1.2: Contribution of contraction modes in an anisotropic cylinder with impact at top (vertically) considering timber pole situation (input frequency 20 kHz)

D – 2 Individual contribution of flexural and shear modes for the anisotropic cylinder with the horizontal impact at the top of the pole

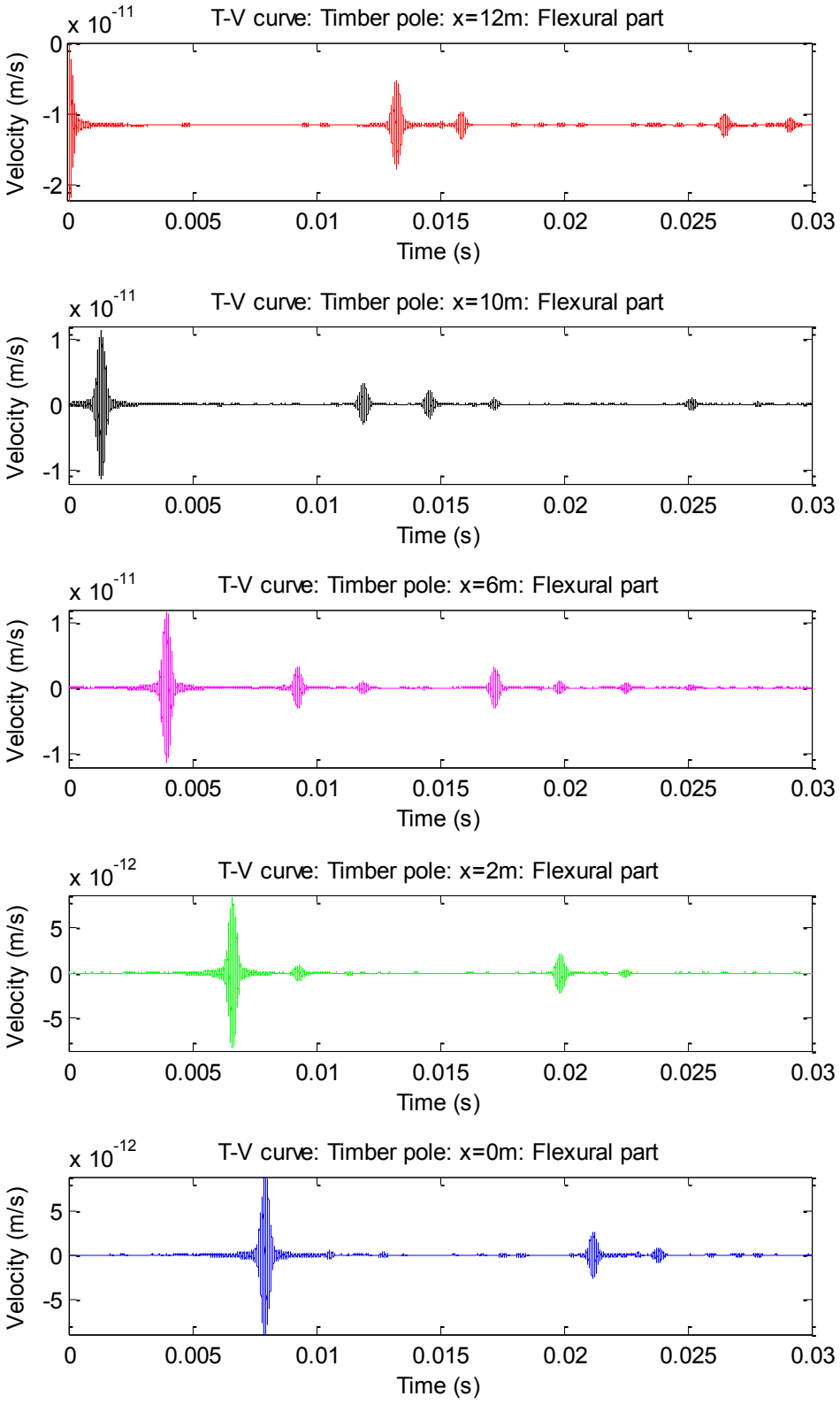

Figure D-2.1: Contribution of flexural modes in an anisotropic cylinder with impact at top (horizontally) considering timber pole situation (input frequency 12 kHz)

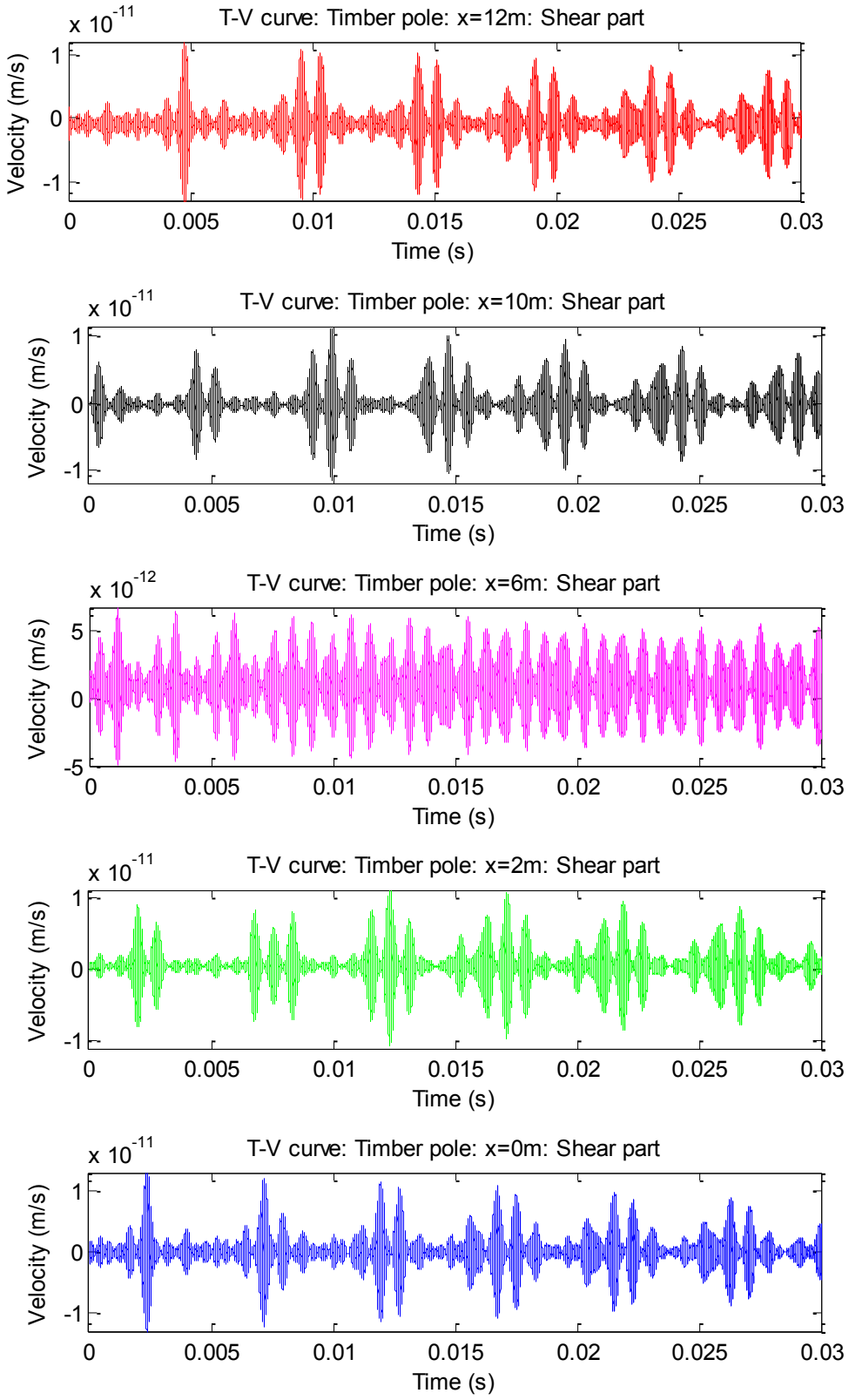

Figure D-2.2: Contribution of shear modes in an anisotropic cylinder with impact at top (horizontally) considering timber pole situation (input frequency 12 kHz)

D – 3 Time domain reconstruction of the anisotropic cylinder with the vertical impact at the middle section of the pole

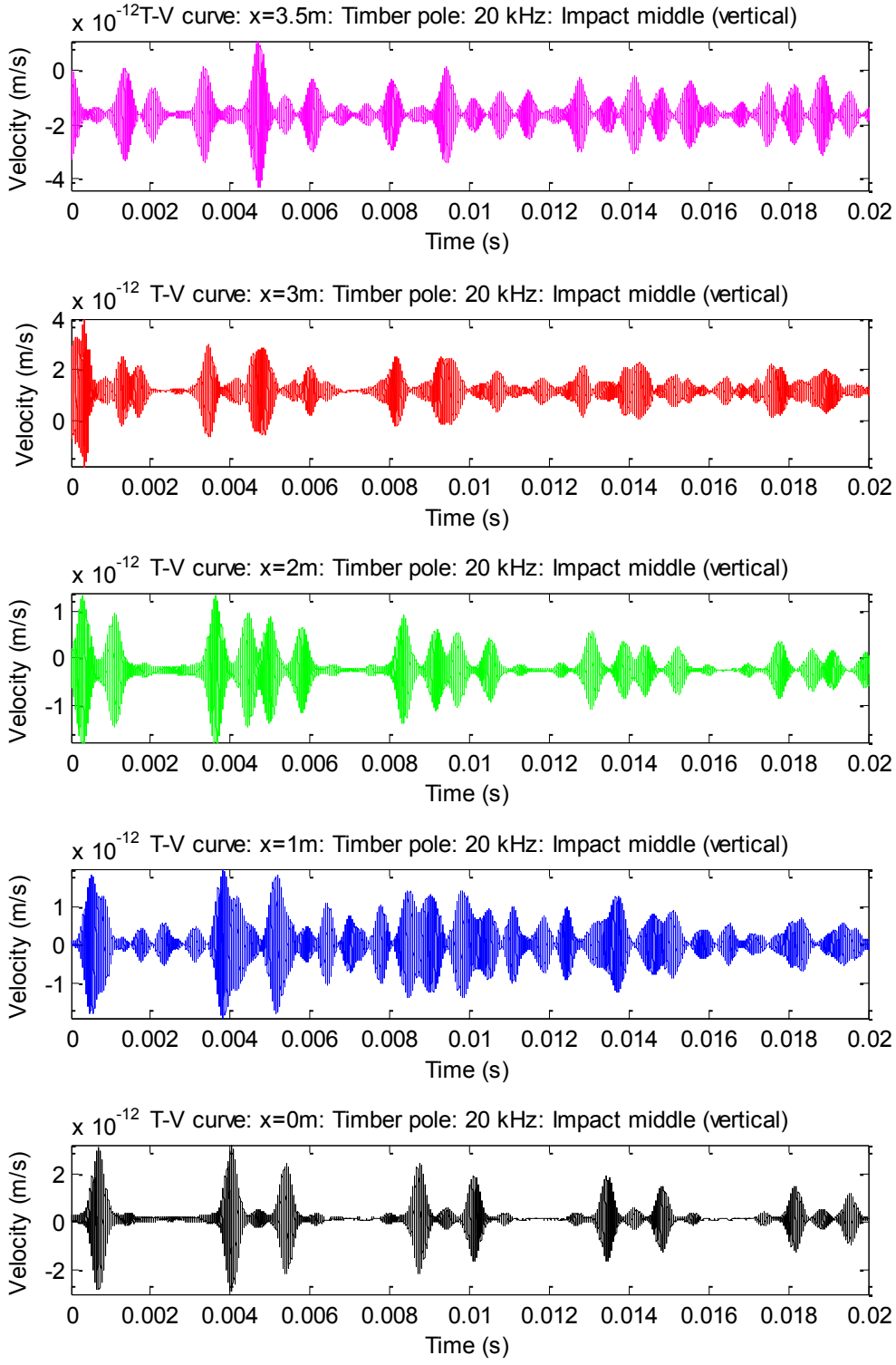

Figure D-3.1: Time domain results of anisotropic cylinder with vertical impact at the middle section of the pole considering timber pole situation (down going wave)

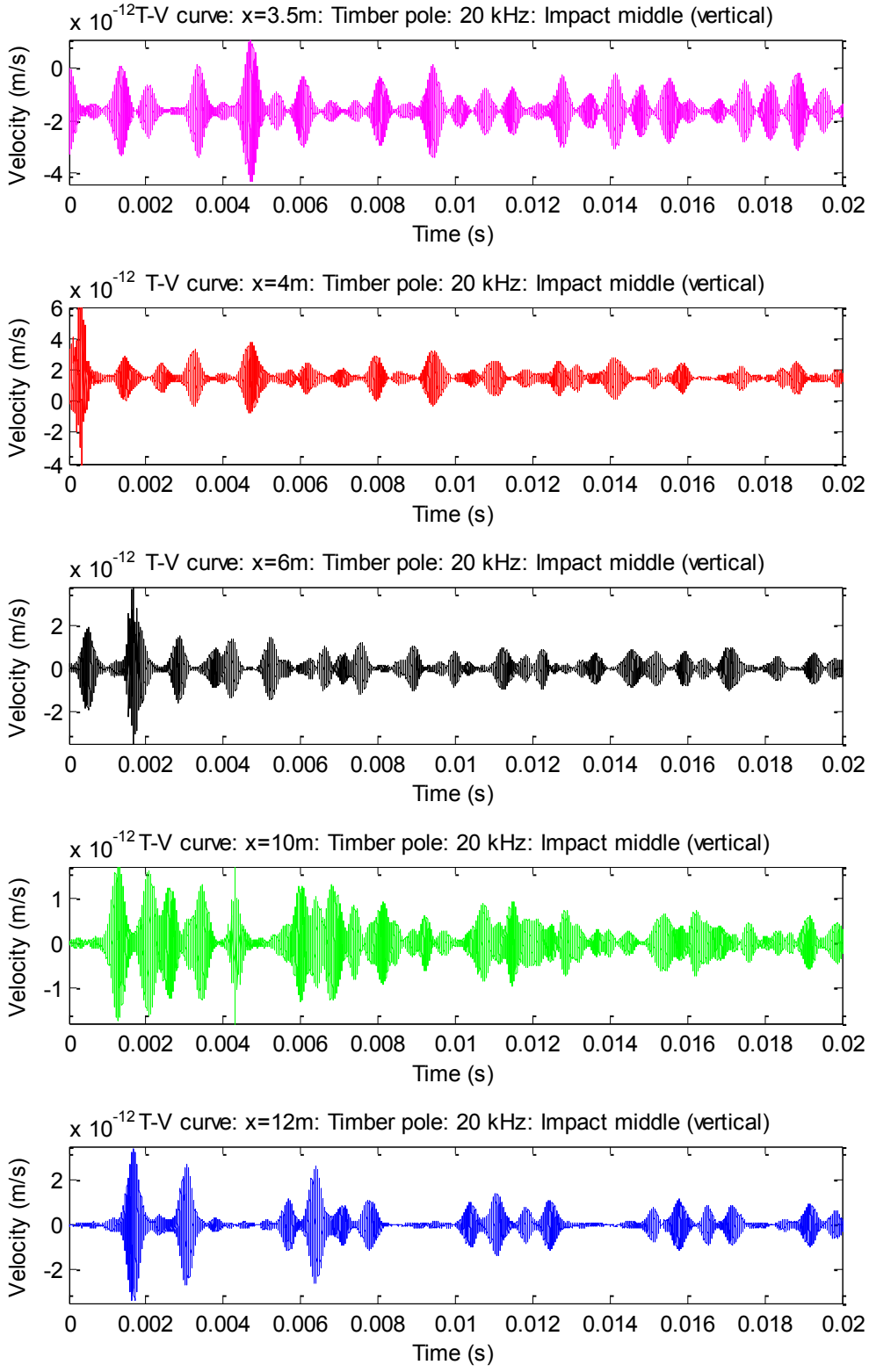

Figure D-3.2: Time domain results of anisotropic cylinder with vertical impact at the middle section of the pole considering timber pole situation (up going wave)

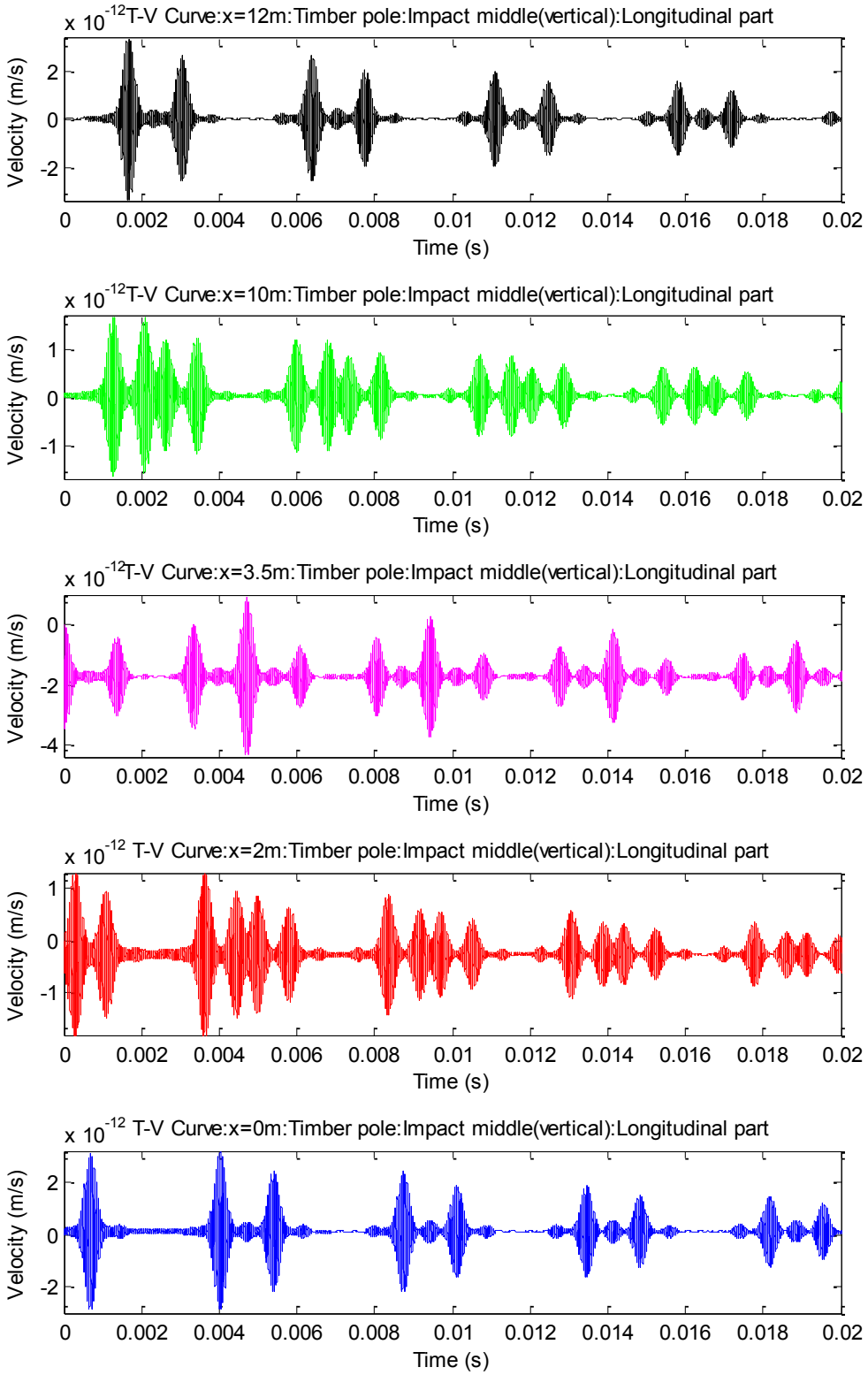

Figure D-3.3: Contribution of longitudinal modes in an anisotropic cylinder with impact at middle (vertically) considering timber pole situation (input frequency 20 kHz)

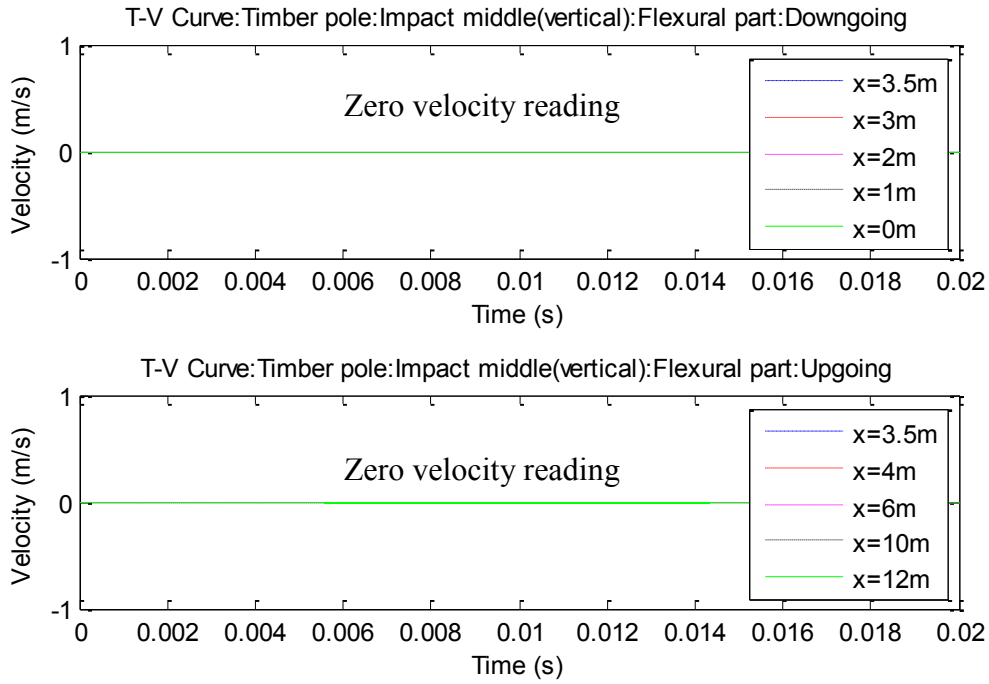

Figure D-3.4: Contribution of flexural modes in an anisotropic cylinder with impact at middle (vertically) considering timber pole situation (input frequency 20 kHz)

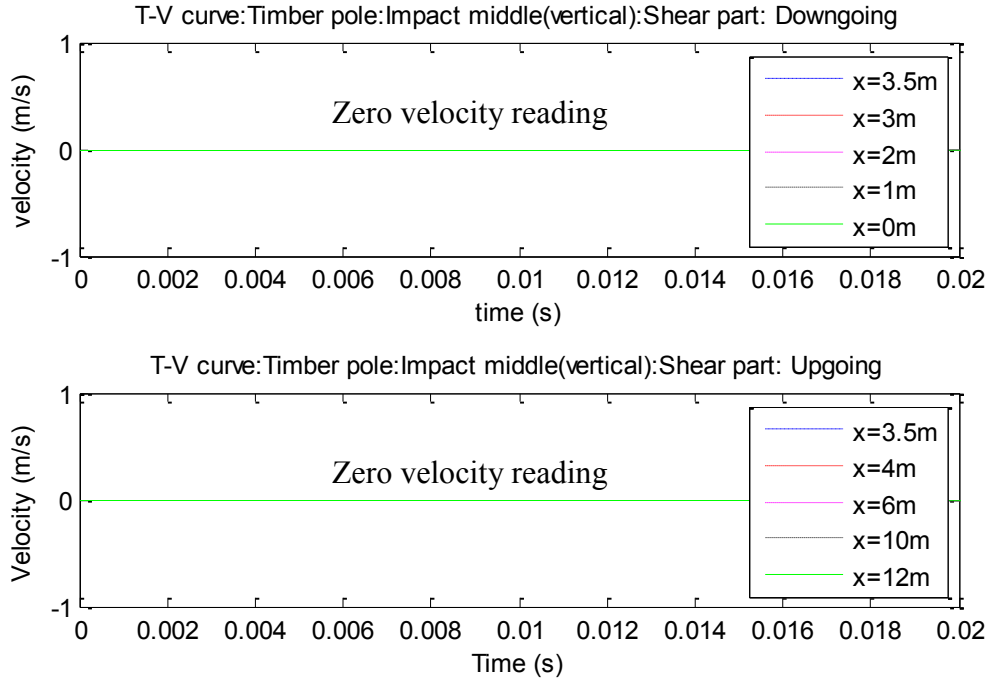

Figure D-3.5: Contribution of shear modes in an anisotropic cylinder with impact at middle (vertically) considering timber pole situation (input frequency 20 kHz)

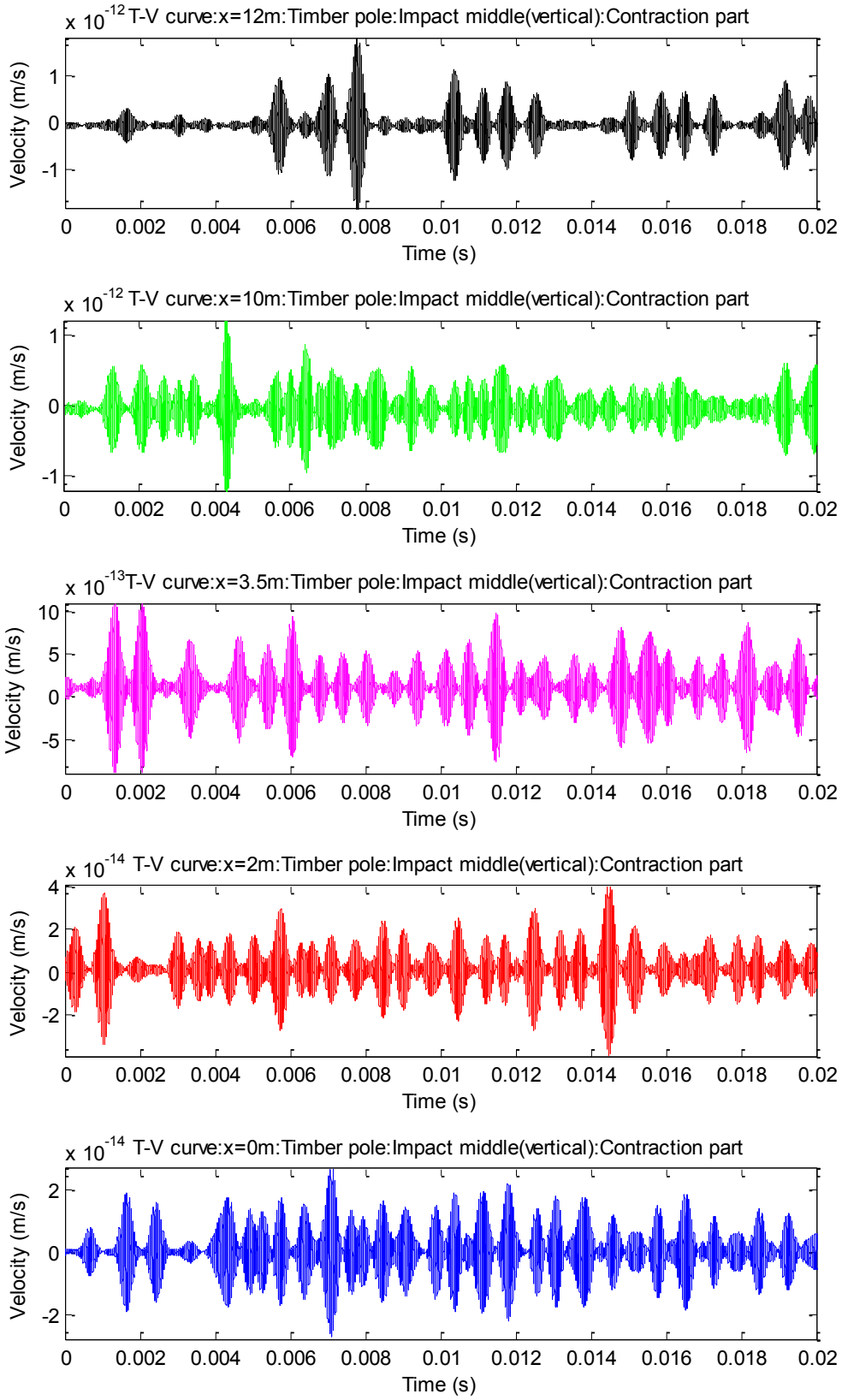

Figure D-3.6: Contribution of contraction modes in an anisotropic cylinder with impact at middle (vertically) considering timber pole situation (input frequency 20 kHz)

D – 4 Time domain reconstruction of the anisotropic cylinder with the horizontal impact at the middle section of the pole

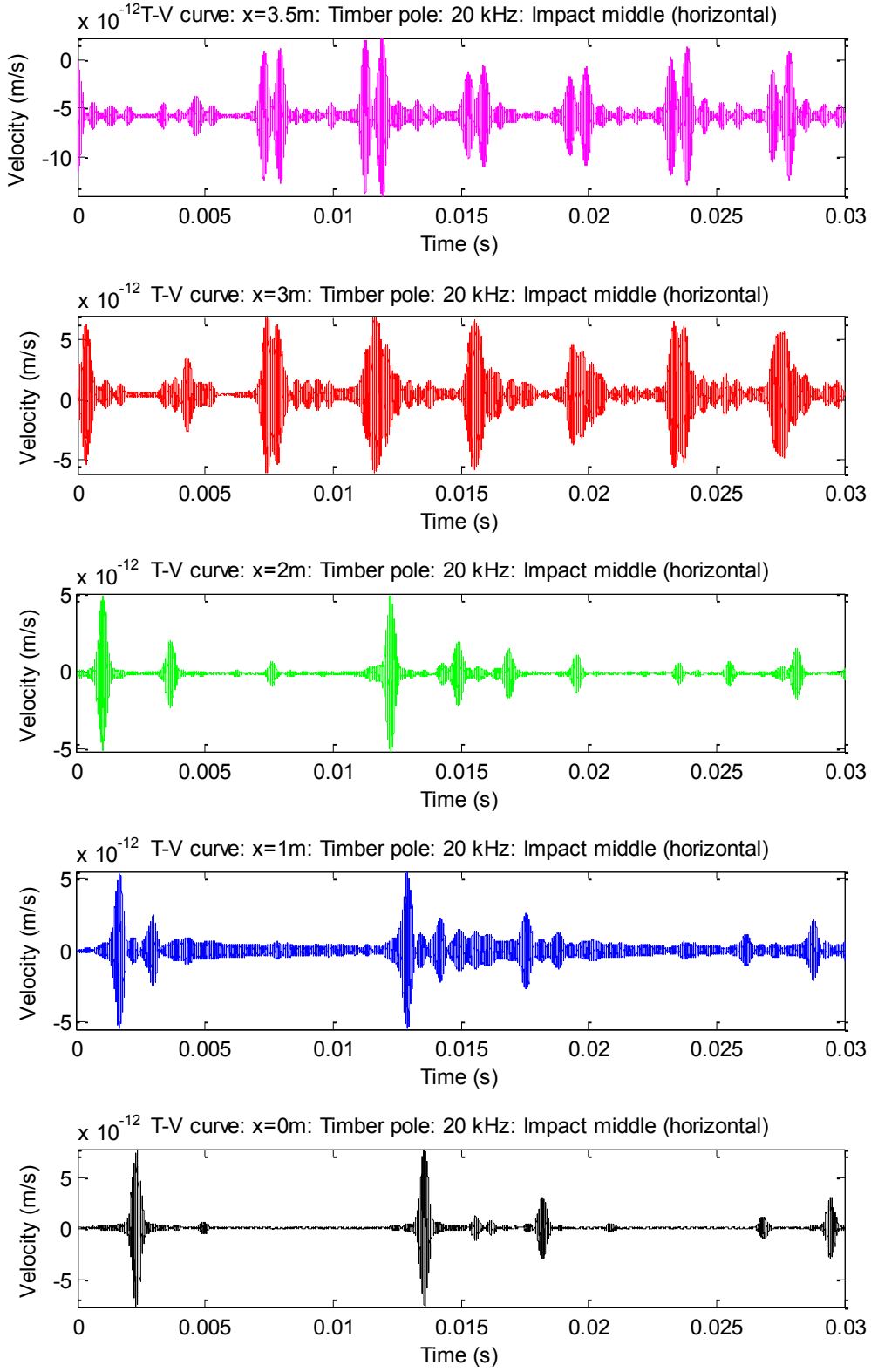

Figure D-4.1: Time domain results of anisotropic cylinder with horizontal impact at the middle section of the pole considering timber pole situation (down going wave)

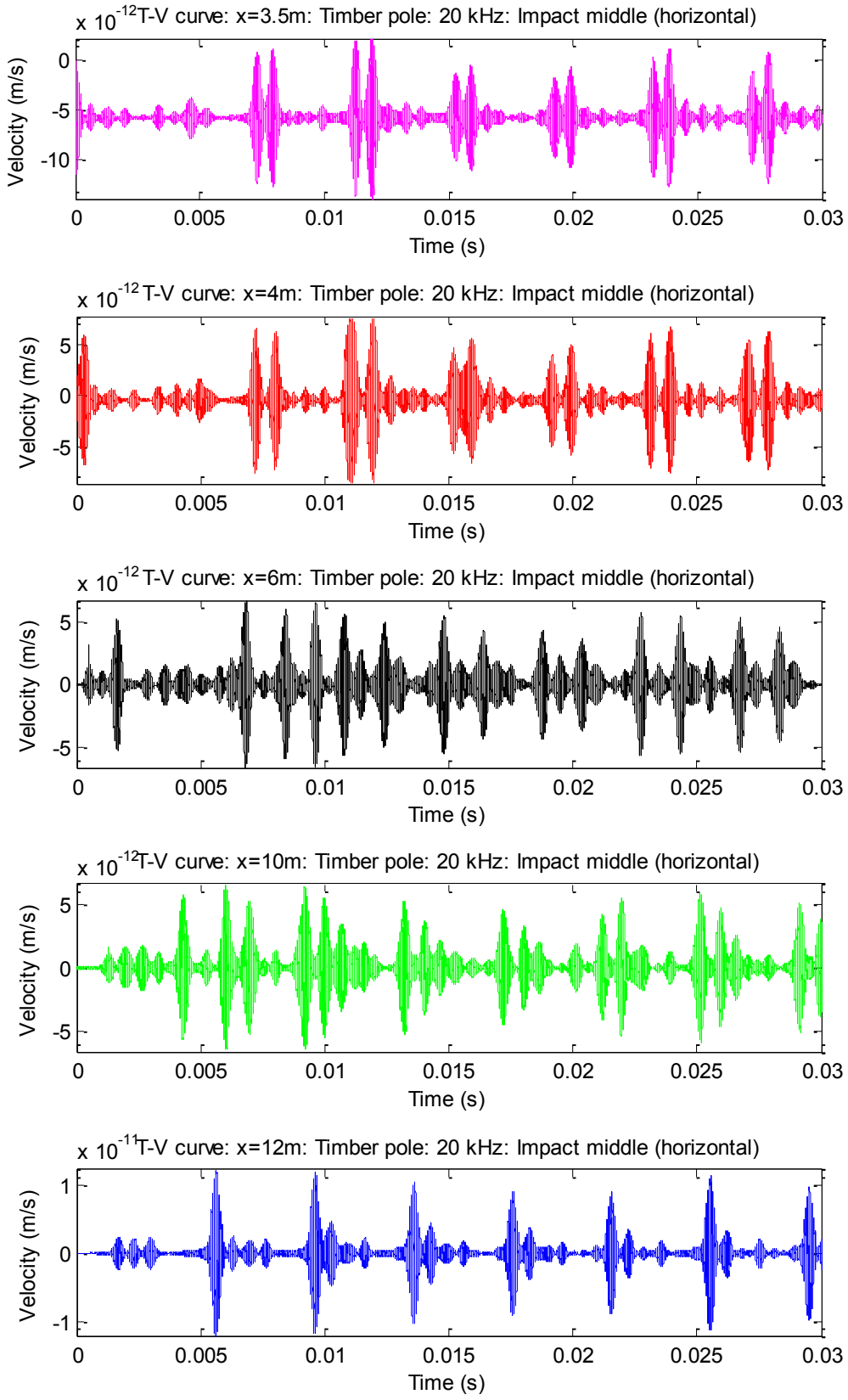

Figure D-4.2: Time domain results of anisotropic cylinder with horizontal impact at the middle section of the pole considering timber pole situation (up going wave)

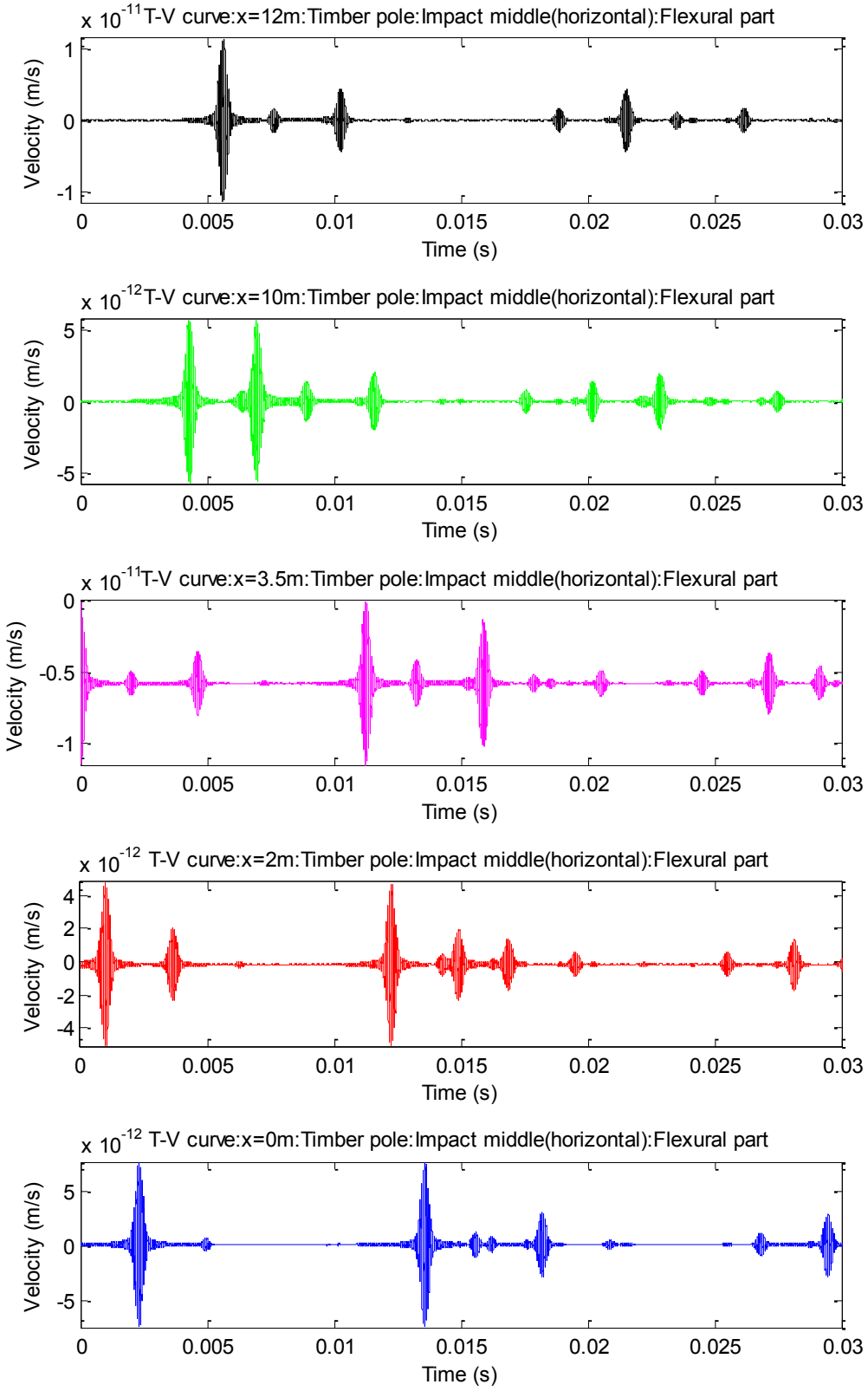

Figure D-4.3: Contribution of flexural modes in an anisotropic cylinder with impact at middle (horizontally) considering timber pole situation (input frequency 20 kHz)

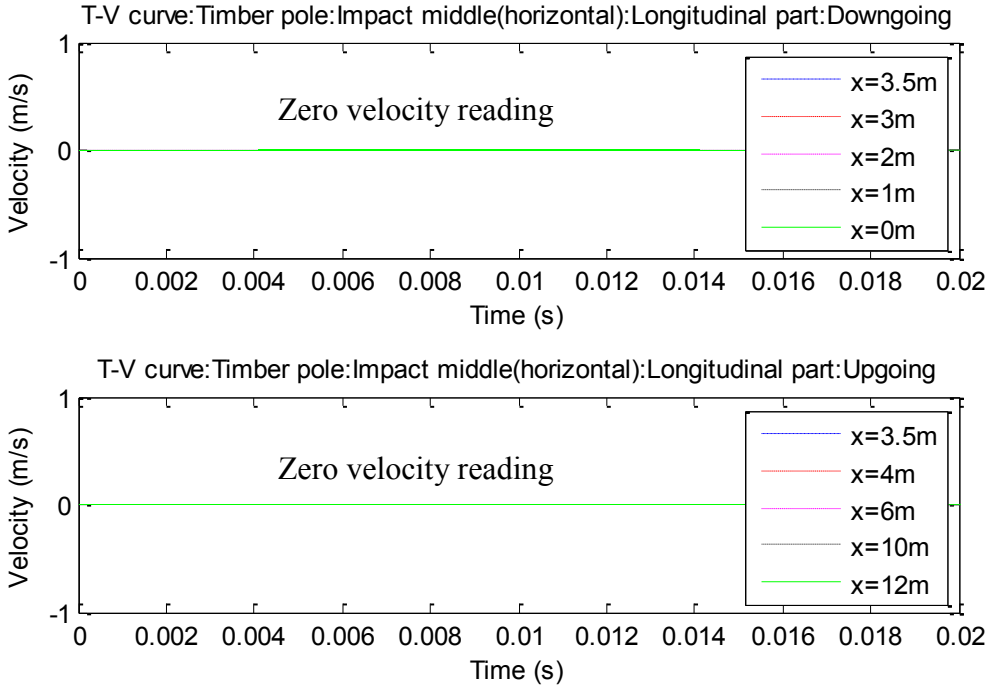

Figure D-4.4: Contribution of longitudinal modes in an anisotropic cylinder with impact at middle (horizontally) considering timber pole situation (input frequency 20 kHz)

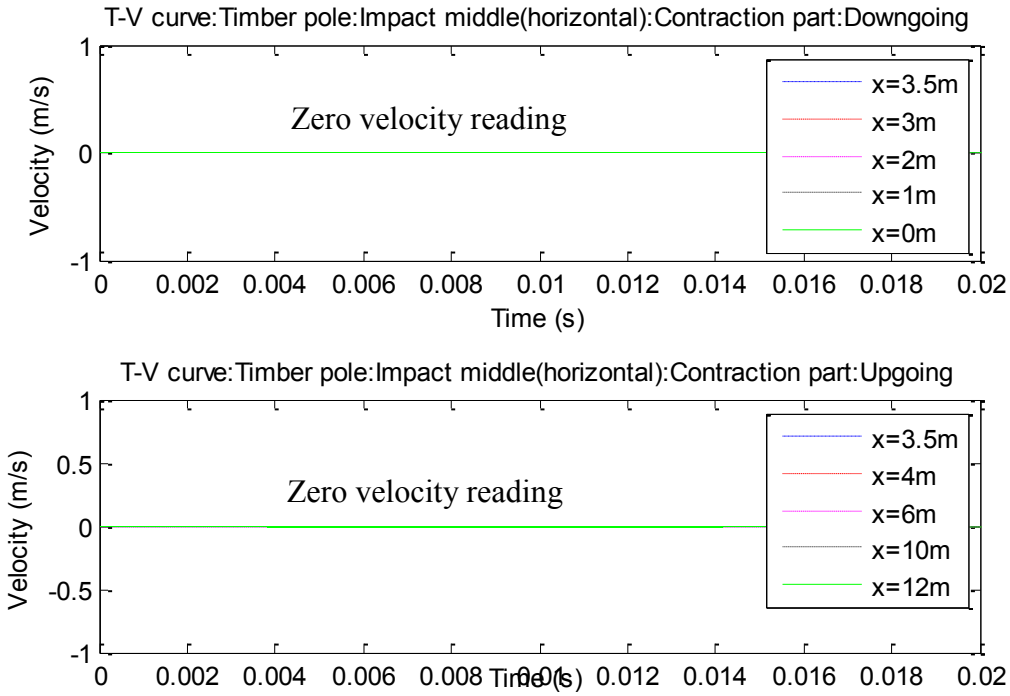

Figure D-4.5: Contribution of contraction modes in an anisotropic cylinder with impact at middle (horizontally) considering timber pole situation (input frequency 20 kHz)

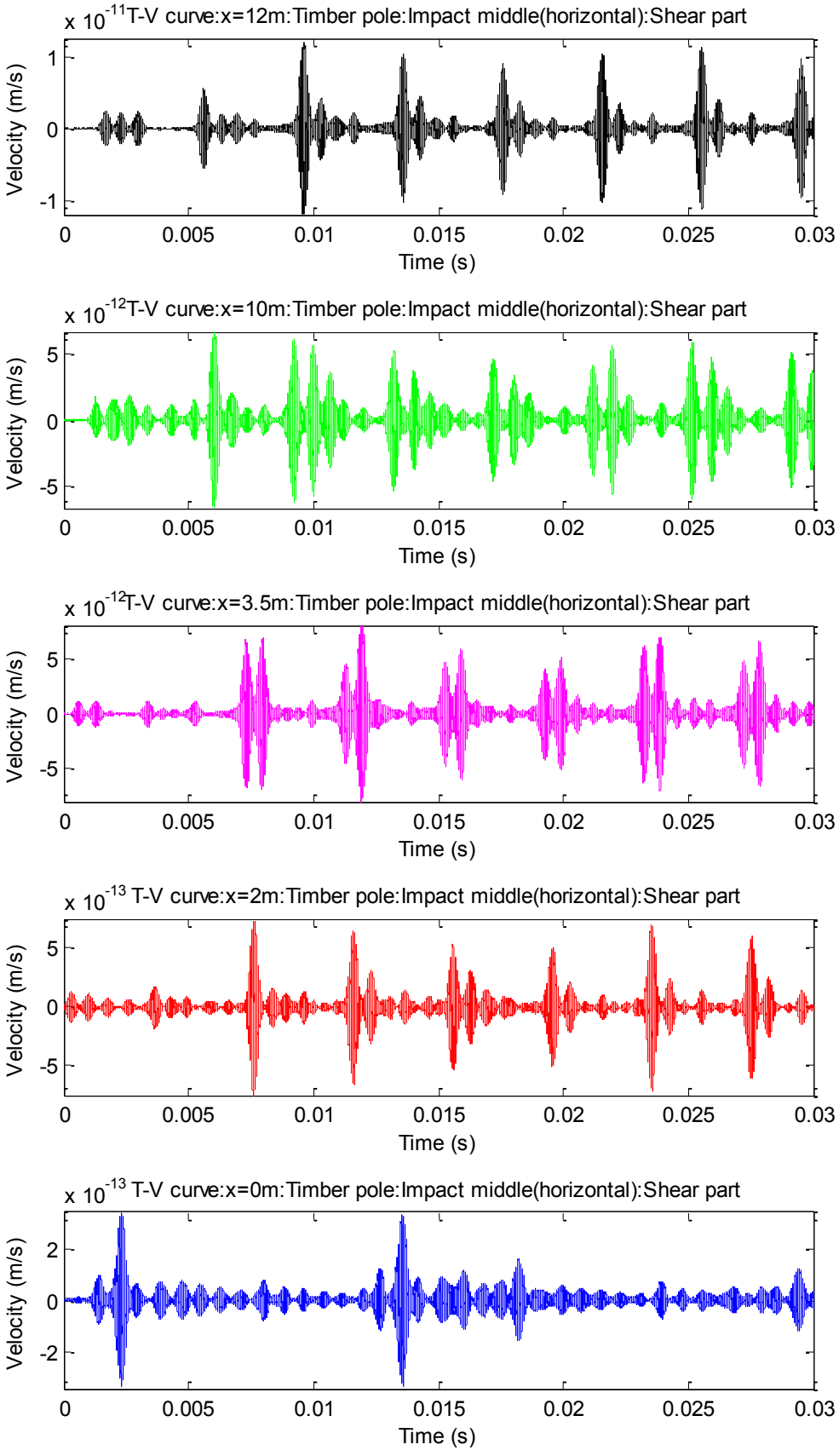

Figure D-4.6: Contribution of shear modes in an anisotropic cylinder with impact at middle (horizontally) considering timber pole situation (input frequency 20 kHz)

Appendix E: The CWT and SKM coefficient plots of a signal from timber pole obtained using FEM

E – 1 CWT coefficient plot at the common frequencies for case 1 and case 2

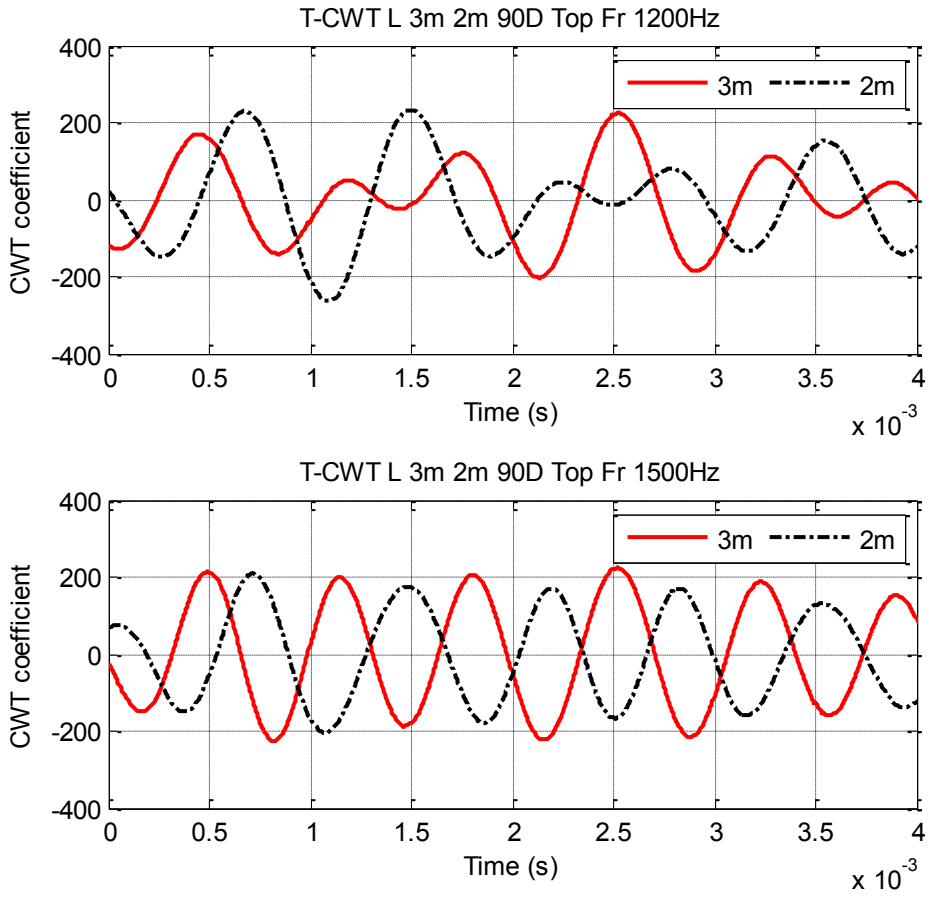

Figure E-1.1: CWT coefficient plots at the common frequencies between two sensors at the location of 90° orientated axially (case 1)

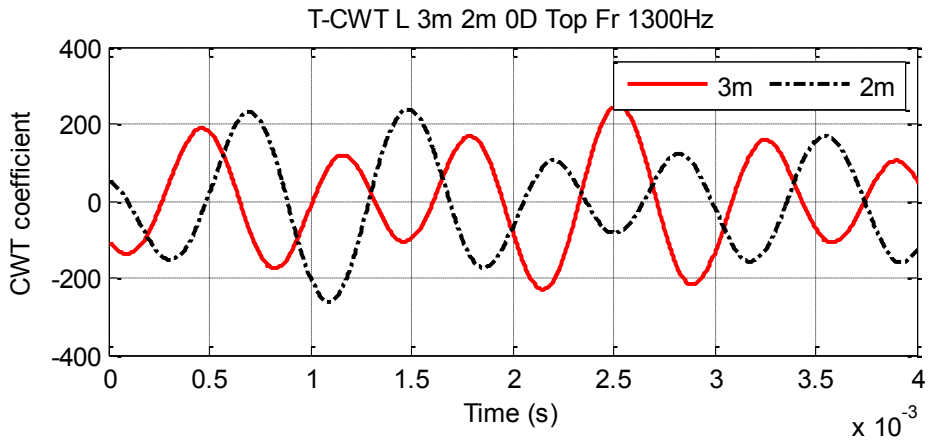

Figure E-1.2: CWT coefficient plots at the common frequency between two sensors at the location of 0° orientated axially (case 1)

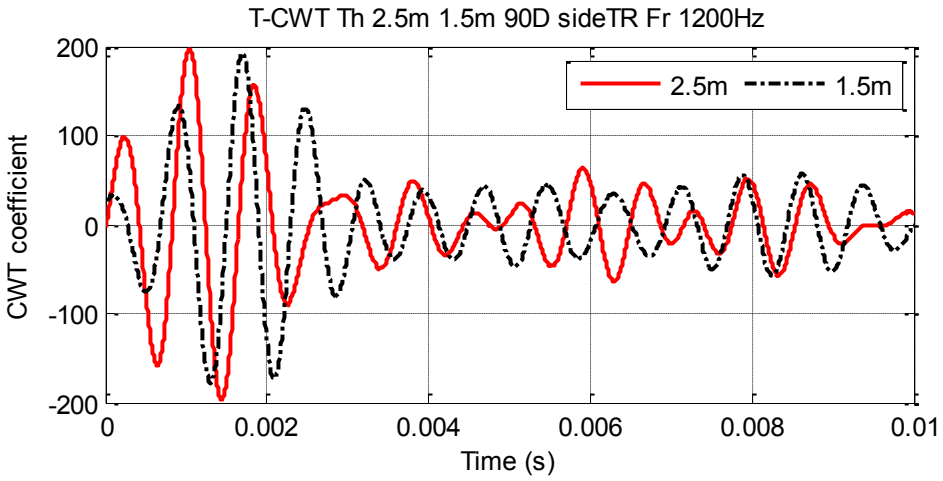

Figure E-1.3: CWT coefficient plots at the common frequency between two sensors at the location of 90° orientated tangentially (case 2)

E – 2 CWT coefficient plot at the common frequencies for case 3

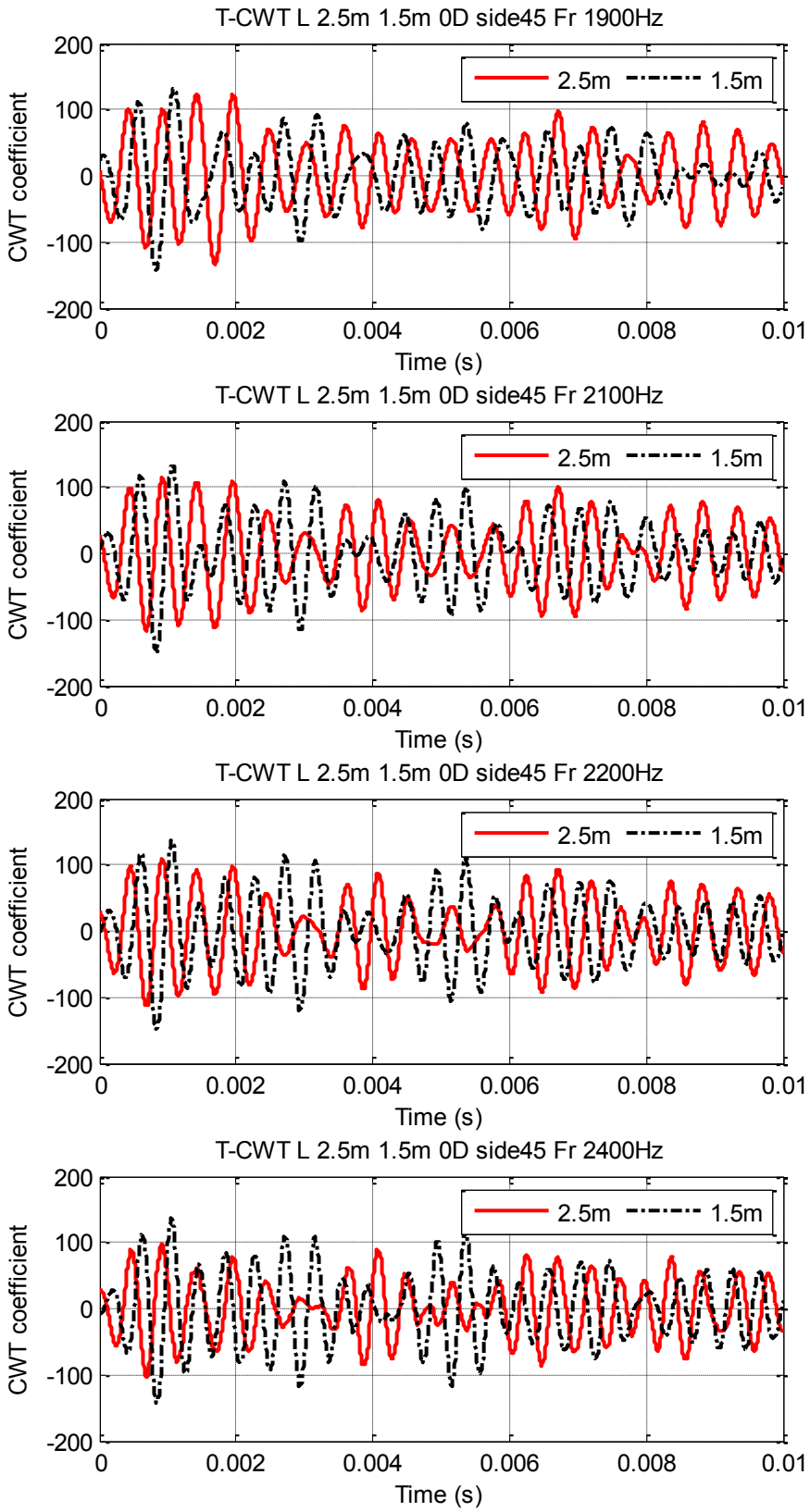

Figure E-2.1: CWT coefficient plots at the common frequencies between two sensors at the location of 0° orientated axially (case 3)

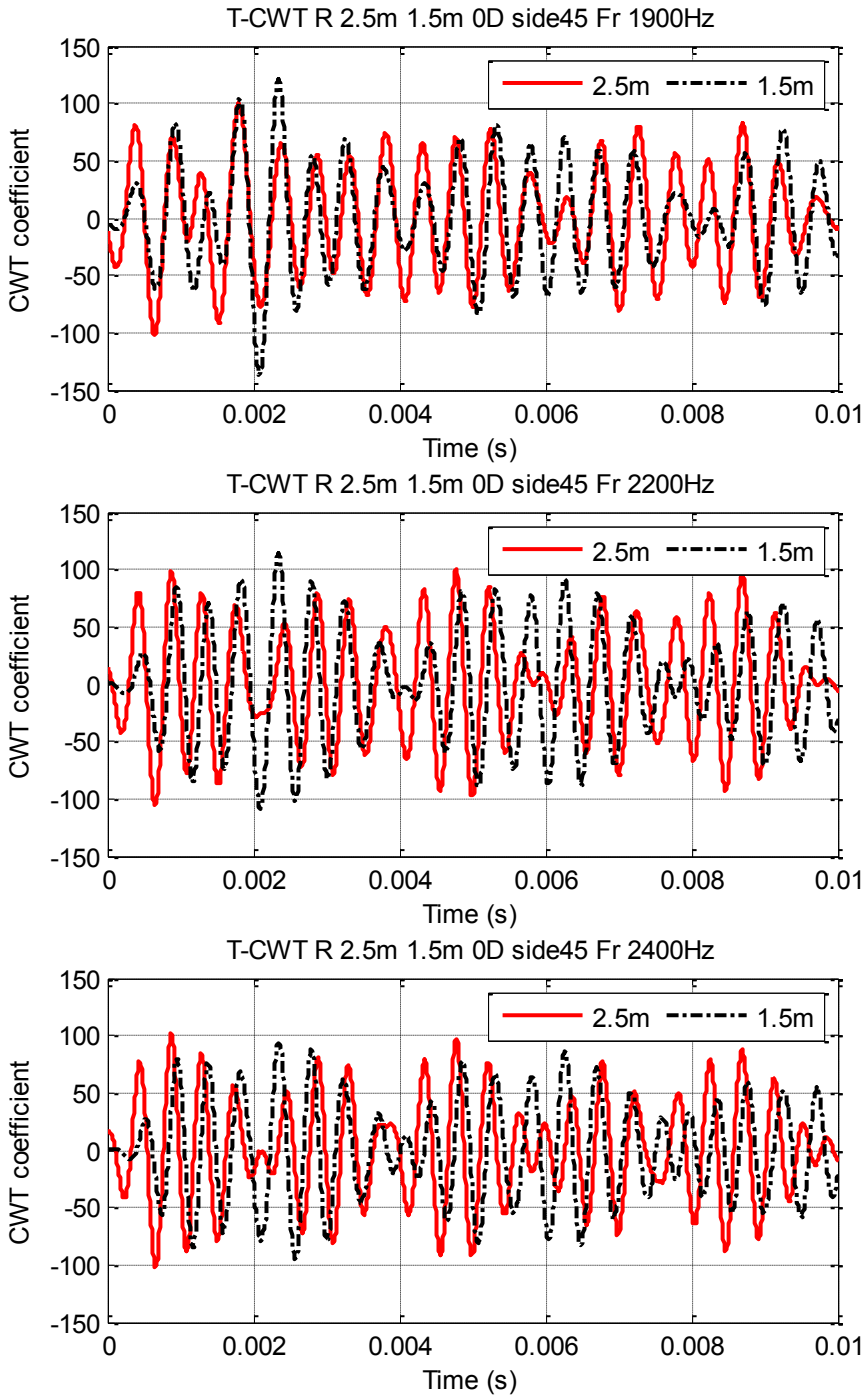

Figure E-2.2: CWT coefficient plots at the common frequencies between two sensors at the location of 0° orientated radially (case 3)

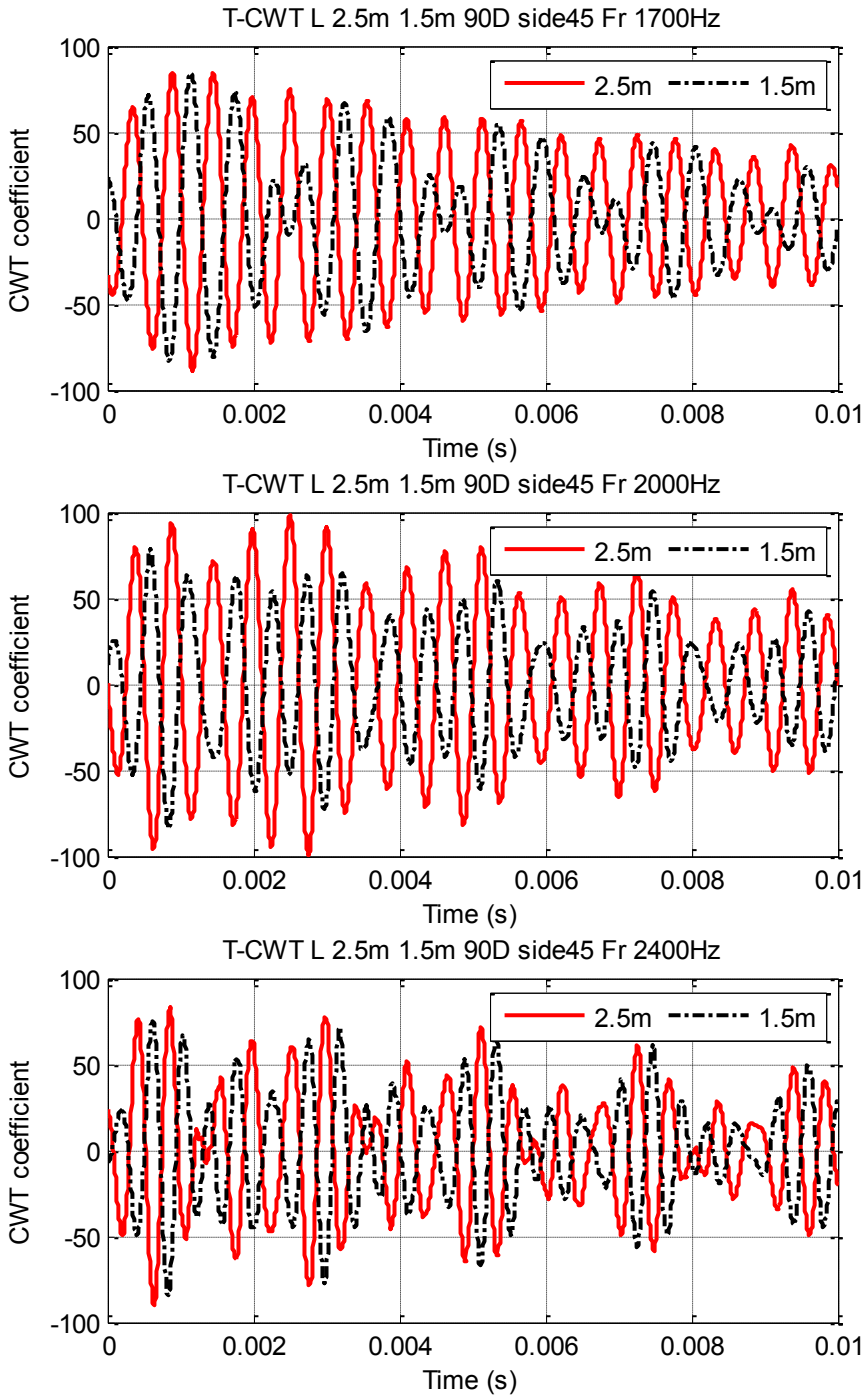

Figure E-2.3: CWT coefficient plots at the common frequencies between two sensors at the location of 90° orientated axially (case 3)

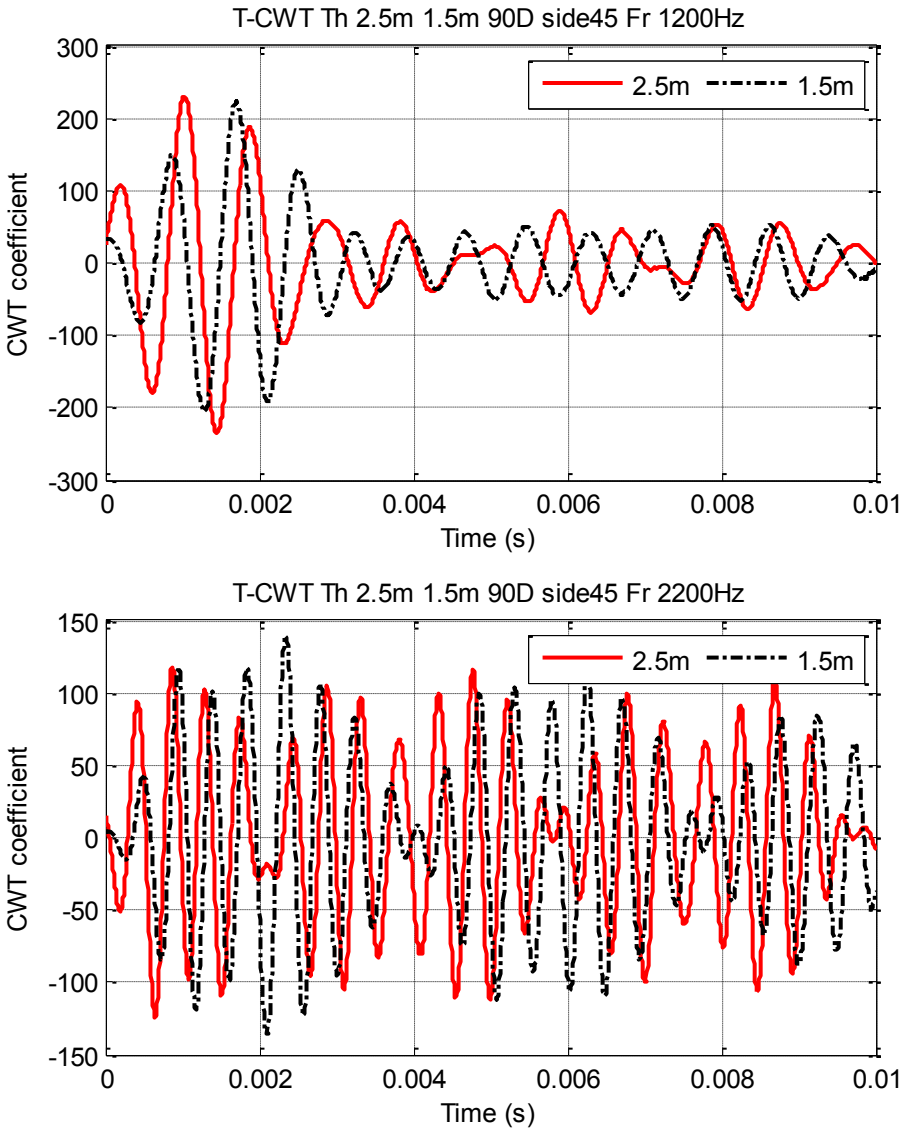

Figure E-2.4: CWT coefficient plots at the common frequencies between two sensors at the location of 90° orientated tangentially (case 1)

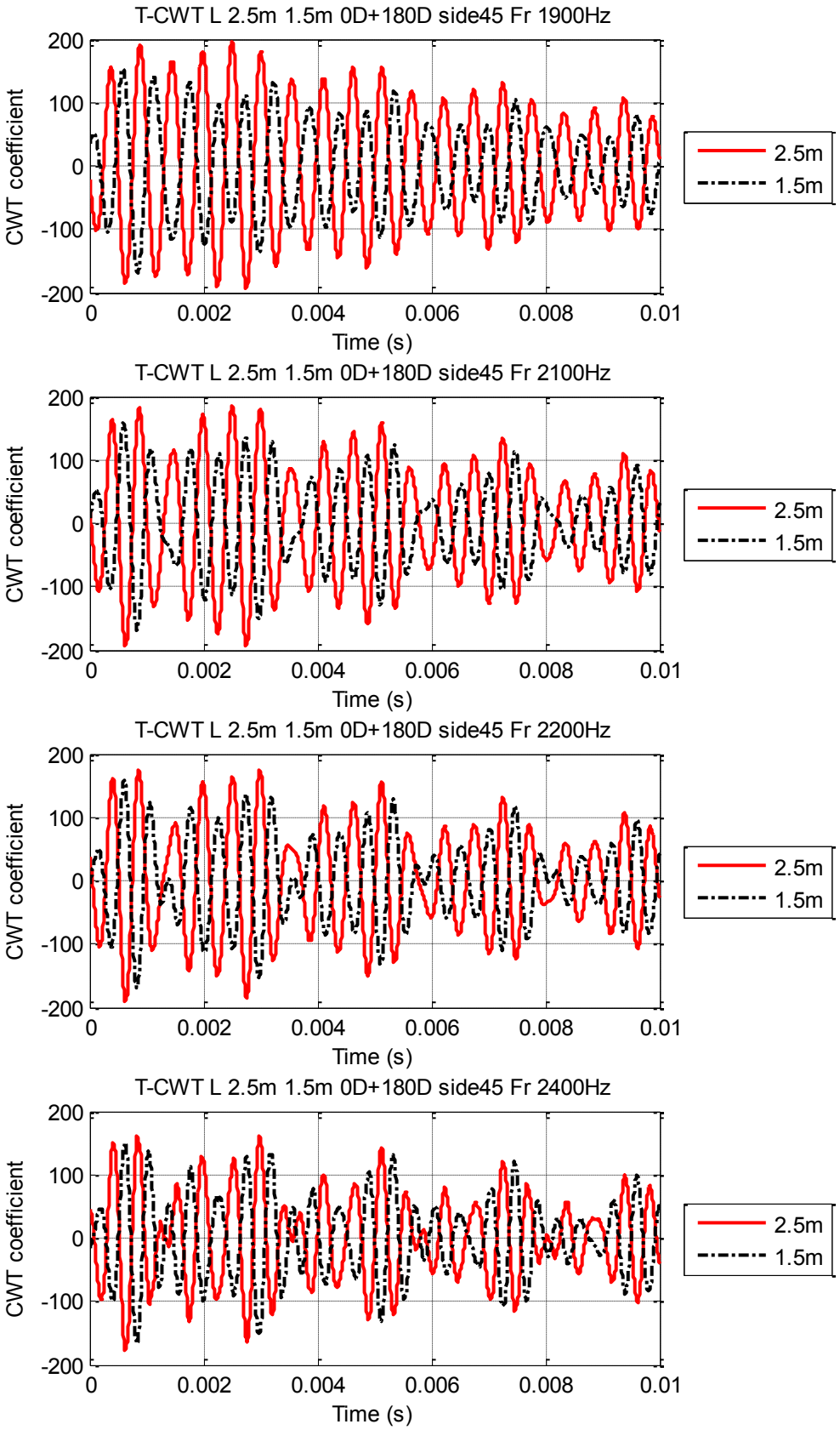

Figure E-2.5: Summation of CWT coefficient plots at the common frequencies of two sensors located at 0° and 180° which are orientated axially (case 3)

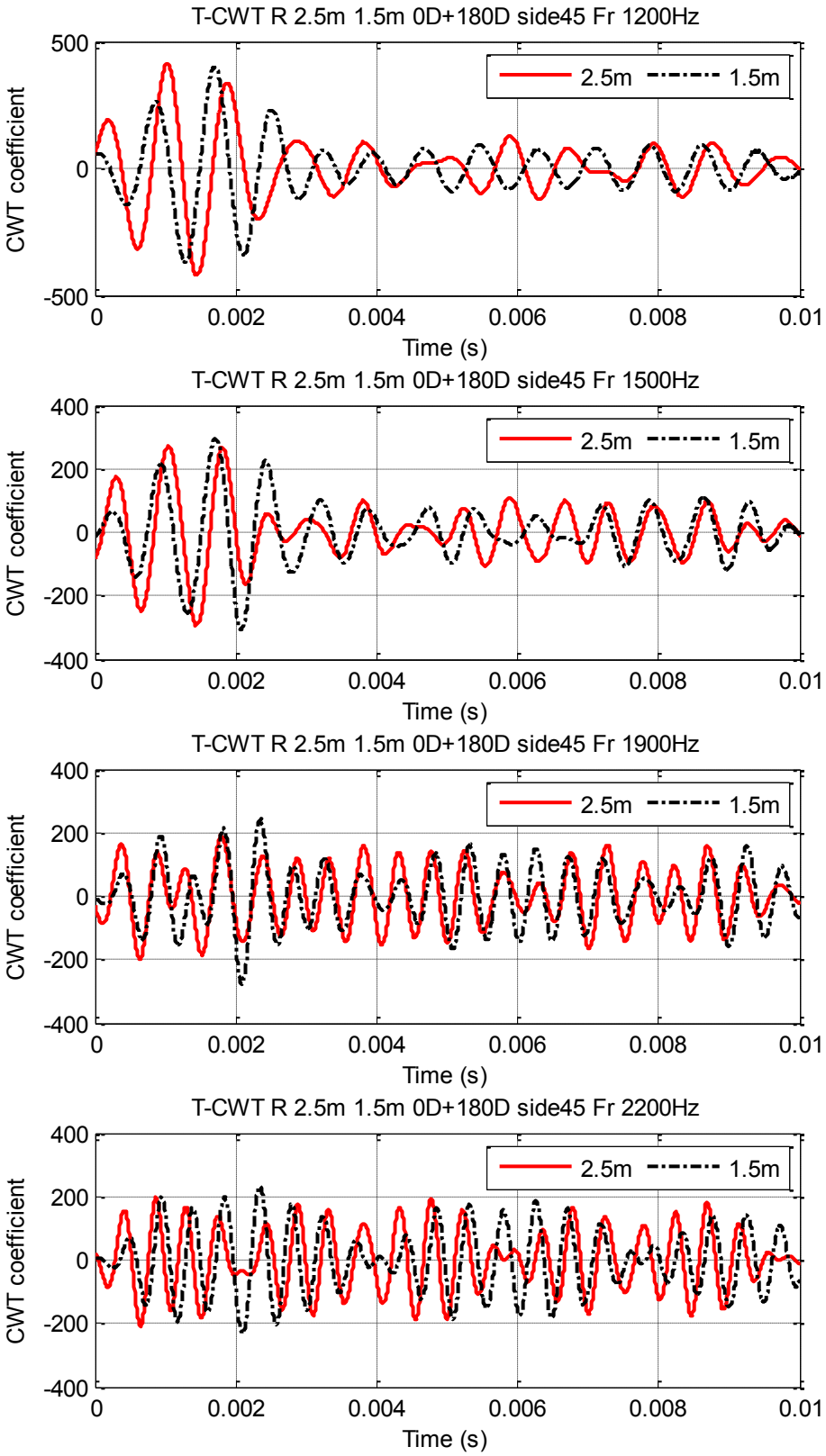

Figure E-2.6: Summation of CWT coefficient plots at the common frequencies of two sensors located at 0° and 180° which are orientated radially (case 3)

E – 3 CWT and SKM coefficient plot at the common frequencies to calculate phase velocity and embedment length

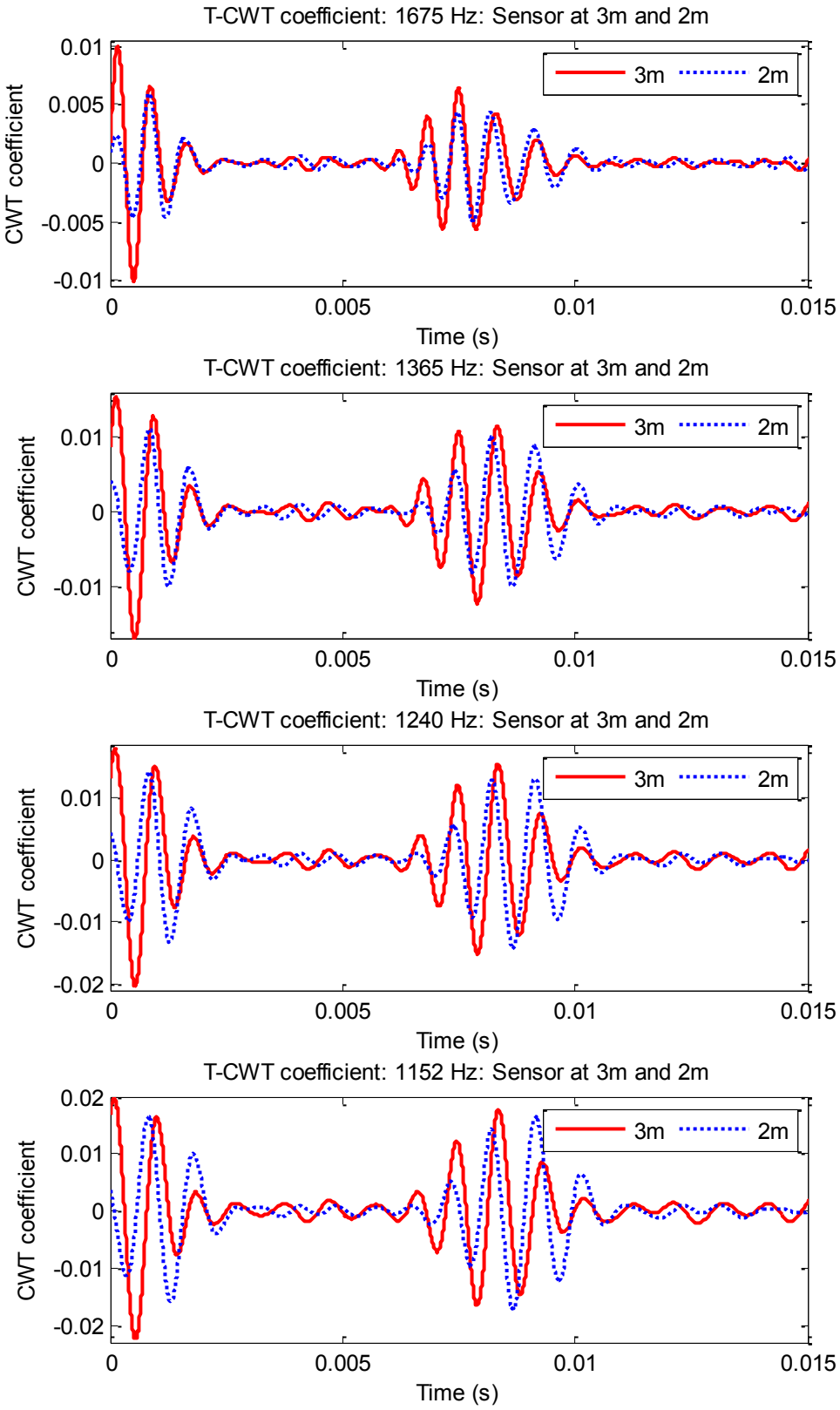

Figure E-3.1: CWT coefficient plots at the common frequencies of 1675, 1365, 1240 and 1152 Hz between two sensors

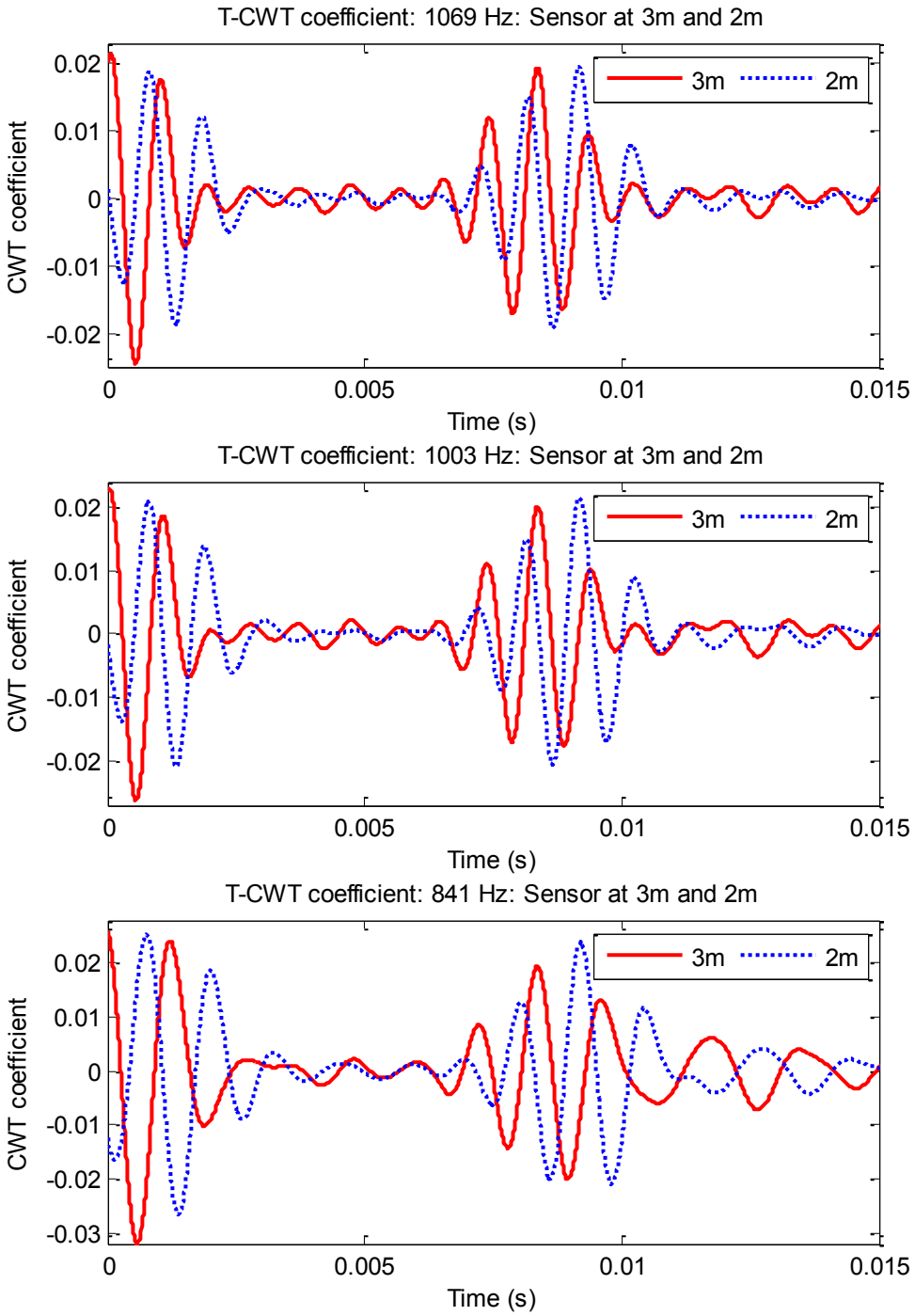

Figure E-3.2: CWT coefficient plots at the common frequencies of 1069, 1003 and 841 Hz between two sensors

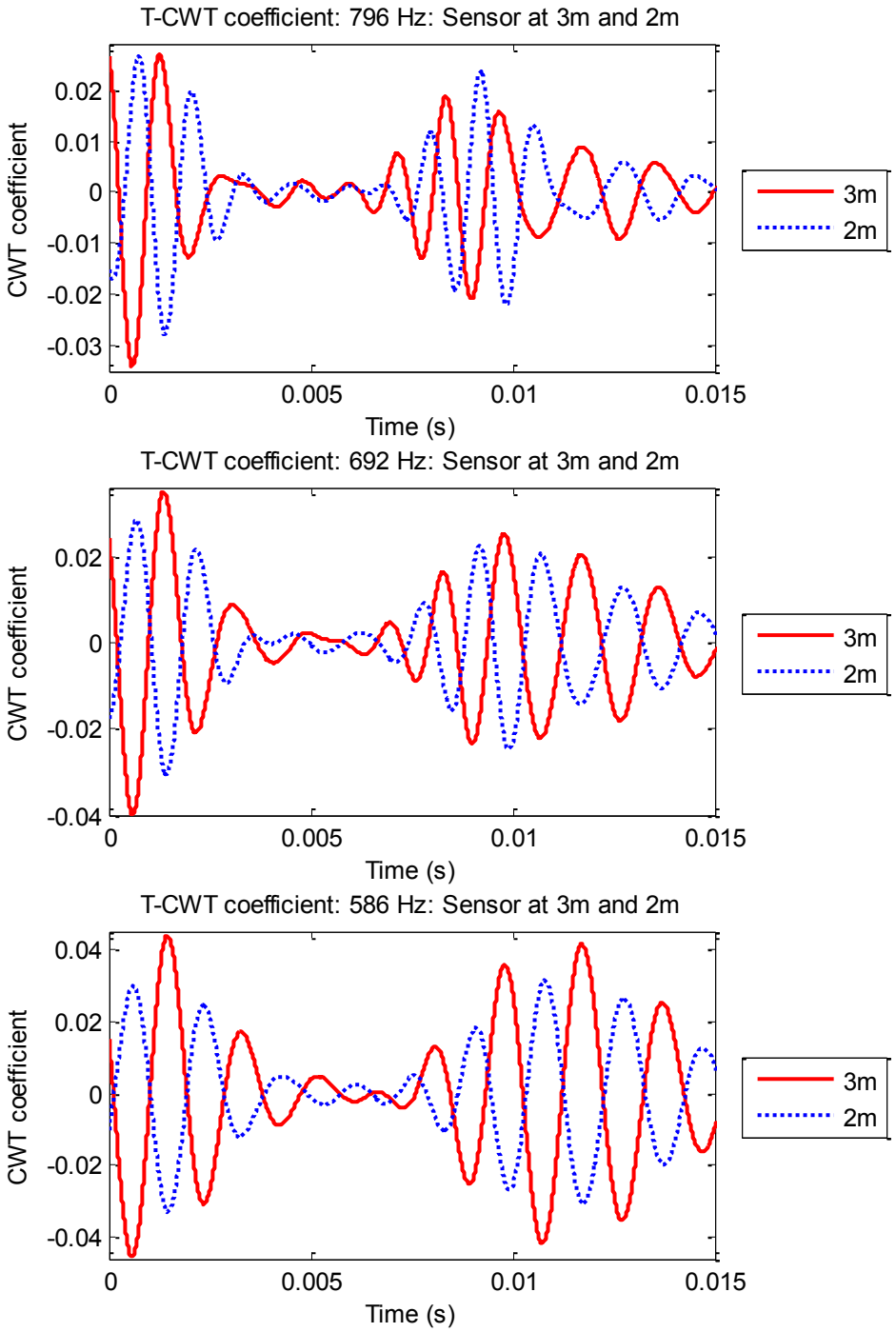

Figure E-3.3: CWT coefficient plots at the common frequencies of 796, 692 and 586 Hz between two sensors

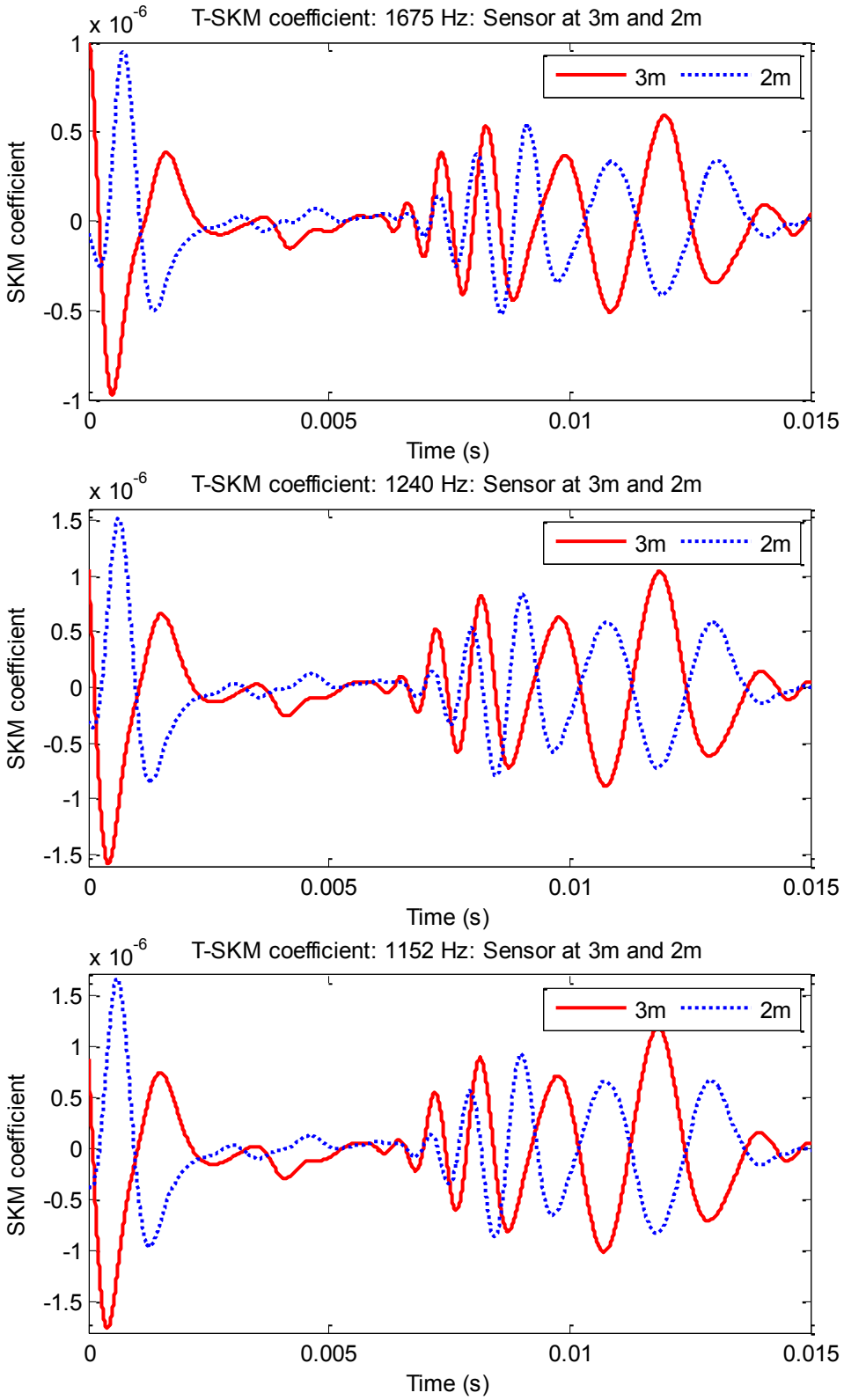

Figure E-3.4: SKM coefficient plots at the common frequencies of 1675, 1240 and 1152 Hz between two sensors

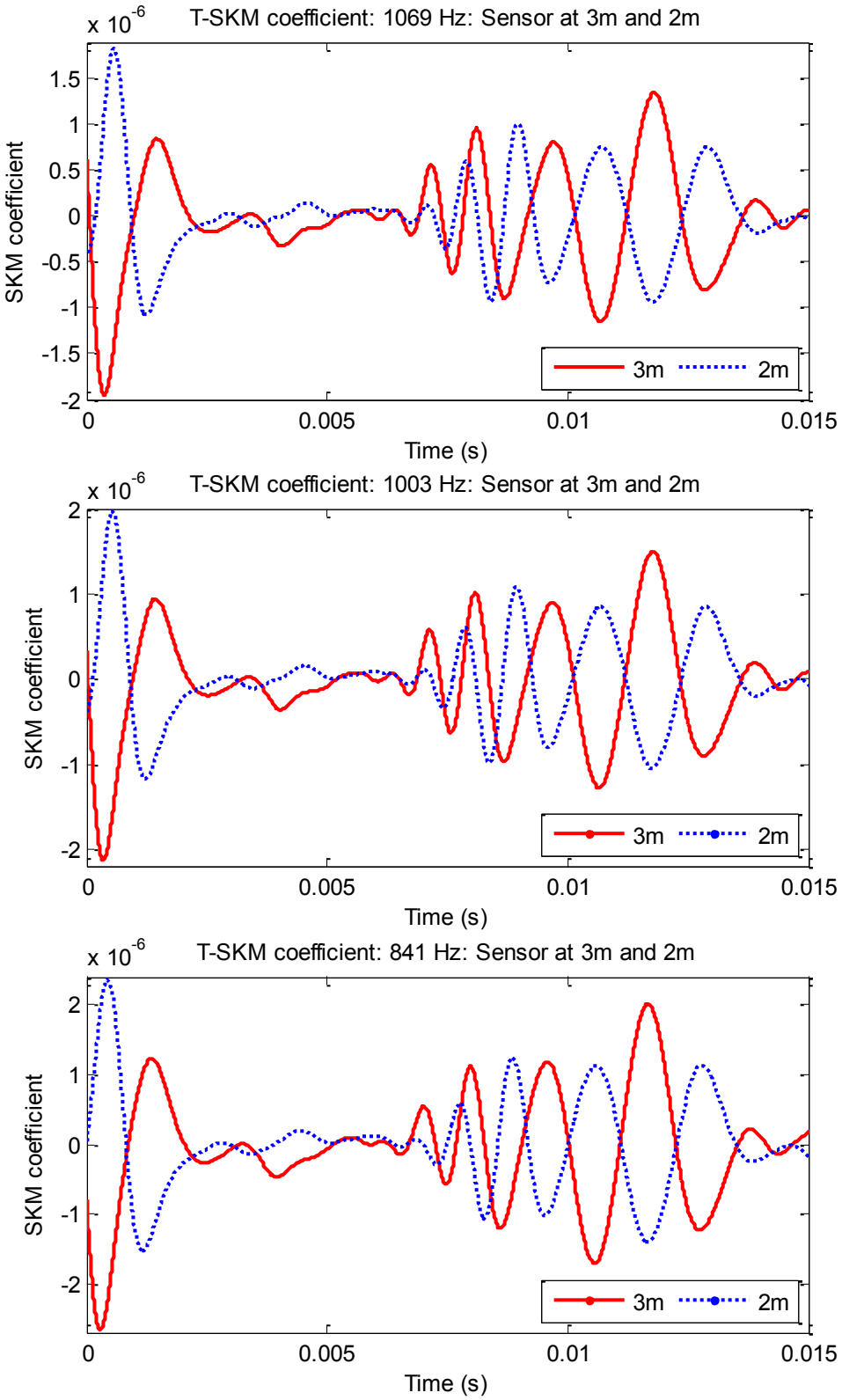

Figure E-3.5: SKM coefficient plots at the common frequencies of 1069, 1003 and 841 Hz between two sensors

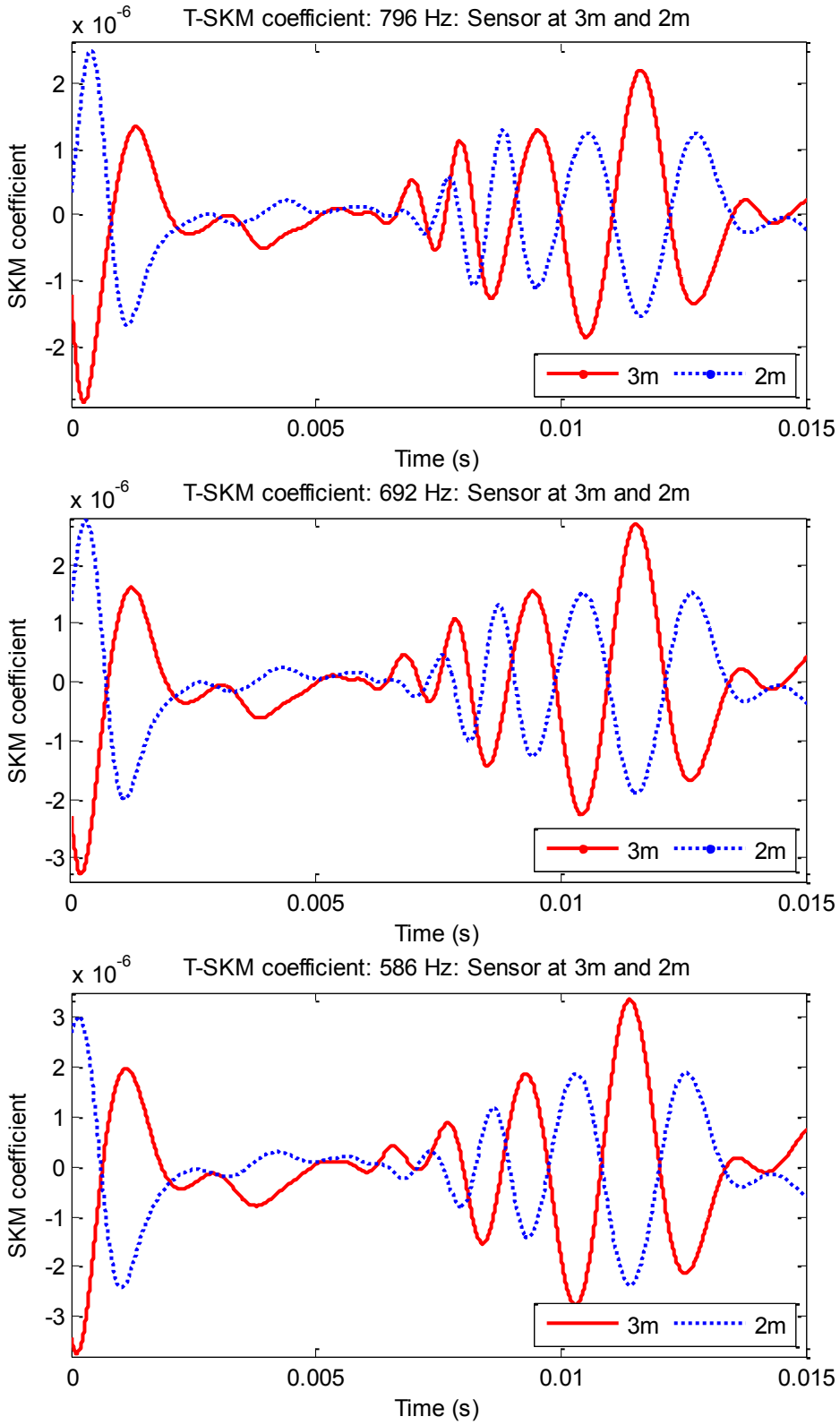

Figure E-3.6: SKM coefficient plots at the common frequencies of 796, 692 and 586 Hz between two sensors